



**HAL**  
open science

# Spin-crossover iron(II) scorpionates and luminescent lanthanide(III) bis-carbacylamidophosphates for thermometry applications

Oleksandr Horniichuk

► **To cite this version:**

Oleksandr Horniichuk. Spin-crossover iron(II) scorpionates and luminescent lanthanide(III) bis-carbacylamidophosphates for thermometry applications. Coordination chemistry. Université Paul Sabatier - Toulouse III; Kiïvs kij nacionalnij unïversitet imeni Tarasa Ševčenko (Kiïv), 2023. English. NNT : 2023TOU30233 . tel-04697625

**HAL Id: tel-04697625**

**<https://theses.hal.science/tel-04697625v1>**

Submitted on 14 Sep 2024

**HAL** is a multi-disciplinary open access archive for the deposit and dissemination of scientific research documents, whether they are published or not. The documents may come from teaching and research institutions in France or abroad, or from public or private research centers.

L'archive ouverte pluridisciplinaire **HAL**, est destinée au dépôt et à la diffusion de documents scientifiques de niveau recherche, publiés ou non, émanant des établissements d'enseignement et de recherche français ou étrangers, des laboratoires publics ou privés.



# THÈSE

En vue de l'obtention du

## DOCTORAT DE L'UNIVERSITÉ DE TOULOUSE

Délivré par :

Université Toulouse 3 Paul Sabatier (UT3 Paul Sabatier)

Cotutelle internationale avec l'Université nationale Taras-Chevtchenko de Kiev (Ukraine)

---

**Présentée et soutenue par :**

**Oleksandr HORNIICHUK**

le vendredi 27 octobre 2023

**Titre :**

Spin-crossover iron(II) scorpionates and luminescent lanthanide(III) bis-carbacylamidophosphates for thermometry applications

---

**École doctorale et discipline ou spécialité :**

ED SDM : Chimie organométallique de coordination - CO 043

**Unité de recherche :**

Laboratoire de chimie de coordination du CNRS

**Directeur/trice(s) de Thèse :**

Azzedine BOUSSEKSOU, Lionel SALMON, Volodymyr AMIRKHANOV

**Jury :**

Prof. Sergey KOLOTILOV (L. V. Pisarzhevsky Institute of physical chemistry of the National Academy of Sciences of Ukraine) - Rapporteur;

Dr. Svitlana ORYSYK (V. I. Vernadsky Institute of general and inorganic chemistry of the National Academy of Sciences of Ukraine) - Rapporteur;

Dr. Carlos BARTUAL MURGUI (Valence University, Spain) - Examineur;

Dr. Maksym SEREDYUK (Taras Shevchenko National University of Kyiv) - Examineur;

Prof. Gwénaél RAPENNE (Université Toulouse 3 Paul Sabatier) - Examineur.

# Acknowledgments

I would like to acknowledge every member of the jury: Dr. Azzedine Bousseksou, Dr. Lionel Salmon, Prof. Volodymyr Amirkhanov, Prof. Sergey Kolotilov, Dr. Carlos Bartual Murgui, Dr. Svitlana Orysyk, Dr. Maksym Seredyuk, Prof. Gwénaél Rapenne for dedicating their time and effort to thoroughly review the manuscript and contribute to the thesis defense process.

I would like to thank to my supervisors Azzedine Bousseksou, Lionel Salmon and Volodymyr Amirkhanov for their unwavering support, guidance and mentorship that have played a pivotal role in helping me to reach this final milestone in my PhD journey. I am truly grateful for all that you have done for me. Also, I would like to thank to Gábor Molnár whose kind advices and meticulous feedback played a substantial role in guiding my research towards the intended course.

I want to express my appreciation to the Switchable Molecular Materials Team (Team P) and the research group of Volodymyr Amirkhanov, to all members, current and former, who I met during the time of my PhD for being great colleagues and friends, and for creating a friendly, familial working environment within the teams. It was a pleasure to work with you, as well as to share good and bad moments.

My deepest thanks to Lijun Zhang and Yuteng Zhang for helping me with vacuum deposition of the SCO thin films, as well as to Karl Ridier for his kind help with the thermometry experiments. I express my sincerest thanks to Viktor Trush, owing to whose immense experience in organic synthesis and mentor skills I have mastered the synthesis of carbacylamidophosphate ligands, which was an integral part of this work. You taught me a lot of synthetic skills I am applying up till today. I sincerely appreciate it and will always remember it. I would like to convey my deepest gratitude to Natalia Kariaka for her thorough feedback and willingness to help. You shared your profound background in lanthanide carbacylamidophosphates' chemistry with me, which helped me to find the best way to design and synthesize the lanthanide complexes presented in this work. I admire your enthusiasm and your diligence. Thank you for all that you have done for me.

I would also like to express my gratitude to Laure Vendier, Sergiu Shova (“Petru Poni” Institute of Macromolecular Chemistry, Iasi), Il’ya Gural’skiy, Svitlana Shishkina (STC “Institute for Single Crystals”), Viktoriya Dyakonenko (STC “Institute for Single Crystals”) and Kostiantyn Domasevitch for their help with the X-ray diffraction experiments, as well as to Jean-Francois Meunier, Aurelian Rotaru (University Stefan cel Mare of Suceava) and Kane Jacob for magnetic measurements, acquisition of  $^{57}\text{Fe}$  Mössbauer spectra and thermal analyses. I extend my sincerest appreciation to Sergii Smola and Natalia Rusakova (A. V. Bogatsky Physico-chemical Institute of the National Academy of Sciences of

Ukraine), Paula Gawryszewska (University of Wroclaw) and Adam Watras (Włodzimierz Trzebiatowski Institute of Low Temperature and Structure Research) for their help with the luminescence measurements.

I thank to Jean-Baptiste Sortais and Anna Bonfiglio (Team A) for their kind help with the equipment for hydrogenation under pressure.

My thanks to trainee Anastasiia Nyrko, who worked with me, for her dedication and enthusiasm for the work.

I would like to acknowledge Zoia Voitenko for her kind support and guidance in the matters of the cotutelle program.

I want to acknowledge with utmost gratitude French Embassy in Ukraine and Campus France (Bourse du Gouvernement Français), as well as Erasmus+ and MSCA4Ukraine for their decision to support financially my thesis project on its different stages.

My deepest thanks to my friends who supported me throughout this time. I hardly imagine to get over this path without you. Special thanks to Ion, Christina, Yael, Vlad and Damian. Over the last year (even more), which was also the final year of PhD for many of you, we went through troubles together and we shared the greatest moments together. It means a lot for me. I am very happy and grateful that I have met you during this journey, and I hope we keep in contact in the future to come.

My warmest thanks to my family. Thank you for always being here for me and always supporting me.

As part of this work was carried out in Ukraine, I would like to acknowledge defenders of Ukraine who together with defending our country and its people are also defending the future of Ukrainian science.

# Table of contents

<b>List of abbreviations and acronyms</b> .....	4
<b>Résumé</b> .....	5
<b>Chapter 1. Introduction</b> .....	29
1.1 Spin-crossover phenomenon.....	29
1.2 Applications of the SCO materials .....	30
1.3 SCO thin films: fabrication and characterization .....	34
1.4 Sublimable SCO complexes .....	39
1.5 Lanthanide(III) complexes with bis-chelating ligands for highly-efficient luminescence.....	45
1.6 Hybrid SCO/luminescent materials .....	55
1.7 Application of SCO and luminescence in micro- and nanothermometry.....	75
1.8 Objectives of this work.....	82
<b>Chapter 2. Iron(II) scorpionates: synthesis, properties and SCO in the bulk complexes</b> .....	85
2.1 Bis[hydrotris(1,2,3-triazol-1-yl)borate]iron(II): spin crossover, solvato- and polymorphism.....	85
2.1.1 <i>Synthesis of hydrotris(1,2,3-triazol-1-yl)borate ligand and the corresponding iron(II) complex</i> .....	85
2.1.2 <i>X-ray crystallography</i> .....	86
2.1.3 <i>Spin crossover properties of [Fe(HB(1,2,3-tz)<sub>3</sub>)<sub>2</sub>]</i> .....	93
2.2 Synthesis of new heteroscorpionate ligands and their iron(II) complexes. Characterization and spin-crossover properties of the coordination compounds. ....	96
2.2.1 <i>Synthesis of the heteroscorpionate ligands and their complexes with Fe<sup>II</sup></i> .....	96
2.2.2 <i>NMR spectroscopy</i> .....	101
2.2.3 <i>IR spectroscopy</i> .....	102
2.2.4 <i>Single crystal and powder X-ray diffraction studies</i> .....	102
2.2.5 <i>Spin crossover in the iron(II) complexes with the heteroscorpionate ligands</i> .....	108
2.3 Partial conclusions .....	111
2.4 Partial perspectives .....	112
2.5 Notes.....	112
<b>Chapter 3. Lanthanide(III) bis-carbacylamidophosphates. Synthesis, characterization and luminescence studies</b> .....	113
3.1 Synthesis of bis-chelating carbacylamidophosphate ligand (H <sub>2</sub> L <sup>8</sup> ) and its binuclear lanthanide(III) complexes [Ln <sub>2</sub> (L <sup>8</sup> ) <sub>3</sub> (phen) <sub>2</sub> ]. Characterization of the compounds. Luminescence in the obtained complexes. ....	114
3.1.1 <i>Synthesis of the ligand and the complexes</i> .....	114
3.1.2 <i>NMR spectroscopy</i> .....	115
3.1.3 <i>IR spectroscopy</i> .....	115

3.1.4 Absorption spectra of the $Nd^{III}$ complex .....	116
3.1.5 The $Y^{III}$ complex phosphorescence spectra .....	117
3.1.6 Luminescence properties of the $Nd^{III}$ , $Sm^{III}$ , $Eu^{III}$ , $Tb^{III}$ , $Dy^{III}$ and $Yb^{III}$ complexes.....	118
3.2 Synthesis and characterization of quadruple-stranded $NEt_4[NaLn_2(L^8)_4(H_2O)]$ and $Na[NaLn_2(L^8)_4(H_2O)] \cdot 2H_2O$ . Structure and luminescence properties.....	123
3.2.1 Synthesis.....	123
3.2.2 X-ray crystallography .....	124
3.2.3 $^1H$ NMR spectroscopy.....	127
3.2.4 IR spectroscopy.....	127
3.2.5 Photoluminescent properties of $NEt_4[NaNd_2(L^8)_4(H_2O)]$ .....	128
3.2.6 Mass spectrometry .....	131
3.3 Partial conclusions .....	131
3.4 Partial perspectives .....	131
3.5 Notes.....	132
<b>Chapter 4. Thin films of bis[hydrotris(1,2,3-triazol-1-yl)borate]iron(II). Application in thermometry.</b> .....	133
4.1 Fabrication and characterization of $[Fe(HB(1,2,3-tz)_3)_2]$ films.....	133
4.2 Microthermometry application of $[Fe(HB(1,2,3-tz)_3)_2]$ films .....	140
4.3 Partial conclusions .....	148
4.4 Partial perspectives .....	148
4.5 Notes.....	148
<b>Conclusions and perspectives</b> .....	150
<b>Experimental part</b> .....	153
1. Experimental techniques and methods .....	153
2. Syntheses of ligands and complexes .....	156
<b>Bibliographic References</b> .....	165
<b>Annexes</b> .....	193
Annex A. X-ray crystallography data.....	193
Annex B. NMR spectra .....	198
Annex C. IR spectra.....	219
Annex D. Variable-temperature SQUID magnetometry data for complex <b>6</b> .....	227
Annex E. Energy diagram of lowest $Ln^{III}$ excited states and the estimated LLTS in <b>8–13</b> .....	228
Annex F. $^5D_0$ luminescence complex <b>10</b> .....	229
Annex G. Luminescence decay curves for complexes <b>10</b> and <b>11</b> .....	230
Annex H. LDI mass spectrum of <b>16</b> .....	231
Annex I. Articles.....	231

## List of abbreviations and acronyms

AFM	Atomic Force Microscopy
CAPh	Carbacylamidophosphate
DCM	Dichloromethane
DMF	<i>N,N</i> -Dimethylformamide
DMSO	Dimethyl sulfoxide
DTA	Differential Thermal Analysis
EWG	Electron-Withdrawing Group
GIXRD	Grazing Incidence X-ray Diffraction
HS	High Spin
HSAB	Hard and Soft Lewis Acid and Base theory
IR	Infrared
LLTS	Lowest Ligands' Triplet State
LS	Low Spin
NIR	Near-infrared
NMR	Nuclear Magnetic Resonance
OLED	Organic Light Emitting Diode
PXRD	Powder X-ray Diffraction
SAPh	Sulfonylamidophosphate
SCO	Spin crossover
SEM	Scanning Electron Microscopy
SQUID	Superconducting Quantum Interference Device
TBA	<i>n</i> -Tetrabutylammonium
TGA	Thermogravimetric Analysis
UV	Ultraviolet
XPS	X-ray Photoelectron Spectroscopy

## Résumé

### Chapitre 1. Introduction

#### 1.1 le phénomène de transition de spin

Le phénomène de transition de spin (TS) désigne un changement d'état de spin des complexes de la première rangée des métaux de transition dont les configurations électroniques de l'ion central sont  $d^4$ - $d^7$ , induit par des stimuli externes tels que la température, la pression, la lumière ou le champ magnétique.<sup>1,2</sup> Le phénomène se produit généralement dans les complexes avec un champ de ligand octaédrique et est le plus abondant pour la configuration électronique  $d^6$ , dont les complexes de fer(II) sont des exemples prédominants. Les complexes métalliques ne peuvent subir une TS que lorsque l'énergie du champ du ligand et l'énergie d'appariement des électrons dans les orbitales d sont comparables. Dans le cas du fer(II), la TS est généralement observée dans les complexes avec des ligands donneurs d'azote où l'environnement de l'ion métallique est généralement  $FeN_6$  ou  $FeN_4O_2$ .<sup>2</sup> Le changement d'état de spin dans les complexes Fe(II) est réalisé via une commutation réversible entre les configurations électroniques diamagnétiques ( $S = 0$ ) bas spin (BS) et paramagnétiques ( $S = 2$ ) haut spin (HS).

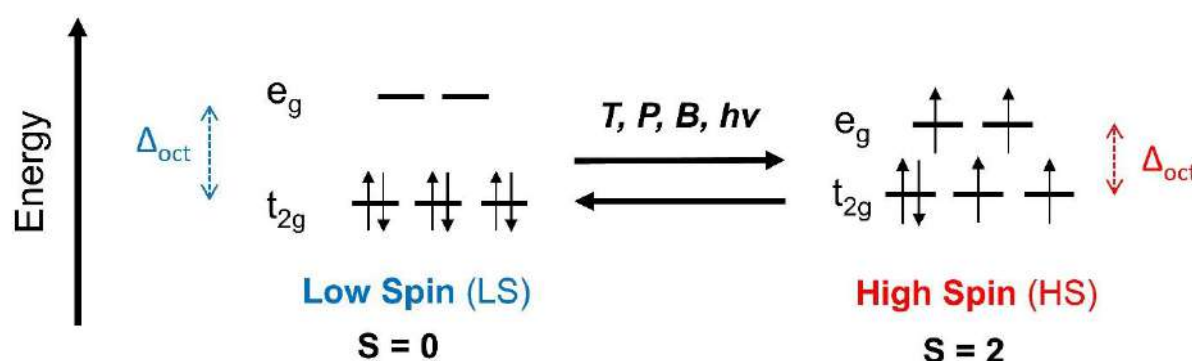


Figure 1.1. Diagramme énergétique des états bas spin et haut spin pour la configuration  $d^6$ .

Ainsi, le changement d'état de spin implique des modifications des propriétés physiques des complexes, à savoir les propriétés magnétiques, les propriétés optiques (par exemple, le thermochromisme),<sup>6,8,9</sup> les changements de distance entre les centres Fe(II) et les atomes donneurs de ligand et, par conséquent, le changement de volume moléculaire.<sup>10</sup>

#### 1.2 Applications des matériaux à transition de spin

Compte tenu de la commutation des propriétés que le phénomène de TS implique sous l'effet d'une perturbation externe et compte tenu du caractère de ce changement, le phénomène présente un intérêt pour diverses applications.<sup>11</sup>

Ainsi, le changement de champ du ligand induit par la transition de spin modifie l'absorption optique du complexe, c'est-à-dire qu'il entraîne un changement de couleur. Si la transition est induite thermiquement, ce changement de couleur est appelé thermochromisme. Les matériaux peuvent être utilisés comme peintures thermochromes, capteurs optiques de température de surface ou pour l'affichage.<sup>8,12</sup>

La transition de l'état bas spin à l'état haut spin implique la population d'orbitales e.g. anti-liantes conduisant à l'allongement des distances entre le Fe(II) et les atomes donneurs des ligands, ce qui implique une expansion du volume moléculaire et de la cellule unitaire. Dans certains complexes, par exemple  $[\text{Fe}(\text{Htrz})_2(\text{trz})]\text{BF}_4$ , l'expansion du volume peut atteindre 10 %.<sup>13</sup> Ces changements radicaux dans la masse de la substance affectent ses propriétés mécaniques et permettent de l'utiliser comme élément actif d'actionneurs mécaniques.<sup>14-16</sup>

Pour être mis en œuvre dans des applications, les complexes sont principalement utilisés sous forme de matériaux, qui peuvent être : des cristaux liquides,<sup>8</sup> des nanoparticules (NPs),<sup>31</sup> des films minces<sup>32-35</sup> et des (nano)composites.<sup>36</sup> Dans le cadre de cette thèse, une attention particulière sera portée à la fabrication et à la caractérisation de films minces à TS.



Figure 1.2. Schéma regroupant les matériaux à transition de spin et leurs applications.

### 1.3 Objectifs de la thèse

Les films minces constituent l'une des formes de matériaux à TS qui se prêtent aux applications. Pour garantir la reproductibilité des propriétés, les films doivent répondre à des critères de qualité, de pureté

et d'homogénéité élevés. Le dépôt thermique sous vide est une technique appropriée qui permet de répondre à ces exigences. Cependant, le nombre de composés à transition de spin qui peuvent être déposés en couches minces par cette technique est relativement limité. Par conséquent, ce domaine de recherche doit être complété par la synthèse de nouveaux composés de coordination à TS susceptibles d'être organisés en couches minces.

La luminescence des ions lanthanides trivalents a attiré l'attention des scientifiques depuis sa découverte, en raison de sa distinction marquée par rapport aux autres luminophores et des avantages qu'elle offre. Les complexes de lanthanide avec des ligands organiques présentent une émission plus brillante que les composés purement inorganiques à base de Ln(III). Une grande pureté de couleur, un fort décalage Stokes et une longue durée de vie de l'émission centrée sur le lanthanide sont des paramètres importants pour la conception de dispositifs électroluminescents et pour les applications biomédicales. Le choix du (des) ligand(s) est important dans la conception de complexes de lanthanides hautement luminescents. Les  $\beta$ -dicétones sont des ligands polyvalents à cette fin. Les analogues structurels des 1,3-dicétones - les carbacylamidophosphates (CAPH) offrent des avantages pour la fixation d'ions métalliques et sont sensibles à la luminescence des lanthanides. Une autre stratégie pour obtenir une émission hautement efficace consiste à augmenter le nombre de centres optiques, ce qui a été clairement démontré dans une série d'hélicates de lanthanides binucléaires avec des ligands bis- $\beta$ -dicétonates. Compte tenu des avantages des ligands CAPH par rapport aux  $\beta$ -dicétones, le développement de ligands CAPH bis-chélateurs et de leurs complexes lanthanides pourrait permettre d'améliorer encore l'émission centrée sur le Ln(III).

La synergie de la transition de spin et de la luminescence est un nouvel horizon dans le domaine des matériaux multifonctionnels. La combinaison des deux dans un même système peut entraîner une interaction entre les deux phénomènes. La commutation de l'état de spin peut induire la commutation de la luminescence, tandis que cette dernière peut être utilisée pour rendre compte de l'état de spin de la partie active du complexe. Divers systèmes hybrides TS-luminescence sont connus à ce jour, depuis les complexes luminescents à TS jusqu'aux matériaux hybrides où les entités luminescentes et à TS sont séparées. Il s'avère difficile d'obtenir de tels composés synergiques, car le fait de combiner les espèces luminescentes et à TS dans une substance peut souvent entraîner l'annulation de l'un des phénomènes. Par ailleurs, les deux phénomènes peuvent être préservés sans qu'il y ait de couplage entre eux. Par conséquent, le développement des systèmes bifonctionnels nécessite une conception moléculaire et cristallographique minutieuse.

Les phénomènes de TS et de luminescence dépendent de la température et fournissent une réponse optique détectable au changement de température, qui peut être utilisée comme outil non invasif pour la thermométrie à l'échelle micro et nanométrique. Le film mince à TS  $[\text{Fe}(\text{HB}(1,2,4\text{-tz})_3)_2]$  déposé

à la surface d'un nanofil chauffé par effet Joule s'est comporté comme un thermomètre de surface binaire en raison du caractère abrupt de la TS. Cela peut trouver une application dans la surveillance de la chaleur locale dans les circuits intégrés. Une surveillance continue de la température en temps réel peut être réalisée dans les matériaux à TS graduelle. Comme il n'existe pas de films minces présentant de telles propriétés, un nouveau complexe de transition de spin évaporable et ses films minces subissant une transition de spin graduelle devraient être préparés pour combler cette lacune.

Les thermomètres moléculaires luminescents basés sur l'émission de lanthanides présentent une grande sensibilité au changement de température dans un large intervalle. Cependant, ces systèmes ne sont pas nombreux. Le développement de nouveaux complexes Ln bimétalliques pourrait augmenter le nombre de ces thermomètres optiques. Grâce à une conception moléculaire ajustable et à la possibilité de contrôler la distance intermétallique, les hélicates binucléaires de lanthanide peuvent être des candidats polyvalents pour assembler les thermomètres moléculaires exploitant le transfert d'énergie inter-ionique.

Ainsi, le chapitre 2 concerne la synthèse de nouveaux ligands scorpionates à base de triazole et leurs complexes de fer(II), des études sur la structure moléculaire, les propriétés physico-chimiques et le comportement magnétique des composés de coordination, en particulier des études du phénomène de TS. Le chapitre 3 est consacré à la synthèse et à la caractérisation de complexes binucléaires de lanthanide(III) à triple et quadruple brins avec un ligand carbacylamidophosphate bis-chélateur. Une attention particulière est accordée à l'étude de la luminescence dans les composés à la fois à l'état solide et en solution. Le chapitre 4 est consacré à l'élaboration de films minces de complexes fer(II)-scorpionate, à la caractérisation des films et à l'essai de ces derniers pour la microthermométrie de surface et l'imagerie thermique.

## **Chapitre 2. Les scorpionates de fer(II) : synthèse et propriétés de transition de spin**

### **2.1 Bis[hydrotris(1,2,3-triazol-1-yl)borate]fer(II) : transition de spin, solvatation et polymorphisme.**

#### ***2.1.1 Synthèse du ligand hydrotris(1,2,3-triazol-1-yl)borate et du complexe de fer(II) correspondant***

Le ligand tris(1,2,3-triazolyl)borate ( $\text{NaL}^1$ ) et son complexe neutre de fer(II)  $[\text{Fe}(\text{HB}(1,2,3\text{-tz})_3)_2]$  (ci-après  $[\text{Fe}(\text{L}^1)_2]$  ou **1**) ont été synthétisés comme indiqué sur le schéma de la Figure 2.1. Le composé de coordination cristallin isolé de la solution aqueuse mère se présente sous forme de dodécahydrate. La forme de poudre anhydre peut être obtenue en chauffant l'hydrate au-dessus de 90 °C.

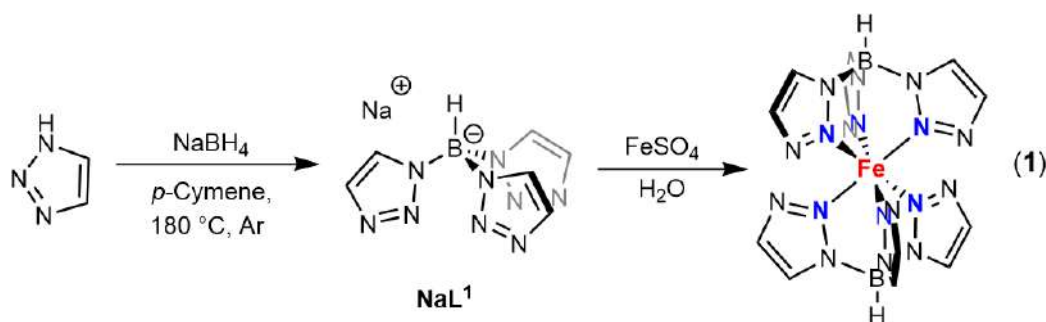


Figure 2.1. Voie synthétique pour obtenir **1**.<sup>205</sup>

### 2.1.2 Cristallographie aux rayons X

Le composé désolvaté **1** cristallise dans le groupe spatial monoclinique  $P2_1/c$  avec 2 molécules  $[\text{Fe}(\text{L}^1)_2]$  par cellule unitaire (figure 2.2).

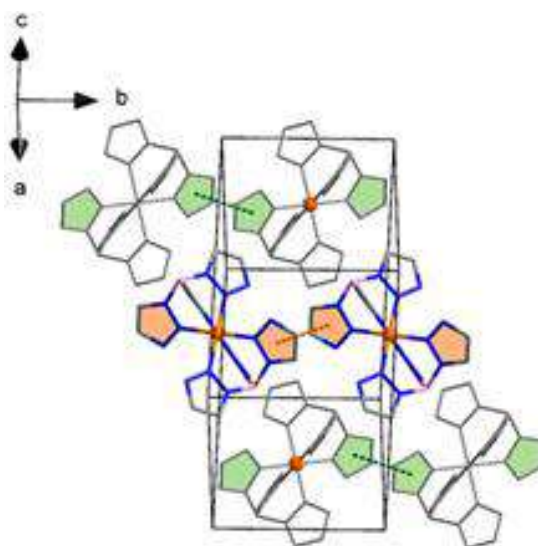


Figure 2.2. Cellule unitaire de **1** avec des interactions d'empilement  $\pi$ - $\pi$  se propageant le long de deux directions opposées dans le plan  $ab$ .

Les sphères de coordination des ions fer(II) dans **1** et les solvatomorphes ont des géométries octaédriques  $[\text{FeN}_6]$  légèrement déformées. Les distances Fe–N sont comprises entre 1,952(3) et 1,972(2) Å, tandis que la valeur moyenne du volume des octaèdres de coordination ( $V_p$ ) est de 10,05 Å<sup>3</sup>, comme attendu pour le fer(II) bas spin.<sup>10</sup> Dans les cristaux de la plupart des solvatomorphes, ainsi que dans **1**, les interactions d'empilement  $\pi$ - $\pi$  jouent un rôle clé dans l'empilement des molécules  $[\text{Fe}(\text{L}^1)_2]$ . Les interactions se produisent entre les cycles aromatiques 1,2,3-triazolyl des molécules adjacentes du complexe (Figure 2.3). Un autre type d'interaction assez faible qui lie les molécules du complexe dans le réseau cristallin est représenté par des interactions C–H $\cdots$ N. Les atomes d'azote exodentés et les

groupements C–H des cycles 1,2,3-triazolyl des molécules voisines  $[\text{Fe}(\text{L}^1)_2]$  sont impliqués dans ces interactions intermoléculaires.

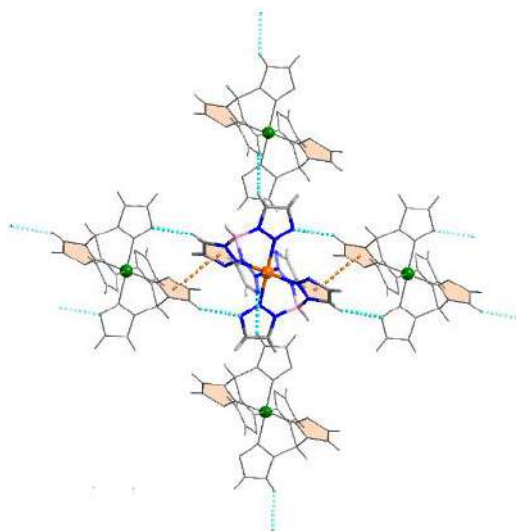


Figure 2.3. Structure cristalline de **1** montrant les interactions intermoléculaires (les interactions d'empilement  $\pi$ - $\pi$  sont représentées dans une seule direction).

### 2.1.3 Propriétés de transition de spin du complexe $[\text{Fe}(\text{HB}(1,2,3\text{-tz})_3)_2]$

La figure 2.4 présente un graphique de la susceptibilité magnétique molaire en fonction de la température.

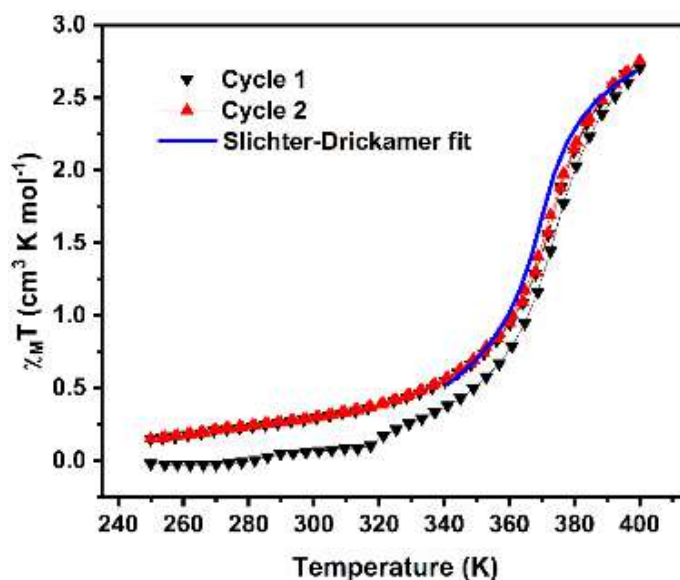


Figure 2.4.  $\chi_M T$  vs  $T$ , enregistrées sur deux cycles thermiques à partir de l'échantillon poudre **1**·**12H<sub>2</sub>O**. Un ajustement Slichter-Drickamer a été réalisé pour la deuxième courbe de chauffage.

Des mesures magnétiques dépendantes de la température ont été effectuées en chauffant d'abord la poudre de **1**·**12H<sub>2</sub>O** de 250 K à 400 K, puis en cyclant l'échantillon déshydraté **1** ainsi obtenu dans la

même plage de température à une vitesse de  $2 \text{ K min}^{-1}$ . Le composé **1** subit un changement d'état de spin progressif entre l'état de bas spin ( $S = 0$ ) et l'état de haut spin ( $S = 2$ ), avec une température de transition  $T_{1/2} = 373 \text{ K}$ .

## 2.2 Synthèse de nouveaux ligands hétéroscorpionates et de leurs complexes de fer(II). Caractérisation et propriétés de TS des composés de coordination.

### 2.2.1 Synthèse des ligands hétéroscorpionates et de leurs complexes de Fe(II)

Tout d'abord, l'hydrotris(pyrazol-1-yl)borate de potassium (ci-après KTp) a été synthétisé selon le protocole développé par Trofimenko,<sup>208</sup> avec une procédure d'élaboration légèrement modifiée. Ensuite, le cation potassium du produit a été échangé contre du tétrabutylammonium ( ${}^n\text{Bu}_4\text{N}^+$  ou TBA) selon la procédure décrite dans la référence 209. Ensuite, le dérivé TBA résultant  ${}^n\text{Bu}_4\text{NTp}$  a été chauffé avec 1 (2) équivalent(s) d'un 1,2,4-triazole monosubstitués contenant un groupe électro-attracteur en position 3 comme illustré à la Figure 2.5.

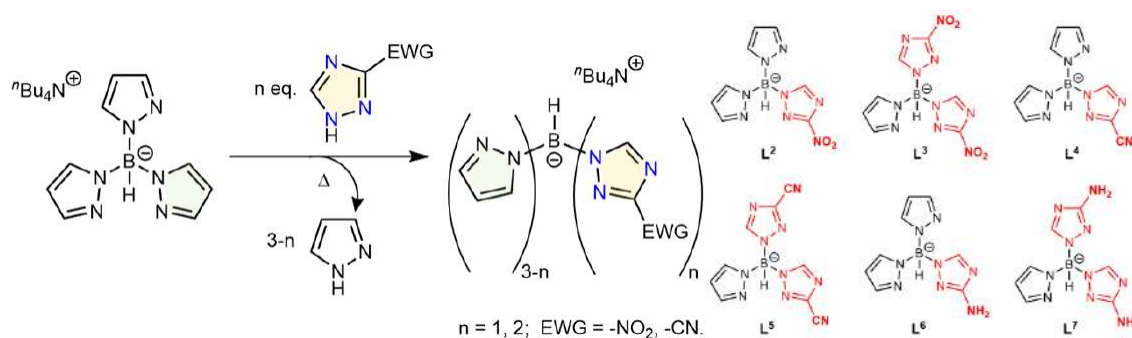


Figure 2.5. Voie synthétique pour obtenir de nouveaux ligands hétéroscorpionates à base de triazole.

Les synthèses des complexes de fer(II) avec les ligands  $L^2$ – $L^5$  ont été réalisées sous atmosphère d'argon dans une solution dégazée de dichlorométhane (DCM) à partir de 2 équivalents du ligand respectif et d'un équivalent de  $\text{FeCl}_2 \cdot 4\text{H}_2\text{O}$ .

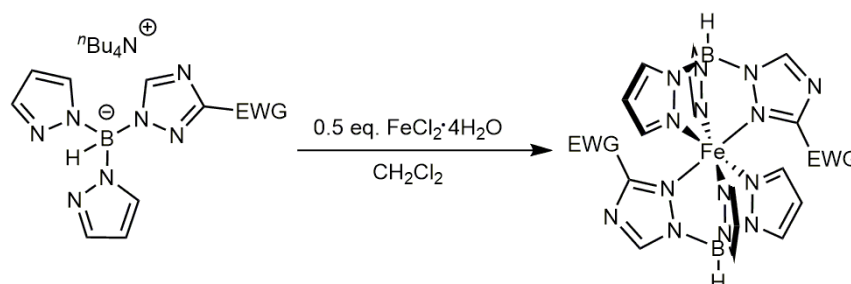


Figure 2.6. Schéma de synthèse pour accéder aux complexes de fer(II) avec les ligands  $L^2$ – $L^5$ . Un ligand monosubstitué a été choisi comme exemple.

La technique classique de réduction catalytique du groupe nitro sous pression d'hydrogène dans un autoclave a servi d'outil fiable pour convertir les substrats substitués en  $\text{NO}_2$  [ $\text{Fe}(L^2)_2$ ] et [ $\text{Fe}(L^3)_2$ ] en di- et tétraamines [ $\text{Fe}(L^6)_2$ ] et [ $\text{Fe}(L^7)_2$ ], respectivement (figure 2.7).

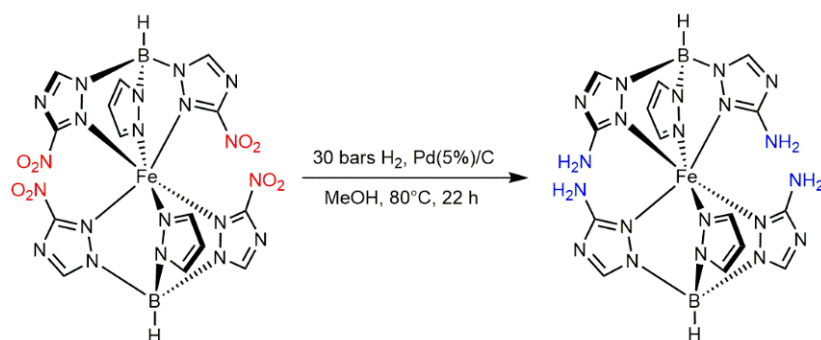


Figure 2.7. Réduction du groupe nitro pour  $[\text{Fe}(\text{L}^3)_2]$ .

### 2.2.2 Études de diffraction des rayons X sur cristal unique et sur poudre

Des cristaux du composé bis[hydrobis(pyrazol-1-yl)(3-amino-1,2,4-triazol-1-yl)]fer(II) (**6**) ont été obtenus à partir d'une solution méthanolique saturée par évaporation lente du solvant. Le complexe cristallise dans le groupe spatial  $P2_1/n$ . L'environnement de coordination du Fe(II) est formé par les deux ligands tridentés coordonnés, dont les atomes donneurs reposent sur les facettes de l'octaèdre. Les unités triazolyle sont situées sur les côtés opposés les uns aux autres sur les sommets axiaux de l'octaèdre (figure 2.8).

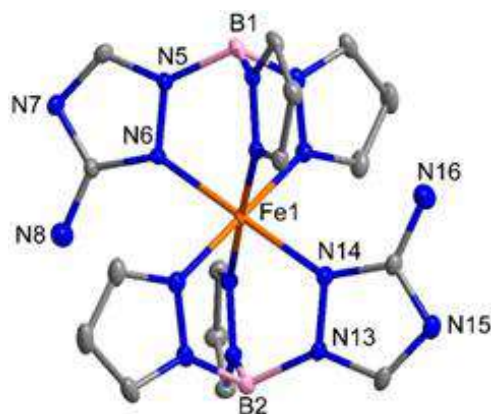


Figure 2.8. Structure cristalline du complexe **6**

La structure cristalline de **6** a été acquise à quatre températures différentes : 100 K, 293 K, 320 K et 393 K. La distance moyenne Fe-N dans le complexe à 100 K est égale à 1,986(11) Å, tandis que le volume de l'octaèdre ( $V_p$ ) à cette température est d'environ 10,46 Å<sup>3</sup>, ce qui est inhérent aux complexes de fer(II) bas spin. La valeur  $d_{\text{Fe-N}}$ , à température ambiante, atteint 2,107(2) Å, ce qui se situe déjà dans la gamme des distances Fe-N trouvées dans les complexes HS. À des températures plus élevées 320 K et 393 K, les distances fer-azote moyennes sont de 2,130(3) Å et 2,159(15) Å, tandis que les valeurs du volume polyédrique sont de 12,80 Å<sup>3</sup> et 13,32 Å<sup>3</sup> respectivement. Le volume de la cellule unitaire ( $V_c$ ) augmente avec la température de 2142.1(10) Å<sup>3</sup> (à 100 K) à 2314.06(10) Å<sup>3</sup> (à 393 K). Ainsi, les distances Fe-N augmentent de 8,7 % dans toute la gamme des températures, tandis que le volume cellulaire augmente de 8,0 %.

Parmi les interactions qui déterminent l'agencement cristallin des molécules  $[\text{Fe}(\text{L}^6)_2]$ , on peut souligner les liaisons H intermoléculaires entre les unités triazoles formées par un atome d'hydrogène du groupe aminé et l'atome d'azote en position 4 de l'hétérocycle (figure 2.9). La distance entre les donneurs et les accepteurs de liaisons hydrogène  $d(\text{D}\cdots\text{A})$  est de 3,014(3) Å pour  $\text{N8}\cdots\text{N15}$  et de 3,010(3) Å pour  $\text{N7}\cdots\text{N16}$  à 100 K. La distance moyenne donneur-accepteur augmente d'environ 2 % à haute température. Des interactions  $\text{C-H}\cdots\pi$  sont également présentes entre les unités triazole et pyrazole des molécules  $[\text{Fe}(\text{L}^6)_2]$  adjacentes.

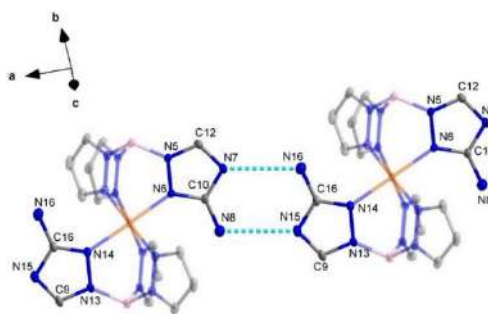


Figure 2.9. Liaison hydrogène entre les molécules  $[\text{Fe}(\text{L}^6)_2]$

### 2.2.3 Transition de spin dans les complexes de fer(II) avec les ligands hétéroscorpionates

Contrairement au groupe nitro, la fonction CN n'a pas d'effet stérique considérable. Ainsi, le complexe **4** portant deux substituants cyano est à l'état bas spin à basse température, ce qui est en accord avec les données structurales des rayons X, et il reste BS à température ambiante où ensuite son  $\chi_{\text{MT}}$  augmente fermement (Figure 2.10). La transition n'est pas terminée à 400 K, et se produit probablement complètement à des températures plus élevées en dehors de la gamme accessible par l'installation de magnétométrie SQUID utilisée. Une tendance similaire est observée pour le composé **5** (dérivé tétracyano), mais le seuil du  $\chi_{\text{MT}}$  est supérieur à 350 K.

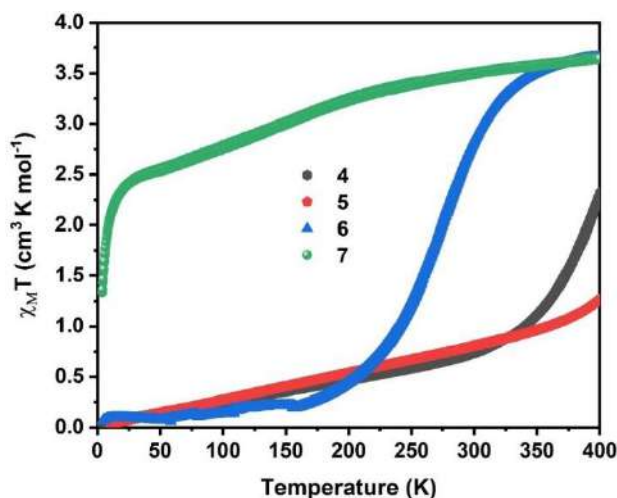


Figure 2.10.  $\chi_{\text{MT}}$  vs  $T$  pour les composés **4–7** en modes chauffage et refroidissement.

Le groupe amino est beaucoup moins volumineux que le groupe nitro, les ligands substitués par NH<sub>2</sub> devraient donc adopter l'ion métallique dans les configurations LS et HS. En effet, les données des mesures magnétiques révèlent une transition de spin complète pour le complexe **6** et un comportement à TS incomplet pour le complexe **7**. Le complexe **6** subit un changement de spin graduel dans la gamme 150–350 K avec T<sub>1/2</sub> centré autour de 276 K avec une petite hystérésis d'environ 2–3 K. Malgré la présence de la liaison hydrogène entre les molécules de [Fe(L<sup>6</sup>)<sub>2</sub>] dans la masse de la substance, la transition est graduelle.

### Chapitre 3. Lanthanide(III) bis-carbacylamidophosphates. Synthèse, caractérisation et étude de la luminescence.

#### 3.1 Synthèse d'un ligand carbacylamidophosphate bis-chélateur (H<sub>2</sub>L<sup>8</sup>) et de ses complexes binucléaires de lanthanide(III) [Ln<sub>2</sub>(L<sup>8</sup>)<sub>3</sub>(phen)<sub>2</sub>]. Caractérisation des composés et luminescence des complexes obtenus.

##### 3.1.1 Synthèse du ligand et des complexes

Les composés de coordination [Ln<sub>2</sub>(L<sup>8</sup>)<sub>3</sub>(phen)<sub>2</sub>] ont été obtenus selon le schéma présenté sur la figure 3.1.

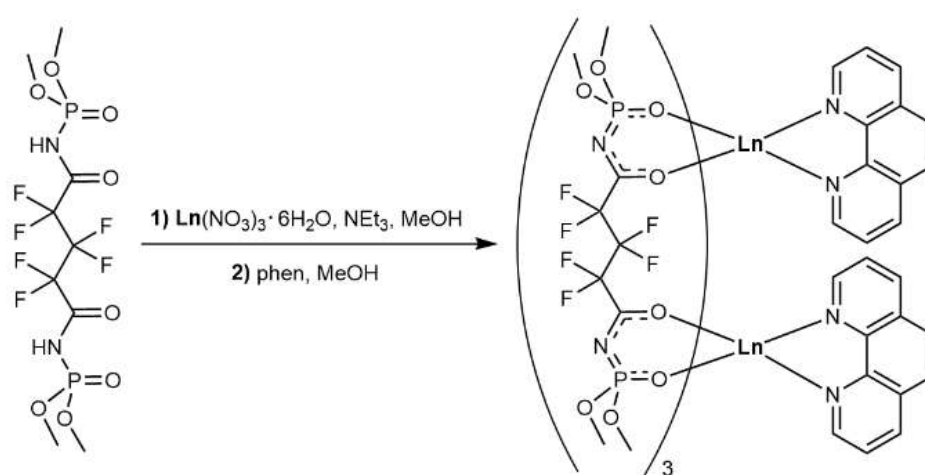


Figure 3.1. Synthesis of [Ln<sub>2</sub>(L<sup>8</sup>)<sub>3</sub>(phen)<sub>2</sub>] complexes. Ln<sup>III</sup> = Nd<sup>III</sup>, Sm<sup>III</sup>, Eu<sup>III</sup>, Tb<sup>III</sup>, Dy<sup>III</sup>, Yb<sup>III</sup>.

##### 3.1.2 Propriétés de luminescence des complexes Nd(III), Sm(III), Eu(III), Tb(III), Dy(III) et Yb(III)

Les spectres d'excitation et de luminescence des complexes, émettant dans le domaine spectral visible, sont présentés dans la figure 3.2. Lors de l'excitation par la lumière UV à 330 nm, [Sm<sub>2</sub>(L<sup>8</sup>)<sub>3</sub>(phen)<sub>2</sub>] (**9**) présente une émission orange. Comme pour les complexes ternaires Sm(III) β-dicétone, la bande de transition <sup>4</sup>G<sub>5/2</sub>→<sup>6</sup>H<sub>9/2</sub> (λ<sub>max</sub> = 645 nm) domine dans le spectre d'émission du complexe.

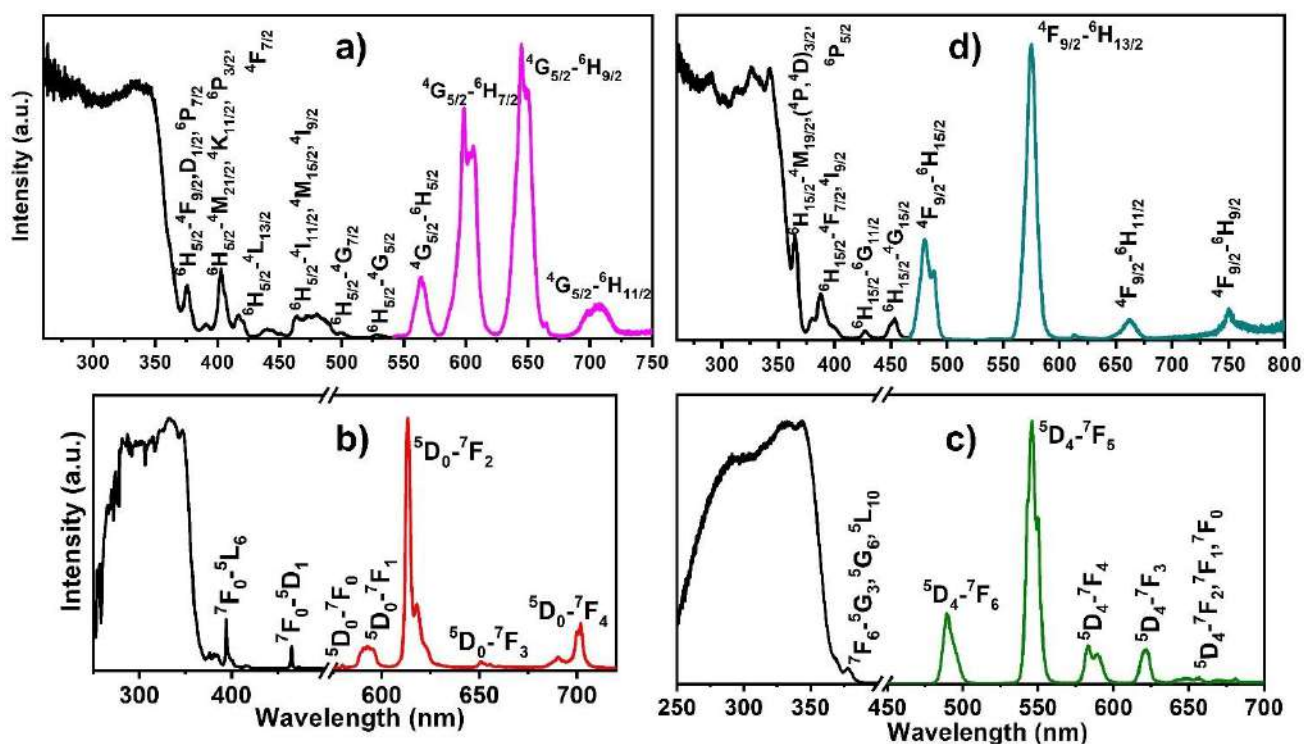


Figure 3.2. Spectres d'excitation (lignes noires) et d'émission (lignes colorées) des complexes  $[\text{Sm}_2(\text{L}^8)_3(\text{phen})_2]$  (a),  $[\text{Eu}_2(\text{L}^8)_3(\text{phen})_2]$  (b),  $[\text{Tb}_2(\text{L}^8)_3(\text{phen})_2]$  (c),  $[\text{Dy}_2(\text{L}^8)_3(\text{phen})_2]$  (d) à l'état solide et à 293 K.

Contrairement au complexe d'euprium, le temps de décroissance de la luminescence de  $[\text{Tb}_2(\text{L}^8)_3(\text{phen})_2]$  augmente avec la diminution de la température : à température ambiante, tobs pour le complexe de terbium est égal à 1,45 ms et à 77 K, il est de 2,00 ms. Compte tenu de l'écart d'énergie relativement faible entre l'état triplet le plus bas des ligands et le niveau émissif  $^5\text{D}_4$  de l'ion Tb(III) dans le complexe étudié ( $\Delta E = 1050 \text{ cm}^{-1}$ ), une activation des processus non radiatifs dans le complexe **11** lors de l'augmentation de la température peut être due à un transfert d'énergie du terbium vers les ligands.

### 3.2 Synthèse et caractérisation des composés à 4 brins $\text{NEt}_4[\text{NaLn}_2(\text{L}^8)_4(\text{H}_2\text{O})]$ et $\text{Na}[\text{NaLn}_2(\text{L}^8)_4(\text{H}_2\text{O})] \cdot 2\text{H}_2\text{O}$ . Structure et propriétés de luminescence.

#### 3.2.1 Synthèse

Dans le cas présent, pour synthétiser les complexes souhaités, le ligand bis-chélatant CAPH a été utilisé sous la forme du sel de sodium  $\text{Na}_2\text{L}^8$  qui a été préparé par déprotonation de  $\text{H}_2\text{L}^8$  à l'aide de méthanolate de sodium. Des complexes quadrangulaires de formules générales  $\text{NEt}_4[\text{NaLn}_2(\text{L}^8)_4(\text{H}_2\text{O})]$  et  $\text{Na}[\text{NaLn}_2(\text{L}^8)_4(\text{H}_2\text{O})] \cdot 2\text{H}_2\text{O}$  ont été synthétisés selon le schéma présenté à la figure 3.3.

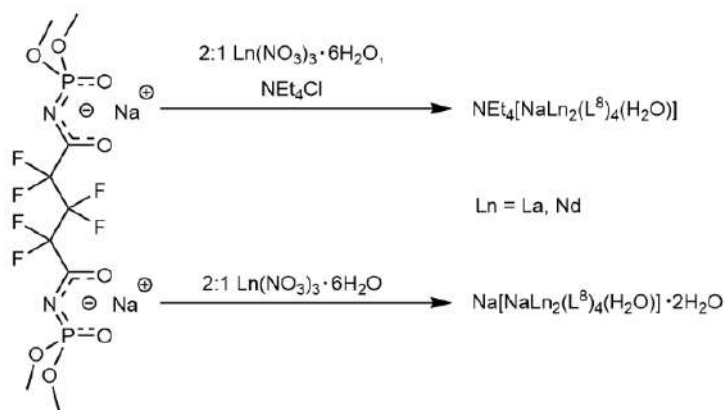


Figure 3.3. Voie de synthèse des complexes binucléaires de lanthanide à quadruple brin.

### 3.2.2 Cristallographie aux rayons X

La structure cristalline du composé  $\text{NEt}_4[\text{NaNd}_2(\text{L}^8)_4(\text{H}_2\text{O})]$  (**16**) est présentée à la figure 3.4.

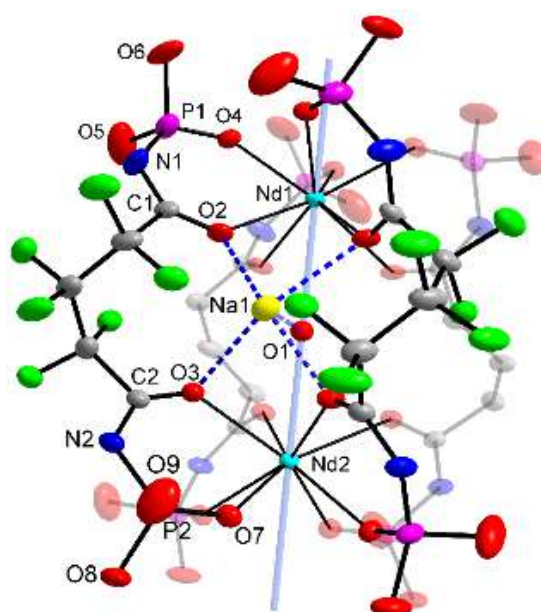


Figure 3.4. Structure de l'anion du complexe  $[\text{NaNd}_2(\text{L}^8)_4(\text{H}_2\text{O})]^-$  **16**.

L'anion complexe  $[\text{NaNd}_2(\text{L}^8)_4(\text{H}_2\text{O})]^-$  a une structure d'hélicate quadruple brin, qui encapsule le cation sodium et une molécule d'eau dans l'environnement chargé négativement des atomes de fluor et de et d'oxygène, qui peut également être considéré comme une cavité de type crypte. Quatre ligands bis-carbamoylphosphates sont coordonnés à deux ions Nd(III) cristallographiquement distincts de manière bidente par l'intermédiaire des atomes d'oxygène des groupes carbonyle et phosphoryle. Les atomes d'oxygène des groupes carbonyles agissent comme des ponts liant également l'ion sodium. Contrairement à la structure discrète de **16**, les cristaux de  $\text{Na}[\text{NaLa}_2(\text{L}^8)_4(\text{H}_2\text{O})] \cdot 2\text{H}_2\text{O}$  (**17**) et  $\text{Na}[\text{NaNd}_2(\text{L}^8)_4(\text{H}_2\text{O})] \cdot 2\text{H}_2\text{O}$  (**18**) sont constitués de chaînes de polymères formées par des atomes

d'oxygène des groupements OCH<sub>3</sub> et phosphoryle et des cations sodium de la sphère externe (figures 3.5).

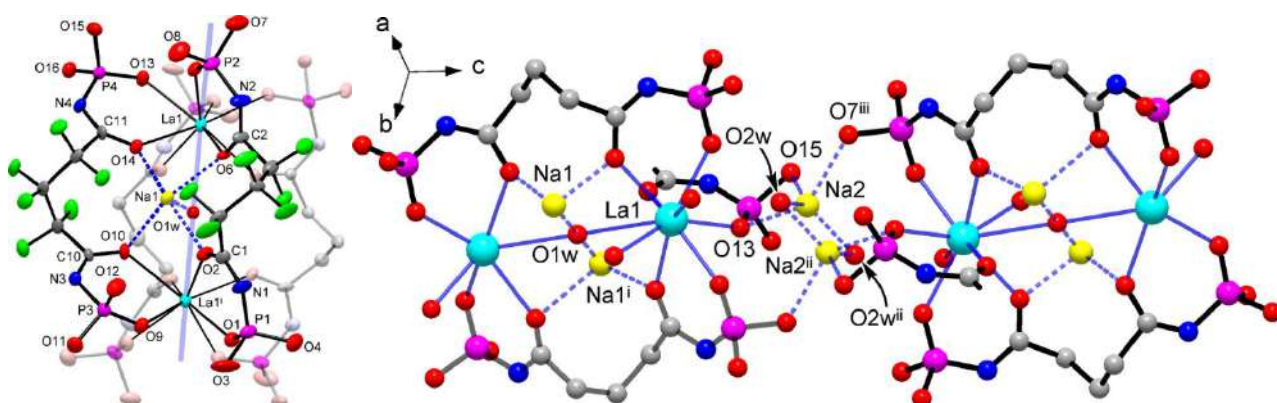


Figure 3.5. Structure du complexe anionique  $[\text{NaLa}_2(\text{L}^8)(\text{H}_2\text{O})]^-$  dans 17.

### 3.2.3 Propriétés photoluminescentes du composé $\text{NEt}_4[\text{NaNd}_2(\text{L}^8)_4(\text{H}_2\text{O})]$

Le complexe  $\text{NEt}_4[\text{NaNd}_2(\text{L}^8)_4(\text{H}_2\text{O})]$  présente une émission IR à 300 et 77 K lors de l'excitation par laser pulsé Nd:YAG à 266 nm. Les spectres d'émission sont présentés dans la figure 3.6. Les bandes étroites autour de 900 et 1060 nm ont été attribuées aux transitions  ${}^4\text{F}_{3/2} \rightarrow {}^4\text{I}_{9/2}$  and  ${}^4\text{F}_{3/2} \rightarrow {}^4\text{I}_{11/2}$  transitions de l'ion Nd(III). Lorsque la température diminue de 300 à 77 K, le canal de relaxation radiative du niveau  ${}^4\text{F}_{3/2}$  change. Ceci est mis en évidence par le changement des intensités relatives des transitions, à 300 K.

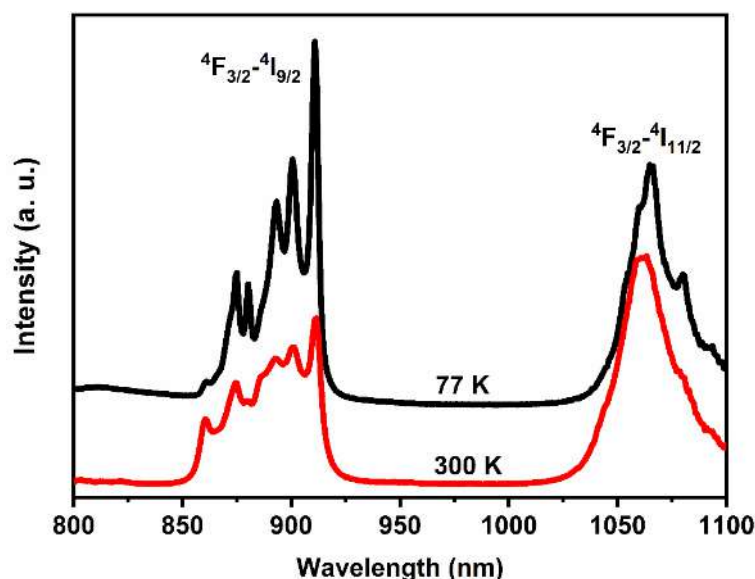


Figure 3.6. Spectre d'émission du complexe  $\text{NEt}_4[\text{NaNd}_2(\text{L}^8)_4(\text{H}_2\text{O})]$  à 300 et 77 K,  $\lambda_{\text{exc}}=266$  nm.

Dans les complexes à quatre unités  $\text{L}^8$  coordonnées, il a été constaté que les anions complexes des composés obtenus ont une structure d'hélicate quadruple brin, qui encapsule le cation sodium et une molécule d'eau dans une cavité de type cryptand. Le complexe  $\text{NEt}_4[\text{NaNd}_2(\text{L}^8)_4(\text{H}_2\text{O})]$  s'est avéré

luminescent dans la région spectrale IR avec une durée de vie d'émission  ${}^4F_{3/2}$  égale à 2  $\mu$ s. Le ligand bis-carbacylamidophosphate appartient à la nouvelle famille des ligands bis-chélateurs et peut être utilisé pour obtenir des complexes Ln comme systèmes modèles pour l'étude du transfert d'énergie inter-ionique ainsi que pour concevoir des complexes hétéro-nucléaires pour la thermométrie par luminescence en exploitant le transfert d'énergie inter-ionique dépendant de la température.

#### **Chapitre 4. Films minces du composé bis[hydrotris(1,2,3-triazol-1-yl)borate]fer(II). Application à la thermométrie.**

Ce chapitre est consacré au dépôt et à la caractérisation de films minces nanométriques d'un composé fer(II)-scorpionate. L'étude du comportement de TS dans les nanomatériaux obtenus est discutée, ainsi que le test des films minces pour une application de thermométrie de surface basée sur la thermorélectance. La première partie traite de l'élaboration et de la caractérisation des films minces à TS, tandis que la deuxième partie est consacré à l'utilisation des films minces pour la technique de microthermométrie de surface basée sur la thermorélectance sur des microfils d'or chauffés par effet Joule et obtenus par photolithographie sur des puces en verre et en silicium. Compte tenu de la grande stabilité thermique du composé bis[hydrotris(1,2,3-triazol-1-yl)borate]de fer(II) (**1**), sa sublimation pour former des films minces à TS avec un caractère graduel est particulièrement intéressante pour élaborer un thermomètre de surface basé sur la thermorélectance. Des techniques de caractérisation telles que la diffraction des rayons X à incidence rasante (GIXRD) et la microscopie à force atomique (AFM) ont été utilisées pour étudier la cristallinité, l'homogénéité, la morphologie de surface et l'épaisseur des films. La TS dans les matériaux a été étudiée au moyen de la spectroscopie UV-Vis à température variable pour les films minces déposés sur des substrats transparents dans cette gamme spectrale. Comme les films conservent la nature graduelle de la TS observée dans le composé massif et son stable lors d'un stockage à long terme dans des conditions ambiantes et lors de nombreux cycles thermiques, il était intéressant de les tester en vue d'une application de microthermométrie. À cette fin, une fine couche du composé bis[hydrotris(1,2,3-triazol-1-yl)borate]fer(II) a été déposée sur un circuit électrique en or comportant un ensemble de microfils physisorbé sur un substrat en verre/silicium oxydé. Les changements de thermorélectance des microfils chauffés par effet Joule et de la surface du substrat autour d'eux ont été suivis au moyen de la microscopie optique dans les domaines de l'UV et du visible. Les données obtenues ont permis d'établir une cartographie précise de la température de la surface des microfils.

##### **4.1 Fabrication et caractérisation de films du composé [Fe(HB(1,2,3-tz)<sub>3</sub>)<sub>2</sub>]**

Des films minces du composé **1** ont été déposés par évaporation thermique sous vide avec des épaisseurs de l'ordre de 20-200 nm. Les diagrammes de diffraction des rayons X des films révèlent un

pic intense à  $2\theta = 12,15^\circ$  (figure 4.1a) qui indique une cristallinité et une orientation cristallographique préférentielle. La figure 4.1a montre également le diagramme de diffraction de la poudre microcristalline, qui présente un pic similaire à  $2\theta = 12,09^\circ$ . Dans le diagramme PXRD simulé de **1**, ce pic correspond à la réflexion 011. Ainsi, on peut suggérer que les cristallites dans les films se développent préférentiellement avec la direction [011] normale à la surface du substrat. Cette observation a été systématiquement confirmée, indépendamment de la nature du substrat (silicium ou silice fondue) et de l'épaisseur du film.

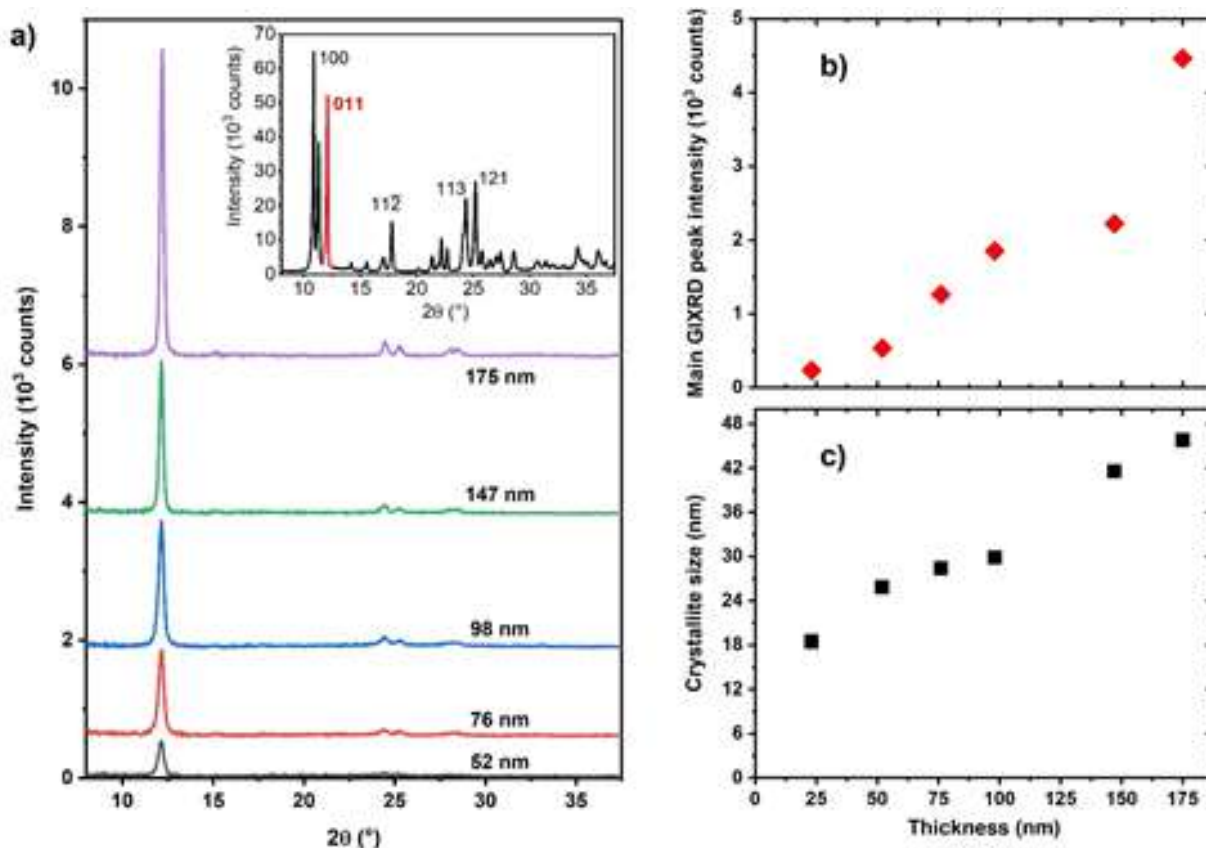


Figure 4.1. Cristallinité des films. a) Diagrammes XRD de films minces nanocristallins de **1** de différentes épaisseurs, déposés sur des substrats de Si. L'encadré montre le diagramme XRD de la poudre microcristalline de **1**. b) Intensité de la réflexion 011 en fonction de l'épaisseur du film. c) Taille moyenne des domaines cristallins (calculée pour la réflexion 011 en utilisant la méthode de Scherrer) en fonction de l'épaisseur du film.

Des données représentatives de topographie de surface AFM de films de **1** de différentes épaisseurs, déposés sur des substrats de silice, sont présentées dans la figure 4.2.

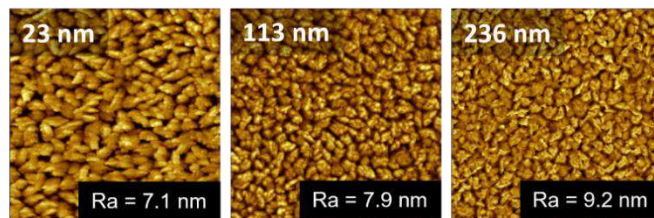


Figure 4.2. Morphologie des films. Images représentatives de topographie AFM de films de **1** avec différentes épaisseurs (23, 113 et 236 nm) déposés sur des substrats de silicium. La taille du balayage est de  $5 \times 5 \mu\text{m}^2$ .

La morphologie de surface nanocristalline des films est évidente avec des valeurs de rugosité RMS typiquement comprises entre 7 et 11 nm. La morphologie des particules ne dépend pas substantiellement de l'épaisseur du film ou de la nature du substrat mais on peut remarquer une densité de cristallites plus importante dans les films plus épais. Afin d'étudier les propriétés de TS des films minces de **1**, des mesures de spectrophotométrie UV-vis à température variable ont été effectuées sur trois à huit cycles de chauffage-refroidissement entre 253 et 453 K à une vitesse de  $2 \text{ K min}^{-1}$ . Les mesures ont été effectuées pour les films déposés sur des substrats transparents en silice fondue. Les spectres d'absorption à température ambiante des films présentent trois bandes d'absorption avec des maxima à 208, 275 et 336 nm (figure 4.3a).

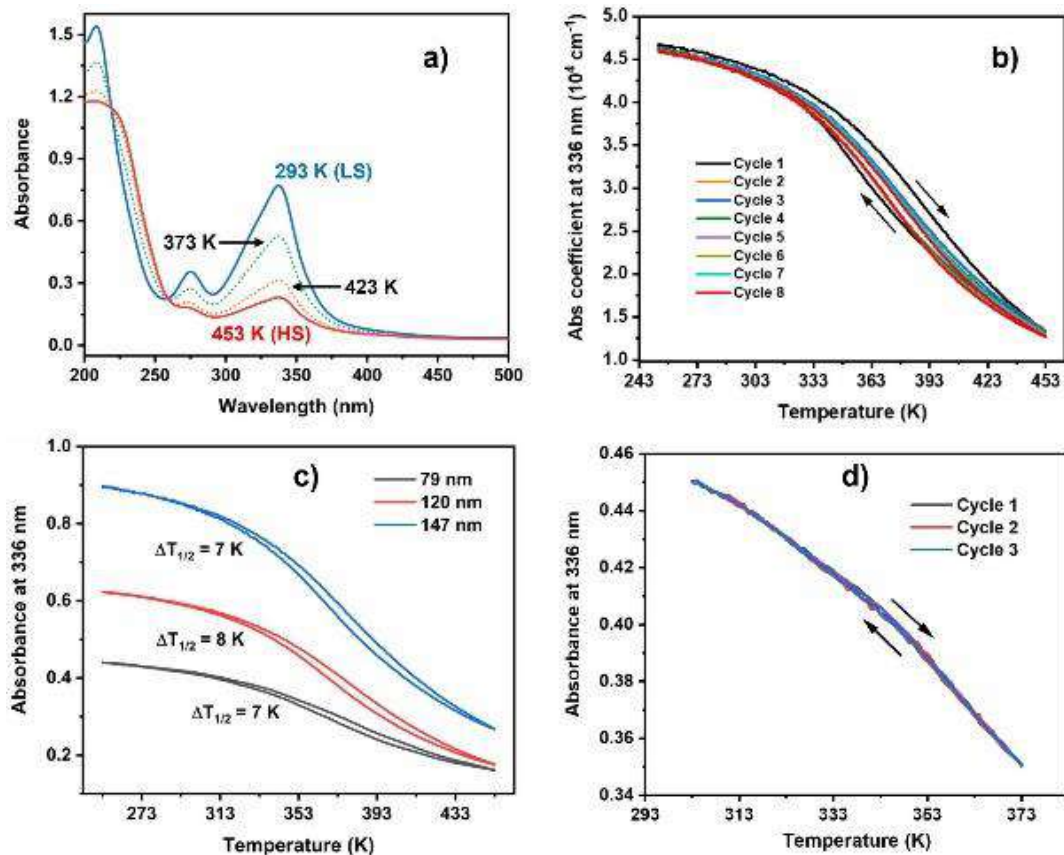


Figure 4.3. Propriétés de TS des films. a) Spectres d'absorbance optique d'un film de **1** de 175 nm d'épaisseur sur un substrat de silice fondue, acquis à des températures sélectionnées. b) Dépendance de

la température de l'absorbance à 336 nm du même film de 175 nm lors de huit cycles de chauffage et de refroidissement entre 253 et 453 K. c) Variation thermique de l'absorbance à 336 nm pour un film de **1** de 79, 120 et 147 nm d'épaisseur, lors de cycles de chauffage et de refroidissement entre 253 et 453 K. c) Variation thermique de l'absorbance à 336 nm d'un film de **1** de 79, 120 et 147 nm d'épaisseur lors de cycles de chauffage-refroidissement entre 253 et 453 K. d) Variation thermique de l'absorbance optique à 336 nm d'un film de **1** de 79 nm d'épaisseur lors de trois cycles de chauffage-refroidissement entre 303 et 373 K.

L'absorbance de ces bandes diminue lors du chauffage, tandis qu'une quatrième bande apparaît à 230 nm et présente une absorbance plus élevée à haute température. En conséquence, les spectres à température variable sont caractérisés par deux points isobétiques à environ 220 et 260 nm. Compte tenu des coefficients d'absorption élevés associés à ces pics, ceux-ci peuvent être attribués avec certitude à des transitions de transfert de charge (métal-ligand et/ou ligand-métal). L'évolution thermique de la bande d'absorption la plus intense à 336 nm a été utilisée pour suivre le changement d'état de spin dans les films. Les courbes de transition typiques, présentées dans la figure 4.3b, révèlent une conversion de spin très progressive entre les états BS et HS, similaire à celle observée pour le composé massif. La température de transition est centrée autour de  $374 \pm 2$  K, indépendamment de l'épaisseur du film (figure 4.3c). La conversion de spin est pratiquement complète à 273 K (état BS pur), tandis qu'une fraction BS résiduelle d'environ 5-10 % est encore observée à 453 K. (N.B. Un chauffage supérieur à environ 453 K entraîne la dégradation des films.) Une caractéristique notable et inhabituelle de la TS dans les films est l'apparition d'une hystérésis thermique, qui n'est pas attendue pour une conversion de spin aussi graduelle. Lors du premier cycle de chauffage-refroidissement, cette boucle d'hystérésis thermique est généralement large, atteignant jusqu'à 35 K de largeur, tandis que lors des cycles suivants, elle se réduit à environ 7 K. Il est toutefois important de noter que la réduction de la durée du cycle thermique entraîne un rétrécissement de la boucle d'hystérésis. En effet, la réduction de la température finale de 453 K à 393 K entraîne une boucle d'hystérésis de 4 K de large, alors que l'hystérésis thermique peut être complètement supprimée en limitant le chauffage de l'échantillon à 373 K, ce qui conduit à des courbes de transition de spin parfaitement réversibles et reproductibles (figure 4.3d).

#### **4.2 Application des films de $[\text{Fe}(\text{HB}(1,2,3\text{-tz})_3)_2]$ à la microthermometry**

Tirant parti des propriétés susmentionnées, des expériences ont été entreprises pour explorer l'utilisation de films minces de **1** comme capteur de température, sondé par réflectivité optique, pour cartographier et mesurer la température de la surface par imagerie thermique par thermoréfectance. En effet, le rôle du film à TS est d'améliorer les propriétés de thermoréfectance des surfaces dans une large gamme de températures - en particulier dans le domaine spectral UV où un changement radical de l'absorbance optique se produit lors du passage de l'état BS à l'état HS ; la thermoréfectance améliorée implique un changement accru de la réflectivité optique induite par la chaleur et, par conséquent, une

plus grande sensibilité thermique pour la mesure de la température de la surface. La figure 4.4a (panneaux supérieurs) montre l'évolution thermique de la réflectivité optique,  $\Delta R/R = (R - R_{298K})/R_{298K}$ , à  $\lambda = 310$  nm (proche de la longueur d'onde d'absorption maximale du complexe) sur des surfaces d'or, de silicium et de verre revêtues de matériaux à TS (120 nm) et non revêtues.

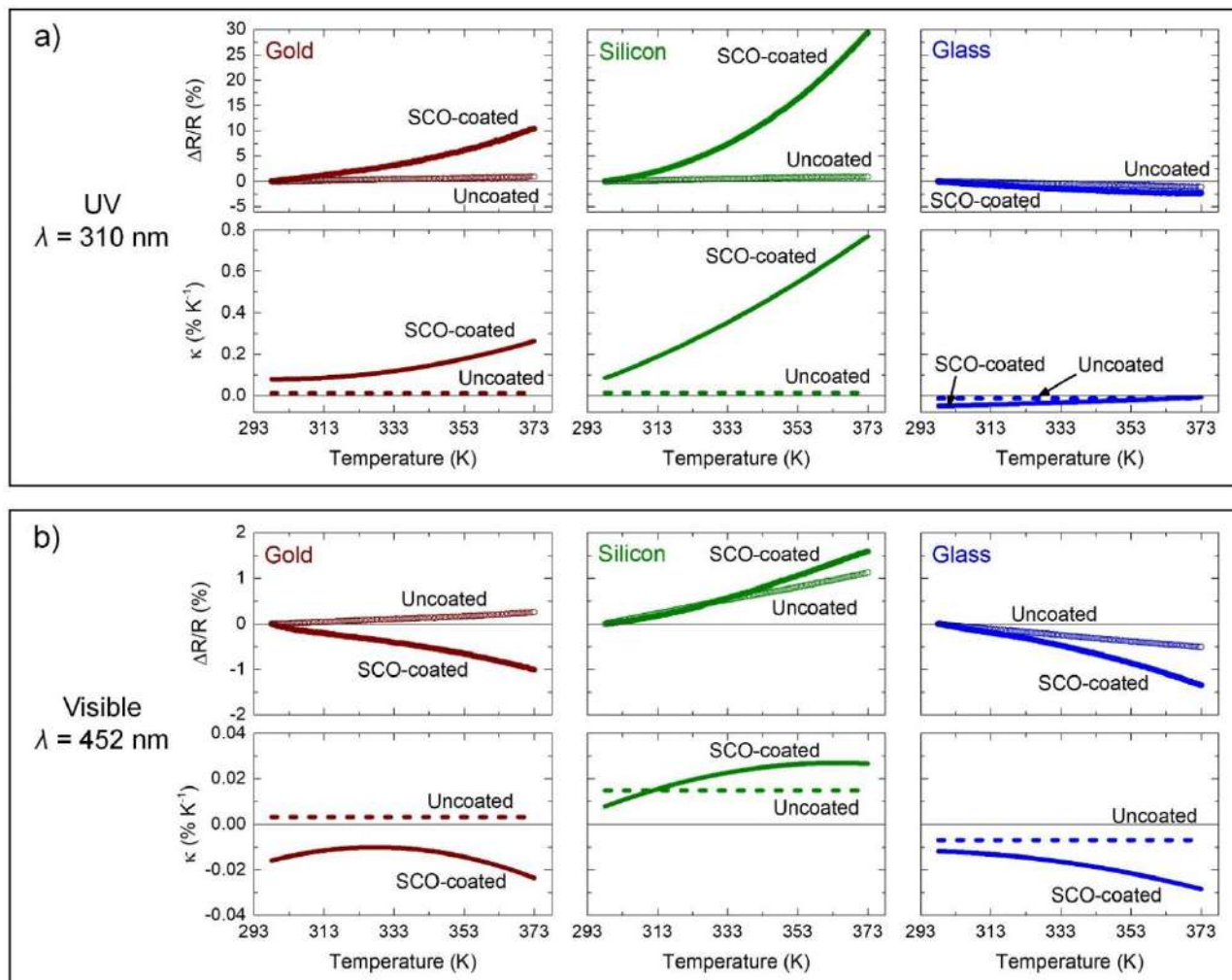


Figure 4.4. Étalonnages thermiques de la réflectivité optique : Évolution thermique du changement de réflectivité optique relative,  $\Delta R/R = (R - R_{298K})/R_{298K}$ , (panneau supérieur) et du coefficient de thermorélectance correspondant,  $\kappa = d(\Delta R/R)/dT$ , (panneau inférieur) pour des surfaces d'or, de silicium et de verre revêtues et non revêtues de film à TS mesuré à  $\lambda = 310$  nm (a) et à  $\lambda = 452$  nm (b) Pour chaque mesure, la surface a été chauffée de 298 à 373 K à une vitesse de balayage de la température de  $2 \text{ K min}^{-1}$ .

Il est remarquable que la présence de la couche à TS améliore de manière significative les propriétés de thermorélectance des surfaces, entraînant un changement relatif de la réflectivité de +29,4 %, +10,4 % et -2,4 % sur les surfaces de silicium, d'or et de verre, respectivement, dans la plage de température comprise entre 298 et 373 K. En comparaison, sur les surfaces non revêtues, ces changements relatifs (thermorélectance ordinaire) restent modérés : +0,9 % sur les surfaces de silicium et d'or et -1,1 % sur le verre. Les changements observés sont beaucoup plus importants sur le silicium (et dans une moindre

mesure sur l'or), qui est une surface réfléchissante dans le domaine UV (par rapport au verre). Sur ces surfaces, la réflectivité optique augmente avec la température ( $\Delta R/R > 0$ ), ce qui est compatible avec une réduction progressive de l'absorbance du film à TS à cette longueur d'onde lors de la transition de spin.

La figure 4.4a (panneaux inférieurs) illustre l'évolution thermique du coefficient de thermoréfectance correspondant ( $\kappa$ ), défini comme  $\kappa = d(\Delta R/R)/dT$ , sur les différentes surfaces étudiées ( $\lambda = 310$  nm). Alors que  $\kappa$  est pratiquement constant pour les surfaces non revêtues dans la plage de température 298-373 K,  $\kappa = +0,013 \% K^{-1}$ ,  $+0,012 \% K^{-1}$  et  $-0,014 \% K^{-1}$  pour les surfaces de silicium, d'or et de verre, respectivement, le coefficient de thermoréfectance n'est pas constant sur les surfaces revêtues de matériau à TS.

Sur l'or,  $\kappa$  passe de  $0,078 \% K^{-1}$  à  $0,26 \% K^{-1}$  lors du chauffage de 298 à 373 K, ce qui correspond à une augmentation du coefficient de thermoréflexion d'un facteur de 6,5 et 22 à 298 et 373 K, respectivement, par rapport à la surface d'or vierge. Enfin, l'effet est moins avantageux sur les substrats en verre transparent où  $\kappa$  passe de  $-0,050 \% K^{-1}$  à  $-0,009 \% K^{-1}$  lors du passage de 298 à 373 K, ce qui signifie que la sensibilité thermique est augmentée d'un facteur 3,6 (en valeur absolue) à 298 K, mais devient inférieure à la thermoréfectance ordinaire à haute température. Il convient de noter ici que d'autres améliorations du coefficient de thermoréfectance peuvent être envisagées, par exemple en utilisant une source lumineuse correspondant à la longueur d'onde de l'absorbance maximale (336 nm) et/ou en augmentant l'épaisseur du film à TS. Toutefois, dans les deux cas, le prix à payer serait une perturbation croissante de la température de surface causée par la présence du film à TS (c'est-à-dire une invasivité accrue), ce qui est particulièrement préjudiciable pour une surveillance rapide ( $< ms$ ) de la température. Comme pour les mesures d'absorbance optique, il convient de noter qu'aucune différence notable n'est observée dans ces courbes d'étalonnage thermique entre les modes de chauffage et de refroidissement (figure 4.5), ce qui signifie que la performance du film à TS, en termes de changement thermique de la réflectivité optique, est entièrement réversible dans la plage de température 298-373 K.

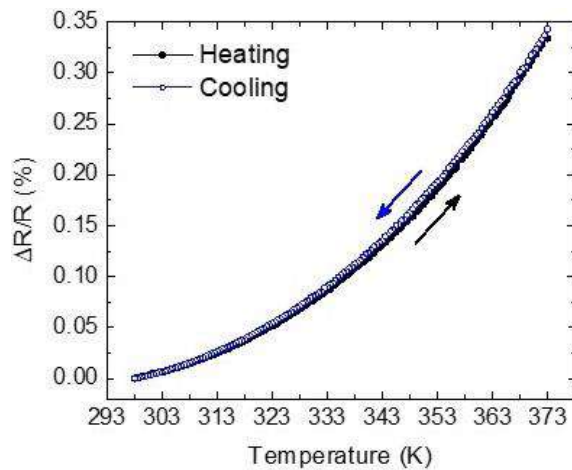


Figure 4.5. Évolution thermique du changement de réflectivité optique,  $\Delta R/R = (R - R_{298K})/R_{298K}$ , mesurée à  $\lambda = 310$  nm sur une surface de silicium revêtue de matériau à TS dans les deux modes de chauffage et de refroidissement.

Il est intéressant de noter, comme le montre la figure 4.4b, que seule une légère amélioration des propriétés de thermoréfectance est mise en évidence sur les surfaces revêtues de matériau à TS dans le domaine visible ( $\lambda = 452$  nm), c'est-à-dire dans un domaine spectral en dehors de la bande d'absorption variable du film à TS. Ce résultat indique que la majeure partie du changement de la réflectivité optique au cours de la transition de spin provient de la variation des propriétés d'absorption du film, plutôt que d'un simple changement de l'indice de réfraction. Dans l'ensemble, ces mesures montrent que la présence du film mince à TS entraîne une augmentation substantielle des propriétés de thermoréfectivité dans la gamme UV, de plus d'un ordre de grandeur par rapport à la thermoréfectivité ordinaire, en particulier sur les surfaces réfléchissantes comme l'or ou le silicium, ce qui implique par conséquent une amélioration considérable de la sensibilité (en termes de signal de réflectivité optique) à tout changement de la température de la surface.

Afin d'étudier le potentiel de ce film mince à TS en termes d'imagerie thermique par thermoréflexion, des microfils d'or chauffés par effet Joule (longueur 1-2 mm, épaisseur 250 nm) sur des puces de verre et de silicium oxydé ont été fabriqués par photolithographie (figure 4.6a). La surface des puces a ensuite été entièrement recouverte d'un film du composé **1** de 120 nm d'épaisseur. Il convient de noter qu'en raison de sa nature isolante, la présence d'un film de **1** sur la surface n'est pas invasive et n'affecte pas les performances électriques du dispositif.

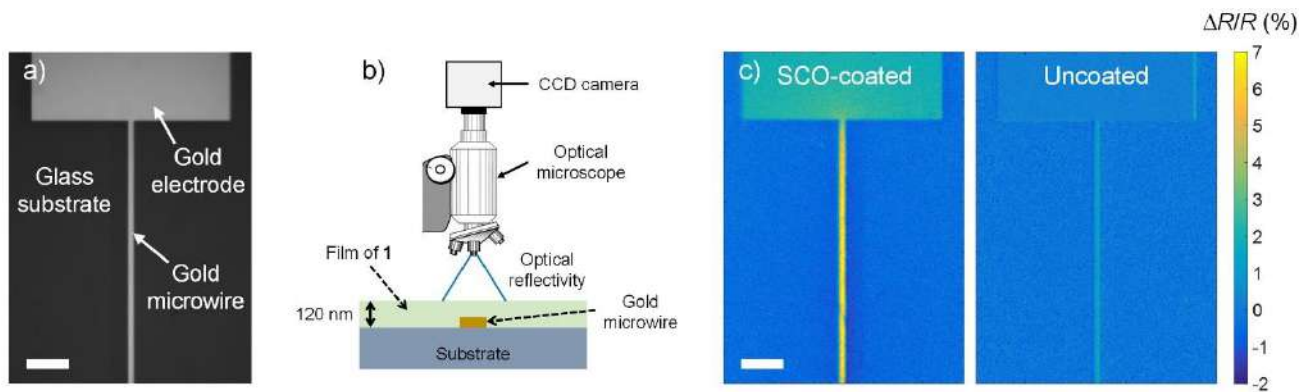


Figure 4.6. Amélioration de la sensibilité thermique. a) Image de réflectivité optique  $R$  d'un micro-fil d'or chauffé par effet Joule (2 mm de long et  $16 \mu\text{m}$  de large) sur un substrat en verre. b) Schéma du dispositif expérimental. c) Changement relatif de la réflectivité optique ( $\lambda = 310 \text{ nm}$ ),  $\Delta R/R = (R_{\text{ON}} - R_{\text{OFF}})/R_{\text{OFF}}$ , suite à l'application d'un courant électrique de 65 mA dans le fil, pour (à gauche) une surface recouverte du film à TS et (à droite) une surface non recouverte. Dans les deux cas, la température de base  $T_b$  de la puce a été maintenue à 298 K. Les barres d'échelle sont de  $100 \mu\text{m}$ .

Des images de réflectivité optique ( $\lambda = 310 \text{ nm}$ ) du microfil sur un substrat de verre revêtu d'un film à TS ont été acquises par microscopie optique à  $T = 298 \text{ K}$  (voir Figure 4.6b), dans les deux états ON ( $I \neq 0$ ) et OFF ( $I = 0$ ) du dispositif de chauffage. La figure 4.6c (à gauche) montre une carte de la variation relative de la réflectivité optique,  $\Delta R/R = (R_{\text{ON}} - R_{\text{OFF}})/R_{\text{OFF}}$ , suite à l'application d'un courant électrique de 65 mA dans le fil. Une forte augmentation de la réflectivité optique est observée sur le fil et, dans une moindre mesure, sur l'électrode. Sur le substrat de verre, à proximité immédiate du fil, une légère diminution de la réflectivité est également observée, ce qui est compatible avec une augmentation de la température suite à l'application du courant électrique. (Comme l'indique la figure 4.5a, la réflectivité optique augmente/diminue sur la surface or/verre à la suite d'une élévation de température). À titre de comparaison, la même expérience a été réalisée avec un microfil identique non revêtu. Comme le montre la figure 4.6c (à droite), la variation de la réflectivité optique associée à l'application du même courant électrique (65 mA) est considérablement plus faible que celle observée pour la surface recouverte du film à TS, ce qui démontre le gain substantiel apporté par la couche à TS thermosensible en termes de propriétés de thermoréflexance et, par conséquent, en termes de sensibilité thermique.

En tirant parti de cette sensibilité thermique accrue, il a été possible de déduire des cartes de température précises des microfils chauffés par effet Joule. En effet, sur la base des courbes d'étalonnage thermique de la réflectivité optique présentées à la figure 4.4a, la carte de réflectivité ( $\Delta R/R$ ) mesurée à la figure 4.6c (gauche) peut être facilement transformée en une carte de température, en convertissant simplement la valeur mesurée de  $\Delta R/R$ , sur chaque pixel de l'image, en une valeur de température. Comme le montre la figure 4.7, cette procédure nous a permis de cartographier le champ de température

de la surface avec une résolution spatiale micrométrique, pour différentes valeurs du courant électrique appliqué.

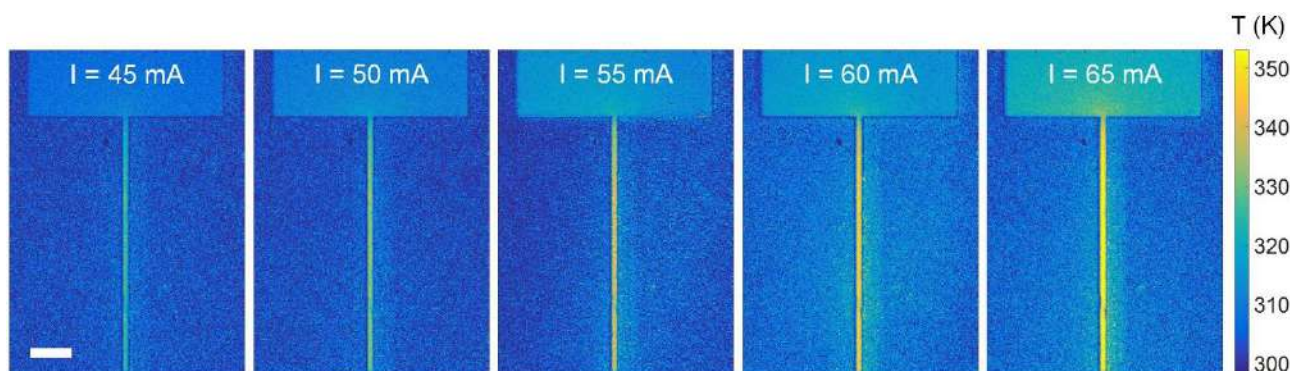


Figure 4.7. Microthermométrie quantitative. Cartes de température d'un micro-fil d'or de 16  $\mu\text{m}$  de large sur un substrat de verre recouvert d'un film à TS pour différents courants électriques appliqués allant de 45 à 65 mA ( $T_b = 298$  K). Les cartes sont déduites des images de réflectivité optique ( $\lambda = 310$  nm),  $\Delta R/R = (R_{\text{ON}} - R_{\text{OFF}})/R_{\text{OFF}}$ , de la surface revêtue du film à TS. La taille des pixels des cartes de température est de  $2,6 \times 2,6 \mu\text{m}^2$ . La barre d'échelle est de 100  $\mu\text{m}$ .

Comme prévu, ces cartes de température montrent que l'échauffement est principalement localisé sur le microfil d'or, tandis qu'une diffusion progressive de la chaleur est également observée dans le substrat et l'électrode métallique lors de l'augmentation du courant électrique, comme cela a déjà été signalé dans l'étude thermométrique pour le composé  $[\text{Fe}(\text{HB}(1,2,4\text{-tz})_3)_2]$ .<sup>29</sup> Toutefois, il convient de noter que les gradients de température observés sur le substrat de verre environnant sont moins marqués que dans le cas du thermomètre  $[\text{Fe}(\text{HB}(1,2,4\text{-tz})_3)_2]$ ,<sup>29</sup> principalement en raison de l'utilisation de fils chauffants par effet Joule plus larges (16  $\mu\text{m}$  de large au lieu de 1  $\mu\text{m}$  de large) dans la présente étude, qui génèrent des gradients thermiques moins prononcés). Ces cartes de température permettent de déduire une température moyenne du micro-fil chauffé par effet Joule  $T_{\text{wire}}$  de 315,9, 320,0, 325,4, 329,9 et 336,6 K pour un courant appliqué de 45, 50, 55, 60 et 65 mA, respectivement. Ces valeurs sont reportées dans la figure 4.8b (carrés vides).

Pour valider les résultats obtenus avec la technique de thermométrie à base du film à TS, la température moyenne du micro-fil chauffé par effet Joule a également été déterminée en mesurant sa résistance électrique. En effet, la variation thermique induite par le courant appliqué génère une variation de la résistance électrique  $\Delta R\Omega$ , proportionnelle à l'élévation moyenne de la température du fil :  $\Delta R\Omega = \alpha \Delta T_{\text{wire}}$ . Pour déterminer la valeur de  $\alpha$ , une calibration thermique de la résistance du microfil a été réalisée, en mesurant l'évolution de  $R\Omega$  à faible courant de polarisation (5 mA) pour différentes températures de base ( $T_b$ ) de la puce. Une dépendance linéaire est observée, donnant une valeur de  $\alpha = 3,84 \times 10^{-2} \Omega \text{ K}^{-1}$  (Figure 4.8a). Par conséquent, au cours des mesures de thermoréflexion, la résistance a été mesurée simultanément pour chaque valeur du courant électrique appliqué, fournissant un moyen de comparaison fiable pour contrôler en temps réel la température moyenne réelle  $T_{\text{wire}}$  du fil chauffé

par effet Joule. La figure 4.8b résume les valeurs de  $T_{\text{wire}}$  obtenues par les deux méthodes pour les différents courants électriques appliqués, la puce étant maintenue à température ambiante ( $T_b = 298 \text{ K}$ ). Comme le montre la figure et comme prévu, la température du fil augmente avec le courant en suivant une évolution quadratique typique (effet Joule). Il est important de noter que les valeurs de température obtenues par ces deux techniques sont en très bon accord, la différence relative observée étant typiquement de 2 à 5 % et toujours inférieure à 2 K.

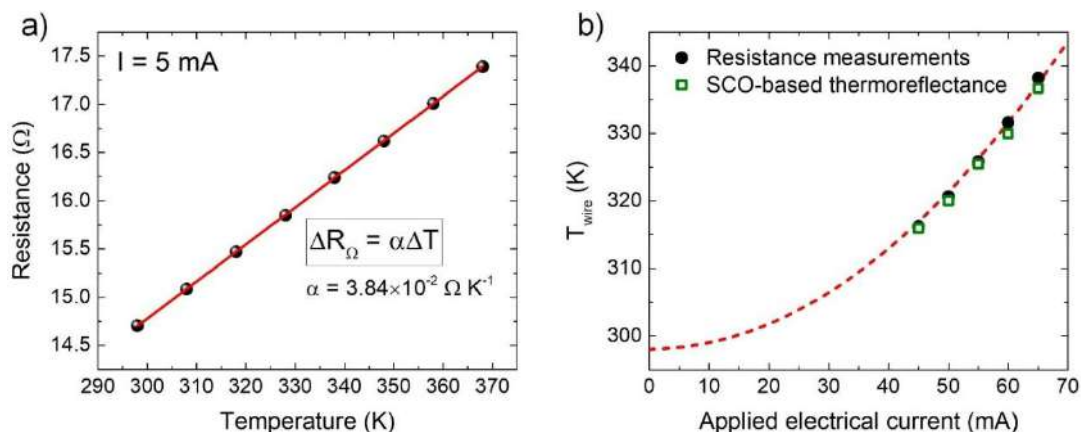


Figure 4.8. Comparaison avec les mesures de résistance électrique. a) Variation de la résistance électrique  $R_{\Omega}$  du microfil, mesurée à faible courant de polarisation (5 mA), en fonction de la température de base ( $T_b$ ) du substrat. Le coefficient de température linéaire du fil est  $\alpha = 3,84 \times 10^{-2} \Omega \text{ K}^{-1}$ . b) Température moyenne du fil chauffé par effet Joule,  $T_{\text{wire}}$ , pour différents courants électriques appliqués allant de 45 à 65 mA ( $T_b = 298 \text{ K}$ ), déduite de l'imagerie thermique par thermoréfectance (carrés vides) et des mesures de résistance électrique (cercles pleins). La ligne pointillée rouge indique l'évolution quadratique typique de la résistance (et donc de la température du fil) avec le courant électrique appliqué.

Dans l'ensemble, ces données démontrent la possibilité d'utiliser des films minces à TS de **1** pour imager la température de surface à l'échelle micrométrique avec une précision thermique de l'ordre de  $\sim 1 \text{ K}$  (en utilisant une simple détection optique basée sur un CCD), en profitant d'une amélioration d'environ un ordre de grandeur du coefficient de thermoréfectance de la lumière UV apportée par la présence de la couche à TS. La résolution spatiale et temporelle ultime du thermomètre à base de matériau à TS n'a pas été étudiée, car cela nécessiterait un équipement plus sophistiqué, bien que le coefficient de thermoréflexion amélioré soit manifestement un atout clé dans ce contexte. En outre, le fait que les films fonctionnent dans la gamme spectrale UV est clairement avantageux pour l'imagerie sub-micrométriques. Par exemple, un puissant objectif de microscope avec une ouverture numérique de 0,9 peut fournir un spot de 0,35 micron à une longueur d'onde de 310 nm. En ce qui concerne la résolution temporelle, le facteur limitant est la vitesse de diffusion de la chaleur dans le film, le phénomène de TS moléculaire étant intrinsèquement plus rapide.<sup>258</sup> En effet, en raison de leur faible diffusivité thermique, le processus de thermalisation de ces films à TS est achevé en  $\sim 1 \mu\text{s}$ , ce qui définit donc la résolution

temporelle accessible du thermomètre de surface. Des expériences sur des films moléculaires similaires indiquent qu'un film de **1** de 100 nm d'épaisseur pourrait potentiellement permettre des mesures de température jusqu'à l'échelle de temps de la  $\mu\text{s}$ .<sup>29</sup> Dans l'ensemble, les caractéristiques thermométriques démontrées dans le présent travail sont virtuellement comparables à ceux obtenus avec le composé  $[\text{Fe}(\text{HB}(1,2,4\text{-tz})_3)_2]$ ,<sup>29</sup> en termes de résolution thermique, spatiale et temporelle accessible. Cependant, il convient de souligner que les approches thermométriques utilisées dans ces deux cas sont totalement différentes, chacune ayant ses avantages et ses inconvénients. L'utilisation du composé  $[\text{Fe}(\text{HB}(1,2,4\text{-triazol-1-yl})_3)_2]$  (siège d'une transition de spin abrupte) a permis une détection binaire de la température de surface, fonctionnant sur n'importe quelle surface sans la nécessité d'une procédure d'étalonnage thermique de la réflectivité optique. Cependant, dans ce cas, les cartes de température de surface n'ont pas pu être acquises en temps réel. Inversement, l'utilisation du composé **1** permet une imagerie thermique en temps réel, sur la base d'un étalonnage thermique préalable de la réflectivité optique. Cependant, comme l'augmentation du coefficient de thermoréflexion induite par le film à TS dépend de la surface, cette méthode de thermométrie n'est pas aussi efficace sur toutes les surfaces.

# Chapter 1. Introduction

## 1.1 Spin-crossover phenomenon

Spin crossover (SCO) phenomenon refers a change in spin state of first-row transition metal complexes with central ion electronic configurations of  $d^4$ – $d^7$  induced by external stimuli that include temperature, pressure, light or magnetic field.<sup>1,2</sup> The phenomenon typically occurs in complexes with octahedral ligand field and is the most abundant for electronic configuration  $d^6$  where iron(II) complexes are prevalent examples.<sup>2</sup> The metal complexes can undergo SCO only when the ligand field energy and the electron pairing energy in the  $d$ -orbitals are comparable.<sup>3,4</sup> In case of iron(II), SCO is commonly observed in complexes with nitrogen-donor ligands where the metal ion environment is usually  $\text{FeN}_6$  or  $\text{FeN}_4\text{O}_2$ .<sup>2</sup> The spin state change in  $\text{Fe}^{\text{II}}$  complexes is realized *via* reversible switching between diamagnetic ( $S = 0$ ) low spin (LS) and paramagnetic ( $S = 2$ ) high spin (HS) electronic configurations (Figure 1.1).<sup>5–7</sup>

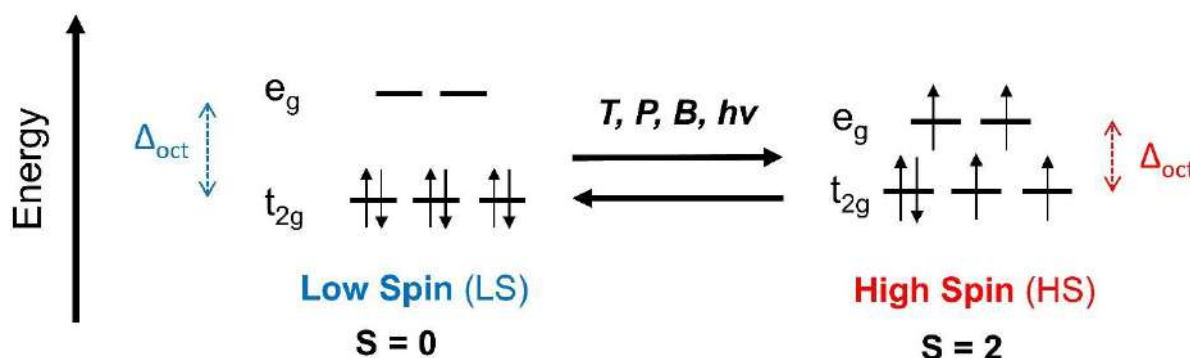


Figure 1.1. Energy diagram of spin crossover LS-HS switching for  $d^6$  configuration.

Thus, the change in spin state involves changes in physical properties of the complexes, namely magnetic properties, optical properties (*e.g.*, thermochromism),<sup>6,8,9</sup> changes in distances between  $\text{Fe}^{\text{II}}$  centers and ligand donor atoms and, consequently, change in molecular volume.<sup>10</sup>

Spin crossover is a cooperative phenomenon, which means that the changes at the molecular level propagate throughout the bulk of the solid *via* cooperative interactions. The degree of the cooperativity depends on the crystal packing and the strength of intermolecular interactions. The latter determine the character of the spin crossover, which can be followed by spin transition curves that can be obtained from a plot of high-spin state fraction ( $\gamma_{\text{HS}}$ ) *vs* temperature (Figure 1.2).<sup>2</sup>

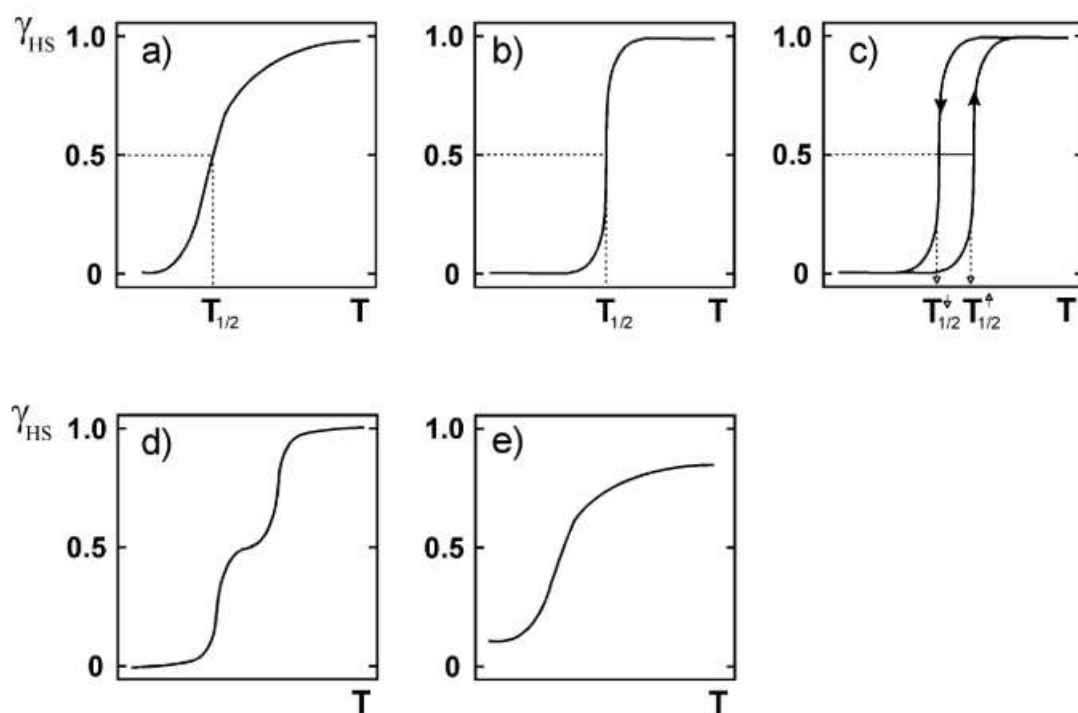


Figure 1.2. Representation of main types of SCO behavior (high spin fraction ( $\gamma_{HS}$ ) plotted as a function of temperature): **a)** gradual complete transition; **b)** abrupt transition; **c)** abrupt transition with hysteresis; **d)** two-step transition; **e)** gradual incomplete transition.<sup>2</sup>

As shown on Figure 1.2, there are several principal types of the spin transition behavior, where each of them correlates with the degree of cooperativity in the substance. Thus, the *gradual* transition points to low cooperativity and is typical for the solids with weak intermolecular interactions, liquid and solid solutions where intermolecular interactions between SCO-active molecules are interfered or disrupted. In contrary, systems with highly cooperative interactions exhibit *abrupt* spin transition and the transition *with hysteresis*, when the cooperativity is especially strong. This type of spin transition is inherent in the substances with supramolecular interactions such as intermolecular hydrogen bonding or  $\pi$ - $\pi$  stacking interactions and in SCO coordination polymers. The *two-step* transition is observed usually in binuclear spin crossover systems or in those containing two SCO-active sites in their crystal lattice. In certain lattices the spin state change cannot propagate throughout the bulk of the solid fully, in which case the transition is *incomplete*.

## 1.2 Applications of the SCO materials

Considering the switching of the properties the SCO phenomenon involves under external perturbation and considering the character of this change, the phenomenon is of interest for application in miscellaneous switchable materials.<sup>11</sup> Some examples of the applications will be considered in this sub-chapter. Thus, the ligand field change induced by spin crossover alters the optical absorption of the

complex, *i.e.*, leads to the color change. In case if the SCO is thermally induced, this color change is called thermochromism (Figure 1.3). Thermochromic materials can be used for thermochromic paints, surface-temperature sensors or in displays.<sup>8,12</sup> Seredyuk *et al.* have synthesized thermochromic SCO liquid crystals operating in near-room-temperature region.<sup>8</sup> Owing to an intrinsic property of liquid crystals to form thin layers, the researchers were able to obtain the liquid crystalline thin films. Thermochromic liquid crystalline materials are interesting for application in screens and displays.

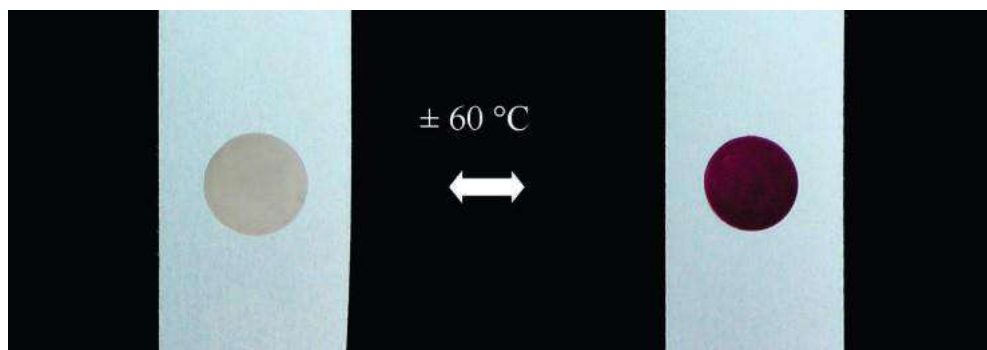


Figure 1.3. Thermochromism in the SCO liquid crystalline thin films upon switching between HS (left) and LS (right) states.<sup>8</sup>

The transition from low spin to high spin state implies the population of antibonding  $e_g$  orbitals leading to elongation of distances between  $\text{Fe}^{\text{II}}$  and donor atoms of the ligand that involves molecular and unit-cell volume expansion. In some complexes, *e.g.*,  $[\text{Fe}(\text{Htrz})_2(\text{trz})]\text{BF}_4$  the volume expansion may reach as much as 10%.<sup>13</sup> Such drastic changes in bulk of the substance affect its mechanic properties and makes it suitable to use for mechanical actuators.<sup>14–16</sup> For example, Bousseksou *et al.* have elaborated macroscale actuators based on  $[\text{Fe}(\text{Htrz})_2(\text{trz})]\text{BF}_4$  nanoparticles.<sup>17</sup> To this purpose, the authors have incorporated the SCO nanoparticles into a polymer matrix and deposited the obtained nanocomposite on top of a freestanding polyester film. Then, the resulting bilayer was cut into six-petal flower shape. Then, the volume change, induced by spin crossover generated macroscale mechanical movements, *i.e.*, opening/closure of the “flower” (Figure 1.4), which was reversible upon heating or cooling of the object. Such switchable materials can be used to fabricate artificial muscles activated under external stimulus.

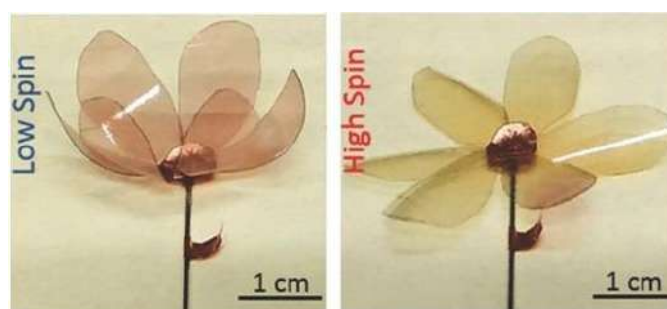


Figure 1.4. SCO-induced mechanical actuation in a macroscale bilayer composite material.<sup>17</sup>

As the SCO phenomenon depends on intermolecular interactions, it can be affected by guest molecules entering the host SCO matrix so the latter can act as a chemical sensor to detect volatile organic compounds, hazardous solvents and even gases.<sup>18–22</sup> Real and co-workers have investigated influence of trapped CS<sub>2</sub> and benzene guest molecules on the spin state of porous coordination polymer [Fe(pyrazine)Pt(CN)<sub>4</sub>].<sup>23</sup> The collaborators have found that accommodation of benzene molecules by the complex favored the high spin state at room temperature, while CS<sub>2</sub> guests stabilized the low spin state (Figure 1.5a). Thus, the response of the host SCO system is determined by nature of the guest. Besides altering of the magnetic properties, the system also showed color change upon guest trapping and desolvation of the host framework (Figure 1.5b). Together with detection of solvents and volatile organic compounds, SCO complexes were also reported to detect marker-gases of spoiled food.<sup>22</sup>

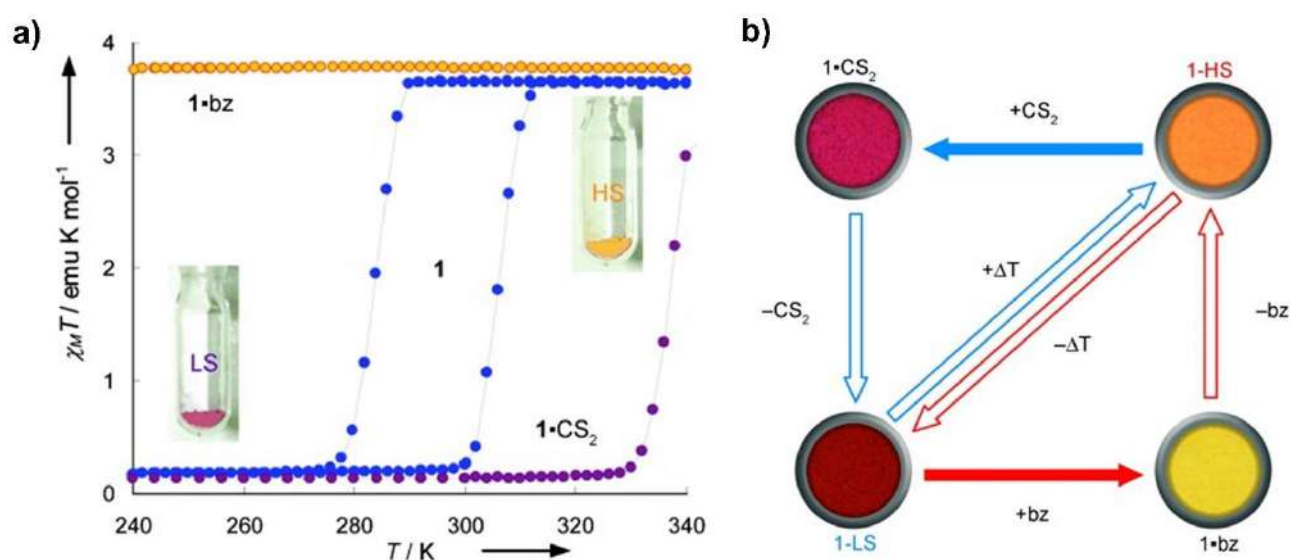


Figure 1.5. a) Thermal variation of molar magnetic susceptibility of pristine [Fe(pyrazine)Pt(CN)<sub>4</sub>] (in blue), its benzene (in yellow) and CS<sub>2</sub> solvates (in purple). Inset photographs show color of the respective solvate powders; b) Color change in response to chemically and thermally induced SCO.<sup>23</sup>

Compounds displaying the transition with hysteresis can be employed for fabrication of memory devices.<sup>7,24–26</sup> Kraieva *et al.* have coated a gold microwire heater with a layer of [Fe(Htrz)<sub>2</sub>(trz)]BF<sub>4</sub> nanoparticles exhibiting hysteretic spin transition (Figure 1.6).<sup>25</sup> Maintaining the device at temperature within the hysteresis loop, and applying an electrical current bias to the microwire heater the authors were able to detect transient heating events. After overpassing the threshold temperature, the complex undergoes transition to the high spin state, in which it can be maintained if the temperature stays within the range of the hysteresis loop. Such a bistability of the SCO layer allows for thermal memory, *i.e.*, *a posteriori* read-out of optical information on the temperature changes. The authors were able also to map the transient thermal events. A possible application of such a temperature sensor is to detect overheating above a threshold temperature in micro- or nanoelectronic devices over their long-term operation. Spin

crossover also involves changes in electrical properties of the substance, such as electrical resistivity, which allows for use in electronic devices.<sup>27</sup> In this context, materials with abrupt transition are interesting in the prospective of use for resistance switching junctions.<sup>28</sup> Another application for the abrupt spin transition concerns binary temperature sensing.<sup>29</sup> In contrary, spin crossover materials with gradual spin transition can serve as continuous thermometers affording their application in micro- and nanothermometry (see sub-chapter 1.7).<sup>29,30</sup>

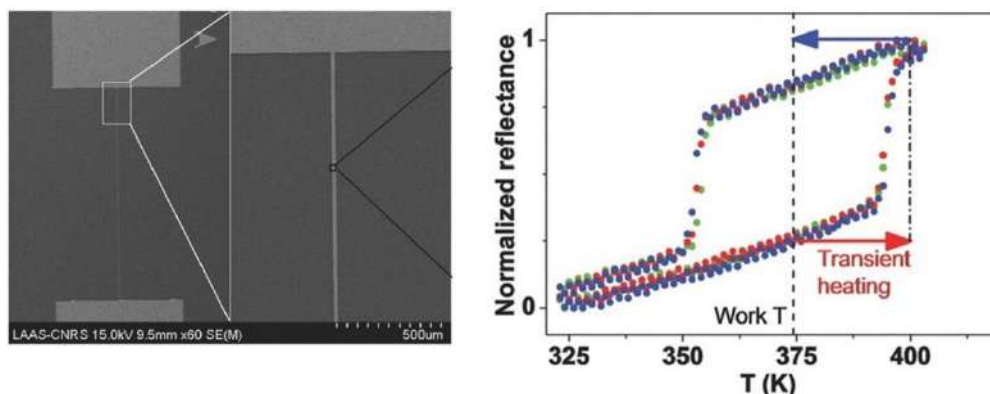


Figure 1.6. Scanning electron microscopy images (left) of the microwire heater coated with  $[\text{Fe}(\text{Htrz})_2(\text{trz})]\text{BF}_4$  layer and temperature-dependent optical reflectivity (right) of the microwire device for three consecutive heating/cooling cycles.<sup>25</sup>

As it was shown in the examples above, in order to be implemented for applications, spin crossover complexes are predominantly used in a form of SCO materials (Figure 1.7), which can be: liquid crystals,<sup>8</sup> nanoparticles (NPs),<sup>31</sup> thin films<sup>32–35</sup> and (nano)composites.<sup>36</sup> Particular attention will be focused on the fabrication and the characterization of SCO thin films in the next sub-chapter.

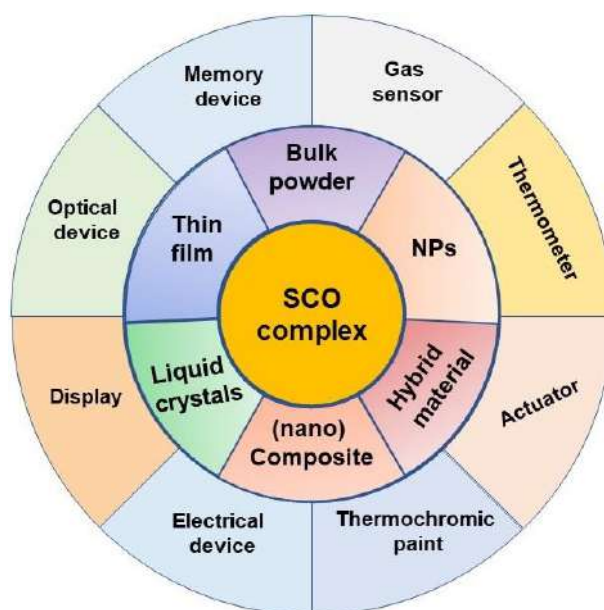


Figure 1.7. Scheme gathering possible material forms in which the SCO compound can be processed and applications of the complexes and materials.

### 1.3 SCO thin films: fabrication and characterization

An important class of SCO materials is represented by thin films.<sup>34,35</sup> Over decades of research, various techniques to obtain the thin films have been developed, which include: *Langmuir-Blodgett technique*,<sup>37,38</sup> *spin coating*,<sup>39,40</sup> *drop casting*,<sup>41</sup> *surface layer-by-layer assembly*,<sup>33,42</sup> *vacuum deposition*,<sup>43,44</sup> etc.<sup>34</sup> Preparation of spin-crossover thin films by *Langmuir-Blodgett technique* involves the use of surface-active SCO complexes that form monolayer on top of water solution, which is then transferred on top of a substrate by dipping the latter into the solution (Figure 1.8a). Multilayer films can also be obtained using this approach. The technique is simple and convenient in realization, however suffers from disadvantages and limitations, such as instability of the SCO compounds on the gas-liquid interface upon transfer onto a substrate, and limited number of amphiphilic spin-crossover molecules, which are challenging to obtain. One of the most used methods to deposit SCO thin films is *spin coating*. In this method, a drop of spin-crossover compound solution in a volatile solvent is deposited onto surface of a rotating substrate (Figure 1.8b). Rotation allows a uniform distribution of the solution on the substrate surface and promotes evaporation of the solvent leading to formation of the thin film. Spin coating often affords homogenous thin films. It is possible to control the thickness and morphology of thin films of functional materials by controlling parameters such as rotation speed, temperature, nature of the solvent and the substrate.<sup>45</sup>

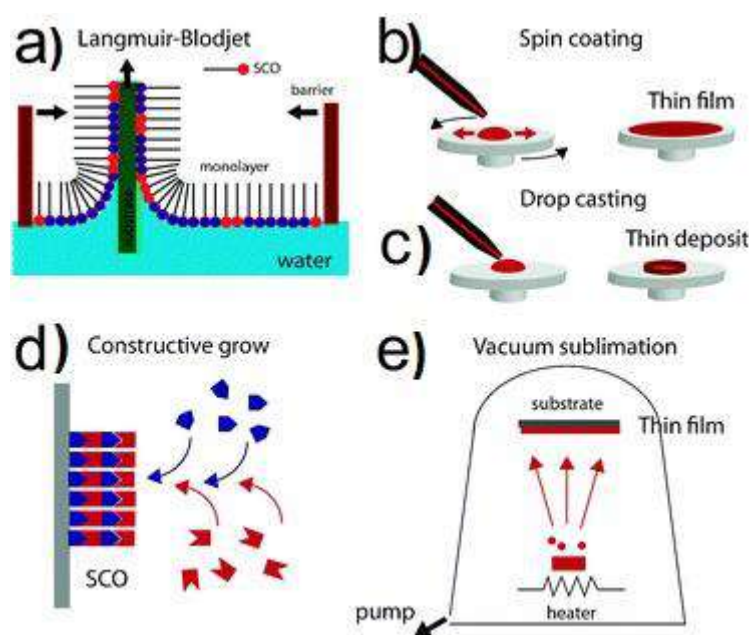


Figure 1.8. Techniques of SCO thin film deposition: a) Langmuir-Blodgett; b) Spin coating; c) Drop casting; d) Surface layer-by-layer assembly; e) Vacuum deposition.<sup>34</sup>

The simplest way of the thin film preparation is *drop casting*, as it requires a simple deposition of a SCO solution onto a substrate, whereupon evaporation of the solvent in controlled conditions results

in thin film formation (Figure 1.8c). The technique is rarely used as the resulting thin films are inhomogeneous. Nevertheless, the method is suitable for preliminary tests for which homogeneity is not mandatory. Alternatively, spin-crossover complexes can be synthesized directly on the substrate surface by means of *surface layer-by-layer assembly*, which includes dipping of a substrate in a series of solutions containing the necessary building-blocks (Figure 1.8d). The method allows to control the orientation of the assembled thin films. *Vacuum deposition* allows to grow pure and high-quality thin films with precise control of the thickness and morphology. In this method, sublimation of a solid SCO complex *via* heating in a high-vacuum chamber is followed by its deposition onto a substrate surface (Figure 1.8e). This thin film deposition technique is promising for elaboration of functional devices and will be discussed further in the current sub-chapter.

Properties of thin films obtained by any of the discussed techniques often depend on their characteristics such as thickness, surface morphology, crystallinity etc. There are various characterization techniques allowing to study these thin film characteristics. One of such techniques is atomic force microscopy (AFM).<sup>46,47</sup> This very high-resolution scanning probe microscopy method deals with either repulsive or attractive forces that atoms of the investigated surface impose on front atoms of a very sharp needle that moves across the surface being in close proximity or even in direct contact with the latter. The needle, which is also referred as tip, is fixed on a flexible cantilever, the back of which is illuminated by a laser. The laser beam is then reflected to a detector, which is sensitive to any deflections of the cantilever over the course of the surface scanning, that are then processed by a computer (Figure 1.9). Processing vertical deviations of the cantilever moving along a line of the surface gives the surface profile, while multiple scans within certain area of the surface allow to obtain an AFM image of the surface within this area (Figure 1.9). The method is operational under air, vacuum or liquid. AFM is a key technique for thin film characterization as it allows nanometer-scale measurements of a range of parameters. One of the parameters that can be determined with precision is thickness. Before the film deposition on the substrate, certain areas of the latter can be covered with a mask material that can be removed after the deposition leaving the pristine substrate surface. The thickness can be deduced from the step in the surface profile taken at the intersection between the thin-film-coated and uncoated substrate surfaces. AFM allows to estimate homogeneity of thin films and to measure how smooth is the thin film surface, which can be determined from average value between the highest and the lowest points of the surface profile giving the parameter known as *mean roughness* ( $R_a$ ) of the surface, that is a characteristic criterion for certain surface morphologies. For example, polycrystalline thin films tend to have grainy morphologies, so their surfaces are rougher than for, *e.g.*, amorphous films. It was demonstrated in the work of Shalabaeva *et al.*, who have deposited nanometric thin films of iron(II) bis[hydrotris(1,2,4-triazol-1-yl)borate] or  $[\text{Fe}(\text{HB}(1,2,4\text{-tz})_3)_2]$  (tz = triazol-1-yl) onto silicon and fused

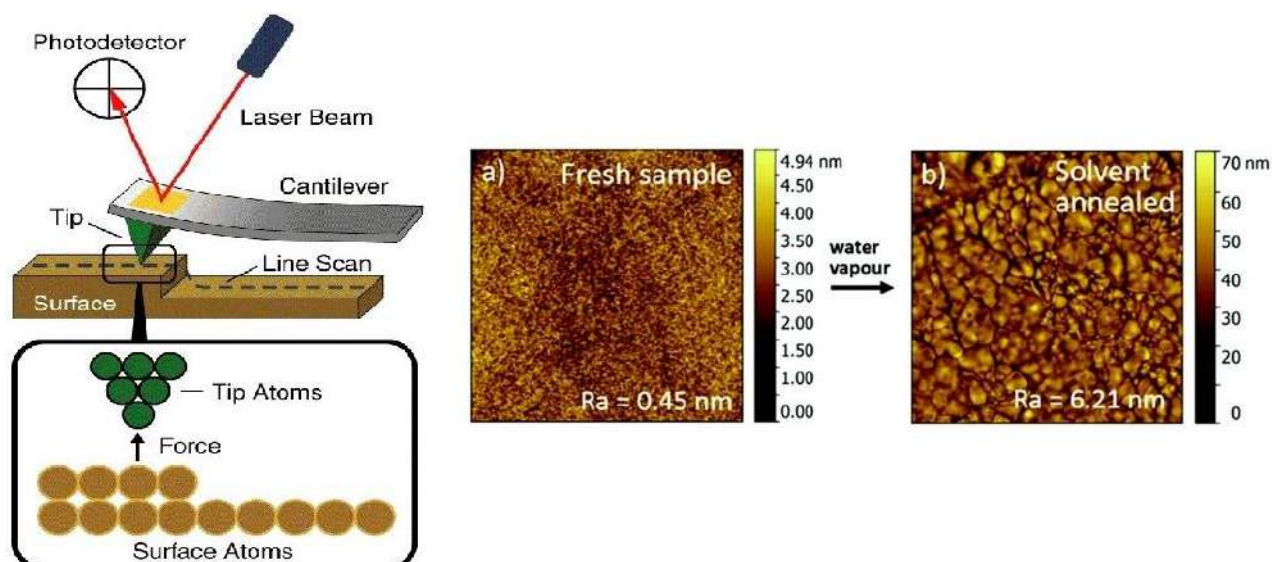


Figure 1.9. AFM operating principle (left)<sup>48</sup> and AFM images of  $[\text{Fe}(\text{HB}(1,2,4\text{-tz})_3)_2]$  thin films both freshly deposited and after treatment with water vapor (right). Image sizes:  $10 \times 10 \mu\text{m}^2$ .<sup>49</sup>

silica substrates by means of thermal vacuum evaporation.<sup>49</sup> The surface area of the films is around  $1 \text{ cm}^2$ . Typical scanning areas of the microscopy on thin films vary from  $4 \mu\text{m}^2$  to  $100 \mu\text{m}^2$ . The latter value is the maximum area that can be scanned by AFM. Scanning different regions of as-deposited films reveals variation of roughness from *ca.* 0.5 nm to 5 nm, which points to inhomogeneity of the films. It is explained by amorphousness of the as-deposited films. Exposure of the films to water vapor induces their crystallization, which leads to changes in the surface morphology and roughness (Figure 1.9). Unlike to the initially amorphous as-deposited films, the resulting polycrystalline films are homogeneous across all the surface area. Alternative method to investigate the surface morphology of thin films is scanning electron microscopy (SEM). This electron microscopy technique implies scanning of the studied surface with a focused electron beam under vacuum conditions (Figure 1.10a).<sup>50,51</sup> Interaction of electrons from the beam with the surface atoms produces various signals (secondary/backscattered electrons, characteristic X-ray) that can be detected and processed to give a two-dimensional (2D) image (Figure 1.10b-d). Incident electrons from the beam have enough energy to knock off electrons from the electron shells of the sample atoms to produce secondary electrons, or, otherwise the incident electrons can be backscattered from the atoms. Both secondary and backscattered electrons are useful for imaging. Though, secondary electrons are typically used for surface morphology studies. SEM affords broader magnification range than AFM, which means that more surface area can be analyzed at a time, even multiple objects on surface can be in focus at a time. Thus, Molnár *et al.* used scanning electron microscopy to study micro- and nanopatterns of  $\text{Fe}(\text{pyrazine})[\text{Pt}(\text{CN})_4]$  coordination polymer they assembled on gold surface by combination of surface layer-by-layer and patterning approaches.<sup>52</sup> Magnification capabilities of the method allowed the researchers to scan arrays of patterns (Figure 1. 10bc) as well as isolated patterns in areas from  $\mu\text{m}^2$  to  $\text{mm}^2$  (Figure 1. 10cd).

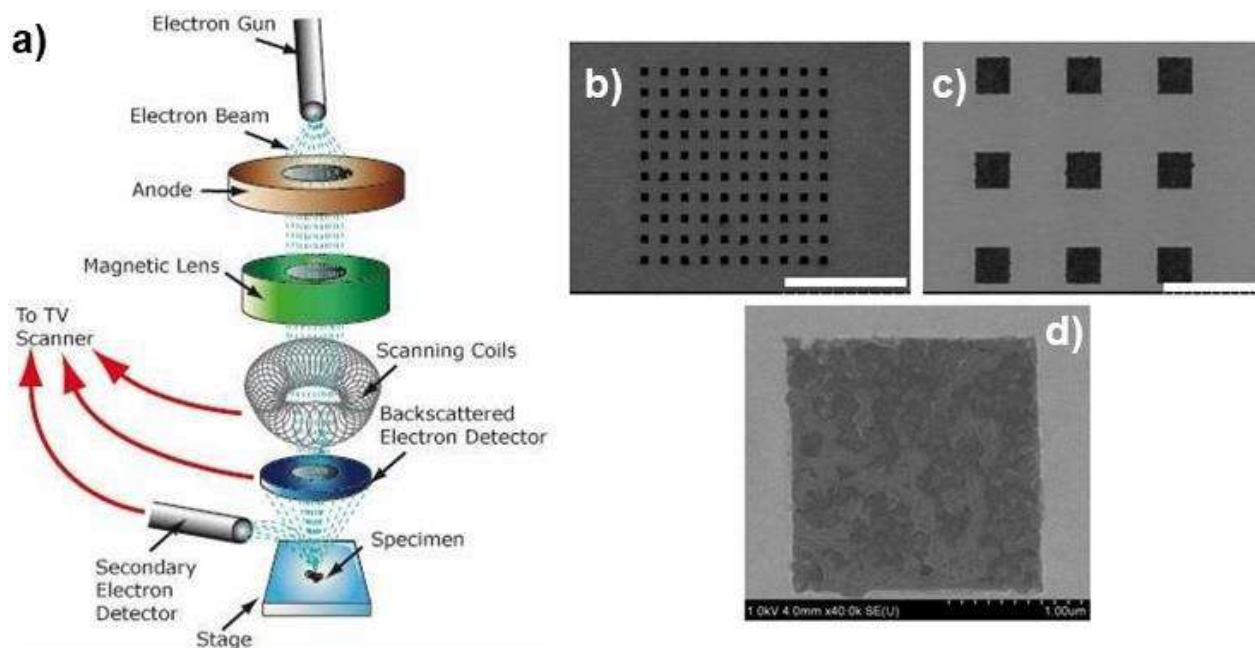


Figure 1.10. Simplified scheme of scanning electron microscope (a);<sup>53</sup> SEM images of 2  $\mu\text{m}$   $\text{Fe}(\text{pyrazine})[\text{Pt}(\text{CN})_4]$  pattern arrays (b,c) and the isolated 2  $\mu\text{m}$  pattern (d). The scale bars are 30  $\mu\text{m}$  (b), 5  $\mu\text{m}$  (c) and 1  $\mu\text{m}$  (d).<sup>52</sup>

Additionally, SEM can provide information on chemical composition of the sample. Thus, vacancy created after knocking off the electron from an inner shell of the atom is filled by electron migrating from the outer shell, which is followed by X-ray emission characteristic for a specific type of atom (Figure 1.11a). This response allows to obtain chemical information, such as elemental composition across certain area of the sample. High energy of incident electrons and emitted characteristic X-rays affords bulk studies of the sample and can be applied, *e.g.*, for analysis of multilayer structures composed of different materials. However, in conventional SEM setup the electron beam can be focused on certain area of the sample and typically does not allow to analyze all the sample surface at a time. Nevertheless, there is another method that makes possible surface analysis across the sample and provides even more chemical information, which is X-ray photoelectron spectroscopy (XPS). This surface technique is based on the opposite principle: detection of electrons knocked off from an atom due to absorption of incident X-rays (Figure 1.11b).<sup>54</sup> In addition to identification of the elements composing the sample surface, more information can be obtained from measurement of kinetic energy of an ejected electron (photoelectron) that allows to calculate binding energy of the electron, which is characteristic and gives information on chemical environment and electronic state of an atom from which it was ejected. Taking advantage from capabilities of the method, Atzori *et al.* have investigated a vacuum-deposited thin film ( $\sim 50$  nm) of  $[\text{Fe}(\text{qnal})_2]$  (qnal = quinoline-naphthaldehyde) and bulk powder of the complex.<sup>55</sup> The authors have

recorded XPS spectra at room temperature for both the thin film and the powder and compared them (Figure 1.12).

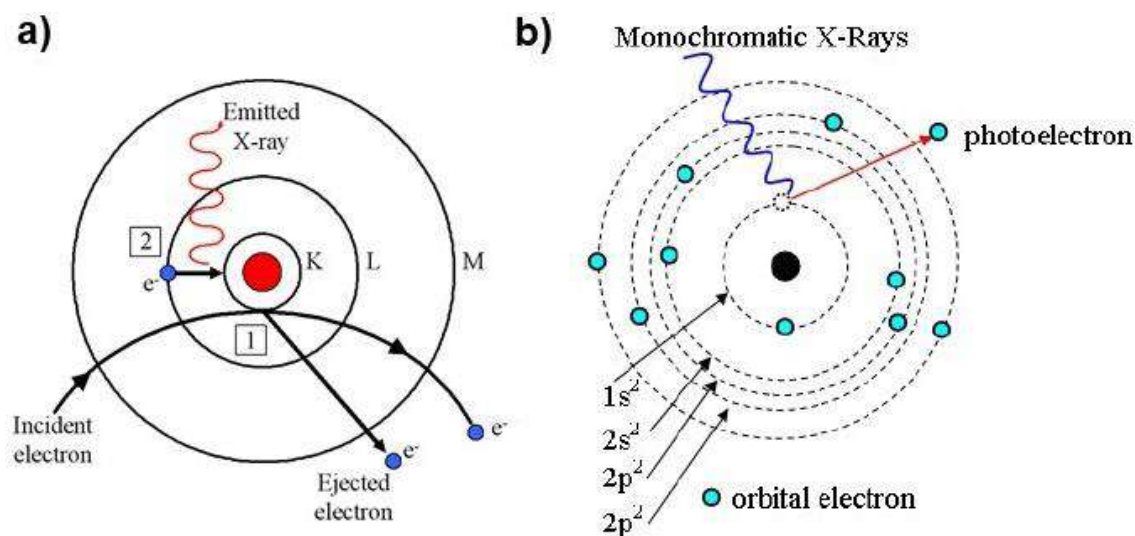


Figure 1.11. Representations of mechanism behind characteristic X-ray emission from an atom subjected to the electron beam (a)<sup>56</sup> and fundamental principle of the XPS (b).<sup>54</sup>

Analysis of Fe2*p* spectral region revealed a very close similarity between the both bulk powder and thin film spectra. Fitting of the spectra showed a shake-up structure inherent in paramagnetic species. Spin-orbit interactions cause appearance of two possible electronic states for the *p*-orbitals leading to two signals in the spectra, which is referred as spin-orbit splitting. The latter is determined as the energy difference between the two peaks. The value of the spin-orbit splitting in the studied materials was of *ca.* 13.3 eV, which is typical for paramagnetic Fe<sup>II</sup> complexes.<sup>57–59</sup> Thus, the researchers have concluded that at room temperature both thin film and bulk powder forms of the complex are in high spin state, which is in well accordance with magnetic measurements. Data from analysis of binding energies in the characteristic regions of lighter elements (C1*s*, N1*s*, O1*s*) composing the complex showed consistency with those obtained from crystallography and vibrational spectroscopies.

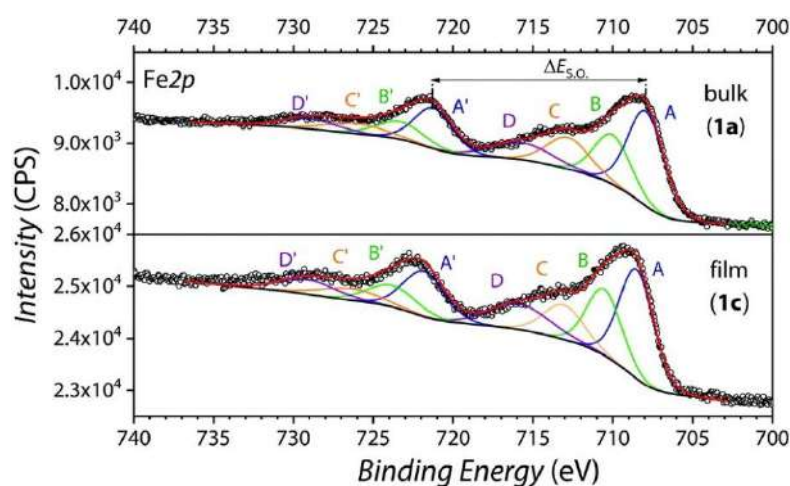


Figure 1.12. XPS spectra of [Fe(qnal)<sub>2</sub>] in bulk (top) and thin film (bottom) form.<sup>55</sup>

Finally, all the three techniques are very useful for thin film characterization. AFM provides information on physical properties of the thin film surface, while signals in SEM besides imaging of the investigated surface can give information on its elemental composition. In XPS, it is possible to analyze electronic states of the surface elements as well as their chemical environment. However, unlike to SEM, XPS can measure only up to 10-nm-thick layers of samples, which makes it a good characterization technique for ultra-thin films, while thicker samples need to be scratched for full analysis.

#### 1.4 Sublimable SCO complexes

The vast majority of applications involving the thin films require high quality, purity and homogeneity of the film. To fulfil these criteria, thermal vacuum deposition serves a powerful means.<sup>43,60</sup> As yet, only a scarce number of SCO complexes are known to be capable of being deposited by this technique (Figure 1.13).<sup>43,44,48,56,60–72</sup> Such a limited range of spin crossover compounds suitable for vacuum deposition can be explained by the fact that the compound-candidates for thermal vacuum evaporation should be prone to sublimation and thus meet certain criteria, such as relatively low molecular weight, charge neutrality, discrete structure and absence of solvent or other guest molecules in its crystal lattice. However, cationic iron(III) complex  $[\text{Fe}(\text{pap})_2]\text{ClO}_4 \cdot \text{H}_2\text{O}$  (pap = *N*-2-pyridylmethylidene-2-hydroxyphenylamino) is the only exclusion to this rule.<sup>64</sup>

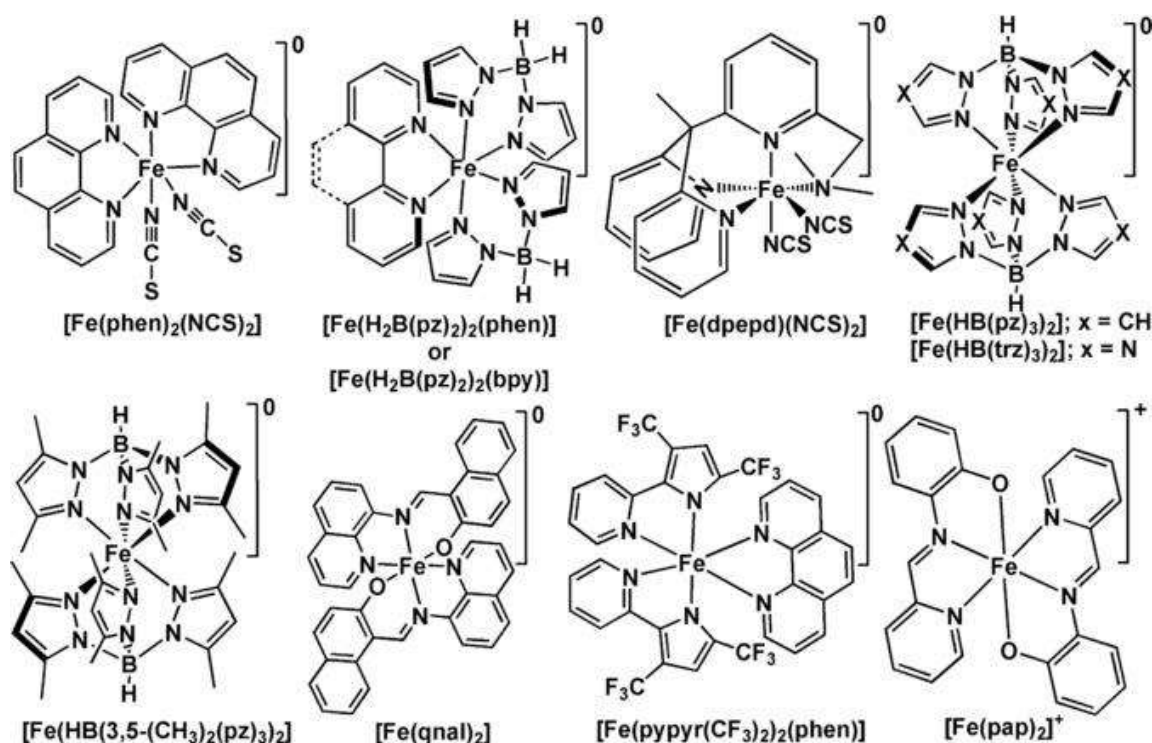


Figure 1.13. Structural formulae of evaporable SCO complexes.<sup>43</sup>

When deposited on a surface, the SCO properties of the thin films are determined by interplay of intermolecular and interfacial interactions, which depends on the thickness of the film and its crystallinity. Thus, tens-to-hundreds-nanometer-scale crystalline films tend to show spin crossover properties comparable to those the substances display in bulk, due to the distance to the interface making the intermolecular interactions more favored.<sup>43</sup> Amorphous or semicrystalline thin films demonstrate irreproducible SCO behavior or incomplete transition.<sup>49</sup> On the other hand, for the monolayer and sub-monolayer films the interfacial interactions play paramount role defining their SCO properties. The proximity to the interface imposes constraints on intermolecular interactions between the complex molecules leading to changes of the character and completeness of SCO comparing to the bulk behavior and may result in coexistence of both spin states at low temperatures.<sup>73,74</sup> Other important factors to consider for fabrication of the ultrathin films are the nature of the substrate and the molecular design of the complex. Thus, heteroleptic Fe<sup>II</sup> complexes [Fe(H<sub>2</sub>B(pz)<sub>2</sub>)<sub>2</sub>phen], [Fe(H<sub>2</sub>B(pz)<sub>2</sub>)<sub>2</sub>bpy] (pz = pyrazol-1-yl; phen = 1,10-phenanthroline; bpy = 2,2'-bipyridine), some of their derivatives substituted at phen or bpy cores and [Fe(pypyr(CF<sub>3</sub>)<sub>2</sub>)<sub>2</sub>phen] (pypyr = 2-(2'-pyridyl)pyrrolide) can undergo surface-induced fragmentation to [FeL<sub>2</sub>] or [FeL]<sup>+</sup> (L = H<sub>2</sub>B(pz)<sub>2</sub> or pypyr respectively) and phen (bpy) on certain metallic substrates at monolayer and sub-monolayer coverages.<sup>75-77</sup> In contrary, homoleptic iron(II) complexes with scorpionate-type tripodal hydrotris(azol-1-yl)borate ligands<sup>78</sup> do not dissociate on surfaces and can represent a stable alternative to their heteroleptic counterparts.<sup>74</sup>

The majority of applications require materials switching around or above room temperature.<sup>6</sup> Among the sublimable SCO complexes, only a few are known to undergo spin crossover above room temperature both in bulk and thin film states, those include [Fe(pypyr(CF<sub>3</sub>)<sub>2</sub>)<sub>2</sub>phen],<sup>79</sup> [Fe(HB(pz)<sub>3</sub>)<sub>2</sub>]<sup>67,68</sup> and [Fe(HB(1,2,4-tz)<sub>3</sub>)<sub>2</sub>] (Figure 1.13).<sup>49</sup> It is noteworthy that the two latter belong to the scorpionate family of complexes. The temperature of spin transition  $T_{1/2}$  for Fe-pypyr thin films (~330 K) is nearly 60 K lower comparing to the bulk substance (390 K), when the other two compounds show comparable SCO properties in bulk and thin film forms ( $T_{1/2} \approx 393$  K and 335 K for the pyrazolyl and triazolyl derivatives, respectively). The properties of [Fe(HB(1,2,4-tz)<sub>3</sub>)<sub>2</sub>] thin films were investigated for 20-200 nm thickness range. It was found that the considered films are of high quality and show unprecedented endurance towards thermal cycling withstanding over 10 million heating-cooling cycles remaining intact.<sup>29</sup> Such an outstanding stability of the films make them appropriate materials to elaborate miscellaneous functional devices for photonics, molecular electronics, actuators, sensors and temperature damping.<sup>29,80-83</sup> Thus, Manrique-Juarez and co-workers have elaborated a microelectromechanical system (MEMS) actuated by spin crossover.<sup>80</sup> The researchers have deposited a 140 nm thin film of [Fe(HB(1,2,4-tz)<sub>3</sub>)<sub>2</sub>] on top of a freestanding silicon microcantilever with an

integrated piezoresistive detection system. Spin transition induced mechanical strain in the system lead to reversible static bending of the cantilever (Figure 1.14). SCO also imposed a dynamical effect on the

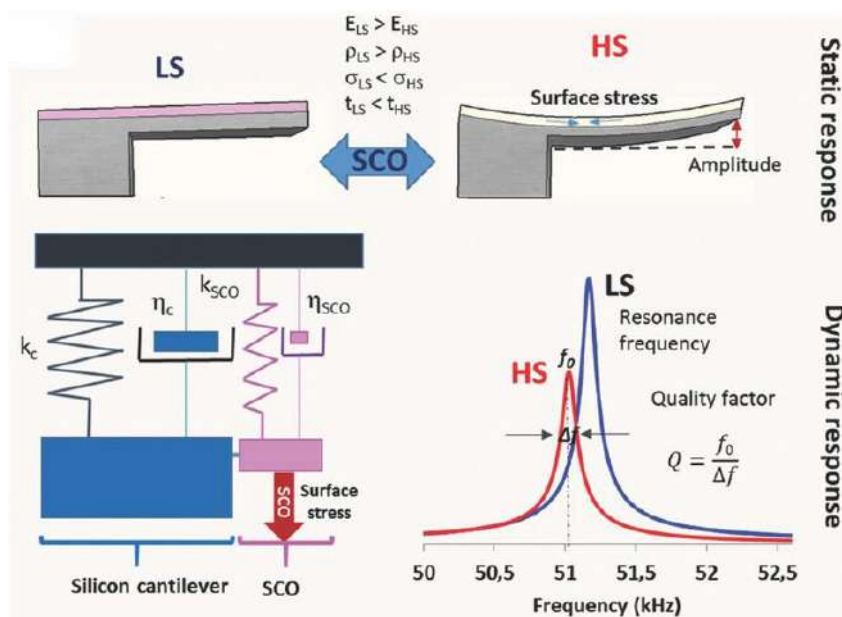


Figure 1.14. Static and dynamical effects imposed on the MEMS by SCO.<sup>15,80</sup>

system, such as a decrease in resonance frequency of the MEMS by  $\sim 66$  Hz in HS state comparing to the LS state (Figure 1.14). Such a mechanical integration of the SCO nanomaterial into the system, makes it attractive for application in mechanical transduction (conversion of mechanical energy to electrical one) controlled by external stimuli. Thin films of the same SCO complex were used in the work of Zhang *et al.*, who fabricated electrical junctions with switchable electrical resistance.<sup>28</sup> The junctions were composed of indium-tin oxide (ITO) anode, layer of  $[\text{Fe}(\text{HB}(1,2,4\text{-tz})_3)_2]$  and metal cathode of aluminum or calcium (Figure 1.15a). The insulating layer of the SCO film had higher resistance in HS state than in low-spin state. The authors have measured current-voltage and current-temperature characteristics of the devices in heating and cooling modes (Figure 1.15b) and found them similar independently on the cathode material. Therefore, the resistance switching is not governed by electron injection from the cathode but rather by transport of charge-carriers that depends on the spin

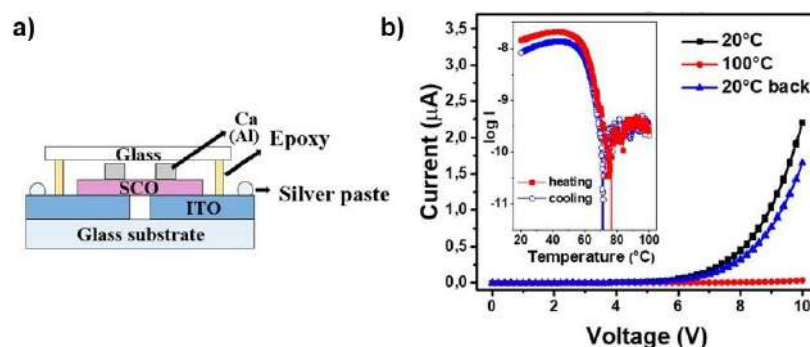


Figure 1.15. a) Scheme of ITO/ $[\text{Fe}(\text{HB}(1,2,4\text{-tz})_3)_2]/\text{M}$  ( $\text{M} = \text{Al}, \text{Ca}$ ) junction; b) Electrical characteristics of ITO/ $[\text{Fe}(\text{HB}(1,2,4\text{-tz})_3)_2]/\text{Al}$  junction measured in heating and cooling modes.<sup>28</sup>

state. Consequently, electrical junctions based on SCO thin films can be used as resistance switches. As follows from the considered examples, spin crossover occurring in a material induces a range of phenomena interesting for various applications, however spin crossover in a single molecule has also attracted an immense interest of researchers. Miyamachi *et al.* reported electrical switching in a single molecule of  $[\text{Fe}(\text{phen})_2(\text{NCS})_2]$  deposited on Cu(100) substrate covered with copper nitride layer by applying a voltage bias to the molecule from a tip of scanning tunneling microscope (Figure 1.16a).<sup>84</sup> Negative voltage applied leads to transition of the molecule to high spin state (higher tunneling current, higher conductance), while applying positive bias returns it to the LS state (Figure 1.16b). By applying sequential pulses of positive and negative biases it was demonstrated that the state of the molecule can be deterministically selected, as after switching the molecule to LS state by a pulse of positive bias it will not switch back to HS state by the second positive pulse, but it is possible applying the negative pulse (Figure 1.16c). Such single-molecule devices can be used in the field of information storage, *e.g.*, spintronics etc. Though the discussed complexes and their thin films are substantively studied and some of them implemented to functional devices, this domain requires new compounds for its development.

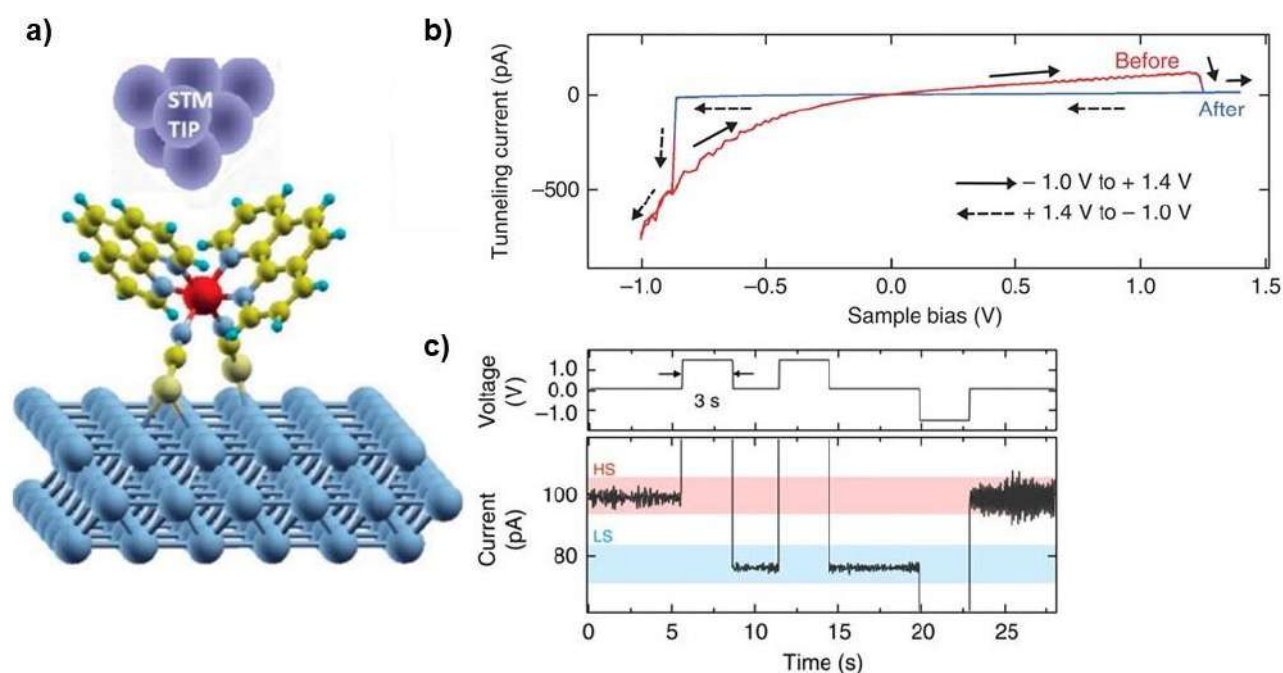


Figure 1.16. a) Isolated  $[\text{Fe}(\text{phen})_2(\text{NCS})_2]$  molecule on CuN/Cu(100) surface electrically switched *via* tip of scanning tunneling microscope; b) Current-voltage characteristics of the isolated molecule; c) Application of two consecutive pulses of positive voltage bias following with negative one demonstrates deterministic character of the switching.<sup>27,84</sup>

Recent works of several research groups reported a potential extension to the family of sublimable spin crossover compounds switching their spin states above room temperature.<sup>85–87</sup> The reported compounds belong to the class of heteroscorpionates. Unlike to common (homo)scorpionates, in heteroscorpionates the N-donor azol-1-yl rings are not identical.<sup>78</sup> Flötotto *et al.* have developed a

synthetic path to access new iron(II) heteroscorpionates, which implies an exchange of pyrazole ring to 4-nitropyrazole one in the initial  $[\text{HB}(\text{pz})_3]^-$  ligand driven by the difference in  $\text{pK}_a$  of the heterocycles (Figure 1.17).<sup>85</sup>

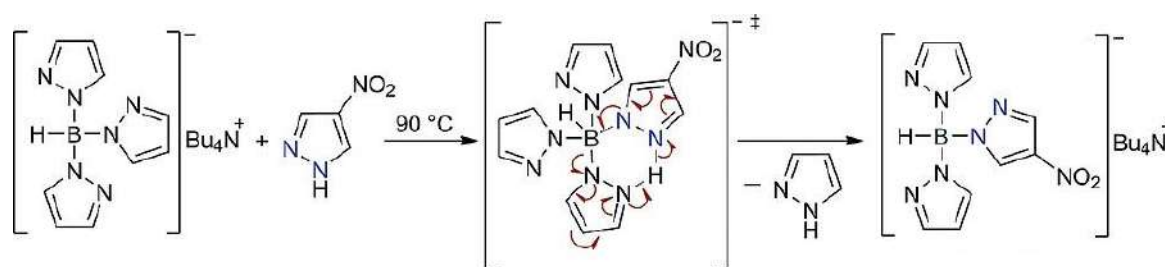


Figure 1.17. Synthesis of heteroscorpionate ligands by heterocycle exchange reported in ref.<sup>85</sup>

They have successfully demonstrated that controlling the temperature and stoichiometry it is possible to selectively substitute from one to all the three pyrazol-1-yl moieties in the anionic ligand with the nitro counterpart. Moreover, susceptibility of  $\text{NO}_2$ -group to reduction offers a route to post-modification of the complexes (Figure 1.18). The authors reported syntheses of the amino-derived ferrous compound  $[\text{Fe}(\text{HB}(4\text{-NH}_2\text{pz})(\text{pz})_2)_2]$  together with its amide, imine and azo products of post-functionalization. All the obtained compounds undergo thermal spin crossover in 340–500 K range of temperatures (Figure 1.19).

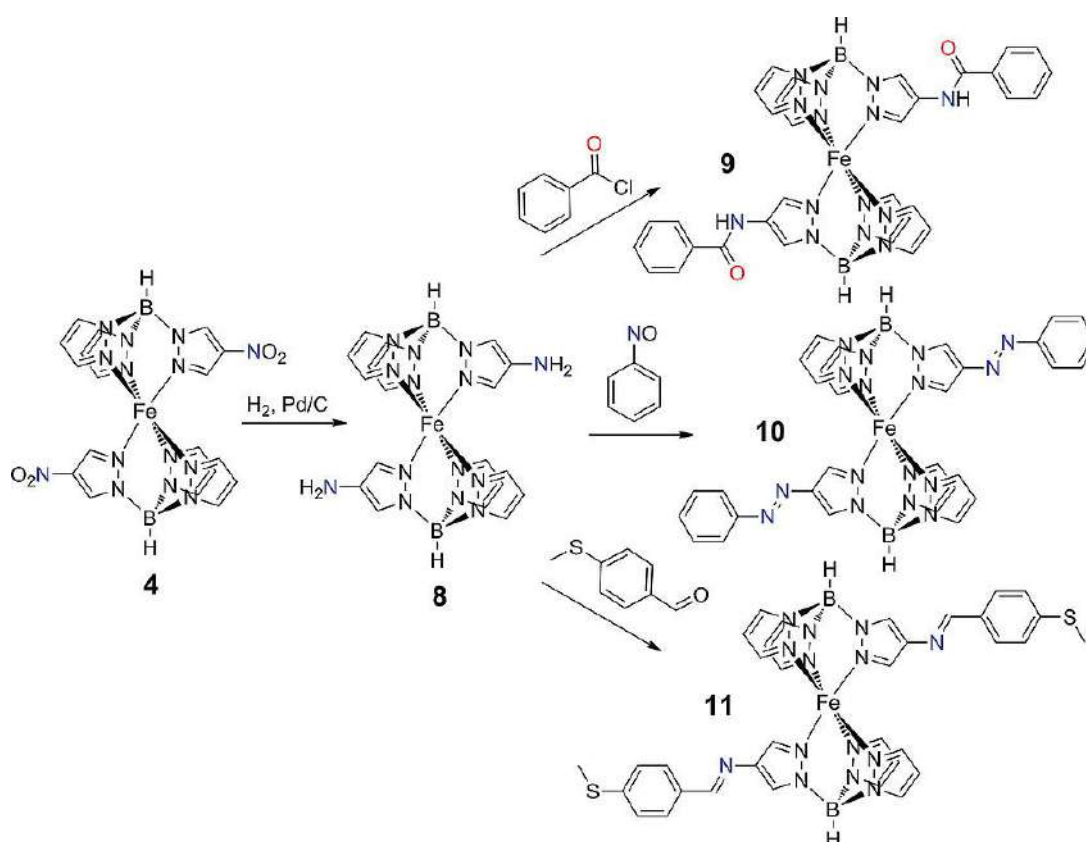


Figure 1.18. Post-synthetic functionalization of the nitro-derived heteroscorpionates.<sup>85</sup>

Though the thermal stability of the compounds was studied, the authors do not report the sublimation of the complexes. Using the above-discussed reaction of pyrazole exchange with 3(5)-nitro- and 4-nitropyrazols, Ma *et al.* have complemented the library of nitro- and amino-decorated iron(II) hydrotris(pyrazol-1-yl)borates.<sup>86</sup>

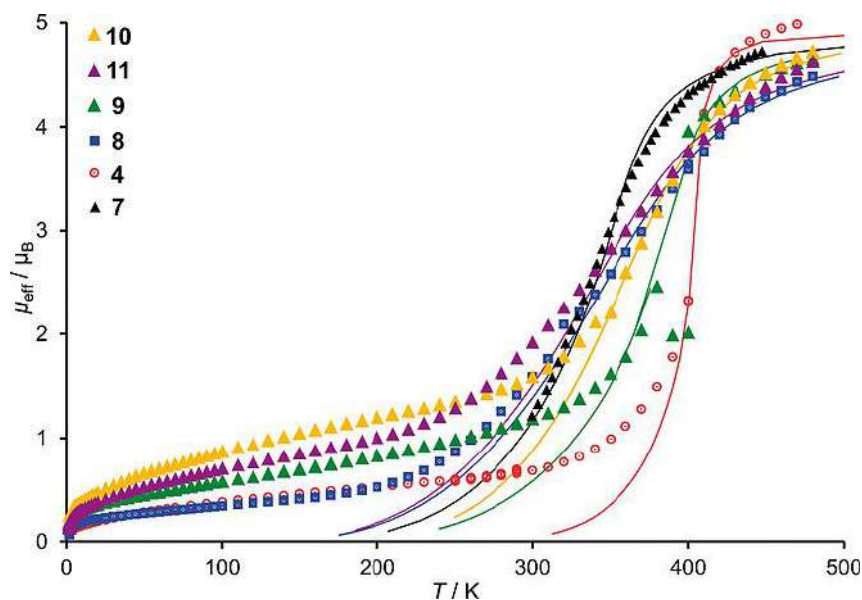


Figure 1.19. Temperature-dependent molecular magnetic moment of the initial nitro-complex and the post-modification products (see Figure 1.18).<sup>85</sup>

The researchers have shown that the occurrence of SCO behavior in the resulting complexes depends on steric and electronic factors determined by the substituent position of the pyrazole ring, its steric demands and electronic properties. For example, the substitution with nitro-group at the position 3 makes thermal spin crossover impossible, as the steric effect of NO<sub>2</sub>-function leads to elongated Fe–N distances of 2.14–2.43 Å typical for high spin iron (II) complexes,<sup>10</sup> thus the ligands can adopt the metal ion exclusively in HS state configuration. As the steric demands of the amino-group are considerably lower, the 3-substituted amino-functionalized complexes maintain the spin crossover behavior. Notably, compound [Fe(HB(3-NH<sub>2</sub>pz)(pz)<sub>2</sub>)<sub>2</sub>] undergoes above-room-temperature spin transition at  $T_{1/2} = 310$  K. The authors' preliminary studies have shown that compounds [Fe(HB(3-NH<sub>2</sub>pz)(pz)<sub>2</sub>)<sub>2</sub>] and [Fe(HB(3-NO<sub>2</sub>pz)(pz)<sub>2</sub>)<sub>2</sub>] can be sublimed under vacuum without any substantial decomposition, which opens opportunity for application in switchable thin film materials. Desrochers *et al.* used the discussed reaction of heterocycle metathesis to replace one 3,5-dimethylpyrazole ring in [HB(3,5-Me<sub>2</sub>pz)<sub>3</sub>]<sup>-</sup> ligand with benzotriazole (btz) to obtain the first ferrous heteroazolyl heteroscorpionate [Fe(HB(3,5-Me<sub>2</sub>pz)<sub>2</sub>(btz)<sub>2</sub>)<sub>2</sub>] (Figure 1.20a).<sup>87</sup> As synthesized, the substance constitutes a mixture of *cis*- and *trans*-isomers separable by column chromatography. Both isomers display spin state change in high temperature region ( $T_{1/2} \approx 385$  K for *cis*-isomer and  $T_{1/2} \approx 372$  K for *trans*-isomer; see Figure 1.20b). The group of authors performed detailed studies of the complexes in solid state and employed a

paramagnetic  $^{11}\text{B}$  NMR to follow the SCO of both isomers in solution. It was also revealed that the exodentate nitrogen atom of benzotriazole in the *cis*-isomer can coordinate to  $\text{SnCl}_2$  to form an adduct. Interestingly, the coordination of tin (II) chloride does not affect the initial spin state of the  $\text{Fe}^{\text{II}}$  complex and causes minimal impact on the benzotriazole  $\pi$ -system.

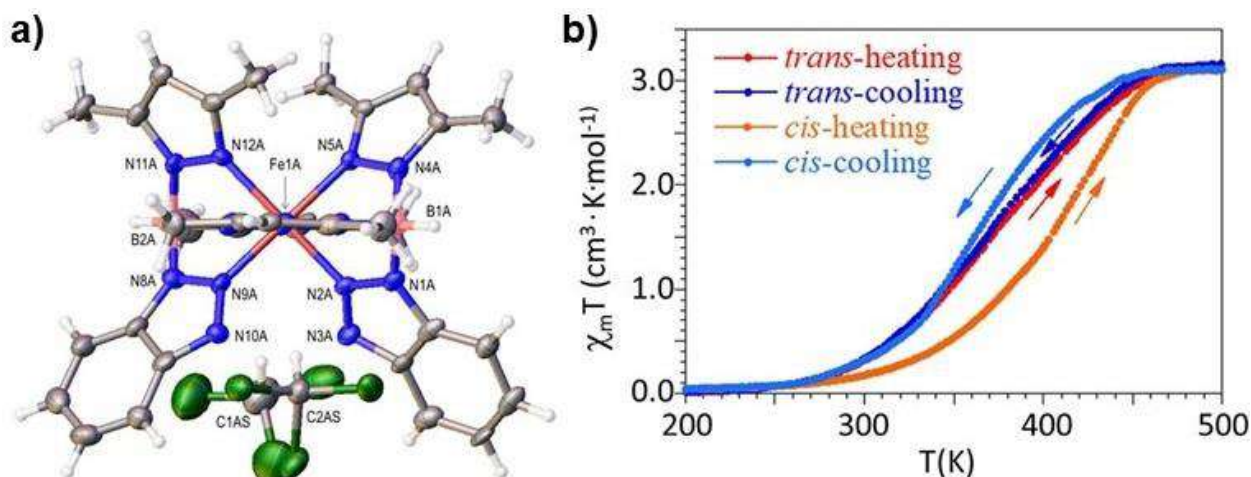


Figure 1.20. a) Crystal structure of *cis*-[Fe(HB(3,5-Me<sub>2</sub>pz)<sub>2</sub>(btz)<sub>2</sub>)<sub>2</sub>] chloroform solvate; b) Temperature-dependent molar magnetic susceptibility of the *cis*- and *trans*-isomer bulk powers in heating and cooling modes.<sup>87</sup>

To conclude, a range of evaporable spin crossover complexes have been synthesized up to date, however this domain of research is still on rise and requires development of new SCO coordination compounds and their thin film materials, properties of which can be predetermined by molecular design.

### 1.5 Lanthanide(III) complexes with bis-chelating ligands for highly-efficient luminescence

Luminescence stands for a phenomenon of light radiation from electronically excited states of species (molecules, ions etc.) as a result of return of the latter to the ground state.<sup>88,89</sup> The substances where luminescence is observed are called *luminophores*. Depending on the *external stimulus* inducing the electron excitation in the substance, there can be defined: photoluminescence (*light*), electroluminescence (*electrical field*), radioluminescence (*ionizing radiation*), chemiluminescence (*chemical process*), sonoluminescence (*ultrasound*), triboluminescence (*grinding*) etc. Hereafter the term *luminescence* will be used to refer *photoluminescence* (if not specified otherwise). The pathway of the de-excitation determines lifetimes of excited states and rates of luminescence, which can be classified as *fluorescence* and *phosphorescence*. As a precondition to fluorescence, a photon of light is absorbed by the substance that leads to transition of one of the singlet ground state ( $S_0$ ) paired electrons (of opposite spins) to a singlet excited state level ( $S_1$ ,  $S_2$ ...), whereafter it returns to the ground state from the lowest  $S_1$  level leading to a photon emission. In case of singlet-singlet electronic transitions, the

electron spin does not change upon the electron excitation and return to the ground state. As the electron spin remains unchanged, the return to the ground state is spin-allowed, so the process is fast, as the typical rate of luminescence is around  $10^8 \text{ s}^{-1}$ , and hence the lifetime is around 10 nanoseconds ( $10 \times 10^{-9} \text{ s}$ ). In turn, phosphorescence occurs from triplet excited state  $T_1$ , where the electron has the same spin as the ground-state electron of  $S_0$ . The triplet-singlet transitions are formally forbidden, so the rates of phosphorescence ( $T_1 \rightarrow S_0$ ) are as slow as  $10^3\text{--}10^0 \text{ s}^{-1}$  and its lifetimes can range from milliseconds to seconds. A process that precedes the phosphorescence is a conversion of  $S_1$  to  $T_1$  through *intersystem crossing* – a non-radiative transition between the excited state levels of different multiplicity. Forbidden transitions between singlet and triplet states can be partially allowed in case if spin-orbit coupling takes place. Spin-orbit coupling is inherent in substances containing heavy atoms (halogens or metal ions), thus the conditions for intersystem crossing and phosphorescence in such samples can be favourable. The excitation energy can also be converted to heat instead of light, which is known as *internal conversion*, which can occur from excited state levels of higher energy to those with lower energy as well as between excited and ground state levels. Internal conversion is a fast ( $10^{-10}\text{--}10^{-8} \text{ s}$ ) non-radiative process that can compete with photon emission processes. The less is the energy difference between levels, the more favourable the internal conversion is. All the considered radiative and nonradiative processes are visualized on Jablonski diagram shown on Figure 1.21.

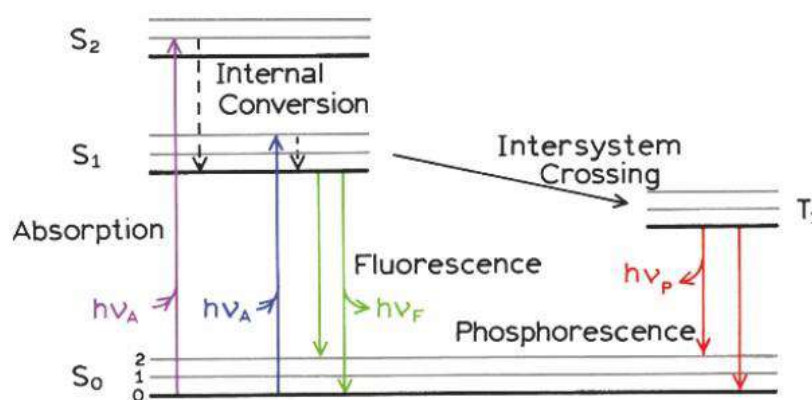


Figure 1.21. Representation of Jablonski diagram.<sup>88</sup>

The luminescence of trivalent lanthanide ions is of high interest owing to benefits it provides comparing to other known luminophores, which include high color purity of the emitted light, luminescence decay times longer than those for organic luminophores and large Stokes shifts.<sup>90</sup> The unique optical properties of these species are conditioned by a distinct electronic structure of  $\text{Ln}^{\text{III}}$ , that have  $[\text{Xe}]4f^n$  ( $n = 0\text{--}14$ ) electronic configuration. The  $4f$  orbitals are shielded by the filled  $5s^25p^6$  subshells which prevents them from interacting with the ion surroundings. As a consequence, in the emission spectra of lanthanide luminophores the  $f\text{--}f$  transitions appear as narrow bands, distinctive for each lanthanide(III) ion and independent on its coordination environment.<sup>91</sup> Most of the ions are

emissive, except for the elements at termini of the lanthanide row, namely  $\text{La}^{\text{III}}$  and  $\text{Lu}^{\text{III}}$ , where the first does not have  $f$ -electrons ( $\text{La}^{\text{III}}$ ), while the last has the  $4f$  sub-shell completely filled ( $\text{Lu}^{\text{III}}$ ). The emission range of the lanthanide ions is broad and covers ultraviolet (UV), visible and near-infrared (NIR) spectral regions (Figure 1.22).<sup>92</sup> Such spectroscopic properties are advantageous in terms of various applications from light-emitting materials for functional devices to luminescent bio-probes.<sup>91</sup> For instance, narrow-band emission is the key to pure colors of the emitted light, which is an important characteristic for electroluminescent devices used in displays and screens,<sup>93</sup> while long luminescence lifetimes and considerable Stokes shifts when coordinated to organic ligands allow to use  $\text{Ln}^{\text{III}}$  as luminescent labels for immunoassays.<sup>94</sup>

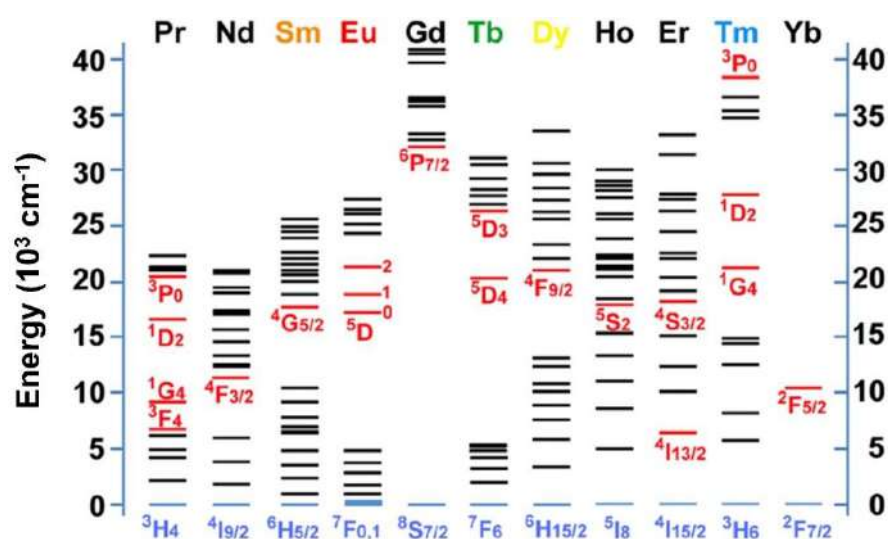


Figure 1.22. Partial energy diagrams of  $\text{Ln}^{\text{III}}$  aquo-ions. The emissive excited state levels are highlighted in red, while the ground state levels are highlighted in blue. The diagrams are also applicable to other lanthanide compounds as the energies of the levels are not impacted by coordination environment of the lanthanide ion.<sup>92,95–97</sup>

However, it should be noted that  $\text{Ln}^{\text{III}}$  ions themselves are not efficient at light absorption, as the  $f$ - $f$  transitions are parity-forbidden, hence the molar extinction coefficients for the lanthanide ions are low ( $\epsilon \approx 1\text{--}10 \text{ M}^{-1}\cdot\text{cm}^{-1}$ ), consequently weak is their emission upon direct excitation.<sup>98</sup> The other obstacle preventing the lanthanides from efficient light emission comes from non-radiative deactivation of the  $\text{Ln}^{\text{III}}$  excited states by vibrations of OH, CH and NH groups.<sup>99,100</sup> The solution to the first problem was discovered in 1942 by Weissman who found that in lanthanide complexes with organic ligands the lanthanide luminescence can also be triggered indirectly, *i.e.* by excitation of the organic ligand molecules.<sup>101</sup> This phenomenon of  $\text{Ln}^{\text{III}}$  luminescence sensitization by organic ligands is called “antenna effect”. The effect is realized by means of light absorption by the ligand, exciting the latter on the singlet state, whereafter it is converted to the triplet state *via* intersystem crossing. Then, the populated triplet state undergoes de-excitation accompanied by non-radiative transfer of energy to the lanthanide ion

inducing an electron excitation in the latter. This type of energy transfer is known as Förster-type energy transfer (FRET).<sup>102</sup> Finally, radiative return to the ground state occurs from the emissive excited state of the lanthanide as shown in Figure 1.23.<sup>93</sup>

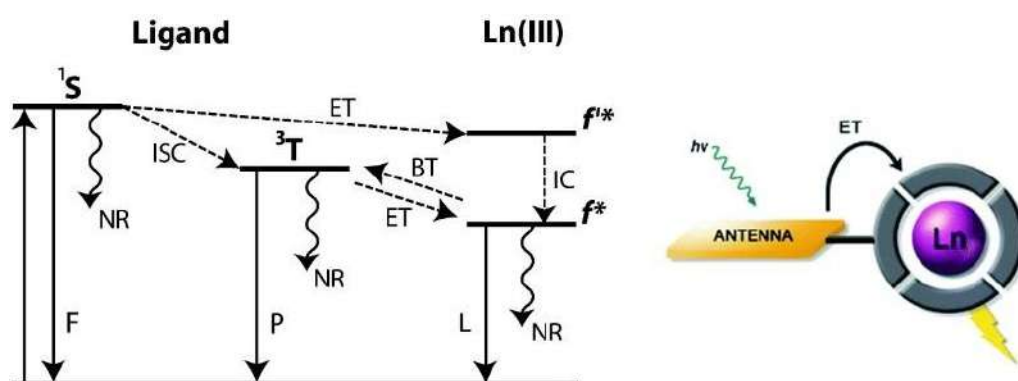


Figure 1.23. Diagram<sup>93</sup> (left) and simplified scheme<sup>103</sup> (right) of the ligand-sensitized lanthanide luminescence mechanism. ( $^1S$  – singlet state;  $^3T$  – triplet state;  $f^{1*}$  –  $\text{Ln}^{\text{III}}$  excited state;  $f^*$  –  $\text{Ln}^{\text{III}}$  emissive excited state; F – fluorescence; P – phosphorescence; L – luminescence; ET – energy transfer; BT – energy back-transfer; ISC – intersystem crossing; IC – internal conversion; NR – non-radiative decay)

The efficiency of luminescence is essentially determined by quantum yield. The overall quantum yield of sensitized luminescence is calculated using the following equation:

$$Q_{\text{Ln}}^{\text{L}} = \eta_{\text{sens}} Q_{\text{Ln}}^{\text{Ln}} \quad (1.1)$$

where  $Q_{\text{Ln}}^{\text{Ln}}$  is the intrinsic quantum yield of the lanthanide emission upon direct  $f$ - $f$  excitation, and  $\eta_{\text{sens}}$  stands for sensitization efficiency. The intrinsic quantum yield in turn takes into consideration the contribution of non-radiative deactivation processes in inner and outer spheres of the complex, and is characterized by radiative rate ( $k_{\text{rad}}$ ) and excited state de-population ( $k_{\text{obs}}$ ) constants, which are inversely proportional to radiative ( $\tau_{\text{rad}}$ ) and excited state ( $\tau_{\text{obs}}$ ) lifetimes respectively (Equation 1.2). Thus, the efficiency of the luminescence depends on two parameters, such as energy transfer ( $\eta_{\text{sens}}$ ) and contribution of non-radiative deactivation processes ( $Q_{\text{Ln}}^{\text{Ln}}$ ). One of the well-known examples of highly-

$$Q_{\text{Ln}}^{\text{Ln}} = \frac{k_{\text{rad}}}{k_{\text{obs}}} = \frac{\tau_{\text{obs}}}{\tau_{\text{rad}}} \quad (1.2)$$

luminescent europium(III) complexes is  $[\text{Eu}(\text{tta})_3(\text{DBSO})_2]$  (tta = thenoyltrifluoroacetylacetonate; DBSO = dibenzyl sulfoxide; Figure 1.24) with the overall quantum yield reaching 85% – one of the highest value measured for  $\text{Eu}^{\text{III}}$  complexes in the solid state.<sup>104</sup> Terbium(III) benzoate shows 100% quantum yield. Although, the high  $Q_{\text{Ln}}^{\text{Ln}}$  cannot be reached by coordinating just any ligand to the metal center. In search of general rules that can be followed to design highly luminescent lanthanide complexes, different scientific teams, after careful research, suggested an assumption that the

luminescence sensitization is realized only through  $S_1(\text{ligand})\text{--}T_1(\text{ligand})\text{--}Ln^*$  energy transfer path, and that the only important parameter in this case is the energy difference between the triplet state of the ligand  $T_1$  and the emitting excited-state level of the lanthanide ion.<sup>105–107</sup>

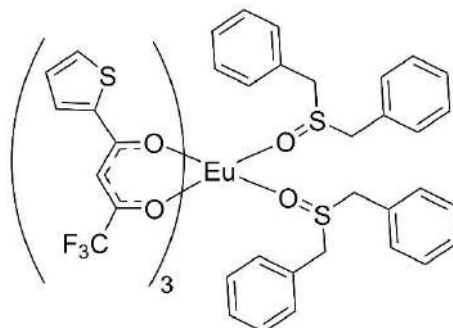


Figure 1.24. Structural formula of  $[Eu(\text{tta})_3(\text{DBSO})_2]$ .

It was found that high quantum yields were observed in coordination compounds of  $\text{Eu}^{\text{III}}$  and  $\text{Tb}^{\text{III}}$  with energy difference between  $T_1$  and  $Ln^*$  lying in  $2500\text{--}3500\text{ cm}^{-1}$  range.<sup>108</sup> The energy differences below this range favor the back-transfer of energy to the triplet state, while the higher differences increase the probability of non-radiative relaxation. In turn, an efficient intersystem crossing from  $S_1$  to  $T_1$  occurs if the energy difference between the levels is  $\sim 5000\text{ cm}^{-1}$ , which should also be considered when designing the ligand. In general, the efficiency of the energy transfer relies on an optimal match between the ligand triplet and  $Ln^{\text{III}}$  excited states, which depends on the nature of the ligand molecules and the lanthanide ion. For instance, in case of europium(III), high luminescence quantum yields were observed in complexes with the triplet state energy close to:  $^5D_2$  level for polyaminocarboxylates,<sup>106</sup>  $^5D_1$  level for  $\beta$ -diketonates<sup>105</sup> and  $^5D_0$  level for coordination compounds with Schiff-base ligands (Figure 1.25).<sup>107</sup> On the other hand, some lanthanide ions emit more efficiently than other in complexes with the same ligands, which can be observed on example of polyaminocarboxylates of  $\text{Eu}^{\text{III}}$  and  $\text{Tb}^{\text{III}}$ , where the latter show higher quantum yields due to larger band gap  $^5D_4\text{--}^7F_6$  in Tb comparing to  $^5D_0\text{--}^7F_0$  in Eu (Figure 1.22).<sup>91,106</sup> The optimal energy gap range between the emitting excited state and the ground state that minimizes the probability of non-radiative deactivation is the key reason that makes  $\text{Eu}^{\text{III}}$ ,  $\text{Gd}^{\text{III}}$  and  $\text{Tb}^{\text{III}}$  better emitters comparing to other lanthanides. This is why the coordination compounds of  $\text{Eu}^{\text{III}}$  and  $\text{Tb}^{\text{III}}$  are of high scientific interest. However, in complexes with organic ligands, the luminescence of  $\text{Gd}^{\text{III}}$  cannot be observed as its emission lies in the UV range where it often overlaps with absorption of the organic molecules of the ligand, so the coordination compounds of gadolinium(III) do not represent interest in terms of metal-centred light emission, however, they are useful for determining of ligand triplet state energy that can be deduced from low-temperature phosphorescence spectra of  $\text{Gd}^{\text{III}}$  complexes with the ligand(s) of interest.

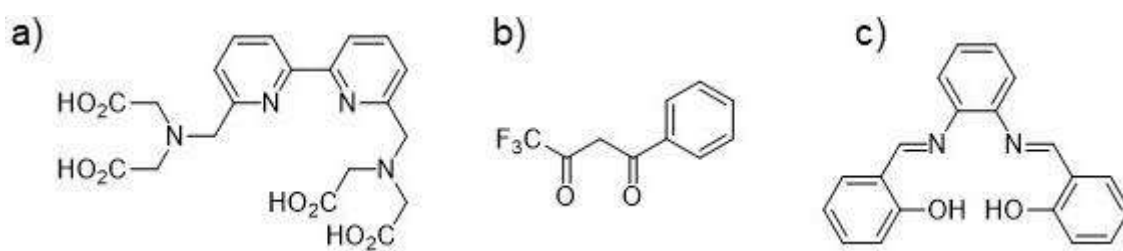


Figure 1.25. Examples of polyaminocarboxylate (a),  $\beta$ -diketone (b) and Schiff base (c) ligands (in neutral form) used in the literature.<sup>105–107</sup>

In order to design highly emissive lanthanide complexes, besides the above-discussed photophysical requirements, chemical aspect should be met. This involves the coordination preferences of  $\text{Ln}^{\text{III}}$  ions and the molecular structure of the ligand. According to hard and soft Lewis acid and base theory (HSAB),<sup>109–111</sup> trivalent lanthanide cations are hard acids, meaning that they coordinate more readily to ligands with hard-base donor atoms to which belong oxygen and nitrogen. The lanthanide ions have a range of possible coordination numbers, which are governed by steric factors and with uncongested ligands can be relatively high (usually from 7 to 9).<sup>112</sup> As a corollary, polydentate chelating ligands are good candidates to form stable complexes. The complex design strategy should also address the problem of vibrational deactivation processes induced by high-energy oscillators, such as OH, NH or CH groups. The emission quenching by O–H vibrations ( $\sim 3600\text{ cm}^{-1}$ ) is often observed in aqueous solutions and isolated complexes where coordination sphere of the lanthanide ion contains water molecules bound to it. Typical mechanism of the deactivation by O–H vibration modes for some  $\text{Ln}^{\text{III}}$  ions is shown on Figure 1.26.

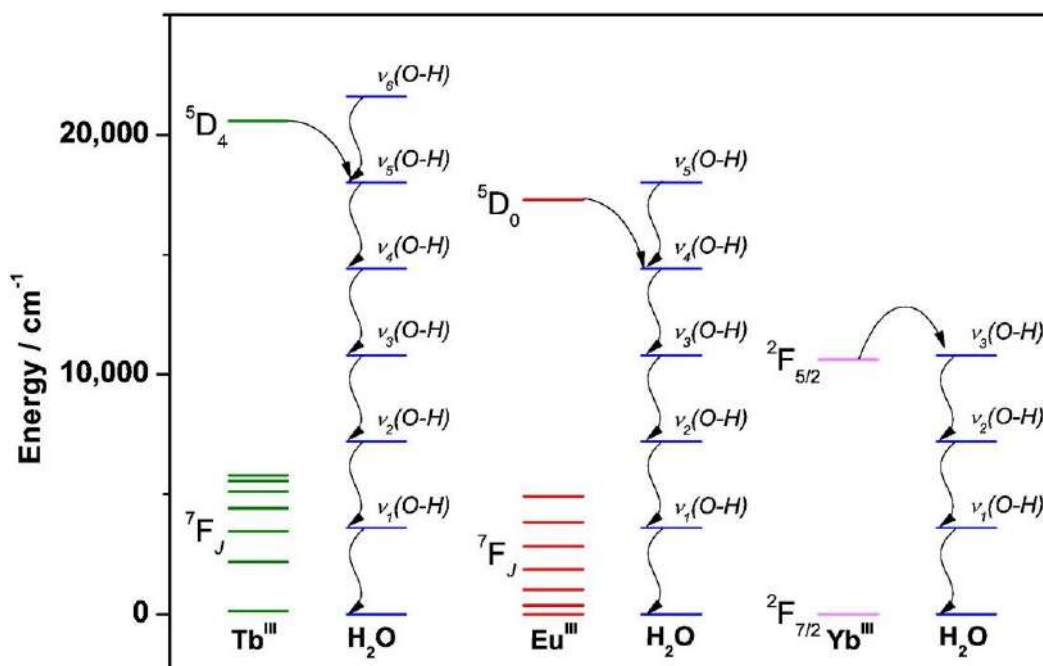


Figure 1.26. Energy diagram showing the mechanism of lanthanide luminescence quenching by O–H vibration modes of water molecule on the examples of  $\text{Tb}^{\text{III}}$ ,  $\text{Eu}^{\text{III}}$  and  $\text{Yb}^{\text{III}}$  ions.<sup>113</sup>

Use of chelating multidentate ligands to saturate the lanthanide coordination sphere allows to prevent the coordination of solvent molecules carrying OH oscillators. Binding sites of some chelating ligands may contain OH and NH ( $\nu_{\text{N-H}} \approx 3300 \text{ cm}^{-1}$ ) groups able to coordinate to the lanthanide ions or located in close proximity to the donor atoms. This problem could be solved by deprotonation (if applicable) of these moieties. Otherwise, hydrogens in these groups can be replaced with deuterium atoms, which significantly lowers the energy of vibrations.<sup>98</sup> In a vast majority of organic ligands the presence of C–H oscillators ( $\sim 2900 \text{ cm}^{-1}$ ) is nearly inevitable, and reducing the number of CH groups is often a more challenging task comparing to OH and NH ones. Nevertheless, it is possible to minimize the quantity of these groups by using organic ligands where C–H moieties are partially substituted with C–F functions, vibrations of which have much lower energy ( $\sim 1400\text{--}1000 \text{ cm}^{-1}$ ). Thus, lanthanide complexes with  $\beta$ -diketones bearing perfluorinated substituents displayed higher quantum yields comparing to their non-fluorinated analogues.<sup>114</sup>

Among miscellaneous classes of lanthanide-based coordination compounds, the complexes with  $\beta$ -diketones (or 1,3-diketones) are one of the most investigated.<sup>115,116</sup> The acidic nature of protons at  $\alpha$ -position of a  $\beta$ -diketone molecule eases its deprotonation resulting in formation of stable  $\beta$ -diketonate anion with negative charge delocalized within OC–CH–CO fragment of the molecule.<sup>117</sup> The 1,3-diketonate anions are bidentate chelating ligands towards  $\text{Ln}^{\text{III}}$  and can form neutral ternary  $\text{Ln}(\beta\text{-diketonate})_3$  or anionic  $\text{Ct}^+[\text{Ln}(\beta\text{-diketonate})_4]^-$  ( $\text{Ct}^+$  = single-charged cation) complexes (Figure 1.27) depending on stoichiometry of the initial reagents.<sup>118</sup>

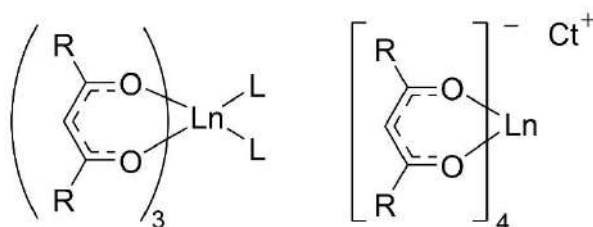


Figure 1.27. General structures for two types of lanthanide  $\beta$ -diketonate: ternary or tris- (left) and anionic tetrakis- (left) complexes. (R = substituent; L = additional neutral ligand;  $\text{Ct}^+$  = single-charged cation).

As the diketonates are bidentate ligands, they do not fully saturate the metal coordination sphere in the ternary complexes permitting solvent molecules to bind to the metal center, which increases the probability of the quenching processes. This problem can be solved by replacing the solvent molecules with neutral bidentate ligands, *e.g.* 1,10-phenanthroline and 2,2'-bipyridine, leading to formation of highly luminescent molecular complexes.<sup>119,120</sup> The neutral molecular  $\text{Ln}^{\text{III}}$  complexes are interesting in the context of vacuum deposition to fabricate electroluminescent devices.<sup>121</sup> Another class of ligands, which deserves a particular interest, is represented by carbacylamidophosphates (CAPH)<sup>122</sup> that are structurally analogous to  $\beta$ -diketones (Figure 1.28) but offer the following advantages: 1) the  $\alpha$ -position

methylene moiety is substituted with NH one, deprotonation of which excludes the presence of the emission quenching vibration modes in close vicinity to the lanthanide center; 2) one of the carbonyl groups is substituted with phosphoryl group, oxygen donor atom of which displays higher affinity to the lanthanide ions comparing to the carbonyl one, thus additionally stabilizing the resulting complexes; 3) P=O stretching vibrations have lower energies ( $\sim 1250\text{ cm}^{-1}$ ) comparing to ones of the carbonyl ( $\sim 1600\text{ cm}^{-1}$ ); 4) substantial thermodynamic stability of the complexes; 5) the phosphorus atom is pentacoordinate, which allows to decorate the ligand with an extra chromophore function; 6) due to the valence capabilities of phosphorus allowing one more substituent, CAPH ligands appear to be more bulky than their  $\beta$ -diketone counterparts that leads to better shielding of the lanthanide emissive centers from external interactions impairing the luminescence.<sup>122–130</sup> Despite the large number of works dedicated to CAPH-based lanthanide complexes, this domain of research is relatively new comparing to the diketonate counterparts, hence there is a room to develop new highly-luminescent lanthanide(III) carbacylamidophosphates.

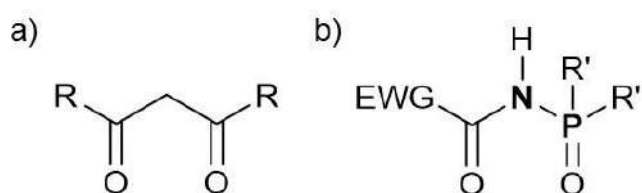


Figure 1.28. General structural formulae of  $\beta$ -diketone (a) and CAPH (b) molecules. (R, R' = substituent; EWG = electron-withdrawing group).

Another powerful strategy to increase the quantum yields is to increase the number of the emission centers (*i.e.* Ln<sup>III</sup> ions) per molecule using bis- or poly-chelating ligands.<sup>131,132</sup> There are numerous reports highlighting the outstanding luminescent properties of binuclear lanthanide complexes of with bis- $\beta$ -diketones – tertridentate bis-chelating counterparts of simple 1,3-diketones containing to chelating sites connected by spacer.<sup>133</sup> In 2004 Bassett *et al.* have reported significantly higher luminescence intensity and quantum yields in binuclear lanthanide complexes with bis- $\beta$ -diketones comparing to their simpler mononuclear  $\beta$ -diketonate analogues. It was shown that binuclear samarium(III) complex with 1,3-bis(3-phenyl-3-oxopropanoyl)benzene exhibits 11 times higher luminescence intensity than analogous mononuclear tris-dibenzoylmethanate complex (Figure 1.29).<sup>131</sup> Later on, a number of works marked considerable quantum yields in binuclear lanthanide bis- $\beta$ -diketonates and confirmed higher luminescence intensities over their mononuclear analogues.<sup>134–140</sup> The metal coordination compounds with bis-chelating ligands can have certain beneficial structural features, for example, the ligands with relatively flexible spaces often form helicate assemblies around metal ions upon coordination. Helicates are supramolecular edifices in which metal ions lie on helical axis, while the coordinated poly-chelating ligands are wrapped about the latter in a spiral manner (Figure 1.30).<sup>141,142</sup>

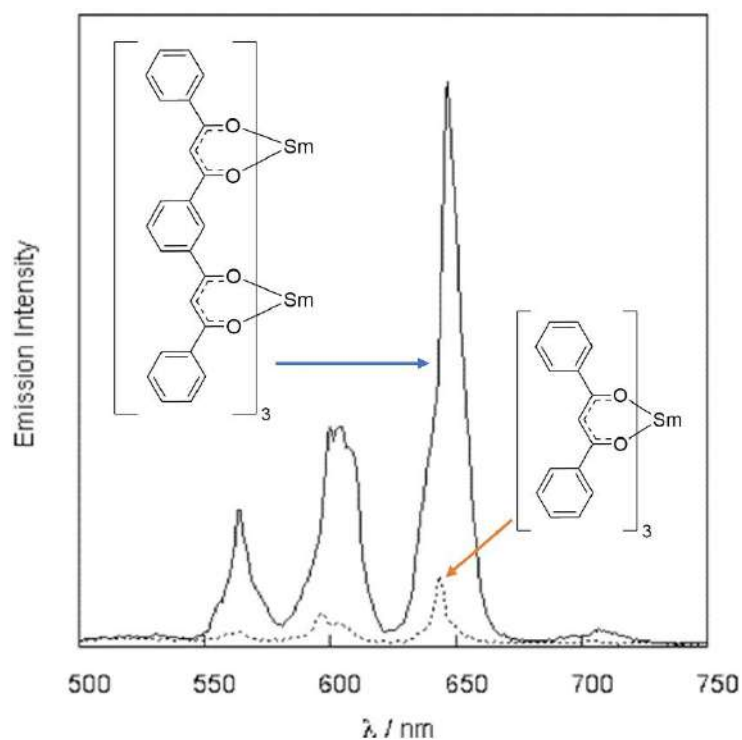


Figure 1.29. Emission spectra of disamarium (III) bis- $\beta$ -diketonate (solid line) and its mononuclear analogue (dashed line) isoabsorptive DMF solutions. Formulae of the complexes are depicted in the left and right insets respectively.<sup>131</sup>

Applied to the lanthanide complexes, the helicate design offers more protection from the external interactions and therefore has a positive impact on the luminescence.<sup>142,143</sup> With bis- $\beta$ -diketonates as well as with other bis-chelating ligands, the lanthanides tend to form triple-stranded (ternary, with three bis-bidentate ligands) and quadruple-stranded helicates (Figure 1.30).<sup>144,145</sup>

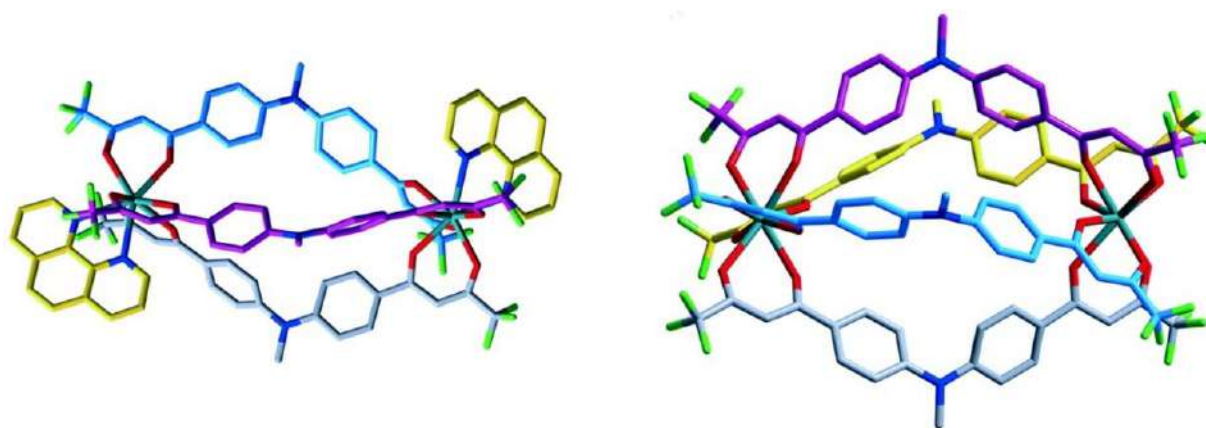


Figure 1.30. Examples of crystal structures of the triple- (left) and quadruple-stranded (right) helicates.<sup>145</sup>

Changing the nature of the spacer (*idem* linker) it is possible to tune or even switch the luminescent properties of the bis- $\beta$ -diketonate complexes.<sup>133</sup> Zhang *et al.* have synthesized a binuclear quadruple-stranded Eu<sup>III</sup> bis-diketonate with diarylethene-type linker and demonstrated a reversible switching of

the europium luminescence by switching between open and closed forms of the bridging diarylethene moiety upon UV or visible light irradiation respectively (Figure 1.31).<sup>146</sup> Investigating phosphorescence spectra of quadruple-stranded gadolinium(III) complex with the considered ligand, the authors have found that the triplet state energy of the open-ring form ligand is of 20833 cm<sup>-1</sup>, which is higher than <sup>5</sup>D<sub>0</sub> level of Eu<sup>III</sup> (17500 cm<sup>-1</sup>) and the energy difference between the levels allows for efficient energy transfer. However, in ring-closed form the triplet state energy is significantly lower (14728 cm<sup>-1</sup>), which makes the energy transfer impossible. Thus, photoswitching between open- and closed-ring form of the ligand leads to tuning of its triplet state and, as a consequence, switching of the metal-centered emission.

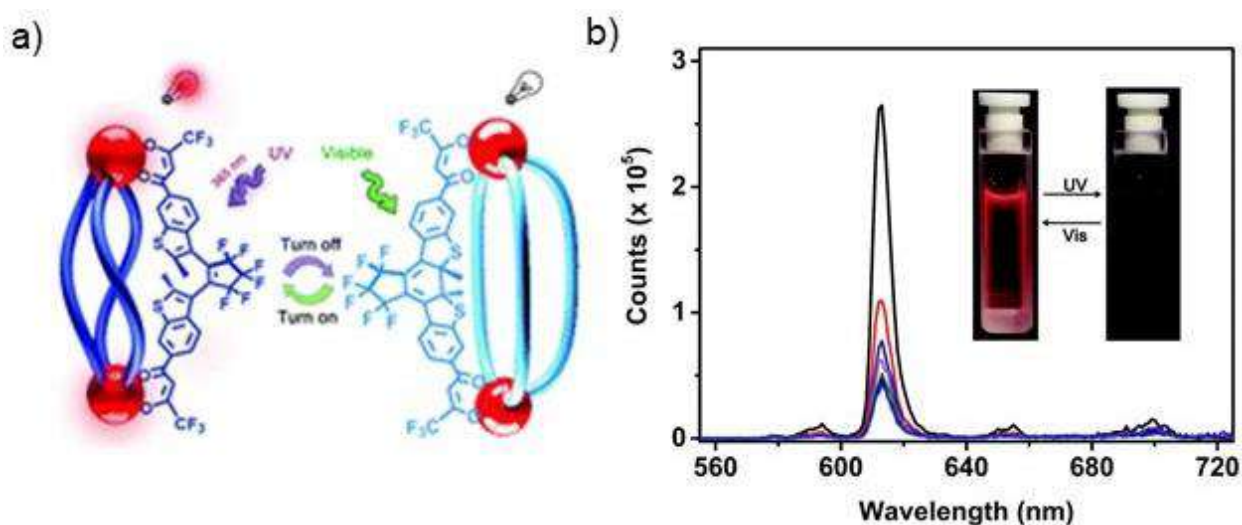


Figure 1.31. a) Representation of the Eu<sup>III</sup> luminescence photoswitching in the quadruple-stranded complex with the diaryl-ethene based ligand; b) Emission spectra of the complex solution in MeOH/CH<sub>2</sub>Cl<sub>2</sub> mixture upon irradiation at 395 nm.<sup>146</sup>

Introduction of fluorescent organic groups, such as tetraphenylethylene (TPE), to the spacer (Figure 1.32a) can be used to achieve a white-light emission, as it was described by Li *et al.* who employed the red emission of Eu<sup>III</sup> together with blue-green aggregation-induced emission of TPE moieties to produce a white-light luminescence in a quadruple-stranded helicate.<sup>147</sup> Interestingly, the TPE- and the Eu-centered emissions can be excited simultaneously in a broad range of excitation wavelengths (310–410 nm). Furthermore, the resulting emission spectra can be tuned depending on the excitation wavelength ( $\lambda_{exc}$ ), and hence – the emission color (Figure 1.32b). Thus, upon excitation with longer wavelengths the TPE emission appears more dominant in the spectra, while at short  $\lambda_{exc}$ , *e.g.* 310 nm, the color of the emission is nearly white (Figure 1.32c). The authors have also managed to incorporate the complex into a polymer matrix to obtain white-light-emitting hybrid films (Figure 1.32d).

Summarizing the discussed nuances of the ligand and complex design to achieve an efficient lanthanide-centered luminescence and considering its possible applications, one can conclude that bis-

chelating CPh ligands and their lanthanide complexes may appear as promising candidates to tackle the existing issues on the way to a highly-efficient Ln<sup>III</sup> emission.

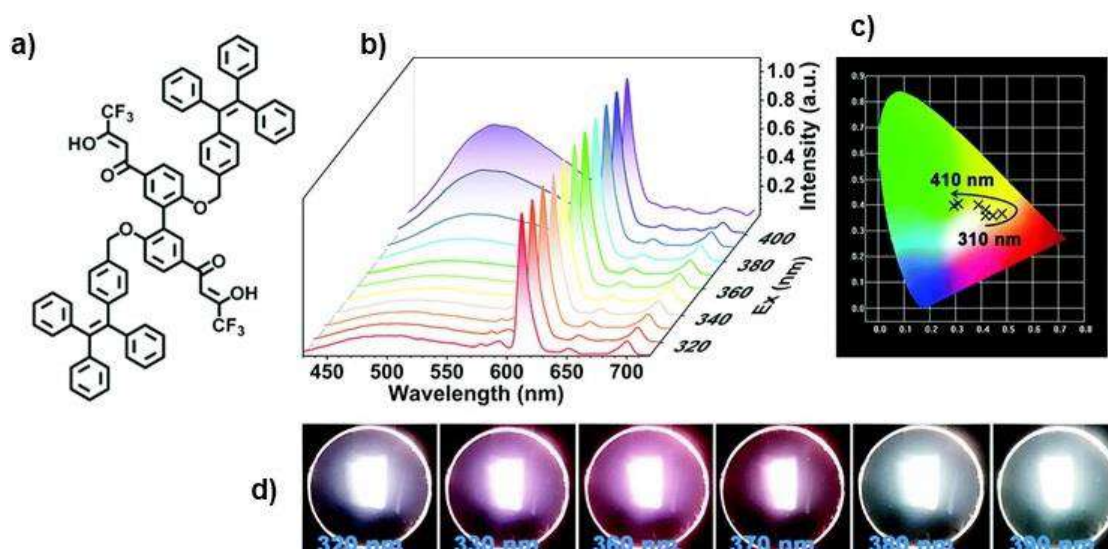


Figure 1.32. a) Structural formula of the TPE-derived bis- $\beta$ -diketone ligand (neutral form) used to construct the quadruple-stranded dieuropium(III) helicate in ref.<sup>147</sup>; b) Emission spectra of the solid-state helicate ( $\lambda_{\text{exc}}$  range: 310–410 nm); c) CIE chromaticity diagram of the complex; d) Photographs of hybrid polymer films (0.5 % content of the helicate) upon excitation at the selected wavelengths.

## 1.6 Hybrid SCO/luminescent materials

The synergy of spin crossover and luminescence phenomena is an area of intensive research over the past few decades.<sup>148</sup> An interplay between the two phenomena can serve a key to fabrication of bifunctional materials.<sup>149</sup> The optical absorption bands of low spin iron(II) can overlap with the emission bands of some luminophores leading to the luminescence quenching as a result of the energy transfer onto the iron center or emission reabsorption, while the absorption of high spin iron(II) may not interfere with the emission of these luminophores, which makes possible the switching of the luminescence using SCO phenomenon.<sup>150</sup> In turn, luminescence can serve a very convenient tool to monitor the spin state of spin-crossover materials.<sup>149</sup> However, combining both properties in one substance is a challenge, as both spin crossover and luminescence are sensitive to changes in chemical environment and structural changes, therefore the attempts to unite these two properties often leads to loss of at least one of them.<sup>148–150</sup> In 1990s–2000s, the first attempts to combine the lanthanide emission and spin crossover were done by Piguet *et al.* who synthesized a series of heterobimetallic *f-d* helicates including Ln<sup>III</sup>-Fe<sup>II</sup> ones.<sup>151–153</sup> The authors' investigation revealed a strong quenching of europium(III) emission in Eu-Fe helicates with LS Fe<sup>II</sup> (Figure 1.33). Nevertheless, even with the highest possible fraction (>0.5) of high-spin iron(II) species, the lanthanide luminescence was not observed. Even in helicate where the iron was fixed in HS state, the energy transfer from the lanthanide to the iron still occurred leading to weak Eu-

centered emission.<sup>151</sup> About 20 years later, a study conducted for similar helicate systems has corroborated the temperature dependence of the Eu<sup>III</sup>-centered luminescence induced by SCO, however its signal remained fairly weak due to high quenching efficiency of 95% for the high-spin iron ions and quantitative for the iron in low spin state.<sup>154</sup> Thus, even the trace fractions of the LS species led to drastic quenching of the lanthanide emission.

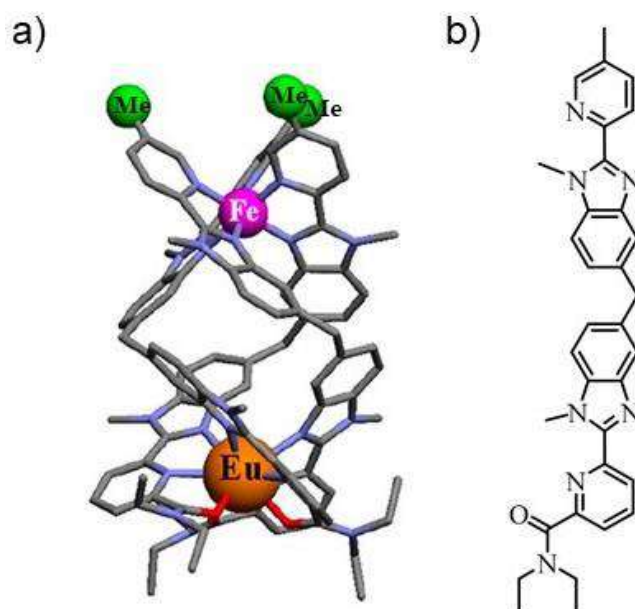


Figure 1.33. Crystal structure of one of Eu-Fe helicates (a) investigated by Piguet *et al.* and structural formula of the ligand (b) constituting the helicate.<sup>154</sup>

Besides these works, there is no other reports on attempts to bridge lanthanide emitters and iron SCO centers in one chemical entity. Nonetheless, there is a different approach allowing to combine luminescent and SCO species together, to preserve both phenomena and to provide the luminescence modulation by spin state switching. This approach was proposed in works of Salmon *et al.*, who associated spin-crossover complexes and organic fluorophores by means of luminescent doping.<sup>30,155,156</sup> The first implementation of the approach involved doping of nanoparticles of iron-triazole complexes (Figure 1.34)  $[\text{Fe}(\text{NH}_2\text{trz})_3](\text{A})_2$  ( $\text{NH}_2\text{trz}$  = 4-amino-1,2,4-triazole;  $\text{A}$  = tosylate ( $\text{OTs}^-$ ) or  $\text{NO}_3^-$ ) with rhodamine-110.<sup>30,155</sup>

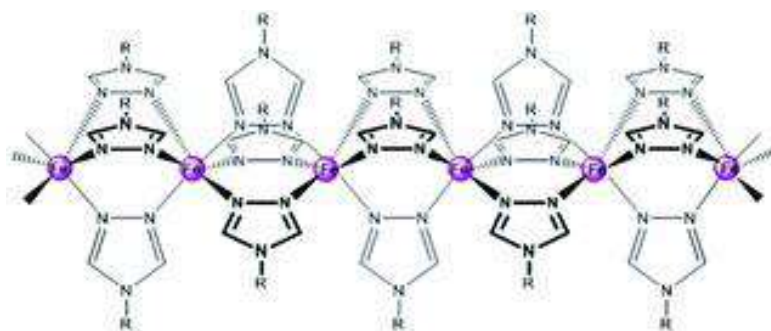


Figure 1.34. General structure of iron-triazole polymeric complexes. Iron (II) centers are highlighted in purple.<sup>156</sup>

Room temperature absorption spectra of  $[\text{Fe}(\text{NH}_2\text{trz})_3](\text{OTs})_2$  nanoparticles suspension contain a band with maximum at 540 nm (Figure 1.35a).

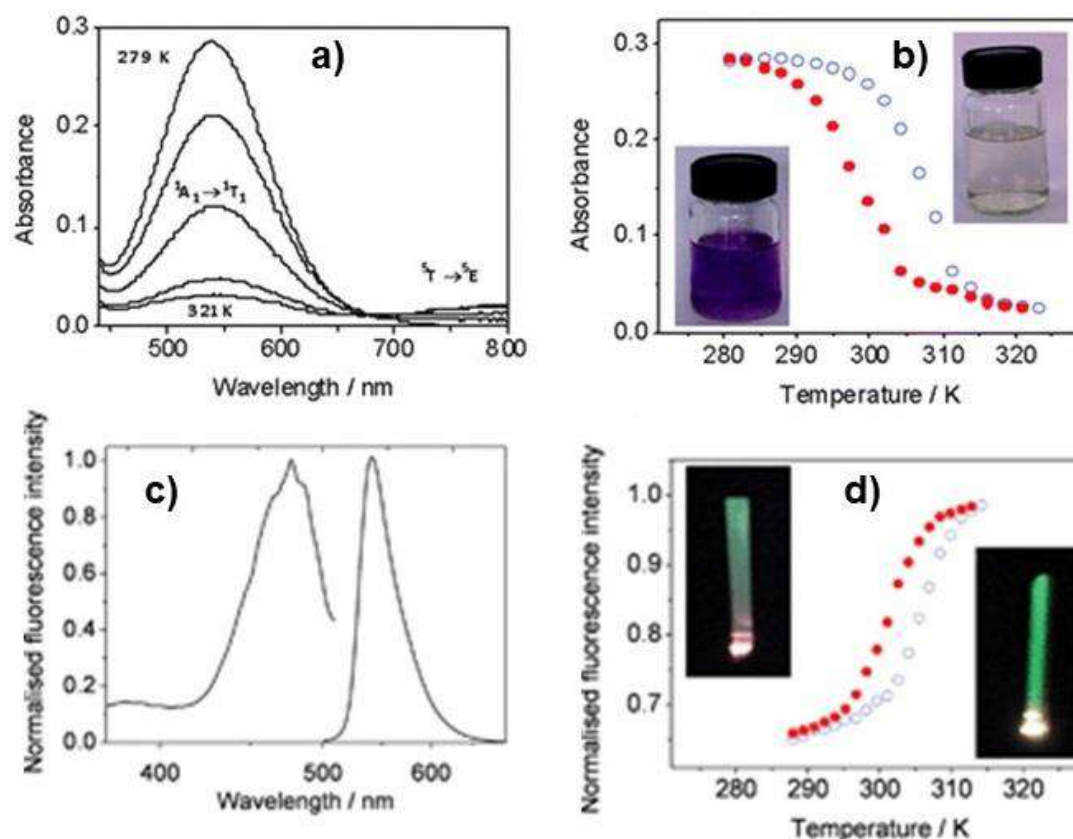


Figure 1.35. a) Absorption spectra of  $[\text{Fe}(\text{NH}_2\text{trz})_3](\text{OTs})_2$  nanoparticles suspension recorded at several selected temperatures; b) Temperature dependance of the suspension absorbance at 540 nm over heating (empty circles) and cooling (filled circles). The inset photographs show the color of the suspension at the lowest (purple) and the highest (colorless) temperature; c) Room temperature fluorescence excitation and emission spectra of the nanoparticles suspension; d) Thermal variation of the fluorescence intensity at 540 nm upon heating (empty circles) and cooling (filled circles). The inset pictures are photographs of the fluorescing sample at low (left) and high (right) temperature.<sup>155</sup>

The band bleaches upon heating of the suspension to 320 K as a result of the LS-to-HS transition. The spin crossover curve obtained by plotting the absorption at maximum versus temperature points to the hysteretic character of the transition (Figure 1.35b). The rhodamine emission band was observed at 540 nm (Figure 1.35c), which means that the absorption of the LS complex fully overlaps with the emission of the fluorophore. As a result, the luminescence is impaired. Nevertheless, the SCO absorption in the visible range fades upon temperature rise favoring the luminescence. The suspension of  $[\text{Fe}(\text{NH}_2\text{trz})_3](\text{OTs})_2$  nanoparticles with the mean size of ca. 10 nm doped with 3% of rhodamine-110 was the optimal system to observe the luminescence modulation with spin state change. The plot of the emission intensity at maximum as a function of temperature showed the increase of the intensity upon heating and decrease – upon cooling, with the presence of the hysteresis (Figure 1.35d). Changing the

anion in the complex from tosylate to nitrate allowed to reduce the average nanoparticles size to 3 nm resulting in change of SCO character to non-hysteretic and gradual. Benefiting from the gradual character of the spin transition and its synergy with luminescence of the dopant, the authors demonstrated the utility of the system for thermometry applications (Figure 1.64). Then, the approach was extended to spin-crossover thin films. The collaborators have prepared spin coated thin films of  $[\text{Fe}(\text{hptrz})_3](\text{OTs})_2$  (hptrz = 4-heptyl-1,2,4-triazole; OTs = tosylate) doped with fluorescent dye – acridine orange.<sup>156</sup> The mechanism of the fluorescence switching is suggested to rely on energy transfer between the fluorophore molecules and  $\text{Fe}^{\text{II}}$  centers. The spectral characteristics of both the organic dye and the SCO complex are in good match to make the considered materials operational. Thus, at room temperature the complex is in low spin state and its electronic spectrum is characterized by broad absorption band covering the range of excitation ( $\lambda_{\text{max}} = 450 \text{ nm}$ ) and emission (550 nm) of the organic fluorophore. Contrarily, at 320 K the complex is HS and the considered spectral region appears to be transparent for excitation and emission of the dye molecules. The materials undergo a reversible abrupt change in fluorescence intensity with the transition curves reproducible over three consecutive thermal cycles (Figure 1.36a).

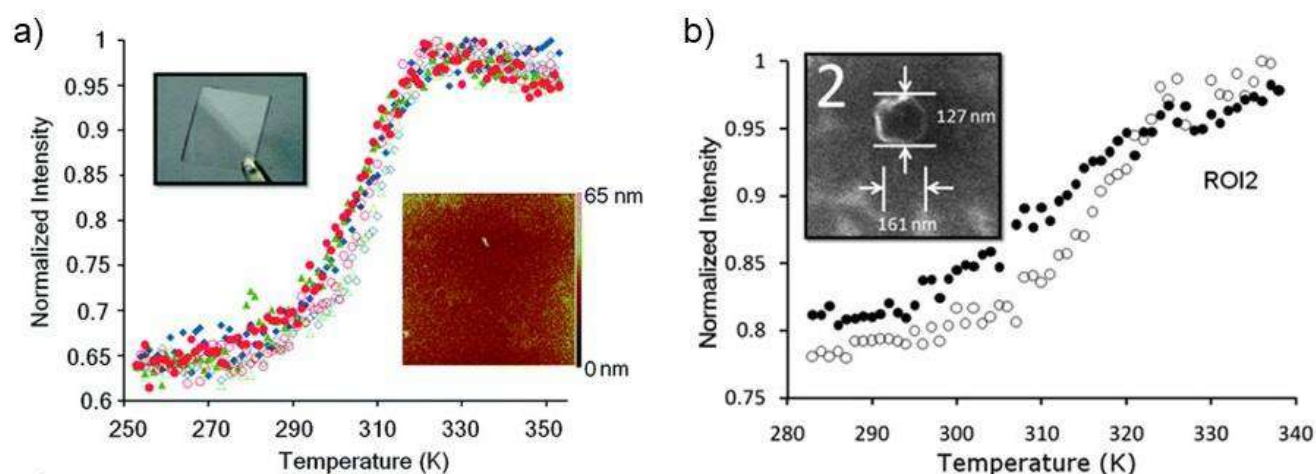


Figure 1.36. Normalized luminescence intensity (at 550 nm) thermal variation for the acridine-doped: a) spin coated thin film (~85 nm) of  $[\text{Fe}(\text{hptrz})_3](\text{OTs})_2$ . The insets are the photograph (left) of the film and AFM image (right) of its surface; b) nano-dot represented on SEM image in the inset. Empty and filled symbols on the plots refer heating and cooling modes respectively.<sup>156</sup>

The luminescence response to the spin state change can be detected even for the films with thickness lower than 100 nm. Together with the nanometric thin films, the authors have also patterned arrays of nano-objects of the considered system on silicon surface. The luminescence response was observed even for the nano-objects as small as 150 nm (Figure 1.36b). The dopant allowed to follow the SCO in single isolated nano-objects by means of fluorescent microscopy. Such a result could not be achieved by reflectance measurements of non-doped SCO nano-objects using conventional bright- and dark-field optical microscopies. Thus, luminescence appears as more sensitive optical response to probe nano-objects, than optical reflectance.

Earlier Matsuda *et al.* have fabricated a working synergetic electroluminescent device composed of indium-tin oxide (ITO) anode, spin-coated film of chlorophyll  $\alpha$  and  $[\text{Fe}(\text{dpp})_2](\text{BF}_4)_2$  (dpp = 2,6-di(pyrazol-1-yl)pyridine), and aluminum cathode (Figure 1.37).<sup>157</sup>

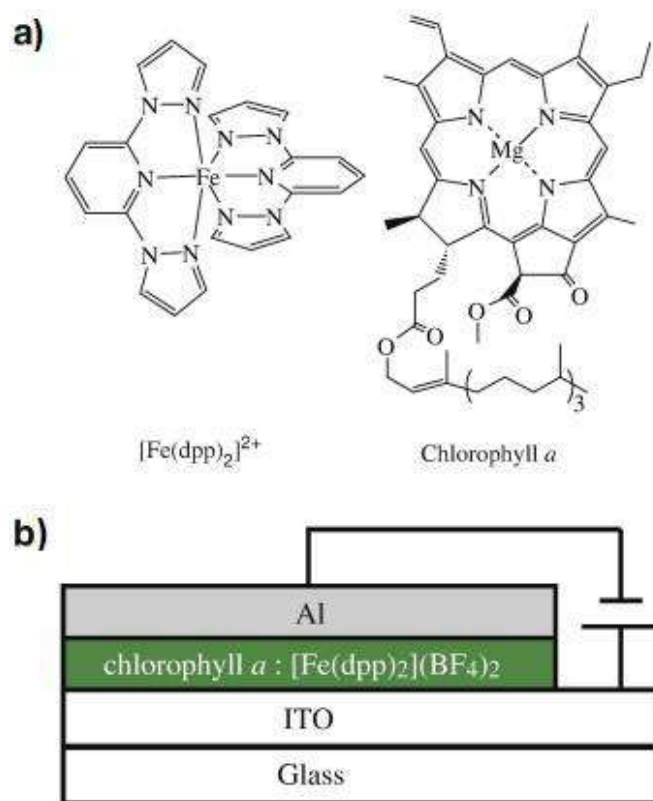


Figure 1.37. a) From left to right: molecular structures of  $[\text{Fe}(\text{dpp})_2]^{2+}$  and chlorophyll  $\alpha$ ; b) Schematic representation of structure of ITO/chlorophyll  $\alpha$  :  $[\text{Fe}(\text{dpp})_2](\text{BF}_4)_2/\text{Al}$  device.<sup>157</sup>

The collaborators have applied voltage to the device and recorded chlorophyll  $\alpha$  electroluminescence spectra at 200 K and 300 K, at which the iron(II) complex ( $T_{1/2} = 260$  K) is low-spin and high-spin respectively. The emission of chlorophyll  $\alpha$  was clearly observed near room temperature, however no luminescence response was detected at 200 K (Figure 1.38a). This on-off switching of the electroluminescence in the device was reproducible for both heating and cooling processes. For comparison, the authors have also fabricated a reference device without the SCO complex and measured the electroluminescence at the same temperatures. In the reference device the luminescence was conserved at both temperatures (Figure 1.38b). The emission of chlorophyll  $\alpha$  is observed at  $\sim 700$  nm and above, which is out of typical absorption range of low-spin  $\text{Fe}^{\text{II}}$  complexes, hence the luminescence switching cannot be related to the spectral overlap in this case. The authors suggested that the action principle of this device relies on blocking of electron/hole injection into the active layer by low-spin  $[\text{Fe}(\text{dpp})_2](\text{BF}_4)_2$ .

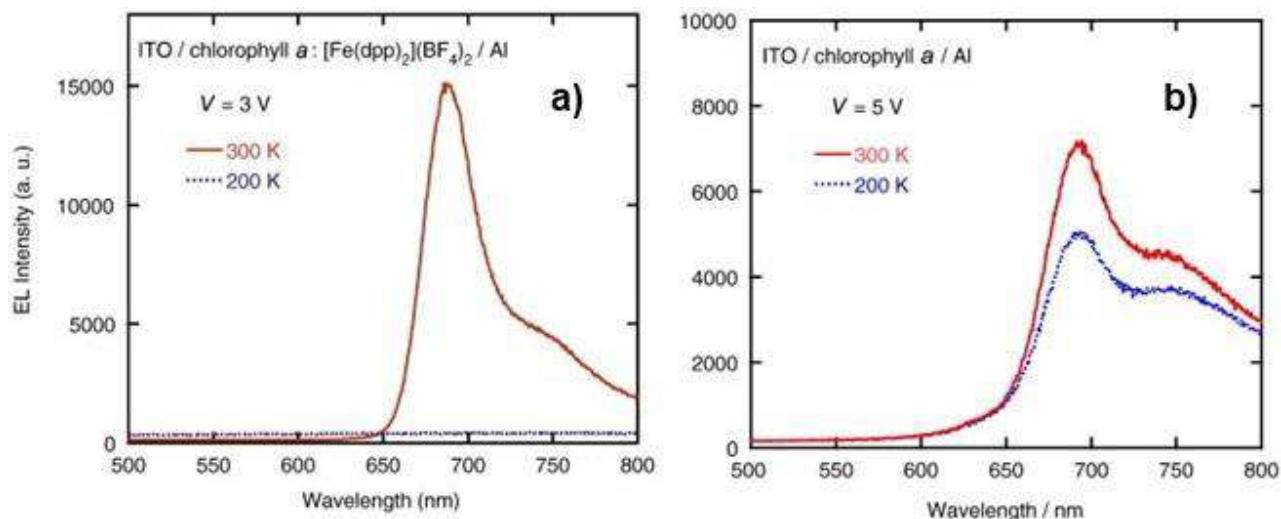


Figure 1.38. Electroluminescence spectra of: a) SCO-containing device; b) reference device without SCO.<sup>157</sup>

The first successful example of a system where the lanthanide luminescence is modulated by SCO was reported by Salmon and co-workers, who have elaborated nanoparticles of  $[\text{Fe}(\text{Htrz})_2(\text{trz})]\text{BF}_4$  covered with silica shell, the surface of which was grafted with terbium(III) ethylenediaminetetraacetate (EDTA) complex (Figure 1.39).<sup>158</sup>

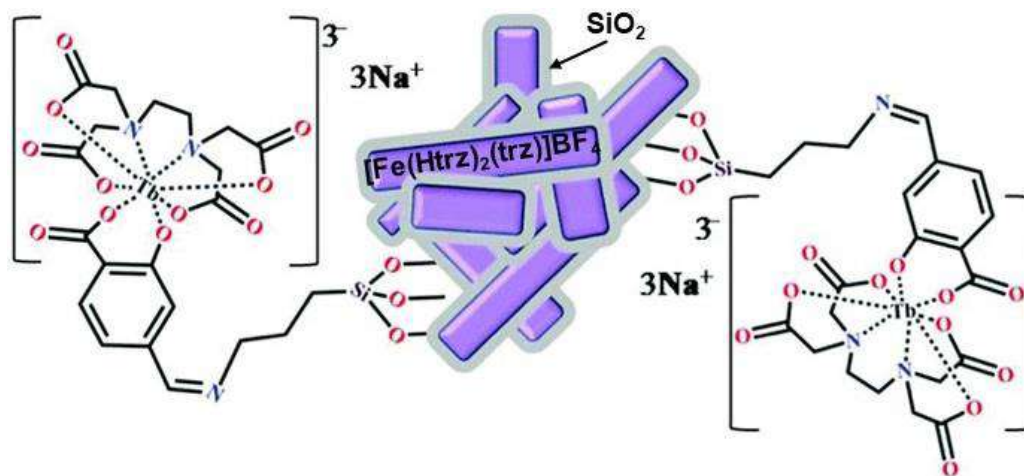


Figure 1.39. Schematic representation of the structure of the Tb-grafted SCO nanocomposite.<sup>158</sup>

To form this nanocomposite, the nanoparticles with SCO core and silica shell and terbium(III) complex were prepared separately at first. The synthesis of the lanthanide precursor started with formation of  $\text{Tb}^{\text{III}}$  complex with fully deprotonated EDTA and 5-formylsalicylic acid, which afterwards reacted with 3-aminopropyltrimethoxysilane. The final product was suitable for grafting onto silica surface, and combining it with the nanoparticles gave the considered nanocomposite. The preparation process is summarized on Figure 1.40.

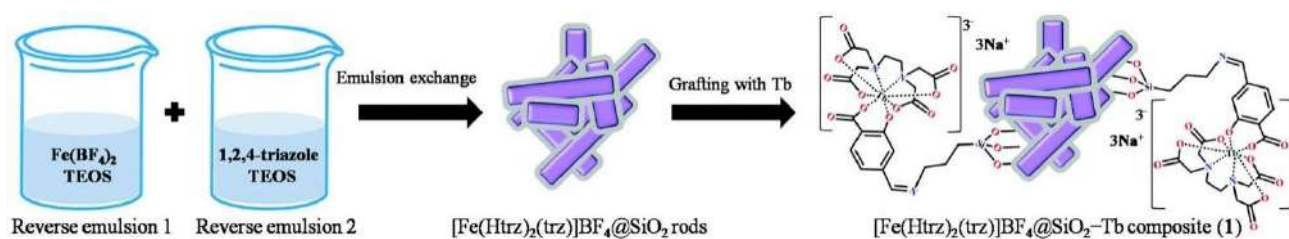


Figure 1.40. Preparation route of the Tb-SCO nanocomposite.<sup>158</sup>

Spin-crossover behavior of the nanocomposite was studied by temperature-dependent magnetic susceptibility measurements. The resulting spin transition curves are featured with broad 34 K width hysteresis loop with transition temperatures of 395 K and 361 K upon heating ( $T_{1/2\uparrow}$ ) and cooling ( $T_{1/2\downarrow}$ ) modes respectively (Figure 1.41a).

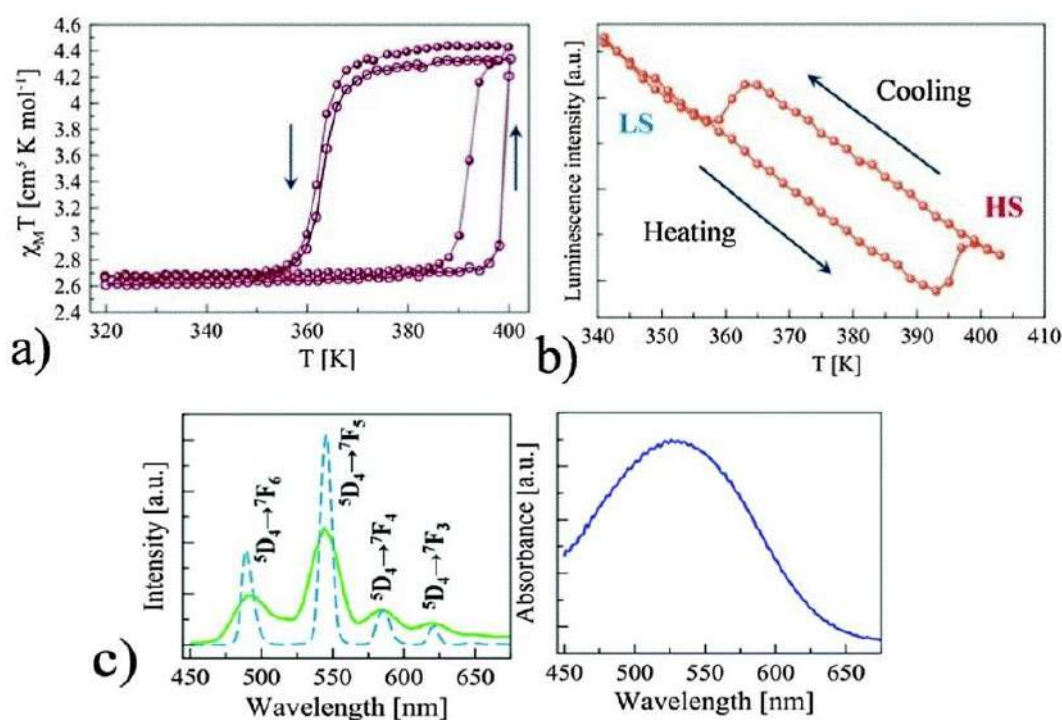


Figure 1.41. a) Variation of molar magnetic susceptibility upon temperature change over two subsequent heating/cooling cycles (empty/closed circles – 1<sup>st</sup>/2<sup>nd</sup> cycle); b) Temperature dependence of the luminescence intensity at 545 nm in heating and cooling modes; c) Room temperature emission spectra (left) of the nanocomposite (green solid line) and free Tb-complex (blue dashed line) and absorption spectrum (right) of [Fe(Htrz)<sub>2</sub>(trz)]BF<sub>4</sub> complex.<sup>158</sup>

In the emission spectrum of the nanocomposite the bands of Tb<sup>III</sup> transitions lie in the region of absorption ( $\lambda_{\text{max}} = 530$  nm) of low spin [Fe(Htrz)<sub>2</sub>(trz)]BF<sub>4</sub> complex (Figure 1.41c). The most intense  $^5\text{D}_4 \rightarrow ^7\text{F}_5$  transition band (at 545 nm) was selected to follow the spin-state dependence of the luminescence intensity. As expected, the luminescence intensity experiences an abrupt increase upon LS-to-HS transition, and its thermal variation curve is also hysteretic (Figure 1.41b). The monotonous

firm decrease of the luminescence upon heating is caused by thermal population of non-radiative states, *i.e.*, thermal quenching occurring in the Tb complex. In the nanocomposite, the SCO and Tb complexes may appear well separated from each other, so the energy transfer is unlikely to occur. Though the emission modulation is possible due to its reabsorption by the LS iron(II) complex, which does not take place when the complex is high spin. The material exhibits reversible thermal switching of the luminescence, can endure several consecutive thermal cycles and demonstrates high photostability. The same principle was applied by the authors to graft the nanoparticles with organic luminophore – pyrene (Figure 1.42).<sup>159</sup>

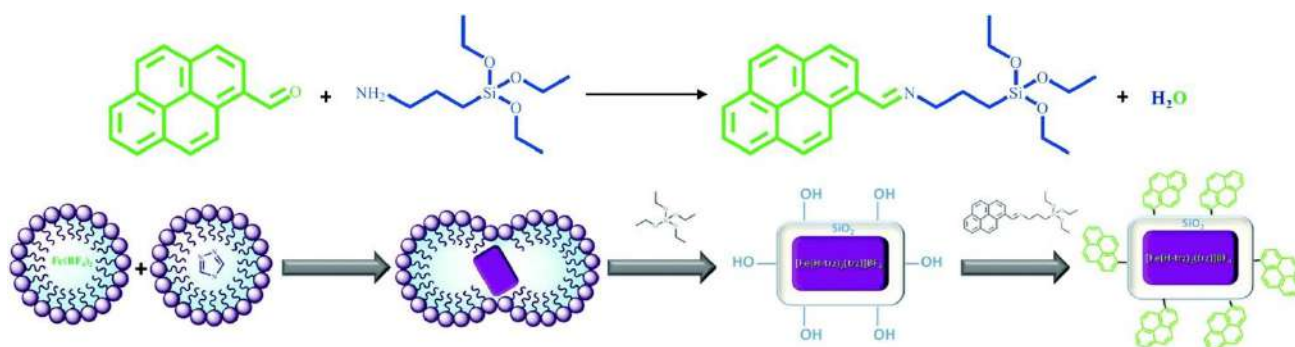


Figure 1.42. Scheme of the pyrene-bearing precursor synthesis (top), nanoparticles preparation (bottom) and grafting of the latter with pyrene.<sup>159</sup>

Pyrene and its derivatives can form excimers – dimers formed by pyrene molecules one of which is in excited state.<sup>160</sup> In emission spectra of pyrenes, excimer bands can be easily distinguished from monomer bands as they appear red-shifted towards the latter. Transitions from S<sub>1</sub> excited state level to vibrational levels of the ground state complicate the structure of the monomer emission spectra, while excimer emission appears as a broad band with single maximum. These spectral features of pyrene unit were also observed in the authors' nanocomposite (Figure 1.43).

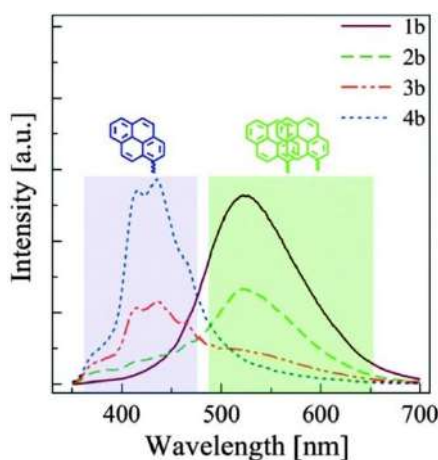


Figure 1.43. Room temperature solid-state emission spectra of the pyrene-grafted SCO nanoparticles (the content of pyrene is indicated in parentheses): 1b (38 % mass), 2b (11 % mass), 3b (4.2 % mass) and 4b (1.7 % mass).<sup>159</sup>

The co-workers have synthesized platelike nanoparticles of 60–150 nm length and 40–90 nm width, where the content of the luminophore varied from 1.7 to 38 % mass. The room-temperature emission spectra of the nanoparticles were essentially determined by the quantity of the grafted luminophore. Thus, the sample with the highest pyrene content exhibited predominantly the excimer emission, while for the one with the lowest luminophore content the monomer emission was dominant (Figure 1.43). The spectra of samples containing 4–11% mass of pyrene displayed both monomer and excimer bands in different ratios. Variable temperature magnetic measurements performed on the nanocomposite over several consecutive thermal cycles reveal a hysteretic character of the spin transition (37 K width hysteresis loop) with  $T_{1/2\uparrow}$  of 384 K and  $T_{1/2\downarrow}$  equal to 347 K (Figure 1.44a). In the first thermal cycle the hysteresis loop is wider probably due to release of the solvent trapped in the sample. The spin transition curves, obtained from following the emission intensity at 550 nm over two heating/cooling cycles, correlate with magnetic measurements data (Figure 1.44b). A slight linear decrease of the luminescence intensity upon heating to around 380 K is caused by thermal quenching similarly to the nanoparticles grafted with the terbium complex. Spin crossover in  $[\text{Fe}(\text{Htrz})_2(\text{trz})]\text{BF}_4$  induces drastic change in the unit cell volume (*ca.* 11.5%) imposing a mechanical strain on the material. The appearance of the strain in the nanocomposite can lead to changes in distances and orientation between the grafted pyrene species impacting the formation of the excimers. This was attributed as a main mechanism behind the synergy between the SCO and luminescence phenomena in the nanocomposite.

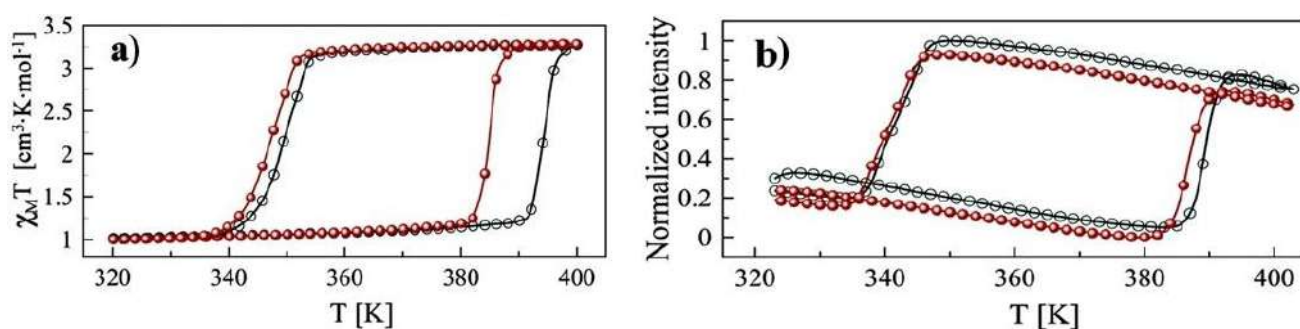


Figure 1.44. Synergy of SCO and luminescence in nanoparticles grafted with pyrene (38 % mass). Molar magnetic susceptibility plotted as a function of temperature (a) and thermal variation of normalized emission intensity at 550 nm (b) measured over two heating/cooling cycles.<sup>159</sup>

Besides the nanocomposites capable of modulation of terbium and pyrene luminescence, the research group has also created SCO nanocomposites with CdTe quantum dots.<sup>161</sup> Mixing nanoparticles of  $[\text{Fe}(\text{Htrz})_2(\text{trz})]\text{BF}_4$  wrapped in a shell of silica or a branch polyethylenimine polymer (BPEI) in a suspension with 2-nm-sized  $\text{CO}_2\text{H}$ -functionalized CdTe nanocrystals gave the bifunctional nanocomposites. The choice of the spin-crossover complex and the luminophore was founded by the very same idea as in the previous examples – the spectral overlap of the SCO LS absorption and

luminophore emission bands. Thus, at room temperature the quantum dots emission band is centered at 555 nm, which is within the range of absorption corresponding to the low-spin SCO complex. Likely to the above-discussed nanocomposites, the coupling between spin crossover and luminescence phenomena was observed, and the latter was reversibly modulated by switching the spin states of the SCO-active component. Though the quantum dots in the considered nanocomposites appeared to be a less photostable luminophore comparing to those in the previously discussed nanocomposites and underwent considerable photo- and photothermal degradation negatively affecting their luminescence properties. This effect is observed as 1-2 % luminescence intensity drop between in the second thermal cycle comparing to the first one (Figure 1.45).

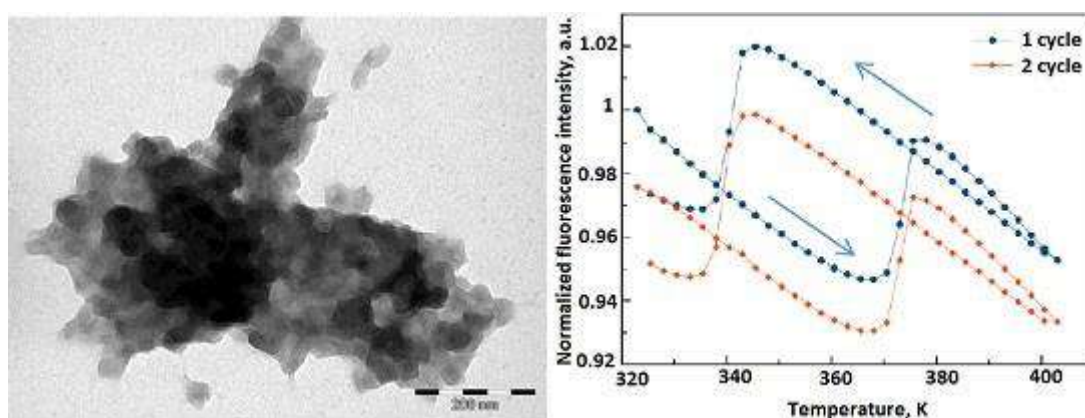


Figure 1.45. Transmission electron microscopy image (left) of the composite nanoparticles consisting of BPEI-wrapped  $[\text{Fe}(\text{Htrz})_2(\text{trz})]\text{BF}_4$  and CdTe quantum dots and their normalized luminescence intensity (550 nm) thermal variation (right) acquired over two thermal cycles.<sup>161</sup>

The operating principle of all the above considered bifunctional materials relies on the overlap of the absorption band of low-spin iron(II) complex and luminophore emission band, however the co-workers have shown that modulation of the luminescence is possible even in absence of any spectral overlap.<sup>162</sup> As a luminophore, the collaborators used a near-infrared emitting cyanine dye Cy7-NHS, with which they functionalized a branch polyethylenimine polymer and associated the resulting product with silica-wrapped  $[\text{Fe}(\text{Htrz})_2(\text{trz})]\text{BF}_4$  nanoparticles (Figure 1.46). The authors aimed to create a hybrid material with spectral overlap of the luminophore NIR emission band (maxima at 752 nm in solid state and 792 nm in solution) and absorption band of the high-spin iron(II) complex (~800 nm) situated in this spectral region, thus expecting the rise of luminescence intensity upon the transition from HS to LS state, in which the complex is NIR-transparent. As in case of the other nanocomposites, luminescence intensity showed strong dependence on the spin state of the spin-crossover component, however, contrarily to the authors' expectations, the emission intensity abruptly dropped upon high-spin to low-spin transition (Figure 1.47).

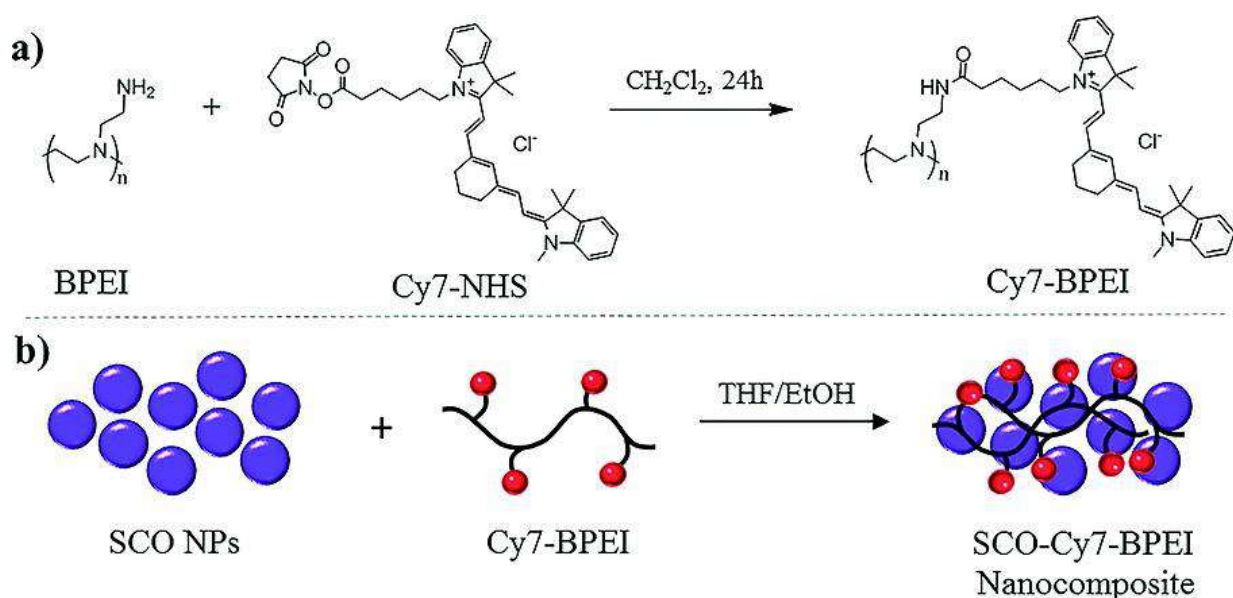


Figure 1.46. a) Functionalization of the branch polyethylenimine polymer with Cy7 dye moiety; b) Preparation of the nanocomposite of SCO with the NIR-luminescent polymer.<sup>162</sup>

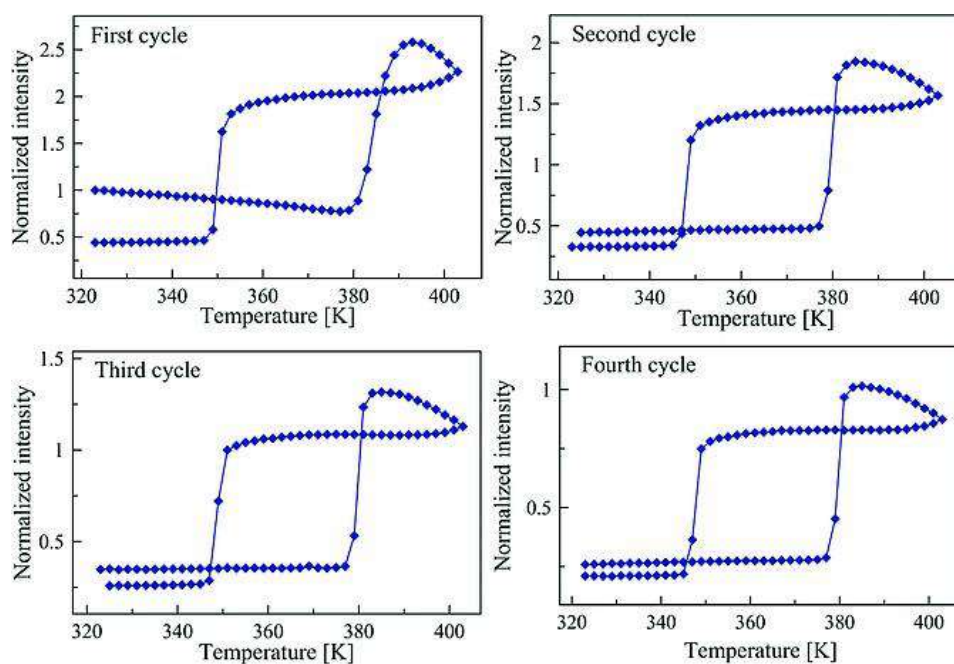


Figure 1.47. Variation of the SCO-Cy7-BPEI nanocomposite luminescence intensity over four consecutive heating/cooling cycles.<sup>162</sup>

Thus, the spectral overlap is not the reason of luminescence dependence on the spin state in this composite, but changes in crystal lattice properties of the complex can be related to the observed luminescence intensity variation.

Alternatively, Sánchez-Molina *et al.* spin-coated bifunctional composite thin film blends of a luminescent semiconducting polyfluorene polymer (poly-9,9'-dioctylfluorene or PFO) and spin-

crossover  $[\text{Fe}(\text{Rtrz})_3](\text{X})_2$  ( $\text{Rtrz} = 4\text{-hexadecyl-4H-1,2,4-triazole}$ ;  $\text{X} = \text{OTs}^-, \text{Cl}^-$ ) complexes (Figure 1.48).<sup>163</sup> The composites were prepared with the SCO content from 50% to 90%. The choice of a counter-anion of the complex impacted the morphology of the polymer. For example, with the tosylate complex the polymer conserves its original glassy phase, however, when blended with the chloride complex the polymer crystallizes in  $\beta$ -phase forming planar polymer chains. A strong coupling between luminescence and spin crossover was observed in the latter composite in 50-90% range of the SCO content. The spin transition had an abrupt character in composites with the complex content from 50% to 80%, while more gradual SCO behavior was inherent in the 90% sample. Conversely, the composite with the tosylate complex displayed the synergy between the phenomena only when the content of the coordination compound was  $\geq 90\%$ . Similarly to the previous example of the bifunctional hybrid material involving a luminescent polymer, the synergy mechanism was attributed to the environmental lattice changes accompanying the spin crossover.

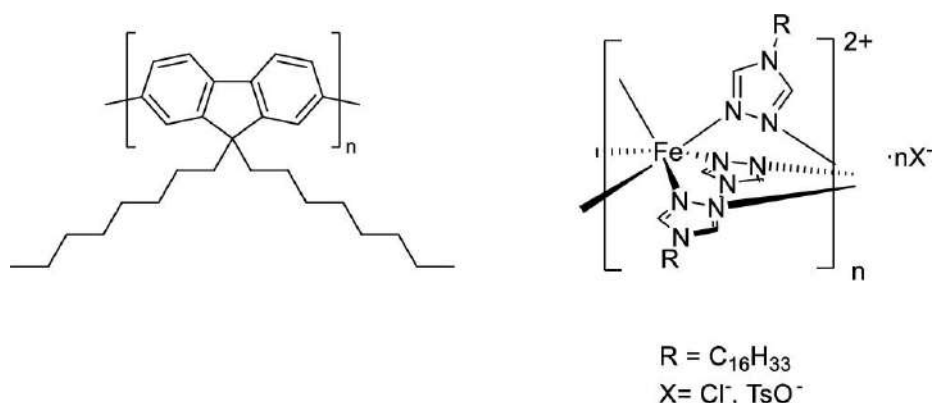


Figure 1.48. Chemical structures of poly-9,9'-dioctylfluorene (left) and  $[\text{Fe}(\text{Rtrz})_3](\text{X})_2$  (right).<sup>163</sup>

In addition to all the discussed luminophores, emission of which was tuned by switching the spin state of the SCO nanoparticles embedded into silica shell, Colacio *et al.* reported on nanocomposites where dansylamido (5-dimethylamino-1-naphthalenesulfonamido) functionalities were grafted onto the nanoparticles.<sup>164,165</sup> In their first work, the co-authors have studied the nanocomposites with  $[\text{Fe}(\text{Htrz})_2(\text{trz})]\text{BF}_4$  core and with the complex where half of  $\text{Fe}^{\text{II}}$  ions were replaced with zinc (II).<sup>164</sup> Both systems showed the synergy between the spin crossover and luminescence. In the metal-diluted system the emission intensities were higher due to lower concentration of  $\text{Fe}^{\text{II}}$  quenchers. In the second work, the researchers have established the mechanism of the luminescence switching in the non-diluted nanocomposite using luminescence lifetime measurements.<sup>165</sup> The authors compared the emission lifetime of the nanocomposite (LS core) and the emission lifetime of dansyl-derived nanoparticles of pure amorphous silica and found that the lifetime for the first one is considerably lower (7.4 ns vs 12.0 ns respectively). Reduction of the emission lifetime indicates a non-radiative deactivation of the emitter excited state by the quencher of luminescence and is associated with Förster-type energy transfer, that,

in the present case, occurs from the excited dansyl species to  $\text{Fe}^{\text{II}}$  (LS) species.<sup>166</sup> The nanocomposite demonstrated reversible luminescence switching, however the emission intensity suffered from an irreversible decrease over consecutive thermal cycling due to decomposition of the dansyl moieties upon heating over 400 K.

Another approach was coined by Bas *et al.*, who used thermal vacuum evaporation to fabricate nanometric bilayer thin films consisting of luminescent complex  $\text{Ir}(\text{ppy})_3$  or tris(2-phenylpyridinato-C2,N)iridium(III) as a bottom layer and  $[\text{Fe}(\text{HB}(1,2,4\text{-tz})_3)_2]$  SCO complex deposited on top of it.<sup>167</sup> Unlike the previous example with the nanocomposite, the operating principle of the considered hybrid material is based on blocking of the UV light in the region of the excitation wavelength of the iridium(III) complex by SCO-active layer, when the latter is in low spin state (Figure 1.49).

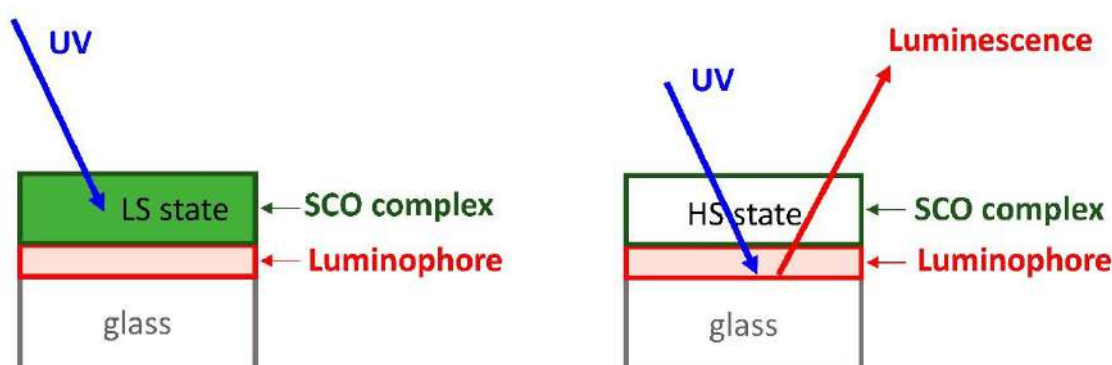


Figure 1.49. Representation of the working principle of the bilayer synergetic SCO-luminescent material.<sup>167</sup>

Upon heating, *i.e.*, upon transition from LS to HS state, a jump in the luminescence was observed, as the absorption of the top layer faded (Figure 1.50).

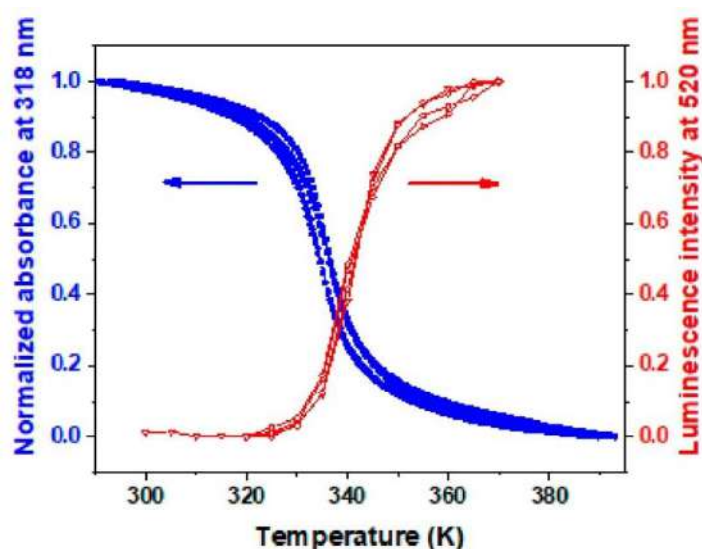


Figure 1.50. Normalized absorbance at 318 nm (blue) and luminescence intensity at 520 nm (red) of the hybrid SCO-luminescent bilayer plotted as a function of temperature.<sup>167</sup>

The reverse effect is observed upon cooling, when the SCO layer returns to low spin state. Importantly, that both optically active layers do not affect each other's intrinsic properties, and the top coating basically plays a role of a thermally switchable light filter that modulates the excitation light intensity.

A much less safe strategy implies a use of ligands that are intrinsically luminescent or bear luminophore functionalities in order to synthesize the luminescent SCO substances. The action principle of this strategy is attributed to the energy transfer from the luminescent ligand to the LS iron ion. The first efforts, involving a luminescent ligand employed to give bifunctional molecules when coordinated to the iron ion, were made by Hasegawa *et al.*, who studied the dependence of fluorescence spectra on the spin state in neutral and cationic SCO complexes of iron(II) with 2,6-bis(benzimidazole-2'-yl)pyridine ligand (Figure 1.51).<sup>168</sup>

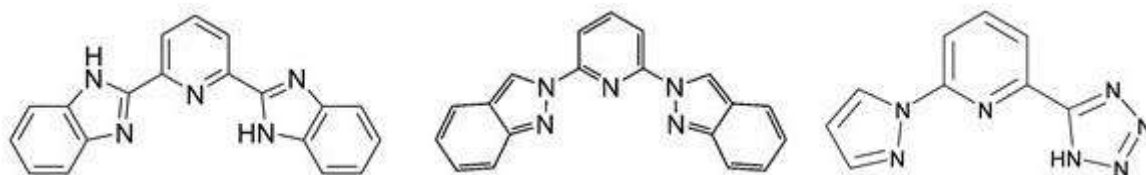


Figure 1.51. Structural formulae of luminescent ligands: 2,6-bis(benzimidazole-2'-yl)pyridine (left); 2,6-bis(indazol-1-yl)pyridine (middle) and 2-pyrazol-1-yl-6-(1H-tetrazol-5-yl)pyridine (right).<sup>168–170</sup>

The thermal variation of the ligand-centered fluorescence indeed correlated with the spin state change in the studied systems and can be used to follow the spin crossover. Despite the successful examples, complexes with similar N-heterocycle tridentate ligands, such as bis(indazolyl)pyridines<sup>169</sup> and pyrazolyl(tetrazolyl)pyridines<sup>170</sup> (Figure 1.51) tend to conserve the ligand emission without any dependence on the spin state of Fe<sup>II</sup> ion, due to absence of the energy transfer from the ligands to the metal. One of the successful examples of synergy between luminescence and SCO in a molecule of complex was achieved by Benaïcha and co-workers, who prepared and studied a mononuclear cationic iron(II) complex with six monodentate triazole-based ligands (naph-tz), in which a fluorescent naphthalimide substituents are attached to position 4 of the 1,2,4-triazole cores (Figure 1.52a).<sup>171</sup> The temperature-dependent fluorescence measurements were done on a single crystal of the complex. The emission spectra of the bifunctional compound contained characteristic extra bands not inherent in the free ligand. One of these bands was prone to a pronounced blue-shift upon elevation of temperature. The co-authors followed the thermal evolution of the band position and revealed a notable change in 70–180 K region where SCO occurs. The spectroscopic and magnetic measurements data well correlated, thus proving the coupling between the fluorescence and spin crossover properties (Figure 1.52b).

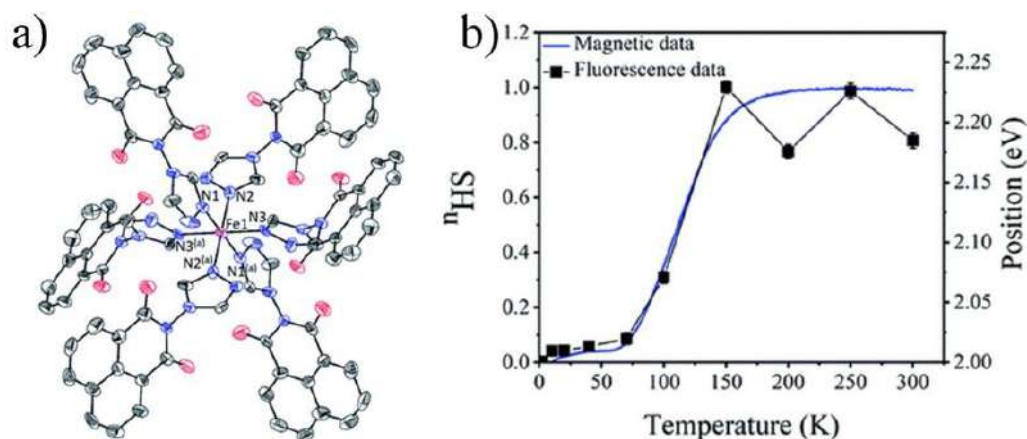


Figure 1.52. a) Crystal structure of  $[\text{Fe}(\text{naph-tz})_6]^{2+}$  complex cation; b) Alteration of the complex high-spin fraction (blue line) and the characteristic band position (black symbols) in its emission spectra upon temperature change.<sup>150,171</sup>

Although, the use of a luminescent tag linked with ligand, does not always lead to the desired interplay between the both properties and sometimes leads to disabling of one of them. This was observed in case of the iron complexes with 2,6-bis(pyrazol-1-yl)pyridine ligands featured with pyrene-based substituents at position 4 of the pyridine ring (Figure 1.53a).<sup>172</sup>

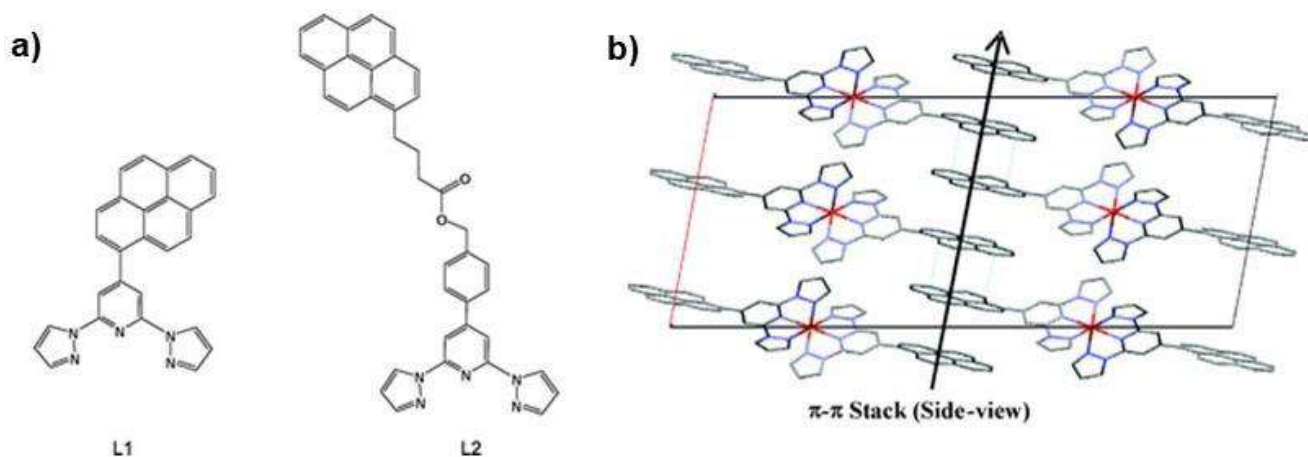


Figure 1.53. a) Structures of the pyrene-decorated 2,6-bis(pyrazol-1-yl)pyridine ligands; b)  $\pi$ - $\pi$  Stacking in a crystal of  $\text{Fe}^{\text{II}}$  complex with ligand L1 shown in a).<sup>172</sup>

Strong intermolecular  $\pi$ - $\pi$  stacking interactions between molecules of the complex, with pyrene function directly bound to the ligand core (Figure 1.53b), impose constraints incompatible with spin crossover, so the complex exists only in HS state. Separation of the polyaromatic substitute from the coordinating unit *via* alkyl-chain linker helps to preserve both fluorescence and spin crossover phenomena, but makes

impossible the energy transfer necessary for the synergy of the properties. Such nuances of the complex design highlight the delicacy of the considered strategy and difficulties to predict the result on planning stage. Nevertheless, only persistent experimental efforts result in compounds with the desired interplay of the properties. One of such an example was presented by Yuan *et al.* who used luminescent pyridinecarbaldehyde rhodamine 6G hydrazone ligand (L) to synthesize the synergetic iron(II) complex (Figure 1.54ab).<sup>173</sup>

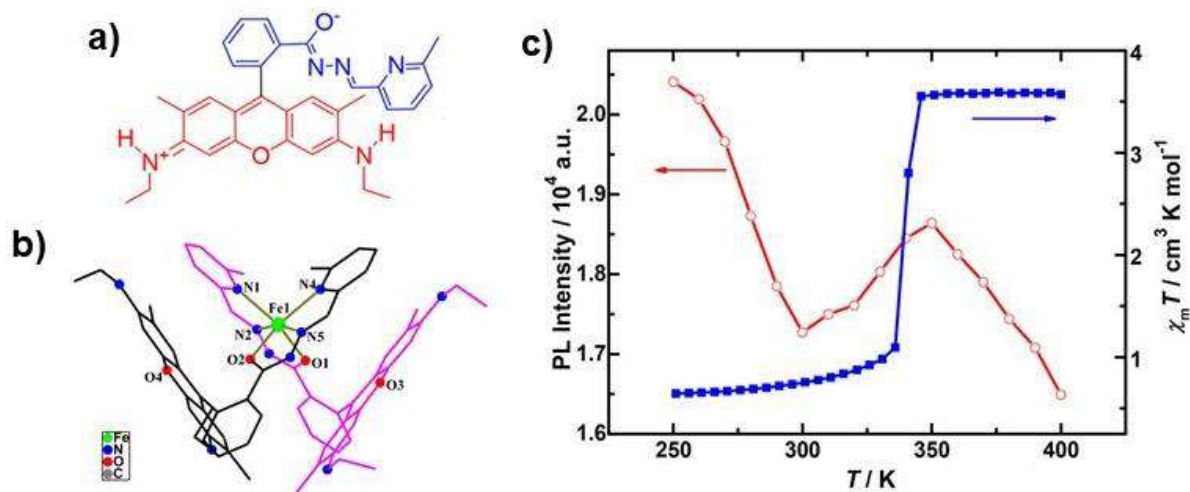


Figure 1.54. Structure of pyridinecarbaldehyde rhodamine 6G hydrazone ligand (a), crystal structure of its  $[\text{FeL}_2]^{2+}$  complex cation (b) and alteration of molar magnetic susceptibility (in blue) and luminescence intensity (in red) of the bifunctional compound in heating mode (c).<sup>173</sup>

The effect of spin crossover on the luminescence intensity was observed around the transition temperature. Thus, upon heating in 250–400 K range, emission intensity of the ligand luminescence at 560 nm experienced first a steep decrease up to 300 K, whereupon it started to increase firmly until 350 K, whereafter the intensity decrease continued (Figure 1.54c).

Other possibility to construct a SCO-luminescence synergetic system is to use post-synthetic modification of ligands in isolated complexes with luminescent moieties, as it was reported by Wang and co-workers.<sup>174</sup> The collaborators used  $[\text{Fe}(\text{NH}_2\text{trz})_3](\text{ClO}_4)_2$ , a SCO one-dimensional (1D) coordination polymer, and labeled it with fluorescent pyrene and Rhodamine B units by means of condensation reaction between the triazole amino-groups and aldehyde group of pyrenecarboxaldehyde or carboxylate group of the rhodamine (Figure 1.55).

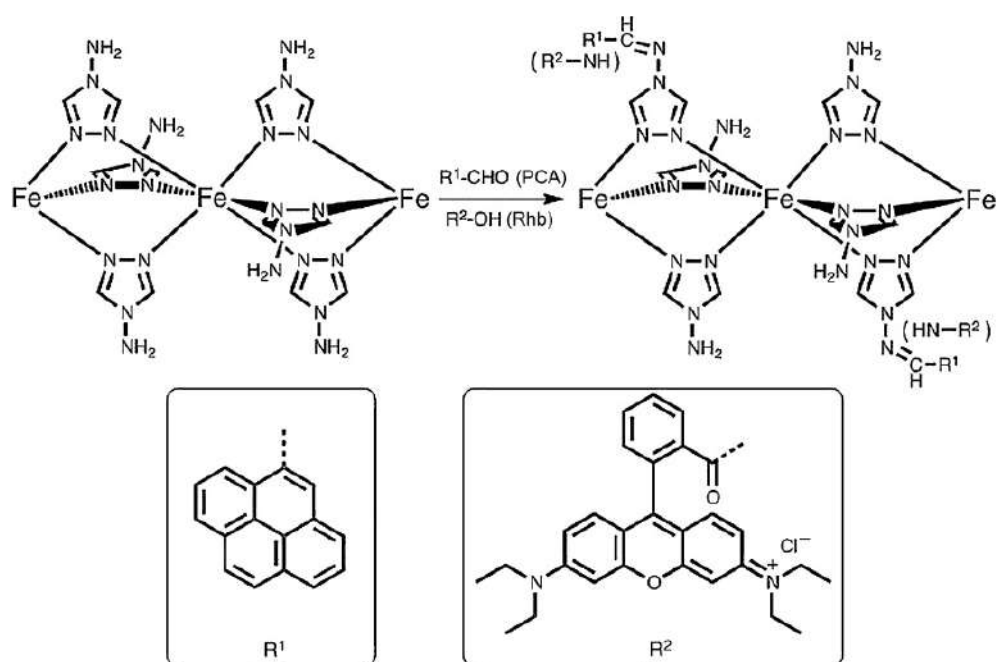


Figure 1.55. Scheme of  $[\text{Fe}(\text{NH}_2\text{trz})_3]^{2+}$  post-modification with pyrene and Rhodamine B luminophore moieties.<sup>174</sup>

In both pyrene- and rhodamine-labeled complexes the fluorescence response can be tuned depending on the spin state. Alternatively, the synergy in iron-triazole systems can be achieved by preparation of complexes with spin-crossover cations and fluorescent polyaromatic anions.<sup>175</sup> Besides iron-triazole systems, there is another bifunctional 1D-polymer, which was reported by Lochenie and co-workers.<sup>176</sup> A fluorescent phenazine-bearing Schiff base was used as a tetradentate chelating ligand and 4,4'-bipyridine was used to bridge the chelated iron species in a 1D chain (Figure 1.56a). Upon excitation with 337 nm light, the compound exhibits luminescence at 550 nm and 673 nm. The intensity of the 550 nm decreased with increase of temperature, while the intensity of the second band remained unchanged (Figure 1.56b). The plot of the intensity ratio  $I_{673}/I_{550}$  versus temperature is in line with molar magnetic susceptibility measurements data (Figure 1.56c).

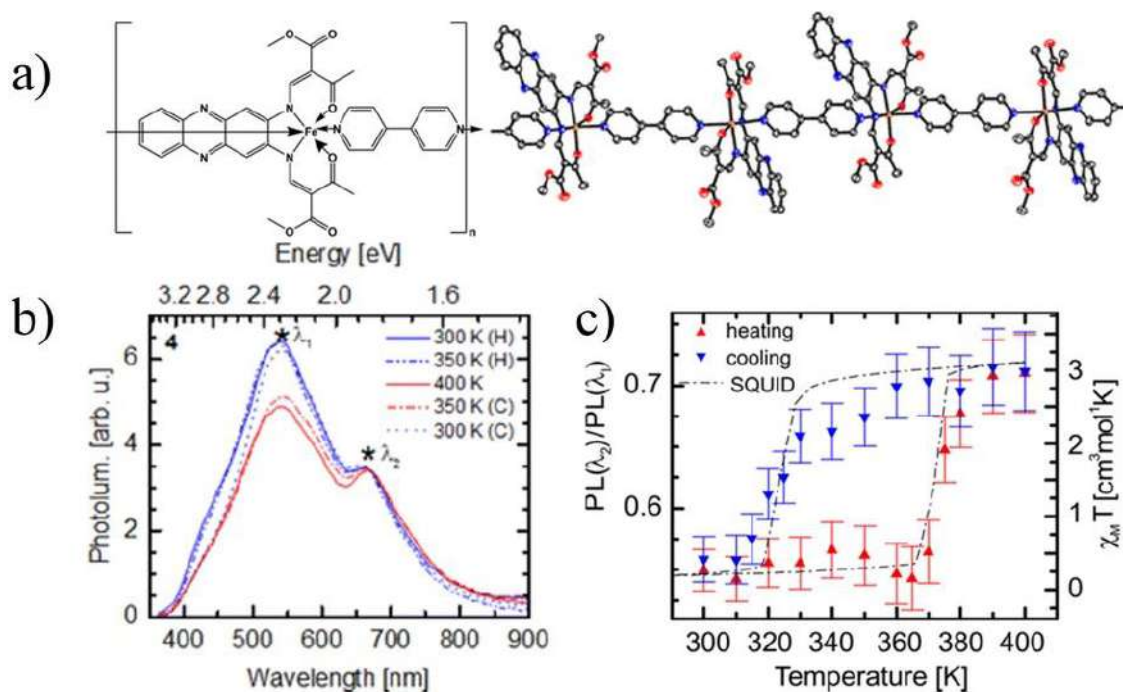


Figure 1.56. a) Structure of the synergetic 1D coordination polymer; b) Temperature-dependent emission spectra of the compound; c) Comparison of the  $\chi_M T(T)$  product and temperature-dependent luminescence ratio at  $\lambda_2 = 686$  nm and  $\lambda_1 = 550$  nm.<sup>150,176</sup>

The examples of the synergetic coordination polymers are not numerous, probably due to a synthetic challenge to provide functional SCO and luminescent species combined in a polymer, especially in case of multidimensional coordination polymers. Nevertheless, a proper ligand design allows to assemble the bifunctional structures of high complexity. Thus, Ge *et al.* have synthesized the first synergetic 2D coordination polymer using 1,1,2,2-tetrakis(4-(pyridin-4-yl)phenyl)ethene (TPPE) – luminescent tetradentate ligand, molecules of which act as “knots” that form this 2D network by “tying” together the closest four  $\text{Fe}^{\text{II}}$  centers chelated by a Schiff base like ligand (Figure 1.57).<sup>177</sup>

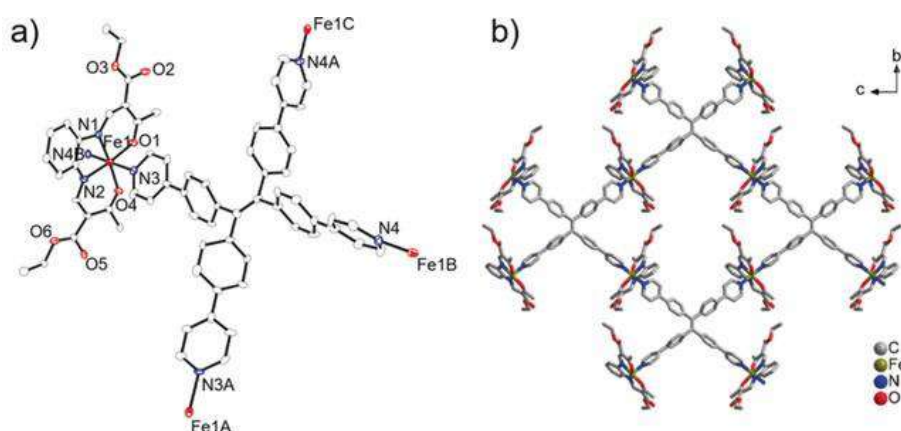


Figure 1.57. Crystal structure of the first-reported luminescent SCO 2D coordination polymer: a) Coordination environment of the iron center; b) A fragment of the 2D network showing the connection manner between TPPE and  $\text{Fe}^{\text{II}}$  centers.<sup>177</sup>

Intensity of TPPE emission in the compound reached its maximum spikewise at the spin transition temperature indicating the presence of synergetic effect between the ligand luminescence and spin crossover of iron(II). More recently, Ghosh and co-authors presented another bifunctional SCO luminescent 2D coordination network assembled using luminescent ditopic ligand 2,5-dipyridylethylene-3,4-ethylenedioxythiophene and  $\text{NCSe}^-$  to complete the metal coordination sphere (Figure 1.58a).<sup>178</sup> The coordination polymer demonstrated reversible gradual SCO behavior with  $T_{1/2} = 150$  K. The luminescence intensity first decreased upon heating up to the spin transition temperature whereafter it reached a plateau, and above 200 K it started to increase significantly pointing to cooperation between the both electronic phenomena (Figure 1.58b).

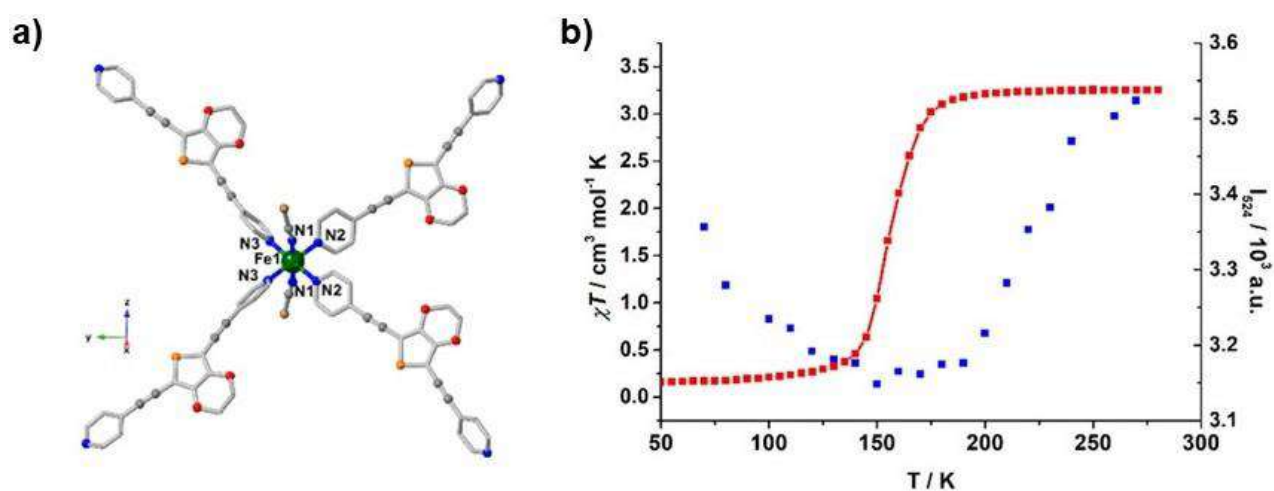


Figure 1.58. a) Crystal of the 3,4-ethylenedioxythiophene-based 2D coordination polymer; b) Comparison of temperature-dependent magnetic susceptibility (red) and luminescence intensity at 524 nm (blue).<sup>178</sup>

Aside from all the approaches considered above, there is a distinct approach allowing spin crossover and luminescence synergy. This approach implies an inclusion of guest luminophore molecules into a SCO-active framework, and firstly was implemented by Delgado *et al.*, who embedded guest pyrene molecules into cavities of host  $\{\text{Fe}(\text{bpben})[\text{Au}(\text{CN})_2]\}$  (bpben = 1,4-bis(4-pyridyl)benzene) 3D framework (Figure 1.59).<sup>179</sup> In the resulting supramolecular assembly both monomer ( $\lambda_{\text{max}} = 392$  nm) and excimer ( $\lambda_{\text{max}} = 478$  nm) emission of pyrene were detected. Moreover, the presence of intermolecular  $\pi$ - $\pi$  stacking interactions between aromatic systems of pyrene guest and the ligand favorize generation of an excited complex or exciplex, however detection of its emission was complicated by overlap with the monomer emission band. Spectral properties of the luminescent guest and the SCO host meet the conditions required for the synergy, as the position of the excimer emission band falls into the region of the metal-to-ligand charge transfer (MLCT) absorption of the low-spin host framework. As a result, the excimer emission is quenched at low temperature due to the radiative energy

transfer (emission-reabsorption), while its intensity increases upon heating. Contrarily, the monomer band strengthened upon cooling.

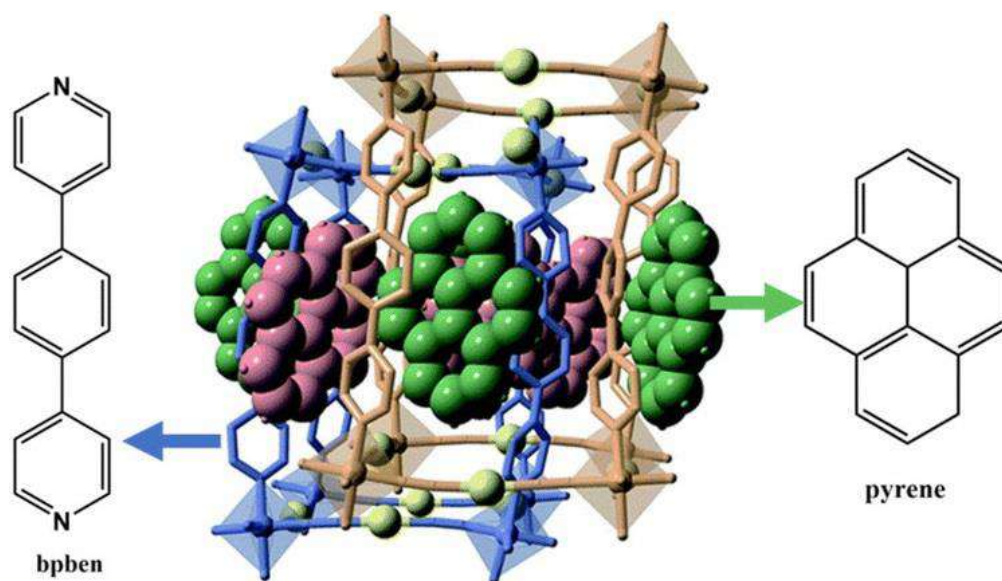


Figure 1.59. Crystal structure of  $\{\text{Fe}(\text{bpben})[\text{Au}(\text{CN})_2]\} \cdot \text{Pyrene}$ .<sup>150,179</sup>

The temperature dependence of the excimer and monomer bands intensity ratio is aligned with the magnetic measurements data. In their further work the authors have assembled two types of the frameworks, one of them contained pyrene guest and exhibited extrinsic luminescence, while another was constructed using luminescent anthracene-bearing bridging ligand (Figure 1.60) and displayed intrinsic luminescence.<sup>180</sup> The formulae for the two types of frameworks were  $\{\text{Fe}(\text{bpb})[\text{M}(\text{CN})_2]_2\} \cdot \text{Pyrene}$  and  $\{\text{Fe}(\text{bpan})[\text{M}(\text{CN})_2]_2\}$  (bpb = bis(4-pyridyl)butadiyne; bpan = bis(4-pyridyl)anthracene; M = Ag, Au). As in the previous example, the host-guest frameworks showed very similar behavior, when the guest excimer emission was quenched upon the transition of the LS host, while the monomer emission was strong at low temperature due to less thermal quenching. The Au-based framework showed incomplete quenching of the excimer emission as a result of incomplete spin transition. A strong SCO-luminescence synergy was observed for the host-guest systems. Anthracene-based  $\{\text{Fe}(\text{bpan})[\text{Ag}(\text{CN})_2]_2\}$  showed similar trend with the excimer band quenched around the spin transition temperature and monomer band strengthened. The presence of the excimer signal in the framework is ascribed to its lattice rigidity and crystallinity of the sample, however the signal is weaker than in the host-guest assemblies due to weaker intermolecular interactions the luminophore entities. In the most recent work, the collaborators synthesized 2D host-guest frameworks based on luminescent 4-(anthracene)pyridine (AnPy, Figure 1.60) as a monodentate ligand binding to iron (II) ions.<sup>181</sup> Unlike to the previously considered systems, complexes  $\{\text{Fe}(\text{AnPy})[\text{M}(\text{CN})_2]_2\} \cdot \text{XBz}$  (M = Ag, Au; XBz – substituted benzene, X = Cl, Br, I, NO<sub>2</sub> or CH<sub>3</sub>) consist of intrinsically luminescent host SCO framework

and non-luminescent guest molecules. Due to combination of steric and electronic effects the trapped guests impose on the host matrix, the SCO behaviour was tuned depending on the nature of the guest molecule. In case of the synergy, changes in the spin-crossover behaviour can impact the luminescence response. Though the conditions for the interplay between the both phenomena were met only for X = I (M = Ag, Au) and X = Cl (M = Au) displaying excimer/exciple emission overlapping with Fe<sup>II</sup> (LS) absorption.

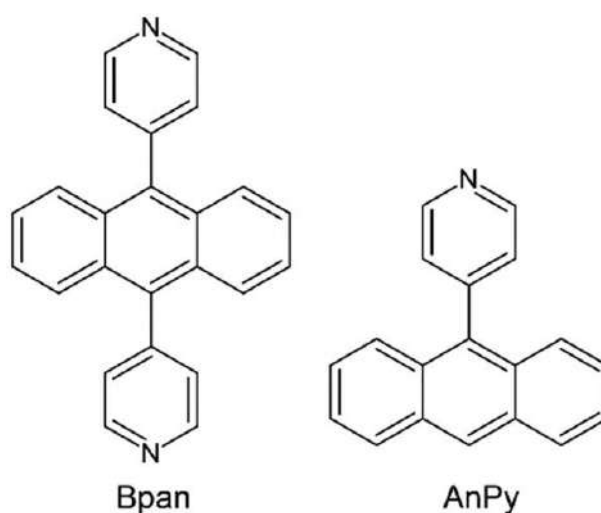


Figure 1.60. Luminescent ligands used in ref.<sup>180</sup> (left) and ref.<sup>181</sup> (right).

In summary, the concept of combining luminescence and spin crossover is relatively new and the above-considered approaches to achieve it indicate its intricacy, as the development of most of the bifunctional systems requires very careful molecular and crystallographic design allowing to conserve both phenomena and providing an interplay between them. Despite the difficulties on the way to engineer molecular SCO-Ln synergetic systems, new efforts are required to seize the lanthanide-luminescence switching mediated by spin crossover.

### 1.7 Application of SCO and luminescence in micro- and nanothermometry

Modern technology often deals with micro- and nanoscale applications, where contact techniques of temperature measurement are undesirable or impossible.<sup>182</sup> Remote temperature sensing and imaging is paramount for biomedical applications, photonics and microelectronics.<sup>183–190</sup> Among the known contactless temperature-probing and imaging techniques, the most abundant of them are based on optical response of the studied body's surface to the thermal variation.<sup>183</sup> Typical temperature-sensitive optical responses include: Planck blackbody radiation,<sup>191–193</sup> luminescence,<sup>194</sup> Raman scattering<sup>190</sup> and thermorefectance.<sup>182,195–197</sup> The latter phenomenon stands for dependance of surface optical reflectance on temperature. Thermometry based on thermorefectance allow high thermal and temporal resolution

and provide possibility to perform both qualitative and quantitative measurements. However, the method has drawbacks: it requires calibration of the surface reflectivity index and depends on the material as surfaces of various materials have different thermorefectance responses, and not all of them show high sensitivity to the temperature change. The latter obstacle can be overcome by coating of the target surfaces with materials that change their optical response depending on temperature. Such coatings can significantly increase the sensitivity by enhancing the thermally governed optical contrast of the coated surface. Spin-crossover compounds can serve as promising candidates to this purpose. Spin crossover entails changes in optical properties of the compound such as absorption and reflection, which correlate with magnetic properties change and can be conveniently followed by optical methods (*e.g.*, optical microscopy).<sup>198</sup> To prove this idea, Ridier *et al.* have deposited a 200-nm thin film of [Fe(HB(1,2,4-tz)<sub>3</sub>)<sub>2</sub>] on the surfaces of glass and oxidized silicon chips patterned with a set of equally-sized gold nanowires (Figure 1.61).<sup>29</sup>

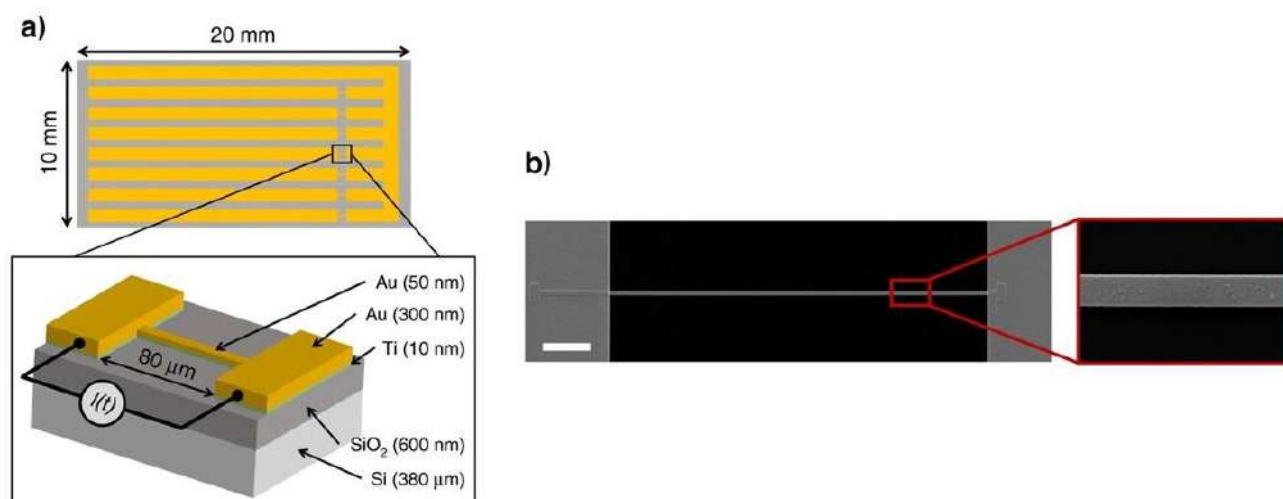


Figure 1.61. a) Schematic drawing of the chips with an array of seven nanowires (80- $\mu\text{m}$ -long, 1- $\mu\text{m}$ -wide and 50-nm-thick) and depiction of a nanowire on top of the oxidized silicon surface; b) Images of 1- $\mu\text{m}$ -wide nanowire obtained using scanning electron microscopy.<sup>29</sup>

The ferrous complex undergoes an abrupt spin transition both in bulk and thin film forms. Accordingly, its optical reflectivity change also has an abrupt character. Applied electrical current induced the Joule heating of a selected nanowire and, consequently, of the SCO layer. The optical absorption of the film decreases upon LS-to-HS transition leading to abrupt increase of the optical reflectivity of the coated gold-nanowire surface, and to decrease for the glass and silicon surfaces. This considerable step in optical reflectivity brings out a well-defined isotherm allowing to record real-time contour maps of the surface temperature distribution without any precedent calibration of the surface optical properties (Figure 1.62).

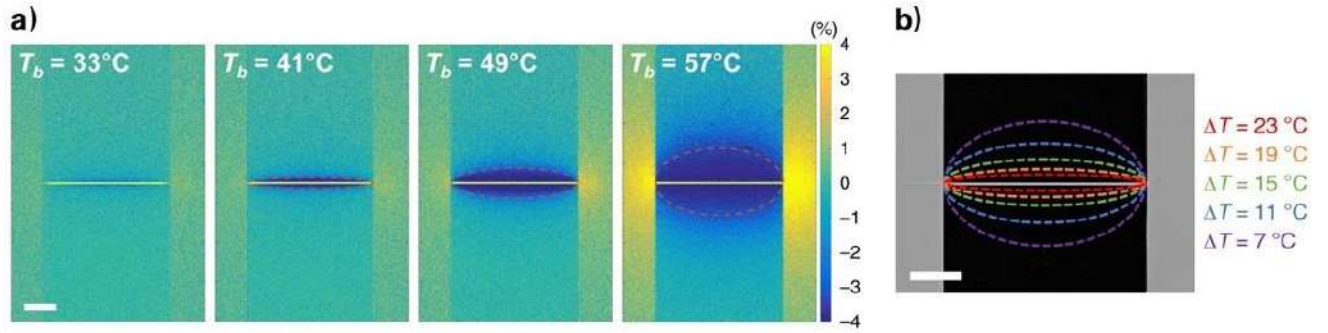


Figure 1.62. a) Optical reflectivity change images of selected nanowire ( $80 \mu\text{m} \times 1 \mu\text{m} \times 50 \text{nm}$ ) obtained at chosen base temperatures. The final images were obtained by difference between the images acquired when the current was applied (on) and when the current was off in relation to current-off image:  $\Delta R/R = (R_{ON} - R_{OFF})/R_{OFF}$ ; b) Surface temperature contour map. The dotted lines represent the position of isotherms at different base temperatures ( $\Delta T = T_{1/2} - T_b$ ).<sup>29</sup>

The contour maps can be obtained by varying the temperature of the entire chip (hereafter *base temperature* or  $T_b$ ) and imaging the optical reflectivity change in the region of the wire, both when the current is on and off (Figure 1.62a). The resulting optical reflectivity change maps allow to extract isotherms for each  $T_b$  (Figure 1.62b). The temperature rise on the isotherms is defined as difference between the spin transition and base temperatures ( $\Delta T = T_{1/2} - T_b$ ). Thermal images of the surface were acquired from scanning of the current-OFF and current-ON reflectivity profiles over a wide base-temperature range. The local heating can be determined for each image pixel (on the wire or area nearby) with sub-micrometric resolution by difference  $\Delta T = T_{1/2}^{OFF} - T_{1/2}^{ON}$  (Figure 1.63).

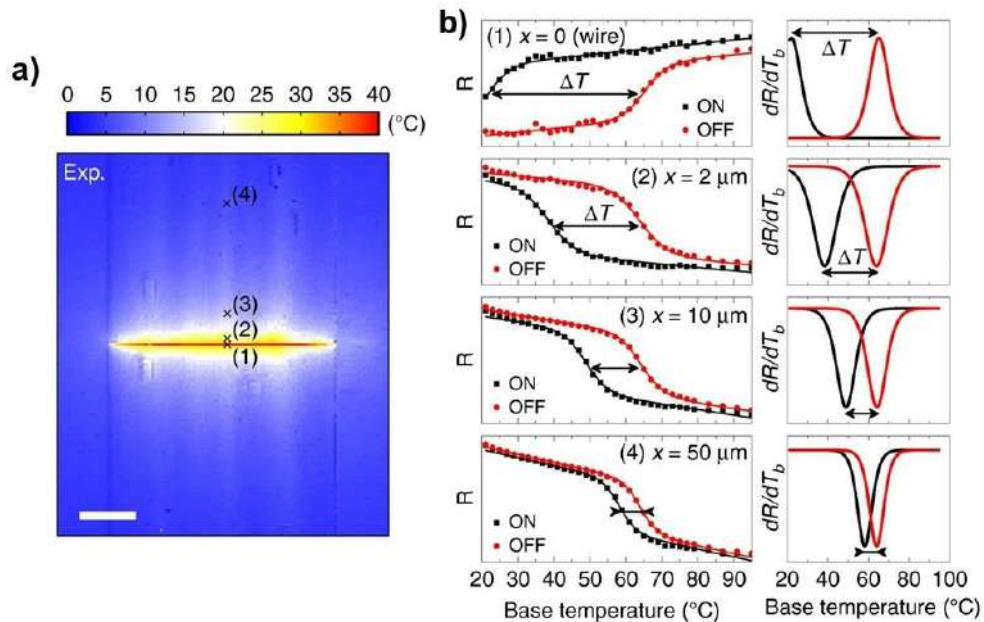


Figure 1.63. a) Temperature map ( $\Delta T$ ) of the Joule-heated nanowire on glass. Crosses mark individual pixels ( $1 \times 1 \mu\text{m}^2$ ); b) Current-ON and current-OFF reflectivity profiles of the pixels marked on the temperature map at different distances from the wire ( $x$ ). Difference between two peaks in the respective derivative curves gives the average temperature rise of a pixel.<sup>29</sup>

The studies have proven that the thermal sensitivity of the coated surfaces ( $-0.35\% \text{ K}^{-1}$  for coated glass) increases about 10 times (at  $T_{1/2}$ ) comparing to the conventional thermorefectance ( $-0.036\% \text{ K}^{-1}$  for pristine glass). The authors' thermometry technique afforded high spatial ( $< \mu\text{m}$ ), temporal ( $\mu\text{s}$ ) and thermal (1 K) resolution. The complex thin film does not affect the overall electrical and thermal performance of the devices, which makes the considered technique non-invasive. After all, the film serves as a prominent binary temperature sensor allowing fast thermal mapping without prior calibration of the surface properties.

Despite the advantages the abrupt spin transition can offer for thermometry, it does not allow a continuous real-time temperature monitoring enabled by the gradual transition. For this purpose, Salmon *et al.* have synthesized a hybrid fluorescent SCO material represented by 3-nm-sized nanoparticles of  $[\text{Fe}(\text{NH}_2\text{trz})_3](\text{NO}_3)_2$  doped with 0.01% of rhodamine-110.<sup>155</sup> The temperature-dependent fluorescence intensity variation of nanoparticle suspension appears as reproducible relatively gradual SCO curve in 293–313 K region with  $T_{1/2} = 303 \text{ K}$  (Figure 1.64a).

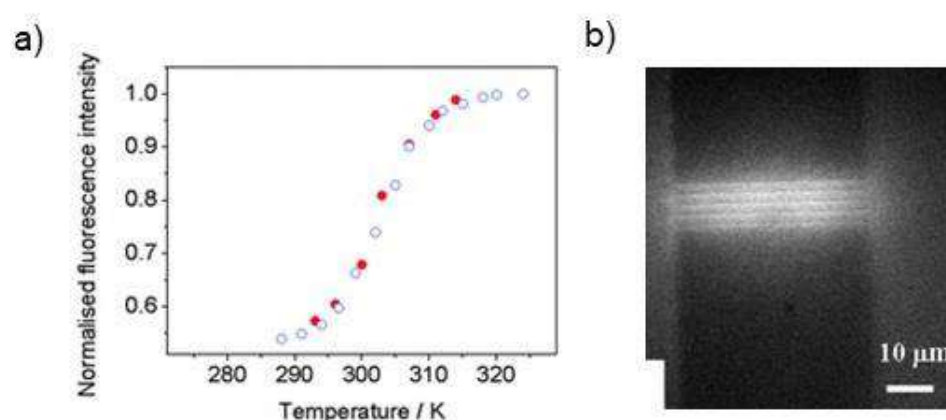


Figure 1.64. a) Thermal variation of fluorescence intensity (at  $\lambda = 540 \text{ nm}$ ) of the rhodamine-110-doped  $[\text{Fe}(\text{NH}_2\text{trz})_3](\text{NO}_3)_2$  nanoparticles suspension upon heating (empty circles) and cooling (filled circles); b) Fluorescent microscopy image of the nanoparticle-coated nickel nanowires obtained by difference between the images taken with current ON and current OFF.<sup>155</sup>

The co-workers have deposited the suspension on top of nickel nanowires patterned on silicon substrate and recorded fluorescent microscopy images both when 6 mA current flowed through the wires and when the current was off. The specific value of the current provided full LS-HS transition. A significant increase in the fluorescent intensity was observed when the current passed through the wires. As expected, the resulting thermal images show a temperature increase in immediate proximity to the nanowires. (Figure 1.64b) The fluorescent SCO thermometer has a perspective of use for high spatial resolution thermometry with the only restriction by the diffraction limit.

The phenomenon of luminescence itself depends on temperature, and this dependence can be used for thermometry purposes.<sup>194</sup> In lanthanide-based compounds, the population of the metal ion

excited state levels is temperature-dependent which reflects on intensity ratio of the emission bands changing with temperature.<sup>199–201</sup> The excited energy levels of the ion must be close enough to each other that one is thermally populated at the expense of the other. The temperature-induced intensity ratio change is also a feature of systems with two different lanthanide ions that are located close to each other, and when there is a temperature-dependent ion-ion energy transfer between them.<sup>202</sup> In this case, with the change of temperature, the ratio of the intensity of two bands changes, *e.g.* in the Tb-Eu systems: of the Eu band and the Tb band. The most studied systems, in this aspect, are lanthanide metal organic frameworks (MOFs).<sup>185</sup> There are also reports on molecular homo- and heterobimetallic thermal sensing systems.<sup>203,204</sup> Thus, Salerno and co-workers studied thermometric properties in dimeric metallacrown complexes bearing two identical lanthanide emitters in  $\text{Ln}_2\text{L}_8$  motif (where L is a hydroxamate) shown on Figure 1.65.<sup>203</sup>

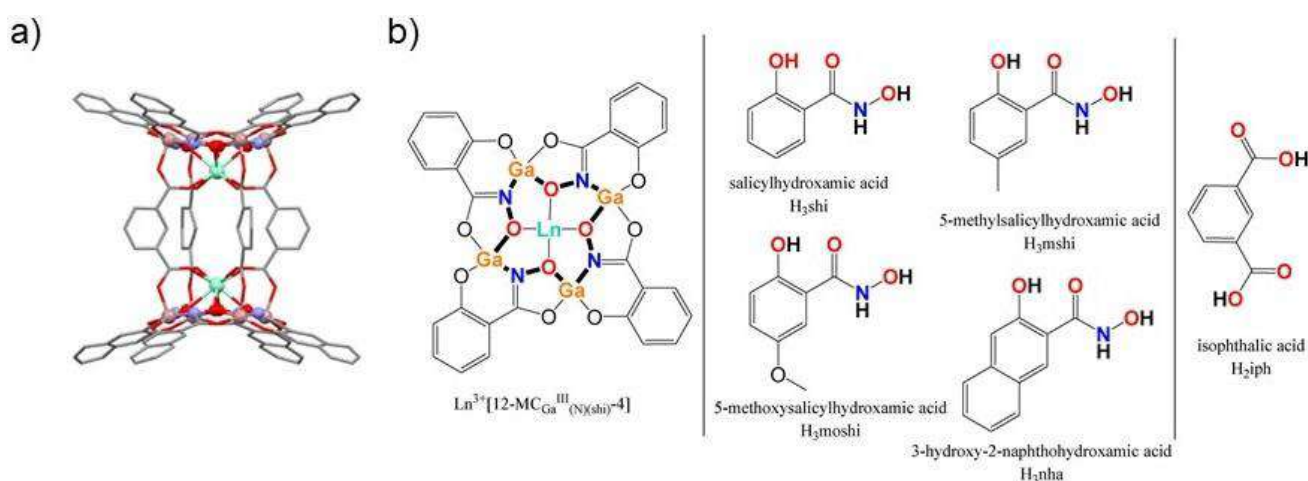


Figure 1.65. a) Structure of  $\text{Ln}_2\text{nha}_8$  ( $\text{nha}$  = 3-hydroxy-2-naphthohydroxamate) metallacrown dimer; b) Example of the metallacrown core (left) and structural formulae of hydroxamate ligands L (right, in bars) used by the authors. Two metallacrown cores are bridged together by isophthalate (right, behind the bars).<sup>203</sup>

The luminescence spectra of binuclear terbium(III) and samarium(III) complexes acquired over 11–400 K temperature range demonstrated a general intensity fade for all of the emission bands with temperature evolution. However, the character and the extent of this change are different for each of the metal ions. It can be observed on the example of selected emission bands in  $\text{Ln}_2\text{moshi}_8$  systems ( $\text{moshi}$  = 5-methoxysalicylhydroxamate). In  $\text{Tb}^{\text{III}}$  complex,  $^5\text{D}_4 \rightarrow ^7\text{F}_5$  line intensity decreases with the temperature rise and retains its band shape, contrarily the intensity of  $^4\text{G}_{5/2} \rightarrow ^6\text{H}_{7/2}$  transition band in  $\text{Sm}_2\text{moshi}_8$  fluctuates negligibly, but significant broadening of the band is observed (Figure 1.66ab). These spectral features are attractive for combination in one system, where the samarium emission band can serve for internal calibration of the terbium emission. To implement this concept, the researchers ground together

a solid-state equimolar mixture of the both complexes. Likely to the intensity of  ${}^5\text{D}_4 \rightarrow {}^7\text{F}_5$  band of the terbium metallacrown alone, the  $({}^5\text{D}_4 \rightarrow {}^7\text{F}_5) / ({}^4\text{G}_{5/2} \rightarrow {}^6\text{H}_{7/2})$  ratio of the band integrated intensities started to decrease brusquely above 150 K and nearly faded away over the course of heating (Figure 1.66c). The peak of thermal sensitivity of the resulting ratiometric luminescent thermometer reached above  $2.5\% \text{ K}^{-1}$  at 220 K (Figure 1.66d). The particularity of the reported thermometer is that it was composed by mixing two independent substances.

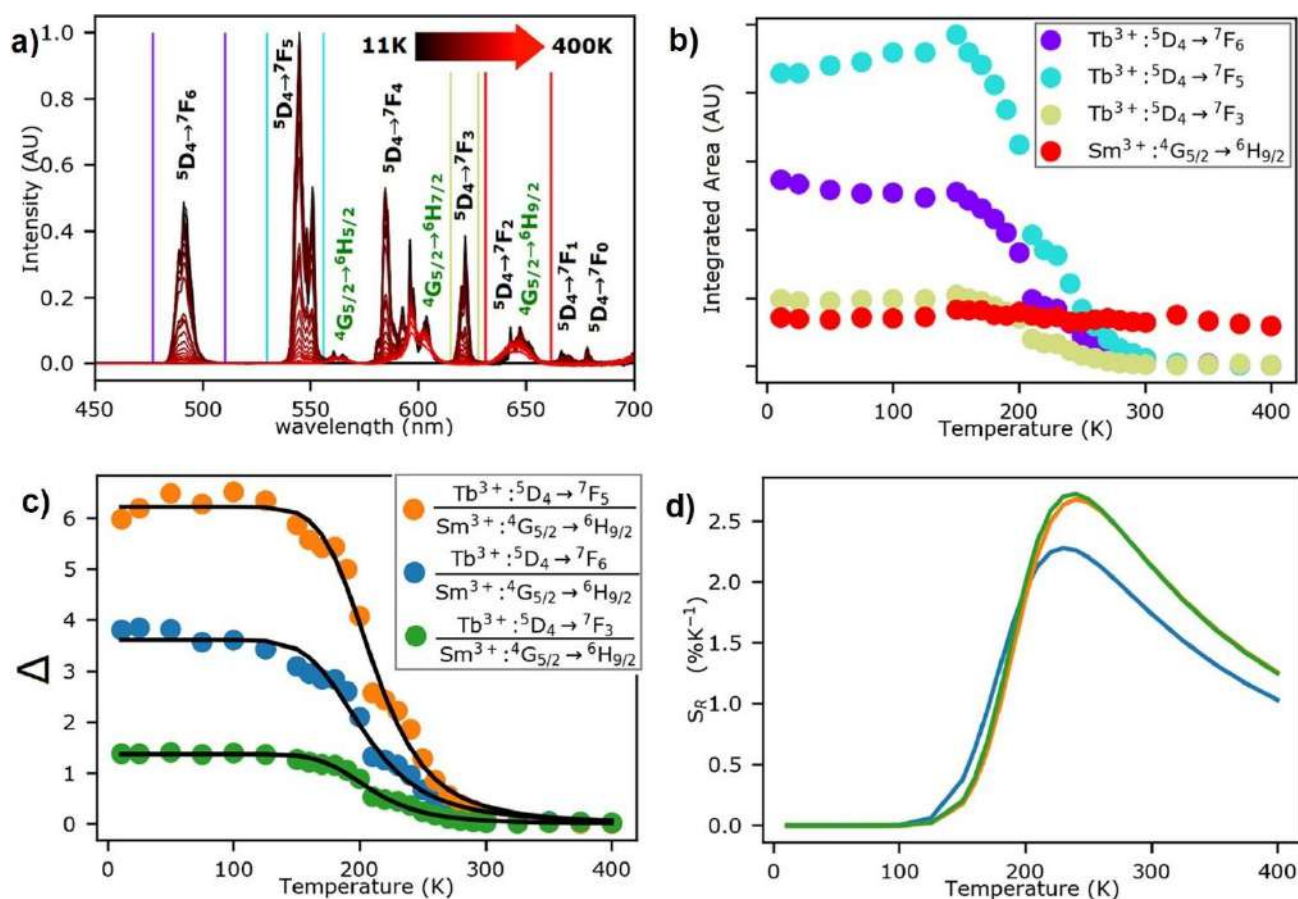


Figure 1.66. Tb<sub>2</sub>moshi<sub>8</sub>:Sm<sub>2</sub>moshi<sub>8</sub> (1:1) optical thermometer: a) thermal evolution of the Tb- (dark red) and Sm-centered (bright red) emission spectra. Tb<sup>III</sup> transitions are marked in black text, while those for Sm<sup>III</sup> – in green; b) Temperature dependance of integrated intensities of selected bands; c) Integrated intensities ratios ( $\Delta$ ) of  $({}^5\text{D}_4 \rightarrow {}^7\text{F}_J, J=3, 5, 6; \text{Tb}^{\text{III}}) / ({}^4\text{G}_{5/2} \rightarrow {}^6\text{H}_{7/2}; \text{Sm}^{\text{III}})$  as a function of temperature; d) Relative sensitivity ( $S_R = 1/\Delta|\partial\Delta/\partial T|$ ) of the optical thermometer plotted vs temperature.<sup>203</sup>

Bao *et al.* have synthesized heterobinuclear complexes using a ligand with two different covalently-linked binding sites coordinating Eu<sup>III</sup> and Tb<sup>III</sup> ions.<sup>204</sup> Ligand bearing a macrocyclic encapsulating site and the bidentate phen unit allows variable coordination the distinct lanthanides by both sites controlled *via* different synthetic paths. Owing to these structural possibilities of the ligand, the authors were able to synthesize heterobimetallic cycTb-phEu and cycEu-phTb complexes (Figure 1.67).

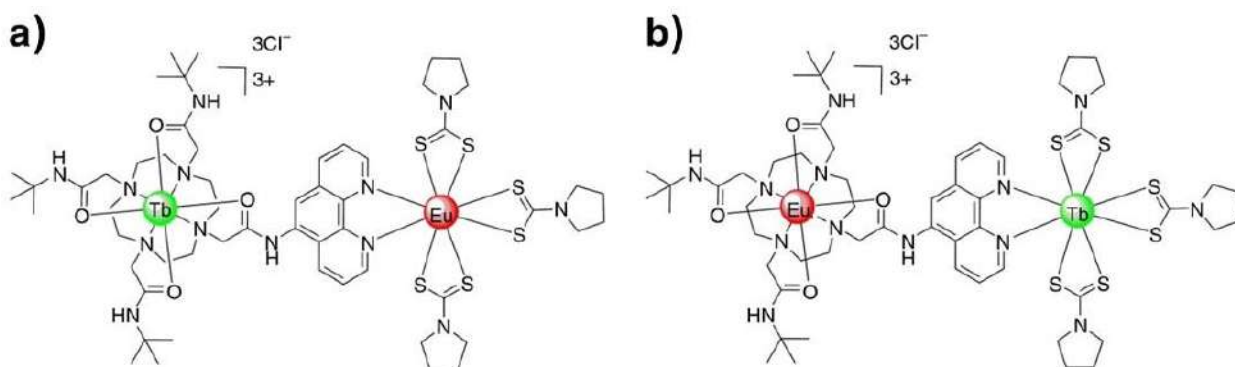


Figure 1.67. Molecular structures of **a)** cycTb-phEu and **b)** cycEu-phTb.<sup>204</sup>

The  $^5D_4$  level of terbium has higher energy comparing to  $^5D_0$  of europium favorizing the energy transfer to the latter ion. The calculated Ln...Ln distance of ca. 10.6 Å makes possible the inter-ion energy transfer. The emission spectra of the both compounds acquired within 10–298 K interval showed temperature-dependent Tb-Eu energy transfer. The investigations revealed an exponential growth of  $(^5D_0 \rightarrow ^7F_4) / (^5D_4 \rightarrow ^7F_5)$  intensity ratio along with the temperature for complex cycEu-phTb (Figure 1.68).

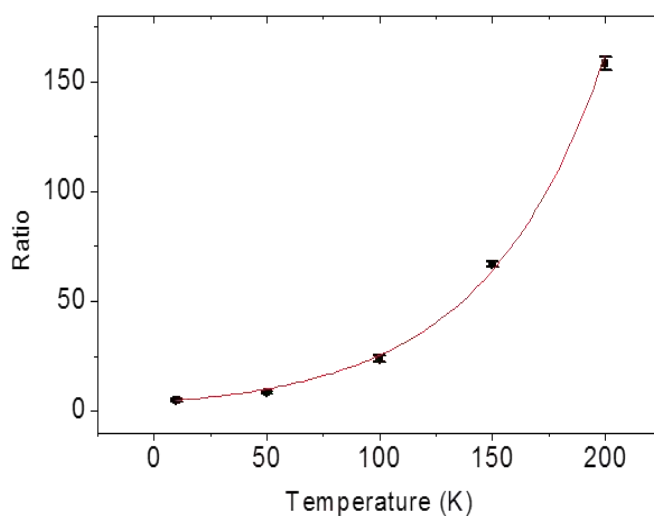


Figure 1.68. Thermal variation of  $(^5D_0 \rightarrow ^7F_4) / (^5D_4 \rightarrow ^7F_5)$  intensity ratio for cycEu-phTb.<sup>204</sup>

The thermal sensitivity of this molecular thermometer was a constant value of 1.86%  $K^{-1}$  and the thermal resolution was  $<1$  K at high temperatures attractive for potential thermometry applications. The concept developed by the co-workers is beneficial in terms of possibility to control synthetically the heterobimetallic complex formation, fixed and relatively close distance between two emitters and fixed stoichiometric ratio of the latter.

Therefore, the phenomena of spin crossover and luminescence possess a great potential for application in noninvasive small-scale thermometry techniques. Vacuum-deposited SCO thin films are convenient thermo-responsive materials to probe the temperature in reduced-size electronic circuits. If

such thin films undergo an abrupt spin transition, they can function as binary thermal sensors. To follow the surface temperature continuously in real time, gradual spin transition is required. As spin-crossover thin films with gradual SCO have not been previously reported, the further research efforts should be focused on development of the appropriate spin-crossover compounds and materials.

Molecular optical thermometers exploiting lanthanide luminescence can serve for temperature sensing in a broad range from cryogenic to biological regions or even higher. However, the number of such examples is scarce. Considering this fact, new lanthanide bimetallic coordination compounds are needed to fill this gap. Binuclear helicates offer a versatile candidature to address this issue, as, with careful molecular design, the distance between the Ln emission centers can be programmed,<sup>142</sup> which is important for thermometers based on the inter-ion energy transfer.

### **1.8 Objectives of this work**

Summarizing the above literature analysis, it can be concluded that spin crossover phenomenon in coordination compounds of iron(II) is extensively studied by numerous research teams owing to a broad extent of properties change it produces in the substance such as optical, magnetic and structural properties change. This variety of responses and characters of the spin transition allows a broad range of applications covering information storage, chemical sensing and mechanical actuation. One of the forms of SCO materials suitable for application is represented by thin films. To ensure the reproducibility of properties, the films should meet criteria of high quality, purity and homogeneity. Thermal vacuum deposition serves as an appropriate technique allowing to fulfill these requirements. However, the number of spin-crossover compounds that can be deposited in thin films by this technique is fairly limited. Consequently, this research field requires to be supplemented with new SCO coordination compounds and thin film materials on their basis.

Luminescence of trivalent lanthanide ions have been attracting scientists' attention since it was discovered, due to its pronounced distinction from other luminophores and advantages it offers. Lanthanide complexes with organic ligands exhibit brighter emission than Ln<sup>III</sup>-based purely inorganic compounds. High color purity, large Stokes shifts and long lifetimes of the lanthanide-centered emission are important parameters to design electroluminescent devices and for bio-medical applications. Choice of ligand(-s) is important in design of highly luminescent lanthanide complexes.  $\beta$ -Diketones are versatile ligands to this purpose. The structural analogues of 1,3-diketones – carbacylamidophosphates (CAPH) offer advantages for sensitization of the lanthanide luminescence and binding of the metal ion. Other strategy to achieve the highly efficient emission is to increase the number of optical centers, which was clearly demonstrated in series of binuclear lanthanide helicates with bis- $\beta$ -diketonate ligands.

Considering the benefits that CAPH ligands have over  $\beta$ -diketones, development of bis-chelating CAPH ligands and their lanthanide complexes may lead to further improvement of  $\text{Ln}^{\text{III}}$ -centered emission.

The synergy of spin crossover and luminescence is a new horizon in the field of multifunctional materials. Combining both in one system may result in an interplay between the phenomena. Spin state switching can induce the switching of luminescence, while the latter can be used to report on the spin state of the SCO-active part. Various hybrid SCO-luminescence systems are known up to date, from luminescent spin-crossover complexes to hybrid materials where luminescent and SCO entities are separated. It is proven to be challenging to obtain such synergetic compounds, since combining the luminescent and spin-crossover species in one substance may often result in canceling of one of the phenomena. Alternatively, both phenomena can be preserved without any coupling between them. Therefore, the further development of the bifunctional systems requires careful molecular and crystallographic design. Examples of the systems with interplay between the lanthanide luminescence and spin crossover are extremely rare. Regardless the difficulties on the way to create such systems, new efforts are required to seize the SCO-governed lanthanide-luminescence switching.

The phenomena of spin crossover and luminescence are temperature-dependent and provide a detectable optical response to the temperature change, which can be used as a noninvasive tool for thermometry at micro- and nanoscale. The SCO thin film of  $[\text{Fe}(\text{HB}(1,2,4\text{-tz})_3)_2]$  deposited on surface of a Joule-heated nanowire behaved as a binary surface thermometer due to the abrupt character of the spin transition. This can find an application in local heating monitoring in integrated circuits. A continuous real-time temperature monitoring can be achieved in the materials with gradual SCO. As there was no report on the thin films with such properties, a new evaporable spin-crossover complex and its thin films undergoing gradual spin transition should be prepared to fill this gap.

Molecular luminescent thermometers based on the lanthanide emission show high sensitivity to the temperature change in a broad interval. Although, such systems are not numerous. The development of new bimetallic Ln complexes may extend the number of such optical thermometers. Due to adjustable molecular design and possibility to control the intermetallic distance, binuclear lanthanide helicates can be versatile candidates to assemble the molecular thermometers exploiting the inter-ion energy transfer.

Following the brief conclusions to the literature review, the next objectives to this research work can be distinguished:

1. Synthesis of novel ligands for coordination to iron(II) to form new sublimable SCO complexes. Investigation of spin crossover behavior of the bulk complexes. Elaboration of thin films of the complexes *via* vacuum deposition of the compounds on various substrates. Investigation of the SCO in the resulting thin films.

2. Synthesis of bis-chelating CAPH for complexation with lanthanide(III) ions to form binuclear complexes. Investigation of photophysical properties of the obtained coordination compounds.
3. Development of new bifunctional molecular systems with modulation of Ln<sup>III</sup> luminescence by SCO and investigation of their properties and synergy between the phenomena in the systems.
4. Research for sublimable spin-crossover complex displaying gradual spin transition in bulk and thin film forms. Deposition of the thin films of the complex on top of small-scale electronic circuits featured with micro- or nanowires. Testing the thin film for continuous real-time thermometry of the wires' surfaces based on thermorefectance.

Thus, chapter 2 concerns the synthesis of novel triazol-based scorpionate ligands and their iron(II) complexes, studies on structure, physico-chemical properties and magnetic behavior of the coordination compounds, in particular, studies of the SCO phenomenon (if present) in the bulk complexes.

Chapter 3 is dedicated to the synthesis and characterization of binuclear triple- and quadruple-stranded lanthanide(III) complexes with a bis-chelating carbacylamidophosphate ligand. Particular attention is paid to investigation of luminescence in the compounds both in solid state and in solution.

Chapter 4 is focused on elaboration of thin films of iron(II) scorpionate complex, characterization of the films and testing the latter for surface microthermometry and thermal imaging of a gold microwire.

## Chapter 2. Iron(II) scorpionates: synthesis, properties and SCO in the bulk complexes.

In order to address the objectives highlighted in chapter 1, which involve expansion of sublimable spin-crossover complexes family and search for the materials with gradual SCO for thermometry applications, the research described in this chapter was done in two directions that are presented in two parts (two main sub-chapters): the first one deals with synthesis and characterization of already reported iron(II) scorpionate, SCO properties of which were not investigated, while the second one is dedicated to the synthesis of new scorpionate ligands and their iron(II) complexes using a versatile synthetic path described in literature, characterization of the compounds and study of magnetic behavior, in particular, spin crossover in the complexes.

Thus, in the first part bis[hydrotris(1,2,3-triazol-1-yl)borate]iron(II) was selected for a detailed investigation of its physico-chemical properties and spin crossover in the bulk form of the compound. The complex was firstly prepared by Jenkins *et al.*,<sup>205</sup> however the researchers did not carry out studies dedicated to SCO in this substance. Considering the fact that the compound is a structural isomer to the well-studied  $[\text{Fe}(\text{HB}(1,2,4\text{-tz})_3)_2]$ , it was interesting to investigate how the change of the exodentate nitrogen atom position from 4 to 3 in the triazolyl ring impacts the crystalline structure and SCO properties of the complex.

Inspiration to design new scorpionate ligands and their  $\text{Fe}^{\text{II}}$  complexes described in the second part was based on the heterocycle metathesis reaction described in the literature,<sup>85,86</sup> where the authors obtained novel spin-crossover complexes by replacing pyrazole units in tris(pyrazol-1-yl)borate derivatives with nitropyrazoles, with the possibility of post-functionalization of the resulting complexes. Instead of nitropyrazoles, 1,2,4-triazoles substituted with an electron withdrawing group ( $-\text{NO}_2$ ,  $-\text{CN}$ ) at the position 3 were used in this work. Nitro-functionalized derivatives proven successfully converted to amines. Structural, spectral and magnetic properties of the obtained complexes were studied and compared to those for their pyrazole-based analogues reported in the literature.

### 2.1 Bis[hydrotris(1,2,3-triazol-1-yl)borate]iron(II): spin crossover, solvato- and polymorphism.

#### 2.1.1 Synthesis of hydrotris(1,2,3-triazol-1-yl)borate ligand and the corresponding iron(II) complex

Commercial reactants and solvents were used directly without further purification. The tris(1,2,3-triazolyl)borate ligand ( $\text{NaL}^1$ ) and its neutral  $[\text{Fe}(\text{HB}(1,2,3\text{-tz})_3)_2]$  iron (II) complex (hereafter  $[\text{Fe}(\text{L}^1)_2]$  or **1**) were synthesized as shown on the scheme in Figure 2.1, according to experimental procedures

reported in the literature.<sup>205</sup> Synthetic procedures are given in the experimental part (p. 154). The crystalline coordination compound isolated from the mother aqueous solution appears as dodecahydrate. The anhydrous powder form can be obtained *via* heating the hydrate above 90 °C.

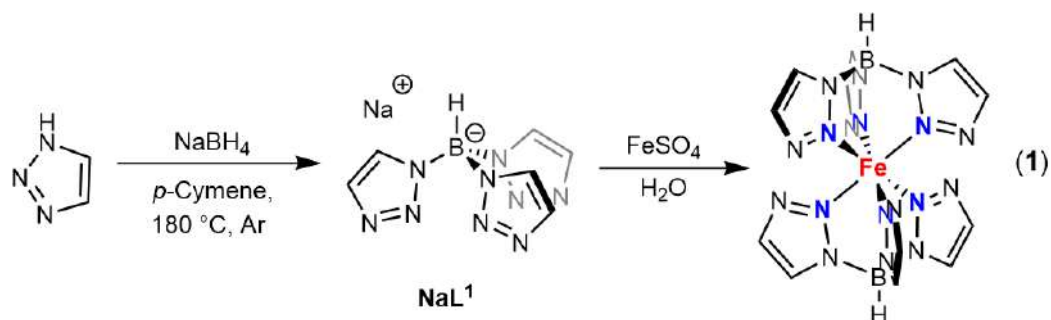


Figure 2.1. Synthetic route to obtain **1**.<sup>205</sup>

### 2.1.2 X-ray crystallography

Complex **1** is soluble in polar solvents, such as water, methanol, dimethylsulfoxide (DMSO), *N,N*-dimethylformamide (DMF) and poorly soluble in much less polar chloroform. The complex tends to form solvates, which can be easily crystallized from the above-mentioned solvents. The number of the solvent molecules per one molecule of the complex depends on the nature of the solvent. For instance, in the case of DMSO, the formation of two solvates **1·2DMSO** and **1·7DMSO** was observed serendipitously from attempts of recrystallization of **1** in the same condition. The methanol- or chloroform-based solvates appear only as **1·2MeOH** and **1·2CHCl<sub>3</sub>**, respectively. The dimethylformamide solvate tends to crystallize with inclusion of one water molecule to form **1·2DMF·H<sub>2</sub>O**. The solvatomorphs **1·2MeOH** and **1·2CHCl<sub>3</sub>** crystallize in monoclinic space groups *P*2<sub>1</sub>/*n* and *P*2<sub>1</sub>/*c*, respectively. **1·2DMF·H<sub>2</sub>O** crystallizes in the orthorhombic *Pbcn* space group. In the case of DMSO-based solvatomorphs, **1·2DMSO** crystallizes in the triclinic  $\bar{P}1$  space group, while **1·7DMSO** adopts a trigonal  $R\bar{3}c$  space group. All the X-ray crystallography data are gathered in Annex A. DMSO molecules in the latter crystals are disordered over six and over two positions, respectively. Upon long-term exposure to ambient air (~hours to days), crystals of solvatomorphs tend to lose their solvents. This process is followed by disintegration of the crystals along with structural changes and can be promoted by heating. Remarkably, crystals of **1·2CHCl<sub>3</sub>** and **1·2MeOH** undergo single-crystal-to-single-crystal transformations upon heating. When heated at 313 K for one day, solvatomorph **1·2CHCl<sub>3</sub>** completely loses its solvent to form stable crystals of **1**. The same transformation occurs in case of its methanol counterpart, but the latter requires heating at 323 K for two days.

The desolvated compound **1** crystallizes in the monoclinic  $P2_1/c$  space group with 2 molecules of  $[\text{Fe}(\text{L}^1)_2]$  per unit cell (Figure 2.2). It should be noted that the crystals used for refining the structure were obtained via a solid-state crystal-to-crystal transformation.

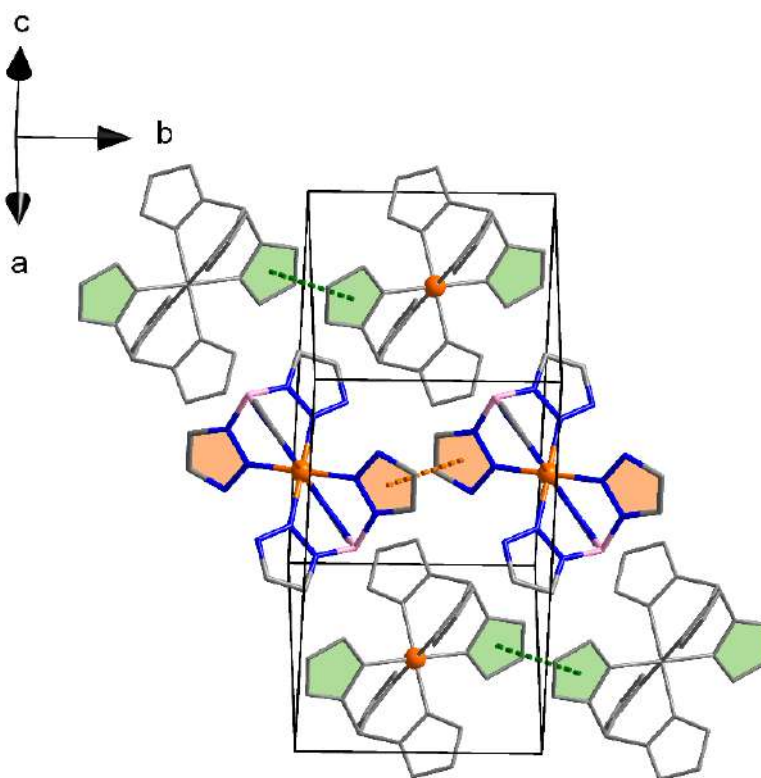


Figure 2.2. Unit cell of **1** with displayed  $\pi$ - $\pi$  stacking interactions propagating along two opposite directions within  $ab$ -plane. Hydrogen atoms are omitted for clarity.

This huge structural rearrangement is related to a chloroform solvent loss, namely c.a. 25% of the volumic contraction occurs ( $1412$  to  $1063 \text{ \AA}^3$ ) that leads to low quality multi-twin crystals. The room temperature (low spin state) unit cell volume per molecule in the crystals of **1** ( $531.8 \text{ \AA}^3$ ) is greater when compared to its 1,2,4-triazolyl isomer ( $516.6 \text{ \AA}^3$ ).<sup>206</sup> While the structure of  $[\text{Fe}(\text{HB}(1,2,3\text{-tz})_3)_2]$  is less dense, the mean intermolecular  $\text{Fe}\cdots\text{Fe}$  separation ( $8.49 \text{ \AA}$ ) is slightly shorter in **1** than in the 1,2,4-triazolyl isomer ( $8.87 \text{ \AA}$ ). The coordination spheres of iron(II) ions in the solvatomorphs (as well as in **1**) have slightly distorted  $[\text{FeN}_6]$  octahedral geometries (Table 2.1). The Fe–N distances lie in the range from  $1.952(3)$  to  $1.972(2) \text{ \AA}$ , while the mean value of coordination octahedra volume ( $V_p$ ) is  $10.05 \text{ \AA}^3$ , as expected for the low spin iron(II).<sup>10</sup> Considering all the solvatomorphs, the average value of the octahedral distortion parameter  $\sum |90^\circ - \theta_{\text{N-Fe-N}}|$  (or  $\Sigma$ ) equals  $21.66^\circ$ . Unfortunately, the high spin structure of **1** could not be assessed because crystals crash at the corresponding high temperatures. Indeed, single crystals of **1**, obtained *via* crystal-to-crystal transformation through thermally induced solvent loss, appear as low quality, highly cracked at room temperature, while further heating is a trigger for crystal degradation.

In the crystals of most of the solvatomorphs, as well as in **1**,  $\pi$ - $\pi$  stacking interactions play a key role in the packing of  $[\text{Fe}(\text{L}^1)_2]$  molecules. The interactions occur between aromatic 1,2,3-triazolyl rings of adjacent complex molecules (Figures 2.2–2.7).

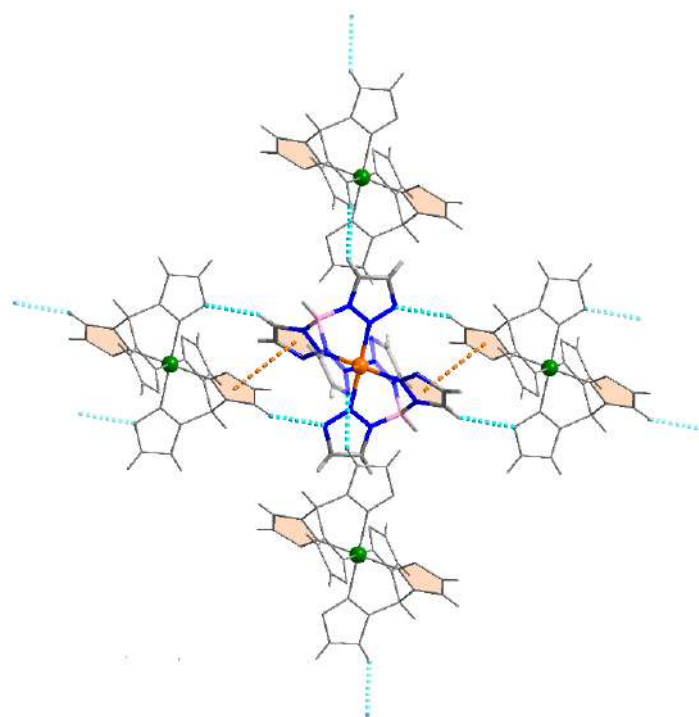


Figure 2.3. Crystal packing in **1** with intermolecular interactions ( $\pi$ - $\pi$  stacking interactions are shown only for one direction).

It is noteworthy, that these interactions are spread along one direction in **1·2DMSO**, however they are bidirectional in **1** (Figure 2.2) and in the rest of the solvatomorphs where they are observed (Figure 2.4). The centroid-centroid distances range from 3.560(3) to 3.6959(17) Å (Table 2.2).

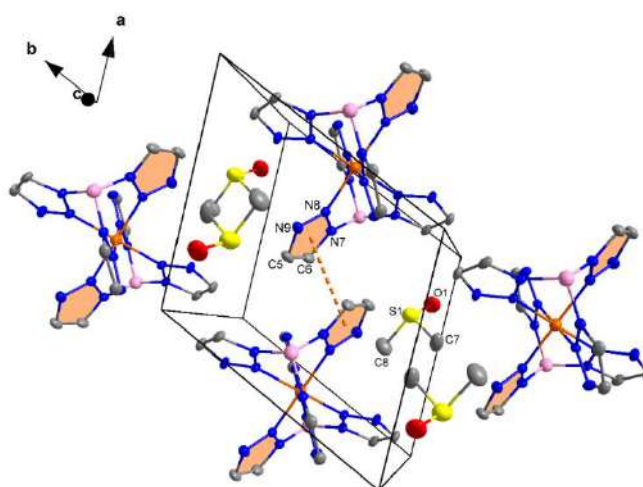


Figure 2.4. Crystal structure of **1·2DMSO** showing intermolecular  $\pi$ - $\pi$  stacking interactions developing along the *a*-axis. Hydrogen atoms are omitted for clarity. Displacement ellipsoids are drawn at 50% probability level.

Another type of interactions that hold molecules of the complex together in the crystal lattices of **1** and **1·Solv** is represented by rather weak C–H···N interactions. The exodentate nitrogen atoms and C–H moieties of 1,2,3-triazolyl rings of neighboring  $[\text{Fe}(\text{L}^1)_2]$  molecules are involved in such intermolecular interactions (Figure 2.3, 2.5–2.8). Likely to  $\pi$ - $\pi$  stacking interactions, C–H···N contacts propagate along a and b crystallographic directions (Figure 2.3), however the structure of **1·2CHCl<sub>3</sub>** reveals only a single propagation direction (Figure 2.6). The parameters of the respective C–H···N contacts are gathered in Table 2.2.

In **1·2DMSO** and **1·2DMF·H<sub>2</sub>O**, the oxygen-containing polar solvents are bound to molecules of **1** via C–H···O contacts (Figures 2.7a, 2.8). In **1·7DMSO**, the molecules of  $[\text{Fe}(\text{L}^1)_2]$  do not display any direct contacts with each other, but interact through solvent molecules by means of C–H···O contacts (Figure 2.9). In **1·2MeOH**, a hydrogen bonding occurs involving the proton of the OH moiety of the solvent and the exodentate nitrogen atom of the triazolyl ring of the complex ( $d(\text{O}\cdots\text{N}) = 2.867(4) \text{ \AA}$ , Figure 2.5a). Chloroform molecules in **1·2CHCl<sub>3</sub>** reveal C–H···N and C–H···Cl interactions with  $[\text{Fe}(\text{L}^1)_2]$  molecules (Figure 2.6).

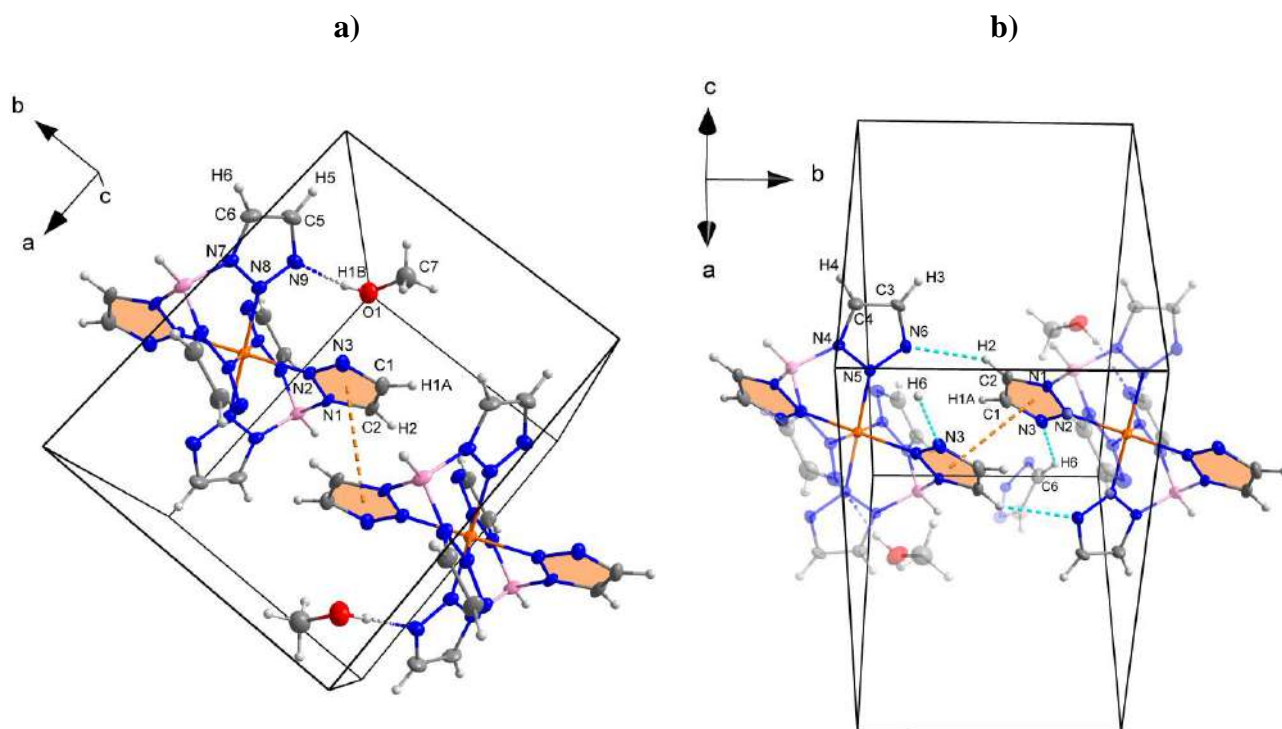


Figure 2.5. Fragments of **1·2MeOH** crystal structure, where hydrogen bonding between  $\text{FeL}_2$  and MeOH molecules (a), C–H···N interactions (b) and intermolecular  $\pi$ - $\pi$  stacking (a, b) are shown. Parts of the molecules in b are omitted or made transparent for clarity.

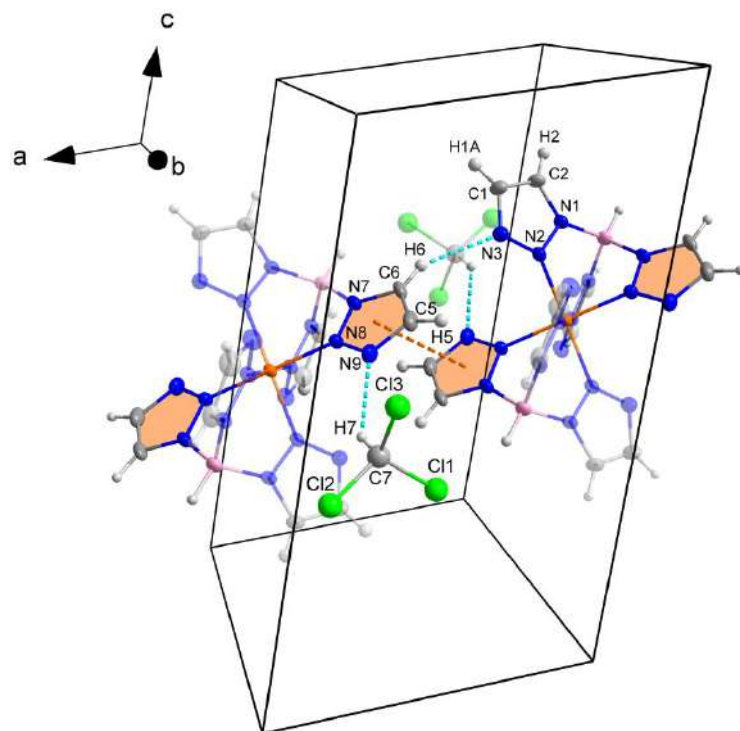


Figure 2.6.  $1 \cdot 2\text{CHCl}_3$  crystal structure fragment with intermolecular interactions between the complex and the solvent molecules. Parts of  $[\text{Fe}(\text{HB}(1,2,3\text{-tz})_3)_2]$  molecules are represented transparent for clarity.

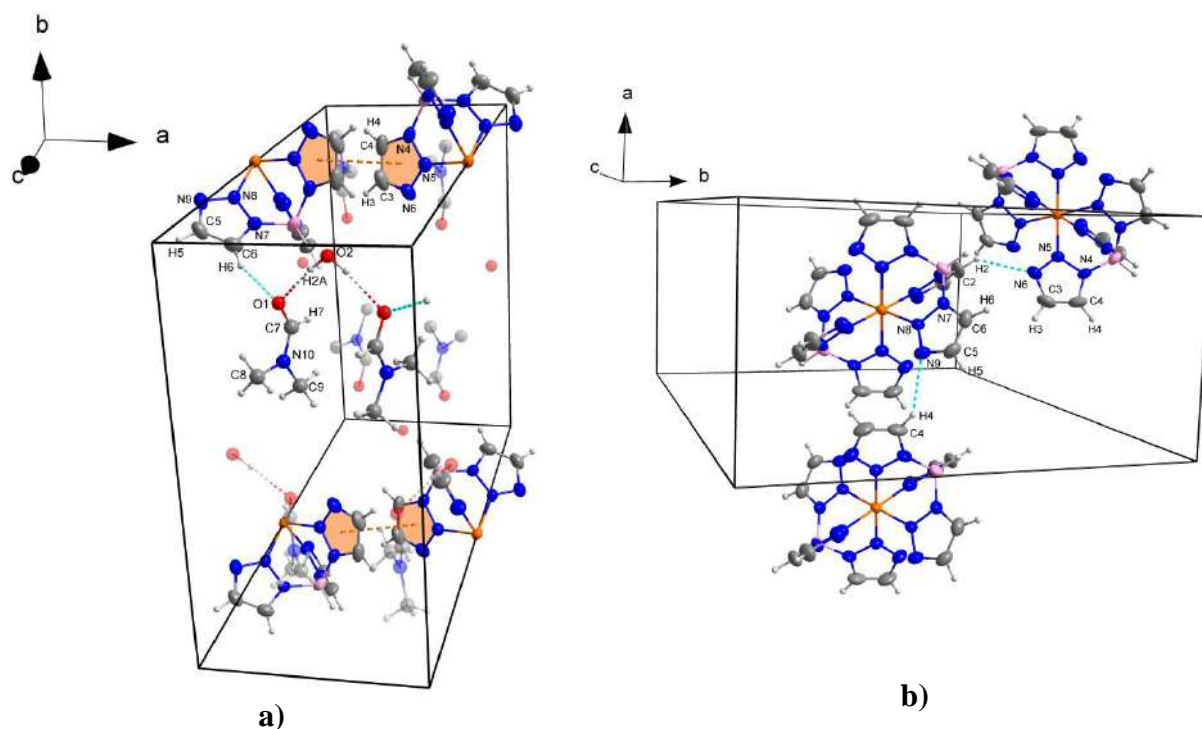


Figure 2.7. Fragments of  $1 \cdot 2\text{DMF} \cdot \text{H}_2\text{O}$  crystal structure representing intermolecular  $\text{C}-\text{H} \cdots \text{O}$  contacts,  $\pi-\pi$  stacking (a) and  $\text{C}-\text{H} \cdots \text{N}$  (b) interactions.

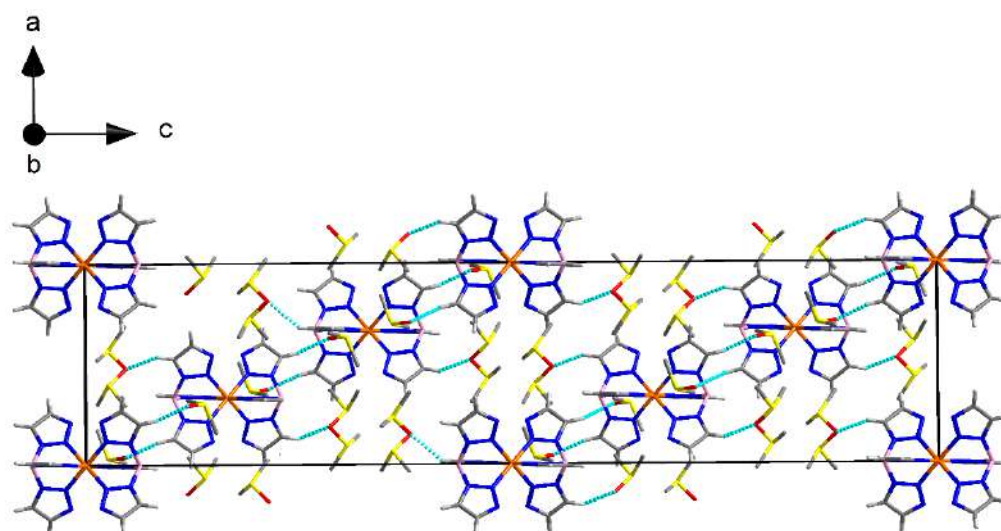


Figure 2.9. Crystal structure (packing diagram) of **1·7DMSO** solvatomorph with intermolecular interactions shown. Hydrogen atoms of the disordered CH<sub>3</sub>-moieties of the solvent are omitted for clarity.

Table 2.1. Selected bond distances and angles of the solvatomorphs.

Compound	1·2DMSO	1·7DMSO	1·2MeOH
<b>Distance, Å</b>			
Fe–N(1)	1.959(3)	1.9674(18)	1.955(2)
Fe–N(2)	1.959(3)	1.9676(17)	1.955(2)
Fe–N(3)	1.952(3)	1.9676(17)	1.958(2)
Fe–N(4)	1.952(3)	1.9676(18)	1.958(2)
Fe–N(5)	1.964(3)	1.9676(17)	1.972(2)
Fe–N(6)	1.964(3)	1.9676(17)	1.972(2)
<b>Angle, ° (average value)</b>			
Cis (intra)	88.27(13)	87.91(7)	88.11(10)
Cis (inter)	91.73(13)	92.09(7)	91.89(10)
Trans	180.0	180.00(9)	180.00(8)
Compound	1·2CHCl <sub>3</sub>	1·2DMF·H <sub>2</sub> O	1
<b>Distance, Å</b>			
Fe–N(1)	1.9600(19)	1.968(3)	1.991(14)
Fe–N(2)	1.9600(19)	1.968(3)	1.991(14)
Fe–N(3)	1.9468(18)	1.958(3)	1.931(18)
Fe–N(4)	1.9468(18)	1.958(3)	1.931(19)
Fe–N(5)	1.9597(18)	1.964(2)	1.950(15)
Fe–N(6)	1.9597(18)	1.964(2)	1.950(15)
<b>Angle, ° (average value)</b>			
Cis (intra)	88.55(8)	88.16(11)	88.07(7)
Cis (inter)	91.45(8)	91.84(11)	91.93(7)
Trans	180.00(3)	180.0	180.0

Table 2.2. Intermolecular  $[\text{Fe}(\text{L}^1)_2] \cdots [\text{Fe}(\text{L}^1)_2]$  interaction parameters.

$\pi$ - $\pi$ stacking interactions			
Compound	$\text{C}_{\text{ring}}-\text{C}'_{\text{ring}}$ (Å)	$\text{C}_{\text{ring}}-\text{Plane}'$ (Å)	Dihedral angle (°)
<b>1·2DMSO</b>	3.640(4)	3.298(7)	25.03
<b>1·2MeOH</b>	3.560(3)	3.275(4)	23.08
<b>1·2CHCl<sub>3</sub></b>	3.6959(17)	3.375(3)	24.05
<b>1·2DMF·H<sub>2</sub>O</b>	3.684(3)	3.377(4)	23.56
<b>1</b>	3.594(17)	3.28(3)	24.13
$\text{C}-\text{H} \cdots \text{N}$ interactions			
Compound	$\text{D}-\text{H} \cdots \text{A}$	$\text{D} \cdots \text{A}$ (Å)	$\angle(\text{D}-\text{H} \cdots \text{A})$ (°)
<b>1·2DMSO</b>	$\text{C3}-\text{H3} \cdots \text{N3}$	3.440(7)	150.0(3)
	$\text{C6}-\text{H6} \cdots \text{N3}$	3.349(6)	137.6(3)
<b>1·2MeOH</b>	$\text{C2}-\text{H2} \cdots \text{N6}$	3.279(4)	146.1(2)
	$\text{C6}-\text{H6} \cdots \text{N3}$	3.196(4)	133.3(2)
<b>1·2CHCl<sub>3</sub></b>	$\text{C6}-\text{H6} \cdots \text{N3}$	3.377(3)	153.97(14)
<b>1·2DMF·H<sub>2</sub>O</b>	$\text{C2}-\text{H2} \cdots \text{N6}$	3.290(4)	135.7(3)
	$\text{C4}-\text{H4} \cdots \text{N9}$	3.345(4)	144.0(2)
<b>1</b>	$\text{C2}-\text{H2} \cdots \text{N6}$	3.14(3)	150.4(17)
	$\text{C6}-\text{H6} \cdots \text{N3}$	3.25(3)	134(2)

### 2.1.3 Spin crossover properties of $[Fe(HB(1,2,3-tz)_3)_2]$

A plot of molar magnetic susceptibility as a function of temperature is shown on Figure 2.10.

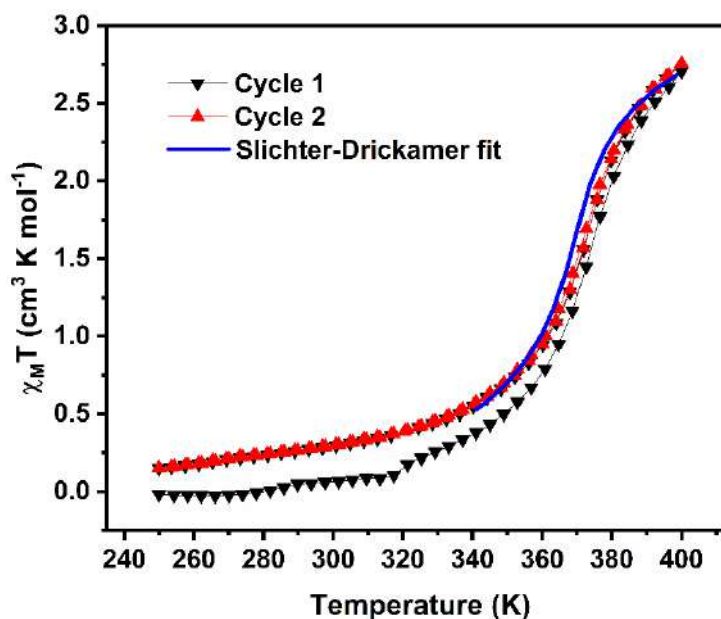


Figure 2.10.  $\chi_M T$  vs  $T$  plot, recorded over two thermal cycles starting with the powder sample  $\mathbf{1} \cdot 12\text{H}_2\text{O}$ . Slichter-Drickamer fit was performed for the second heating curve.

Temperature dependent magnetic measurements were conducted by first heating the powder of  $\mathbf{1} \cdot 12\text{H}_2\text{O}$  from 250 K to 400 K, followed by cycling the as obtained dehydrated sample of  $\mathbf{1}$  in the same temperature range at a rate of  $2 \text{ K min}^{-1}$ . Compound  $\mathbf{1}$  undergoes a gradual spin crossover between the low spin ( $S = 0$ ) and the high spin ( $S = 2$ ) states, with a transition temperature  $T_{1/2} = 373 \text{ K}$ . One must note that the SCO is not fully completed at 400 K, which is the highest attainable temperature by the magnetometer used, but variable-temperature Raman spectroscopic measurements conducted in the 303–433 K range reveal the flattening of the SCO curve slightly above 400 K (Figure 2.11). The Raman spectra were collected for dehydrated crystal of  $\mathbf{1}$  (Figure 2.11a). The spectra revealed reversibility upon cooling to room temperature at the end of the thermal cycle. Intensity of the signals in  $1160\text{--}1280 \text{ cm}^{-1}$  region of the spectra tends to decrease upon heating, that makes them useful to track the spin crossover properties. Plotting integral intensity ratio of the bands at  $1205 \text{ cm}^{-1}$  and  $1263 \text{ cm}^{-1}$  versus temperature yields the spin crossover curve, that is in accordance with magnetic measurements data (Figure 2.11b). The variable temperature magnetic data could be conveniently fitted by the conventional Slichter-Drickamer (SD) model<sup>207</sup> (Figure 2.10), providing estimation<sup>207</sup> of the enthalpy change ( $\Delta H = 14 \text{ kJ mol}^{-1}$ ), entropy change ( $\Delta S = 38 \text{ J K}^{-1} \text{ mol}^{-1}$ ) and cooperativity ( $\Gamma = 5387 \pm 52 \text{ J mol}^{-1}$ ) associated with the SCO phenomenon. One can remark here the relatively low entropy change and high cooperativity of the spin crossover in  $\mathbf{1}$ , similar to the values reported previously for the 1,2,4-triazolyl isomer ( $\Delta S = 48 \text{ J K}^{-1} \text{ mol}^{-1}$ ,  $\Gamma = 5700 \pm 50 \text{ J/mol}$ ).<sup>206</sup>

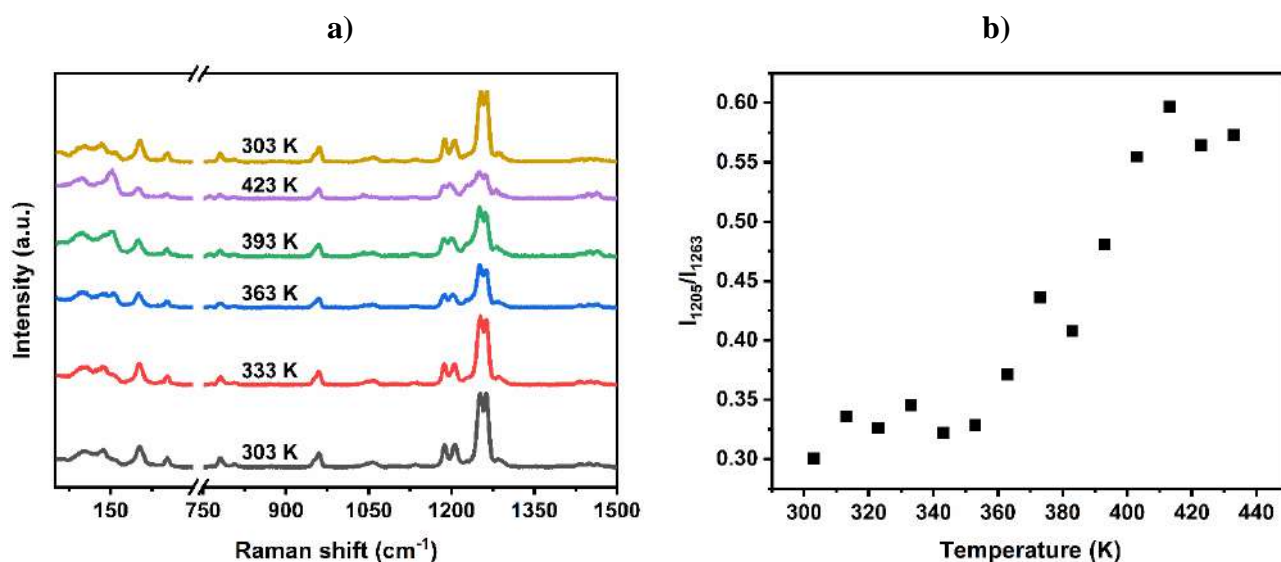


Figure 2.11. Raman spectra of **1** at different temperatures (a) and plot of 1205/1263 cm<sup>-1</sup> bands' integral intensity ratio as a function of temperature (b).

At first glance, one may ascribe the different magnetic behavior on the first heating to solvent loss. Indeed, TG-DTA data acquired for compound **1·12H<sub>2</sub>O** reveals dehydration in the temperature range between *ca.* 313 and 363 K (Figure 2.12). However, the DSC curve obtained for the hydrated powder displays several intense and broad endothermic peaks during the first heating (Figure 2.13), which cannot be solely ascribed to the water loss, but denote also other (overlapped) physical phenomena, including obviously the SCO, but also various structural changes (*vide infra*). Remarkably, the DSC trace on cooling and on successive thermal cycling display a single exothermic (endothermic) peak at 366 K (373 K) on cooling (heating). The peak temperature as well as the associated enthalpy change of *ca.* 14 kJ mol<sup>-1</sup> agrees with the SD fit of the magnetic susceptibility data, allowing us to assign this peak to the sole SCO phenomenon.

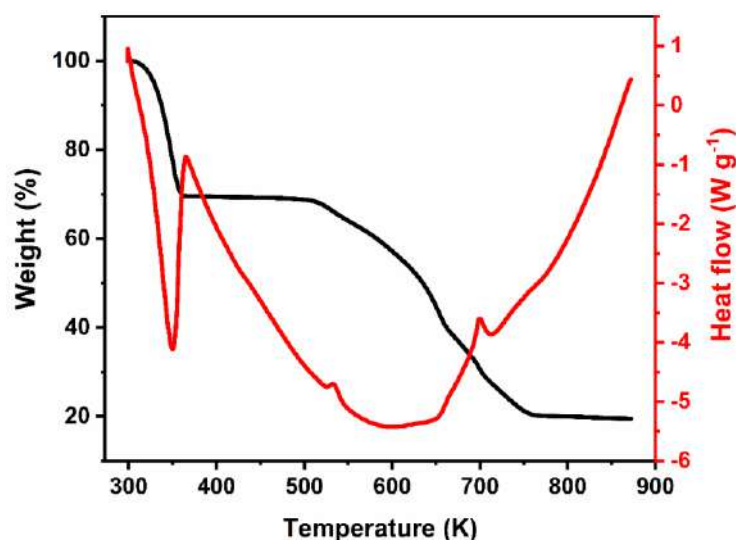


Figure 2.12. TGA and DTA curves for **1·12H<sub>2</sub>O**.

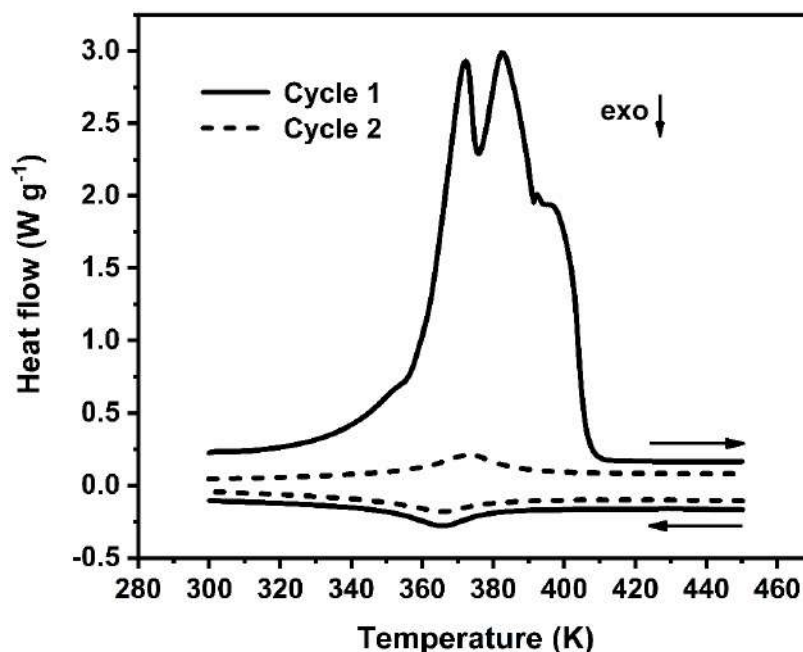


Figure 2.13. DSC curves recorded starting with crystalline powder sample of **1**·12H<sub>2</sub>O at 10 K min<sup>-1</sup> rate over two successive heating/cooling cycles.

In order to further investigate the possible interplay between solvent loss, structural changes and SCO in **1**, variable temperature powder XRD measurements were carried out in the 333–493 K temperature range following heating of **1**·12H<sub>2</sub>O at 328 K for 1 h. The powder patterns recorded at 333, 363 and 393 K are substantially different – denoting successive dehydration/structural changes (Figure 2.14). Of particular interest is that the experimental powder pattern recorded at 363 K shows the best match with the diffraction pattern simulated using the single crystal structural data of **1** (Figure 2.15).

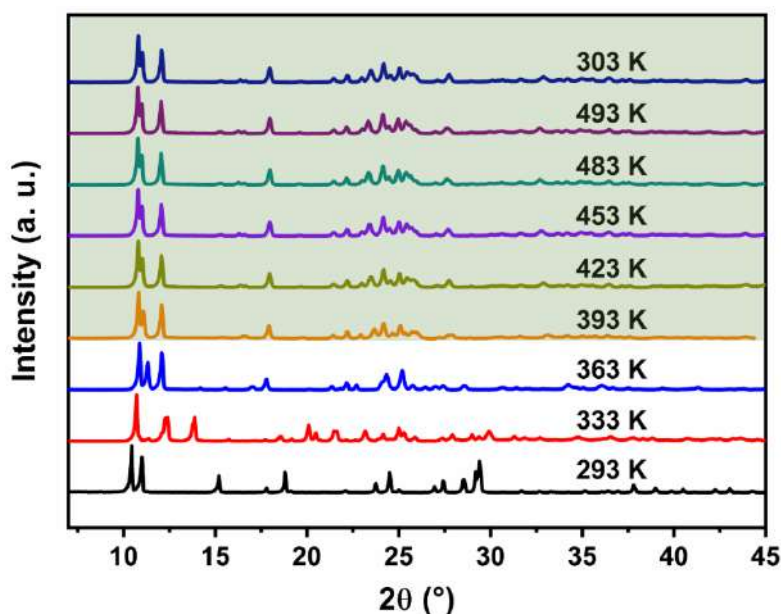


Figure 2.14. Powder X-Ray diffraction patterns for bulk powders of **1**·12H<sub>2</sub>O (293 K) and **1** recorded at different temperatures.

Then, further heating up to 493 K and cooling back to 303 K does not reveal any substantial change in the diffractograms (apart small shifts and broadenings of the peak positions – depending on the temperature). This finding is in line with the calorimetric and magnetic measurements, pointing to the occurrence of a very gradual and reversible SCO following a first heating of the sample up to *ca.* 400 K.

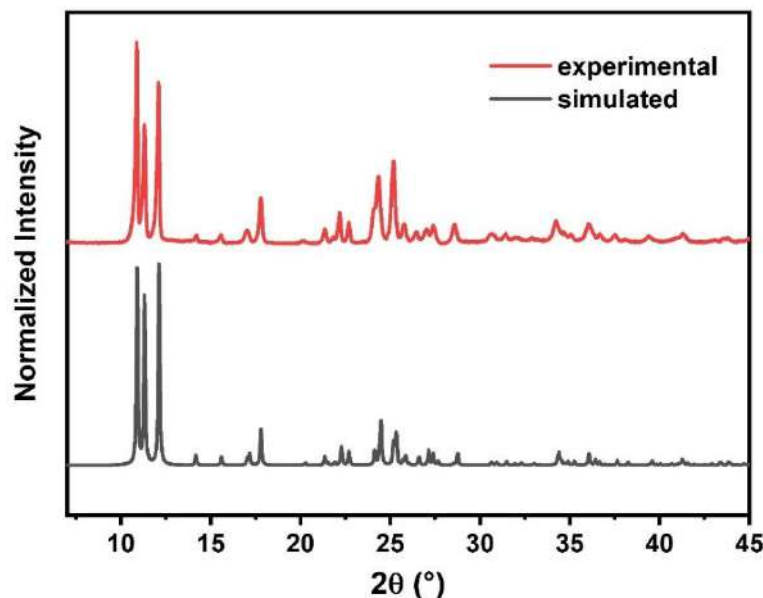


Figure 2.15. Experimental and simulated PXRD patterns of **1**.

## 2.2 Synthesis of new heteroscorpionate ligands and their iron(II) complexes. Characterization and spin-crossover properties of the coordination compounds.

### 2.2.1 Synthesis of the heteroscorpionate ligands and their complexes with $Fe^{II}$

A choice of the synthetic path to access new heteroscorpionate ligands was inspired by refs.<sup>85,86</sup> (see chapter 1). Though, instead of nitropyrazoles involved in heterocycle metathesis reactions reported in the mentioned references, 1,2,4-triazoles decorated with electron-withdrawing group (EWG) at position 3 were used in the present case. At first, potassium hydrotris(pyrazol-1-yl)borate (hereafter KTp) was synthesized following the protocol developed by Trofimenko,<sup>208</sup> with slightly modified work-up procedure (see experimental part, p. 155). Then, potassium cation in the product was exchanged to tetrabutylammonium ( $nBu_4N^+$  or TBA) according to the procedure reported in ref.<sup>209</sup> Then, the resulting TBA derivative  $nBu_4NTp$  was heated with 1 (2) equivalents of an EWG-bearing 1,2,4-triazole to give mono(di)substituted products as shown on Figure 2.16. As electron-withdrawing groups, nitro-group and cyano-group were selected. Thus, commercially available 3-nitro-1,2,4-triazole and 3-cyano-1,2,4-triazole were used for the reaction of heterocycle exchange to afford the new heteroscorpionate ligands. The reactions between  $nBu_4NTp$  and the triazole reactants were conducted without any solvent under conditions of static vacuum to promote the pyrazole release (see experimental part, pp. 155–156). The

heterocycle exchange proceeded similarly to the reported reactions with nitropyrazoles. The degree of substitution of pyrazole moieties with triazole ones was controlled by stoichiometry and temperature alike. Thus, to replace one pyrazole unit ( $n = 1$ , Figure 2.16), heating of the reaction mixture at 90 °C was sufficient for the reaction to proceed. The optimal temperature range for the monosubstitution was set between 90 and 105 °C. The primary evidence of the reaction is condensation of the eliminated pyrazole crystals on walls of the reaction vessel. The latter can be distilled under dynamic vacuum and collected in a receiving flask. This allowed to monitor conveniently the reaction completion by measuring the weight of the released pyrazole. To this purpose, the latter was distilled off from the reaction vessel every one hour, and the collected distillate was weighted. The major quantity of pyrazole was released in the first hour of the reaction. Heating the reaction mixture for the following hour yielded the rest of pyrazole. At this stage, the pyrazole release stopped. In case of monosubstitution, the pyrazole release was quantitative, and most of the by-product was released within the first hour of the reaction.

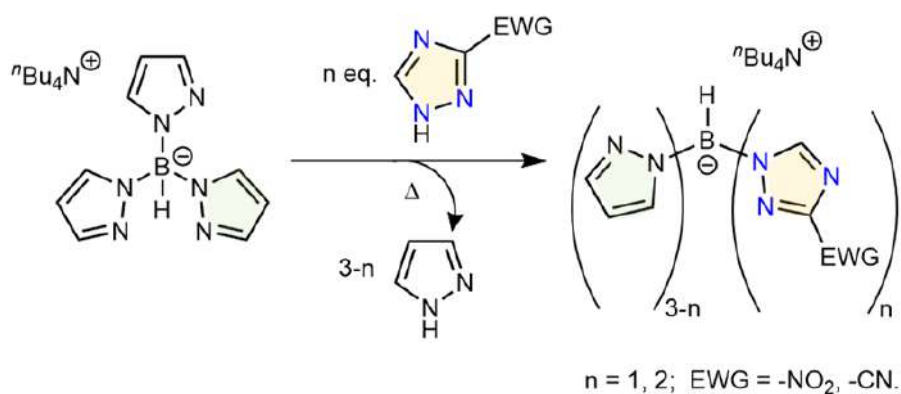


Figure 2.16. Synthetic path to obtain new triazole-based heteroscorpionate ligands.

Formation of the disubstituted derivatives was possible *via* heating of the stoichiometric reactants' mixture to 130 °C. After around 95 % of pyrazole was eliminated, its release ceased maximum after 3 h of heating. As in case of the analogous reactions with nitropyrazoles, the heterocycle metathesis involving the above-mentioned triazole reactants leads to selective formation of the desired mono- and disubstituted products, which can be controlled by temperature and stoichiometry. Though, attempts of trisubstitution, requiring 3 equivalents of a triazole reactant and higher temperatures (about 150 °C), lead to formation of a mixture of products with different degree of substitution and by-products that were formed, most probably, as a result of side reactions taking place at high temperatures. The separation of products in this mixture appeared to be challenging.

In the literature,<sup>85,86</sup> the authors propose the heterocycle metathesis mechanism (Figure 1.17) based on considerations of HSAB theory, according to which more acidic nitropyrazoles ( $\text{pK}_a = 9.50\text{--}9.75$ ) attacking the boron core, readily give their pyrrole-type protons to more basic pyrazolyl moiety, that eliminates as a free pyrazole ( $\text{pK}_a = 14.21$ ).<sup>210</sup> Given that the acidity of 1,2,4-triazole ( $\text{pK}_a = 9.89$ )<sup>211</sup>

is close to such for nitropyrazoles, it was interesting to carry out this reaction with unsubstituted triazole. Though the synthetic conditions for the mono- and disubstitution were the same as in case of the substituted triazoles, the reactions with pristine triazole did not provide the same selectivity and resulted in a mixture of products that are challenging to separate. Similar results were achieved, when triazole bearing electron-donating amino-group at position 3 was used as the reactant in an attempt to synthesize directly an amino-functionalized heteroscorpionate ligand. Considering the fact of the electron density donation from the amino-group to the aromatic core,  $pK_a$  of 3-amino-1,2,4-triazole is expected to be higher than such in the pristine triazole, consequently, such a result was expected. Consequently, these results point to the conclusion that the presence of EWG in the triazole precursor is crucial for the heterocycle metathesis to proceed as it provides a sufficient difference in  $pK_a$  between a triazole reactant and pyrazole, to shift the equilibrium towards formation of the desired heteroscorpionates.

The scope of the ligands, discussed in the current sub-chapter, is summarized on Figure 2.17.

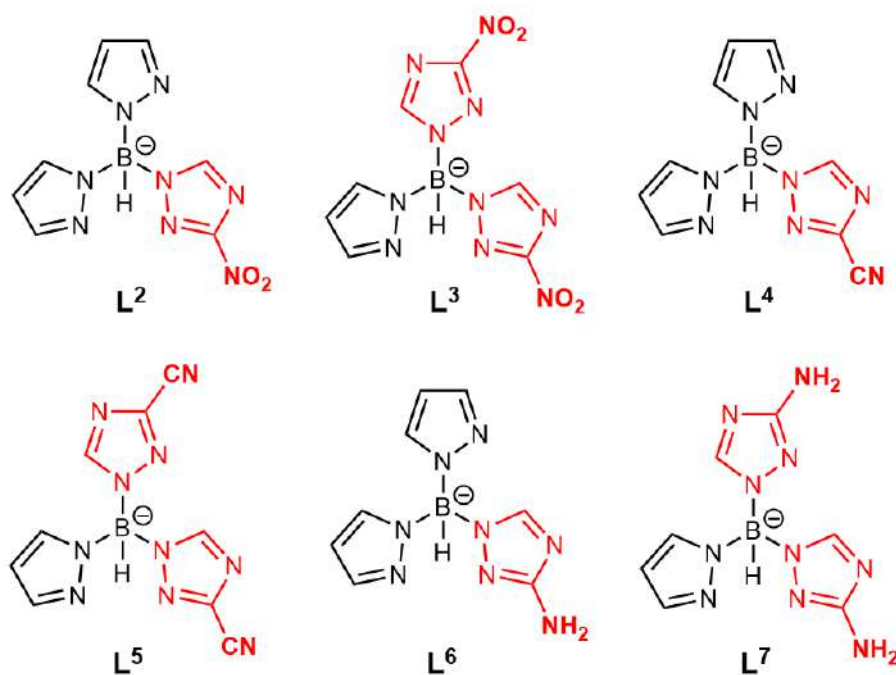


Figure 2.17. Scope of the new heteroscorpionate ligands in the current work.

As nitro-group can be reduced to a primary amine, it was interesting to convert a nitro-derived ligand to an  $NH_2$ -bearing ligand that can be either directly coordinated to  $Fe^{II}$  or undergo functionalization of the amino-group with subsequent coordination of a modified ligand to the metal ion. For this purpose, monosubstituted nitro-derived ligand  ${}^nBu_4NL^2$  (Figure 2.17) was selected as a subject to reduction. The reduction reaction conditions were similar to those in case of complexes reported in ref.,<sup>86</sup> which involve the use of an organic reducing agent, palladium catalyst, protic solvent and microwave heating. In the present case, 1,4-cyclohexadiene was used as a reducing agent, palladium (5

% wt.) on carbon was selected as a catalyst, while alcohols such as methanol or ethanol were used as solvents pure or in the alcohol:toluene (3:1) mixture likely to the reported ones by Ma *et al.*<sup>86</sup> The first approach implied microwave heating (closed-vessel mode) of  $n\text{Bu}_4\text{NL}^2$  stirred methanolic solution at 120 °C for 5 minutes with excess (6 equivalents) of 1,4-cyclohexadiene and in the presence (8 % mol.) of Pd/C. Colorless crystals isolated after concentration of the obtained solution were analyzed by means of single crystal X-ray diffraction. Instead of the expected amino-derived hydroborate anion, the resulting crystal structure revealed an associate composed of 3-amino-1,2,4-triazole anion binding three neutral pyrazole molecules *via* hydrogen bonding (Figure 2.18). The negatively charged associate is compensated by TBA cation. Such a result indicates a degradation of the hydroborate anion, possibly due to solvolysis under the given conditions. The fact of the degradation is supported by NMR spectroscopy data. Solution  $^1\text{H}$  NMR of an aliquot of the reaction mixture taken after 5 minutes of the reaction revealed two signals of free-pyrazole aromatic protons, while in the spectra of the scorpionate ligands, three signals are typically observed for pyrazole bound to boron (see the NMR spectra in Annex B). Changing the reaction conditions, *e.g.*, reducing the temperature together with increasing the time only retarded the degradation, however did not prevent it. Moreover, even after leaving the mixture of the reactants and the reagents overnight at room temperature with no stirring degradation signs, such as presence of the liberated pyrazole, could be detected. Varying the solvents did not have any notable impact on the reaction outcome. Such a chemical behavior is probably related to the presence of the palladium catalyst that in the protic solvent medium can promote the solvolysis of the hydroborate as it is known in case of borohydride.<sup>212</sup> Considering such a fragility of the hydroborate anion, direct reduction of nitro-group in  $L^2$  and  $L^3$  to obtain  $L^6$  and  $L^7$  is probably not the most appropriate strategy. Reduction of  $\text{NO}_2$ -group of the ligands in their iron(II) complexes (post-functionalization) is another approach, which is discussed further together with synthesis of the coordination compounds based on the heteroscorpionate ligands.

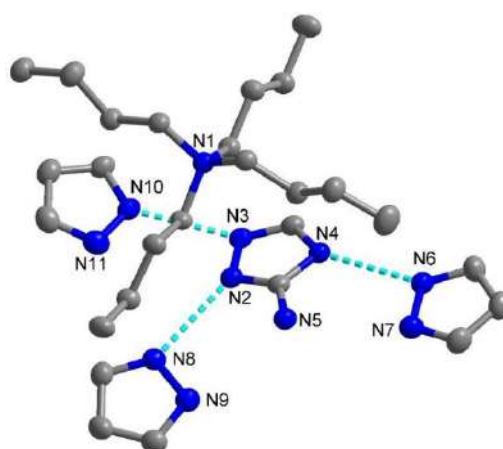


Figure 2.18. Crystal structure of the product formed in an attempt of reduction of  $n\text{Bu}_4\text{NL}^2$ . Hydrogen atoms are omitted for clarity. Displacement ellipsoids are drawn at 50% probability level.

Alike to the protocols described in ref.,<sup>86</sup> syntheses of iron(II) complexes with ligands L<sup>2</sup>–L<sup>5</sup> were performed under argon atmosphere in degassed dichloromethane (DCM) solution starting from 2 equivalents of the respective ligand and 1 equivalent of FeCl<sub>2</sub>·4H<sub>2</sub>O (Figure 2.19).

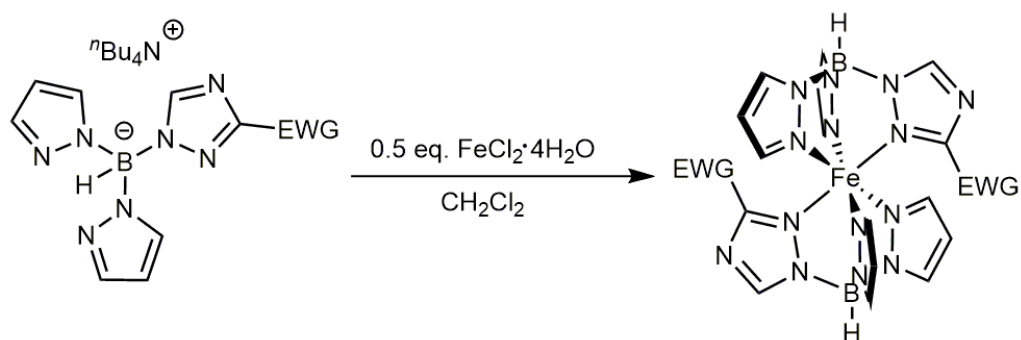


Figure 2.19. Synthetic scheme to access iron(II) complexes with ligands L<sup>2</sup>–L<sup>5</sup> (EWG = -NO<sub>2</sub>, -CN). A monosubstituted ligand was chosen as an example. The synthetic scheme remains the same in case if a disubstituted ligand is chosen as the reactant.

In the context of successful examples on post-synthetic modification of the complexes with nitro-functionalized heteroscorpionates reported in the literature,<sup>85,86</sup> it was interesting to perform the post-functionalization on the complexes' counterparts obtained in this work. Attempts to reduce complexes [Fe(L<sup>2</sup>)<sub>2</sub>] under microwave conditions suggested by Ma *et al.*<sup>86</sup> and tried for uncoordinated L<sup>2</sup> faced issues to obtain any reproducible result, which is related to the absence of possibility of control over the reaction outcome to obtain the desired product, fairly low yields (2–33 %) of the reduction reaction product. Conversely, classical technique of catalytic nitro-group reduction under pressure of hydrogen in an autoclave served a reliable tool to convert NO<sub>2</sub>-decorated substrates [Fe(L<sup>2</sup>)<sub>2</sub>] and [Fe(L<sup>3</sup>)<sub>2</sub>] into di- and tetraamines [Fe(L<sup>6</sup>)<sub>2</sub>] and [Fe(L<sup>7</sup>)<sub>2</sub>], respectively (Figure 2.20). The reaction conditions were similar to those proposed by Flötotto *et al.* for the pyrazole-based counterpart.<sup>85</sup>

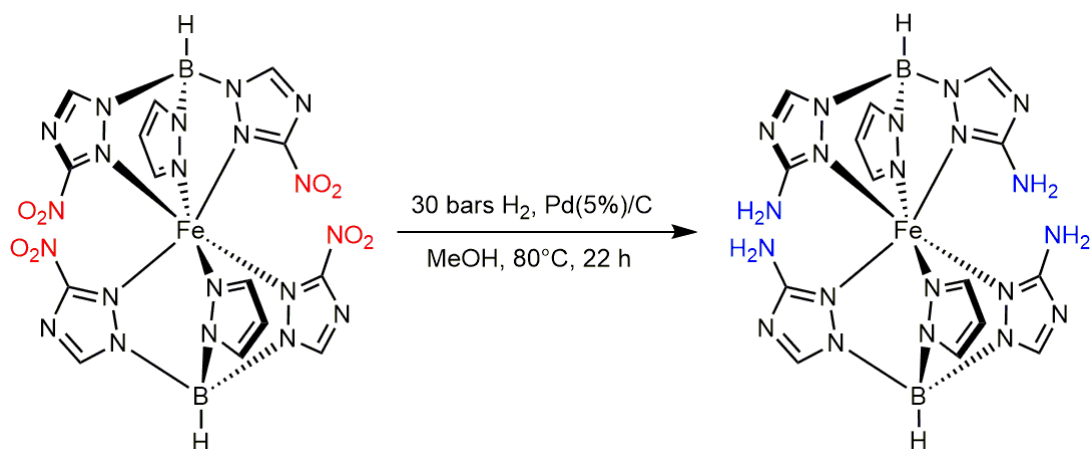


Figure 2.20. Reduction of NO<sub>2</sub>-groups in [Fe(L<sup>3</sup>)<sub>2</sub>].

The synthetic procedures to access the ligands and their iron(II) complexes are provided in the experimental part (pp. 155–158).

### 2.2.2 NMR spectroscopy

In proton NMR spectra of the ligands (provided in Annex B), pyrazolyl moiety is characterized by three signals: two doublets at about 7.61 and 7.58 ppm (average chemical shift values) assigned to protons at position 5 and 3 of the pyrazole ring, and triplet at around 6.20 ppm corresponding to proton at the position 4. The triazolyl units bear only a single proton, singlet signal of which appears at 7.93 (7.99) ppm for L<sup>2</sup> (L<sup>4</sup>) and at 8.20 ppm in case of L<sup>3</sup> and L<sup>5</sup>. The integral intensity ratio of the triazole singlet to the pyrazole multiplets (s:d:d:t) is 1:2:2:2 for L<sup>2</sup>, L<sup>4</sup> and 2:1:1:1 for L<sup>3</sup> and L<sup>5</sup>, which is in line with the expected structures of the respective heteroscorpionate anions.

<sup>13</sup>C NMR spectra of ligands featured with nitro-groups are characterized by presence of four signals in the aromatic region of the spectra: one weak-field signal (~149 ppm) corresponding to the carbon nucleus at position 5 of the triazolyl-moiety and three signals in 140–105 ppm region from the pyrazole carbon nuclei. Large number of scans (>3000) in the NMR experiment may allow to observe a weak signal of carbon nucleus at position 3 of the triazole ring. For example, the signal can be observed for L<sup>2</sup> at 152.39 ppm. In the spectra of the cyano-functionalized ligands, an extra signal of low intensity observed at 114.61 ppm for L<sup>4</sup> and at 114.22 for L<sup>5</sup> is assigned to the carbon nucleus of CN-group. Alike to the nitro-derivatives, large scan numbers allow to observe the position-3 aromatic carbon signal at 139.29 and 139.81 ppm for L<sup>4</sup> and L<sup>5</sup> respectively.

Boron NMR spectra of all the ligands contain one doublet lying in the region from -2.59 to -1.57 ppm. The presence of the sole signal in the spectra as well as multiplicity of the signal correlates well with the fact that the compounds contain only one type of boron nuclei directly linked to proton nuclei of identical nuclear spin.

NMR spectra of the heteroscorpionate ligands recorded in weeks or months after their synthesis reveal signs of stability issues in the ligands upon their storage in ambient conditions. Thus, an extra signal appears in <sup>11</sup>B NMR spectra as a singlet at around 18 ppm, which is characteristic for boric acid and its esters.<sup>213</sup> While in proton NMR, an extra weak-field singlet appears in 8.3–8.0 ppm region, most probably corresponding to the free triazole species. It should be noted that these impurity signals are observed as well in the spectra of the crude products. Likely to the observations of L<sup>2</sup> degradation under the reduction conditions described in sub-chapter 2.2.1, the considered observations stress on the fact that the heteroscorpionates have an inclination to degrade over time in ambient conditions, probably due to slow hydrolysis of the hydroborate species caused by the moisture of the ambient air. This fact should be taken into account during the planning of the ligand synthesis and as well as synthesis of the complexes. Thus, such practices as use of the ligands shortly after their synthesis, or use of anaerobic

techniques for preparation, handling and storage of the compounds can be applied to ensure the substance purity and to minimize or to avoid the undesired degradation processes.

### 2.2.3 IR spectroscopy

The IR spectra are presented in Annex C. A characteristic vibration band for boron-based scorpionate ligands is B–H stretch appearing well apart from other bands within 2460–2526  $\text{cm}^{-1}$  range in case of the considered ligands and complexes. As it was observed for the pyrazole-based scorpionates in ref.,<sup>86</sup> the B–H stretching vibration appeared to be sensitive to coordination of the scorpionate ligands to the metal ion. Following the coordination B–H band position experienced shift towards higher wavenumbers by 27–45  $\text{cm}^{-1}$  for  $\text{NO}_2$ -bearing ligands and by 50–56  $\text{cm}^{-1}$  in case of the CN-derivatives. The high-frequency shift of the B–H stretch is related to withdrawal of the electron density from the ligand, and consequently, from the boron, upon the coordination. In IR spectra of the amino-functionalized complexes, the B–H band is located at lower wavenumbers than for the rest of the complexes, *e.g.*, 2474  $\text{cm}^{-1}$  for  $[\text{Fe}(\text{L}^6)_2]$  vs 2487  $\text{cm}^{-1}$  for  $[\text{Fe}(\text{L}^2)_2]$  and 2470  $\text{cm}^{-1}$  for  $[\text{Fe}(\text{L}^7)_2]$  vs 2512  $\text{cm}^{-1}$  for  $[\text{Fe}(\text{L}^3)_2]$ , which is expected given the electron-donating effect of  $\text{NH}_2$ -group increasing the electron density at boron.

Additional characteristic band, positioned away from the rest of the bands, is caused by stretching vibration of nitril-group's triple bond inherent in  $\text{L}^4$ ,  $\text{L}^5$ , **4** and **5**. In the compounds the band position is situated in narrow 2245–2251  $\text{cm}^{-1}$  range. Unlike to B–H stretch, the position of the  $\text{C}\equiv\text{N}$  stretching vibration band did not experience any significant shift upon the ligand coordination, though the band is useful for identification of the respective compounds.

IR spectra of nitro-compounds are typically featured with characteristic asymmetric and symmetric stretching vibrations of  $\text{NO}_2$ -group. However, they are usually located in the finger-print region containing a set of other bands that are positioned tightly, which might complicate the assignment of the nitro-group vibrations. Thus, in the spectra of the nitro-ligands and their complexes, no bands were found that can be clearly assigned to the  $\text{NO}_2$ -stretches.

### 2.2.4 Single crystal and powder X-ray diffraction studies

Single crystals of  ${}^n\text{Bu}_4\text{NL}^2$  suitable for X-ray diffraction grow in the crude product oily substance in 1 day. Crystal structure of the heteroscorpionate ligand is shown on Figure 2.21. The compound crystallizes in monoclinic  $P2_1/n$  space group, with the desired structure of the heteroscorpionate tetrahedral anion with hydrogen, two pyrazolyl substituents and one 3-nitro-1,2,4-triazolyl function attached to boron as well as tetrabutylammonium as a counter-cation.

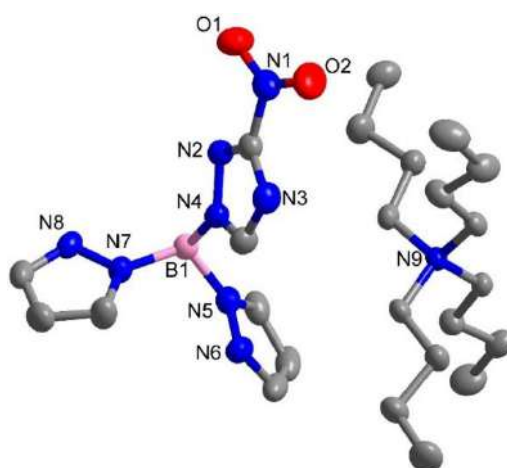


Figure 2.21. Crystal structure of  ${}^n\text{Bu}_4\text{NL}^2$ . Hydrogen atoms are omitted for clarity. Only atom labels of heteroatoms are shown for clarity considerations alike. Displacement ellipsoids are drawn at 50% probability level.

Efforts to obtain crystals for the rest of the ligands were not successful. Crystallization of complexes **2** and **3** by slow evaporation of their saturated solutions or vapor diffusion techniques yielded only polycrystalline aggregates or very small crystals quality of which did not meet requirements for the single crystal X-ray diffraction experiment. Similarly, the endeavor to crystallize complexes **5** and **7** proved unsuccessful.

Single crystals of bis[hydrobis(pyrazol-1-yl)(3-amino-1,2,4-triazol-1-yl)]iron(II) (**6**) were grown from saturated methanolic solution by means of slow evaporation of the solvent. The complex crystallizes in  $P2_1/n$  space group (see Annex A). Coordination environment of  $\text{Fe}^{\text{II}}$  is formed by the two coordinated tridentate ligands, the donor atoms of which are resting on the facets of octahedron. The triazolyl units are situated on the opposite sides to each other on the axial vertices of the octahedron. Thus, the obtained complex appears in the *trans*- form. Despite the probability of existence of both *cis*- and *trans*-isomers, only *trans*-isomer of **6** was observed. Crystal structure of **6** is shown on Figure 2.22.

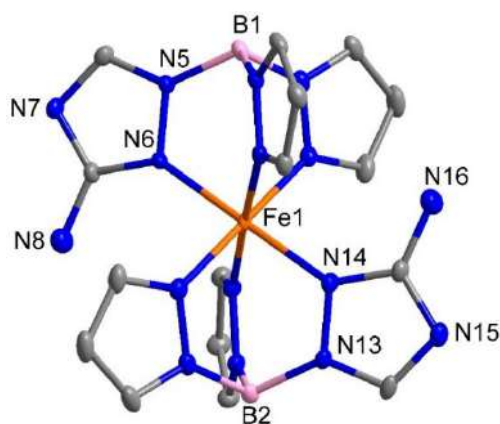


Figure 2.22. Crystal structure of complex **6**. Hydrogen atoms, as well as atom labels of carbon, and nitrogen of the pyrazolyl fragments are omitted for clarity. Displacement ellipsoids are drawn at 50% probability level.

Crystal structure of **6** was acquired at four different temperatures: 100 K, 293 K, 320 K and 393 K. The average distance Fe–N ( $\bar{d}_{\text{Fe-N}}$ ) in the complex at 100 K equals 1.986(11) Å, while the octahedron volume ( $V_p$ ) at this temperature is around 10.46 Å<sup>3</sup>, which is inherent in low spin iron(II) complexes. The  $\bar{d}_{\text{Fe-N}}$  value, at room temperature, reaches 2.107(2) Å, which already falls within the range of Fe–N distances found in the HS complexes. At higher temperatures of 320 K and 393 K the mean iron-nitrogen distances are 2.130(3) Å and 2.159(15) Å, while the polyhedral volume values are of 12.80 Å<sup>3</sup> and 13.32 Å<sup>3</sup> respectively. Octahedron distortion parameter  $\Sigma$  at termini of the low and high temperature values equals 16.77° and 47.53° respectively. The unit cell volume ( $V_c$ ) increases with temperature from 2142.1(10) Å<sup>3</sup> (at 100 K) to 2314.06(10) Å<sup>3</sup> (at 393 K). Thus Fe–N distances increase by 8.7 % in the full range of temperatures, while the cell volume – by 8.0 %. Though, the percentage of the parameters thermal evolution should be considered with care, as the thermal expansion in the given temperature range may be non-negligible. The evolution of the structural parameters with temperature for complex **6** is summarized in Table 2.3. (See detailed crystallographic data in Annex A).

Table 2.3. Selected structural parameters of **6** at selected temperatures.

Temperature, K	$\bar{d}_{\text{Fe-N}}$ , Å	$\Sigma$ , °	$V_p$ , Å <sup>3</sup>	$V_c$ , Å <sup>3</sup>
100	1.986(11)	16.77	10.46	2142.1(10)
293	2.107(2)	38.59	12.41	2256.1(11)
320	2.130(3)	42.81	12.80	2269.4(2)
393	2.159(15)	47.53	13.32	2314.06(10)

Besides the metal octahedron distortions accompanying the spin crossover, there are also distortions at the ligands. In scorpionate ligands, two main types of distortions in response to iron-nitrogen distance increase were established: twisting of a heterocycle ring defined by B–N–N–Fe torsion angle, and pyramidalization of boron tetrahedron defined by distance from boron to the centroid of B–N-bonded N<sub>3</sub> plane or B–Ct(N<sub>3</sub>).<sup>214</sup> These SCO-responsive parameters were measured in coordination compound **6**. It was found that temperature had no considerable effect on twisting of heterocycle rings. Thus at 100 K, the triazole rings are twisted to a quite small extent: torsion angles B1–N5–N6–Fe1 and B2–N13–N14–Fe1 are -0.05° and 1.32° respectively. While at 393 K, these values change to -2.21° and -0.08° respectively. Similarly to those for the triazole rings, B–N–N–Fe torsion angles of the pyrazole changed only by 2.38° maximum. Contrarily, the elongation of iron-nitrogen bonds induces pyramidalization of the boron geometry, *i.e.*, decrease of the distance between boron and centroid of the mean plane of the boron-bound nitrogen atoms B–Ct(N<sub>3</sub>) from 0.57(2) Å at 100 K to 0.522(2) Å at 393 K, which leads to an increase of the ligand bite angle.

Among the interactions determining the crystal packing of  $[\text{Fe}(\text{L}^6)_2]$  molecules one can highlight the intermolecular H-bonding between the triazole units formed by a hydrogen atom of amino-group (H-bond donor or D) and nitrogen atom at position 4 (H-bond acceptor or A) of the heterocycle ring (Figure 2.23). Hydrogen bonding connects the complex molecules in a 1D cascade growing along  $a$  crystallographic axis. The distance between hydrogen-bond donors and acceptors  $d(\text{D}\cdots\text{A})$  is 3.014(3) Å for  $\text{N8}\cdots\text{N15}$  and 3.010(3) Å for  $\text{N7}\cdots\text{N16}$  at 100 K. The mean donor-acceptor distance increases by *ca.* 2% at high temperature. Alternatively,  $\text{C}-\text{H}\cdots\pi$  interactions are present between the triazole and pyrazole units of adjacent  $[\text{Fe}(\text{L}^6)_2]$  molecules (Figure 2.24).

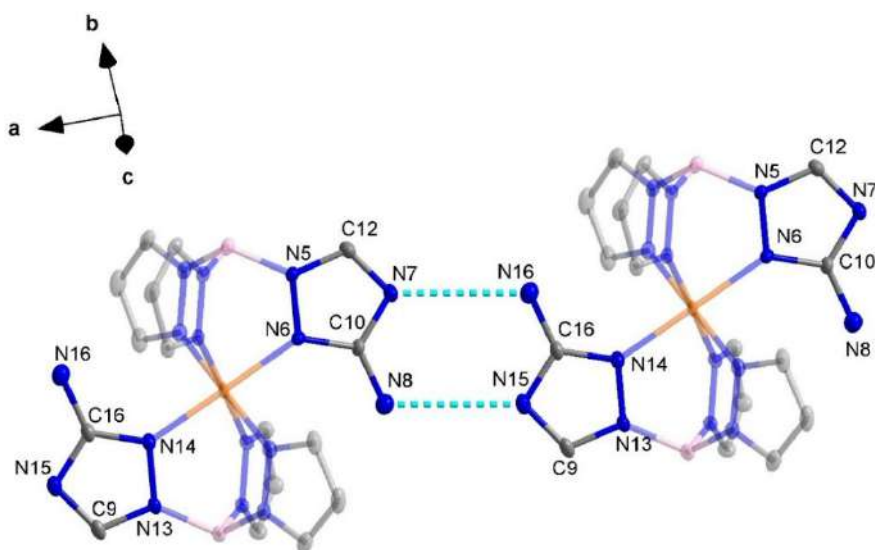


Figure 2.23. Hydrogen bonding between  $[\text{Fe}(\text{L}^6)_2]$  molecules in the crystal of the substance. Hydrogen atoms are omitted for clarity.

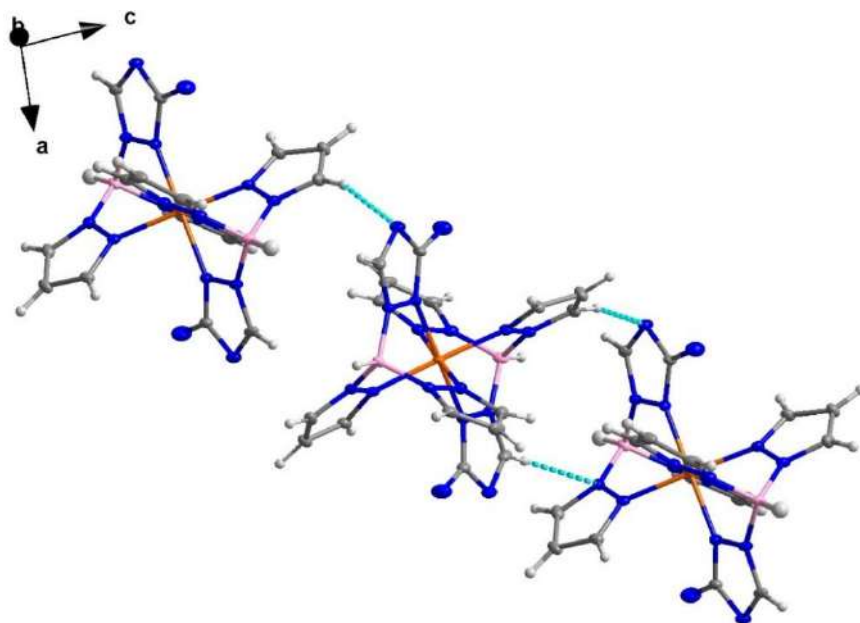


Figure 2.24. Intermolecular  $\text{C}-\text{H}\cdots\pi$  interactions between the pyrazole and triazole rings in **6**.

X-ray diffractogram acquired on powder of **6** at room temperatures matches one simulated from the single crystal diffraction data (Figure 2.25).

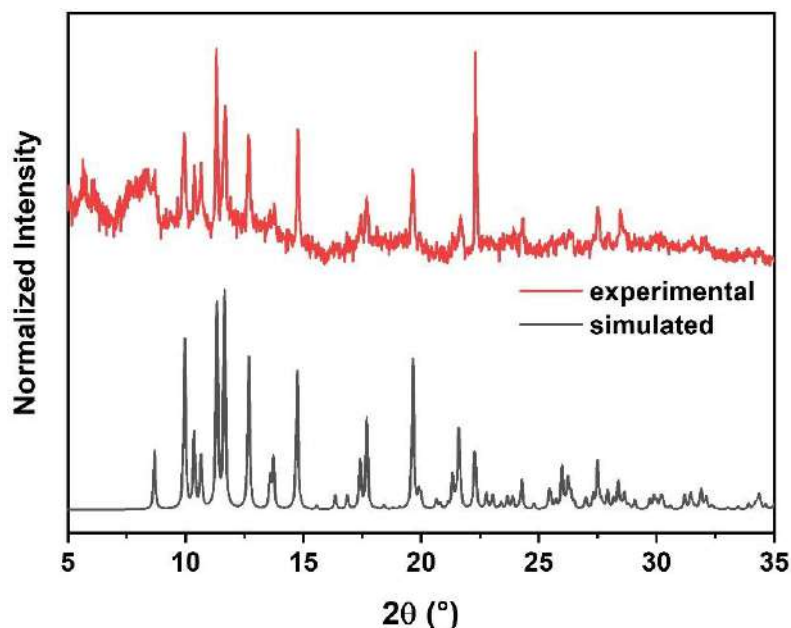


Figure 2.25. Simulated powder pattern from the respective single crystal XRD data (dark grey line) and experimental PXR pattern (red line) of **6**.

Single crystals of complex **4** were obtained by slow evaporation of its saturated DCM solution. Elongated prismatic crystals correspond to the compound that crystallizes in monoclinic  $C2/c$  space group as a *trans*-isomer (Figure 2.26a). Together with the prismatic crystals, seldom small orthorhombic crystals can be found in the same crystallization batch. These crystals show distinct unit cell parameters and correspond to the *cis*-isomer of the complex that crystallizes as DCM solvate [*cis*-Fe(L<sup>4</sup>)<sub>2</sub>] $\cdot$ CH<sub>2</sub>Cl<sub>2</sub> (Figure 2.26b) in  $P2_1/n$  space group (see detailed crystallographic data in Annex A). Thus, crystallization of the both isomers was observed for complex **4**. Though, unlike to the case described in ref.,<sup>87</sup> no separation of the isomers was achieved by means of column chromatography. Moreover, the PXR pattern of the same crystallization batch does not contain reflection peaks that might correspond to the *cis*-isomer (Figure 2.27). These observations suggest that the later may form during the crystallization, however as a very minor product.

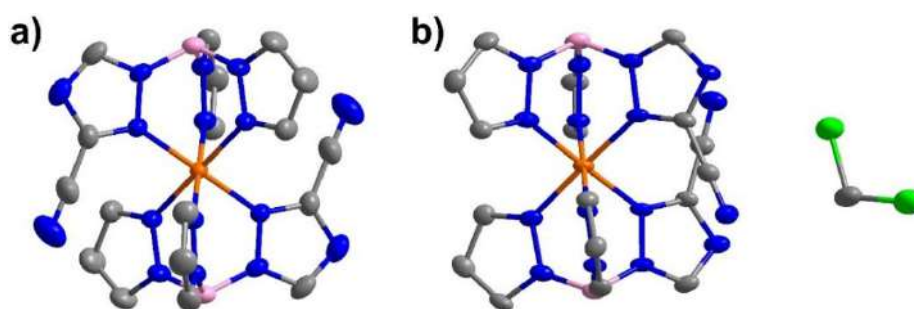


Figure 2.26. Crystal structures of *trans*- (a) and *cis*-isomer (b) of **4**. Hydrogen atoms are omitted for clarity. Displacement ellipsoids are drawn at 50% probability level.

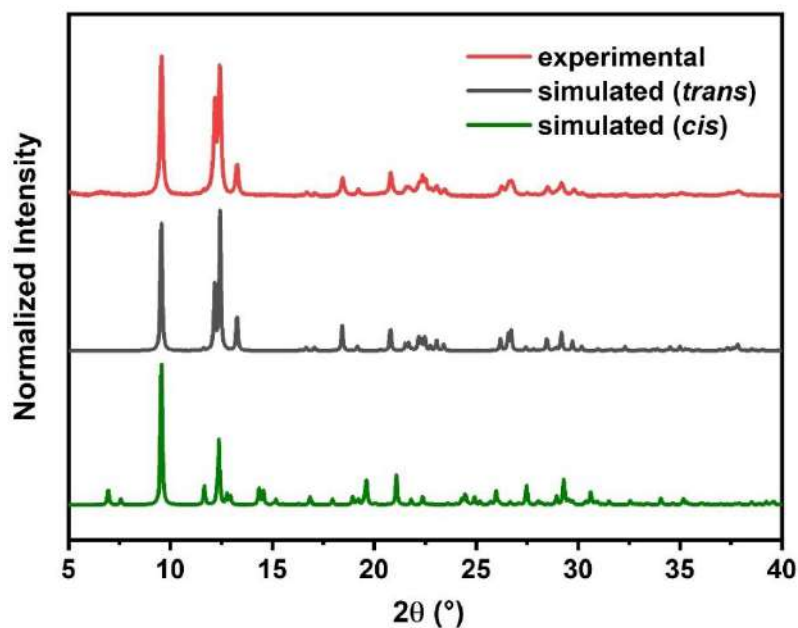


Figure 2.27. Simulated powder XRD patterns for the *cis*- and *trans*-isomer of **4** and the experimental pattern for the bulk powder of the compound acquired at room temperature.

At 100 K, average Fe–N distance value is 1.976(14) Å in *trans*- and 1.968(4) Å in *cis*-isomer. The octahedron volume at the given temperature equals to 10.27 Å<sup>3</sup> and 10.16 Å<sup>3</sup> in *trans*- and *cis*-isomers respectively. These values indicate that both isomers of the complex are low spin at this temperature. The octahedron distortion of the low-spin *trans*-isomer appears to be higher (19.80°) than such in the LS *cis*-isomer (16.10°). Crystal packing of the isomers is dominated by C–H⋯N and C–H⋯π interactions between the complex molecules (Figure 2.28).

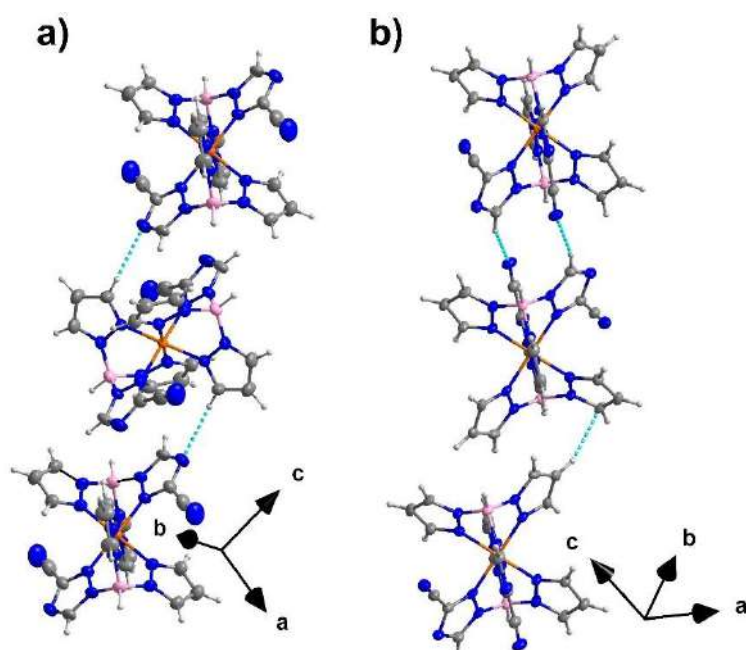


Figure 2.28. C–H⋯N intermolecular interactions in *trans*- (top) and both C–H⋯N together with C–H⋯π interactions in *cis*-isomer (bottom) of **4**.

The mean D···A distances characterizing the C–H···N interactions in the both isomers are 3.453(3) Å in the *trans*- and 3.377(6) Å in the *cis*-isomer. In case of the C–H··· $\pi$  interactions in the *cis*-isomer, the CH/ $\pi$ -plane distance equals 2.762(4) Å, while the C–H··· $\pi$  access angle is of 146.0(4)°, which is in line with typical reported values for such type of interactions.<sup>215</sup>

### 2.2.5 Spin crossover in the iron(II) complexes with the heteroscorpionate ligands

Magnetic behavior of the complexes under temperature variation was studied by means of variable-temperature SQUID magnetometry on bulk powders of the complexes. Molar magnetic susceptibility ( $\chi_M T$ ) was measured in 4–300 K (for **2**, **3**) and 4–400 K (for **4–7**) temperature range.

Nitro-functionalized complexes **2** and **3** are high spin at room temperature and retain their HS state at low temperatures until their  $\chi_M T$  starts to decrease brusquely below 50 K due to the zero-field splitting (Figure 2.29). This behavior was observed also for their heteroanalogues containing 3-nitropyrazolyl moieties instead of the nitrotriazole ones.<sup>86</sup> Referring to the crystallography data, Ma *et al.* suggested that the effect of sterically demanding NO<sub>2</sub>-substituent situated closely to the metal center allows the ligands to adopt exclusively HS Fe<sup>II</sup>.

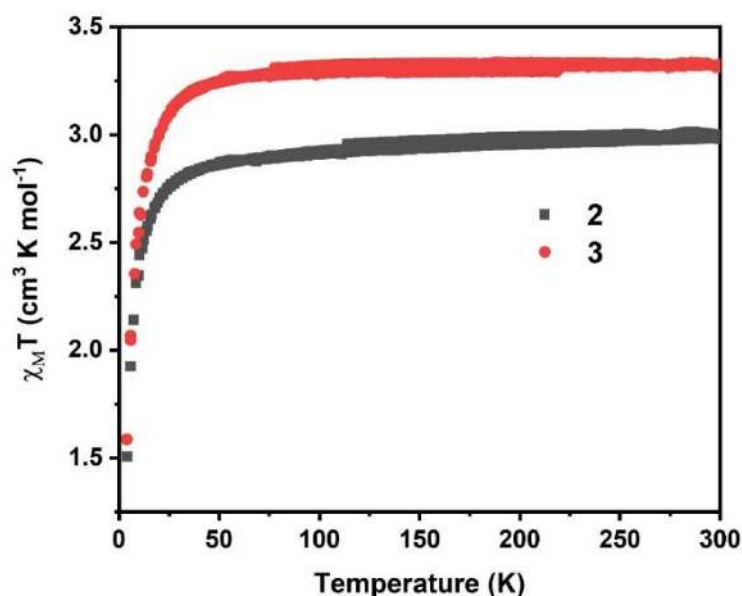


Figure 2.29. Molar magnetic susceptibility of **2** (dark grey symbols) and **3** (red symbols) as a function of temperature in both cooling and heating modes.

Unlike to nitro-group, CN-function has no considerable steric effect. Thus, complex **4** bearing two cyano-substituents is low spin at low temperatures, which is in agreement with the X-ray structural data, and it remains LS at room temperature whereafter its  $\chi_M T$  firmly increases (Figure 2.30). The transition is not over at 400 K, and probably occurs completely at higher temperatures out of range attainable by the SQUID magnetometry setup used. Similar trend is observed in **5** (tetracyano-derivative), however the threshold of  $\chi_M T$  is above 350 K.

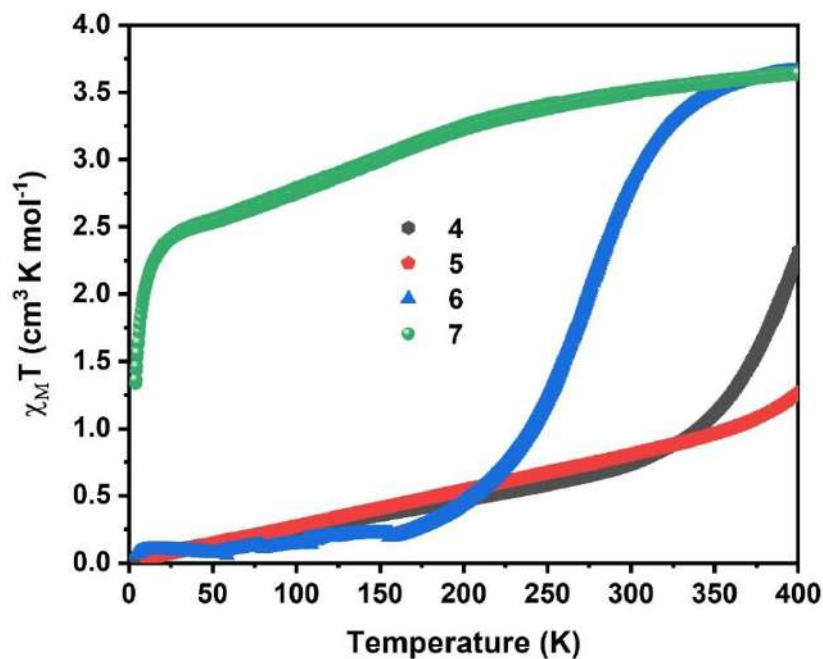


Figure 2.30.  $\chi_M T$  vs  $T$  products for compounds 4–7 in heating and cooling modes.

Amino-group is much less bulky comparing to nitro-group, thus the  $\text{NH}_2$ -substituted ligands are expected to adopt the metal ion in both LS and HS configurations. Indeed, the magnetic measurements data reveal complete spin transition in diamino-featured complex **6** and incomplete SCO behavior in tetraamino-derived complex **7** (Figure 2.30). The SCO behavior in the complexes is reproducible over three consecutive thermal cycles. Complex **6** undergoes gradual spin crossover in 150–350 K range with  $T_{1/2}$  centered around 276 K with small hysteresis of *ca.* 2–3 K. The SCO curves of **6** acquired over three consecutive heating/cooling cycles together with the hysteresis loop are shown in Annex D. Despite the presence of the hydrogen bonding between  $[\text{Fe}(\text{L}^6)_2]$  molecules in bulk of the substance, the character of SCO is gradual. Although the magnetometry data and the crystallography data correlate well with each other. Comparing the SCO behavior in complex **6** to such for bis[hydrotris(1,2,3-triazol-1-yl)borate]iron(II) one may note that the spin transition in bis[hydrobis(pyrazol-1-yl)(3-amino-1,2,4-triazol-1-yl)]iron(II) is more gradual. Though, hydrogen bonding present in the crystal is supposed to favor more abrupt spin transition. It should be noted however that the H-bonding in the structure is spread only in one dimension, while in  $[\text{Fe}(\text{HB}(1,2,3\text{-tz})_3)_2]$  and  $[\text{Fe}(\text{HB}(1,2,4\text{-tz})_3)_2]$  similar by nature intermolecular C–H $\cdots$ N interactions form a 2D and 3D supramolecular networks respectively, which may promote the cooperativity. Thus, such a gradual SCO behavior in **6** may be explained by absence of any multidimensional supramolecular network and lack of other strong intermolecular different from hydrogen bonding. Besides the structural and magnetochemical characterization, Mössbauer spectra were acquired for the bulk powder of bis[hydrobis(pyrazol-1-yl)(3-amino-1,2,4-triazol-1-yl)]iron(II) (**6**) at six different temperature points within 80–320 K range (Figure 2.31).

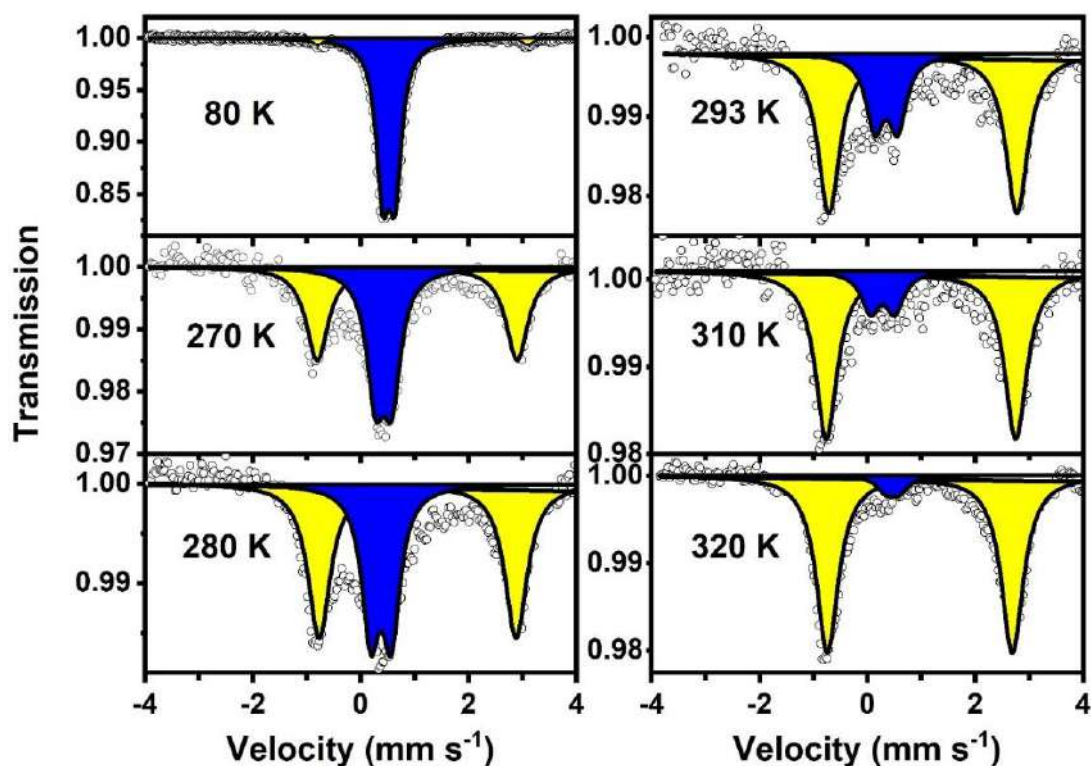


Figure 2.31. Mössbauer spectra recorded for the bulk powder of **6** at selected temperatures.

The high spin fraction increased with temperature. The spectrum acquired at 80 K allows to conclude that the substance is virtually fully low spin ( $\gamma_{\text{HS}} = 4\%$ ) at this temperature (Figure 2.31). At 320 K the HS fraction reaches 94% (Figure 2.31). Expectedly,  $\gamma_{\text{HS}}$  is at equilibrium at 270 K ( $\gamma_{\text{HS}} = 50\%$ ), while at room temperature the compound is 74% high spin.

The isomeric shifts, quadruple splittings, half widths at half maximum (HWHM), acquisition time and high-spin fraction for each temperature are given in Table 2.4.

Table 2.4. Selected parameters determined from the Mössbauer spectra of **6** at selected temperatures. Values in brackets stand for the standard deviation. Fixed values are underlined.

$T$ , K	$\delta^{\text{HS}}$ ; $\delta^{\text{LS}}$ , $\text{mm}\cdot\text{s}^{-1}$	$\Delta E_{\text{q}}^{\text{HS}}$ ; $\Delta E_{\text{q}}^{\text{LS}}$ , $\text{mm}\cdot\text{s}^{-1}$	HWHM, $\text{mm}\cdot\text{s}^{-1}$	Acquisition time, d	$\gamma_{\text{HS}}$ , %
<b>80</b>	1.15(2); 0.525(1)	3.89(5); 0.226(2)	0.13(4); 0.146(2)	3	4.0(9)
<b>270</b>	1.05(2); 0.43(1)	3.70(3); 0.30(2)	<u>0.25</u> ; <u>0.2</u>	2	50(3)
<b>280</b>	1.057(8); 0.378(9)	3.65(2); 0.38(2)	<u>0.25</u> ; <u>0.2</u>	5	58(2)
<b>293</b>	1.03(1); <u>0.35</u>	3.48(2); 0.42(5)	<u>0.25</u> ; <u>0.2</u>	3	74(3)
<b>310</b>	1.00(2); 0.28(8)	3.51(4); <u>0.45</u>	<u>0.25</u> ; <u>0.2</u>	5	84(5)
<b>320</b>	0.975(5); <u>0.47</u>	3.43(1); <u>0.25</u>	<u>0.25</u> ; <u>0.2</u>	7	94(2)

The full correlation between the temperature-dependent magnetic susceptibility and Mössbauer spectral data is depicted on Figure 2.32.

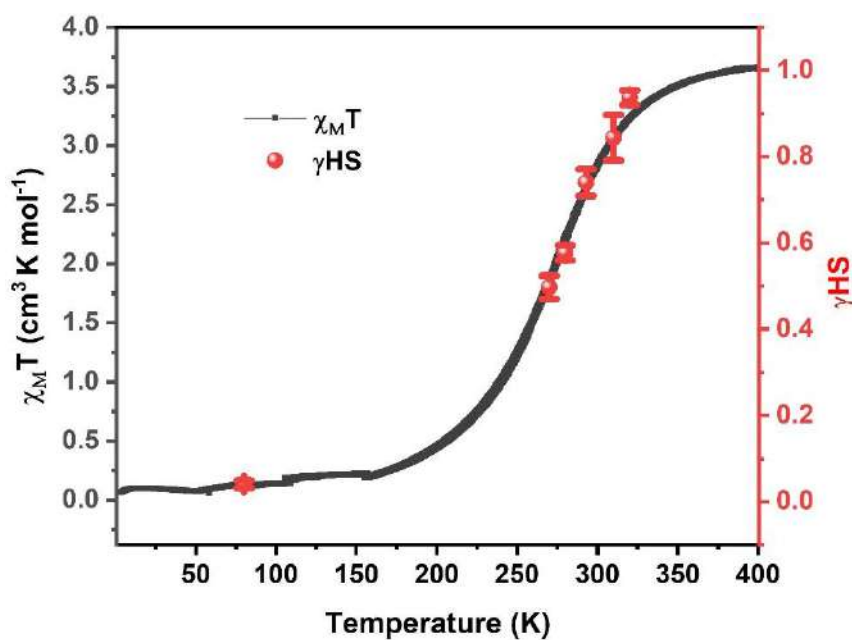


Figure 2.32. Correlation of molar magnetic susceptibility thermal variation for **6** (black symbols) and  $\gamma_{\text{HS}}$  (red symbols with error bars) extracted from the Mössbauer spectra of the complex acquired at five different temperatures.

The collected structural, magnetochemical and spectroscopic data on the properties of the complexes, when compared to those reported for the 3-nitro- and 3-aminopyrazolyl analogues can yield in some clues on the structure-property relationship. Indeed, iron(II) complexes with heteroscorpionate ligands substituted with bulky  $\text{NO}_2$ -group at 3-position of a heterocycle do not undergo spin crossover as only HS configuration is sterically favorable for them. Changing nitro-group to non-bulky CN-group affords low spin complexes which may undergo SCO at high temperatures. Concerning the amino-derivatives, one may conclude that replacing 3-aminopyrazole unit with 3-amino-1,2,4-triazole ones makes HS state more favorable at lower temperatures, thus lowering  $T_{1/2}$  or even favoring the incomplete SCO behavior.

### 2.3 Partial conclusions

The physical and spin crossover properties of  $[\text{Fe}(\text{HB}(1,2,3\text{-tz})_3)_2]$  were investigated. Similar to other unsubstituted tris(1-azolyl)borate iron(II) complexes, the complex exhibits reversible spin crossover above room temperature. The SCO in this complex is gradual and is centered at 373 K. Interestingly, the first heating of the hydrated complex is accompanied by a series of structural phase transitions resulting in different polymorphic phases of the compound. Crystal structures of the anhydrous complex and most of the solvatomorphs share the same types of interactions between the molecules of complex, including  $\pi$ - $\pi$  stackings and weak  $\text{C-H}\cdots\text{N}$  hydrogen bond interactions.

Heteroscorpionate ligands  ${}^n\text{Bu}_4\text{N}(\text{L}^2\text{-L}^5)$  and complexes **2–7** were synthesized and characterized for the first time. Magnetic behavior of the complexes investigated. It was found that nitro-derivatives

do not undergo SCO, thus remaining high spin at low temperatures, while cyano-derivatives tend to remain in LS in a broad temperature range including above-room-temperature region. Amino-derived complex **6** displays a very gradual spin transition that covers broad temperature range that covers cryogenic, room-temperature and above-room-temperature which might be interesting for thermometry applications. Contrarily, another NH<sub>2</sub>-derived complex **7** undergoes an incomplete spin transition.

## 2.4 Partial perspectives

- To test complexes **1** and **6** for evaporability and to elaborate thin films of the complexes and investigate properties and SCO in the latter.
- To test the films with desired properties for application in thermometry.
- To test the amino-derivatives as building blocks to enlarge the family of SCO scorpionates.

## 2.5 Notes

Preparation of this chapter involved the use of materials from the following publication (all the publications are presented in Annex I):

1. Horniichuk, O. Y.; Ridier, K.; Molnár, G.; Kotsyubynsky, V. O.; Shova, S.; Amirkhanov, V. M.; Gural'skiy, I. A.; Salmon, L.; Bousseksou, A. Solvatomorphism, Polymorphism and Spin Crossover in Bis[Hydrotris(1,2,3-Triazol-1-Yl)Borate]Iron(II). *New J. Chem.* **2022**, *46* (24), 11734–11740. <https://doi.org/10.1039/D2NJ01471H>.

# Chapter 3. Lanthanide(III) bis-carbacylamidophosphates. Synthesis, characterization and luminescence studies.

With accordance to the objectives highlighted in chapter 1, the current chapter is aimed at the development of novel binuclear lanthanide complexes of helicate family, displaying efficiently-sensitized Ln<sup>III</sup>-centered luminescence. Design of the ligand should involve presence of two binding sites allowing coordination of two lanthanide ions, relative flexibility of the ligand molecule permitting the formation of a helicate motif as well as addressing the requirements for efficient sensitization of the lanthanide luminescence. Considering the benefits of  $\beta$ -diketinate binding sites and advantages of carbacylamidophosphate (CAPH) ones over the latter, it was interesting to seek for a bis-chelating CAPH ligand, design of which would imply minimized non-radiative deactivation processes together with a good shielding of the lanthanide ions from external luminescence-quenching interactions (*e.g.*, vibrations of high-energy oscillators at solvent molecules). To meet these requirements tetramethyl *N,N'*-(2,2,3,3,4,4-hexafluoro-1,5-dioxopentane-1,5-diyl)bis(phosphoramidate) – bis-chelating CAPH reported earlier<sup>216</sup> was selected as an appropriate candidate. The ligand is featured with two carbacylamidophosphate chelating sites linked by perfluorinated propylene spacer, both together ensure the absence of high-energy oscillators in close vicinity to the lanthanide ions.

As well as chapter 2, the current chapter consists of two main sub-chapters. The first one deals with triple-stranded (ternary) binuclear lanthanide complexes with the bis-chelating CAPH ligand and ancillary 1,10-phenantroline ligands saturating the Ln<sup>III</sup> coordination spheres. The sub-chapter is dedicated to the detailed spectroscopic studies in particular on the Ln<sup>III</sup>-centered luminescence in the complexes.

In the second sub-chapter, structural and spectroscopic features of quadruple-stranded binuclear Ln<sup>III</sup> complexes with the bis-chelating CAPH are considered. In particular, NIR Nd<sup>III</sup> luminescence, its quenching mechanism and temperature dependance are discussed.

### 3.1 Synthesis of bis-chelating carbacylamidophosphate ligand ( $H_2L^8$ ) and its binuclear lanthanide(III) complexes $[Ln_2(L^8)_3(phen)_2]$ . Characterization of the compounds. Luminescence in the obtained complexes.

#### 3.1.1 Synthesis of the ligand and the complexes

All the synthetic procedures are provided in the experimental part (pp. 159–162). The synthesis of the ligand – tetramethyl  $N,N'$ -(2,2,3,3,4,4-hexafluoro-1,5-dioxopentane-1,5-diyl)bis(phosphoramidate), hereafter  $H_2L^8$ , was reported earlier.<sup>216</sup> Though, in this work the procedure has been slightly modified, and the compound was synthesized according to the scheme depicted in Figure 3.1.

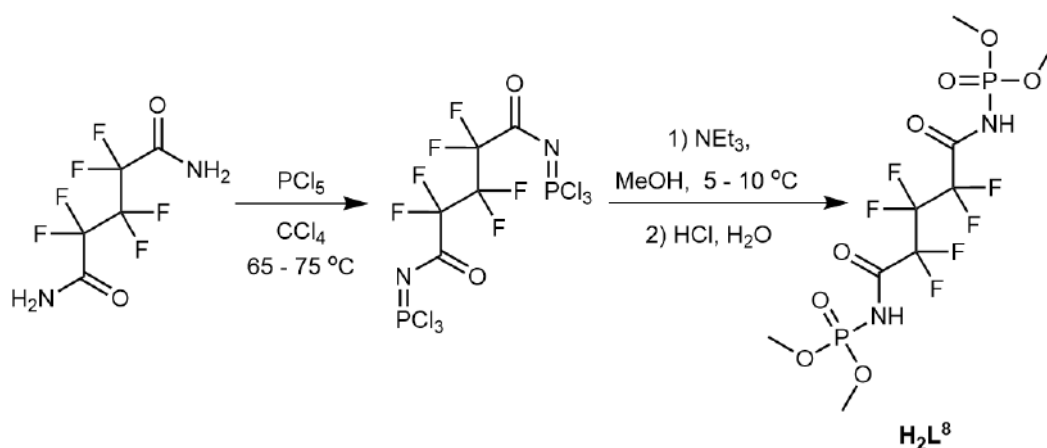


Figure 3.1. Synthesis of tetramethyl  $N,N'$ -(2,2,3,3,4,4-hexafluoro-1,5-dioxopentane-1,5-diyl)bis(phosphoramidate) or  $H_2L^8$  – bis-chelating CAPH ligand.

Coordination compounds  $[Ln_2(L^8)_3(phen)_2]$  were obtained according to the scheme displayed in Figure 3.2.

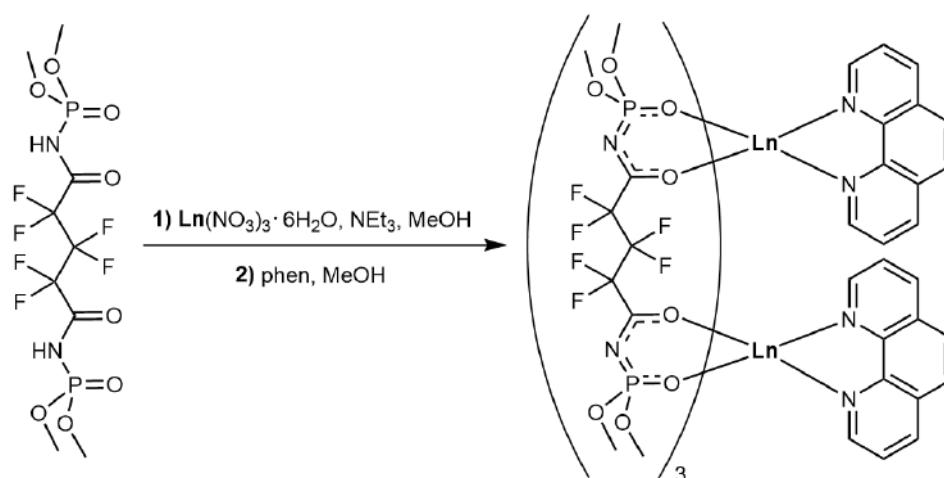


Figure 3.2. Synthesis of  $[Ln_2(L^8)_3(phen)_2]$  complexes.  $Ln^{III} = Nd^{III}, Sm^{III}, Eu^{III}, Tb^{III}, Dy^{III}, Yb^{III}$ .

### 3.1.2 NMR spectroscopy

The NMR spectra discussed in this sub-chapter are provided in Annex B.  $^1\text{H}$  NMR spectrum of  $[\text{Y}_2(\text{L}^8)_3(\text{phen})_2]$  (**14**) displays a doublet at  $\delta$  3.57 assigned to protons of ester groups of the CAPH ligands and a series of peaks in region of  $\delta$  7.8–9.2 assigned to 1,10-phenanthroline ligands. By integrating of areas of peaks corresponding to the both ligands it was found that their ratio ( $\text{L}^8$  : phen) in the complex equals 3:2. No signal of the amide protons of the CAPH ligand was found in the  $^1\text{H}$  NMR spectrum of complex **14**, which is a consequence of coordination of tetramethyl *N,N'*-(2,2,3,3,4,4-hexafluoro-1,5-dioxopentane-1,5-diyl)bis(phosphoramidate) to  $\text{Y}^{\text{III}}$  ion in a doubly deprotonated form. Deprotonation of the CAPH ligand in  $[\text{Y}_2(\text{L}^8)_3(\text{phen})_2]$  also leads to the shift of the signal of  $\text{OCH}_3$ -groups in the complex  $^1\text{H}$  NMR spectrum to high field compared to the spectrum of  $\text{H}_2\text{L}^8$ .<sup>216</sup> For paramagnetic lanthanides ( $\text{Nd}^{\text{III}}$ ,  $\text{Sm}^{\text{III}}$ ,  $\text{Eu}^{\text{III}}$ ) complexes the signals in their  $^1\text{H}$  NMR spectra are broadened and shifted however the integral intensities ratio do not change. For the rest of the obtained complexes the  $^1\text{H}$  NMR spectra were not informative.

### 3.1.3 IR spectroscopy

The characteristic IR spectra data for  $\text{H}_2\text{L}^8$  and the complexes are given in Table 3.1 and shown in Annex C.

Table 3.1. Main IR absorption bands and their assignments for the synthesized compounds.

Compound	Band assignment, $\text{cm}^{-1}$				
	$\nu(\text{N-H})$	$\nu(\text{C=O})$	$\nu(\text{Amide-2})$	$\nu(\text{P=O})$	$\nu(\text{PN})$
$\text{H}_2\text{L}^8$	3095	1746	1478	1212	877
$[\text{Ln}_2(\text{L}^8)_3(\text{phen})_2]$	-	1604–1613	1399–1406	1160–1165	962–964

The complexes have similar IR spectra with resembling position of characteristic bands, suggesting the similar coordination modes. An absence of  $\nu(\text{N-H})$  absorption band in the region near  $3100 \text{ cm}^{-1}$  in the IR spectra of the complexes indicates the coordination of the CAPH ligands to the rare earth ions doubly deprotonated form is in good agreement with  $^1\text{H}$  NMR data. The low frequency shift of  $\nu(\text{P=O})$  and  $\nu(\text{C=O})$  bands and high frequency shift of  $\nu(\text{P-N})$  bands in the IR spectra of the complexes with respect to  $\text{H}_2\text{L}^8$  spectrum point to participation of the both phosphoryl and carbonyl groups in metal binding and

existence of  $\pi$ -conjugation in  $-\text{OCNPO}-$  chelating core. A number of bands with middle and low intensity at 1520, 1430, 1350, 846 and 733  $\text{cm}^{-1}$  points to the presence of 1,10-phenanthroline ligands in the complexes (see Annex C). The IR spectrum of the neodymium complex concentrated solution in DMSO is shown in Annex C alike. Only the most intense absorption bands of the complex, which do not overlap with solvent absorption bands, can be observed in the spectrum. The position of  $\nu(\text{P}=\text{O})$  absorption band is the same for the complex in KBr pellet and in solution, while  $\nu(\text{C}=\text{O})$  and  $\delta(\text{POC})$  absorption bands slightly moved for near 20  $\text{cm}^{-1}$  to higher or lower frequencies respectively. Considering an insignificant difference in positions of characteristic absorption bands in the IR spectra for the solid complex and its solution the retention of CAPH ligand type of coordination in the complex in solution in DMSO can be concluded.

### 3.1.4 Absorption spectra of the $\text{Nd}^{\text{III}}$ complex

Among the lanthanide(III) ions  $\text{Nd}^{\text{III}}$  has been used most frequently as an absorption probe for Ln-ligand interactions. The absorption band associated with  $^4\text{I}_{9/2} \rightarrow ^4\text{G}_{5/2}$  and  $^2\text{G}_{7/2}$  transitions of  $\text{Nd}^{\text{III}}$  exhibits strong "hypersensitive" behaviour.<sup>217-219</sup> The intensity of these bands is mostly influenced among all the  $f-f$  transitions due to the changes in the nearest surrounding of the  $\text{Nd}^{\text{III}}$  ion, making it particularly suitable for probing the coordination environment around the ion. View of the spectra in the region of  $^4\text{I}_{9/2} \rightarrow ^2\text{P}_{1/2}$  transition indicates the splitting of the ground level in the ligand field of the  $\text{Nd}^{\text{III}}$  environment.<sup>220</sup>

The absorption spectra of the neodymium complex were recorded at 293 K in the ranges of  $^4\text{I}_{9/2} \rightarrow ^2\text{P}_{1/2}$  and  $^4\text{I}_{9/2} \rightarrow ^4\text{G}_{5/2}, ^2\text{G}_{7/2}$  transitions for solid sample and for the complex 0.008 M solution in DMSO (Figure 3.3).

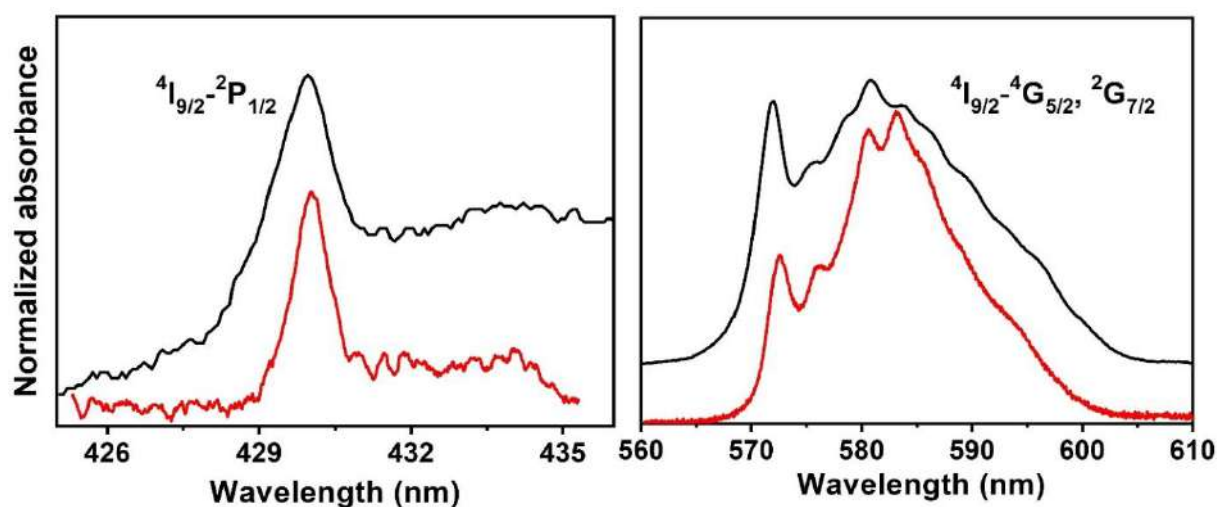


Figure 3.3. Normalized absorption spectra of  $[\text{Nd}_2(\text{L}^8)_3(\text{phen})_2]$  solid sample (black lines) and solution in DMSO (red lines) in the regions of  $^4\text{I}_{9/2} \rightarrow ^2\text{P}_{1/2}$  (left panel) and  $^4\text{I}_{9/2} \rightarrow ^4\text{G}_{5/2}, ^2\text{G}_{7/2}$  (right panel) transitions.

A single band with maximum at 430.0 nm in region of  $^4I_{9/2} \rightarrow ^2P_{1/2}$  transition points on identical or very similar neodymium ions positions in the complex. In the region of  $^4I_{9/2} \rightarrow ^4G_{5/2}$ ,  $^2G_{7/2}$  transitions the electronic absorption spectra of  $[\text{Nd}_2(\text{L}^8)_3(\text{phen})_2]$  (**8**) show absorption features similar to those reported previously for mononuclear neodymium complexes with different CPh and SPh ligands displaying octacoordinated central ion geometries.<sup>221–223</sup> From the similar bands positions in the spectra of solid  $[\text{Nd}_2(\text{L}^8)_3(\text{phen})_2]$  complex and its solution it can be concluded that in solution the central ion of the complex is eight-coordinated and the  $\text{Nd}^{\text{III}}$ -ligand bond covalence is the same as for the solid sample.

### 3.1.5 The $\text{Y}^{\text{III}}$ complex phosphorescence spectra

It is well known that the energy level matching between the lowest ligand triplet state and excited levels of  $\text{Ln}^{\text{III}}$  ions plays an important role in determining the luminescent properties of complexes. Energy level of the lowest ligands triplet state (LLTS) for the complexes under study ( $21550 \text{ cm}^{-1}$ ) was calculated from the shortest wavelength peak<sup>224</sup> of the phosphorescence spectrum of solid  $[\text{Y}_2(\text{L}^8)_3(\text{phen})_2]$  complex (Figure 3.4, solid line). LLTS is obviously higher than emissive levels of  $\text{Nd}^{\text{III}}$ ,  $\text{Sm}^{\text{III}}$ ,  $\text{Eu}^{\text{III}}$ ,  $\text{Tb}^{\text{III}}$ ,  $\text{Dy}^{\text{III}}$  and  $\text{Yb}^{\text{III}}$  ions. The energy gaps between the ligands' lowest triplet state and emissive levels of the mentioned lanthanides in the complexes under study are 10050, 3850, 4250, 1050, 450 and  $11550 \text{ cm}^{-1}$  respectively (see Annex E).

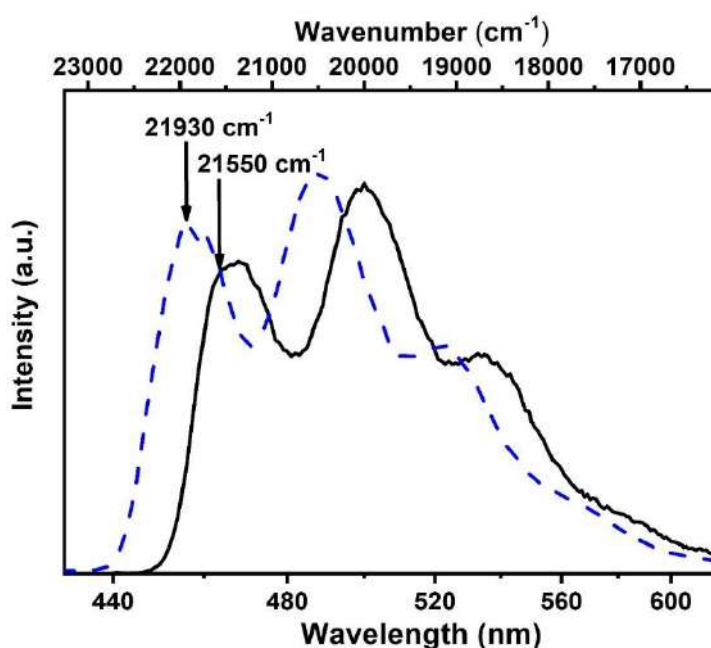


Figure 3.4. The phosphorescence spectra of  $[\text{Y}_2(\text{L}^8)_3(\text{phen})_2]$  complex at 77 K ( $\lambda_{\text{exc}}=330 \text{ nm}$ ) in solid state (solid line) and for frozen solution in DMSO (dashed line).

In 0.001 M solution in DMSO the phosphorescence spectrum of the  $\text{Y}^{\text{III}}$  complex was shifted to higher frequencies for  $380 \text{ cm}^{-1}$  (Figure 3.4, dashed line) due to the complex interaction with the solvent.

### 3.1.6 Luminescence properties of the $\text{Nd}^{\text{III}}$ , $\text{Sm}^{\text{III}}$ , $\text{Eu}^{\text{III}}$ , $\text{Tb}^{\text{III}}$ , $\text{Dy}^{\text{III}}$ and $\text{Yb}^{\text{III}}$ complexes

The excitation and emission spectra of the obtained complexes are shown in the Figures 3.5–3.6. The excitation spectra were recorded by monitoring the strongest emission bands of corresponding lanthanide ions. The spectra consist of a broad intense band in the 250–380 nm region, which can be assigned to the  $\pi$ - $\pi^*$  electronic transitions of the ligands, and of less intense and narrow bands of  $f$ - $f$  transitions of the lanthanide ions. Such a ratio of the bands' intensities points on efficient sensitization of lanthanide luminescence by organic ligands. Upon excitation by UV light all the complexes show characteristic  $\text{Ln}^{\text{III}}$  emission with a series of narrow bands corresponding to the respective lanthanide ion. No ligand fluorescence was observed in the emission spectra of the complexes pointing on efficient energy transfer from ligands to lanthanides.

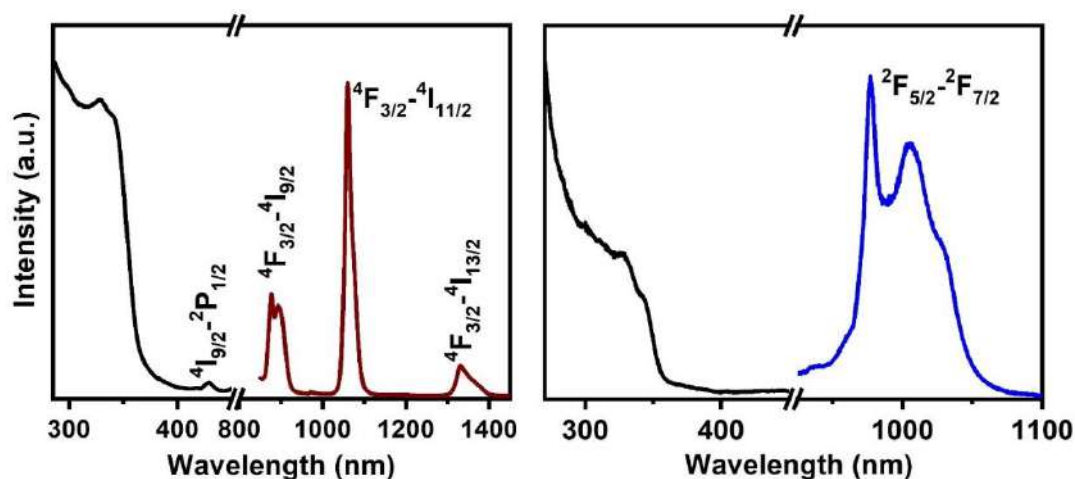


Figure 3.5. Luminescence excitation (black lines) and emission (colored lines) spectra of  $[\text{Nd}_2(\text{L}^8)_3(\text{phen})_2]$  (left panel) and  $[\text{Yb}_2(\text{L}^8)_3(\text{phen})_2]$  (right panel) solid samples at 293 K.

The spectroscopic properties of  $\text{Nd}^{\text{III}}$  and  $\text{Yb}^{\text{III}}$  complexes emitting in the near-infrared (NIR) range have been increasingly studied in recent times because of their diagnostic or tagging applications.<sup>225–229</sup> Considering that in the coordination compounds under study the energy level of lowest ligands triplet state was higher than emissive levels of  $\text{Nd}^{\text{III}}$  ( $^4\text{F}_{3/2}$ ,  $\sim 11\,500\text{ cm}^{-1}$ ) and  $\text{Yb}^{\text{III}}$  ( $^2\text{F}_{5/2}$ ,  $\sim 10\,000\text{ cm}^{-1}$ ) ions the luminescence excitation and luminescence spectra for complexes **8** and **14** were recorded (Figure 3.5). Upon excitation of the complex  $[\text{Nd}_2(\text{L}^8)_3(\text{phen})_2]$  by UV light at 330 nm, characteristic  $\text{Nd}^{\text{III}}$   $4f$ -luminescence was observed in the IR spectral region (Figure 3.5, left panel). The observed bands were assigned to the  $^4\text{F}_{3/2} \rightarrow ^4\text{I}_{9/2}$ ,  $^4\text{F}_{3/2} \rightarrow ^4\text{I}_{11/2}$  and  $^4\text{F}_{3/2} \rightarrow ^4\text{I}_{13/2}$  transitions. The bands, observed in the emission spectra of the complex  $[\text{Yb}_2(\text{L}^8)_3(\text{phen})_2]$ , were assigned to the  $^2\text{F}_{5/2} \rightarrow ^2\text{F}_{7/2}$  transition of the  $\text{Yb}^{\text{III}}$  ion (Figure 3.5, right panel). The electronic line corresponding to the  $^2\text{F}_{5/2}(0') \rightarrow ^2\text{F}_{7/2}(0)$  transition has a maximum at 977 nm. The broad peaks in 1000–1050 nm region arise from the  $M_J$  splitting of  $^2\text{F}_{7/2}$  state as the consequence of ligand-field effects.

The luminescence excitation and luminescence spectra of the complexes, emitting in the visible spectral range are shown in Figure 3.6. Sm<sup>III</sup> compounds are the objects of extensive studies because of their application as luminescence orange emitters for laser active materials.<sup>230–232</sup> Sm<sup>III</sup> exhibits an orange emission, which is normally much weaker than Eu<sup>III</sup> and Tb<sup>III</sup> emission due to the small energy gap between excited and ground states, that makes multiphonon relaxation much easier. Upon excitation by UV light at 330 nm [Sm<sub>2</sub>(L<sup>8</sup>)<sub>3</sub>(phen)<sub>2</sub>] (**9**) shows orange 4*f*-emission (Figure 3.6a). Similar to ternary Sm<sup>III</sup> β-diketone based complexes<sup>233</sup> the band of magnetic dipole forbidden and electronic-dipole allowed hypersensitive transition <sup>4</sup>G<sub>5/2</sub>→<sup>6</sup>H<sub>9/2</sub> (λ<sub>max</sub> = 645 nm) dominates in the emission spectrum of complex [Sm<sub>2</sub>(L<sup>8</sup>)<sub>3</sub>(phen)<sub>2</sub>]. A band of transition <sup>4</sup>G<sub>5/2</sub>→<sup>6</sup>H<sub>7/2</sub> (λ<sub>max</sub> = 598 nm) is less intense and the bands of <sup>4</sup>G<sub>5/2</sub>→<sup>6</sup>H<sub>5/2</sub> (λ<sub>max</sub> = 564 nm) and <sup>4</sup>G<sub>5/2</sub>→<sup>6</sup>H<sub>11/2</sub> (λ<sub>max</sub> = 708 nm) transitions are of the lowest intensity.

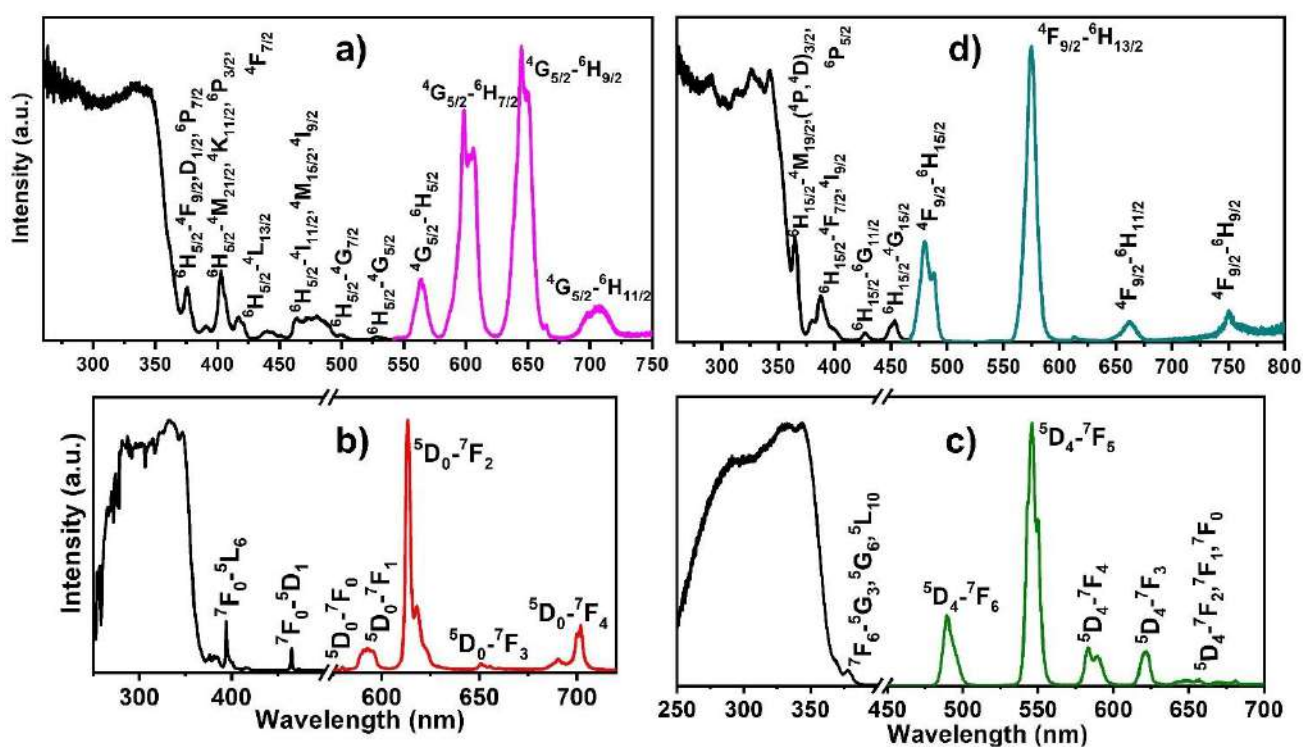


Figure 3.6. Luminescence excitation (black lines) and emission (colored lines) spectra of the complexes [Sm<sub>2</sub>(L<sup>8</sup>)<sub>3</sub>(phen)<sub>2</sub>] (**a**), [Eu<sub>2</sub>(L<sup>8</sup>)<sub>3</sub>(phen)<sub>2</sub>] (**b**), [Tb<sub>2</sub>(L<sup>8</sup>)<sub>3</sub>(phen)<sub>2</sub>] (**c**), [Dy<sub>2</sub>(L<sup>8</sup>)<sub>3</sub>(phen)<sub>2</sub>] (**d**) solid samples at 293 K.

Extensive research into Eu<sup>III</sup> and Tb<sup>III</sup> complexes possessing long luminescent lifetimes has focused on their use as labels and biological probes<sup>234–239</sup> or as emitting components in electroluminescent devices for light-emitting diodes.<sup>240–242</sup> The luminescence properties of [Eu<sub>2</sub>(L<sup>8</sup>)<sub>3</sub>(phen)<sub>2</sub>] (**10**) and [Tb<sub>2</sub>(L<sup>8</sup>)<sub>3</sub>(phen)<sub>2</sub>] (**11**) complexes were investigated at room temperature and at 77 K as well as in solution in DMSO (Figures 3.6–3.8 and Annex F).

At both temperatures the solid europium complex exhibited  $^5D_0$  and  $^5D_1$  emission (Figures 3.6b and Annex F). The  $^5D_0$  emission spectra of the  $\text{Eu}^{\text{III}}$  complex, solid state and solution, are dominated by the band of the  $^5D_0 \rightarrow ^7F_2$  transition (Figures 3.6b, 3.7). High intensity of  $^5D_0 \rightarrow ^7F_2$  band compared to such for  $^5D_0 \rightarrow ^7F_1$  points to low symmetry of the  $\text{Eu}^{\text{III}}$  coordination environment in the complex under study. The intensity ratio of the bands of  $^5D_0 \rightarrow ^7F_2$  and  $^5D_0 \rightarrow ^7F_1$  transitions (red/orange ratio) was found to be independent on temperature and equal 6.5 for the solid sample and 3.9 for the complex solution, which can be due to increasing of symmetry of  $\text{Eu}^{\text{III}}$  ion surroundings in the complex solution compared to the solid sample. The obtained red/orange ratio for the solid sample is comparable with that found for mononuclear CAPH-based europium complexes with 1,10-phenanthroline.<sup>221,243,244</sup> One component band of  $^5D_0 \rightarrow ^7F_0$  transition is observed at 580 nm in the both spectra measured for solid sample and solution.

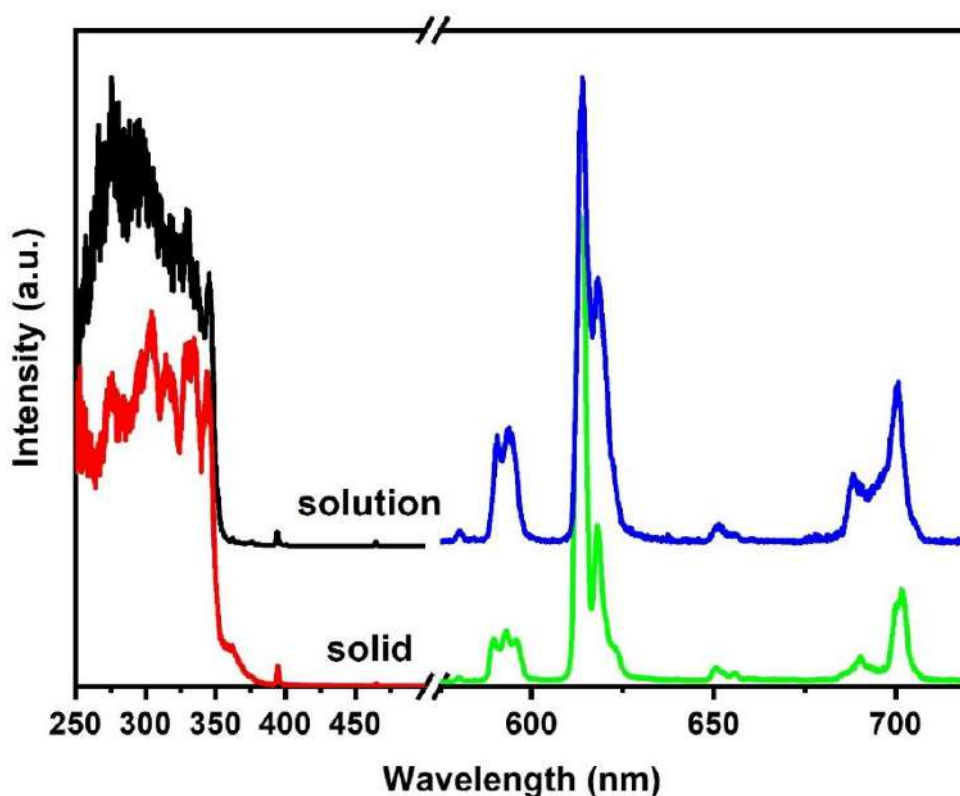


Figure 3.7. Luminescence excitation (red and black lines) and  $^5D_0$  luminescence (green and blue) spectra of the complex  $[\text{Eu}_2(\text{L}^8)_3(\text{phen})_2]$  in solid state and for frozen solution in DMSO at 77 K.

The typical luminescence decay profiles for europium and terbium complexes in a semilog scale are shown in Annex G. All decay curves for solid samples are well reproduced by single exponential function, which suggests that only one species exists in the excited states of the complexes. The luminescence decay time of the europium complex did not depend on the excitation wavelength but decreased slightly with temperature (Table 3.2).

Table 3.2. Decay times values (ms) for complex **10** in solid state and in solution. The accuracy of measurements was within 10 %. (“-” – was not measured).

Temperature, K	298	77
solid sample		
$\lambda_{\text{exc}} = 280 \text{ nm}$	1.88	1.50
$\lambda_{\text{exc}} = 330 \text{ nm}$	1.74	1.53
solution in DMSO		
$\lambda_{\text{exc}} = 280 \text{ nm}$	1.14	1.29
$\lambda_{\text{exc}} = 330 \text{ nm}$	1.24	-

In the solution luminescence decay time for complex **10** was found to be equal 1.2 ms that is lower compared to solid sample and can be a result of quenching of  $\text{Eu}^{\text{III}}$  luminescence by the solvent molecules. Some luminescence characteristics radiative ( $k_r$ ) and non-radiative ( $k_{nr}$ ) decay rates, observed ( $\tau_{\text{obs}}$ ) and radiative ( $\tau_{\text{rad}}$ ) luminescence lifetime and  $^5\text{D}_0$  intrinsic quantum yield ( $Q^{\text{LnLn}}$ ) for solid complex  $[\text{Eu}_2(\text{L}^8)_3(\text{phen})_2]$  and some selected mixed-ligand europium complexes with  $\beta$ -diketones and CAPHs and 1,10-phenanthroline are given in Table 3.3.

Table 3.3. Selected luminescence characteristics for  $[\text{Eu}_2(\text{L}^8)_3(\text{phen})_2]$  and some mixed-ligand europium complexes with  $\beta$ -diketones or CAPH-type ligands and phen at 298 K. Acronyms for ligands are deciphered at the bottom of the table.

Complex	$\lambda_{\text{exc}}$ , nm	$I(^5\text{D}_0 \rightarrow ^7\text{F}_2)/I(^5\text{D}_0 \rightarrow ^7\text{F}_1)$	$\tau_{\text{obs}}$ , ms (293K)	$\tau_{\text{rad}}$ , ms	$A_r$ , $\text{s}^{-1}$	$A_{nr}$ , $\text{s}^{-1}$	$Q^{\text{LnLn}}$ , %	ref.
$[\text{Eu}_2(\text{L}^8)_3(\text{phen})_2]$	280	6.5	1.88	2.06	485	28	91	present study
$[\text{Eu}(\text{Pip})_3\text{phen}]$	337	8.7	1.58	1.78	564	68	89	243
$[\text{Eu}(\text{CAPH}^1)_3\text{phen}]$	254	4.6	1.58	2.85	346	286	55	221
$[\text{Eu}(\text{CAPH}^2)_3\text{phen}]$	254	5.7	1.54	2.03	494	156	76	244
$[\text{Eu}_2(\text{BTP})_3(\text{phen})_2]$	324	7.3	0.91	1.17	857	246	78	245
$[\text{Eu}_2(\text{BTB})_3(\text{phen})_2]$	-	15.6	0.55	1.16	853	973	47	136

HPip = 2,2,2-trichloro-N-(dipiperidin-1-ylphosphoryl)acetamide,  $\text{CAPH}^1$  = dimethyl-N-benzoylamidophosphate,  $\text{CAPH}^2$  = N-(diphenylphosphoryl)benzamide, BTP = 1,3-bis(4,4,4-trifluoro-1,3-dioxobutyl)-phenyl, BTB = 3,3'-bis(4,4,4-trifluoro-1,3-dioxobutyl)biphenyl.

The  $^5D_0$  intrinsic quantum yield ( $Q^{Ln_{Ln}}$ ) for the europium complex was estimated from the emission spectrum and measured  $^5D_0$  luminescence lifetime using the Equation 1.2, whereby  $\tau_{rad}$  is the radiative lifetime of  $^5D_0$  state estimated from the emission data using the following equation:

$$\frac{1}{\tau_{rad}} = A_{MD,0} n^3 \left( \frac{I_{tot}}{I_{MD}} \right) \quad (3.1)$$

where  $A_{MD,0}$  is the theoretical probability of spontaneous emission for magnetic-dipole (MD) transition  $^5D_0 \rightarrow ^7F_1$  equal to  $14.65 \text{ s}^{-1}$ ,  $n$  – refractive index, considered to be 1.5 (a value commonly encountered for coordination compounds) and  $(I_{tot}/I_{MD})$  is the ratio of the total integrated emission from the Eu ( $^5D_0$ ) level to the integrated intensity of MD transition  $^5D_0 \rightarrow ^7F_1$ .<sup>108,246</sup>

The total decay rates ( $k_r + k_{nr}$ ) for the europium complex under study are dominated by radiative contribution ( $k_r$ ) resulting in very high intrinsic quantum yield equal 91 %, which is significantly higher compared to the most of the mentioned in the Table 3.3 related mixed-ligand europium complexes with 1,10-phenanthroline. The observed ( $\tau_{obs}$ ) and radiative ( $\tau_{rad}$ ) luminescence lifetimes for complex  $[Eu_2(L^8)_3(phen)_2]$  are comparable with those found for CAPH based mixed-ligand europium complexes of general formula  $Eu(CAPH)_3phen$  and higher compared to bis- $\beta$ -diketones based binuclear mixed-ligand europium complexes of general formula  $[Eu_2(bis-\beta-dik)_3(phen)_2]$ .

Unlike the europium complex the luminescence decay time of  $[Tb_2(L^8)_3(phen)_2]$  increase with the temperature decreasing: at room temperature:  $\tau_{obs}$  for the terbium complex equals 1.45 ms and at 77 K it is 2.00 ms (see Annex G). Considering rather small energy gap between the ligands' lowest triplet state and  $^5D_4$  emissive level of  $Tb^{III}$  ion in the complex under study ( $\Delta E = 1050 \text{ cm}^{-1}$ ), an activation of non-radiative processes in **11** upon temperature increasing can be due to energy back transfer from terbium to ligands. It is known that in  $Tb^{III}$  complexes the ligand-to-metal energy transfer processes are efficient if the energy gap between the lowest ligand triplet state and  $^5D_4$  emissive level of  $Tb^{III}$  ( $\Delta E$ ) exceeds  $1850 \text{ cm}^{-1}$ .<sup>106</sup>

The emission spectrum of the terbium complex in solution at 298 K is very similar to that recorded for the solid sample, while at 77 K both  $Tb^{III}$  centered luminescence and the ligands phosphorescence was observed in the emission spectrum (Figure 3.8). According to the phosphorescence spectrum of the  $Y^{III}$  complex in solution in DMSO (Figure 3.4) the energy gaps between the ligands' lowest triplet state and emissive levels of  $Tb^{III}$  ion equals  $1430 \text{ cm}^{-1}$ , that is rather small and makes possible back from terbium to ligands energy transfer and enables rather effective ligand phosphorescence. The luminescence decay time of the terbium complex in solution was dependent on temperature (see Annex G). At room temperature  $\tau_{obs} = 1.37 \text{ ms}$  was similar to that found for solid

sample. At 77 K the decay curve departs from monoexponentiality probably due to the ligands' phosphorescence.

The Dy<sup>III</sup> luminescence mainly takes place from <sup>4</sup>F<sub>9/2</sub> level. The <sup>4</sup>F<sub>9/2</sub> level is separated from the lower lying state <sup>6</sup>F<sub>1/2</sub> by about 7500 cm<sup>-1</sup>, therefore multiphonon relaxation process is of low efficiency. In the visible range, the Dy<sup>III</sup> ion possesses two intense fluorescence bands located at 480 nm (blue region) and 570 nm (yellow region), corresponding to the <sup>4</sup>F<sub>9/2</sub> → <sup>6</sup>H<sub>15/2</sub> and <sup>4</sup>F<sub>9/2</sub> → <sup>6</sup>H<sub>13/2</sub> transitions, respectively. The yellow emission (<sup>4</sup>F<sub>9/2</sub> → <sup>6</sup>H<sub>13/2</sub>) of Dy<sup>III</sup> is called hypersensitive transition and its intensity strongly depends on Dy<sup>III</sup> ion coordination environment. Therefore, the luminescence of Dy<sup>III</sup> ion can be successfully used as structural probe of the chemical environment and recently Dy<sup>III</sup> complexes have been studied as emitting layers in OLEDs for white light generation. For complex [Dy<sub>2</sub>(L<sup>8</sup>)<sub>3</sub>(phen)<sub>2</sub>] the <sup>4</sup>F<sub>9/2</sub> → <sup>6</sup>H<sub>13/2</sub> yellow emission (λ<sub>max</sub>=575 nm) is dominant in its luminescence spectrum, indicating that Dy<sup>III</sup> ion is located in low-symmetry local site environment (Figure 3.6d). A band of transition <sup>4</sup>F<sub>9/2</sub> → <sup>6</sup>H<sub>15/2</sub> (λ<sub>max</sub> = 480 nm) is of a less intense and the bands of <sup>4</sup>F<sub>9/2</sub> → <sup>6</sup>H<sub>11/2</sub> (λ<sub>max</sub> = 662 nm) and <sup>4</sup>F<sub>9/2</sub> → <sup>6</sup>H<sub>9/2</sub> (λ<sub>max</sub> = 750 nm) transitions are of the lowest intensity.

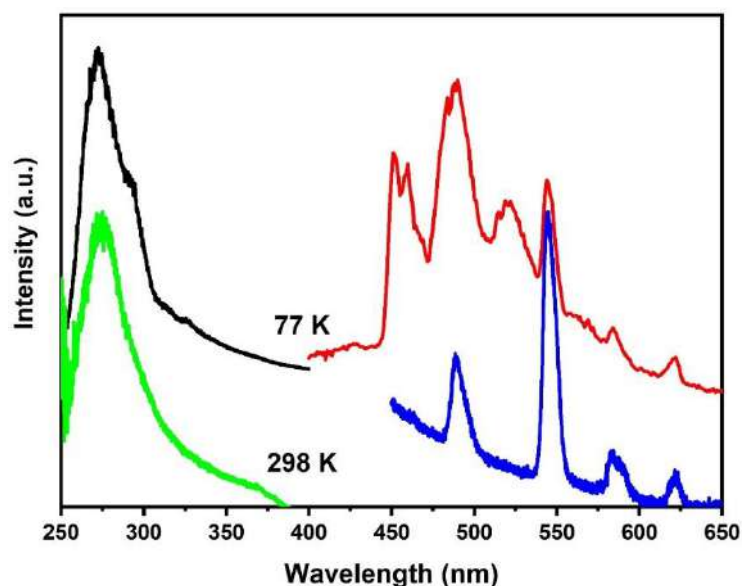


Figure 3.8. Luminescence excitation (green and black lines) and emission (blue and red lines) spectra of complex [Tb<sub>2</sub>(L<sup>8</sup>)<sub>3</sub>(phen)<sub>2</sub>] in solution in DMSO at 298 K and at 77 K.

### 3.2 Synthesis and characterization of quadruple-stranded NEt<sub>4</sub>[NaLn<sub>2</sub>(L<sup>8</sup>)<sub>4</sub>(H<sub>2</sub>O)] and Na[NaLn<sub>2</sub>(L<sup>8</sup>)<sub>4</sub>(H<sub>2</sub>O)]·2H<sub>2</sub>O. Structure and luminescence properties.

#### 3.2.1 Synthesis

In the present case, to synthesize the desired complexes the bis-chelating CAPH ligand was used in the form of sodium salt Na<sub>2</sub>L<sup>8</sup> that was prepared by deprotonation of H<sub>2</sub>L<sup>8</sup> using sodium methoxide in methanol according to the previously described procedures.<sup>122</sup> Quadruple-stranded complexes of

general formulae  $\text{NEt}_4[\text{NaLn}_2(\text{L}^8)_4(\text{H}_2\text{O})]$  and  $\text{Na}[\text{NaLn}_2(\text{L}^8)_4(\text{H}_2\text{O})]\cdot 2\text{H}_2\text{O}$  were synthesized according to the scheme presented in Figure 3.9.

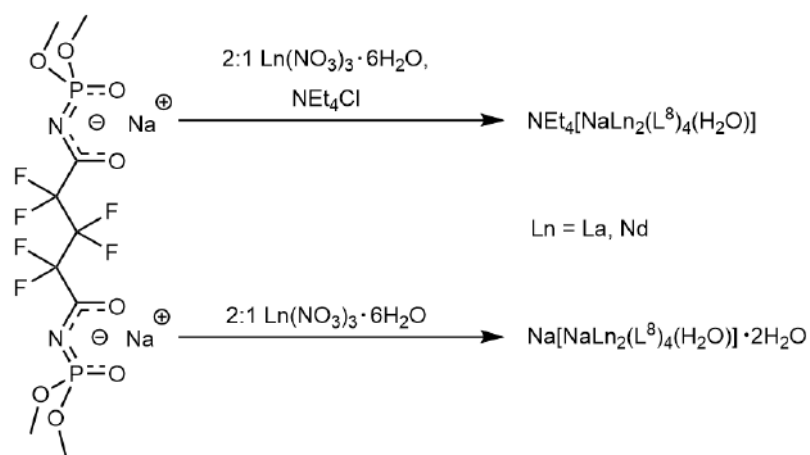


Figure 3.9. Synthetic path for the quadruple-stranded binuclear lanthanide complexes.

### 3.2.2 X-ray crystallography

The crystal data and structure refinement for complexes  $\text{NEt}_4[\text{NaNd}_2(\text{L}^8)_4(\text{H}_2\text{O})]$  (**16**),  $\text{Na}[\text{NaLa}_2(\text{L}^8)_4(\text{H}_2\text{O})]\cdot 2\text{H}_2\text{O}$  (**17**) and  $\text{Na}[\text{NaNd}_2(\text{L}^8)_4(\text{H}_2\text{O})]\cdot 2\text{H}_2\text{O}$  (**18**) are given in Annex A. The single crystals of the complexes were obtained from the solution in 2-propanol/acetone mixture. The crystal structure of compound **16** is shown in Figure 3.10.

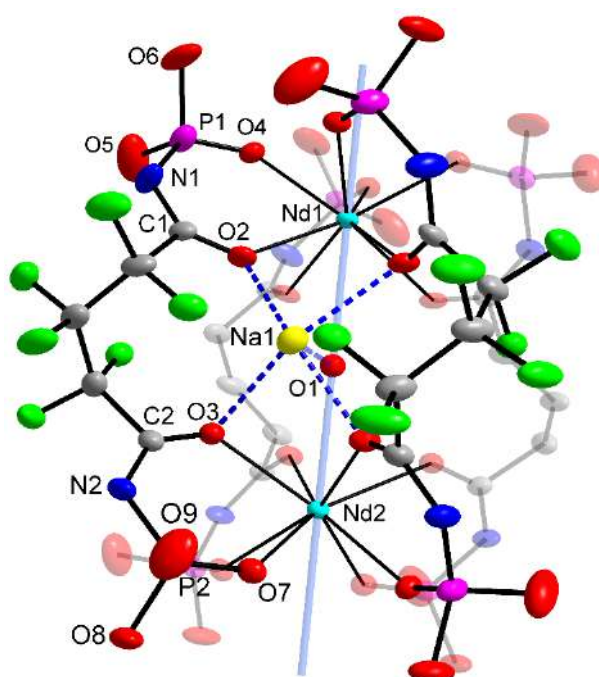


Figure 3.10. Structure of the complex anion  $[\text{NaNd}_2(\text{L}^8)_4(\text{H}_2\text{O})]^-$  in **16**, with the displacement ellipsoids drawn at the 30% probability level (methyl groups are omitted for clarity). The light blue line indicates axis of the complex, with O1 atom situated on a center of inversion. The Na1 ion is equally disordered over four inversion-related positions (only one of them is shown here).

The complex anion  $[\text{NaNd}_2(\text{L}^8)_4(\text{H}_2\text{O})]^-$  has a structure of quadruple-stranded helicate, which encapsulates sodium cation and a molecule of water into the negatively charged environment of the ligand fluorine and carbonyl oxygen atoms, which can also be treated as a cryptand-like cavity. The water molecule is located between two neodymium ions lying on helical axis, while the sodium ion is situated at the periphery of the cryptand-like cavity, where it is bound to the oxygen atom of the water molecule, carbonyl oxygen and fluorine atoms of the ligand. Four bis-carbacylamidophosphate ligands are coordinated to two crystallographically distinct  $\text{Nd}^{\text{III}}$  ions in bidentate-chelating manner via oxygen atoms of carbonyl and phosphoryl groups. Oxygen atoms of carbonyl groups act as bridges also binding the sodium ion. Such a structure allows to assume, that the sodium cation may act as a template participating in helicate self-assembly.

The  $\text{Nd}\cdots\text{Nd}$  distance in the complex under study equals  $5.703(9)$  Å that is the shortest reported  $\text{Ln}\cdots\text{Ln}$  distance for quadruple-stranded binuclear lanthanide complexes. The  $\text{Nd}-\text{O}(\text{C})$  bond lengths are of  $2.501(7)$  Å and  $2.516(6)$  Å for  $\text{Nd1}$  and  $\text{Nd2}$  respectively. The  $\text{Nd}-\text{O}(\text{P})$  bond lengths respectively equal  $2.429(6)$  Å and  $2.433(6)$  Å, thus being shorter than in the case of carbonyl oxygen atoms due to the higher affinity of phosphoryl oxygen to lanthanide ions. The  $\text{P}-\text{O}$  and  $\text{C}-\text{O}$  bond lengths of the ligand in  $\text{NEt}_4[\text{NaNd}_2(\text{L}^8)_4(\text{H}_2\text{O})]$  (**16**) have greater average values comparing to such of free ligand ( $d(\text{P}-\text{O})_{\text{ligand}} = 1.4598(12)$  Å and  $d(\text{C}-\text{O})_{\text{ligand}} = 1.202(2)$  Å)<sup>216</sup> and are equal  $1.461(7)$  Å and  $1.22(1)$  Å, respectively. The average values of  $\text{P}-\text{N}$  and  $\text{C}-\text{N}$  bond lengths of the ligand in the complex are reduced comparing to those in free ligand ( $d(\text{P}-\text{N})_{\text{ligand}} = 1.6751(14)$  Å and  $d(\text{C}-\text{N})_{\text{ligand}} = 1.361(2)$  Å) (Table 3.4).

According to the data obtained using SHAPE 2.1 software,<sup>247</sup> the coordination polyhedra of  $\text{Nd}$  (III) ions in **16** could be interpreted as distorted square antiprism (Figure 3.11).

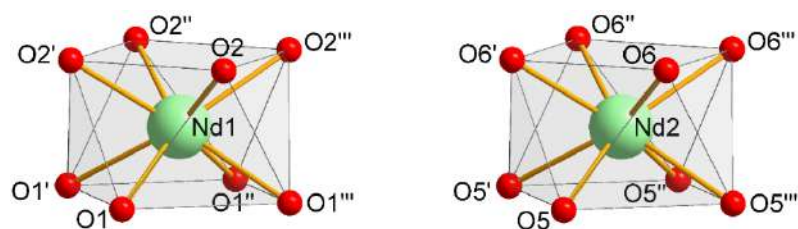


Figure 3.11. Polyhedra of  $\text{Nd1}$  and  $\text{Nd2}$  ions. Twisted square antiprisms (coordination number = 8).

There are four  $\text{NEt}_4[\text{NaNd}_2(\text{L}^8)_4(\text{H}_2\text{O})]$  units per unit cell, where both  $\text{Nd}^{\text{III}}$  ions are homochiral in each helicate.  $\text{NEt}_4^+$  and sodium cations are disordered over four positions.

The average value of  $\text{OPO}$  angle is  $108.98^\circ$ , consequently the phosphorus atoms surroundings in the complex anion have slightly distorted tetrahedral configuration. The values of essential angles and bond distances are given in Table 3.4.

Table 3.4. Principal bond lengths and angles in the crystal structures of the helicates.

Bond length, Å			
	<b>16</b>	<b>17</b>	<b>18</b>
Ln–O(C)	2.501(7)–2.516(6)	2.557(6)–2.561(12)	2.480(7)–2.487(15)
Ln–O(P)	2.429(6)–2.433(6)	2.435(6)–2.474(5)	2.392(8)–2.440(6)
O–C	1.220(12)–1.222(11)	1.22(2)–1.25(2)	1.28(2)–1.29(3)
P–O	1.444(7)–1.461(7)	1.460(6)–1.481(5)	1.459(10)–1.466(8)
P–N	1.646(10)–1.655(9)	1.613(9)–1.626(9)	1.612(13)–1.623(12)
C–N	1.301(13)–1.303(12)	1.334(19)–1.339(16)	1.28(2)–1.30(3)
Angle, °			
O–Ln–O	71.3(2)–71.8(2)	70.2(3)–70.66(17)	71.5(4)–72.0(2)
C–O–Ln	136.9(6)–137.0(6)	137.8(11)–140.0(7)	138.4(15)–138.5(9)
P–O–Ln	135.0(4)–135.7(4)	136.6(3)–137.0(4)	135.0(4)–137.0(6)
O–P–O	104.6(5)–113.4(5)	92.4(7)–124.3(6)	99.4(9)–120.6(7)
O–P–N	103.0(5)–119.9(4)	106.2(4)–120.0(4)	104.8(7)–119.3(5)
C–N–P	120.0(7)–122.3(7)	122.6(10)–124.7(10)	124.2(12)–125.0(12)
O–C–N	130.7(9)–132.3(9)	129.1(14)–129.5(15)	127(2)–128.9(15)
O–Ln–O	71.3(2)–71.8(2)	70.2(3)–70.66(17)	71.5(4)–72.0(2)

Unlike the discrete structure of **16**, the crystals of  $\text{Na}[\text{NaLa}_2(\text{L}^8)_4(\text{H}_2\text{O})]\cdot 2\text{H}_2\text{O}$  (**17**) and  $\text{Na}[\text{NaNd}_2(\text{L}^8)_4(\text{H}_2\text{O})]\cdot 2\text{H}_2\text{O}$  (**18**) consist of polymer chains formed by oxygen atoms of  $\text{OCH}_3$  and phosphoryl moieties and outer-sphere sodium cations (Figures 3.12, 3.13).

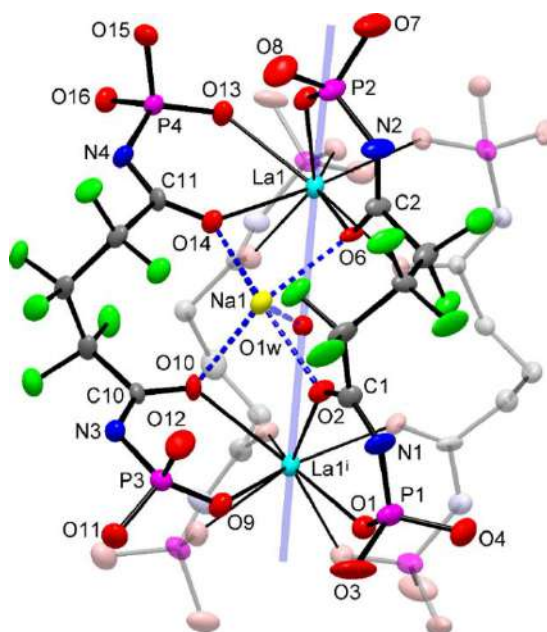


Figure 3.12. Structure of the complex anion  $[\text{NaLa}_2(\text{L}^8)_4(\text{H}_2\text{O})]^-$  in **17**, with the displacement ellipsoids drawn at the 30% probability level. Only one orientation of the disordered ligands is shown and  $\text{CH}_3$  groups are omitted for clarity. Blue line indicates axis of the complex, with O1W atom situated on a center of inversion. The Na1 ion is equally disordered over two inversion-related positions (only one of them is shown here).

The complexes under consideration are hydrates, since they also contain two molecules of water in their outer-spheres. Considered water molecules tend to bind the outer-sphere sodium. The other

significant attribute of the helicates **17** and **18** lies in the presence of opposite helicity species in the same unit cell in 1:1 ratio which is not likely to the crystals of **16** with one definite helicity. Both lanthanide ions in the helicate units are crystallographically equivalent.

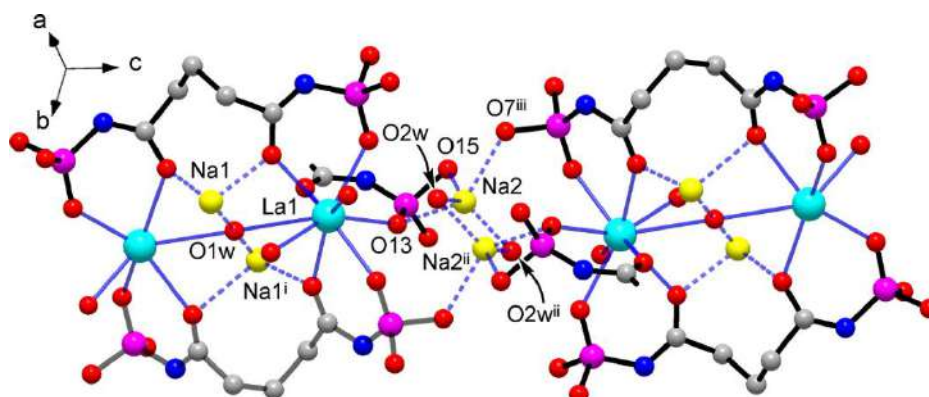


Figure 3.13. Connection of the anionic species  $[\text{NaLa}_2(\text{L}^8)_4(\text{H}_2\text{O})]^-$  and outer Na2 cations in the crystal structure of **17** resulting in 1D linear chains along c-axis direction in the crystal. Na2 is equally disordered across a center of inversion. Part of the organic ligands are omitted for clarity.

### 3.2.3 $^1\text{H}$ NMR spectroscopy

When considering the  $^1\text{H}$  NMR spectrum of  $\text{H}_2\text{L}^8$  there could be found two types of signals: one of them is associated with the protons of four methoxy-groups and appears in the spectrum as a doublet at 3.74 ppm, the other one is broadened signal at 11.38 ppm, which corresponds to NH protons. In the spectra of  $\text{Na}_2\text{L}^8$  and the complexes the signals of amide protons are absent. The signals of methoxy-groups' protons in the spectra of  $\text{Na}_2\text{L}^8$  and the diamagnetic complexes  $\text{NEt}_4[\text{NaLa}_2(\text{L}^8)_4(\text{H}_2\text{O})]$  (**15**) and  $\text{Na}[\text{NaLa}_2(\text{L}^8)_4(\text{H}_2\text{O})]\cdot 2\text{H}_2\text{O}$  (**17**) are shifted to high field compared to  $\text{H}_2\text{L}^8$  and come out as doublets at 3.44, 3.59 and 3.53 ppm respectively. The upfield shift is caused by redistribution of electron density in the ligand molecule as a consequence of deprotonation, coordination and  $\pi$ -conjugation in chelate cycle. In the spectra of  $\text{NEt}_4[\text{NaNd}_2(\text{L}^8)_4(\text{H}_2\text{O})]$  (**16**) and  $\text{Na}[\text{NaNd}_2(\text{L}^8)_4(\text{H}_2\text{O})]\cdot 2\text{H}_2\text{O}$  (**18**) the signal of methoxy-groups' protons is downfield shifted to 4.17 and 3.92 ppm due to paramagnetic nature of  $\text{Nd}^{\text{III}}$ . For the compounds **15** and **17** the integral intensities ratio of the tetraethylammonium protons' signals to the ligand protons' signals agrees with X-ray data and confirms the complexes established composition.

### 3.2.4 IR spectroscopy

The obtained complexes have very similar IR spectra (see Annex C). The spectrum of  $\text{H}_2\text{L}^8$  exhibits N–H stretching vibrations band at  $3095\text{ cm}^{-1}$ , while in the spectra of the complexes as well as  $\text{Na}_2\text{L}^8$  this band is absent. This fact indicates the coordination of the ligand to the lanthanide ions in deprotonated form. The other vibration bands sensitive towards deprotonation and coordination are

C=O, P=O stretching vibrations and Amide-2 band. Comparing the spectra of the complexes to the spectrum for the neutral ligand, it could be easily noticed that C=O, P=O and Amide-2 bands are bathochromically shifted compared to such in H<sub>2</sub>L<sup>8</sup> by 122–125 cm<sup>-1</sup>, 68–72 cm<sup>-1</sup> and 51–53 cm<sup>-1</sup> respectively. The shift of these stretching bands is caused by bond order decreasing as a result of ligand deprotonation and coordination that is in agreement with X-Ray data for the complex and neutral ligand.<sup>216</sup>

The IR spectrum of the complex **16** in region 60–600 cm<sup>-1</sup> is shown in Annex C. The bands of Ln–O stretching modes, OLnO bending modes and chelate ring “breathing” can be observed in this region. The chelate rings are characterized by three types of vibrations: chelate ring breathing, in-plane bending and out-of-plane bending. These modes are observed in 625–840, 420–540 and 180–395 cm<sup>-1</sup> regions.<sup>248,249</sup> Some of these bands are split due to coupling with  $\nu(\text{Ln-O})$  and  $\delta(\text{OLnO})$  vibrations. The  $\nu(\text{Ln-O})$  stretching vibrations are strongly coupled with chelate ring deformations<sup>250</sup>. Therefore, the bands sensitive to changes in the metal could be observed, even above 400 cm<sup>-1</sup>. Theoretical calculations for mononuclear neodymium CAPH based complexes showed that the  $\nu(\text{Ln-O})$  stretching motions couple with the chelate ring vibrations with their contribution 10–30 %.<sup>249</sup> These bands are observed in the broad frequency region 630–320 cm<sup>-1</sup>. The bending vibrations OLnO are observed as the broad and middle intensity bands in the IR spectrum in region 50–280 cm.

Based on previously reported data for CAPH based lanthanide complexes<sup>248,249</sup> the vibrations in the IR spectrum of of complex **16** at 336, 352, 375, 387, 410, 463, 497 and 552 cm<sup>-1</sup> were assigned to Ln–O stretching modes coupled with chelate ring “breathing”. The bands at 270 and 170 cm<sup>-1</sup> and their shoulders in were assigned to OLnO bending modes coupled with chelate ring “breathing”.

### **3.2.5 Photoluminescent properties of $\text{NEt}_4[\text{NaNd}_2(\text{L}^8)_4(\text{H}_2\text{O})]$**

Complex  $\text{NEt}_4[\text{NaNd}_2(\text{L}^8)_4(\text{H}_2\text{O})]$  exhibits the IR-emission at 300 and 77 K upon excitation by 266 nm harmonic line of the Nd:YAG pulsed laser. The emission spectra are shown in Figure 3.14. The narrow bands at around 900 and 1060 nm were assigned to  ${}^4\text{F}_{3/2} \rightarrow {}^4\text{I}_{9/2}$  and  ${}^4\text{F}_{3/2} \rightarrow {}^4\text{I}_{11/2}$  transitions of Nd<sup>III</sup> ion. When temperature decreases from 300 to 77 K, the radiative relaxation channel of the  ${}^4\text{F}_{3/2}$  level changes. This is evidenced by the change in the relative intensities of the transitions, in 300 K  $I({}^4\text{F}_{3/2} \rightarrow {}^4\text{I}_{9/2}) < I({}^4\text{F}_{3/2} \rightarrow {}^4\text{I}_{11/2})$ , and in 77 K  $I({}^4\text{F}_{3/2} \rightarrow {}^4\text{I}_{9/2}) > I({}^4\text{F}_{3/2} \rightarrow {}^4\text{I}_{11/2})$ . The integral intensity ratio of  ${}^4\text{F}_{3/2} \rightarrow {}^4\text{I}_{9/2} / {}^4\text{F}_{3/2} \rightarrow {}^4\text{I}_{11/2}$  equals 0.97 at 300 K and 1.3 at 77 K.

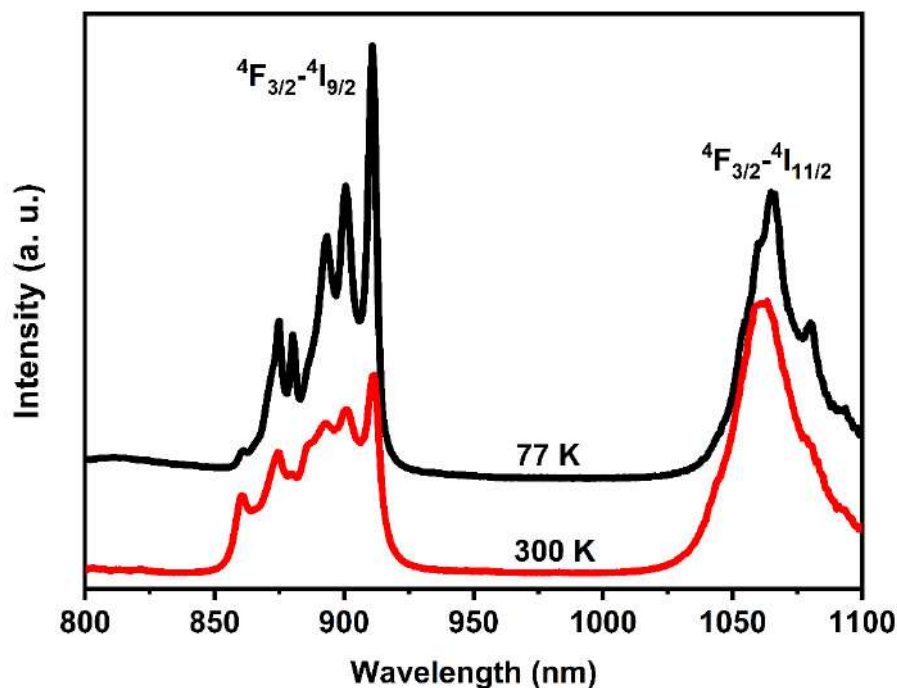


Figure 3.14. The emission spectra of  $\text{NEt}_4[\text{NaNd}_2(\text{L}^8)_4(\text{H}_2\text{O})]$  complex at 300 and 77 K,  $\lambda_{\text{exc}}=266$  nm.

In the case of inorganic Nd compounds, due to the relatively large energy gap between the  $^4\text{F}_{3/2}$  and  $^4\text{I}_{15/2}$  levels (about  $5500\text{ cm}^{-1}$ ), the participation of multi-phonon relaxation in the depopulation of the  $^4\text{F}_{3/2}$  level is relatively small and the lifetime of the  $^4\text{F}_{3/2}$  level can reach about  $150\ \mu\text{s}$ .<sup>251</sup> The situation is different regarding the Nd coordination compounds. Organic ligands have high-energy vibrations and are effective in quenching the Nd emission by the so-called multi-phonon quenching process. This is an extremely effective mechanism for the non-radiative conversion of the energy of  $\text{Ln}^{\text{III}}$  electronic states into molecular groups resonant vibrational states. The emission is quenched as a result of coupling with, for example, high-energy vibrations of  $\nu(\text{OH})$  of water or  $\nu(\text{CH})$  of aliphatic groups. To reduce this quenching process, the CH groups in the ligand have been partially replaced with CF groups, which are characterized by a much lower vibration energy. The lifetime of the  $^4\text{F}_{3/2}$  emission level spans from 0.1 to about  $5\ \mu\text{s}$  for Nd compounds with organic ligands.<sup>227,252,253</sup> A slight extension of this value is observed in fluorinated coordination compounds ( $\sim 25\ \mu\text{s}$ ).<sup>227</sup> However, in the case of the  $\text{NEt}_4[\text{NaNd}_2(\text{L}^8)_4(\text{H}_2\text{O})]$  complex with the fluorinated ligand, the  $^4\text{F}_{3/2}$  emission lifetime is very short ( $2\ \mu\text{s}$ ) and is non-exponential, as shown in Figure 3.15.

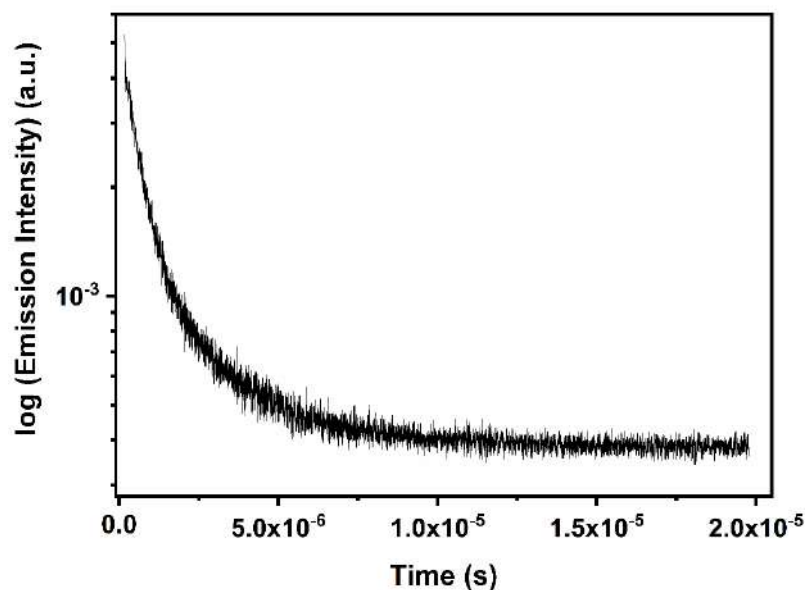


Figure 3.15. Decay luminescence curve for  $\text{NEt}_4[\text{NaNd}_2(\text{L}^8)_4(\text{H}_2\text{O})]$  at 300 K.

The average lifetime ( $\tau$ ) was calculated using Equation 3.2.<sup>254</sup>

$$\tau = \frac{\int_0^{\infty} tI(t)dt}{\int_0^{\infty} I(t)dt} \quad (3.2)$$

where  $t$  stands for the measurement time, while  $I(t)$  is the decay function. The non-exponential character of the lifetime is due to the ion-ion energy transfer. As shown in the crystallographic part, the distance  $\text{Nd}\cdots\text{Nd}$  equals 5.703(9) Å. At such close distances between the Nd ions, the  ${}^4\text{F}_{3/2}$  emission quenching occurs through the cross-relaxation process.<sup>255</sup> The cross-relaxation process is possible if there is a neighboring neodymium ion in the ground state in the vicinity of the excited  $\text{Nd}^{\text{III}}$  ion. The excited  $\text{Nd}^{\text{III}}$  ion undergoes the  ${}^4\text{F}_{3/2} \rightarrow {}^4\text{I}_{15/2}$  transition and the adjacent ion undergoes the  ${}^4\text{I}_{9/2} \rightarrow {}^4\text{I}_{15/2}$  transition, thus both ions occupy the  ${}^4\text{I}_{15/2}$  levels. Narrow energy gaps between levels below the  ${}^4\text{I}_{15/2}$  state favor multiphonon relaxation, and the ions revert to the ground state along the non-radiative pathway. The cross-relaxation process is possible due to the coincidence of energy differences between  ${}^4\text{F}_{3/2} - {}^4\text{I}_{15/2}$  and  ${}^4\text{I}_{9/2} - {}^4\text{I}_{15/2}$ .

Due to the above-mentioned emission quenching process, such dimer systems may not be of interest in terms of photophysical properties. On the other hand, we have shown that the Nd-Nd distance allows the non-radiative interionic energy transfer. Thus, the investigated ligand can be used, e.g., to design heteronuclear complexes for luminescence thermometry, showing interionic temperature-dependent energy transfer.

### 3.2.6 Mass spectrometry

The helicate **16** was also characterized by laser desorption/ionization mass spectrometry. The mass spectrum of **16**, recorded in the negative ionization mode, displays a cluster of peaks possessing the correct isotopic distribution, which corresponds to doubly charged anion  $[\text{Nd}_2(\text{L}^8)_4]^{2-}$  species (see Annex H). In contrary to the crystal structure data, the single charged anion associate  $[\text{Nd}_2(\text{L}^8)_4+\text{Na}+\text{H}_2\text{O}]^-$  is not observed. The mass spectra of the rest of compounds exhibit similar patterns.

### 3.3 Partial conclusions

The triple- and quadruple-stranded binuclear  $\text{Ln}^{\text{III}}$  complexes with tetramethyl *N,N'*-(2,2,3,3,4,4-hexafluoro-1,5-dioxopentane-1,5-diyl)bis(phosphoramidate) were synthesized and characterized for the first time.

In  $[\text{Ln}_2(\text{L}^8)_3(\text{phen})_2]$  series, UV light excitation induced bright characteristic emission of the lanthanide ions due to effective energy transfer from the organic ligands to the  $\text{Ln}^{\text{III}}$  ions. The europium and terbium complexes were found to be luminescent both in solid and solution in DMSO with emission decay time in range of 1.2–2.0 ms depending on temperature. The energy level of the ligands' lowest triplet state in the complexes was found to match better to resonance level of  $\text{Eu}^{\text{III}}$  than to  $\text{Tb}^{\text{III}}$  ion. In solid state at room temperature the  $\text{Eu}^{\text{III}}$  complex displays a very high intrinsic quantum yield of 91% and decay time of 1.88 ms.

In the complexes with four coordinated  $\text{L}^8$  units it was found that the complex anions in the obtained compounds have a structure of quadruple-stranded helicate, which encapsulates sodium cation and a molecule of water into a cryptand-like cavity. Complex  $\text{NEt}_4[\text{NaNd}_2(\text{L}^8)_4(\text{H}_2\text{O})]$  was found to be luminescent in IR spectral region with the  ${}^4\text{F}_{3/2}$  emission lifetime equal 2  $\mu\text{s}$ . The bis-carbacylamidophosphate ligand belongs to the new family of bis-chelating ligands and can be used to obtain Ln complexes as model systems for the study of interionic energy transfer as well as to design heteronuclear complexes for luminescence thermometry exploiting the interionic temperature-dependent energy transfer.

### 3.4 Partial perspectives

- To perform a detailed study on temperature dependance of the luminescence in the obtained complexes. In particular, in  $\text{NEt}_4[\text{NaNd}_2(\text{L}^8)_4(\text{H}_2\text{O})]$ .
- To design and to develop heterobinuclear  $\text{Ln}^{\text{III}}\text{-Fe}^{\text{II}}$  systems displaying the synergy between the lanthanide luminescence and spin crossover.

- To design heteronuclear lanthanide(III) helicates displaying with temperature-dependent interionic energy transfer and to test them for application in the luminescence thermometry.

### 3.5 Notes

Preparation of this chapter involved the use of materials from the publications provided below (all the publications are presented in Annex I). The materials from the first reference were reproduced with permission from Springer Nature (License 5591411446149).

1. Horniichuk, O. Y.; Kariaka, N. S.; Smola, S. S.; Rusakova, N. V.; Trush, V. O.; Sliva, T. Y.; Amirkhanov, V. M. Efficient Sensitized Luminescence of Binuclear Ln(III) Complexes Based on a Chelating Bis-Carbacylamidophosphate. *J. Fluoresc.* **2021**, *31* (4), 1029–1039. <https://doi.org/10.1007/s10895-021-02733-0>.
2. Horniichuk, O. Y.; Trush, V. A.; Kariaka, N. S.; Shishkina, S. V.; Dyakonenko, V. V.; Severinovskaya, O. V.; Gawryszewska, P.; Domasevitch, K. V.; Watras, A.; Amirkhanov, V. M. Novel Quadruple-Stranded Heterometallic Ln<sub>2</sub>Na Complexes Hosting Sodium Ions inside the Cryptand-like Cavity. *New J. Chem.* **2021**, *45* (47), 22361–22368. <https://doi.org/10.1039/D1NJ04353F>.

# Chapter 4. Thin films of bis[hydrotris(1,2,3-triazol-1-yl)borate]iron(II). Application in thermometry.

This chapter is dedicated to deposition and characterization of nanometric thin films of an iron(II)-scorpionate complex. Investigation of the SCO behavior in the obtained nanomaterials is discussed, as well as testing the thin films for application in surface thermometry based on thermorefectance. Alike to chapters 2 and 3, the current chapter consists of two parts, *i.e.*, two sub-chapters. The first one deals with elaboration and characterization of the SCO thin films, while the second sub-chapter is devoted to employment of the thin films for thermorefectance-based surface microthermometry technique on Joule-heated microwires photolithography-patterned on top of glass and silicon chips. Considering the high thermal stability of bis[hydrotris(1,2,3-triazol-1-yl)borate]iron(II) (**1**) together with reproducible gradual spin crossover in the above-room-temperature range (see chapter 2), sublimation of the compound to form SCO thin films exhibiting a gradual SCO is of particular interest to elaborate a continuous surface thermometer based on thermorefectance. Thus, the compound was selected as an appropriate candidate for vacuum deposition to give SCO thin films. Characterization techniques such as grazing incidence X-ray diffraction (GIXRD) and atomic force microscopy (AFM) were used to study the crystallinity, homogeneity, surface morphology and thickness of the films. The SCO in the materials was investigated by means of variable-temperature UV-Vis spectroscopy for thin films deposited on substrates transparent in the respective spectral regions. As the films conserved the gradual nature of the SCO observed in the bulk compound, demonstrated subsequent stability towards long-term storage in ambient conditions and towards numerous thermal cycling, it was interesting to test them for application in thermorefectance-based surface microthermometry. For this purpose, a thin film of bis[hydrotris(1,2,3-triazol-1-yl)borate]iron(II) was deposited on top of a gold electric circuit featured with a set of gold microwires settled on top of glass/oxidized silicon substrate. The changes in thermorefectance of Joule-heated microwires and substrate surface around them were followed by means of microscopy in UV and visible ranges. The resulting data allowed precise temperature mapping of the microwire surface.

## 4.1 Fabrication and characterization of [Fe(HB(1,2,3-tz)<sub>3</sub>)<sub>2</sub>] films

Thin films of **1** were deposited by vacuum thermal evaporation with thicknesses in the 20–200 nm range on silicon (100) and fused silica substrates (see experimental part, p. 153). The thickness of the films was monitored *in situ* by means of quartz crystal microbalance, while *ex situ* thickness verification was performed *via* spectral reflectance measurements and AFM. The spectral reflectance measurements were conducted first on a reflectance standard of SiO<sub>2</sub> film on Si, and then on the SCO

films deposited on the silicon substrates. To measure the thickness by means of AFM, a scratch reaching the substrate was inflicted on an investigated film beforehand. Afterwards AFM measurement was acquired in the region of the scratch. By measuring the height of several scratch profiles, it was possible to obtain the sought thickness value (Figure 4.1).

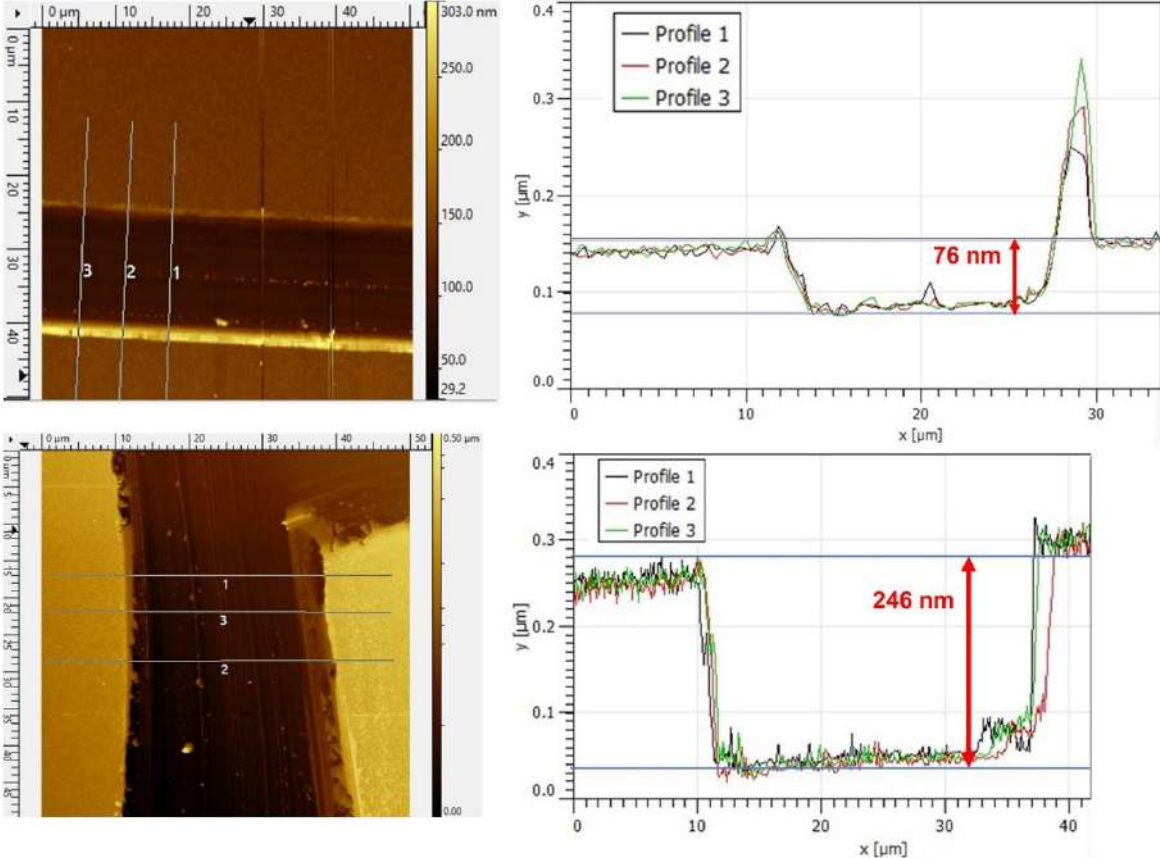


Figure 4.1. AFM thickness verification. AFM images of scratches on 76-nm- (top left) and 246-nm-thick (bottom left) films of **1** deposited on silicon (100) substrates with the numbered profile lines. The extracted scratch profiles (top and bottom right) of the respective thin films with the measured profile height, *i.e.*, film thickness.

The thickness values of the films measured by both spectral reflectance and AFM are summarized in Table 4.1.

Table 4.1. Thin film thickness verification by spectral reflectance and AFM (“-” – not measured). The spectral reflectance measurements offer thickness values exclusively for the films deposited on silicon. This distinction arises from the infeasibility of measuring films on fused silica due to low reflectance of the substrate.

Substrates	Thickness (spectral reflectance), nm	Thickness (AFM), nm
Si (100) / Fused silica	23	-
Si (100) / Fused silica	76	76 / 79
Si (100) / Fused silica	113	113 / 124
Si (100) / Fused silica	175	-
Si (100) / Fused silica	236	246 / -

Representative AFM surface topography data of films of **1** with different thicknesses, deposited on silicon and fused silica substrates, are shown in Figure 4.2. The nanocrystalline surface morphology of the films is obvious with RMS roughness values typically between 7 and 11 nm. The particle morphology does not substantially depend on the film thickness or the nature of the substrate (Figure 4.2), but one can notice a denser packing in the thicker films.

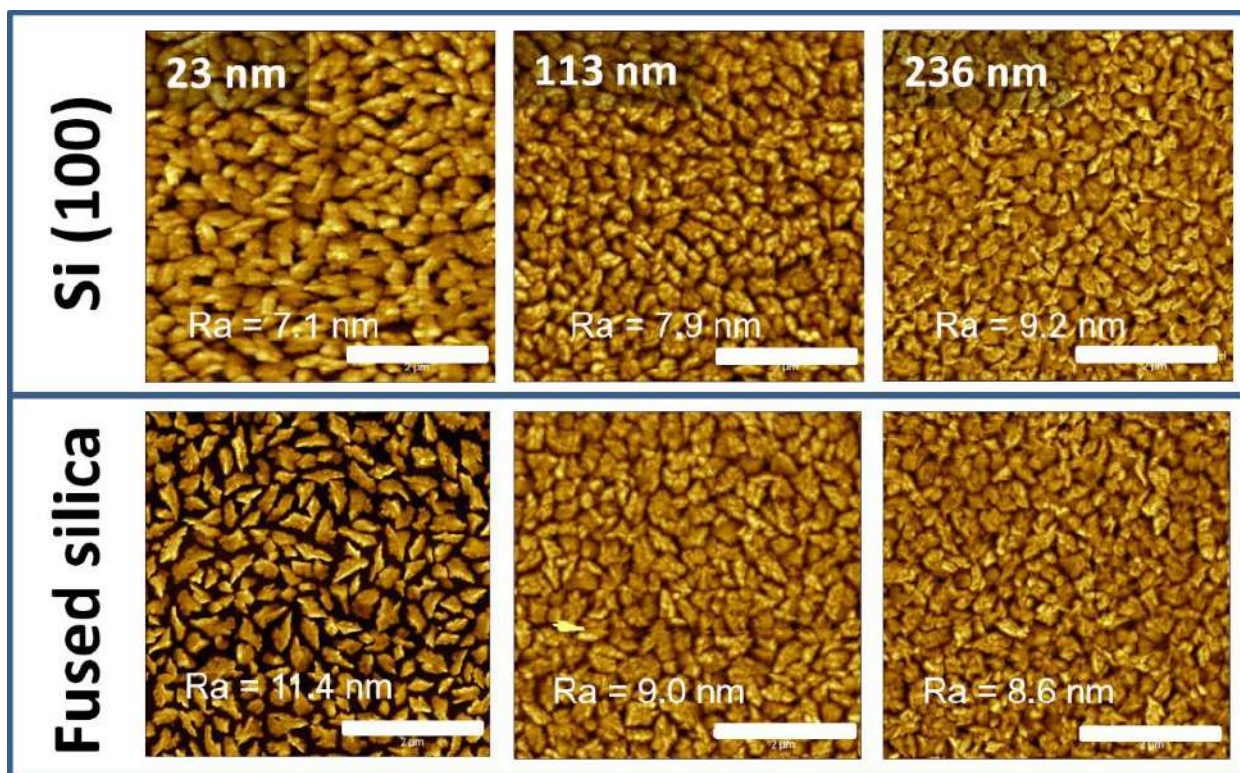


Figure 4.2. AFM topography images of 23, 113 and 236-nm-thick films of **1** deposited on silicon (top panel) and fused silica (bottom panel) substrates. The scan size is  $5 \times 5 \mu\text{m}^2$ . The scale bars are  $2 \mu\text{m}$ .

The X-ray diffraction patterns of the films reveal an intense peak at  $2\theta = 12.15^\circ$  (Figure 4.3a) that points to crystallinity and preferential crystallographic orientation of the as-deposited films. Figure 4.3a also shows the diffraction pattern of the microcrystalline bulk powder, which displays a similar peak at  $2\theta = 12.09^\circ$ . In the simulated PXRD pattern of **1** this peak corresponds to the 011 reflection. Thus, it can be suggested that crystallites in the films grow preferentially with the [011] direction of the monoclinic unit cell normal to the substrate surface (Figure 4.4). This observation was systematically confirmed, irrespective of the substrate material (silicon or fused silica) and the film thickness. The diffractograms did not undergo significant changes upon long-term storage (months) of the films in ambient conditions. It is interesting to note here that the complex  $[\text{Fe}(\text{HB}(1,2,4\text{-triazol-1-yl})_3)_2]$ , which is the structural isomer of **1**, forms an amorphous film upon vacuum thermal deposition and only a subsequent solvent vapor annealing affords for the formation of a textured, crystalline film.<sup>49</sup> The 011

diffraction peak intensity of the as-deposited films of **1** correlates with the thickness, indicating a similar degree of crystallinity and texture for each film in the investigated thickness range (Figure 4.3b).

From the width of the 011 diffraction peak, the average size of the coherent crystalline domains can be calculated using the Scherrer equation.<sup>256</sup> As for the absolute values, care must be taken because the peak widths were corrected for instrument broadening, but not for other possible effects, such as micro-strain. Nevertheless, the tendency shown in Figure 4.3c clearly evidences that the size of the crystalline domains grows steadily with the film thickness.

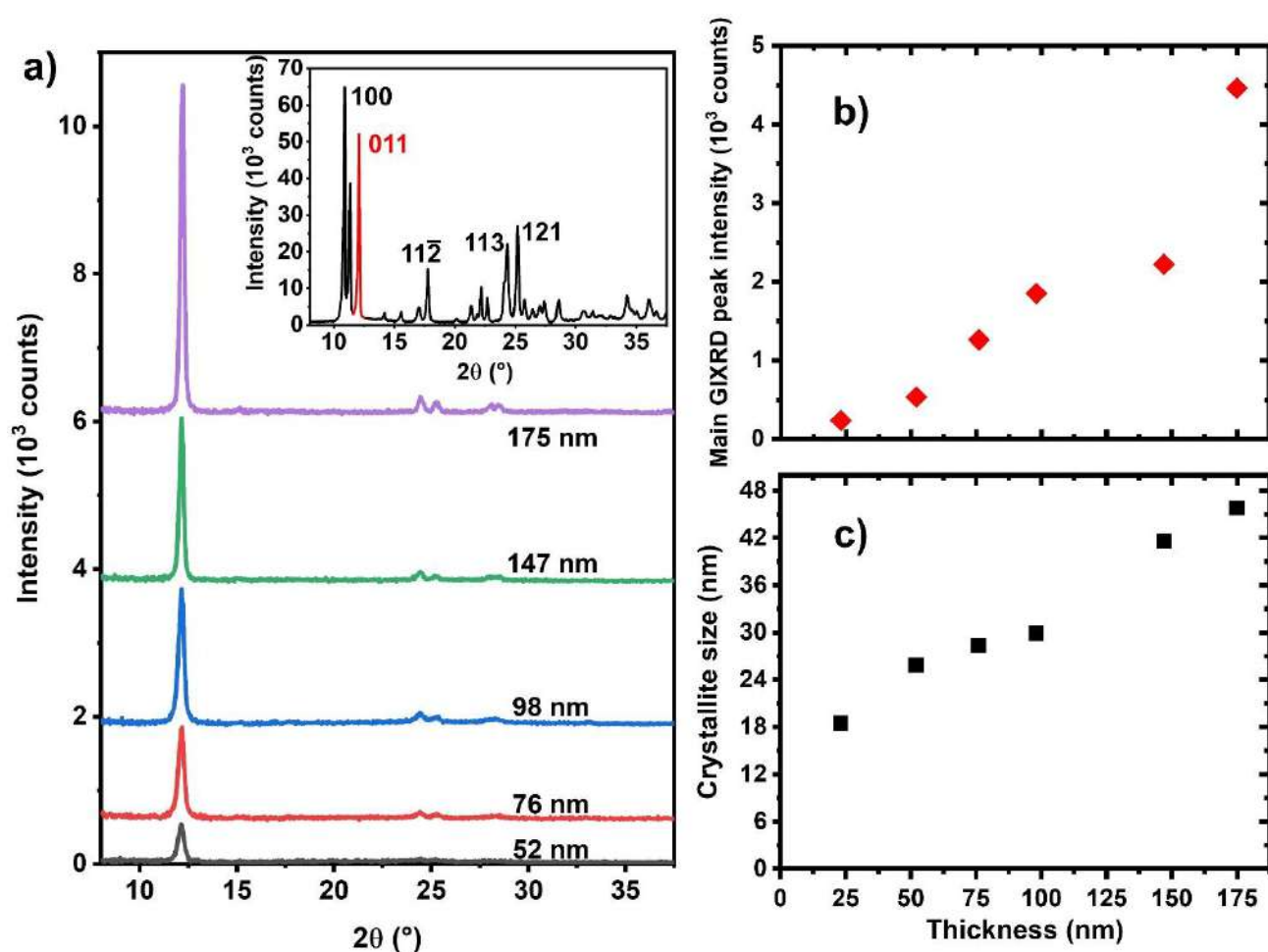


Figure 4.3. Crystallinity of the films. a) XRD patterns of nanocrystalline thin films of **1** with various thicknesses, deposited on Si substrates. The inset shows the XRD pattern of the microcrystalline powder of **1**. b) Intensity of the 011 reflection as a function of the film thickness. c) Average size of the crystalline domains (calculated for the 011 reflection using the Scherrer method) as a function of the film thickness.

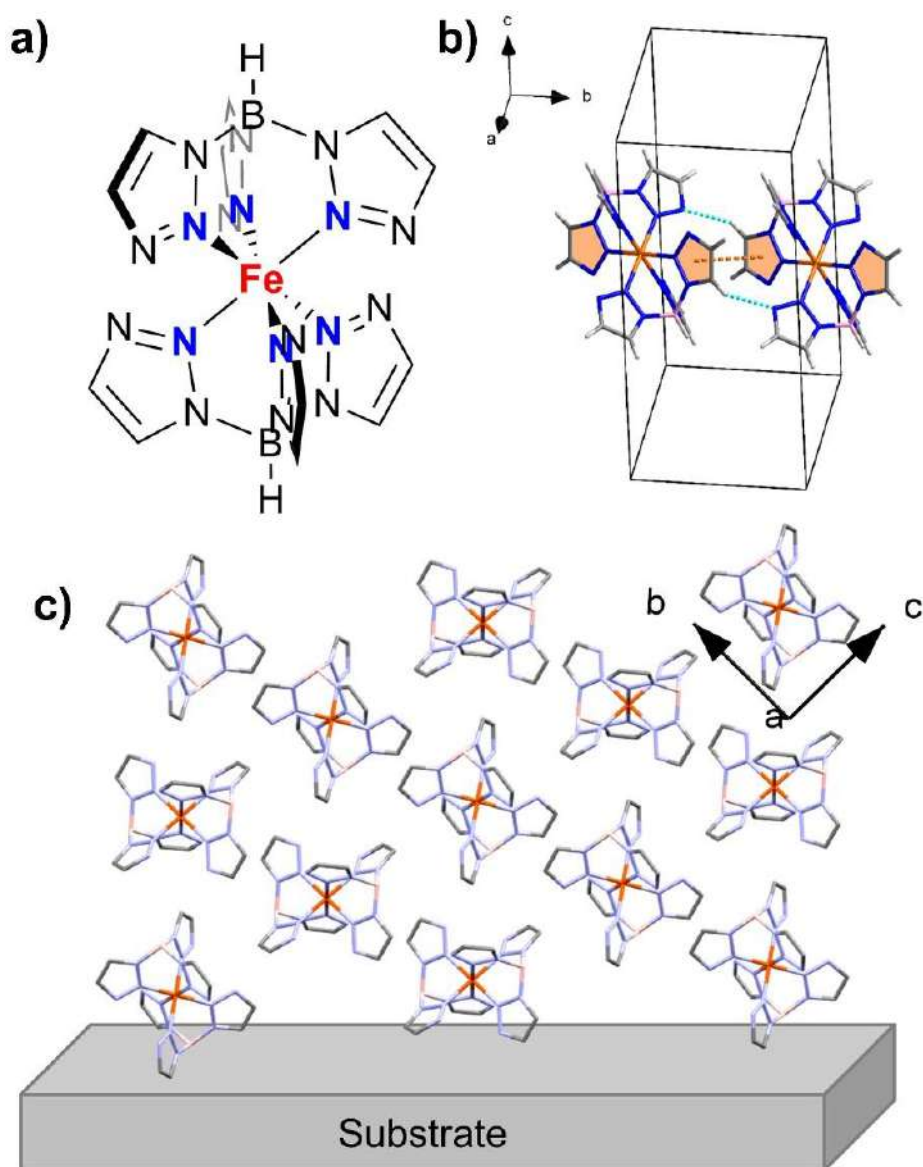


Figure 4.4. Molecular structure (a), fragment of the crystal structure (b) displaying intermolecular interactions for  $[\text{Fe}(\text{HB}(1,2,3\text{-triazol-1-yl})_3)_2]$  and schematic representation (c) of the complex molecules arrangement in the oriented thin films.

In order to investigate the SCO properties in the thin films of **1**, variable-temperature UV-vis spectrophotometry measurements were conducted over three to eight heating-cooling cycles between 253 and 453 K at  $2 \text{ K min}^{-1}$  rate. The measurements were performed for the films deposited on transparent fused silica substrates with thicknesses ranging from 79 to 175 nm. The room-temperature absorbance spectra of the films display three absorption bands with maxima at 208, 275 and 336 nm (Figure 4.5a). The absorbance level of these bands decreases upon heating, while a fourth band appears at 230 nm and exhibits higher absorbance at high temperatures (Figure 4.5a). As a result, the variable temperature spectra are characterized by two isosbestic points at *ca.* 220 and 260 nm. Taking into

account the high absorption coefficients associated with these peaks, they can be safely assigned to charge transfer (metal-to-ligand and/or ligand-to-metal) transitions.

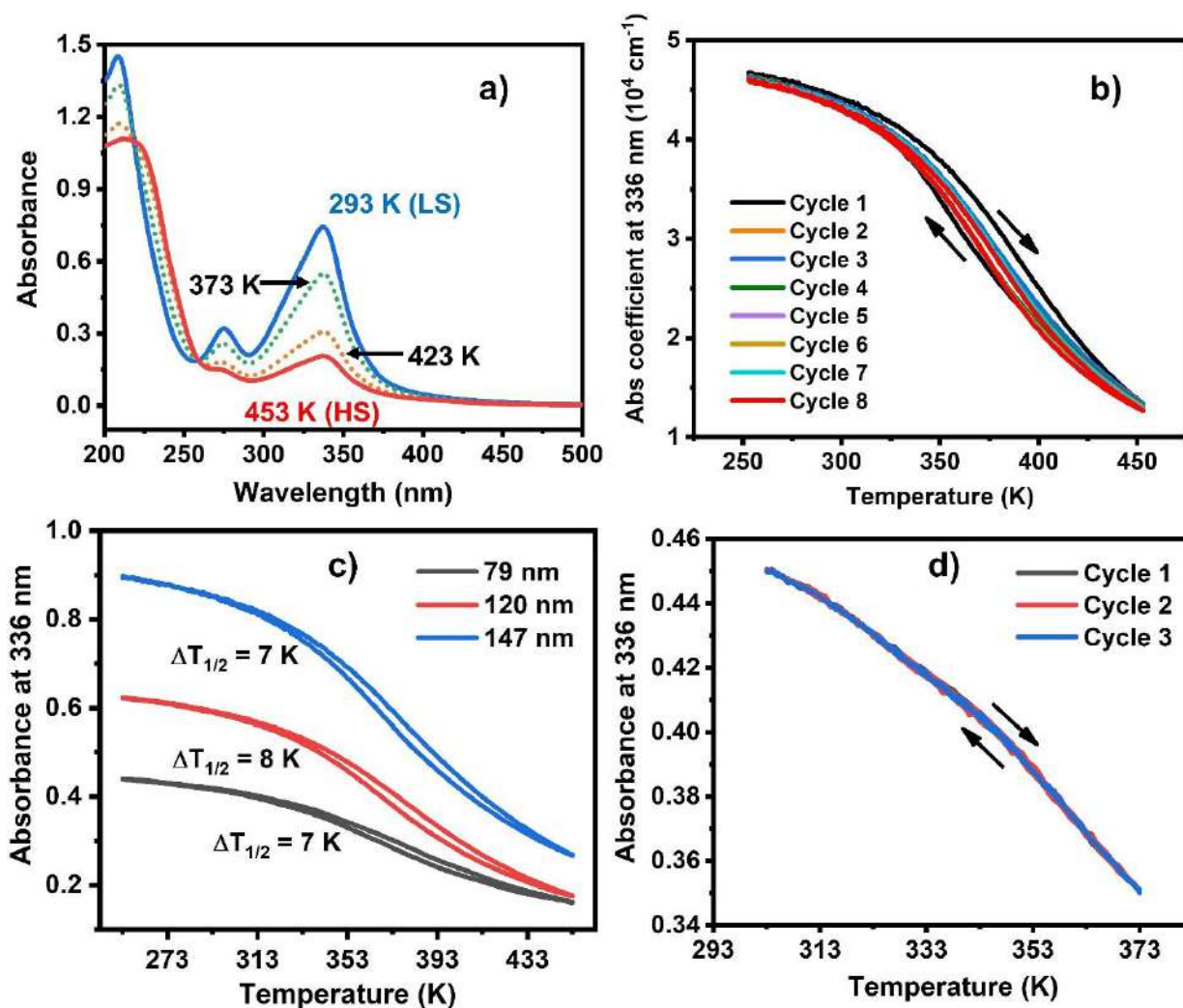


Figure 4.5. SCO properties of the films. a) Optical absorbance spectra of a 175-nm-thick film of **1** on fused silica substrate, acquired at selected temperatures. b) Temperature dependence of the absorbance at 336 nm of the same 175-nm film upon eight heating-cooling cycles between 253 and 453 K. c) Thermal variation of the absorbance at 336 nm for a 79, 120 and 147-nm-thick film of **1** upon heating-cooling cycles between 253 and 453 K. d) Thermal variation of the optical absorbance at 336 nm for a 79-nm-thick film of **1** upon three heating-cooling cycles from 303 to 373 K.

Thermal evolution of the highest intensity absorption band at 336 nm was used to follow the occurrence of a spin-state change in the films. Typical transition curves, displayed in Figure 4.5b, reveal a very gradual spin conversion between the LS and HS states, similar to the one observed in the bulk powder. The transition temperature is centered around  $374 \pm 2$  K, independently of the film thickness (Figure 4.5c). The transition is virtually complete at 273 K (pure LS state), whereas a residual LS fraction of *ca.* 5–10 % is still observed at 453 K. (*N.B.* Heating above *ca.* 453 K leads to the degradation of the films.) A notable, unusual characteristic of the SCO in the films of **1** is the occurrence of a thermal

hysteresis, which is not expected for such a gradual spin conversion. At the first heating-cooling cycle this thermal hysteresis loop is usually broad reaching up to 35 K in width, while on further cycling it narrows down to *ca.* 7 K. Importantly, it was found, however, that reducing the thermal cycling span leads to a narrowing of the hysteresis loop. Indeed, reducing the end temperature from 453 K to 393 K results in a 4-K-wide hysteresis loop, whereas the thermal hysteresis can be completely removed by limiting the heating of the sample to 373 K, leading to perfectly reversible and reproducible spin-transition curves (Figure 4.5d and Figure 4.6).

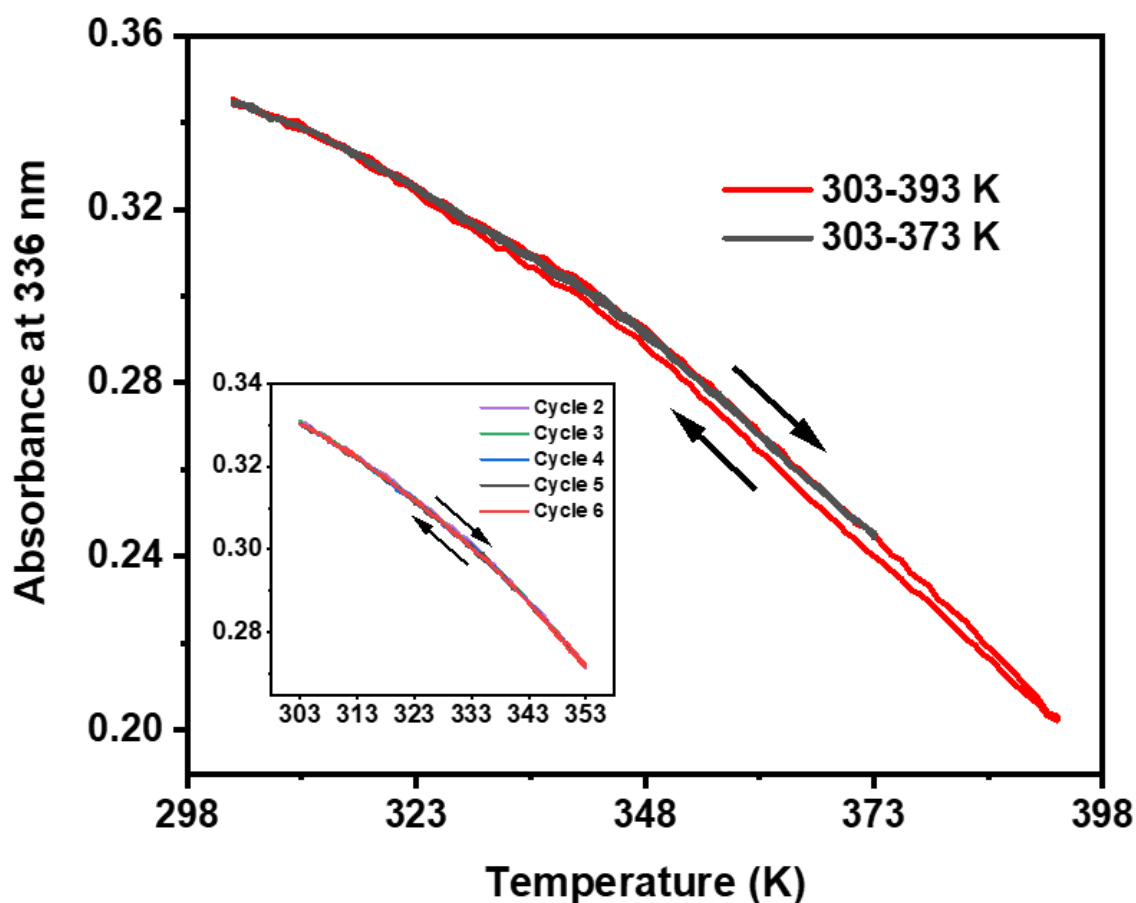


Figure 4.6. Thermal variation of the optical absorbance at 336 nm from 303 to 393 K (red curves) and from 303 to 373 K (grey curves) for a 79-nm-thick film of **1** deposited on a fused silica substrate. The inset shows the thermal variation of the optical absorbance at 336 nm for the film upon five heating-cooling cycles in 303–353 K temperature range. While a narrow thermal hysteresis ( $\approx$  4 K wide) is observed for the heating-cooling cycles between 303 and 393 K, no thermal hysteresis is observed when cycling in the 303–373 K range.

To summarize the somewhat unusual SCO properties of the vacuum-deposited films of **1**, it can be stated that they display a very gradual spin conversion between *ca.* 273 and 473 K, similar to that of the bulk powder. Up to *ca.* 373 K (i.e., the half-transition), the SCO is perfectly reversible, without any thermal hysteresis, thus providing scope for real-time thermometry applications. However, when heating above this temperature, a more and more broad thermal hysteresis loop opens. This hysteresis obviously

does not refer to the usually encountered cooperative phenomena in SCO materials. Instead, it is likely an indication of small, irreversible changes in the material when cycling at high temperature. Due to this phenomenon, accurate thermal sensing is not possible in the full 373–453 K range, but still it is possible to acquire thermal images. Finally, above *ca.* 453 K, the films start to degrade, presumably due to the sublimation of the molecules. At present, there is no unequivocal explanation for the opening of the thermal hysteresis loop above 373 K. Preliminary AFM and GIXRD data acquired on samples cycled at high temperatures reveal the existence of structural changes in the films as well as a visible modification of their surface morphology (Figure 4.7), but further work will be necessary to reach a clear-cut conclusion.

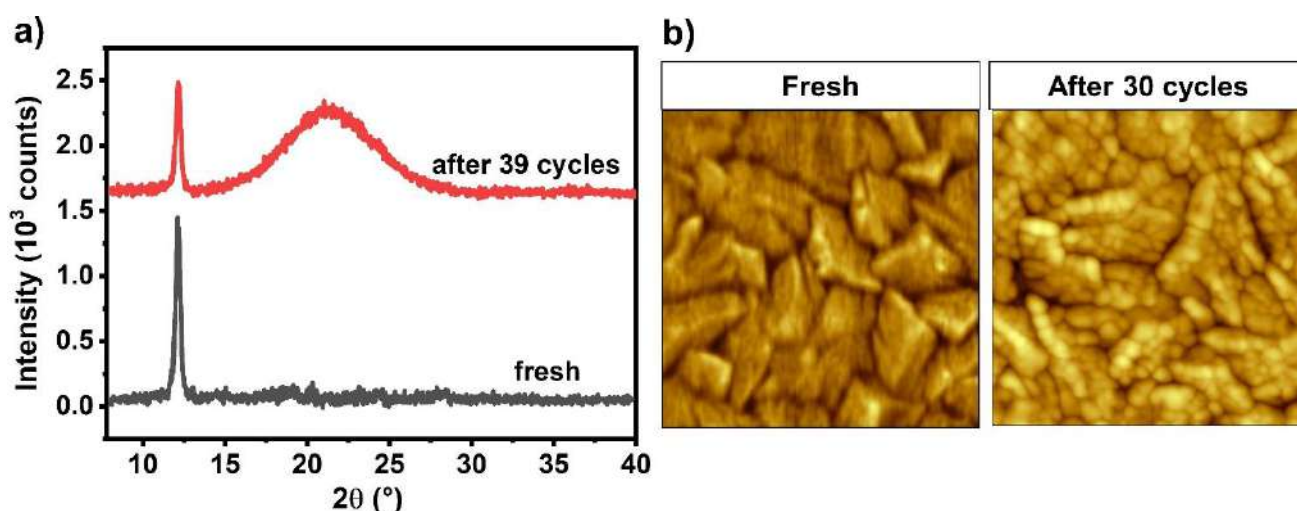


Figure 4.7. a) GIXRD patterns for a 79-nm-thick film of **1** deposited on fused silica substrate for both the freshly deposited film (in grey) and the film after 39 heating-cooling cycles (in red) in the 253–453 K temperature range. b) AFM topography images of the same 79-nm-thick film, (left) freshly deposited and (right) after 30 thermal cycles in the 253–453 K temperature range. The scan size is  $2 \times 2 \mu\text{m}^2$ . These data show that the thermal cycling at high temperature is accompanied by a visible change of the surface topography and by structural changes in the film that result in the exposure of the underlying substrate as revealed by the appearance of a wide bump around  $2\theta \approx 20^\circ$  (possibly due to structural reorganization and/or thickness reduction following sublimation).

#### 4.2 Microthermometry application of $[\text{Fe}(\text{HB}(1,2,3\text{-tz})_3)_2]$ films

Taking advantage of the above-mentioned properties, experiments were undertaken to explore the use of thin films of **1** as a temperature sensor, probed by optical reflectivity, for mapping and measuring the surface temperature through thermorefectance thermal imaging. Indeed, the role of the SCO film is to enhance the thermorefectance properties of surfaces in a broad temperature range – especially in the UV spectral domain where a drastic change of the optical absorbance occurs when switching between the LS and HS states; the improved thermorefectance involving an increased

thermally induced change in optical reflectivity and, therefore, a greater thermal sensitivity for measuring the surface temperature.

All the experimental details on the microthermometry experiments discussed in the current sub-chapter are provided in the experimental part (pp. 153–154).

Figure 4.8a (top panels) shows the thermal evolution of optical reflectivity,  $\Delta R/R = (R - R_{298K})/R_{298K}$ , at  $\lambda = 310$  nm (close to the maximum absorbance wavelength) on SCO-coated (120 nm) and uncoated gold, silicon and glass surfaces in the heating mode.

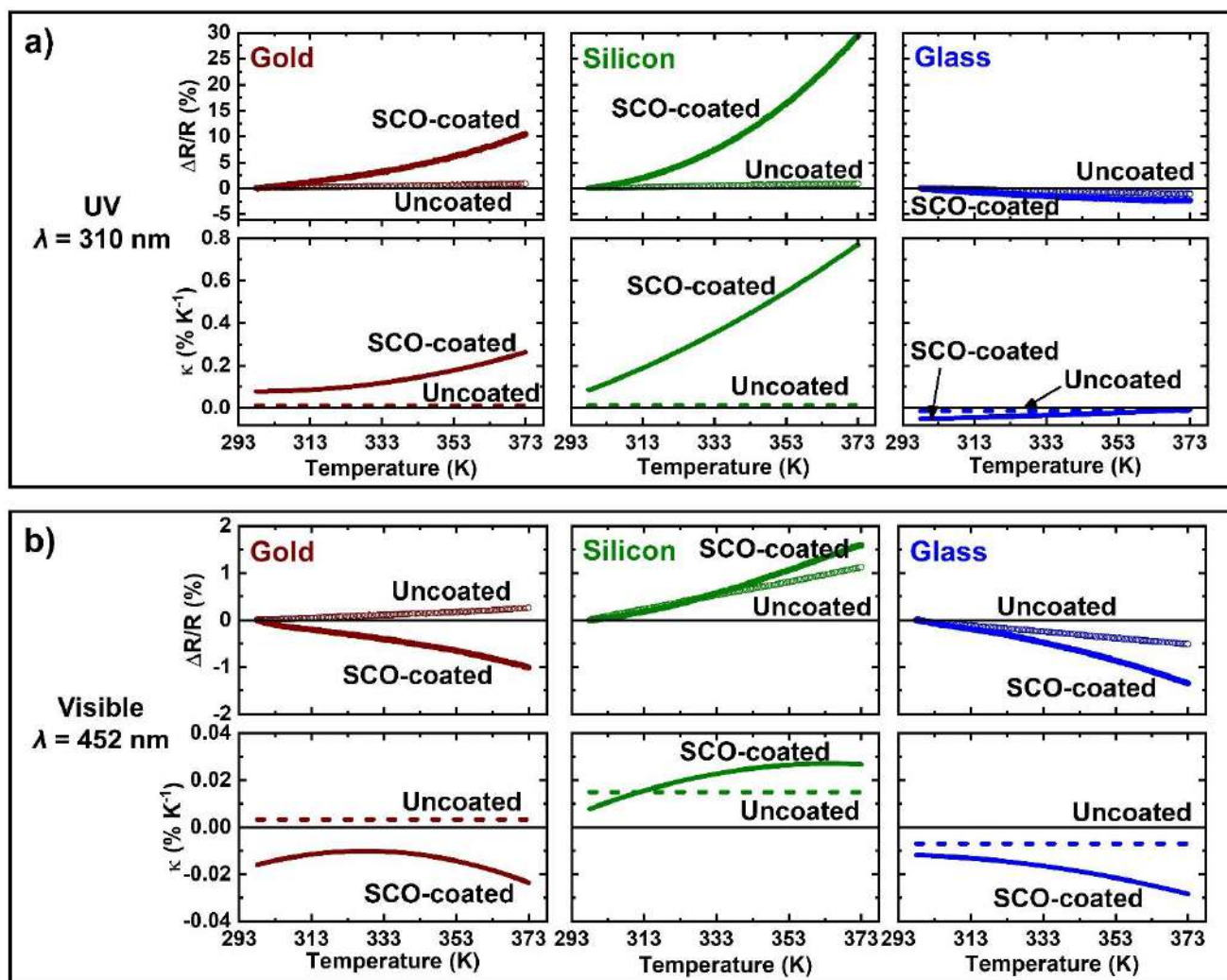


Figure 4.8. Thermal calibrations of the optical reflectivity. a) Thermal evolution of the relative optical reflectivity change,  $\Delta R/R = (R - R_{298K})/R_{298K}$ , (top panel) and of the corresponding thermoreflectance coefficient,  $\kappa = d(\Delta R/R)/dT$ , (bottom panel) measured at  $\lambda = 310$  nm on SCO-coated and uncoated surfaces of gold, silicon and glass. b) Thermal evolution of the relative optical reflectivity change,  $\Delta R/R$ , (top panel) and of the corresponding thermoreflectance coefficient,  $\kappa$ , (bottom panel) measured at  $\lambda = 452$  nm on SCO-coated and uncoated surfaces of gold, silicon and glass. For each measurement, the surface was heated from 298 to 373 K at a temperature scan rate of  $2 \text{ K min}^{-1}$ .

Remarkably, the presence of the SCO layer significantly enhances the thermoreflectance properties of surfaces, providing a relative change of the reflectivity by +29.4 %, +10.4 % and -2.4 % on silicon, gold

and glass surfaces, respectively, in the temperature range between 298 and 373 K. By comparison, on uncoated surfaces, these relative changes (ordinary thermoreflectance) remain moderate: +0.9 % on silicon and gold surfaces and -1.1 % on glass. The observed changes are much greater on silicon (and to a lesser extent on gold), which is a reflective surface in the UV range (compared to glass). On these surfaces, the optical reflectivity is found to increase with temperature ( $\Delta R/R > 0$ ), which is compatible with a progressive reduction of the absorbance of the SCO film at this wavelength upon the spin transition. Figure 4.8a (bottom panels) depicts the thermal evolution of the corresponding thermoreflectance coefficient ( $\kappa$ ), defined as  $\kappa = d(\Delta R/R)/dT$ , on the various investigated surfaces ( $\lambda = 310$  nm). While  $\kappa$  is virtually constant for uncoated surfaces in the temperature range 298–373 K,  $\kappa = +0.013$  % K<sup>-1</sup>, +0.012 % K<sup>-1</sup> and -0.014 % K<sup>-1</sup> for silicon, gold and glass surfaces, respectively, the thermoreflectance coefficient is not constant on SCO-coated surfaces due to the spin-transition phenomenon. On SCO-coated silicon,  $\kappa$  varies from 0.085 % K<sup>-1</sup> at 298 K to 0.77 % K<sup>-1</sup> at 373 K. In other words, the thermoreflectance coefficient (i.e., the thermal sensitivity) is multiplied by 6.5 at 298 K up to a factor of 59 at 373 K due to the presence of the SCO layer. On gold,  $\kappa$  changes from 0.078 % K<sup>-1</sup> to 0.26 % K<sup>-1</sup> when heating from 298 to 373 K, which corresponds to an increase of the thermoreflectance coefficient by a factor of 6.5 and 22 at 298 and 373 K, respectively, compared to the pristine gold surface. Finally, the effect is less advantageous on transparent glass substrates where  $\kappa$  changes from -0.050 % K<sup>-1</sup> to -0.009 % K<sup>-1</sup> when heating from 298 to 373 K, which means that the thermal sensitivity is increased by a factor 3.6 (in absolute value) at 298 K, but becomes lower than the ordinary thermoreflectance at high temperature. One should note here that further enhancements of the thermoreflectance coefficient can be anticipated, for instance by using a light source matching the wavelength of maximum absorbance (336 nm) and/or by increasing the thickness of the SCO film. However, in both cases, the price to pay would be an increasing disturbance of the surface temperature caused by the presence of the SCO film (i.e., increased invasiveness), which is particularly detrimental for fast (< ms) temperature monitoring. As with the optical absorbance measurements, it should be noted that no notable difference is observed in these thermal calibration curves between heating and cooling modes (Figure 4.9), which signifies that the performance of the SCO film, in terms of thermal change of the optical reflectivity, is fully reversible in the temperature range 298–373 K.

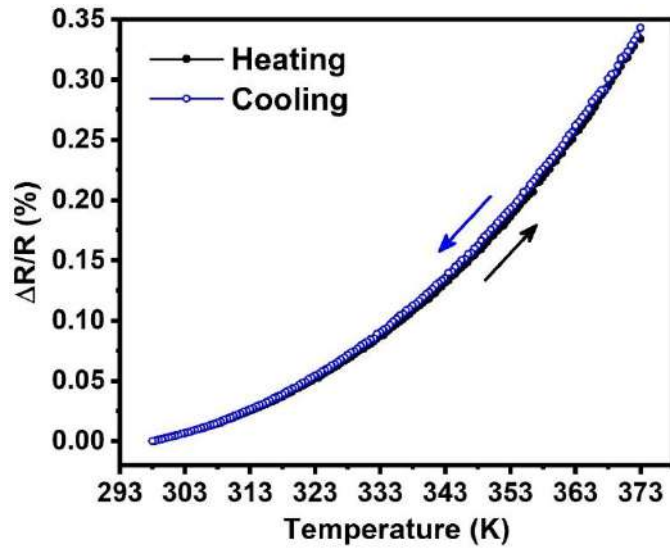


Figure 4.9. Thermal evolution of the optical reflectivity change,  $\Delta R/R = (R - R_{298K})/R_{298K}$ , measured at  $\lambda = 310$  nm on SCO-coated silicon surface in both heating and cooling modes. These data show that the thermal change of the optical reflectivity of the SCO-coated surface is fully reversible in the temperature range 298–373 K.

Interestingly, as shown in Figure 4.8b, only a slight improvement of the thermorefectance properties is evidenced on the SCO-coated surfaces in the visible range ( $\lambda = 452$  nm), i.e., in a spectral domain out of the SCO-dependent absorption band of the film. This result indicates that most of the change of the optical reflectivity along the spin transition arises from the variation of the absorption properties of the film, rather than a simple change of the refractive index. On the whole, these measurements show that the presence of the SCO thin film entails a substantial increase of the thermorefectance properties in the UV range, by more than one order of magnitude compared to the ordinary thermorefectance, especially on reflective surfaces like gold or silicon, which consequently implies a sizeable enhancement of the sensitivity (in terms of optical reflectivity signal) to any change of the surface temperature. The thermorefectance coefficients for the pristine and SCO-coated surfaces at terminal temperature points as well as at the both wavelengths of the incident light are summarized in Table 4.2.

Table 4.2. Thermorefectance coefficients of the uncoated and SCO-coated surfaces at selected temperatures and irradiation wavelengths.

Surface	T, K	$\kappa$ , % K <sup>-1</sup> ( $\lambda = 310$ nm)		$\kappa$ , % K <sup>-1</sup> ( $\lambda = 452$ nm)	
		Uncoated	SCO-coated	Uncoated	SCO-coated
Gold	298	0.012	0.078	0.003	-0.016
	373	0.012	0.260	0.003	-0.024
Silicon	298	0.013	0.085	0.015	0.008
	373	0.013	0.77	0.015	0.027
Glass	298	-0.014	-0.050	-0.007	-0.012
	373	-0.014	-0.009	-0.007	-0.028

In order to investigate the potential of this SCO thin film in terms of thermorefectance thermal imaging, a variety of Joule-heated gold microwires (length 1–2 mm, thickness 250 nm) on top of glass and oxidized silicon chips were fabricated by means of photolithography (Figure 4.10a).<sup>25,29,257</sup> The latter method involves applying a photosensitive material (photoresist) onto a substrate and exposing it to light through a mask, causing the resist's chemical transformation. After development, a thin gold layer is deposited, and unwanted gold is removed using a solvent (lift-off), leaving gold only in patterned regions. After the photolithography procedure, the surface of the resulting chips was entirely covered with a 120-nm-thick film of **1**. Note that due to its insulating nature, the presence of the molecular films of **1** on the surface is not invasive and does not perturb the electrical performance of the device.

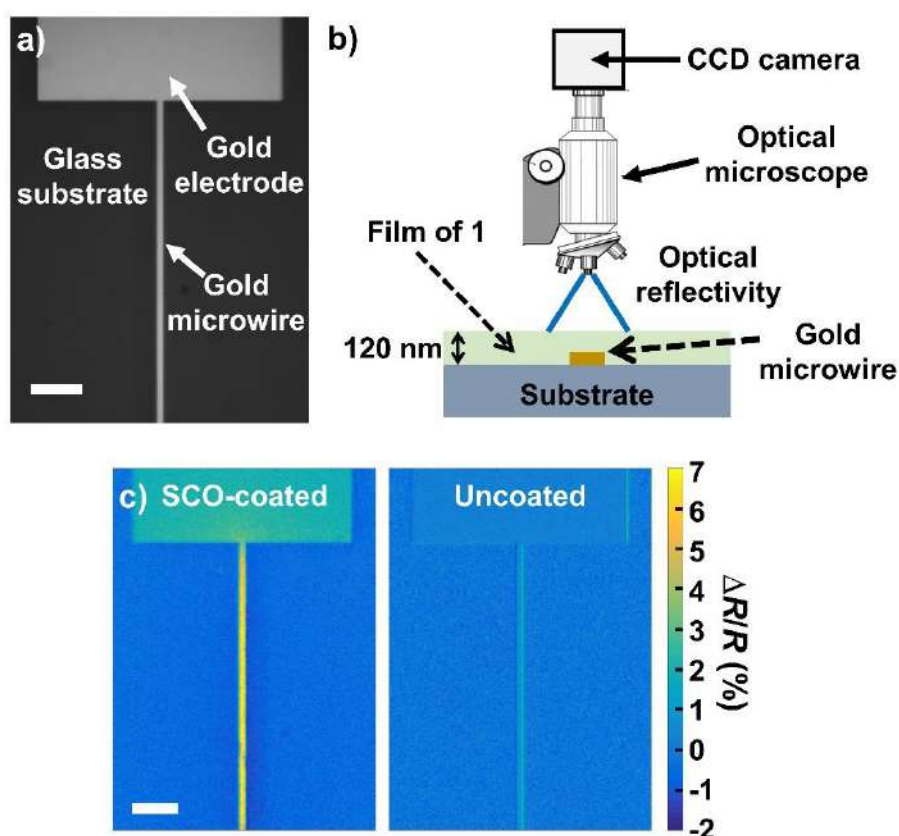


Figure 4.10. Thermal sensitivity improvement. a) Optical reflectivity  $R$  image of a Joule-heated gold microwire (2-mm-long and 16- $\mu\text{m}$ -wide) on top of a glass substrate. b) Scheme of the experimental setup. c) Relative change of optical reflectivity ( $\lambda = 310 \text{ nm}$ ),  $\Delta R/R = (R_{ON} - R_{OFF})/R_{OFF}$ , following the application of an electrical current of 65 mA in the wire, for (left) an SCO-coated surface and (right) an uncoated surface. In both cases, the base temperature  $T_b$  of the chip was maintained at 298 K. The scale bars are 100  $\mu\text{m}$ .

Optical reflectivity images ( $\lambda = 310 \text{ nm}$ ) of a SCO-coated microwire (length 2 mm, width 16  $\mu\text{m}$ ) on a glass substrate were acquired by optical microscopy at  $T = 298 \text{ K}$  (see Figure 4.10b), in both ON ( $I \neq 0$ ) and OFF ( $I = 0$ ) states of the heating device. Figure 4.10c (left) shows a map of the relative change of optical reflectivity,  $\Delta R/R = (R_{ON} - R_{OFF})/R_{OFF}$ , following the application of an electrical current of 65 mA in the wire. A strong increase of the optical reflectivity is observed on the wire, and, to a lesser

extent on the gold electrode. On the glass substrate, in the immediate vicinity of the wire, a slight decrease of the reflectivity is also observed, which is compatible with an increase of the temperature following the application of the electrical current. (As indicated in Figure 4.8a, the optical reflectivity increases/decreases on gold/glass surface following a temperature rise). For comparison, the same experiment was performed with an identical microwire on an uncoated, pristine chip. As shown in Figure 4.10c (right), the variation of optical reflectivity associated with the application of the same electrical current (65 mA) is considerably lower than that observed for the SCO-coated surface, which demonstrates the substantial gain provided by the thermosensitive SCO layer in terms of thermorefectance properties and, therefore, in terms of thermal sensitivity.

Taking advantage of this enhanced thermal sensitivity, it was possible to deduce accurate temperature maps of the Joule-heated microwires. Indeed, based on the thermal calibration curves of the optical reflectivity shown in Figure 4.8a, the reflectivity ( $\Delta R/R$ ) map measured in Figure 4.10c (left) can be easily transformed into a temperature map, by simply converting the measured value of  $\Delta R/R$ , on each pixel of the image, into a temperature value. As shown in Figure 4.11, this procedure allowed us to map the temperature field of the surface with a micrometric spatial resolution, for different values of the applied electrical current.

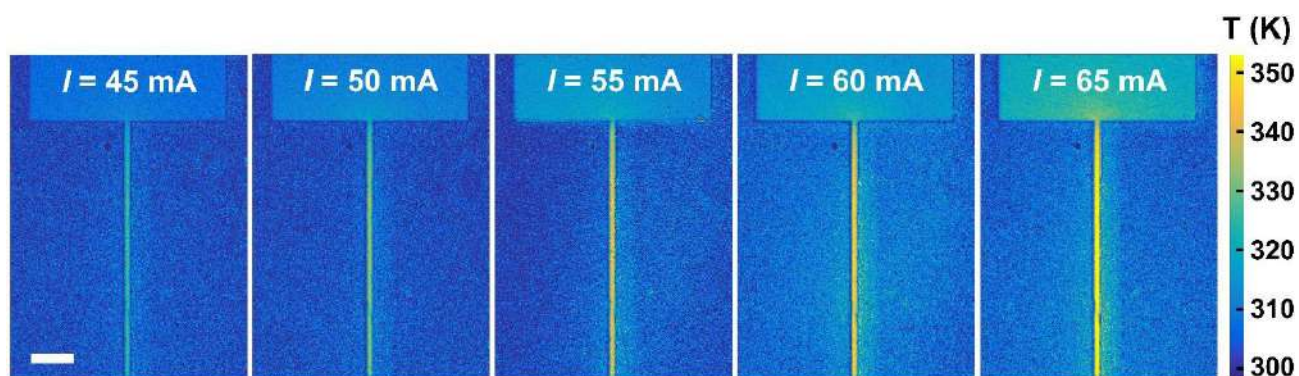


Figure 4.11. Quantitative microthermometry. Temperature maps of a SCO-coated, 16- $\mu\text{m}$ -wide gold microwire on top of a glass substrate for various applied electrical currents ranging from 45 to 65 mA ( $T_b = 298$  K). The maps are deduced from the optical reflectivity ( $\lambda = 310$  nm) images,  $\Delta R/R = (R_{ON} - R_{OFF})/R_{OFF}$ , of the SCO-coated surface. The pixel size of the temperature maps is  $2.6 \times 2.6 \mu\text{m}^2$ . The scale bar is 100  $\mu\text{m}$ .

As expected, these temperature maps show that the heating is mainly localized on the gold microwire, while a progressive diffusion of heat is also observed into the substrate and the metallic electrode when increasing the electrical current, as already reported in the thermometry study for  $[\text{Fe}(\text{HB}(1,2,4\text{-tz})_3)_2]$ .<sup>29</sup> (*N.B.* However, it should be noted that the temperature gradients observed on the surrounding glass substrate are less marked than in case of  $[\text{Fe}(\text{HB}(1,2,4\text{-tz})_3)_2]$  thermometer<sup>29</sup> mainly because of the use of wider Joule-heating wires (16- $\mu\text{m}$ -wide instead of 1- $\mu\text{m}$ -wide), in the present

study, which generate less pronounced thermal gradients.) From these temperature maps, it is possible deduce an average temperature of the Joule-heated microwire  $T_{wire}$  of 315.9, 320.0, 325.4, 329.9 and 336.6 K for an applied current of 45, 50, 55, 60 and 65 mA, respectively. These values are reported in Figure 4.12b (empty squares).

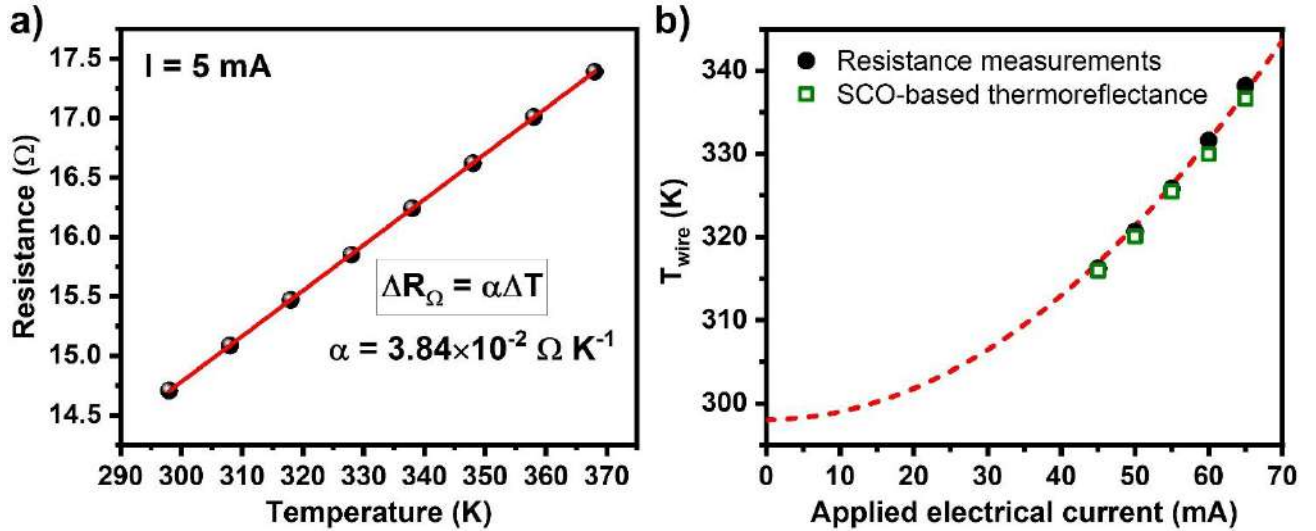


Figure 4.12. Comparison with electrical resistance measurements. a) Variation of the electrical resistance  $R_{\Omega}$  of the microwire, measured at low-bias current (5 mA), as a function of the base temperature ( $T_b$ ) of the substrate, controlled with a variable-temperature stage. The linear temperature coefficient of the wire is  $\alpha = 3.84 \times 10^{-2} \Omega K^{-1}$ . b) Average temperature of the Joule-heated wire,  $T_{wire}$ , for various applied electrical currents ranging from 45 to 65 mA ( $T_b = 298$  K), inferred from SCO-based thermoreflectance thermal imaging (empty squares) and from electrical resistance measurements (filled circles). The red dotted line indicates the typical quadratic evolution of the resistance (and thus of the wire temperature) with the applied electrical current.

To validate the results obtained with the discussed SCO-based thermometry technique, the average temperature of the Joule-heated microwire was also determined by measuring its electrical resistance. Indeed, the thermal variation induced by the applied current generates a change of electrical resistance  $\Delta R_{\Omega}$ , proportional to the mean temperature rise of the wire:  $\Delta R_{\Omega} = \alpha \Delta T_{wire}$ . To determine the value of  $\alpha$ , a thermal calibration of the resistance of the microwire was performed, by measuring the evolution of  $R_{\Omega}$  at low-bias current (5 mA) for various base temperatures ( $T_b$ ) of the chip. A linear dependence is observed, giving a value of  $\alpha = 3.84 \times 10^{-2} \Omega K^{-1}$  (Figure 4.12a). Therefore, in the course of the thermoreflectance measurements, the resistance was simultaneously measured for each value of the applied electrical current, providing a reliable comparative means to monitor in real time the actual average temperature  $T_{wire}$  of the Joule-heated wire. Figure 4.12b summarizes the values of  $T_{wire}$  obtained from the two methods for the different applied electrical currents bias, the chip being kept at room temperature ( $T_b = 298$  K). As shown in Figure 4.12b, and as expected, the temperature of the wire increases with the current following a typical quadratic evolution (Joule effect). Importantly, that the

temperature values obtained from these two techniques are in very good agreement, the observed relative difference being typically 2–5 % and always lower than 2 K.

On the whole, these data demonstrate the possibility of using SCO thin films of **1** for imaging the surface temperature at the micrometric scale with a thermal accuracy of the order of  $\sim 1$  K (using a simple CCD-based optical detection), by taking advantage of a *ca.* one order of magnitude enhancement of the UV-light thermorefectance coefficient brought into by the presence of the SCO layer. The ultimate spatial and temporal resolution of the SCO-based thermometer was not investigated, as this would require more sophisticated equipment, though the enhanced thermorefectance coefficient is obviously a key asset in this context. Furthermore, the fact that the films operate in the UV spectral range is clearly advantageous for imaging sub-micrometer features. For example, a powerful NA = 0.9 microscope objective could provide a 0.35-micron spot imaging at a wavelength of 310 nm. As for the temporal resolution, the limiting factor is the heat diffusion rate in the film, the molecular SCO phenomenon being intrinsically faster.<sup>258</sup> Indeed, due to their low thermal diffusivity, the thermalization process of such SCO films is completed in  $\sim 1$   $\mu\text{s}$ ,<sup>258</sup> which thus defines the accessible temporal resolution of the surface thermometer. Experiments on similar molecular films indicate that a 100-nm-thick film of **1** could potentially afford for temperature measurements down to the  $\mu\text{s}$  timescale.<sup>29</sup> Overall, the thermometric characteristics demonstrated in the present work are virtually comparable to those obtained with the compound  $[\text{Fe}(\text{HB}(1,2,4\text{-tz})_3)_2]$ ,<sup>29</sup> in terms of accessible thermal, spatial and temporal resolution. However, it is worth to emphasize that the thermometric approaches used in these two cases are totally different, each having their advantages and disadvantages. The use of  $[\text{Fe}(\text{HB}(1,2,4\text{-triazol-1-yl})_3)_2]$  (abrupt spin transition) allowed for a binary detection of the surface temperature, working on any surface without the need of thermal calibration procedure of the optical reflectivity. However, in this case, surface temperature maps could not be acquired in real time. Conversely, the use of compound **1** allows for real-time thermal imaging, based on a prior thermal calibration of the optical reflectivity. However, as the enhancement of the thermorefectance coefficient induced by the SCO film is surface dependent, this thermometry method is not equally effective on all surfaces.

In summary, the thermometry method involving thin film materials of  $[\text{Fe}(\text{HB}(1,2,3\text{-tz})_3)_2]$  presented in this chapter allows for microthermometry with thermal, spatial and temporal resolution of the order of  $10^0$  K,  $\mu\text{m}$  and  $\mu\text{s}$  respectively. The thermal and temporal resolution for the presented technique are comparable to such reported for the method utilizing the thin films of  $[\text{Fe}(\text{HB}(1,2,4\text{-tz})_3)_2]$ , though the latter has higher spatial resolution of sub- $\mu\text{m}$  order.<sup>29</sup> Nonetheless, neither of the above-mentioned thermometers reaches the highest thermal and temporal resolution of  $10^{-2}$  K and  $10^{-1}$   $\mu\text{s}$  attainable by thermorefectance-based thermometry.<sup>183</sup> Among the other widely used contactless optical thermometry techniques, the proposed method outperforms the IR thermography in terms of spatial (10

$\mu\text{m}$ ) and temporal resolution ( $10 \mu\text{s}$ ), and luminescence-based thermometry methods – in temporal resolution ( $10 \mu\text{s}$ ).<sup>183</sup> Thermal sensitivity (thermoreflectance coefficient) of the method is dependent on temperature and nature of the material's surface. Thus, the SCO-coating increased the thermal sensitivity of the silicon surface by around 7 times at room temperature and by almost 60 times at 373 K. In case of the gold surface, the thin film deposited on top lead to increase of the thermoreflectance coefficient by a factor comparable to such for the silicon surface at room temperature and by 22 times at 373 K. Though, for the SCO-coated glass surface the thermal sensitivity increased only by *ca.* 4 times at 298 K and ordinary thermoreflectance prevailed at high temperatures.

### 4.3 Partial conclusions

The thin films of  $[\text{Fe}(\text{HB}(1,2,3\text{-tz})_3)_2]$  in 20–200 nm thickness range were deposited and characterized for the first time. It was found the obtained dense, textured, nanocrystalline films conserve the gradual character of the spin transition between *ca.* 273 and 473 K, inherent in the bulk powder of the complex. The studied thin films are the first known to meet the requirements for real-time thermal imaging applications in a broad range of temperatures. The very gradual SCO in the films afforded for a novel, quantitative microthermometry approach, in which the SCO thin film is used for significant enhancement of the thermoreflectance coefficient (of UV-light) of the SCO-coated surface. The key principle for the demonstrated thermal sensitivity gain lies in the considerable change of the absorbance of the films in the UV range throughout the spin transition. The presented microthermometry method allows for  $\sim 1$  K,  $\mu\text{m}$  and  $\mu\text{s}$  thermal, spatial and temporal resolution respectively

### 4.4 Partial perspectives

- To investigate iron(II) SCO complexes with the heteroscorpionate ligands (see chapter 2) for evaporability.
- To study the SCO behavior in the obtained films.
- To test the eligibility of the latter for the thermoreflectance-based surface microthermometry applications.

### 4.5 Notes

In preparation of this chapter, materials from the publication cited below were used. The materials were reprinted from the reference with permission from Copyright © 2022 American Chemical Society.

1. Horniichuk, O. Y.; Ridier, K.; Zhang, L.; Zhang, Y.; Molnár, G.; Salmon, L.; Bousseksou, A. High-Sensitivity Microthermometry Method Based on Vacuum-Deposited Thin Films

Exhibiting Gradual Spin Crossover above Room Temperature. *ACS Appl. Mater. Interfaces* **2022**, *14* (46), 52140–52148. <https://doi.org/10.1021/acsami.2c13834>.

# Conclusions and perspectives

This work dealt with various approaches to develop stimuli-responsive coordination compounds aimed at small-scale thermometry applications. Two optical responses achievable in the coordination compounds were selected to reach the goal, namely thermorefectance and luminescence.

The first response implies the temperature dependence of the optical reflectance of a given material surface. Thermorefectance-based thermometry provides high spatial and temporal resolution as well as possibility for quantitative and qualitative measurements. Though, the thermorefectance coefficient depends on the material, and not every material displays high sensitivity of the response. Thus, in this work, the issue was addressed by the use of a coating of the SCO [Fe(HB(1,2,3-tz)<sub>3</sub>)<sub>2</sub>] complex. As a preliminary, physico-chemical properties of the bulk powder of the compound were investigated in detail. It was found that the compound undergoes gradual spin crossover in a broad temperature range with  $T_{1/2}$  of 373 K. The compound demonstrated evaporability suitable for thermal vacuum evaporation that allowed to deposit nanometric, homogenous, crystalline thin films that conserved the gradual character of the spin conversion with the equilibrium temperature in the frame of 374±2 K. The films exhibited a dramatic change in their absorbance due to the spin transition induced by heating/cooling. Stability of the thin films and reproducibility of their properties make them good candidates for thermometry applications. Dramatic absorbance change in the films allowed to enhance the thermorefectance response of the SCO-coated gold, glass and silicon surfaces. For some of them the thermal sensitivity gain reached more than one order of magnitude. Applied to gold microwires settled on glass or oxidized silicon chips, the films allowed for high-sensitivity thermorefectance thermal imaging with a thermal accuracy of the order of ~1 K and a temporal resolution of ~1 μs.

In addition, six novel iron(II) complexes incorporating six new heteroscorpionate ligands were synthesized and characterized. SCO behavior (or its absence) in the compounds depended on the steric effect of the substituent (-NO<sub>2</sub>, -CN or -NH<sub>2</sub>) of the triazole ring at the position proximal to the metal ion. The SCO-active new complexes potentially may provide an extension to the family of thin film thermo-responsive materials. Gradual spin transition in diamine complex [Fe(L<sup>6</sup>)<sub>2</sub>] represents a particular interest as it covers from cryogenic to above-room-temperature ranges (150–350 K), which is interesting for thermometry applications. Moreover, the versatile reactivity of NH<sub>2</sub>-group may allow to use the amino-derivatives as building-blocks to extend the family of evaporable SCO compounds.

The second optical response, which is luminescence, can also be temperature dependent as, *e.g.*, luminescence intensity or integral intensity ratio of certain emission bands can be sensitive to temperature changes. A promising class of luminescent coordination compounds is represented by

lanthanide complexes. Though, to achieve an efficient luminescence, careful design of the ligand(s) and the resulting complex is required. Thus, the ligand design should ensure the minimal number (or absence) of high-energy oscillators at its binding site and shielding of the lanthanide ions from coordination/interactions with luminescence quenchers such as solvent molecules. In addition, bi- or polynuclear lanthanide complexes show higher luminescence intensity than mononuclear. To address these requirements tetramethyl *N,N'*-(2,2,3,3,4,4-hexafluoro-1,5-dioxopentane-1,5-diy)bis(phosphoramidate) ( $\text{H}_2\text{L}^8$ ) was chosen as an appropriate ligand. In the ligand molecule, the number of high-energy oscillators is minimized and its design allows coordination of two lanthanide ions. Thus, a series of triple-stranded  $[\text{Ln}_2(\text{L}^8)_3(\text{phen})_2]$  and quadruple-stranded  $\text{NEt}_4[\text{NaLn}_2(\text{L}^8)_4(\text{H}_2\text{O})]$  and  $\text{Na}[\text{NaLn}_2(\text{L}^8)_4(\text{H}_2\text{O})]\cdot 2\text{H}_2\text{O}$  complexes were synthesized and characterized for the first time. Efficient sensitization of the luminescence was achieved in  $[\text{Ln}_2(\text{L}^8)_3(\text{phen})_2]$ . Solid triple-stranded europium(III) complex  $[\text{Eu}_2(\text{L}^8)_3(\text{phen})_2]$  demonstrated an outstanding intrinsic quantum yield of 91 %, which is higher than such for bis- $\beta$ -diketonate analogues. In  $\text{NEt}_4[\text{NaNd}_2(\text{L}^8)_4(\text{H}_2\text{O})]$  short distance of 5.703(9) Å between  $\text{Nd}^{\text{III}}$  ions favors an interion energy transfer, which leads to short  $^4\text{F}_{3/2}$  emission lifetime of 2  $\mu\text{s}$ . Intensity of  $^4\text{F}_{3/2} \rightarrow ^4\text{I}_{9/2}$  and  $^4\text{F}_{3/2} \rightarrow ^4\text{I}_{11/2}$  varies with temperature, and the integral intensity ratio of the bands is temperature-dependent alike. Though, the  $\text{Nd}^{\text{III}}$  emission in  $\text{NEt}_4[\text{NaNd}_2(\text{L}^8)_4(\text{H}_2\text{O})]$  is weak, which is problematic for thermometry applications based on luminescence. Nevertheless, the bis-chelating CAPH ligand can be used to develop highly-emissive heterobimetallic (*e.g.*,  $\text{Eu}^{\text{III}}$ - $\text{Tb}^{\text{III}}$ ) complexes with temperature-dependent interion energy transfer suitable for luminescence thermometry applications.

The research directions outlined in the perspectives revolve around spin crossover (SCO) complexes and their thin films as well as luminescent dilanthanide complexes, particularly with the aim of creating functional materials for thermometry applications.

Regarding the future researches on SCO materials, initial investigations involve studying iron(II) SCO complexes with heteroscorpionate ligands, assessing their evaporability, and delving into their spin crossover behavior within thin films. Additional aspect of this exploration seeks to expand the family of the spin crossover complexes with scorpionate ligands by utilizing the amino-derivatives as building blocks. As these complex thin films are being elaborated, their properties and suitability for thermoreflectance-based surface microthermometry applications will be thoroughly examined. This dual focus on SCO phenomena and thermometry highlights the intention to develop advanced materials with tailored characteristics for precise temperature measurement techniques.

A focal point of interest involves more detailed studying the temperature-dependent luminescence in  $\text{NEt}_4[\text{NaNd}_2(\text{L}^8)_4(\text{H}_2\text{O})]$  (**16**) and related complexes. This exploration seeks to uncover

how luminescence properties change with varying temperatures, potentially revealing insights into their behavior and potential applications. Considering the weak luminescence of  $\text{NEt}_4[\text{NaNd}_2(\text{L}^8)_4(\text{H}_2\text{O})]$  **16**, it would be interesting to develop more potent systems, *e.g.*, heterobinuclear  $\text{Eu}^{\text{III}}\text{-Tb}^{\text{III}}$  helicates based on the tetramethyl *N,N'*-(2,2,3,3,4,4-hexafluoro-1,5-dioxopentane-1,5-diyl)bis(phosphoramidate)  $\text{H}_2\text{L}^8$  bis-chelating CAPH ligand displaying the temperature-dependent interionic energy transfer that could be used for luminescence thermometry. Simultaneously, the research aims to design heterobinuclear  $\text{Ln}^{\text{III}}\text{-Fe}^{\text{II}}$  systems that showcase the synergy between lanthanide luminescence and spin crossover phenomena. This interdisciplinary approach could lead to the development of multifunctional materials with novel properties and functionalities.

## Experimental part

### 1. Experimental techniques and methods

**Chapter 2.** IR spectra were recorded on a Perkin Elmer FT-IR Frontier MIR/FIR spectrometer, using a diamond ATR (Attenuated Total Reflection). NMR spectra were recorded with a Bruker Avance III 400 (400 MHz) at 298 K using deuterated solvents CD<sub>3</sub>OD and CD<sub>2</sub>Cl<sub>2</sub>. The chemical shifts,  $\delta$ , for <sup>1</sup>H, <sup>13</sup>C and <sup>11</sup>B NMR are expressed in ppm. <sup>11</sup>B NMR spectra were recorded using BF<sub>3</sub>·OEt<sub>2</sub> as an external reference. Elemental analyses (for C, H and N) were performed using a Perkin Elmer 2400 series II Instrument. Single-crystal X-ray diffraction analysis for **1** and its solvatomorphs was performed on an Oxford-Diffraction XCALIBUR E CCD diffractometer with graphite-monochromated Mo-K $\alpha$  radiation. The unit cell determination and data integration were carried out using the CrysAlisPro package from Oxford Diffraction. Multi-scan correction for absorption was applied. All the structures were solved using an intrinsic phasing method using SHELXT and refined by full-matrix least-squares on  $F^2$  with SHELXL<sup>259,260</sup> using the graphical interface of Olex2.<sup>261</sup> Non-hydrogen atoms were refined anisotropically. Aromatic hydrogen atoms were geometrically fixed and refined using a riding model. Single-crystal X-ray diffraction analysis for <sup>n</sup>Bu<sub>4</sub>NL<sup>2</sup> was performed on an Xcalibur, Eos, Gemini ultra diffractometer at 173 K using Cu K $\alpha$  ( $\lambda = 1.54184 \text{ \AA}$ ) radiation. Single crystals of complexes **4** (*trans*-isomer) were analyzed on a Bruker Kappa Apex II diffractometer equipped with a 30 W air-cooled microfocus source using MoK $\alpha$  radiation ( $\lambda = 0.71073 \text{ \AA}$ ). A suitable single crystal *cis*-isomer of **4** was analyzed using Rigaku XtaLAB Synergy Dualflex diffractometer equipped with PhotonJet X-ray source (Cu,  $\lambda=1.54184 \text{ \AA}$ ). Variable temperature powder X-ray diffraction patterns for **1** were recorded using a Panalytical X'Pert diffractometer equipped with a Cu X-ray tube, a Ge(111) incident beam monochromator ( $\lambda = 1.5406 \text{ \AA}$ ) and an X'Celerator detector. X-ray powder diffractograms for complexes **4** and **6** were recorded on capillaries, on a Rigaku Smartlab Powder Diffractometer using a Cu source ( $\lambda_{K\alpha 1} = 1.54056 \text{ \AA}$ ) and a high energies linear detector (D Tex Ultra 250 from Rigaku). The diffractometer was used in a theta/theta configuration with a multilayer mirror optics (CBO series for Smartlab). Data were recorded with  $2\theta$  between 5 and 70° or 5 and 50° (step: 0.01° or 0.02°). Variable-temperature Raman spectra for compound **1** were acquired by means of an Xplora (Horiba) Raman microspectrometer, using the 532 nm line of a Nd-YAG laser (0.1 mW). The sample temperature was controlled using a Linkam THMS600 liquid nitrogen cryostat. Differential thermal analysis and thermogravimetric (DTA–TG) data for bulk powder of **1**·**12H<sub>2</sub>O** were acquired simultaneously using a Perkin-Elmer Diamond thermal analyzer under a 100 ml min<sup>-1</sup> nitrogen flow at 10 K min<sup>-1</sup>. DSC analysis of **1**·**12H<sub>2</sub>O** was carried out on a Netsch DSC 3500 Sirius instrument under nitrogen purging gas (20 ml min<sup>-1</sup>) at a heating/cooling rate of 10 K min<sup>-1</sup>. Variable-temperature magnetic susceptibility data for **1**

were obtained in 250–400 K range, while for complexes **2** and **3** – in 4–300 K range, at cooling and heating rates of 2 K min<sup>-1</sup> under a field of 1 kOe using a Quantum Design MPMS magnetometer. For complexes **4–7** the data were acquired in 4–400 K range on Quantum Design MPMS3 SQUID magnetometer using the same parameters. <sup>57</sup>Fe Mössbauer spectra were recorded using a conventional constant-acceleration-type spectrometer equipped with a 50 mCi <sup>57</sup>Co source and a liquid nitrogen cryostat. Least-squares fittings of the Mössbauer spectra were carried out with the assumption of Lorentzian line shapes using the Recoil software.<sup>262</sup>

**Chapter 3.** IR measurements were performed on a Perkin–Elmer Spectrum BX spectrometer on solid state samples in form of KBr pellets and for complex **8** solution in DMSO with concentration close to saturated solution, placing a drop of the solution between KBr pellets. FTIR spectrum of **16** in nujol suspensions was performed using a Bruker IFS66/S FITIR spectrometer in the 60–600 cm<sup>-1</sup> region. NMR spectra for solutions in DMSO-*d*<sub>6</sub> were obtained on an AVANCE 400 Bruker NMR spectrometer at room temperature. Elemental analyses (C, H, and N) were performed on an EL III Universal CHNOS Elemental Analyzer and by using standard titrimetric methods for lanthanide ions. The absorption spectra for complex **8** were recorded on an UV-Vis spectrophotometer Specord M 40 Carl Zeiss for solid samples and on KSVU-23 “LOMO” spectrometer using quartz cell of 1 cm path length for the solution of the complex in DMSO (0.008 mol/dm<sup>3</sup>). Photoluminescence excitation and emission spectra of complexes **8–13** were measured at 298 and 77 K on a Fluorolog FL 3-22 (Horiba Jobin Yvon) spectrofluorimeter coupled to a R928 Hamamatsu photomultiplier, using the right-angle detection mode. The excitation source was a 450W Xe arc lamp. The emission spectra were corrected for detection and optical spectral response of the spectrofluorimeter and the excitation spectra were corrected for the spectral distribution of the lamp intensity using a photodiode reference detector. All the spectra were acquired through an UV filter (350 nm cut-off). Solid samples for photoluminescence measurements at room temperature were loaded in a solid sample cuvette supplied with Fluorolog FL 3-22 or in quartz capillaries in case of experiments at 77 K. Concentrations of the complexes’ solutions in DMSO for photoluminescence measurements were 1.0–5.0×10<sup>-4</sup> M. The solution was placed in quartz cuvettes in case of experiment at room temperature or in quartz capillaries in case of experiments at 77 K. The luminescence lifetime measurements were acquired with the same instrument using a pulsed Xe–Hg lamp (6 μs pulse at half width and 20–30 μs low-intensity tail). The luminescence lifetime values are averages of at least three independent measurements which were made by monitoring the decay at the maxima of the emission spectra. The decay time values were estimated with an error of 10 %. Phosphorescence spectra were registered for complex **14** in solid state and for its frozen 0.001 M solution in DMSO at 77 K, enforcing a 0.05 ms delay, and repeating measurements at least 3 times. Emission spectra for compound **16** were recorded at 77 and 300 K using a Hamamatsu PMA-12 photonic

multichannel analyzer equipped with BT-CCD line with corrected response in the whole range (350–1100 nm). As an excitation source a fourth harmonic ( $\lambda_{\text{exc}} = 266$  nm) of Nd:YAG laser was used ( $f = 10$  Hz,  $t_{\text{pulse}} < 20$  ns,  $E_{\text{pulse}} = 10$  mJ). For measurement at 77 K Linkam THMS600 cooling/heating stage was used. Decay curves were recorded using McPherson spectrometer equipped with Hamamatsu R928 and R5108 photomultiplier tubes and Tektronix MDO-4052 digital oscilloscope. Excitation source was the same as for emission spectra. MS analysis for **16** was performed by the method of laser desorption/ionization on an Autoflex II (Bruker Daltonics, Germany) mass spectrometer with nitrogen laser ( $\lambda = 337$  nm). Experiments were carried out in linear mode for negative ions in the mass range 100 to 2000 m/z. Resulting mass spectra were obtained by assuming the data of 200 laser shots and processing by the software FlexAnalysis (Bruker Daltonics, Germany). The data of X-Ray diffraction for **16** were collected and examined on an Xcalibur 3 diffractometer equipped with CCD Sapphire and graphite-monochromated MoK $\alpha$  radiation ( $\lambda = 0.71073$  Å). The diffraction data for **17** were collected at 173 K using a Stoe IPDS-2T diffractometer. For **18**, the measurements were performed on a Stoe Stadivari diffractometer with a Dectris Pilatus 300K detector and with an Cu microfocus source (Cu-K $\alpha$ ,  $\lambda = 1.54186$  Å) at 173 K. Face-indexed numerical absorption correction using X-RED and X-SHAPE<sup>263,264</sup> was applied.

**Chapter 4.** Thin films of **1** were obtained by means of thermal evaporation in a PREVAC thermal deposition system at a base pressure of *ca.*  $9 \times 10^{-7}$  mbar. The bulk powder of the complex was heated at 210 °C in a quartz crucible and evaporated at a rate of  $0.04$  Å s<sup>-1</sup>. The film thickness and the evaporation rate were followed *in situ* using a quartz crystal microbalance. The thickness of the films was verified *ex situ* by spectral reflectance measurements (F20, Filmetrics) and by AFM (SmartSPM, Horiba). The films were deposited onto crystalline silicon (100 orientation) and amorphous fused silica substrates, which were cleaned beforehand *via* 5 min sonication in acetone and ethanol. The GIXRD experiments were carried out in ambient conditions by means of a PANalytical X'Pert PRO MPD system using Cu-K $\alpha$  radiation (45 kV and 40 mA) and a parallel-beam configuration. The incident beam optics consisted of a mirror with a  $1/32^\circ$  divergence slit. A parallel plate collimator ( $0.18^\circ$ ) and Soller slits ( $0.04^\circ$ ) were mounted on the path of the diffracted beam. An X'Celerator detector in receiving slit mode was used for X-ray collection. AFM surface topography analysis was conducted in amplitude-modulation mode at room temperature using SmartSPM. The temperature-dependent absorbance spectra of the thin films were collected at wavelengths between 200 and 600 nm using a Cary 50 (Agilent Technologies) spectrophotometer and a Linkam FTIR-600 heating-cooling stage. The sample chamber was purged with dry nitrogen and spectra were acquired in the 253–453 K range with  $2$  K min<sup>-1</sup> rate.

Gold microwires (length 1–2 mm, thickness 250 nm and width 2–16  $\mu\text{m}$ ) were patterned on glass and thermally oxidized silicon substrates by a photolithography method, as reported earlier.<sup>25,29,257</sup> The

substrates (and the microwires) were then coated with a 120-nm-thick film of **1** by vacuum thermal evaporation. The SCO-coated chip was connected to a source-meter (Keithley 2611A) *via* an eight-track connector<sup>29</sup> and mounted on a variable-temperature microscope stage (Linkam Scientific Instruments, LTS120) to control the base temperature ( $T_b$ ) of the entire circuit. The microwire electrical characterizations and operation were carried out by applying current and not voltage bias in order to guarantee a reproducible Joule heating. Optical reflectivity images were recorded at  $\lambda = 310$  nm (LED source) and  $\lambda = 452$  nm (halogen lamp with a spectral range reduced by a band-pass filter) using a custom-made optical microscope (compatible with UV light) equipped with a  $\times 5$  magnification objective (numerical aperture, NA= 0.12) and a CCD camera (Andor Technology Clara,  $1392 \times 1040$  pixels of  $6.45 \mu\text{m}$  size).

## 2. Syntheses of ligands and complexes

**Chapter 2.** If not specified otherwise, all reactants and reagents used in this study were procured from commercial suppliers and employed as received.  $\text{NaL}^1$  and  $[\text{Fe}(\text{L}^1)_2]$  were synthesized according to the literature.<sup>205</sup> The procedures are given below. Solvent purification system PS-MD-5 (Inert Corporation, USA) was used to provide dry air-free dichloromethane for synthesis of iron(II) complexes **2–5**. Synthesis of KTp was performed according to the procedure developed by Trofimenko,<sup>208</sup> with modifications specified in the respective protocol below.  ${}^n\text{Bu}_4\text{NTp}$  was synthesized according to the literature protocol.<sup>209</sup> Synthesis of the iron(II) complexes **2–5** was carried out under argon atmosphere using common anaerobic Schlenk techniques. Reduction of the nitro-derived complexes **2** and **3** was conducted in 50-ml autoclave (Autoclave-Maxitech, France) pressurized with hydrogen gas.

**Sodium hydrotris(1,2,3-triazol-1-yl)borate ( $\text{NaL}^1$ ).** In a 50-ml round-bottom flask with paracymene (15 ml), sodium borohydride (0.14 g, 3.62 mmol), and 1,2,3-triazole (1.00 g, 14.5 mmol) were mixed and agitated. A white solid developed after the reaction was heated to  $180^\circ\text{C}$  for a week. After the reaction mixture had been brought to room temperature, a 60 ml fine sintered-glass frit was used to collect the white precipitation, which was then washed with toluene ( $3 \times 10$  ml) and hexanes ( $3 \times 10$  ml). Tetrahydrofuran (10 ml) and the solid were transferred to a 20-ml scintillation vial and agitated for 4 h. The solvent was decanted after. Additional THF (5 ml) was added, and the precipitate was filtered using a medium sintered glass frit, and dried under reduced pressure to give 0.50 g of white powder of the product. Yield: 58 %. The spectroscopic results for this compound matched the previously published one.

**Bis[hydrotris(1,2,3-triazol-1-yl)borate]iron(II) [ $\text{Fe}(\text{L}^1)_2$ ] (**1**).** In two separate 100-ml Erlenmeyer flasks iron(II) sulfate heptahydrate (0.12 g, 0.41 mmol) and  $\text{NaL}^1$  (0.20 g, 0.82 mmol) were dissolved in water (17 ml and 50 ml, respectively). The aqueous solution of  $\text{NaL}^1$  was added drop-wise to the iron

salt solution. The latter gradually turned pink upon the addition of the ligand solution. The resulting solution was left for 3 days to afford 0.11 g of red crystals of the product appearing as a dodecahydrate. Yield: 40 %. Heating above 90 °C allows to obtain the anhydrous product. Spectroscopic data matched the reported ones for this complex. The elemental analyses confirmed the composition of the complex both in the hydrated and anhydrous forms. **[Fe(L<sup>1</sup>)<sub>2</sub>·12H<sub>2</sub>O (1·12H<sub>2</sub>O)**. C<sub>12</sub>H<sub>38</sub>B<sub>2</sub>FeN<sub>18</sub>O<sub>12</sub> (M = 704.07). Anal. calc.: C, 20.47; H, 5.44; N, 35.81%. Found: C, 20.55; H, 5.42; N, 35.55%. **[Fe(L<sup>1</sup>)<sub>2</sub>] (1)**. C<sub>12</sub>H<sub>14</sub>B<sub>2</sub>N<sub>18</sub>Fe (M = 487.88) Anal. calc.: C, 29.55; H, 2.89; N, 51.68%. Found: C, 29.51; H, 2.86; N, 51.57%.

**Potassium hydrotris(pyrazol-1-yl)borate (KTp)**. The stepwise heating of KBH<sub>4</sub> (2.07 g, 38 mmol) and pyrazole (10.39 g, 153 mmol) powders mixture to 195 °C was performed according to the protocol reported by Trofimenko.<sup>208</sup> After around 3 h of heating under vigorous stirring of the formed melt, the hydrogen evolution ceased. Then the mixture was cooled down to 150 °C and stirred overnight at this temperature. Afterwards the temperature was raised to 195 °C once again and the melt was vigorously stirred for another 3 h, whereupon it was cooled down to 65 °C. Once the temperature was reached, 30 ml of hot diethyl ether was added and the resulting mixture was stirred for 5 min. The white precipitate formed was filtered, thoroughly washed with the hot ether and dried in air to give 7.50 g of the product appearing as a white powder. Yield: 78 %. <sup>1</sup>H NMR (400 MHz, CD<sub>3</sub>OD) δ 7.51 (d, *J* = 2.0 Hz, 3H), 7.15 (d, *J* = 2.0 Hz, 3H), 6.15 (t, *J* = 2.0 Hz, 3H); <sup>11</sup>B NMR (128 MHz, CD<sub>3</sub>OD) δ -1.15 (d).

***n*-Tetrabutylammonium (3-nitro-1,2,4-triazol-1-yl)di(pyrazol-1-yl)hydroborate (<sup>n</sup>Bu<sub>4</sub>NL<sup>2</sup>)**. <sup>n</sup>Bu<sub>4</sub>NTp (1.99 g, 4.39 mmol) and 3-nitro-1,2,4-triazole (0.50 g, 4.39 mmol) powders were mixed in a Schlenk tube equipped with magnetic stirring bar and an air-cooled distillation condenser connected to a receiving flask. Then, reduced pressure in the setup was created using a vacuum pump. Afterwards, the setup was sealed under reduced pressure. Bottom of the Schlenk tube was immersed into an oil bath resting on a magnetic stirring and heating plate. Then, the reaction mixture was heated at 100 °C under stirring for 2 h. The solid mixture started to melt at 90 °C. Condensation of crystalline pyrazole on the colder parts of the tube walls was observed under these conditions. The deposited pyrazole was distilled under vacuum each 1 h. Crude oily product is obtained as a result. The temperature was reduced then to 75 °C, and water (20 ml) was added to the crude product and the obtained mixture was stirred at this temperature for 5 min. Then the stirring was stopped and the mixture was cooled down to the room temperature. The oily product collected at the bottom of the tube and on the walls. The aqueous phase was removed by decantation and the residue was dried in vacuum yielding 1.68 g of the product as a clear yellow oil. Yield: 76 %. Single crystals, suitable for X-ray diffraction, form in the crude product left overnight at room temperature. IR (neat, cm<sup>-1</sup>): 2963<sub>m</sub>, 2937<sub>w</sub>, 2877<sub>w</sub>, 2460<sub>w</sub> (ν(B–H)), 1526<sub>m</sub>, 1540<sub>m</sub>, 1492<sub>s</sub>, 1474<sub>s</sub>, 1384<sub>vs</sub>, 1298<sub>vs</sub>, 1165<sub>s</sub>, 1109<sub>m</sub>, 1080<sub>m</sub>, 1030<sub>m</sub>; <sup>1</sup>H NMR (400 MHz, CD<sub>2</sub>Cl<sub>2</sub>) δ

7.93 (s, 1H), 7.56–7.54 (m, 4H), 6.18 (t,  $J = 2.2$ , 2H), 3.10–3.01 (m, 8H), 1.62–1.49 (m, 8H), 1.43–1.29 (m, 8H), 0.97 (t,  $J = 7.3$  Hz, 12H);  $^{13}\text{C}$  NMR (101 MHz,  $\text{CD}_2\text{Cl}_2$ )  $\delta$  152.39, 149.11, 140.39, 134.16, 104.26, 59.05, 24.14, 19.98, 13.69;  $^{11}\text{B}$  NMR (128 MHz,  $\text{CD}_2\text{Cl}_2$ )  $\delta$  -1.57 (d);  $\text{C}_{24}\text{H}_{44}\text{BN}_9\text{O}_2$  ( $M = 501.49$ ). Anal. calc.: C, 57.48; H, 8.84; N, 25.14 %. Found: C, 57.39; H, 8.88; N, 25.27 %.

***n*-Tetrabutylammonium bis(3-nitro-1,2,4-triazol-1-yl)(pyrazol-1-yl)hydroborate ( ${}^n\text{Bu}_4\text{NL}^3$ ).** The same setup as in case of  ${}^n\text{Bu}_4\text{NL}^2$  was used and the procedure was similar, with difference in stoichiometry and temperature. Thus,  ${}^n\text{Bu}_4\text{NTp}$  (1.00 g, 2.20 mmol) and 3-nitro-1,2,4-triazole (0.50 g, 4.39 mmol) were heated at 130 °C under stirring for 3 h. Pyrazole was distilled off each 1 h. Purification step of stirring the crude product in water was done as described in the previous protocol. The product appears as a viscous clear dark-yellow oil. 1g. Yield: 83 %. IR (neat,  $\text{cm}^{-1}$ ): 2964 $m$ , 2936 $w$ , 2876 $w$ , 2472 $w$  ( $\nu(\text{B-H})$ ), 1541 $s$ , 1494 $s$ , 1413 $m$ , 1384 $m$ , 1297 $vs$ , 1167 $s$ , 1104 $m$ , 1024 $m$ ;  $^1\text{H}$  NMR (400 MHz,  $\text{CD}_2\text{Cl}_2$ )  $\delta$  8.20 (s, 2H), 7.72 (d,  $J = 2.2$  Hz, 1H), 7.65 (d,  $J = 2.2$  Hz, 1H), 6.26 (d,  $J = 2.2$  Hz, 1H), 3.21–3.05 (m, 8H), 1.62 (p,  $J = 7.3$  Hz, 8H), 1.38 (h,  $J = 7.3$  Hz, 8H), 0.97 (t,  $J = 7.3$  Hz, 12H);  $^{13}\text{C}$  NMR (101 MHz,  $\text{CD}_2\text{Cl}_2$ )  $\delta$  149.54, 148.35, 141.64, 135.34, 105.10, 59.30, 24.15, 20.02, 13.63;  $^{11}\text{B}$  NMR (128 MHz,  $\text{CD}_2\text{Cl}_2$ )  $\delta$  -2.30 (d);  $\text{C}_{23}\text{H}_{42}\text{BN}_{11}\text{O}_4$  ( $M = 547.47$ ). Anal. calc.: C, 50.46; H, 7.73; N, 28.14 %. Found: C, 50.47; H, 7.88; N, 28.35 %.

The CN-bearing derivatives of  $\text{L}^4$  and  $\text{L}^5$  were obtained following the same protocols as for their nitro-featured counterparts.

***n*-Tetrabutylammonium (3-cyano-1,2,4-triazol-1-yl)di(-pyrazol-1-yl)hydroborate ( ${}^n\text{Bu}_4\text{NL}^4$ ).** Clear colorless oily product. Yield: 69 %. IR (neat,  $\text{cm}^{-1}$ ): 2963 $m$ , 2937 $w$ , 2876 $w$ , 2455 $w$  ( $\nu(\text{B-H})$ ), 2245 $w$  ( $\nu(\text{C}\equiv\text{N})$ ), 1500 $w$ , 1470 $s$ , 1413 $w$ , 1384 $s$ , 1291 $s$ , 1161 $vs$ , 1107 $vs$ , 1096 $vs$ , 1034 $vs$ ;  $^1\text{H}$  NMR (400 MHz,  $\text{CD}_2\text{Cl}_2$ )  $\delta$  7.99 (s, 1H), 7.52 (d,  $J = 2.1$  Hz, 2H), 7.50 (d,  $J = 2.1$  Hz, 2H), 6.16 (t,  $J = 2.1$ , 2H), 3.10–2.93 (m, 8H), 1.61–1.49 (m, 8H), 1.44–1.30 (m, 8H), 0.99 (t,  $J = 7.3$  Hz, 12H);  $^{13}\text{C}$  NMR (101 MHz,  $\text{CD}_2\text{Cl}_2$ )  $\delta$  149.35, 140.28, 139.29, 134.12, 114.61, 104.20, 59.10, 24.19, 20.03, 13.72.  $^{11}\text{B}$  NMR (128 MHz,  $\text{CD}_2\text{Cl}_2$ )  $\delta$  -1.66 (d);  $\text{C}_{25}\text{H}_{44}\text{BN}_9$  ( $M = 481.50$ ). Anal. calc.: C, 62.36; H, 9.21; N, 26.18 %. Found: C, 62.70; H, 9.52; N, 26.09 %.

***n*-Tetrabutylammonium bis(3-cyano-1,2,4-triazol-1-yl)(pyrazol-1-yl)hydroborate ( ${}^n\text{Bu}_4\text{NL}^5$ ).** Colorless clear oil. Yield: 94 %. IR (neat,  $\text{cm}^{-1}$ ): 2964 $m$ , 2937 $w$ , 2877 $w$ , 2476 $w$  ( $\nu(\text{B-H})$ ), 2247 $w$  ( $\nu(\text{C}\equiv\text{N})$ ), 1506 $w$ , 1470 $s$ , 1415 $w$ , 1386 $m$ , 1315 $s$ , 1166 $vs$ , 1104 $s$ , 1030 $vs$ ;  $^1\text{H}$  NMR (400 MHz,  $\text{CD}_2\text{Cl}_2$ )  $\delta$  8.19 (s, 2H), 7.65 (d,  $J = 2.2$  Hz, 1H), 7.60 (d,  $J = 2.2$  Hz, 1H), 6.23 (t,  $J = 2.2$ , 1H), 3.15–3.03 (m, 8H), 1.67–1.52 (m, 8H), 1.45–1.31 (m, 8H), 0.98 (t,  $J = 7.3$  Hz, 12H);  $^{13}\text{C}$  NMR (101 MHz,  $\text{CD}_2\text{Cl}_2$ )  $\delta$  149.58, 141.27, 139.81, 134.96, 114.22, 104.91, 59.32, 24.17, 20.02, 13.66;  $^{11}\text{B}$  NMR (128 MHz,  $\text{CD}_2\text{Cl}_2$ )  $\delta$  -

2.59 (d); C<sub>25</sub>H<sub>42</sub>BN<sub>11</sub> (M = 507.50). Anal. calc.: C, 59.17; H, 8.34; N, 30.36 %. Found: C, 59.40; H, 8.33; N, 30.40 %.

All the ligands are poorly soluble in water, soluble in alcohols, DCM and aprotic polar organic solvents, in particular, tetrahydrofuran (THF), acetonitrile and acetone.

Synthetic procedures to access iron(II) complexes with ligands L<sup>2</sup>–L<sup>5</sup> were conducted as follows.

**Bis[hydrobis(pyrazol-1-yl)(3-nitro-1,2,4-triazol-1-yl)]iron(II) [Fe(L<sup>2</sup>)<sub>2</sub>] (2).** To a solution of <sup>n</sup>Bu<sub>4</sub>NL<sup>2</sup> (1.60 g, 3.20 mmol) in dry air-free DCM (95 ml), FeCl<sub>2</sub>·4H<sub>2</sub>O (0.32 g, 1.60 mmol) was added under argon. The solution gradually turned dark pink following the FeCl<sub>2</sub> consumption. After vigorous stirring for 1 h at room temperature, the solvent was removed under reduced pressure, and the residue left was suspended in water (60 ml). The formed precipitate was filtered, thoroughly washed with water and dried in air to afford 0.76 g of a brick-red powder of the product. Yield: 83 %. The compound is insoluble in water, poorly soluble in alcohols, soluble in DCM, THF and acetone. IR (neat, cm<sup>-1</sup>): 3116w, 2487w (ν(B–H)), 1552m, 1501s, 1402m, 1307s, 1167s, 1050s; C<sub>16</sub>H<sub>16</sub>B<sub>2</sub>FeN<sub>16</sub>O<sub>4</sub> (M = 573.88). Anal. calc.: C, 33.49; H, 2.81; N, 39.05 %. Found: C, 33.20; H, 2.61; N, 38.88 %.

**Bis[hydrobis(3-nitro-1,2,4-triazol-1-yl)(pyrazol-1-yl)]iron(II) [Fe(L<sup>3</sup>)<sub>2</sub>] (3).** Synthetic procedure for this compound is the same as for **2**, however the isolation of the product was carried out differently. Thus, to a solution of <sup>n</sup>Bu<sub>4</sub>NL<sup>3</sup> (0.88 g, 1.61 mmol) in dry air-free DCM (50 ml), FeCl<sub>2</sub>·4H<sub>2</sub>O (0.16 g, 0.80 mmol) was added under argon. After vigorous stirring for 1 h at room temperature, the solvent was removed under vacuum. The residue was suspended in minimal amount of ethanol. The formed precipitate was filtered, washed with cold EtOH and air-dried to afford 0.35 g of product as a yellow powder. Solubility properties are similar to those for **2**, however the compound is solubilized more readily with alcohols. Yield: 64 %. IR (neat, cm<sup>-1</sup>): 3144w, 2517w (ν(B–H)), 1554m, 1501s, 1421m, 1311vs, 1173s, 1046m; C<sub>14</sub>H<sub>12</sub>B<sub>2</sub>FeN<sub>20</sub>O<sub>8</sub> (M = 665.85). Anal. calc.: C, 25.25; H, 1.82; N, 42.07 %. Found: C, 25.41; H, 1.86; N, 41.95 %.

**Bis[hydrobis(pyrazol-1-yl)(3-cyano-1,2,4-triazol-1-yl)]iron(II) [Fe(L<sup>4</sup>)<sub>2</sub>] (4).** The synthesis and work up procedure were the same as in **2**. The substance appears as a brick-red powder. Yield: 65 %. Solubility of the compound is similar to such in complex **2**. Single crystals suitable for X-ray diffraction were obtained by slow solvent evaporation from saturated DCM solution. IR (neat, cm<sup>-1</sup>): 3114w, 2511w (ν(B–H)), 2248w (ν(C≡N)), 1501w, 1469w, 1406m, 1315m, 1220m, 1171m, 1112m, 1049m, 755s, 713vs; C<sub>18</sub>H<sub>16</sub>B<sub>2</sub>FeN<sub>16</sub> (M = 533.90). Anal. calc.: C, 40.49; H, 3.02; N, 41.98 %. Found: C, 40.53; H, 2.95; N, 41.82 %.

**Bis[hydrobis(3-cyano-1,2,4-triazol-1-yl)(pyrazol-1-yl)]iron(II) [Fe(L<sup>5</sup>)<sub>2</sub>] (5).** FeCl<sub>2</sub>·4H<sub>2</sub>O (0.31 g, 1.56 mmol) was added to a vigorously stirred solution of <sup>n</sup>Bu<sub>4</sub>NL<sup>5</sup> (1.56 g, 3.07 mmol) in dry air-free DCM (75 ml). In 5 min of stirring, a bright red precipitate appeared. The mixture was stirred for 1 h. Afterwards, the precipitate was filtered. Formation of the precipitate continued in the filtrate, thus the latter was concentrated and the precipitate was filtered. For further purification the precipitations may be subjected to washing with minimal quantities of ethanol as in case of **3**. Eventually, additional quantity of product is accessible by evaporation of the second filtrate and treatment of the residue with ethanol. 0.42 g. Yield: 47 %. The compound is insoluble in water, poorly soluble in DCM, soluble in alcohols and acetone. IR (neat, cm<sup>-1</sup>): 3126<sub>w</sub>, 2526<sub>w</sub> (ν(B–H)), 2251<sub>w</sub> (ν(C≡N)), 1505<sub>w</sub>, 1464<sub>w</sub>, 1405<sub>w</sub>, 1337<sub>m</sub>, 1317<sub>w</sub>, 1167<sub>m</sub>, 1109<sub>w</sub>, 1020<sub>m</sub>, 761<sub>s</sub>, 712<sub>vs</sub>; C<sub>18</sub>H<sub>12</sub>B<sub>2</sub>FeN<sub>20</sub> (M = 585.90). Anal. calc.: C, 36.90; H, 2.06; N, 47.81 %. Found: C, 36.40; H, 2.33; N, 47.49 %.

**Bis[hydrobis(pyrazol-1-yl)(3-amino-1,2,4-triazol-1-yl)]iron(II) [Fe(L<sup>6</sup>)<sub>2</sub>] (6).** Compound **2** (0.36 g, 0.63 mmol) and Pd/C (11 mg) were placed into an autoclave. The charged autoclave was degassed. Then, methanol (18 ml) was added. The resulting stirred suspension was heated to 80 °C and hydrogenated at 15 bars for 22 h. After cooling down to room temperature and depressurizing, the content of the autoclave was poured into methanol (460 ml), and the obtained suspension was heated to sub-reflux under stirring in order to dissolve the product. Afterwards, the mixture was filtered to remove the catalyst. The filtrate was concentrated until formation of a precipitate. The latter was filtered, washed with cold methanol and air-dried to afford 0.23 g of a deep purple powder of the product. Yield: 71 %. The complex is poorly soluble in methanol. Single crystals suitable for X-ray diffraction are accessible by slow evaporation of the saturated methanolic solution. IR (neat, cm<sup>-1</sup>): 3474<sub>w</sub>, 3307<sub>w</sub> (ν<sub>as</sub>(NH<sub>2</sub>)), 3215<sub>w</sub> (ν<sub>s</sub>(NH<sub>2</sub>)), 3168<sub>w</sub> (NH<sub>2</sub>), 2474<sub>w</sub> (ν(B–H)), 1634<sub>m</sub>, 1548<sub>s</sub>, 1505<sub>m</sub>, 1392<sub>m</sub>, 1302<sub>s</sub>, 1206<sub>s</sub>, 1166<sub>s</sub>, 1107<sub>s</sub>, 1045<sub>s</sub>, 1023<sub>s</sub>; C<sub>16</sub>H<sub>20</sub>B<sub>2</sub>FeN<sub>16</sub> (M = 513.91). Anal. calc.: C, 37.39; H, 3.92; N, 43.61 %. Found: C, 37.63; H, 3.57; N, 43.49 %.

**Bis[hydrobis(3-amino-1,2,4-triazol-1-yl)(pyrazol-1-yl)]iron(II) [Fe(L<sup>7</sup>)<sub>2</sub>] (7).** The stirred suspension of **3** (0.29 g, 0.44 mmol) and Pd/C (10 mg) in methanol (20 ml) was heated at 80 °C and hydrogenated at 30 bars for 22 h. After the hydrogenation, the catalyst was filtered and the solvent was removed *in vacuo* to afford 0.22 g of the product as a dark green solid. Yield: 91 %. The substance is soluble in alcohols. IR (neat, cm<sup>-1</sup>): 3464<sub>w</sub>, 3324<sub>w</sub> (ν<sub>as</sub>(NH<sub>2</sub>)), 3210<sub>w</sub> (ν<sub>s</sub>(NH<sub>2</sub>)), 3114<sub>w</sub> (NH<sub>2</sub>), 2470<sub>w</sub> (ν(B–H)), 1614<sub>m</sub>, 1538<sub>s</sub>, 1505<sub>m</sub>, 1417<sub>w</sub>, 1388<sub>w</sub>, 1304<sub>m</sub>, 1210<sub>w</sub>, 1166<sub>s</sub>, 1110<sub>m</sub>, 1055<sub>s</sub>, 1025<sub>s</sub>, 1012<sub>s</sub>; C<sub>16</sub>H<sub>20</sub>B<sub>2</sub>FeN<sub>16</sub> (M = 513.91). Anal. calc.: C, 30.69; H, 4.05; N, 51.13 %. Found: C, 30.45; H, 4.30; N, 51.26 %.

**Chapter 3.** Lanthanide nitrates Ln(NO<sub>3</sub>)<sub>3</sub>·6H<sub>2</sub>O of commercial grade were used without further purification. Synthetic procedure for tetramethyl *N,N'*-(2,2,3,3,4,4-hexafluoro-1,5-dioxopentane-1,5-

diyl)bis(phosphoramidate) or  $H_2L^8$  was slightly modified comparing to the reported one and given below. Sodium salt  $Na_2L^8$  was prepared by deprotonation of the neutral ligand with methanolic solution of sodium methoxide according to the procedures reported earlier.<sup>122</sup>

**Tetramethyl  $N,N'$ -(2,2,3,3,4,4-hexafluoro-1,5-dioxopentane-1,5-diyl)bis(phosphoramidate) ( $H_2L^8$ ).** Fine powders of 2,2,3,3,4,4-hexafluoropentanediamide (13.25 g, 56 mmol) and phosphorus pentachloride (23.18 g, 112 mmol) were combined in a 500-ml round-bottom flask equipped with a water-cooled condenser connected to a bubble counter. Tetrachloromethane (50 ml) was added to the flask and the resulting mixture was heated to 65 °C and stirred at this temperature until the hydrogen chloride evolution rate slowed down. Afterwards the temperature was increased to about 75 °C and the reaction was allowed to continue until hydrogen chloride evolution ceased. Then the mixture was cooled down to room temperature and the solvent was removed in vacuum. The resulting residue was dissolved in tetrahydrofuran (70 ml) and added dropwise to a stirred solution of triethylamine (62 ml, 445 mmol) in methanol (150 ml) cooled down to -5 °C. The temperature upon addition was kept in the range of 0–5 °C. The obtained solution was allowed to warm up to room temperature and left to stay overnight. Then the solvents were evaporated under vacuum. The obtained residue was dissolved in water (100 ml), whereupon acetic acid was carefully added to the solution until its medium became weakly acidic. The white precipitate formed was filtered, washed with water and dried in air to give 17.30 g of the product as a white powder. Yield: 68%. IR (KBr,  $cm^{-1}$ ): 3095 $w$  ( $\nu(N-H)$ ), 1746 $s$  ( $\nu(C=O)$ ), 1478 $m$  (Amide-2), 1212 $s$  ( $\nu(P=O)$ );  $^1H$  NMR (400 MHz, DMSO- $d_6$ )  $\delta$  11.38 (d, NH, 2H), 3.74 (d,  $J = 11.6$  Hz, 12H).

**General synthetic procedure for  $[Ln_2(L^8)_3(phen)_2]$  (8-14).**  $Ln(NO_3)_3 \cdot 6H_2O$  (0.10 mmol) was dissolved in methanol (2 ml) and  $HC(OC_2H_5)_3$  (0.1 ml, 0.60 mmol) as dehydrating agent was added to the solution. Afterwards, the solution was boiled for a minute, cooled down to room temperature and then added to a solution of  $H_2L^8$  (0.068 g, 0.15 mmol) and of triethylamine (0.041 ml, 0.30 mmol) in methanol. Finally a solution of 1,10-phenanthroline (0.018 g, 0.10 mmol) in methanol was added to the resulting mixture to give an oily precipitation colored as respective metal aqua ion. The obtained mixture was boiled for 5 minutes. Then the leach was decanted. The precipitation was thoroughly washed with 2-propanol, filtered off and dried on air. The color of the obtained complexes corresponds to the respective metal aqua ion. The compounds are well soluble in DMSO and DMF.

**$[Nd_2(L^8)_3(phen)_2]$  (8):** Yield: 74 %; IR (KBr,  $cm^{-1}$ ): 3008 $w$  ( $\nu(CH)$ ), 2958 $w$  ( $\nu(CH)$ ), 2855 $w$  ( $\nu(CH)$ ), 1608 $vs$  ( $\nu(C=O)$ ), 1519 $m$  ( $\nu(CC)_{phen}$ ), 1424 $m$  ( $\nu(CC)_{phen}$ ), 1403 $s$  ( $\nu$ (Amide-2)), 1350 $w$ , 1160 $vs$  ( $\nu(P=O)$ ), 1043 $vs$  ( $\delta$ (POC)), 962 $m$  ( $\nu(PN)$ ), 916 $w$ , 847 $s$ , 810 $m$ , 770 $w$ , 731 $m$ , 534 $w$ , 498 $w$ , 463 $w$ ;  $^1H$  NMR (400 MHz, DMSO- $d_6$ )  $\delta$  9.08 (br, 4H), 8.46 (br, 4H), 7.96 (br, 4H), 7.76 (br, 4H), 4.12 (br, 36H);

$C_{51}H_{52}N_{10}O_{24}P_6F_{18}Nd_2$  (M = 2005.31). Anal. calc.: Nd, 14.4; C, 30.55; H, 2.61; N, 6.98 %. Found: Nd, 14.6; C, 30.57; H, 2.63; N, 6.95%.

**[Sm<sub>2</sub>(L<sup>8</sup>)<sub>3</sub>(phen)<sub>2</sub>] (9):** Yield: 76 %; IR (KBr, cm<sup>-1</sup>): 3002w (ν(CH)), 2958w (ν(CH)), 2856w (ν(CH)), 1604vs (ν(C=O)), 1521m (ν(CC)<sub>phen</sub>), 1427m (ν(CC)<sub>phen</sub>), 1403s ν(Amide-2), 1350w, 1162vs (ν(P=O)), 1041vs (δ(POC)), 963m (ν(PN)), 916w, 809m, 770w, 731m, 540w, 498w, 460w; <sup>1</sup>H NMR (400 MHz, DMSO-*d*<sub>6</sub>), δ 9.48 (br, 4H), 8.96 (br, 4H), 8.43 (br, 4H), 8.22 (br, 4H), 3.99 (br, 36H);  $C_{51}H_{52}N_{10}O_{24}P_6F_{18}Sm_2$  (M = 2017.55). Anal. calc.: Sm, 14.9; C, 30.36; H, 2.60; N, 6.94 %. Found: Sm, 15.0; C, 30.38; H, 2.63; N, 6.92 %.

**[Eu<sub>2</sub>(L<sup>8</sup>)<sub>3</sub>(phen)<sub>2</sub>] (10):** Yield: 76 %; IR (KBr, cm<sup>-1</sup>): 3008w (ν(CH)), 2958w (ν(CH)), 2855w (ν(CH)), 1604vs (ν(C=O)), 1520m (ν(CC)<sub>phen</sub>), 1428m (ν(CC)<sub>phen</sub>), 1399s ν(Amide-2), 1350w, 1163vs (ν(P=O)), 1043vs (δ(POC)), 962m (ν(PN)), 916w, 846s, 809m, 770w, 731m, 541w, 500w, 462w; <sup>1</sup>H NMR (400 MHz, DMSO-*d*<sub>6</sub>) δ 9.09 (br, 4H), 8.53 (br, 4H), 7.99 (br, 4H), 7.73 (br, 4H), 2.90 (br, 36H);  $C_{51}H_{52}N_{10}O_{24}P_6F_{18}Eu_2$  (M = 2020.75). Anal. calc.: Eu, 15.0; C, 30.31; H, 2.59; N, 6.93 %. Found: Eu, 15.4; C, 30.33; H, 2.60; N, 6.90 %.

**[Tb<sub>2</sub>(L<sup>8</sup>)<sub>3</sub>(phen)<sub>2</sub>] (11):** Yield: 75%; IR (KBr, cm<sup>-1</sup>): 3007w (ν(CH)), 2958w (ν(CH)), 2854w (ν(CH)), 1610vs (ν(C=O)), 1522m (ν(CC)<sub>phen</sub>), 1427m (ν(CC)<sub>phen</sub>), 1404s ν(Amide-2), 1350w, 1165vs (ν(P=O)), 1042vs (δ(POC)), 964m (ν(PN)), 918w, 847s, 811m, 770w, 731m, 536w, 501w, 464w;  $C_{51}H_{52}N_{10}O_{24}P_6F_{18}Tb_2$  (M = 2034.68). Anal. calc.: Tb, 15.6; C, 30.11; H, 2.58; N, 6.88 %. Found: Tb, 15.9; C, 30.14; H, 2.61; N, 6.86 %.

**[Dy<sub>2</sub>(L<sup>8</sup>)<sub>3</sub>(phen)<sub>2</sub>] (12):** Yield: 73 %; IR (KBr, cm<sup>-1</sup>): 3007w (ν(CH)), 2959w (ν(CH)), 2856w (ν(CH)), 1607vs (ν(C=O)), 1522m (ν(CC)<sub>phen</sub>), 1424m (ν(CC)<sub>phen</sub>), 1405s ν(Amide-2), 1350w, 1164vs (ν(P=O)), 1043vs (δ(POC)), 964m (ν(PN)), 918w, 812m, 771w, 730m, 540w, 498w, 462w;  $C_{51}H_{52}N_{10}O_{24}P_6F_{18}Dy_2$  (M = 2041.83). Anal. calc.: Dy, 15.9; C, 30.00; H, 2.57; N, 6.86 %. Found: Dy, 16.3; C, 30.04; H, 2.59; N, 6.84 %.

**[Yb<sub>2</sub>(L<sup>8</sup>)<sub>3</sub>(phen)<sub>2</sub>] (13):** Yield: 77 %; IR (KBr, cm<sup>-1</sup>): 3011w (ν(CH)), 2958w (ν(CH)), 2856w (ν(CH)), 1607vs (ν(C=O)), 1522m (ν(CC)<sub>phen</sub>), 1427m (ν(CC)<sub>phen</sub>), 1406s ν(Amide-2), 1350w, 1165vs (ν(P=O)), 1041vs (δ(POC)), 964m (ν(PN)), 920w, 847s, 813m, 771w, 731m, 540w, 498w, 462w;  $C_{51}H_{52}N_{10}O_{24}P_6F_{18}Yb_2$  (M = 2062.93). Anal. calc.: Yb, 16.8; C, 29.69; H, 2.54; N, 6.79 %. Found: Yb, 17.1; C, 29.72; H, 2.58; N, 6.76 %.

**[Y<sub>2</sub>(L<sup>8</sup>)<sub>3</sub>(phen)<sub>2</sub>] (14):** Was synthesized following the same procedure for its lanthanide counterparts. Yield: 74 %; IR (KBr, cm<sup>-1</sup>): 3004w (ν(CH)), 2958w (ν(CH)), 2855w (ν(CH)), 1613vs (ν(C=O)), 1522m (ν(CC)<sub>phen</sub>), 1428m (ν(CC)<sub>phen</sub>), 1406s ν(Amide-2), 1350w, 1165vs (ν(P=O)), 1043vs (δ(POC)), 964m

( $\nu(\text{PN})$ ), 919 $w$ , 847 $s$ , 813 $m$ , 771 $w$ , 732 $m$ , 542 $w$ , 495 $w$ , 466 $w$ ;  $^1\text{H NMR}$  (400 MHz,  $\text{DMSO-}d_6$ )  $\delta$  9.19 (br, 4H), 8.55 (br, 4H), 8.03 (s, 4H), 7.83 (br, 4H), 3.56 (d,  $J = 11.1$  Hz, 36H);  $\text{C}_{51}\text{H}_{52}\text{N}_{10}\text{O}_{24}\text{P}_6\text{F}_{18}\text{Y}_2$  ( $M = 1894.64$ ). Anal. calc.: Y, 9.4; C, 32.33; H, 2.77; N, 7.39 %. Found: Y, 9.7; C, 32.35; H, 2.79; N, 7.35 %.

**$\text{Na}_2\text{L}^8$** . Yield: 93%; IR (KBr,  $\text{cm}^{-1}$ ): 1630 $s$  ( $\nu(\text{C=O})$ ), 1406 $m$  (Amide-2), 1202 $s$  ( $\nu(\text{P=O})$ );  $^1\text{H NMR}$  (400 MHz,  $\text{DMSO-}d_6$ , 25 °C):  $\delta = 3.44$  ppm (d,  $J = 11.0$  Hz, 12H);  $\text{C}_9\text{H}_{12}\text{N}_2\text{O}_8\text{P}_2\text{F}_6\text{Na}_2$  ( $M = 498.12$ ). Anal. calc.: C, 21.70; H, 2.43; N, 5.62%. Found: C, 21.72; H, 2.46; N, 5.58%.

**Synthesis of  $\text{NEt}_4[\text{NaLn}_2(\text{L}^8)_4(\text{H}_2\text{O})]$  {Ln = La (15), Nd (16)}**.  $\text{Ln}(\text{NO}_3)_3 \cdot 6\text{H}_2\text{O}$  (0.10 mmol) was dissolved in 2-propanol (2.5 ml), afterwards a dehydrating agent – triethyl orthoformate (0.15 ml, 0.90 mmol) was added to the solution and the latter was heated up to boiling for 1 minute. The obtained solution was cooled down to room temperature, then mixed with the combined solutions of  $\text{Na}_2\text{L}^8$  (0.10 g, 0.20 mmol) and  $\text{NEt}_4\text{Cl}$  (0.008 g, 0.05 mmol) in acetone (10 ml). The obtained mixture was heated up and boiled for a minute, then cooled down to the room temperature. After the filtration of  $\text{NaNO}_3$  and  $\text{NaCl}$  precipitate, the clear solution was allowed to stand for few days to yield colorless (15) and lilac-colored (16) prismatic crystals of the desired products. The complexes are moderately soluble in polar solvents, mainly in methanol, acetonitrile and acetone. It is notable that double excess of  $\text{NEt}_4\text{Cl}$  does not influence on the final composition of the complex.

**$\text{NEt}_4[\text{NaLa}_2(\text{L}^8)_4(\text{H}_2\text{O})]$  (15)**. Yield: 60%; IR (KBr,  $\text{cm}^{-1}$ ): 1621 $s$  ( $\nu(\text{C=O})$ ), 1411 $m$  (Amide-2), 1159 $s$  ( $\nu(\text{P=O})$ );  $^1\text{H NMR}$  (400 MHz,  $\text{DMSO-}d_6$ , 25 °C):  $\delta = 3.59$  ppm (d,  $J = 11.2$  Hz, 48H,  $\text{L}^{2-}$ ), 3.25 ppm (q,  $J = 7.0$  Hz, 8H,  $\text{NEt}_4^+$ ), 1.21 ppm (t,  $J = 7.0$  Hz, 12H,  $\text{NEt}_4^+$ );  $\text{C}_{44}\text{H}_{70}\text{N}_9\text{O}_{33}\text{P}_8\text{F}_{24}\text{NaLa}_2$  ( $M = 2257.63$ ). Anal. calc.: C, 23.41; H, 3.13; N, 5.58%. Found: C, 23.03; H, 3.08; N, 5.59%.

**$\text{NEt}_4[\text{NaNd}_2(\text{L}^8)_4(\text{H}_2\text{O})]$  (16)**. Yield: 62%; IR (KBr,  $\text{cm}^{-1}$ ): 1623 $s$  ( $\nu(\text{C=O})$ ), 1410 $m$  (Amide-2), 1160 $s$  ( $\nu(\text{P=O})$ );  $^1\text{H NMR}$  (400 MHz,  $\text{DMSO-}d_6$ , 25 °C):  $\delta = 4.17$  ppm (br, 48H,  $\text{L}^{2-}$ ), 3.21 ppm (q,  $J = 7.1$  Hz, 8H,  $\text{NEt}_4^+$ ), 1.19 ppm (t,  $J = 7.1$  Hz, 12H,  $\text{NEt}_4^+$ );  $\text{C}_{44}\text{H}_{70}\text{N}_9\text{O}_{33}\text{P}_8\text{F}_{24}\text{NaNd}_2$  ( $M = 2268.30$ ). Anal. calc.: C, 23.30; H, 3.11; N, 5.56%. Found: C, 22.55; H, 3.07; N, 5.51%.

**Synthesis of  $\text{Na}[\text{NaLn}_2(\text{L}^8)_4(\text{H}_2\text{O})] \cdot 2\text{H}_2\text{O}$  [Ln = La (17), Nd (18)]** The procedure is mainly the same as for  $\text{NEt}_4[\text{NaLn}_2(\text{L}^8)_4(\text{H}_2\text{O})]$  excluding the use of  $\text{NEt}_4\text{Cl}$ . The resulting crystalline products possess similar color and solubility properties to 15 and 16.

**$\text{Na}[\text{NaLa}_2(\text{L}^8)_4(\text{H}_2\text{O})] \cdot 2\text{H}_2\text{O}$  (17)**. Yield: 61%; IR (KBr,  $\text{cm}^{-1}$ ): 1622 $s$  ( $\nu(\text{C=O})$ ), 1412 $m$  (Amide-2), 1160 $s$  ( $\nu(\text{P=O})$ );  $^1\text{H NMR}$  (400 MHz,  $\text{DMSO-}d_6$ , 25 °C):  $\delta = 3.53$  ppm (d,  $J = 11.2$  Hz, 48H,  $\text{L}^{2-}$ ).  $\text{C}_{36}\text{H}_{54}\text{N}_8\text{O}_{35}\text{P}_8\text{F}_{24}\text{Na}_2\text{La}_2$  ( $M = 2186.43$ ). Anal. calc.: C, 19.78; H, 2.49; N, 5.13%. Found: C, 19.81; H, 2.53; N, 5.09%.

**Na[NaNd<sub>2</sub>(L<sup>8</sup>)<sub>4</sub>(H<sub>2</sub>O)]·2H<sub>2</sub>O (18).** Yield: 64%; IR (KBr, cm<sup>-1</sup>): 1624<sub>s</sub> (ν(C=O)), 1411<sub>m</sub> (Amide-2), 1161<sub>s</sub> (ν(P=O)); <sup>1</sup>H NMR (400 MHz, DMSO-*d*<sub>6</sub>, 25 °C): δ = 3.92 ppm (br, 48H, L<sup>2-</sup>); C<sub>36</sub>H<sub>54</sub>N<sub>8</sub>O<sub>35</sub>P<sub>8</sub>F<sub>24</sub>Na<sub>2</sub>Nd<sub>2</sub> (M = 2197.09). Anal. calc.: C, 19.68; H, 2.48; N, 5.10%. Found: C, 19.73; H, 2.50; 5.07%.

## Bibliographic References

- (1) *Spin-Crossover Materials: Properties and Applications*; Halcrow, M. A., Ed.; John Wiley & Sons Ltd: Oxford, UK, 2013. <https://doi.org/10.1002/9781118519301>.
- (2) Gütlich, P.; Goodwin, H. A. Spin Crossover—An Overall Perspective. In *Spin Crossover in Transition Metal Compounds I*; Gütlich, P., Goodwin, H. A., Eds.; Springer-Verlag Berlin Heidelberg: Berlin, Heidelberg, 2004; Vol. 233, pp 1–47. <https://doi.org/10.1007/b13527>.
- (3) Ewald, A. H.; Martin, R. L.; Ross, I. G.; White, A. H. Anomalous Behaviour at the 6A1-2T2 Crossover in Iron (III) Complexes. *Proc. R. Soc. London. Ser. A. Math. Phys. Sci.* **1964**, 280 (1381), 235–257. <https://doi.org/10.1098/rspa.1964.0143>.
- (4) Bousseksou, A. Spin Crossover Phenomenon. *C. R. Chim.* **2018**, 21 (12), 1055–1300.
- (5) Gütlich, P.; Hauser, A.; Spiering, H. Thermal and Optical Switching of Iron(II) Complexes. *Angew. Chem. Int. Ed.* **1994**, 33 (20), 2024–2054. <https://doi.org/10.1002/anie.199420241>.
- (6) Bousseksou, A.; Molnár, G.; Salmon, L.; Nicolazzi, W. Molecular Spin Crossover Phenomenon: Recent Achievements and Prospects. *Chem. Soc. Rev.* **2011**, 40 (6), 3313. <https://doi.org/10.1039/c1cs15042a>.
- (7) Kahn, O.; Martinez, C. J. Spin-Transition Polymers: From Molecular Materials Toward Memory Devices. *Science (80-. )*. **1998**, 279 (5347), 44–48. <https://doi.org/10.1126/science.279.5347.44>.
- (8) Seredyuk, M.; Gaspar, A. B.; Ksenofontov, V.; Reiman, S.; Galyametdinov, Y.; Haase, W.; Rentschler, E.; Gütlich, P. Room Temperature Operational Thermochromic Liquid Crystals. *Chem. Mater.* **2006**, 18 (10), 2513–2519. <https://doi.org/10.1021/cm052632w>.
- (9) Krober, J.; Coddjovi, E.; Kahn, O.; Groliere, F.; Jay, C. A Spin Transition System with a Thermal Hysteresis at Room Temperature. *J. Am. Chem. Soc.* **1993**, 115 (21), 9810–9811. <https://doi.org/10.1021/ja00074a062>.
- (10) Guionneau, P.; Marchivie, M.; Bravic, G.; Létard, J.-F.; Chasseau, D. Structural Aspects of Spin Crossover. Example of the [FeIII<sub>n</sub>(NCS)<sub>2</sub>] Complexes. In *Spin Crossover in Transition Metal Compounds II*; Gütlich, P., Goodwin, H. A., Eds.; Springer Berlin Heidelberg: Berlin, Heidelberg, 2004; pp 97–128. <https://doi.org/10.1007/b95414>.
- (11) Senthil Kumar, K.; Ruben, M. Emerging Trends in Spin Crossover (SCO) Based Functional Materials and Devices. *Coord. Chem. Rev.* **2017**, 346, 176–205.

<https://doi.org/10.1016/j.ccr.2017.03.024>.

- (12) Kahn, O.; Kröber, J.; Jay, C. Spin Transition Molecular Materials for Displays and Data Recording. *Adv. Mater.* **1992**, *4* (11), 718–728. <https://doi.org/10.1002/adma.19920041103>.
- (13) Grosjean, A.; Daro, N.; Pechev, S.; Etrillard, C.; Chastanet, G.; Guionneau, P. Crystallinity and Microstructural Versatility in the Spin-Crossover Polymeric Material [Fe(Htrz)<sub>2</sub>(Trz)](BF<sub>4</sub>). *Eur. J. Inorg. Chem.* **2018**, *2018* (3–4), 429–434. <https://doi.org/10.1002/ejic.201701150>.
- (14) Chen, Y.-C.; Meng, Y.; Ni, Z.-P.; Tong, M.-L. Synergistic Electrical Bistability in a Conductive Spin Crossover Heterostructure. *J. Mater. Chem. C* **2015**, *3* (5), 945–949. <https://doi.org/10.1039/C4TC02580F>.
- (15) Molnár, G.; Rat, S.; Salmon, L.; Nicolazzi, W.; Bousseksou, A. Spin Crossover Nanomaterials: From Fundamental Concepts to Devices. *Adv. Mater.* **2018**, *30* (5), 1703862. <https://doi.org/10.1002/adma.201703862>.
- (16) Piedrahita-Bello, M.; Angulo-Cervera, J. E.; Enriquez-Cabrera, A.; Molnár, G.; Tondu, B.; Salmon, L.; Bousseksou, A. Colossal Expansion and Fast Motion in Spin-Crossover@polymer Actuators. *Mater. Horiz.* **2021**, *8* (11), 3055–3062. <https://doi.org/10.1039/d1mh00966d>.
- (17) Manrique-Juárez, M. D.; Mathieu, F.; Laborde, A.; Rat, S.; Shalabaeva, V.; Demont, P.; Thomas, O.; Salmon, L.; Leichle, T.; Nicu, L.; Molnár, G.; Bousseksou, A. Micromachining-Compatible, Facile Fabrication of Polymer Nanocomposite Spin Crossover Actuators. *Adv. Funct. Mater.* **2018**, *28* (29), 1801970. <https://doi.org/10.1002/adfm.201801970>.
- (18) Quintero, C. M.; Félix, G.; Suleimanov, I.; Costa, J. S.; Molnár, G.; Salmon, L.; Nicolazzi, W.; Bousseksou, A. Hybrid Spin-Crossover Nanostructures. *Beilstein J. Nanotechnol.* **2014**, *5* (1), 2230–2239. <https://doi.org/10.3762/bjnano.5.232>.
- (19) Bartual-Murgui, C.; Akou, A.; Thibault, C.; Molnár, G.; Vieu, C.; Salmon, L.; Bousseksou, A. Spin-Crossover Metal-Organic Frameworks: Promising Materials for Designing Gas Sensors. *J. Mater. Chem. C* **2015**, *3* (6), 1277–1285. <https://doi.org/10.1039/c4tc02441a>.
- (20) Ni, Z.-P.; Liu, J.-L.; Hoque, M. N.; Liu, W.; Li, J.-Y.; Chen, Y.-C.; Tong, M.-L. Recent Advances in Guest Effects on Spin-Crossover Behavior in Hofmann-Type Metal-Organic Frameworks. *Coord. Chem. Rev.* **2017**, *335*, 28–43. <https://doi.org/10.1016/j.ccr.2016.12.002>.
- (21) Nakaya, M.; Ohtani, R.; Hayami, S. Guest Modulated Spin States of Metal Complex Assemblies. *Eur. J. Inorg. Chem.* **2020**, *2020* (39), 3709–3719. <https://doi.org/10.1002/ejic.202000553>.

- (22) Sun, L.; Rotaru, A.; Garcia, Y. A Non-Porous Fe(II) Complex for the Colorimetric Detection of Hazardous Gases and the Monitoring of Meat Freshness. *J. Hazard. Mater.* **2022**, *437* (December 2021), 129364. <https://doi.org/10.1016/j.jhazmat.2022.129364>.
- (23) Ohba, M.; Yoneda, K.; Agustí, G.; Muñoz, M. C.; Gaspar, A. B.; Real, J. A.; Yamasaki, M.; Ando, H.; Nakao, Y.; Sakaki, S.; Kitagawa, S. Bidirectional Chemo-Switching of Spin State in a Microporous Framework. *Angew. Chem. Int. Ed.* **2009**, *48* (26), 4767–4771. <https://doi.org/10.1002/anie.200806039>.
- (24) Murray, K. S.; Kepert, C. J. Cooperativity in Spin Crossover Systems: Memory, Magnetism and Microporosity. In *Spin Crossover in Transition Metal Compounds I*; Gülich, P., Goodwin, H. A., Eds.; Springer-Verlag Berlin Heidelberg: Berlin, Heidelberg, 2004; pp 195–228. <https://doi.org/10.1007/b13536>.
- (25) Kraieva, O.; Quintero, C. M.; Suleimanov, I.; Hernandez, E. M.; Lagrange, D.; Salmon, L.; Nicolazzi, W.; Molnár, G.; Bergaud, C.; Bousseksou, A. High Spatial Resolution Imaging of Transient Thermal Events Using Materials with Thermal Memory. *Small* **2016**, *12* (46), 6325–6331. <https://doi.org/10.1002/sml.201601766>.
- (26) Ekanayaka, T. K.; Hao, G.; Mosey, A.; Dale, A. S.; Jiang, X.; Yost, A. J.; Sapkota, K. R.; Wang, G. T.; Zhang, J.; N'Diaye, A. T.; Marshall, A.; Cheng, R.; Naeemi, A.; Xu, X.; Dowben, P. A. Nonvolatile Voltage Controlled Molecular Spin-State Switching for Memory Applications. *Magnetochemistry* **2021**, *7* (3), 37. <https://doi.org/10.3390/magnetochemistry7030037>.
- (27) Lefter, C.; Davesne, V.; Salmon, L.; Molnár, G.; Demont, P.; Rotaru, A.; Bousseksou, A. Charge Transport and Electrical Properties of Spin Crossover Materials: Towards Nanoelectronic and Spintronic Devices. *Magnetochemistry* **2016**, *2* (1), 18. <https://doi.org/10.3390/magnetochemistry2010018>.
- (28) Zhang, Y.; Séguy, I.; Ridier, K.; Shalabaeva, V.; Piedrahita-Bello, M.; Rotaru, A.; Salmon, L.; Molnár, G.; Bousseksou, A. Resistance Switching in Large-Area Vertical Junctions of the Molecular Spin Crossover Complex [Fe(HB(Tz)<sub>3</sub>)<sub>2</sub>]: ON/OFF Ratios and Device Stability. *J. Phys. Condens. Matter* **2020**, *32* (21), 214010. <https://doi.org/10.1088/1361-648X/ab741e>.
- (29) Ridier, K.; Bas, A. C.; Zhang, Y.; Routaboul, L.; Salmon, L.; Molnár, G.; Bergaud, C.; Bousseksou, A. Unprecedented Switching Endurance Affords for High-Resolution Surface Temperature Mapping Using a Spin-Crossover Film. *Nat. Commun.* **2020**, *11* (1), 1–9. <https://doi.org/10.1038/s41467-020-17362-7>.

- (30) Quintero, C.; Molnár, G.; Salmon, L.; Tokarev, A.; Bergaud, C.; Bousseksou, A. Design of Fluorescent Spin-Crossover Nanoparticles for Thermometry Applications. In *16th International Workshop on Thermal Investigations of ICs and Systems, THERMINIC 2010*; IEEE: Barcelona, Spain, 2010; pp 1–5.
- (31) Salmon, L.; Catala, L. Spin-Crossover Nanoparticles and Nanocomposite Materials. *C. R. Chim.* Elsevier Masson SAS December 1, 2018, pp 1230–1269. <https://doi.org/10.1016/j.crci.2018.07.009>.
- (32) Kitchen, J. A.; White, N. G.; Gandolfi, C.; Albrecht, M.; Jameson, G. N. L.; Tallon, J. L.; Brooker, S. Room-Temperature Spin Crossover and Langmuir–Blodgett Film Formation of an Iron(II) Triazole Complex Featuring a Long Alkyl Chain Substituent: The Tail That Wags the Dog. *Chem. Commun.* **2010**, 46 (35), 6464. <https://doi.org/10.1039/c0cc01008a>.
- (33) Bartual-Murgui, C.; Salmon, L.; Akou, A.; Thibault, C.; Molnár, G.; Mahfoud, T.; Sekkat, Z.; Real, J. A.; Bousseksou, A. High Quality Nano-Patterned Thin Films of the Coordination Compound {Fe(Pyrazine)[Pt(CN)<sub>4</sub>] } Deposited Layer-by-Layer. *New J. Chem.* **2011**, 35 (10), 2089–2094. <https://doi.org/10.1039/c1nj20212j>.
- (34) Cavallini, M. Status and Perspectives in Thin Films and Patterning of Spin Crossover Compounds. *Phys. Chem. Chem. Phys.* **2012**, 14 (34), 11867. <https://doi.org/10.1039/c2cp40879a>.
- (35) Mallah, T.; Cavallini, M. Surfaces, Thin Films and Patterning of Spin Crossover Compounds. *C. R. Chim.* **2018**, 21 (12), 1270–1286. <https://doi.org/10.1016/j.crci.2018.02.007>.
- (36) Enriquez-Cabrera, A.; Rapakousiou, A.; Piedrahita Bello, M.; Molnár, G.; Salmon, L.; Bousseksou, A. Spin Crossover Polymer Composites, Polymers and Related Soft Materials. *Coord. Chem. Rev.* **2020**, 419, 213396. <https://doi.org/10.1016/j.ccr.2020.213396>.
- (37) Soyer, H.; Dupart, E.; Gómez-García, C. J.; Mingotaud, C.; Delhaès, P. First Magnetic Observation of a Spin Crossover in a Langmuir–Blodgett Film. *Adv. Mater.* **1999**, 11 (5), 382–384. [https://doi.org/10.1002/\(SICI\)1521-4095\(199903\)11:5<382::AID-ADMA382>3.0.CO;2-U](https://doi.org/10.1002/(SICI)1521-4095(199903)11:5<382::AID-ADMA382>3.0.CO;2-U).
- (38) Roubeau, O.; Agricole, B.; Clérac, R.; Ravaine, S. Triazole-Based Magnetic Langmuir–Blodgett Films: Paramagnetic to Spin-Crossover Behavior. *J. Phys. Chem. B* **2004**, 108 (39), 15110–15116. <https://doi.org/10.1021/jp048194i>.
- (39) Tissot, A.; Bardeau, J.-F.; Rivière, E.; Brisset, F.; Boillot, M.-L. Thermo- and Photoswitchable Spin-Crossover Nanoparticles of an Iron(II) Complex Trapped in Transparent Silica Thin Films.

- Dalton Trans.* **2010**, 39 (33), 7806. <https://doi.org/10.1039/c0dt00321b>.
- (40) Akou, A.; Gural'skiy, I. A.; Salmon, L.; Bartual-Murgui, C.; Thibault, C.; Vieu, C.; Molnár, G.; Bousseksou, A. Soft Lithographic Patterning of Spin Crossover Complexes. Part 2: Stimuli-Responsive Diffraction Grating Properties. *J. Mater. Chem.* **2012**, 22 (9), 3752–3757. <https://doi.org/10.1039/c2jm15663f>.
- (41) Kuroiwa, K.; Shibata, T.; Sasaki, S.; Ohba, M.; Takahara, A.; Kunitake, T.; Kimizuka, N. Supramolecular Control of Spin-Crossover Phenomena in Lipophilic Fe(II)-1,2,4-Triazole Complexes. *J. Polym. Sci. Part A Polym. Chem.* **2006**, 44 (17), 5192–5202. <https://doi.org/10.1002/pola.21601>.
- (42) Cobo, S.; Molnár, G.; Real, J. A.; Bousseksou, A. Multilayer Sequential Assembly of Thin Films That Display Room-Temperature Spin Crossover with Hysteresis. *Angew. Chem. Int. Ed.* **2006**, 45 (35), 5786–5789. <https://doi.org/10.1002/anie.200601885>.
- (43) Kumar, K. S.; Ruben, M. Sublimable Spin-Crossover Complexes: From Spin-State Switching to Molecular Devices. *Angew. Chem. Int. Ed.* **2021**, 60 (14), 7502–7521. <https://doi.org/10.1002/anie.201911256>.
- (44) Gavara-Edo, M.; Valverde-Muñoz, F. J.; Córdoba, R.; Muñoz, M. C.; Herrero-Martín, J.; Real, J. A.; Coronado, E. Sublimable Complexes with Spin Switching: Chemical Design, Processing as Thin Films and Integration in Graphene-Based Devices. *J. Mater. Chem. C* **2023**. <https://doi.org/10.1039/D2TC04120K>.
- (45) Jenekhe, S. A. The Rheology and Spin Coating of Polyimide Solutions. *Polym. Eng. Sci.* **1983**, 23 (15), 830–834. <https://doi.org/10.1002/pen.760231508>.
- (46) Binnig, G.; Quate, C. F.; Gerber, C. Atomic Force Microscope. *Phys. Rev. Lett.* **1986**, 56 (9), 930–933. <https://doi.org/10.1103/PhysRevLett.56.930>.
- (47) Meyer, G.; Amer, N. M. Optical-beam-deflection Atomic Force Microscopy: The NaCl (001) Surface. *Appl. Phys. Lett.* **1990**, 56 (21), 2100–2101. <https://doi.org/10.1063/1.102985>.
- (48) Agarwal, D. H.; Bhatt, P. M.; Pathan, A. M.; Patel, H.; Joshi, U. S. Development of Portable Experimental Set-up for AFM to Work at Cryogenic Temperature. In *AIP Conference Proceedings*; 2012; Vol. 1447, pp 531–532. <https://doi.org/10.1063/1.4710113>.
- (49) Shalabaeva, V.; Rat, S.; Manrique-Juarez, M. D.; Bas, A.-C.; Vendier, L.; Salmon, L.; Molnár, G.; Bousseksou, A. Vacuum Deposition of High-Quality Thin Films Displaying Spin Transition near Room Temperature. *J. Mater. Chem. C* **2017**, 5 (18), 4419–4425.

- <https://doi.org/10.1039/C7TC00999B>.
- (50) McMullan, D. Scanning Electron Microscopy 1928-1965. *Scanning* **2006**, *17* (3), 175–185. <https://doi.org/10.1002/sca.4950170309>.
- (51) Min, H. S. Scanning Electron Microscopy Analysis of Thin Films: A Review. In *Research Aspects in Chemical and Materials Sciences Vol. 5*; B P International, 2022; pp 16–28. <https://doi.org/10.9734/bpi/racms/v5/4419E>.
- (52) Molnár, G.; Cobo, S.; Real, J. A.; Carcenac, F.; Daran, E.; Vieu, C.; Bousseksou, A. A Combined Top-Down/Bottom-Up Approach for the Nanoscale Patterning of Spin-Crossover Coordination Polymers. *Adv. Mater.* **2007**, *19* (16), 2163–2167. <https://doi.org/10.1002/adma.200700448>.
- (53) Siek, M. M. Electrochemical Preparation of Ag- and Au-Based Plasmonic Platforms; Doctoral thesis, Institute for Basic Science, Ulsan, South Korea, 2015. <https://doi.org/10.13140/RG.2.2.24644.01924>.
- (54) Kamarulzaman, N.; Hilmi, M. Synthesis and Stoichiometric Analysis of a Li-Ion Battery Cathode Material. In *Stoichiometry and Materials Science - When Numbers Matter*; Innocenti, A., Kamarulzaman, N., Eds.; InTech, 2012; pp 247–262. <https://doi.org/10.5772/33189>.
- (55) Atzori, M.; Poggini, L.; Squillantini, L.; Cortigiani, B.; Gonidec, M.; Bencok, P.; Sessoli, R.; Mannini, M. Thermal and Light-Induced Spin Transition in a Nanometric Film of a New High-Vacuum Processable Spin Crossover Complex. *J. Mater. Chem. C* **2018**, *6* (33), 8885–8889. <https://doi.org/10.1039/C8TC02685H>.
- (56) Mcaneney, J. Characteristics of Thin and Ultrathin Film Ferroelectric Capacitor Structures; Doctoral thesis, Queen's University, Belfast, UK, 2005.
- (57) Yin, L.; Adler, I.; Tsang, T.; Matienzo, L. J.; Grim, S. O. Paramagnetism and Shake-up Satellites in X-Ray Photoelectron Spectra. *Chem. Phys. Lett.* **1974**, *24* (1), 81–84. [https://doi.org/10.1016/0009-2614\(74\)80219-8](https://doi.org/10.1016/0009-2614(74)80219-8).
- (58) Burger, K.; Furlani, C.; Mattogno, G. XPS Structural Characterization of Spin-State Crossover in FeII(NCS)2 (Ophen)2. *J. Electron Spectros. Relat. Phenomena* **1980**, *21* (3), 249–256. [https://doi.org/10.1016/0368-2048\(80\)85052-3](https://doi.org/10.1016/0368-2048(80)85052-3).
- (59) Ellingsworth, E. C.; Turner, B.; Szulczewski, G. Thermal Conversion of [Fe(Phen)3](SCN)2 Thin Films into the Spin Crossover Complex Fe(Phen)2(NCS)2. *RSC Adv.* **2013**, *3* (11), 3745. <https://doi.org/10.1039/c3ra22534h>.

- (60) Kipgen, L.; Bernien, M.; Tuzcek, F.; Kuch, W. Spin-Crossover Molecules on Surfaces: From Isolated Molecules to Ultrathin Films. *Adv. Mater.* **2021**, *33* (24), 2008141. <https://doi.org/10.1002/adma.202008141>.
- (61) Davesne, V.; Gruber, M.; Studniarek, M.; Doh, W. H.; Zafeiratos, S.; Joly, L.; Sirotti, F.; Silly, M. G.; Gaspar, A. B.; Real, J. A.; Schmerber, G.; Bowen, M.; Weber, W.; Boukari, S.; Da Costa, V.; Arabski, J.; Wulfhekel, W.; Beaurepaire, E. Hysteresis and Change of Transition Temperature in Thin Films of Fe{[Me2Pyrz]3BH}2, a New Sublimable Spin-Crossover Molecule. *J. Chem. Phys.* **2015**, *142* (19), 194702. <https://doi.org/10.1063/1.4921309>.
- (62) Gruber, M.; Miyamachi, T.; Davesne, V.; Bowen, M.; Boukari, S.; Wulfhekel, W.; Alouani, M.; Beaurepaire, E. Spin Crossover in Fe(Phen)2 (NCS)2 Complexes on Metallic Surfaces. *J. Chem. Phys.* **2017**, *146* (9), 092312. <https://doi.org/10.1063/1.4973511>.
- (63) Iasco, O.; Boillot, M.-L.; Bellec, A.; Guillot, R.; Rivière, E.; Mazerat, S.; Nowak, S.; Morineau, D.; Brosseau, A.; Miserque, F.; Repain, V.; Mallah, T. The Disentangling of Hysteretic Spin Transition, Polymorphism and Metastability in Bistable Thin Films Formed by Sublimation of Bis(Scorpionate) Fe(  $\text{Scp}$  ) Molecules. *J. Mater. Chem. C* **2017**, *5* (42), 11067–11075. <https://doi.org/10.1039/C7TC03276E>.
- (64) Jasper-Tönnies, T.; Gruber, M.; Karan, S.; Jacob, H.; Tuzcek, F.; Berndt, R. Deposition of a Cationic Fe III Spin-Crossover Complex on Au(111): Impact of the Counter Ion. *J. Phys. Chem. Lett.* **2017**, *8* (7), 1569–1573. <https://doi.org/10.1021/acs.jpcclett.7b00457>.
- (65) Mosey, A.; Dale, A. S.; Hao, G.; N'Diaye, A.; Dowben, P. A.; Cheng, R. Quantitative Study of the Energy Changes in Voltage-Controlled Spin Crossover Molecular Thin Films. *J. Phys. Chem. Lett.* **2020**, *11* (19), 8231–8237. <https://doi.org/10.1021/acs.jpcclett.0c02209>.
- (66) Beniwal, S.; Sarkar, S.; Baier, F.; Weber, B.; Dowben, P. A.; Enders, A. Site Selective Adsorption of the Spin Crossover Complex Fe(Phen)2(NCS) on Au(111). *J. Phys. Condens. Matter* **2020**, *32* (32), 324003. <https://doi.org/10.1088/1361-648X/ab808d>.
- (67) Salmon, L.; Molnár, G.; Cobo, S.; Oulié, P.; Etienne, M.; Mahfoud, T.; Demont, P.; Eguchi, A.; Watanabe, H.; Tanaka, K.; Bousseksou, A. Re-Investigation of the Spin Crossover Phenomenon in the Ferrous Complex [Fe(HB(Pz)3)2]. *New J. Chem.* **2009**, *33* (6), 1283. <https://doi.org/10.1039/b902811k>.
- (68) Mahfoud, T.; Molnár, G.; Cobo, S.; Salmon, L.; Thibault, C.; Vieu, C.; Demont, P.; Bousseksou, A. Electrical Properties and Non-Volatile Memory Effect of the [Fe(HB(Pz)3)2] Spin Crossover Complex Integrated in a Microelectrode Device. *Appl. Phys. Lett.* **2011**, *99* (5),

- 9–11. <https://doi.org/10.1063/1.3616147>.
- (69) Palamarciuc, T.; Oberg, J. C.; El Hallak, F.; Hirjibehedin, C. F.; Serri, M.; Heutz, S.; Létard, J.-F.; Rosa, P. Spin Crossover Materials Evaporated under Clean High Vacuum and Ultra-High Vacuum Conditions: From Thin Films to Single Molecules. *J. Mater. Chem.* **2012**, *22* (19), 9690. <https://doi.org/10.1039/c2jm15094h>.
- (70) Bernien, M.; Wiedemann, D.; Hermanns, C. F.; Krüger, A.; Rolf, D.; Kroener, W.; Müller, P.; Grohmann, A.; Kuch, W. Spin Crossover in a Vacuum-Deposited Submonolayer of a Molecular Iron(II) Complex. *J. Phys. Chem. Lett.* **2012**, *3* (23), 3431–3434. <https://doi.org/10.1021/jz3011805>.
- (71) Pronschinske, A.; Bruce, R. C.; Lewis, G.; Chen, Y.; Calzolari, A.; Buongiorno-Nardelli, M.; Shultz, D. A.; You, W.; Dougherty, D. B. Iron(II) Spin Crossover Films on Au(111): Scanning Probe Microscopy and Photoelectron Spectroscopy. *Chem. Commun.* **2013**, *49* (89), 10446. <https://doi.org/10.1039/c3cc44904a>.
- (72) Naggert, H.; Rudnik, J.; Kipgen, L.; Bernien, M.; Nickel, F.; Arruda, L. M.; Kuch, W.; Näther, C.; Tuczek, F. Vacuum-Evaporable Spin-Crossover Complexes: Physicochemical Properties in the Crystalline Bulk and in Thin Films Deposited from the Gas Phase. *J. Mater. Chem. C* **2015**, *3* (30), 7870–7877. <https://doi.org/10.1039/C5TC00930H>.
- (73) Pronschinske, A.; Chen, Y.; Lewis, G. F.; Shultz, D. A.; Calzolari, A.; Buongiorno Nardelli, M.; Dougherty, D. B. Modification of Molecular Spin Crossover in Ultrathin Films. *Nano Lett.* **2013**, *13* (4), 1429–1434. <https://doi.org/10.1021/nl304304e>.
- (74) Bairagi, K.; Bellec, A.; Fourmental, C.; Iasco, O.; Lagoute, J.; Chacon, C.; Girard, Y.; Rousset, S.; Choueikani, F.; Otero, E.; Ohresser, P.; Saintavit, P.; Boillot, M.-L.; Mallah, T.; Repain, V. Temperature-, Light-, and Soft X-Ray-Induced Spin Crossover in a Single Layer of Fe II - Pyrazolylborate Molecules in Direct Contact with Gold. *J. Phys. Chem. C* **2018**, *122* (1), 727–731. <https://doi.org/10.1021/acs.jpcc.7b11874>.
- (75) Gopakumar, T. G.; Bernien, M.; Naggert, H.; Matino, F.; Hermanns, C. F.; Bannwarth, A.; Mühlenberend, S.; Krüger, A.; Krüger, D.; Nickel, F.; Walter, W.; Berndt, R.; Kuch, W.; Tuczek, F. Spin-Crossover Complex on Au(111): Structural and Electronic Differences Between Mono- and Multilayers. *Chem. Eur. J.* **2013**, *19* (46), 15702–15709. <https://doi.org/10.1002/chem.201302241>.
- (76) Ossinger, S.; Naggert, H.; Kipgen, L.; Jasper-Toennies, T.; Rai, A.; Rudnik, J.; Nickel, F.; Arruda, L. M.; Bernien, M.; Kuch, W.; Berndt, R.; Tuczek, F. Vacuum-Evaporable Spin-

- Crossover Complexes in Direct Contact with a Solid Surface: Bismuth versus Gold. *J. Phys. Chem. C* **2017**, *121* (2), 1210–1219. <https://doi.org/10.1021/acs.jpcc.6b10888>.
- (77) Rohlf, S.; Grunwald, J.; Jasper-Toennies, T.; Johannsen, S.; Diekmann, F.; Studniarek, M.; Berndt, R.; Tucek, F.; Rossnagel, K.; Gruber, M. Influence of Substrate Electronic Properties on the Integrity and Functionality of an Adsorbed Fe(II) Spin-Crossover Compound. *J. Phys. Chem. C* **2019**, *123* (29), 17774–17780. <https://doi.org/10.1021/acs.jpcc.9b02845>.
- (78) Trofimenko, S. *Scorpionates: The Coordination Chemistry of Polypyrazolylborate Ligands*, 1st ed.; Imperial College Press: London, United Kingdom, 1999.
- (79) Rohlf, S.; Gruber, M.; Flöser, B. M.; Grunwald, J.; Jarausch, S.; Diekmann, F.; Kalläne, M.; Jasper-Toennies, T.; Buchholz, A.; Plass, W.; Berndt, R.; Tucek, F.; Rossnagel, K. Light-Induced Spin Crossover in an Fe(II) Low-Spin Complex Enabled by Surface Adsorption. *J. Phys. Chem. Lett.* **2018**, *9* (7), 1491–1496. <https://doi.org/10.1021/acs.jpcclett.8b00338>.
- (80) Manrique-Juarez, M. D.; Mathieu, F.; Shalabaeva, V.; Cacheux, J.; Rat, S.; Nicu, L.; Leichlé, T.; Salmon, L.; Molnár, G.; Bousseksou, A. A Bistable Microelectromechanical System Actuated by Spin-Crossover Molecules. *Angew. Chem. Int. Ed.* **2017**, *56* (28), 8074–8078. <https://doi.org/10.1002/anie.201702739>.
- (81) Shalabaeva, V.; Ridier, K.; Rat, S.; Manrique-Juarez, M. D.; Salmon, L.; Séguy, I.; Rotaru, A.; Molnár, G.; Bousseksou, A. Room Temperature Current Modulation in Large Area Electronic Junctions of Spin Crossover Thin Films. *Appl. Phys. Lett.* **2018**, *112* (1), 013301. <https://doi.org/10.1063/1.5017458>.
- (82) Zhang, Y.; Ridier, K.; Shalabaeva, V.; Séguy, I.; Pelloquin, S.; Camon, H.; Calvez, S.; Routaboul, L.; Salmon, L.; Molnár, G.; Bousseksou, A. A Molecular Spin-Crossover Film Allows for Wavelength Tuning of the Resonance of a Fabry-Perot Cavity. *J. Mater. Chem. C* **2020**, *8* (24), 8007–8011. <https://doi.org/10.1039/d0tc02094j>.
- (83) Ridier, K.; Zhang, Y.; Piedrahita-Bello, M.; Quintero, C. M.; Salmon, L.; Molnár, G.; Bergaud, C.; Bousseksou, A. Heat Capacity and Thermal Damping Properties of Spin-Crossover Molecules: A New Look at an Old Topic. *Adv. Mater.* **2020**, *32* (21), 2000987. <https://doi.org/10.1002/adma.202000987>.
- (84) Miyamachi, T.; Gruber, M.; Davesne, V.; Bowen, M.; Boukari, S.; Joly, L.; Scheurer, F.; Rogez, G.; Yamada, T. K.; Ohresser, P.; Beaurepaire, E.; Wulfhekel, W. Robust Spin Crossover and Memristance across a Single Molecule. *Nat. Commun.* **2012**, *3* (1), 938. <https://doi.org/10.1038/ncomms1940>.

- (85) Flötotto, H.; Secker, T.; Kögerler, P.; Besson, C. Amine-Functionalized Spin Crossover Building Blocks. *Eur. J. Inorg. Chem.* **2019**, No. 43, 4621–4624. <https://doi.org/10.1002/ejic.201900916>.
- (86) Ma, C.; Besson, C. Precise Control of the Degree and Regioselectivity of Functionalization in Nitro- and Amino-Functionalized Di(Trispyrazolylborato)Iron(II) Spin Crossover Complexes. *Dalton Trans.* **2021**, 50 (48), 18077–18088. <https://doi.org/10.1039/D1DT03445F>.
- (87) Desrochers, P. J.; Abdulrahim, A.; Demaree, K. R.; Fortner, J. A.; Freeman, J. D.; Provorse Long, M.; Martin, M. E.; Gómez-García, C. J.; Gerasimchuk, N. Rational Design of Iron Spin-Crossover Complexes Using Heteroscorpionate Chelates. *Inorg. Chem.* **2022**, 61 (47), 18907–18922. <https://doi.org/10.1021/acs.inorgchem.2c02856>.
- (88) Lakowicz, J. R. *Principles of Fluorescence Spectroscopy*, 3rd ed.; Lakowicz, J. R., Ed.; Springer US: Boston, MA, 2006. <https://doi.org/10.1007/978-0-387-46312-4>.
- (89) Braslavsky, S. E. Glossary of Terms Used in Photochemistry, 3rd Edition (IUPAC Recommendations 2006). *Pure Appl. Chem.* **2007**, 79 (3), 293–465. <https://doi.org/10.1351/pac200779030293>.
- (90) Bünzli, J. C. G.; Piguet, C. Taking Advantage of Luminescent Lanthanide Ions. *Chem. Soc. Rev.* **2005**, 34 (12), 1048–1077. <https://doi.org/10.1039/b406082m>.
- (91) Eliseeva, S. V.; Bünzli, J. C. G. Lanthanide Luminescence for Functional Materials and Bio-Sciences. *Chem. Soc. Rev.* **2010**, 39 (1), 189–227. <https://doi.org/10.1039/b905604c>.
- (92) Gomez, G. E. Luminescent Metal-Organic Frameworks (LMOFS) as Multifunctional Materials for Applications in Solid-State Lighting and Sensing. *An. Asoc. Quim. Argent.* **2019**, 106 (2), 97–114.
- (93) de Bettencourt-Dias, A. Lanthanide-Based Emitting Materials in Light-Emitting Diodes. *Dalton Trans.* **2007**, No. 22, 2229. <https://doi.org/10.1039/b702341c>.
- (94) Bünzli, J.-C. G.; Comby, S.; Chauvin, A.-S.; Vandevyver, C. D. B. New Opportunities for Lanthanide Luminescence. *J. Rare Earths* **2007**, 25 (3), 257–274. [https://doi.org/10.1016/S1002-0721\(07\)60420-7](https://doi.org/10.1016/S1002-0721(07)60420-7).
- (95) Carnall, W. T.; Fields, P. R.; Rajnak, K. Electronic Energy Levels of the Trivalent Lanthanide Aquo Ions. IV. Eu 3+. *J. Chem. Phys.* **1968**, 49 (10), 4450–4455. <https://doi.org/10.1063/1.1669896>.

- (96) Carnall, W. T.; Fields, P. R.; Rajnak, K. Electronic Energy Levels in the Trivalent Lanthanide Aquo Ions. I. Pr <sup>3+</sup>, Nd <sup>3+</sup>, Pm <sup>3+</sup>, Sm <sup>3+</sup>, Dy <sup>3+</sup>, Ho <sup>3+</sup>, Er <sup>3+</sup>, and Tm <sup>3+</sup>. *J. Chem. Phys.* **1968**, *49* (10), 4424–4442. <https://doi.org/10.1063/1.1669893>.
- (97) Carnall, W. T.; Fields, P. R.; Rajnak, K. Electronic Energy Levels of the Trivalent Lanthanide Aquo Ions. III. Tb <sup>3+</sup>. *J. Chem. Phys.* **1968**, *49* (10), 4447–4449. <https://doi.org/10.1063/1.1669895>.
- (98) Bünzli, J.-C. G. On the Design of Highly Luminescent Lanthanide Complexes. *Coord. Chem. Rev.* **2015**, *293–294*, 19–47. <https://doi.org/10.1016/j.ccr.2014.10.013>.
- (99) Beeby, A.; Clarkson, I. M.; Dickins, R. S.; Faulkner, S.; Parker, D.; Royle, L.; de Sousa, A. S.; Williams, J. A. G.; Woods, M. Non-Radiative Deactivation of the Excited States of Europium, Terbium and Ytterbium Complexes by Proximate Energy-Matched OH, NH and CH Oscillators: An Improved Luminescence Method for Establishing Solution Hydration States. *J. Chem. Soc. Perkin Trans. 2* **1999**, *2* (3), 493–504. <https://doi.org/10.1039/a808692c>.
- (100) Maas, H.; Currao, A.; Calzaferri, G. Encapsulated Lanthanides as Luminescent Materials. *Angew. Chem. Int. Ed.* **2002**, *41* (14), 2495–2497. [https://doi.org/10.1002/1521-3773\(20020715\)41:14<2495::AID-ANIE2495>3.0.CO;2-G](https://doi.org/10.1002/1521-3773(20020715)41:14<2495::AID-ANIE2495>3.0.CO;2-G).
- (101) Weissman, S. I. Intramolecular Energy Transfer The Fluorescence of Complexes of Europium. *J. Chem. Phys.* **1942**, *10* (4), 214–217. <https://doi.org/10.1063/1.1723709>.
- (102) Förster, T. Excitation Transfer and Internal Conversion. *Chem. Phys. Lett.* **1971**, *12* (2), 422–424. [https://doi.org/10.1016/0009-2614\(71\)85102-3](https://doi.org/10.1016/0009-2614(71)85102-3).
- (103) Bodman, S. E.; Butler, S. J. Advances in Anion Binding and Sensing Using Luminescent Lanthanide Complexes. *Chem. Sci.* **2021**, *12* (8), 2716–2734. <https://doi.org/10.1039/D0SC05419D>.
- (104) Malta, O. L.; Brito, H. F.; Menezes, J. F. S.; Gonçalves e Silva, F. R.; de Mello Donegá, C.; Alves, S. Experimental and Theoretical Emission Quantum Yield in the Compound Eu(Thenoyltrifluoroacetate)<sub>3</sub>·2(Dibenzyl Sulfoxide). *Chem. Phys. Lett.* **1998**, *282* (3–4), 233–238. [https://doi.org/10.1016/S0009-2614\(97\)01283-9](https://doi.org/10.1016/S0009-2614(97)01283-9).
- (105) Sato, S.; Wada, M. Relations between Intramolecular Energy Transfer Efficiencies and Triplet State Energies in Rare Earth β-Diketone Chelates. *Bull. Chem. Soc. Jpn.* **1970**, *43* (7), 1955–1962. <https://doi.org/10.1246/bcsj.43.1955>.
- (106) Latva, M.; Takalo, H.; Mukkala, V.-M.; Matachescu, C.; Rodríguez-Ubis, J. C.; Kankare, J.

- Correlation between the Lowest Triplet State Energy Level of the Ligand and Lanthanide(III) Luminescence Quantum Yield. *J. Lumin.* **1997**, 75 (2), 149–169. [https://doi.org/10.1016/S0022-2313\(97\)00113-0](https://doi.org/10.1016/S0022-2313(97)00113-0).
- (107) Archer, R. D.; Chen, H.; Thompson, L. C. Synthesis, Characterization, and Luminescence of Europium(III) Schiff Base Complexes. *Inorg. Chem.* **1998**, 37 (8), 2089–2095. <https://doi.org/10.1021/ic960244d>.
- (108) Bünzli, J.-C. G.; Eliseeva, S. V. Basics of Lanthanide Photophysics. In *Lanthanide Luminescence. Springer Series on Fluorescence*; Hänninen, P., Härmä, H., Eds.; Springer, Berlin, Heidelberg: Berlin, Heidelberg, 2010; Vol. 7, pp 1–45. [https://doi.org/10.1007/4243\\_2010\\_3](https://doi.org/10.1007/4243_2010_3).
- (109) Pearson, R. G. Hard and Soft Acids and Bases. *J. Am. Chem. Soc.* **1963**, 85 (22), 3533–3539. <https://doi.org/10.1021/ja00905a001>.
- (110) Pearson, R. G. Recent Advances in the Concept of Hard and Soft Acids and Bases. *J. Chem. Educ.* **1987**, 64 (7), 561–567. <https://doi.org/10.1021/ed064p561>.
- (111) Pearson, R. G. Hard and Soft Acids and Bases—the Evolution of a Chemical Concept. *Coord. Chem. Rev.* **1990**, 100, 403–425. [https://doi.org/10.1016/0010-8545\(90\)85016-L](https://doi.org/10.1016/0010-8545(90)85016-L).
- (112) Cotton, S. A.; Harrowfield, J. M. Lanthanides: Coordination Chemistry. In *Encyclopedia of Inorganic and Bioinorganic Chemistry*; John Wiley & Sons, Ltd: Chichester, UK, 2012. <https://doi.org/10.1002/9781119951438.eibc2062>.
- (113) Monteiro, J. H. S. K. Recent Advances in Luminescence Imaging of Biological Systems Using Lanthanide(III) Luminescent Complexes. *Molecules* **2020**, 25 (9), 2089. <https://doi.org/10.3390/molecules25092089>.
- (114) Filipescu, N.; Sager, W. F.; Serafin, F. A. Substituent Effects on Intramolecular Energy Transfer. II. Fluorescence Spectra of Europium and Terbium  $\beta$ -Diketone Chelates. *J. Phys. Chem.* **1964**, 68 (11), 3324–3346. <https://doi.org/10.1021/j100793a039>.
- (115) Binnemans, K. Rare-Earth Beta-Diketonates. In *Handbook on the Physics and Chemistry of Rare Earths*; Bünzli, J.-C. G., Pecharsky, V. K., Eds.; Elsevier: Amsterdam, The Netherlands, 2005; pp 107–272. [https://doi.org/10.1016/S0168-1273\(05\)35003-3](https://doi.org/10.1016/S0168-1273(05)35003-3).
- (116) Nehra, K.; Dalal, A.; Hooda, A.; Bhagwan, S.; Saini, R. K.; Mari, B.; Kumar, S.; Singh, D. Lanthanides  $\beta$ -Diketonate Complexes as Energy-Efficient Emissive Materials: A Review. *J. Mol. Struct.* **2022**, 1249, 131531. <https://doi.org/10.1016/j.molstruc.2021.131531>.

- (117) Emsley, J. The Composition, Structure and Hydrogen Bonding of the  $\beta$ -Diketones. In *Complex Chemistry*; Springer Berlin Heidelberg: Berlin, Heidelberg, 2007; pp 147–191.  
<https://doi.org/10.1007/BFb0111456>.
- (118) Mara, D.; Artizzu, F.; Laforce, B.; Vincze, L.; Van Hecke, K.; Van Deun, R.; Kaczmarek, A. M. Novel Tetrakis Lanthanide  $\beta$ -Diketonate Complexes: Structural Study, Luminescence Properties and Temperature Sensing. *J. Lumin.* **2019**, *213* (February), 343–355.  
<https://doi.org/10.1016/j.jlumin.2019.05.035>.
- (119) Xiang, N.-J.; Leung, L. M.; So, S.-K.; Gong, M.-L. Preparation and Photoluminescence of a Novel  $\beta$ -Diketone Ligand Containing Electro-Transporting Group and Its Europium(III) Ternary Complex. *Spectrochim. Acta Part A Mol. Biomol. Spectrosc.* **2006**, *65* (3–4), 907–911.  
<https://doi.org/10.1016/j.saa.2006.01.030>.
- (120) Wang, D.; Pi, Y.; Zheng, C.; Fan, L.; Hu, Y.; Wei, X. Preparation and Photoluminescence of Some Europium (III) Ternary Complexes with  $\beta$ -Diketone and Nitrogen Heterocyclic Ligands. *J. Alloys Compd.* **2013**, *574*, 54–58. <https://doi.org/10.1016/j.jallcom.2013.04.049>.
- (121) Zheng, Y.; Fu, L.; Zhou, Y.; Yu, J.; Yu, Y.; Wang, S.; Zhang, H. Electroluminescence Based on a  $\beta$ -Diketonate Ternary Samarium Complex. *J. Mater. Chem.* **2002**, *12* (4), 919–923.  
<https://doi.org/10.1039/b110373c>.
- (122) Amirkhanov, V.; Ovchynnikov, V. A.; Trush, V. A.; Gawryszewska, P.; Trush, V. A.; Gawryszewska, P.; Jerzykiewicz, L. B. Powerful New Ligand Systems: Carbacylamidophosphates (CAPH) and Sulfonylamidophosphates (SAPH). In *Ligands. Synthesis, Characterization and Role in Biotechnology*; Gawryszewska, P., Smoleński, P., Eds.; NOVA publishers: New York, 2014; pp 199–248.
- (123) Amirkhanov, V. M.; Sieler, J.; Trush, V. A.; Ovchynnikov, V. A.; Domasevitch, K. V. Synthesis, IR and X-Ray Studies of a Dioxouranium(VI) Nitrate Complex with N,N'-Tetraethyl-N''-Trichloroacetylphosphortriamide. *Z. Naturforsch. B* **1997**, *52* (10), 1194–1198.  
<https://doi.org/10.1515/znb-1997-1008>.
- (124) Znovjyak, K. O.; Moroz, O. V.; Ovchynnikov, V. A.; Sliva, T. Y.; Shishkina, S. V.; Amirkhanov, V. M. Synthesis and Investigations of Mixed-Ligand Lanthanide Complexes with N,N'-Dipyrrolidine-N''-Trichloroacetylphosphortriamide, Dimethyl-N-Trichloroacetylamidophosphate, 1,10-Phenanthroline and 2,2'-Bipyrimidine. *Polyhedron* **2009**, *28* (17), 3731–3738. <https://doi.org/10.1016/j.poly.2009.08.017>.
- (125) Znovjyak, K. O.; Ovchynnikov, V. A.; Moroz, O. V.; Shishkina, S. V.; Amirkhanov, V. M.

- Bis{N-[Bis(Pyrrolidin-1-Yl)Phosphoryl]-2,2,2-Trichloroacetamide}dinitratodioxidouranium(VI). *Acta Crystallogr. Sect. E: Struct. Rep. Online* **2010**, *66* (3), m322–m322. <https://doi.org/10.1107/S1600536810006422>.
- (126) Znovjyak, K. O.; Ovchynnikov, V. A.; Sliva, T. Y.; Shishkina, S. V.; Amirkhanov, V. M. Bis(N-{bis[Methyl(Phenyl)Amino]Phosphoryl}-2,2,2-Trichloroacetamide)Dinitratodioxidouranium(VI). *Acta Crystallogr. Sect. E: Struct. Rep. Online* **2010**, *66* (3), m306–m306. <https://doi.org/10.1107/S1600536810005611>.
- (127) Tang, S.-F.; Lorbeer, C.; Wang, X.; Ghosh, P.; Mudring, A.-V. Highly Luminescent Salts Containing Well-Shielded Lanthanide-Centered Complex Anions and Bulky Imidazolium Countercations. *Inorg. Chem.* **2014**, *53* (17), 9027–9035. <https://doi.org/10.1021/ic500979p>.
- (128) Litsis, O. O.; Shatrava, I. O.; Amirkhanov, O. V.; Ovchynnikov, V. A.; Sliva, T. Y.; Shishkina, S. V.; Dyakonenko, V. V.; Shishkin, O. V.; Amirkhanov, V. M. New Carbacylamidophosphates (CAPH) and CAPH-Containing Coordination Compounds: Structural Peculiarities. *Struct. Chem.* **2016**, *27* (1), 341–355. <https://doi.org/10.1007/s11224-015-0701-x>.
- (129) Yakovlev, O. O.; Kariaka, N. S.; Trush, V. A.; Smola, S. S.; Siczek, M.; Amirkhanov, V. M. Luminescent Properties and Structure of New CAPH-Based Lanthanide Complexes [LnL3Q], Containing Additional Bis-Heterocyclic Aromatic Ligand-Antenna 2-(1,3,4-Oxadiazole-2-Yl) Pyridine. *Opt. Mater. (Amst)*. **2018**, *75*, 459–464. <https://doi.org/10.1016/j.optmat.2017.10.044>.
- (130) Kariaka, N. S.; Trush, V. A.; Dyakonenko, V. V.; Shishkina, S. V.; Smola, S. S.; Rusakova, N. V.; Sliva, T. Y.; Gawryszewska, P.; Carneiro Neto, A. N.; Malta, O. L.; Amirkhanov, V. M. New Luminescent Lanthanide Tetrakis-Complexes NEt4[LnL4] Based on Dimethyl-N-Benzoylamidophosphate. *ChemPhysChem* **2022**, *23* (14), e202200129. <https://doi.org/10.1002/cphc.202200129>.
- (131) Bassett, A. P.; Magennis, S. W.; Glover, P. B.; Lewis, D. J.; Spencer, N.; Parsons, S.; Williams, R. M.; De Cola, L.; Pikramenou, Z. Highly Luminescent, Triple- and Quadruple-Stranded, Dinuclear Eu, Nd, and Sm(III) Lanthanide Complexes Based on Bis-Diketonate Ligands. *J. Am. Chem. Soc.* **2004**, *126* (30), 9413–9424. <https://doi.org/10.1021/ja048022z>.
- (132) Zhu, T.; Chen, P.; Li, H.; Sun, W.; Gao, T.; Yan, P. Structural Effects on the Photophysical Properties of Mono-β-Diketonate and Bis-β-Diketonate Eu III Complexes. *Phys. Chem. Chem. Phys.* **2015**, *17* (24), 16136–16144. <https://doi.org/10.1039/C5CP01392E>.
- (133) Clegg, J. K.; Li, F.; Lindoy, L. F. Oligo-β-Diketones as Versatile Ligands for Use in Metallo-Supramolecular Chemistry: Recent Progress and Perspectives. *Coord. Chem. Rev.* **2022**, *455*,

214355. <https://doi.org/10.1016/j.ccr.2021.214355>.

- (134) Luo, Y.; Chen, Z.; Tang, R.; Xiao, L.; Peng, H. Investigations into the Synthesis and Fluorescence Properties of Eu(III), Tb(III), Sm(III) and Gd(III) Complexes of a Novel Bis- $\beta$ -Diketone-Type Ligand. *Spectrochim. Acta Part A Mol. Biomol. Spectrosc.* **2008**, *69* (2), 513–516. <https://doi.org/10.1016/j.saa.2007.04.029>.
- (135) He, P.; Wang, H. H.; Liu, S. G.; Shi, J. X.; Wang, G.; Gong, M. L. Visible-Light Excitable Europium (III) Complexes with 2,7-Positional Substituted Carbazole Group-Containing Ligands. *Inorg. Chem.* **2009**, *48* (23), 11382–11387. <https://doi.org/10.1021/ic901210c>.
- (136) Li, H.-F.; Yan, P.; Chen, P.; Wang, Y.; Xu, H.; Li, G. Highly Luminescent Bis-Diketone Lanthanide Complexes with Triple-Stranded Dinuclear Structure. *Dalton Trans.* **2012**, *41* (3), 900–907. <https://doi.org/10.1039/C1DT11496D>.
- (137) Hou, Y.; Shi, J.; Chu, W.; Sun, Z. Synthesis, Crystal Structure, and Near-IR Luminescent Properties of Lanthanide Bis( $\beta$ -Diketonate) Complexes. *Eur. J. Inorg. Chem.* **2013**, *2013* (17), 3063–3069. <https://doi.org/10.1002/ejic.201300013>.
- (138) Shi, J.; Hou, Y.; Chu, W.; Shi, X.; Gu, H.; Wang, B.; Sun, Z. Crystal Structure and Highly Luminescent Properties Studies of Bis- $\beta$ -Diketonate Lanthanide Complexes. *Inorg. Chem.* **2013**, *52* (9), 5013–5022. <https://doi.org/10.1021/ic302726z>.
- (139) Li, B.; Li, H.; Chen, P.; Sun, W.; Wang, C.; Gao, T.; Yan, P. Enhancement of Near-Infrared Luminescence of Ytterbium in Triple-Stranded Binuclear Helicates. *Phys. Chem. Chem. Phys.* **2015**, *17* (45), 30510–30517. <https://doi.org/10.1039/C5CP05888K>.
- (140) Li, B.; Li, H.; Chen, P.; Sun, W.; Wang, C.; Gao, T.; Yan, P. Insight into the Roles of Structures and Energy Levels of Mono- and Bis- $\beta$ -Diketones on Sensitizing Nd(III) NIR-Luminescence. *Dalton Trans.* **2016**, *45* (28), 11459–11470. <https://doi.org/10.1039/c6dt01609j>.
- (141) Lehn, J. M.; Rigault, A.; Siegel, J.; Harrowfield, J.; Chevrier, B.; Moras, D. Spontaneous Assembly of Double-Stranded Helicates from Oligobipyridine Ligands and Copper(I) Cations: Structure of an Inorganic Double Helix. *Proc. Natl. Acad. Sci.* **1987**, *84* (9), 2565–2569. <https://doi.org/10.1073/pnas.84.9.2565>.
- (142) Piguet, C.; Bernardinelli, G.; Hopfgartner, G. Helicates as Versatile Supramolecular Complexes. *Chem. Rev.* **1997**, *97* (6), 2005–2062. <https://doi.org/10.1021/cr960053s>.
- (143) Piguet, C.; Williams, A. F.; Bünzli, J. C. G.; Bernardinelli, G.; Hopfgartner, G. Self-Assembly and Photophysical Properties of Lanthanide Dinuclear Triple-Helical Complexes. *J. Am. Chem.*

- Soc.* **1993**, *115* (18), 8197–8206. <https://doi.org/10.1021/ja00071a032>.
- (144) Chauvin, A. S.; Comby, S.; Song, B.; Vandevyver, C. D. B.; Thomas, F.; Bünzli, J. C. G. A Polyoxyethylene-Substituted Bimetallic Europium Helicate for Luminescent Staining of Living Cells. *Chem. Eur. J.* **2007**, *13* (34), 9515–9526. <https://doi.org/10.1002/chem.200700883>.
- (145) Chen, P.; Li, H.; Sun, W.; Tang, J.; Zhang, L.; Yan, P. Crystallization of Triple- and Quadruple-Stranded Dinuclear Bis- $\beta$ -Diketonate-Dy(III) Helicates: Single Molecule Magnetic Behavior. *CrystEngComm* **2015**, *17* (37), 7227–7232. <https://doi.org/10.1039/c5ce01067e>.
- (146) Zhang, Y.; Zhou, Y.; Gao, T.; Yan, P.; Li, H. Metal-Directed Synthesis of Quadruple-Stranded Helical Eu(III) Molecular Switch: A Significant Improvement in Photocyclization Quantum Yield. *Chem. Commun.* **2020**, *56* (86), 13213–13216. <https://doi.org/10.1039/D0CC05698G>.
- (147) Li, Y.; Zhou, Y.; Yao, Y.; Gao, T.; Yan, P.; Li, H. White-Light Emission from the Quadruple-Stranded Dinuclear Eu(III) Helicate Decorated with Pendent Tetraphenylethylene (TPE). *New J. Chem.* **2021**, *45* (16), 7196–7203. <https://doi.org/10.1039/D1NJ00700A>.
- (148) Javed, M. K.; Sulaiman, A.; Yamashita, M.; Li, Z. Shedding Light on Bifunctional Luminescent Spin Crossover Materials. *Coord. Chem. Rev.* **2022**, *467*, 214625. <https://doi.org/10.1016/j.ccr.2022.214625>.
- (149) Shepherd, H. J.; Quintero, C. M.; Molnár, G.; Salmon, L.; Bousseksou, A. Luminescent Spin-Crossover Materials. In *Spin-Crossover Materials*; Halcrow, M. A., Ed.; John Wiley & Sons Ltd: Oxford, UK, 2013; pp 347–373. <https://doi.org/10.1002/9781118519301.ch13>.
- (150) Sun, K.; Xue, J.-P.; Yao, Z.-S.; Tao, J. Synergistic Strategies for the Synthesis of Fe(II)-Based Bifunctional Fluorescent Spin-Crossover Materials. *Dalton Trans.* **2022**, *51* (42), 16044–16054. <https://doi.org/10.1039/D2DT02604J>.
- (151) Edder, C.; Piguet, C.; Bünzli, J.-C. G.; Hopfgartner, G. High-Spin Iron(II) as a Semitransparent Partner for Tuning Europium(III) Luminescence in Heterodimetallic d-f Complexes. *Chem. Eur. J.* **2001**, *7* (14), 3014–3024. [https://doi.org/10.1002/1521-3765\(20010716\)7:14<3014::AID-CHEM3014>3.0.CO;2-D](https://doi.org/10.1002/1521-3765(20010716)7:14<3014::AID-CHEM3014>3.0.CO;2-D).
- (152) Piguet, C.; Rivara-Minten, E.; Bernardinelli, G.; Bünzli, J. G.; Hopfgartner, G. Non-Covalent Lanthanide Podates with Predetermined Physicochemical Properties: Iron(II) Spin-State Equilibria in Self-Assembled Heterodinuclear d-f Supramolecular Complexes. *J. Chem. Soc. Dalton Trans.* **1997**, No. 3, 421–434. <https://doi.org/10.1039/a605986d>.
- (153) Piguet, C.; Rivara-Minten, E.; Hopfgartner, G.; Bünzli, J.-C. G. Molecular Magnetism and

- Iron(II) Spin-State Equilibrium as Structural Probes in Heterodinuclear d-f Complexes. *Helv. Chim. Acta* **1995**, 78 (7), 1651–1672. <https://doi.org/10.1002/hlca.19950780704>.
- (154) Lathion, T.; Fürstenberg, A.; Besnard, C.; Hauser, A.; Bousseksou, A.; Piguet, C. Monitoring Fe(II) Spin-State Equilibria via Eu(III) Luminescence in Molecular Complexes: Dream or Reality? *Inorg. Chem.* **2020**, 59 (2), 1091–1103. <https://doi.org/10.1021/acs.inorgchem.9b02713>.
- (155) Salmon, L.; Molnár, G.; Zitouni, D.; Quintero, C.; Bergaud, C.; Micheau, J.-C.; Bousseksou, A. A Novel Approach for Fluorescent Thermometry and Thermal Imaging Purposes Using Spin Crossover Nanoparticles. *J. Mater. Chem.* **2010**, 20 (26), 5499. <https://doi.org/10.1039/c0jm00631a>.
- (156) Quintero, C. M.; Gural'skiy, I. A.; Salmon, L.; Molnár, G.; Bergaud, C.; Bousseksou, A. Soft Lithographic Patterning of Spin Crossover Complexes. Part 1: Fluorescent Detection of the Spin Transition in Single Nano-Objects. *J. Mater. Chem.* **2012**, 22 (9), 3745. <https://doi.org/10.1039/c2jm15662h>.
- (157) Matsuda, M.; Isozaki, H.; Tajima, H. Reproducible on–off Switching of the Light Emission from the Electroluminescent Device Containing a Spin Crossover Complex. *Thin Solid Films* **2008**, 517 (4), 1465–1467. <https://doi.org/10.1016/j.tsf.2008.09.034>.
- (158) Suleimanov, I.; Kraieva, O.; Molnár, G.; Salmon, L.; Bousseksou, A. Enhanced Luminescence Stability with a Tb–Spin Crossover Nanocomposite for Spin State Monitoring. *Chem. Commun.* **2015**, 51 (82), 15098–15101. <https://doi.org/10.1039/C5CC06426K>.
- (159) Suleimanov, I.; Kraieva, O.; Sánchez Costa, J.; Fritsky, I. O.; Molnár, G.; Salmon, L.; Bousseksou, A. Electronic Communication between Fluorescent Pyrene Excimers and Spin Crossover Complexes in Nanocomposite Particles. *J. Mater. Chem. C* **2015**, 3 (19), 5026–5032. <https://doi.org/10.1039/C5TC00667H>.
- (160) Duhamel, J. Internal Dynamics of Dendritic Molecules Probed by Pyrene Excimer Formation. *Polymers (Basel)*. **2012**, 4 (1), 211–239. <https://doi.org/10.3390/polym4010211>.
- (161) Kraieva, O.; Suleimanov, I.; Molnár, G.; Salmon, L.; Bousseksou, A. CdTe Quantum Dot Fluorescence Modulation by Spin Crossover. *Magnetochemistry* **2016**, 2 (1), 11. <https://doi.org/10.3390/magnetochemistry2010011>.
- (162) Suleimanov, I.; Molnár, G.; Salmon, L.; Bousseksou, A. Near-Infrared Luminescence Switching in a Spin-Crossover Polymer Nanocomposite. *Eur. J. Inorg. Chem.* **2017**, 2017 (28), 3446–

3451. <https://doi.org/10.1002/ejic.201700426>.
- (163) Sánchez-Molina, I.; Nieto-Castro, D.; Moneo-Corcuera, A.; Martínez-Ferrero, E.; Galán-Mascarós, J. R. Synergic Bistability between Spin Transition and Fluorescence in Polyfluorene Composites with Spin Crossover Polymers. *J. Phys. Chem. Lett.* **2021**, *12* (43), 10479–10485. <https://doi.org/10.1021/acs.jpcclett.1c02811>.
- (164) Titos-Padilla, S.; Herrera, J. M.; Chen, X.-W.; Delgado, J. J.; Colacio, E. Bifunctional Hybrid SiO<sub>2</sub> Nanoparticles Showing Synergy between Core Spin Crossover and Shell Luminescence Properties. *Angew. Chem. Int. Ed.* **2011**, *50* (14), 3290–3293. <https://doi.org/10.1002/anie.201007847>.
- (165) Herrera, J. M.; Titos-Padilla, S.; Pope, S. J. A.; Berlanga, I.; Zamora, F.; Delgado, J. J.; Kamenev, K. V.; Wang, X.; Prescimone, A.; Brechin, E. K.; Colacio, E. Studies on Bifunctional Fe(II)-Triazole Spin Crossover Nanoparticles: Time-Dependent Luminescence, Surface Grafting and the Effect of a Silica Shell and Hydrostatic Pressure on the Magnetic Properties. *J. Mater. Chem. C* **2015**, *3* (30), 7819–7829. <https://doi.org/10.1039/C5TC00685F>.
- (166) Balzani, V.; Bergamini, G.; Campagna, S.; Puntoriero, F. Photochemistry and Photophysics of Coordination Compounds: Overview and General Concepts. In *Photochemistry and Photophysics of Coordination Compounds I*; Balzani, V., Campagna, S., Eds.; Springer Berlin Heidelberg: Berlin, Heidelberg, 2007; Vol. 280, pp 1–36. [https://doi.org/10.1007/128\\_2007\\_132](https://doi.org/10.1007/128_2007_132).
- (167) Bas, A.-C.; Thompson, X.; Salmon, L.; Thibault, C.; Molnár, G.; Palamarciuc, O.; Routaboul, L.; Bousseksou, A. Bilayer Thin Films That Combine Luminescent and Spin Crossover Properties for an Efficient and Reversible Fluorescence Switching. *Magnetochemistry* **2019**, *5* (2), 28. <https://doi.org/10.3390/magnetochemistry5020028>.
- (168) Hasegawa, M.; Renz, F.; Hara, T.; Kikuchi, Y.; Fukuda, Y.; Okubo, J.; Hoshi, T.; Linert, W. Fluorescence Spectra of Fe(II) Spin Crossover Complexes with 2,6-Bis(Benzimidazole-2'-Yl)Pyridine. *Chem. Phys.* **2002**, *277* (1), 21–30. [https://doi.org/10.1016/S0301-0104\(01\)00706-6](https://doi.org/10.1016/S0301-0104(01)00706-6).
- (169) Santoro, A.; Kershaw Cook, L. J.; Kulmaczewski, R.; Barrett, S. A.; Cespedes, O.; Halcrow, M. A. Iron(II) Complexes of Tridentate Indazolylpyridine Ligands: Enhanced Spin-Crossover Hysteresis and Ligand-Based Fluorescence. *Inorg. Chem.* **2015**, *54* (2), 682–693. <https://doi.org/10.1021/ic502726q>.
- (170) Senthil Kumar, K.; Šalitraš, I.; Heinrich, B.; Fuhr, O.; Ruben, M. A Charge Neutral Iron(II)

- Complex with an above Room Temperature Spin Crossover (SCO) and Hysteresis Loop. *J. Mater. Chem. C* **2015**, *3* (44), 11635–11644. <https://doi.org/10.1039/C5TC02079D>.
- (171) Benaicha, B.; Van Do, K.; Yangui, A.; Pittala, N.; Lusson, A.; Sy, M.; Bouchez, G.; Fourati, H.; Gómez-García, C. J.; Triki, S.; Boukheddaden, K. Interplay between Spin-Crossover and Luminescence in a Multifunctional Single Crystal Iron(II) Complex: Towards a New Generation of Molecular Sensors. *Chem. Sci.* **2019**, *10* (28), 6791–6798. <https://doi.org/10.1039/C9SC02331C>.
- (172) González-Prieto, R.; Fleury, B.; Schramm, F.; Zoppellaro, G.; Chandrasekar, R.; Fuhr, O.; Lebedkin, S.; Kappes, M.; Ruben, M. Tuning the Spin-Transition Properties of Pyrene-Decorated 2,6-Bispyrazolylpyridine Based Fe(II) Complexes. *Dalton Trans.* **2011**, *40* (29), 7564. <https://doi.org/10.1039/c1dt10420a>.
- (173) Yuan, J.; Wu, S.-Q.; Liu, M.-J.; Sato, O.; Kou, H.-Z. Rhodamine 6G-Labeled Pyridyl Aroylhydrazone Fe(II) Complex Exhibiting Synergetic Spin Crossover and Fluorescence. *J. Am. Chem. Soc.* **2018**, *140* (30), 9426–9433. <https://doi.org/10.1021/jacs.8b00103>.
- (174) Wang, C.-F.; Li, R.-F.; Chen, X.-Y.; Wei, R.-J.; Zheng, L.-S.; Tao, J. Synergetic Spin Crossover and Fluorescence in One-Dimensional Hybrid Complexes. *Angew. Chem. Int. Ed.* **2015**, *54* (5), 1574–1577. <https://doi.org/10.1002/anie.201410454>.
- (175) Matsukizono, H.; Kuroiwa, K.; Kimizuka, N. Self-Assembly-Directed Spin Conversion of Iron(II) 1,2,4-Triazole Complexes in Solution and Their Effect on Photorelaxation Processes of Fluorescent Counter Ions. *Chem. Lett.* **2008**, *37* (4), 446–447. <https://doi.org/10.1246/cl.2008.446>.
- (176) Lochenie, C.; Schötz, K.; Panzer, F.; Kurz, H.; Maier, B.; Puchtler, F.; Agarwal, S.; Köhler, A.; Weber, B. Spin-Crossover Iron(II) Coordination Polymer with Fluorescent Properties: Correlation between Emission Properties and Spin State. *J. Am. Chem. Soc.* **2018**, *140* (2), 700–709. <https://doi.org/10.1021/jacs.7b10571>.
- (177) Ge, J.; Chen, Z.; Zhang, L.; Liang, X.; Su, J.; Kurmoo, M.; Zuo, J. A Two-Dimensional Iron(II) Coordination Polymer with Synergetic Spin-Crossover and Luminescent Properties. *Angew. Chem. Int. Ed.* **2019**, *58* (26), 8789–8793. <https://doi.org/10.1002/anie.201903281>.
- (178) Ghosh, S.; Kamilya, S.; Pramanik, T.; Rouzières, M.; Herchel, R.; Mehta, S.; Mondal, A. ON/OFF Photoswitching and Thermoinduced Spin Crossover with Cooperative Luminescence in a 2D Iron(II) Coordination Polymer. *Inorg. Chem.* **2020**, *59* (18), 13009–13013. <https://doi.org/10.1021/acs.inorgchem.0c02136>.

- (179) Delgado, T.; Meneses-Sánchez, M.; Piñeiro-López, L.; Bartual-Murgui, C.; Muñoz, M. C.; Real, J. A. Thermo- and Photo-Modulation of Exciplex Fluorescence in a 3D Spin Crossover Hofmann-Type Coordination Polymer. *Chem. Sci.* **2018**, *9* (44), 8446–8452. <https://doi.org/10.1039/C8SC02677G>.
- (180) Meneses-Sánchez, M.; Piñeiro-López, L.; Delgado, T.; Bartual-Murgui, C.; Muñoz, M. C.; Chakraborty, P.; Real, J. A. Extrinsic vs. Intrinsic Luminescence and Their Interplay with Spin Crossover in 3D Hofmann-Type Coordination Polymers. *J. Mater. Chem. C* **2020**, *8* (5), 1623–1633. <https://doi.org/10.1039/C9TC06422B>.
- (181) Turo-Cortés, R.; Meneses-Sánchez, M.; Delgado, T.; Bartual-Murgui, C.; Muñoz, M. C.; Real, J. A. Coexistence of Luminescence and Spin-Crossover in 2D Iron(II) Hofmann Clathrates Modulated through Guest Encapsulation. *J. Mater. Chem. C* **2022**, *10* (29), 10686–10698. <https://doi.org/10.1039/D2TC02039D>.
- (182) Christofferson, J.; Maize, K.; Ezzahri, Y.; Shabani, J.; Wang, X.; Shakouri, A. Microscale and Nanoscale Thermal Characterization Techniques. *J. Electron. Packag.* **2008**, *130* (4), 041101–041106. <https://doi.org/10.1115/1.2993145>.
- (183) Brites, C. D. S.; Lima, P. P.; Silva, N. J. O.; Millán, A.; Amaral, V. S.; Palacio, F.; Carlos, L. D. Thermometry at the Nanoscale. *Nanoscale* **2012**, *4* (16), 4799–4829. <https://doi.org/10.1039/c2nr30663h>.
- (184) Kim, M. M.; Giry, A.; Mastiani, M.; Rodrigues, G. O.; Reis, A.; Mandin, P. Microscale Thermometry: A Review. *Microelectron. Eng.* **2015**, *148*, 129–142. <https://doi.org/10.1016/j.mee.2015.11.002>.
- (185) Rocha, J.; Brites, C. D. S.; Carlos, L. D. Lanthanide Organic Framework Luminescent Thermometers. *Chem. - A Eur. J.* **2016**, *22* (42), 14782–14795. <https://doi.org/10.1002/chem.201600860>.
- (186) Chen, C.; Shen, T.; Du, Z.; Zhang, J.; Wang, J.; Marconnet, A.; Pan, L. Microscale Two-Dimensional (2D) Temperature Mapping by Ratiometric Fluorescence Imaging under Orthogonal Excitations. *Exp. Therm. Fluid Sci.* **2018**, *94* (May 2017), 168–171. <https://doi.org/10.1016/j.expthermflusci.2018.02.009>.
- (187) Jauffred, L.; Samadi, A.; Klingberg, H.; Bendix, P. M.; Oddershede, L. B. Plasmonic Heating of Nanostructures. *Chem. Rev.* **2019**, *119* (13), 8087–8130. <https://doi.org/10.1021/acs.chemrev.8b00738>.

- (188) Ghifari, N.; Rassouk, S.; Hayat, Z.; Taleb, A.; Chahboun, A.; El Abed, A. I. Dye-Doped ZnO Microcapsules for High Throughput and Sensitive Optofluidic Micro-Thermometry. *Micromachines* **2020**, *11* (1), 100. <https://doi.org/10.3390/mi11010100>.
- (189) Mykhaylyk, V.; Kraus, H.; Zhydachevskyy, Y.; Tsiumra, V.; Luchechko, A.; Wagner, A.; Suchocki, A. Multimodal Non-Contact Luminescence Thermometry with Cr-Doped Oxides. *Sensors* **2020**, *20* (18), 5259. <https://doi.org/10.3390/s20185259>.
- (190) Zani, V.; Pedron, D.; Pilot, R.; Signorini, R. Contactless Temperature Sensing at the Microscale Based on Titanium Dioxide Raman Thermometry. *Biosensors* **2021**, *11* (4), 102. <https://doi.org/10.3390/bios11040102>.
- (191) Goodson, K. E.; Ashegh, M. Near-Field Optical Thermometry. *Microscale Thermophys. Eng.* **1997**, *1* (3), 225–235. <https://doi.org/10.1080/108939597200241>.
- (192) Fletcher, D. Thermal Microscopy with a Microfabricated Solid Immersion Lens. *Microscale Thermophys. Eng.* **2003**, *7* (4), 267–273. <https://doi.org/10.1080/10893950390245985>.
- (193) Teysieux, D.; Thiery, L.; Cretin, B. Near-Infrared Thermography Using a Charge-Coupled Device Camera: Application to Microsystems. *Rev. Sci. Instrum.* **2007**, *78* (3), 034902. <https://doi.org/10.1063/1.2714040>.
- (194) Jaque, D.; Vetrone, F. Luminescence Nanothermometry. *Nanoscale* **2012**, *4* (15), 4301–4326. <https://doi.org/10.1039/c2nr30764b>.
- (195) Cahill, D. G.; Ford, W. K.; Goodson, K. E.; Mahan, G. D.; Majumdar, A.; Maris, H. J.; Merlin, R.; Phillpot, S. R. Nanoscale Thermal Transport. *J. Appl. Phys.* **2003**, *93* (2), 793–818. <https://doi.org/10.1063/1.1524305>.
- (196) Christofferson, J.; Shakouri, A. Thermoreflectance Based Thermal Microscope. *Rev. Sci. Instrum.* **2005**, *76* (2), 024903. <https://doi.org/10.1063/1.1850632>.
- (197) Tessier, G.; Bardoux, M.; Boué, C.; Filloy, C.; Fournier, D. Back Side Thermal Imaging of Integrated Circuits at High Spatial Resolution. *Appl. Phys. Lett.* **2007**, *90* (17), 171112. <https://doi.org/10.1063/1.2732179>.
- (198) Morscheidt, W.; Jeftic, J.; Codjovi, E.; Linares, J.; Bousseksou, A.; Constant-Machado, H.; Varret, F. Optical Detection of the Spin Transition by Reflectivity: Application To. *Meas. Sci. Technol.* **1998**, *9* (8), 1311–1315. <https://doi.org/10.1088/0957-0233/9/8/025>.
- (199) Haro-González, P.; Martín, I. R.; Martín, L. L.; León-Luis, S. F.; Pérez-Rodríguez, C.; Lavín,

- V. Characterization of Er<sup>3+</sup> and Nd<sup>3+</sup> Doped Strontium Barium Niobate Glass Ceramic as Temperature Sensors. *Opt. Mater. (Amst)*. **2011**, *33* (5), 742–745.  
<https://doi.org/10.1016/j.optmat.2010.11.026>.
- (200) Heyes, A. L.; Seefeldt, S.; Feist, J. P. Two-Colour Phosphor Thermometry for Surface Temperature Measurement. *Opt. Laser Technol.* **2006**, *38* (4–6), 257–265.  
<https://doi.org/10.1016/j.optlastec.2005.06.012>.
- (201) Allison, S. W.; Gillies, G. T. Remote Thermometry with Thermographic Phosphors: Instrumentation and Applications. *Rev. Sci. Instrum.* **1997**, *68* (7), 2615–2650.  
<https://doi.org/10.1063/1.1148174>.
- (202) Cui, Y.; Xu, H.; Yue, Y.; Guo, Z.; Yu, J.; Chen, Z.; Gao, J.; Yang, Y.; Qian, G.; Chen, B. A Luminescent Mixed-Lanthanide Metal–Organic Framework Thermometer. *J. Am. Chem. Soc.* **2012**, *134* (9), 3979–3982. <https://doi.org/10.1021/ja2108036>.
- (203) Salerno, E. V.; Carneiro Neto, A. N.; Eliseeva, S. V.; Hernández-Rodríguez, M. A.; Lutter, J. C.; Lathion, T.; Kampf, J. W.; Petoud, S.; Carlos, L. D.; Pecoraro, V. L. Tunable Optical Molecular Thermometers Based on Metallocrowns. *J. Am. Chem. Soc.* **2022**, *144* (40), 18259–18271. <https://doi.org/10.1021/jacs.2c04821>.
- (204) Bao, G.; Wong, K.-L.; Jin, D.; Tanner, P. A. A Stoichiometric Terbium-Europium Dyad Molecular Thermometer: Energy Transfer Properties. *Light Sci. Appl.* **2018**, *7* (1), 96.  
<https://doi.org/10.1038/s41377-018-0097-7>.
- (205) Hughes, B. C.; Lu, Z.; Jenkins, D. M. The Final Unadorned Tris(Azoly)Borate: Finishing What Trofimenko Started in 1966. *Chem. Commun.* **2014**, *50* (40), 5273–5275.  
<https://doi.org/10.1039/C3CC47151A>.
- (206) Rat, S.; Ridier, K.; Vendier, L.; Molnár, G.; Salmon, L.; Bousseksou, A. Solvatomorphism and Structural-Spin Crossover Property Relationship in Bis[Hydrotris(1,2,4-Triazol-1-Yl)Borate]Iron(II). *CrystEngComm* **2017**, *19* (24), 3271–3280.  
<https://doi.org/10.1039/C7CE00741H>.
- (207) Slichter, C. P.; Drickamer, H. G. Pressure-Induced Electronic Changes in Compounds of Iron. *J. Chem. Phys.* **1972**, *56* (5), 2142–2160. <https://doi.org/10.1063/1.1677511>.
- (208) Trofimenko, S. Poly(1-pyrazolyl)Borates, Their Transition-Metal Complexes, and Pyrazaboles. In *Inorganic Syntheses*; 1970; Vol. 12, pp 99–109.
- (209) Bour, J. R.; Camasso, N. M.; Sanford, M. S. Oxidation of Ni(II) to Ni(IV) with Aryl

- Electrophiles Enables Ni-Mediated Aryl–CF<sub>3</sub> Coupling. *J. Am. Chem. Soc.* **2015**, *137* (25), 8034–8037. <https://doi.org/10.1021/jacs.5b04892>.
- (210) Yagil, G. The Proton Dissociation Constant of Pyrrole, Indole and Related Compounds. *Tetrahedron* **1967**, *23* (6), 2855–2861. [https://doi.org/10.1016/0040-4020\(67\)85151-2](https://doi.org/10.1016/0040-4020(67)85151-2).
- (211) Radzaminska-Lenarcik, E.; Pyszka, I.; Urbaniak, W. New Polymer Inclusion Membranes in the Separation of Palladium, Zinc and Nickel Ions from Aqueous Solutions. *Polymers (Basel)*. **2021**, *13* (9), 1424. <https://doi.org/10.3390/polym13091424>.
- (212) Sun, J.; Fu, Y.; He, G.; Sun, X.; Wang, X. Catalytic Hydrogenation of Nitrophenols and Nitrotoluenes over a Palladium/Graphene Nanocomposite. *Catal. Sci. Technol.* **2014**, *4* (6), 1742–1748. <https://doi.org/10.1039/C4CY00048J>.
- (213) Wrackmeyer, B.; Tok, O. L. Indirect Nuclear Spin-Spin Coupling Constants 1J(17O, 11B). First Observation And Calculation Using Density Functional Theory (Dft). *Z. Naturforsch. B* **2006**, *61* (8), 949–955. <https://doi.org/10.1515/znb-2006-0804>.
- (214) Reger, D. L.; Gardinier, J. R.; Elgin, J. D.; Smith, M. D.; Hautot, D.; Long, G. J.; Grandjean, F. Structure-Function Correlations in Iron(II) Tris(Pyrazolyl)Borate Spin-State Crossover Complexes. *Inorg. Chem.* **2006**, *45* (22), 8862–8875. <https://doi.org/10.1021/ic0607437>.
- (215) Nishio, M. The CH/π Hydrogen Bond in Chemistry. Conformation, Supramolecules, Optical Resolution and Interactions Involving Carbohydrates. *Phys. Chem. Chem. Phys.* **2011**, *13* (31), 13873. <https://doi.org/10.1039/c1cp20404a>.
- (216) Trush, V. A.; Gubina, K. E.; Gumeniuk, Y. O.; Sliva, T. Y.; Konovalova, I. S. Tetramethyl N , N'-(2,2,3,3,4,4-Hexafluoro-1,5-Dioxopentane-1,5-Diyl)Bis(Phosphoramidate). *Acta Crystallogr. Sect. E Struct. Reports Online* **2012**, *68* (4), o1127–o1127. <https://doi.org/10.1107/S1600536812011191>.
- (217) Jørgensen, C. K.; Judd, B. R. Hypersensitive Pseudoquadrupole Transitions in Lanthanides. *Mol. Phys.* **1964**, *8* (3), 281–290. <https://doi.org/10.1080/00268976400100321>.
- (218) Choppin, G. R.; Henrie, D. E.; Buijs, K. Environmental Effects on F-f Transitions. I. Neodymium(III). *Inorg. Chem.* **1966**, *5* (10), 1743–1748. <https://doi.org/10.1021/ic50044a023>.
- (219) Henrie, D. E.; Choppin, G. R. Environmental Effects on f–f Transitions. II. “Hypersensitivity” in Some Complexes of Trivalent Neodymium. *J. Chem. Phys.* **1968**, *49* (2), 477–481. <https://doi.org/10.1063/1.1670099>.

- (220) Gawryszewska, P.; Sokolnicki, J.; Legendziewicz, J. Photophysics and Structure of Selected Lanthanide Compounds. *Coord. Chem. Rev.* **2005**, *249* (21–22), 2489–2509. <https://doi.org/10.1016/j.ccr.2005.06.021>.
- (221) Kariaka, N. S.; Trush, V. A.; Gawryszewska, P.; Dyakonenko, V. V.; Shishkina, S. V.; Sliva, T. Y.; Amirkhanov, V. M. Spectroscopy and Structure of [LnL3bipy] and [LnL3phen] Complexes with CAPH Type Ligand Dimethylbenzoylamidophosphate. *J. Lumin.* **2016**, *178*, 392–399. <https://doi.org/10.1016/j.jlumin.2016.06.018>.
- (222) Kariaka, N. S.; Trush, V. A.; Medvediev, V. V.; Dyakonenko, V. V.; Shishkin, O. V.; Smola, S. S.; Fadeyev, E. M.; Rusakova, N. V.; Amirkhanov, V. M. Coordination Compounds Based on CAPH Type Ligand: Synthesis, Structural Characteristics and Luminescence Properties of Tetrakis-Complexes CsLnL4 with Dimethylbenzoylamidophosphate. *J. Coord. Chem.* **2016**, *69* (1), 123–134. <https://doi.org/10.1080/00958972.2015.1115024>.
- (223) Olyshevets, I. P.; Dyakonenko, V. V.; Shyshkina, S. V.; Trush, V. O.; Sliva, T. Y.; Amirkhanov, V. M. Synthesis, Structural and Spectral Studies of Anionic Tetrakis-Complexes of Lanthanides CsLnL4 with SAPH-Ligand – Dimethyl(Phenylsulfonyl)Amidophosphate. *Vopr. Khimii i Khimicheskoi Tekhnologii* **2018**, No. 6, 56–62. <https://doi.org/10.32434/0321-4095-2018-121-6-56-62>.
- (224) Gutierrez, F.; Tedeschi, C.; Maron, L.; Daudey, J.-P.; Azema, J.; Tisnès, P.; Picard, C.; Poteau, R. Quantum Chemistry-Based Interpretations on the Lowest Triplet State of Luminescent Lanthanides Complexes. Part 2. Influence of the Electrostatic Interactions on the Triplet State Energy of Terbium Complexes. *J. Mol. Struct. THEOCHEM* **2005**, *756* (1–3), 151–162. <https://doi.org/10.1016/j.theochem.2005.09.004>.
- (225) Shevchuk, S. V.; Rusakova, N. V.; Turianskaya, A. M.; Korovin, Y. V.; Nazarenko, N. A.; Gren, A. I. Infrared Luminescence of Ytterbium Ion in Complexes with Calix[4]Resorcinarenes. *J. Fluoresc.* **1998**, *8* (3), 225–228. <https://doi.org/10.1023/A:1022505716725>.
- (226) Quici, S.; Cavazzini, M.; Marzanni, G.; Accorsi, G.; Armaroli, N.; Ventura, B.; Barigelletti, F. Visible and Near-Infrared Intense Luminescence from Water-Soluble Lanthanide [Tb(III), Eu(III), Sm(III), Dy(III), Pr(III), Ho(III), Yb(III), Nd(III), Er(III)] Complexes. *Inorg. Chem.* **2005**, *44* (3), 529–537. <https://doi.org/10.1021/ic0486466>.
- (227) Comby, S.; Bünzli, J.-C. G. Lanthanide Near-Infrared Luminescence in Molecular Probes and Devices. In *Handbook on the Physics and Chemistry of Rare Earths*; Gschneidner, K. A., Bünzli, J.-C. G., Pecharsky, V. K., Eds.; Elsevier Science: Amsterdam, The Netherlands, 2007;

- (228) Zhang, J.; Petoud, S. Azulene-Moiety-Based Ligand for the Efficient Sensitization of Four Near-Infrared Luminescent Lanthanide Cations: Nd<sup>3+</sup>, Er<sup>3+</sup>, Tm<sup>3+</sup>, and Yb<sup>3+</sup>. *Chem. Eur. J.* **2008**, *14* (4), 1264–1272. <https://doi.org/10.1002/chem.200701068>.
- (229) Gawryszewska, P.; Moroz, O. V.; Trush, V. A.; Amirkhanov, V. M.; Lis, T.; Sobczyk, M.; Siczek, M. Spectroscopy and Structure of LnIII Complexes with Sulfonylamidophosphate-Type Ligands as Sensitizers of Visible and Near-Infrared Luminescence. *ChemPlusChem* **2012**, *77* (6), 482–496. <https://doi.org/10.1002/cplu.201200026>.
- (230) Solarz, P.; Sobczyk, M. Spectroscopic Properties of Sm<sup>3+</sup> in KZnLa(PO<sub>4</sub>)<sub>2</sub> in IR–VUV Region. *Opt. Mater. (Amst)*. **2012**, *34* (11), 1826–1832. <https://doi.org/10.1016/j.optmat.2012.05.011>.
- (231) Sobczyk, M.; Szymański, D. A Study of Optical Properties of Sm<sup>3+</sup> Ions in α-Na<sub>3</sub>Y(VO<sub>4</sub>)<sub>2</sub> Single Crystals. *J. Lumin.* **2013**, *142*, 96–102. <https://doi.org/10.1016/j.jlumin.2013.03.062>.
- (232) Sobczyk, M.; Korzeniowski, K.; Guzik, M.; Cybińska, J.; Gerasymchuk, Y.; Trush, V. A.; Legendziewicz, J. Spectroscopic Behaviour of Na[Sm(SP)<sub>4</sub>] (Where SP = C<sub>6</sub>H<sub>5</sub>S(O)<sub>2</sub>NP(O)(OCH<sub>3</sub>)<sub>2</sub>-) and Its Polymeric Material-New Orange Emitting Phosphors. *J. Lumin.* **2018**, *193*, 90–97. <https://doi.org/10.1016/j.jlumin.2017.08.064>.
- (233) Brito, H. .; Malta, O. .; Felinto, M. C. F. .; Teotonio, E. E. .; Menezes, J. F. .; Silva, C. F. .; Tomiyama, C. .; Carvalho, C. A. . Luminescence Investigation of the Sm(III)-β-Diketonates with Sulfoxides, Phosphine Oxides and Amides Ligands. *J. Alloys Compd.* **2002**, *344* (1–2), 293–297. [https://doi.org/10.1016/S0925-8388\(02\)00372-9](https://doi.org/10.1016/S0925-8388(02)00372-9).
- (234) Mathis, G. Rare Earth Cryptates and Homogeneous Fluoroimmunoassays with Human Sera. *Clin. Chem.* **1993**, *39* (9), 1953–1959. <https://doi.org/10.1093/clinchem/39.9.1953>.
- (235) Hemmilä, I.; Mikkala, V.-M.; Takalo, H. Development of Luminescent Lanthanide Chelate Labels for Diagnostic Assays. *J. Alloys Compd.* **1997**, *249* (1–2), 158–162. [https://doi.org/10.1016/S0925-8388\(96\)02834-4](https://doi.org/10.1016/S0925-8388(96)02834-4).
- (236) Bazin, H.; Trinquet, E.; Mathis, G. Time Resolved Amplification of Cryptate Emission: A Versatile Technology to Trace Biomolecular Interactions. *Rev. Mol. Biotechnol.* **2002**, *82* (3), 233–250. [https://doi.org/10.1016/S1389-0352\(01\)00040-X](https://doi.org/10.1016/S1389-0352(01)00040-X).
- (237) Hemmilä, I.; Laitala, V. Progress in Lanthanides as Luminescent Probes. *J. Fluoresc.* **2005**, *15* (4), 529–542. <https://doi.org/10.1007/s10895-005-2826-6>.

- (238) Ghose, S.; Trinquet, E.; Laget, M.; Bazin, H.; Mathis, G. Rare Earth Cryptates for the Investigation of Molecular Interactions in Vitro and in Living Cells. *J. Alloys Compd.* **2008**, *451* (1–2), 35–37. <https://doi.org/10.1016/j.jallcom.2007.04.054>.
- (239) Montgomery, C. P.; Murray, B. S.; New, E. J.; Pal, R.; Parker, D. Cell-Penetrating Metal Complex Optical Probes: Targeted and Responsive Systems Based on Lanthanide Luminescence. *Acc. Chem. Res.* **2009**, *42* (7), 925–937. <https://doi.org/10.1021/ar800174z>.
- (240) Kido, J.; Okamoto, Y. Organo Lanthanide Metal Complexes for Electroluminescent Materials. *Chem. Rev.* **2002**, *102* (6), 2357–2368. <https://doi.org/10.1021/cr010448y>.
- (241) Binnemans, K. Lanthanide-Based Luminescent Hybrid Materials. *Chem. Rev.* **2009**, *109* (9), 4283–4374. <https://doi.org/10.1021/cr8003983>.
- (242) Xu, H.; Sun, Q.; An, Z.; Wei, Y.; Liu, X. Electroluminescence from Europium(III) Complexes. *Coord. Chem. Rev.* **2015**, *293–294*, 228–249. <https://doi.org/10.1016/j.ccr.2015.02.018>.
- (243) Litsis, O. O.; Ovchynnikov, V. A.; Scherbatskii, V. P.; Nedilko, S. G.; Sliva, T. Y.; Dyakonenko, V. V.; Shishkin, O. V.; Davydov, V. I.; Gawryszewska, P.; Amirkhanov, V. M. Lanthanide Mixed-Ligand Complexes of the [Ln(CAPh)<sub>3</sub>(Phen)] and [LaxEu<sub>1-x</sub>(CAPh)<sub>3</sub>(Phen)] (CAPh = Carbacylamidophosphate) Type. A Comparative Study of Their Spectral Properties. *Dalton Trans.* **2015**, *44* (35), 15508–15522. <https://doi.org/10.1039/C5DT02557E>.
- (244) Kariaka, N. S.; Trush, V. A.; Smola, S. S.; Fadeyev, E. M.; Odynets, I. V.; Sliva, T. Y.; Amirkhanov, V. M. Tris -(Diphenylphosphoryl)Benzamide Lanthanides (III) Trinitrates as a Basis for Creating the Luminophore Materials. *Reports Natl. Acad. Sci. Ukr.* **2016**, No. 5, 85–94. <https://doi.org/10.15407/dopovidi2016.05.085>.
- (245) Gu, H.; Hou, Y.; Xu, F.; Wang, S. Electrospinning Preparation, Thermal, and Luminescence Properties of Eu<sub>2</sub>(BTP)<sub>3</sub>(Phen)<sub>2</sub> Complex Doped in PMMA. *Colloid Polym. Sci.* **2015**, *293* (8), 2201–2208. <https://doi.org/10.1007/s00396-015-3614-8>.
- (246) de Sá, G. .; Malta, O. .; de Mello Donegá, C.; Simas, A. .; Longo, R. .; Santa-Cruz, P. .; da Silva, E. . Spectroscopic Properties and Design of Highly Luminescent Lanthanide Coordination Complexes. *Coord. Chem. Rev.* **2000**, *196* (1), 165–195. [https://doi.org/10.1016/S0010-8545\(99\)00054-5](https://doi.org/10.1016/S0010-8545(99)00054-5).
- (247) Lluell, M.; Casanova, D.; Girera, J.; Alemany, P.; Alvarez, S. SHAPE. Barcelona, Spain 2010.
- (248) Amirkhanov, W.; Jaficzak, C.; Macalik, L.; Hanuza, J.; Legendziewicz, J. Synthesis and

- Spectroscopic Investigations of Lanthanide Compounds with Phosphoro-Azo Derivatives of  $\beta$  Diketones. *J. Appl. Spectrosc.* **1995**, 62 (4), 613–624.
- (249) Sokolnicki, J.; Legendziewicz, J.; Amirkhanov, W.; Ovchinnikov, V.; Macalik, L.; Hanuza, J. Comparative Optical Studies of Lanthanide Complexes with Three Types of Phosphoro-Azo Derivatives of  $\beta$ -Diketones. *Spectrochim. Acta Part A Mol. Biomol. Spectrosc.* **1999**, 55 (2), 349–367. [https://doi.org/10.1016/S1386-1425\(98\)00193-0](https://doi.org/10.1016/S1386-1425(98)00193-0).
- (250) Fujita, J.; Martell, A. E.; Nakamoto, K. Infrared Spectra of Metal Chelate Compounds. VIII. Infrared Spectra of Co (III) Carbonato Complexes. *J. Chem. Phys.* **1962**, 36 (2), 339–345. <https://doi.org/10.1063/1.1732506>.
- (251) Sobczyk, M. Optical Properties of  $\alpha$ -Nd<sup>3+</sup>: Na<sub>3</sub>Y(VO<sub>4</sub>)<sub>2</sub> Single Crystals -Potential Laser Materials. *Opt. Mater. (Amst)*. **2013**, 35 (5), 852–859. <https://doi.org/10.1016/j.optmat.2012.10.043>.
- (252) Kasprzycka, E.; Trush, V. A.; Jerzykiewicz, L.; Amirkhanov, V. M.; Watras, A.; Sokolnicki, J.; Malta, O. L.; Gawryszewska, P. Lanthanide Complexes with Phosphorylated 2-Naphthylsulfonamides Ligands as Electromagnetic Radiation Converters. *Dye. Pigment.* **2019**, 160, 439–449. <https://doi.org/10.1016/j.dyepig.2018.08.015>.
- (253) Pham, Y. H.; Trush, V. A.; Korabik, M.; Amirkhanov, V. M.; Gawryszewska, P. Nd<sup>3+</sup> and Yb<sup>3+</sup> Complexes with N-(Diphenylphosphoryl)Pyrazine-2-Carboxamide as UV-NIR Radiation Converters and Single-Ion Magnets. *Dye. Pigment.* **2021**, 108986. <https://doi.org/10.1016/j.dyepig.2020.108986>.
- (254) Inokuti, M.; Hirayama, F. Influence of Energy Transfer by the Exchange Mechanism on Donor Luminescence. *J. Chem. Phys.* **1965**, 43 (6), 1978–1989. <https://doi.org/10.1063/1.1697063>.
- (255) Blasse, G.; Grabmaier, B. C. *Luminescent Materials*; Springer-Verlag, 1994.
- (256) Langford, J. I.; Wilson, A. J. C. Scherrer after Sixty Years: A Survey and Some New Results in the Determination of Crystallite Size. *J. Appl. Crystallogr.* **1978**, 11 (2), 102–113. <https://doi.org/10.1107/S0021889878012844>.
- (257) Quintero, C. M.; Kraieva, O.; Carcenac, F.; Lagrange, D.; Yaremchuk, N. A.; Molnár, G.; Bergaud, C. Joule Heated Metallic Microwire Devices for Sub-Microsecond T-Jump Experiments. *Microelectronics J.* **2015**, 46 (12), 1167–1174. <https://doi.org/10.1016/j.mejo.2015.06.024>.
- (258) Ridier, K.; Bas, A.; Shalabaeva, V.; Nicolazzi, W.; Salmon, L.; Molnár, G.; Bousseksou, A.;

- Lorenc, M.; Bertoni, R.; Collet, E.; Cailleau, H. Finite Size Effects on the Switching Dynamics of Spin-Crossover Thin Films Photoexcited by a Femtosecond Laser Pulse. *Adv. Mater.* **2019**, *31* (25), 1901361. <https://doi.org/10.1002/adma.201901361>.
- (259) Sheldrick, G. M. A Short History of SHELX. *Acta Crystallogr. Sect. A Found. Crystallogr.* **2008**, *64* (1), 112–122. <https://doi.org/10.1107/S0108767307043930>.
- (260) Sheldrick, G. M. Crystal Structure Refinement with SHELXL. *Acta Crystallogr. Sect. C Struct. Chem.* **2015**, *71* (1), 3–8. <https://doi.org/10.1107/S2053229614024218>.
- (261) Dolomanov, O. V.; Bourhis, L. J.; Gildea, R. J.; Howard, J. A. K.; Puschmann, H. OLEX2: A Complete Structure Solution, Refinement and Analysis Program. *J. Appl. Crystallogr.* **2009**, *42* (2), 339–341. <https://doi.org/10.1107/S0021889808042726>.
- (262) Lagarec, K.; Rancourt, D. G. Extended Voigt-Based Analytic Lineshape Method for Determining N-Dimensional Correlated Hyperfine Parameter Distributions in Mössbauer Spectroscopy. *Nucl. Instruments Methods Phys. Res. Sect. B Beam Interact. with Mater. Atoms* **1997**, *129* (2), 266–280. [https://doi.org/10.1016/S0168-583X\(97\)00284-X](https://doi.org/10.1016/S0168-583X(97)00284-X).
- (263) Stoe & Cie. X-RED. Stoe & Cie GmbH: Darmstadt, Germany 2001.
- (264) Stoe & Cie. X-SHAPE. Stoe & Cie GmbH: Darmstadt, Germany 1999.

## X-ray crystallography data

Crystal data and structure refinement of **1** and its solvatomorphs.

Compound	<b>1·2DMSO</b>	<b>1·7DMSO</b>	<b>1·2MeOH</b>
Formula weight	644.14	1034.74	551.96
Temperature (K)	293	160	180
Space group	$P\bar{1}$	$R\bar{3}c$	$P2_1/n$
<i>a</i> (Å)	8.3929(13)	13.3415(3)	10.4567(8)
<i>b</i> (Å)	9.0045(15)	13.3415(3)	8.2415(5)
<i>c</i> (Å)	10.0309(16)	48.9618(11)	13.9101(8)
$\alpha$ , (°)	86.465(13)	90	90
$\beta$ , (°)	84.490(13)	90	99.208(7)
$\gamma$ , (°)	65.635(16)	120	90
Cell volume, (Å <sup>3</sup> )	687.2(2)	7547.4(4)	1183.31(14)
Z	1	6	2
$\rho_{\text{calc}}$ (g/cm <sup>3</sup> )	1.557	1.358	1.549
$\mu$ (mm <sup>-1</sup> )	0.755	0.647	0.692
Reflections collected/unique	5142/2408	10071/2021	8240/2322
GoF	0.996	1.060	1.084
Final <i>R</i> indices [ <i>I</i> >2 $\sigma$ ( <i>I</i> )]	$R_1=0.0591$ , $wR_2=0.0894$	$R_1=0.0441$ , $wR_2=0.1023$	$R_1=0.0538$ , $wR_2=0.0862$
<i>R</i> indices (all data)	$R_1=0.0944$ , $wR_2=0.1033$	$R_1=0.0577$ , $wR_2=0.1088$	$R_1=0.0768$ , $wR_2=0.0932$
Compound	<b>1·2CHCl<sub>3</sub></b>	<b>1·2DMF·H<sub>2</sub>O</b>	<b>1</b>
Formula weight	726.62	652.09	487.88
Temperature (K)	180	293	293
Space group	$P2_1/c$	$Pbcn$	$P2_1/c$
<i>a</i> (Å)	8.2460(4)	8.3469(5)	8.2563(13)
<i>b</i> (Å)	12.1991(4)	15.7421(7)	8.2491(19)
<i>c</i> (Å)	14.6014(6)	22.5116(9)	15.902(4)
$\alpha$ , (°)	90	90	90
$\beta$ , (°)	105.973(4)	90	100.91(2)
$\gamma$ , (°)	90	90	90
Cell volume, (Å <sup>3</sup> )	1412.11(10)	2958.0(3)	1063.5(4)
Z	2	4	2
$\rho_{\text{calc}}$ (g/cm <sup>3</sup> )	1.709	1.464	1.524
$\mu$ (mm <sup>-1</sup> )	1.147	0.570	0.753
Reflections collected/unique	9532/3251	10062/2601	2425/2425
GoF	1.047	1.053	1.104
Final <i>R</i> indices [ <i>I</i> >2 $\sigma$ ( <i>I</i> )]	$R_1=0.0403$ , $wR_2=0.0802$	$R_1=0.0537$ , $wR_2=0.0945$	$R_1=0.2410$ , $wR_2=0.5271$
<i>R</i> indices (all data)	$R_1=0.0519$ , $wR_2=0.0848$	$R_1=0.0890$ , $wR_2=0.1082$	$R_1=0.2663$ , $wR_2=0.5393$

Crystal data and structure refinement of ***n*Bu<sub>4</sub>NL<sup>2</sup>** and complexes **4** and **6** (at 100 K only).

Compound	<b><i>n</i>Bu<sub>4</sub>NL<sup>2</sup></b>	<b>4</b> ( <i>trans</i> )	<b>4</b> ( <i>cis</i> )·CH <sub>2</sub> Cl <sub>2</sub>	<b>6</b>
Formula weight	501.49	533.90	618.84	513.91
Temperature (K)	173	100	100	100
Space group	<i>P</i> 2 <sub>1</sub> / <i>n</i>	<i>C</i> 2/ <i>c</i>	<i>P</i> 2 <sub>1</sub> / <i>n</i>	<i>P</i> 2 <sub>1</sub> / <i>n</i>
<i>a</i> (Å)	11.9642(1)	9.6251(18)	7.4188(2)	10.364(3)
<i>b</i> (Å)	15.7273(1)	18.494(3)	23.3314(7)	16.490(4)
<i>c</i> (Å)	15.0760(2)	13.335(3)	15.4739(3)	12.598(3)
α, (°)	90	90	90	90
β, (°)	92.122(1)	91.540(6)	101.793(2)	95.789(8)
γ, (°)	90	90	90	90
Cell volume, (Å <sup>3</sup> )	2834.82(5)	2372.9(8)	2621.86(12)	2142.1(10)
Z	4	4	4	4
ρ <sub>calc</sub> (g/cm <sup>3</sup> )	1.175	1.494	1.568	1.581
μ (mm <sup>-1</sup> )	0.620	0.680	6.873	0.749
Reflections collected/unique	89937/5001	34154/3978	21400/4449	58852/4388
GoF	1.046	0.853	1.102	0.990
Final <i>R</i> indices [ <i>I</i> >2σ( <i>I</i> )]	<i>R</i> <sub>1</sub> =0.0413, <i>wR</i> <sub>2</sub> =0.1105	<i>R</i> <sub>1</sub> =0.0368, <i>wR</i> <sub>2</sub> =0.1021	<i>R</i> <sub>1</sub> =0.0755, <i>wR</i> <sub>2</sub> =0.2096	<i>R</i> <sub>1</sub> =0.0372, <i>wR</i> <sub>2</sub> =0.0949
<i>R</i> indices (all data)	<i>R</i> <sub>1</sub> =0.0496, <i>wR</i> <sub>2</sub> =0.1177	<i>R</i> <sub>1</sub> =0.0543, <i>wR</i> <sub>2</sub> =0.1211	<i>R</i> <sub>1</sub> =0.0863, <i>wR</i> <sub>2</sub> =0.2143	<i>R</i> <sub>1</sub> =0.0458, <i>wR</i> <sub>2</sub> =0.1009

Selected geometric parameters for compound **4** (both *trans*- and *cis*-isomers) at 100 K.

Compound			
<b>4</b> ( <i>trans</i> )		<b>4</b> ( <i>cis</i> )·CH <sub>2</sub> Cl <sub>2</sub>	
Fe—N	Distance (Å)	Fe—N	Distance (Å)
Fe1—N5 <sup>i</sup>	1.9835(14)	Fe1—N11	1.963 (4)
Fe1—N3 <sup>i</sup>	1.9821(15)	Fe1—N9	1.964 (4)
Fe1—N1 <sup>i</sup>	1.9618(14)	Fe1—N1	1.969 (4)
Fe1—N1	1.9618(14)	Fe1—N5	1.971 (4)
Fe1—N3	1.9821(15)	Fe1—N3	1.972 (5)
Fe1—N5	1.9835(14)	Fe1—N13	1.973 (4)
N—Fe—N	Angle (°)	N—Fe—N	Angle (°)
N5 <sup>i</sup> —Fe1—N3 <sup>i</sup>	89.23 (6)	N1—Fe1—N13	90.35 (17)
N5 <sup>i</sup> —Fe1—N1 <sup>i</sup>	91.96 (6)	N5—Fe1—N13	179.03 (18)
N3 <sup>i</sup> —Fe1—N1 <sup>i</sup>	92.22 (6)	N3—Fe1—N13	91.04 (17)
N5 <sup>i</sup> —Fe1—N1	88.04 (6)	N11—Fe1—N9	87.87 (18)
N3 <sup>i</sup> —Fe1—N1	87.78 (6)	N11—Fe1—N1	177.69 (17)
N1 <sup>i</sup> —Fe1—N1	179.99	N9—Fe1—N1	90.50 (18)
N5 <sup>i</sup> —Fe1—N3	90.77 (6)	N11—Fe1—N5	91.58 (17)
N3 <sup>i</sup> —Fe1—N3	179.99	N9—Fe1—N5	90.74 (17)
N1 <sup>i</sup> —Fe1—N3	87.78 (6)	N1—Fe1—N5	90.08 (17)
N1—Fe1—N3	92.22 (6)	N11—Fe1—N3	93.67 (19)
N5 <sup>i</sup> —Fe1—N5	179.99	N9—Fe1—N3	178.10 (17)
N3 <sup>i</sup> —Fe1—N5	90.77 (6)	N1—Fe1—N3	88.00 (18)

Selected geometric parameters for compound **4** (both *trans*- and *cis*-isomers) at 100K.  
(continuation)

<b>N—Fe—N</b>	<b>Angle (°)</b>	<b>N—Fe—N</b>	<b>Angle (°)</b>
N1 <sup>i</sup> —Fe1—N5	88.04 (6)	N5—Fe1—N3	88.10 (17)
N1—Fe1—N5	91.96 (6)	N11—Fe1—N13	88.02 (17)

Unit cell parameters of **6** at selected temperatures.

Parameter	Temperature (K)			
	<b>100</b>	<b>293</b>	<b>320</b>	<b>393</b>
<i>a</i> (Å)	10.364(3)	10.547(3)	10.5951(7)	10.6457(2)
<i>b</i> (Å)	16.490(4)	16.596(4)	16.5995(9)	16.6839(5)
<i>c</i> (Å)	12.598(3)	12.943(4)	12.9503(8)	13.0720(3)
$\beta$ , (°)	95.789(8)	95.213(10)	94.867(6)	94.662(2)
Cell volume, (Å <sup>3</sup> )	2142.1(10)	2256.1(11)	2269.4(2)	2314.06(10)

Selected structural parameters for **6** at selected temperatures.

Distance (Å)	Temperature (K)			
	<b>100</b>	<b>293</b>	<b>320</b>	<b>393</b>
Fe1—N6	1.9797(19)	2.079(2)	2.103(3)	2.1268(18)
Fe1—N14	1.9774(19)	2.082(2)	2.105(3)	2.1315(19)
Fe1—N10	1.988(2)	2.119(2)	2.130(3)	2.165(2)
Fe1—N2	1.986(2)	2.107(3)	2.132(3)	2.1668(19)
Fe1—N4	1.995(2)	2.136(2)	2.154(3)	2.178(2)
Fe1—N12	1.999(2)	2.121(3)	2.153(3)	2.1868(19)
	Temperature (K)			
Angle (°)	<b>100</b>	<b>293</b>	<b>320</b>	<b>393</b>
N6—Fe1—N14	179.13(8)	179.36(9)	179.11(12)	178.85(8)
N6—Fe1—N10	91.80(8)	94.06(9)	94.52(12)	94.98(7)

Selected structural parameters for **6** at selected temperatures (continuation).

	Temperature (K)			
Angle (°)	<b>100</b>	<b>293</b>	<b>320</b>	<b>393</b>
N14—Fe1—N10	87.89(8)	86.57(9)	86.35(12)	86.08(8)
N6—Fe1—N2	87.83(8)	86.18(10)	85.88(12)	85.42(8)
N14—Fe1—N2	91.36(8)	93.83(10)	94.30(12)	95.02(8)
N10—Fe1—N2	89.69(8)	91.41(9)	91.61(12)	92.12(8)
N6—Fe1—N4	89.27(8)	87.46(9)	87.14(11)	86.84(7)
N14—Fe1—N4	91.01(8)	91.90(9)	92.00(12)	92.13(8)
N10—Fe1—N4	177.99(8)	177.28(9)	177.09(12)	177.10(8)
N2—Fe1—N4	88.66(8)	86.44 (9)	86.13(12)	85.76(8)
N6—Fe1—N12	91.73(8)	92.57(9)	92.74(11)	93.07(7)
N14—Fe1—N12	89.08(8)	87.44(10)	87.11(12)	86.54(8)
N10—Fe1—N12	88.82(8)	86.64(9)	86.03(12)	85.66(8)
N2—Fe1—N12	178.43(8)	177.60(9)	177.17(12)	177.20(8)
N4—Fe1—N12	92.84(8)	95.55(9)	96.28 (12)	96.51(8)

Crystal data and structure refinement of complexes **16–18**.

Compound	<b>16</b>	<b>17</b>	<b>18</b>
Formula weight	2268.30	2186.43	2197.09
Temperature (K)	100	173	173
Space group	<i>P</i> 4 <sub>2</sub> 1 <sub>2</sub>	<i>P</i> -1	<i>P</i> -1
<i>a</i> (Å)	17.8807(6)	12.3617(9)	12.1643(2)
<i>b</i> (Å)	17.8807(6)	12.7385(9)	12.6444(2)
<i>c</i> (Å)	16.2846(6)	14.0359(12)	14.1504(3)
$\alpha$ , (°)	90	104.654(6)	105.257(2)
$\beta$ , (°)	90	103.976(6)	104.052(2)
$\gamma$ , (°)	90	109.378(5)	109.3800(10)
Cell volume, (Å <sup>3</sup> )	5206.5(4)	1884.6(3)	1845.88(6)
<i>Z</i>	2	1	1
$\rho_{\text{calc}}$ (g/cm <sup>3</sup> )	1.446	1.927	1.976
$\mu$ (mm <sup>-1</sup> )	1.223	1.448	13.769
Reflections collected/unique	4579/4061	8230/6755	7381/6805
GoF	1.078	1.020	1.062
Final <i>R</i> indices [ <i>I</i> >2 $\sigma$ ( <i>I</i> )]	<i>R</i> <sub>1</sub> =0.0496, <i>wR</i> <sub>2</sub> =0.1405	<i>R</i> <sub>1</sub> =0.0405, <i>wR</i> <sub>2</sub> =0.1010	<i>R</i> <sub>1</sub> =0.0508, <i>wR</i> <sub>2</sub> =0.1491
<i>R</i> indices (all data)	<i>R</i> <sub>1</sub> =0.0565, <i>wR</i> <sub>2</sub> =0.1336	<i>R</i> <sub>1</sub> =0.0528, <i>wR</i> <sub>2</sub> =0.0962	<i>R</i> <sub>1</sub> =0.0538, <i>wR</i> <sub>2</sub> =0.1459

**Notes on the solution and refinement of the structures of complexes 16–18**

The structures were solved by direct method and refined against  $F^2$  by full-matrix least-squares method in anisotropic approximation for all atoms except hydrogen using the SHELXTL software package.<sup>259,260</sup> For the structure of **16** the H atoms were located from the difference maps of electron density and refined by “riding” model with  $U_{\text{iso}} = 1.2U_{\text{eq}}$  of the carrier non-hydrogen atom.

In case of the complexes **17** and **18**, the refinement met severe problems associated with disorder of the structure components and possible twinning. Significant residual electron density peaks near La (Nd) ions indicated contribution from a second domain. The attempt to index and integrate the diffraction data as a two-domain system or to derive an appropriate twinning scheme was not successful. Therefore, La (Nd) ions were considered as disordered, with partial contribution factors of 0.93, 0.07 (**17**) and 0.95, 0.05 (**18**) suggested by refinement of thermal parameters. Only major component of the disorder was then refined anisotropically. More important that interlay of two chemically identical helicate moieties of opposite chirality results in equal disorder of the organic linkage and either encapsulated or outer Na cations. Refinements in acentric space group *P*1 did not provide an ordered model, while preserving all features of the disorder. This was resolved with partial occupancy factors of 0.5 for all atoms of two unique ligands and two unique Na ions. With exception of peripheral C-atoms of the methoxy groups, it

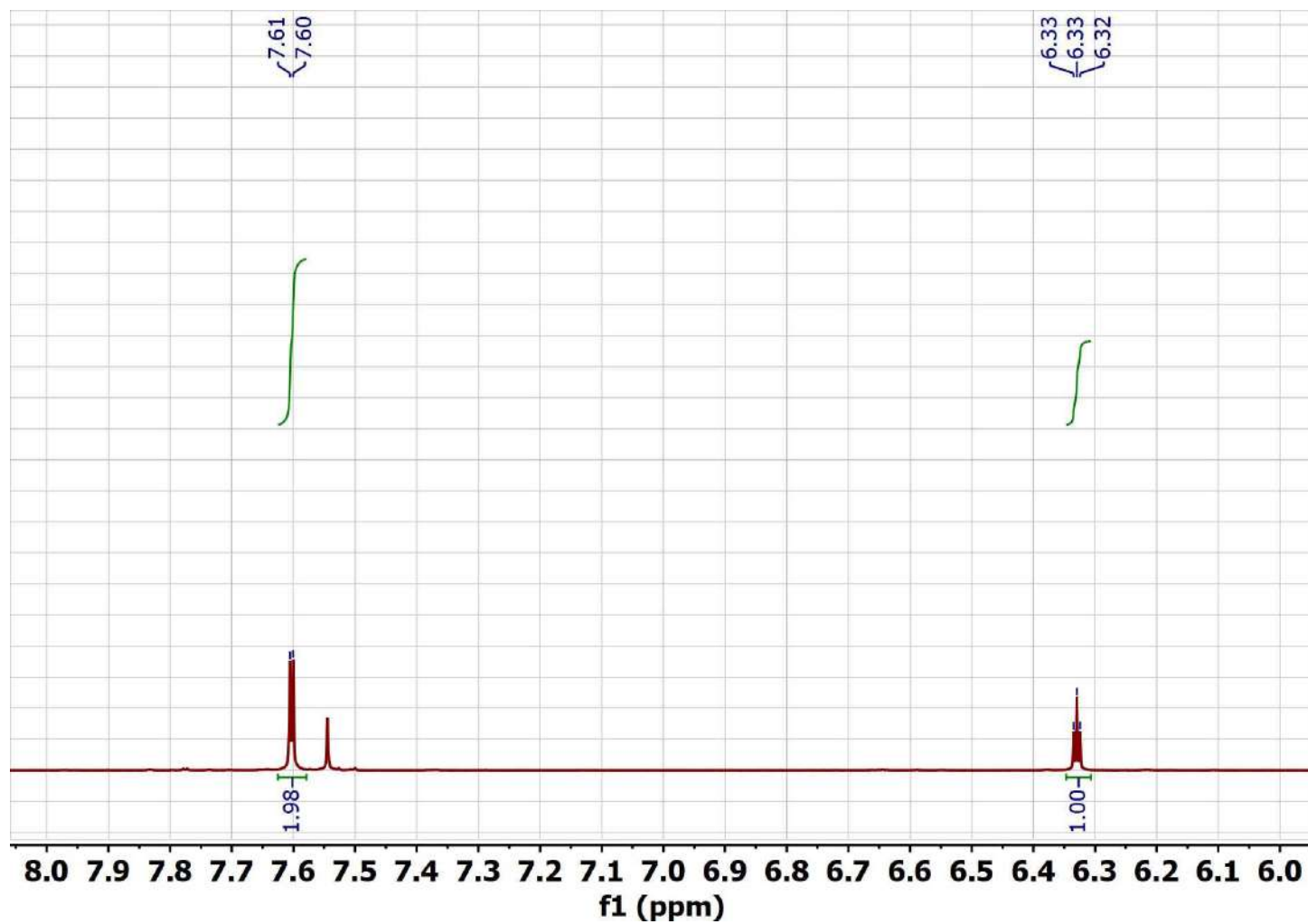
was possible to refine anisotropic model. A set of restraints was applied to improve the refinement stability. In particular, similarity restraints were used for thermal motion of some closely separated components of the disorder as well as for some chemically identical bonds of P–OCH<sub>3</sub> fragments. Due to the nature of the disorder, the hydrogen atoms were not added.

Analysis of the Ln<sup>3+</sup> coordination geometry in the complexes **16**, **17** and **18** using SHAPE 2.1 software.

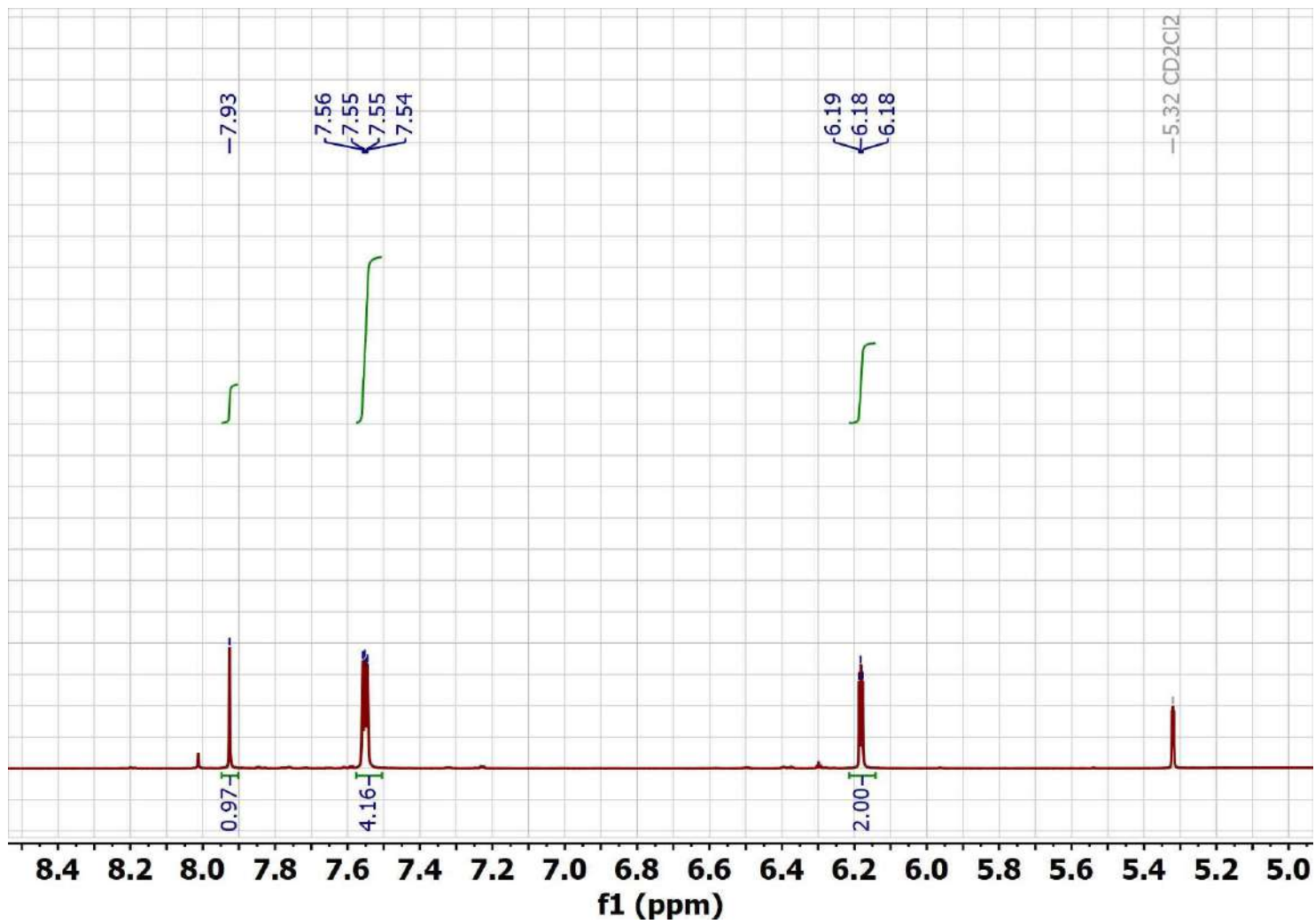
	<b>16</b> (Nd1)	<b>16</b> (Nd2)	<b>17</b> (La1)	<b>18</b> (Nd1)
Octagon (D8h)	25.210	25.050	26.949	25.226
Heptagonal pyramid (C7v)	24.672	24.671	22.738	24.439
Hexagonal bipyramid (D6h)	17.196	17.526	12.110	16.350
Cube (Oh)	9.614	9.975	5.895	9.426
Square antiprism (D4d)	0.168	0.202	1.869	0.321
Triangular dodecahedron (D2d)	2.658	2.786	2.889	2.623
Johnson gyrobifastigium J26 (D2d)	16.621	16.767	14.362	15.465
Johnson elongated triangular bipyramid J14 (D3h)	28.333	28.312	25.743	27.116
Biaugmented trigonal prism J50 (C2v)	2.880	2.855	4.399	2.878
Biaugmented trigonal prism (C2v)	1.978	1.843	3.666	1.922
Snub diphenoid J84 (D2d)	5.373	5.430	6.335	5.145
Triakis tetrahedron (Td)	10.476	10.833	6.624	10.202
Elongated trigonal bipyramid (D3h)	23.497	23.540	22.025	22.384

## NMR spectra

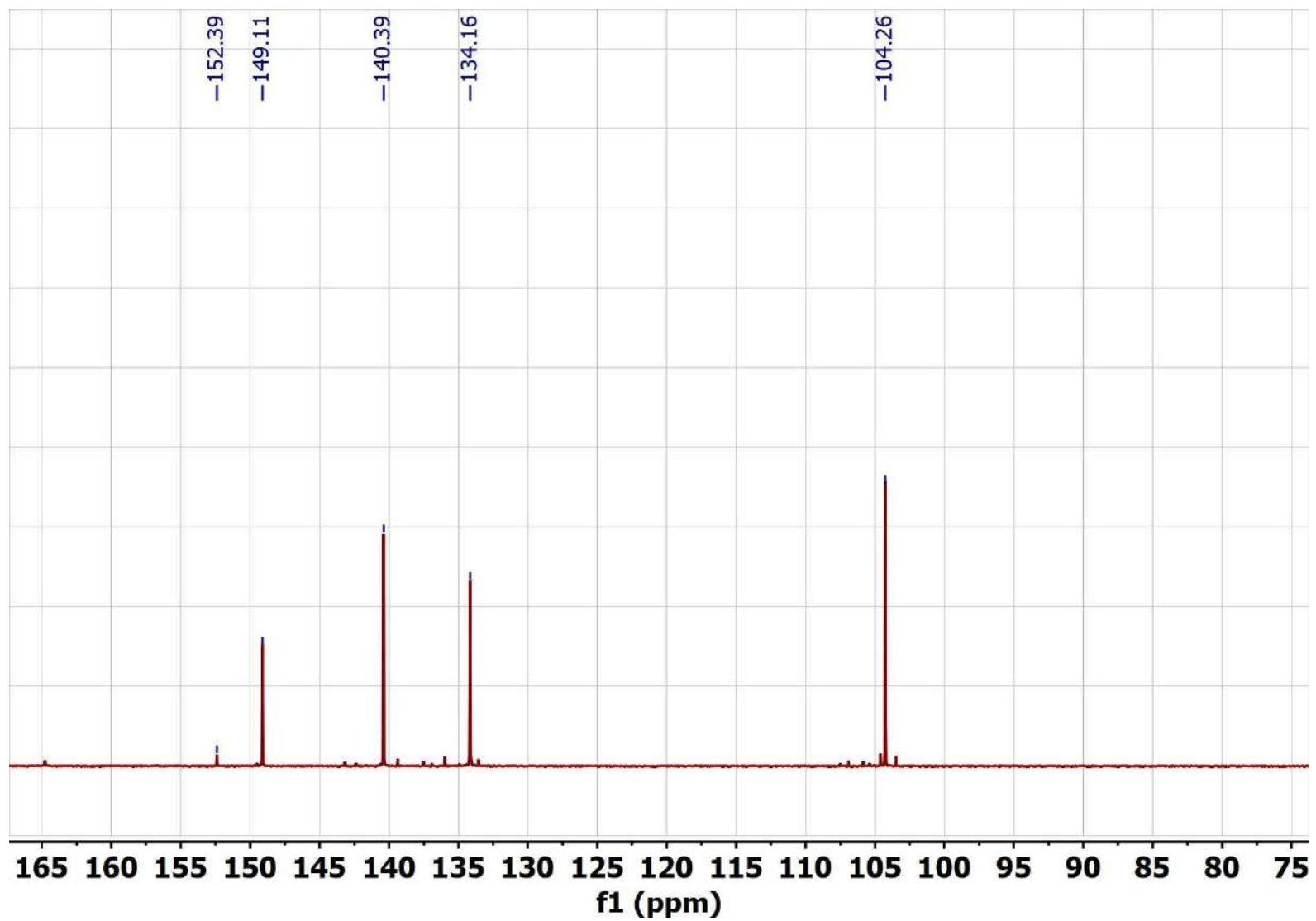
$^1\text{H}$  NMR spectrum (aromatic region) of product obtained in an attempt to reduce  $n\text{Bu}_4\text{NL}^2$  (solvent –  $\text{CD}_3\text{OD}$ ).



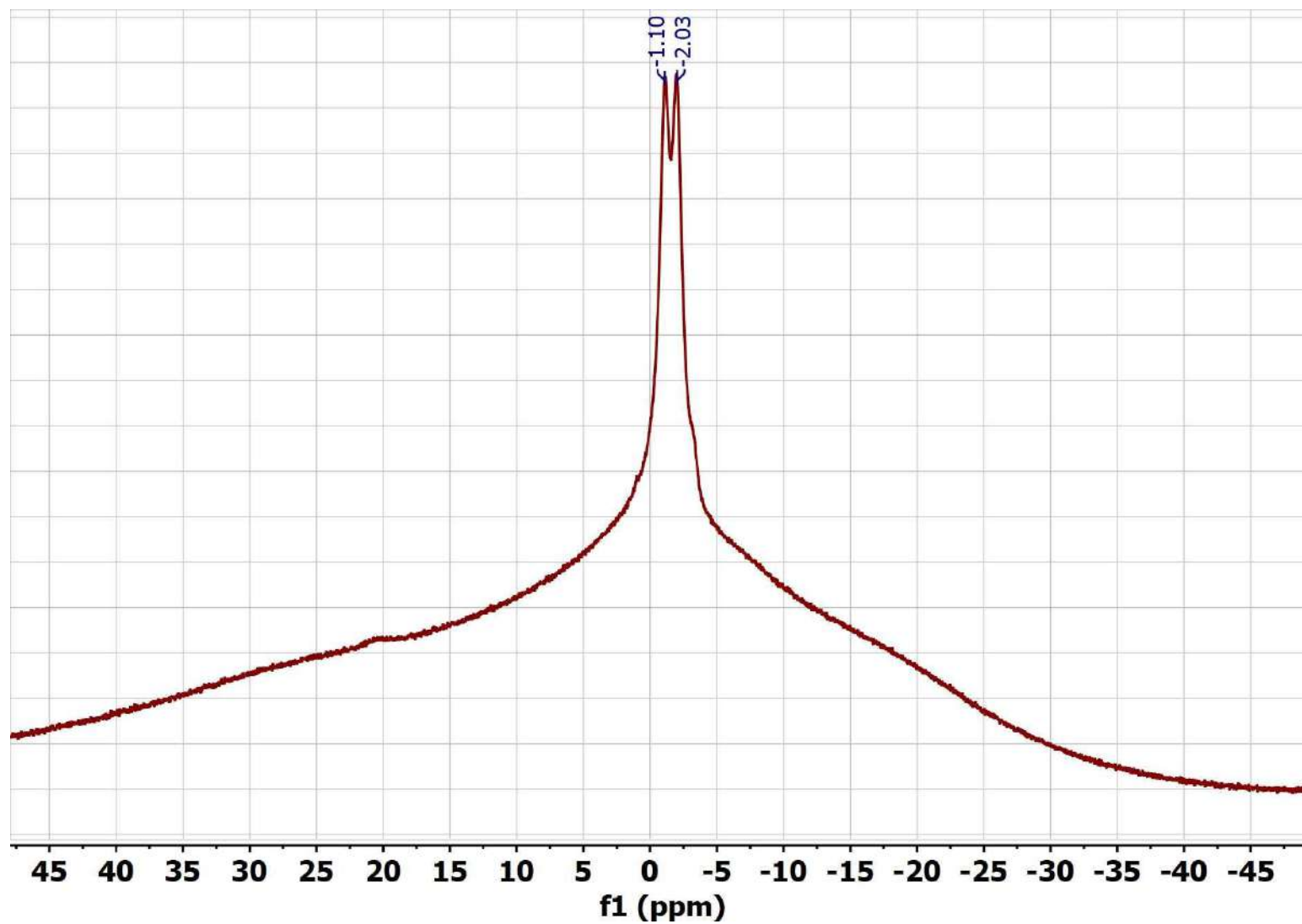
$^1\text{H}$  NMR spectrum (aromatic region) of  ${}^n\text{Bu}_4\text{NL}^2$  in  $\text{CD}_2\text{Cl}_2$ .



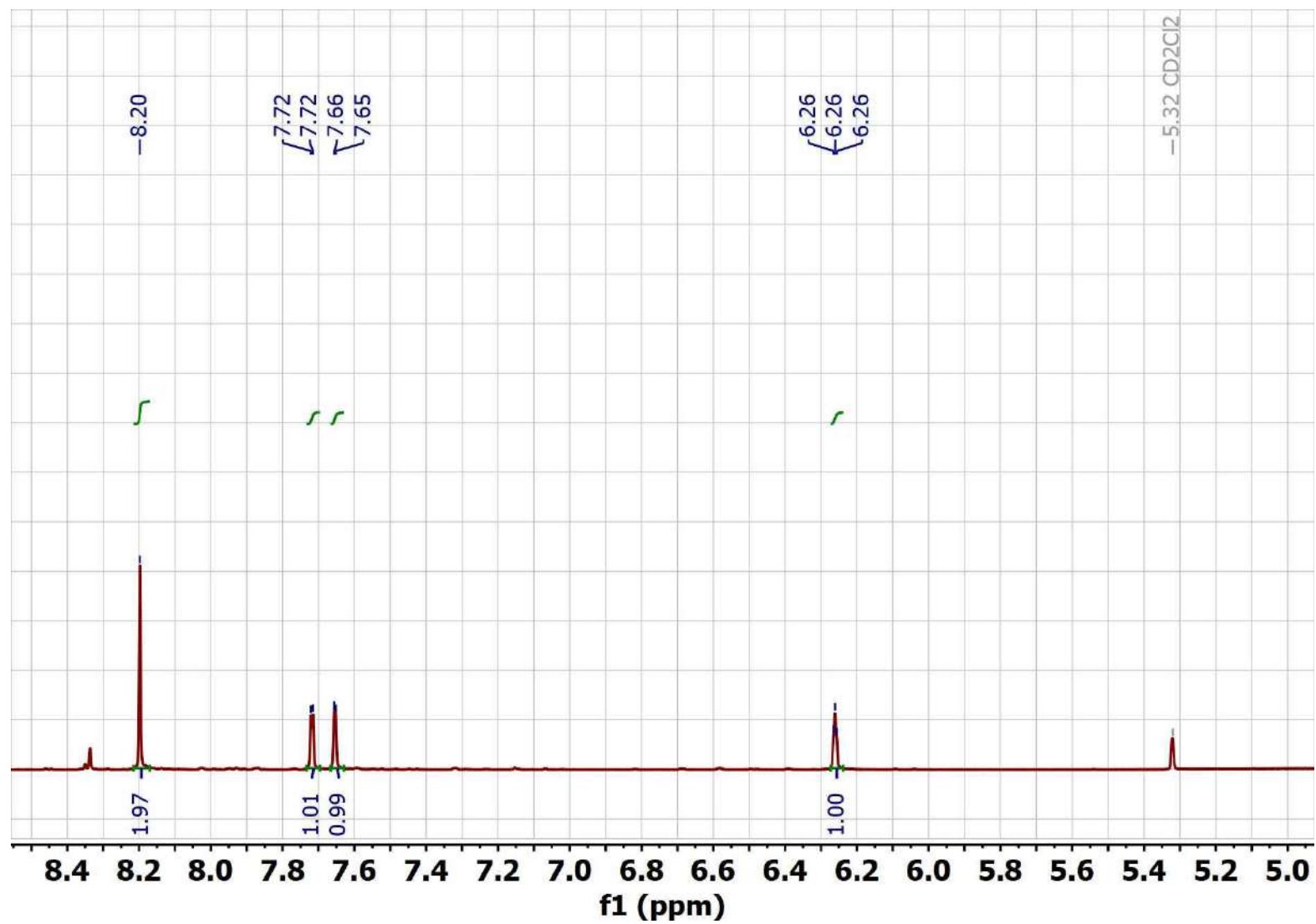
$^{13}\text{C}$  NMR spectrum (aromatic region) of  ${}^n\text{Bu}_4\text{NL}^2$  in  $\text{CD}_2\text{Cl}_2$ .



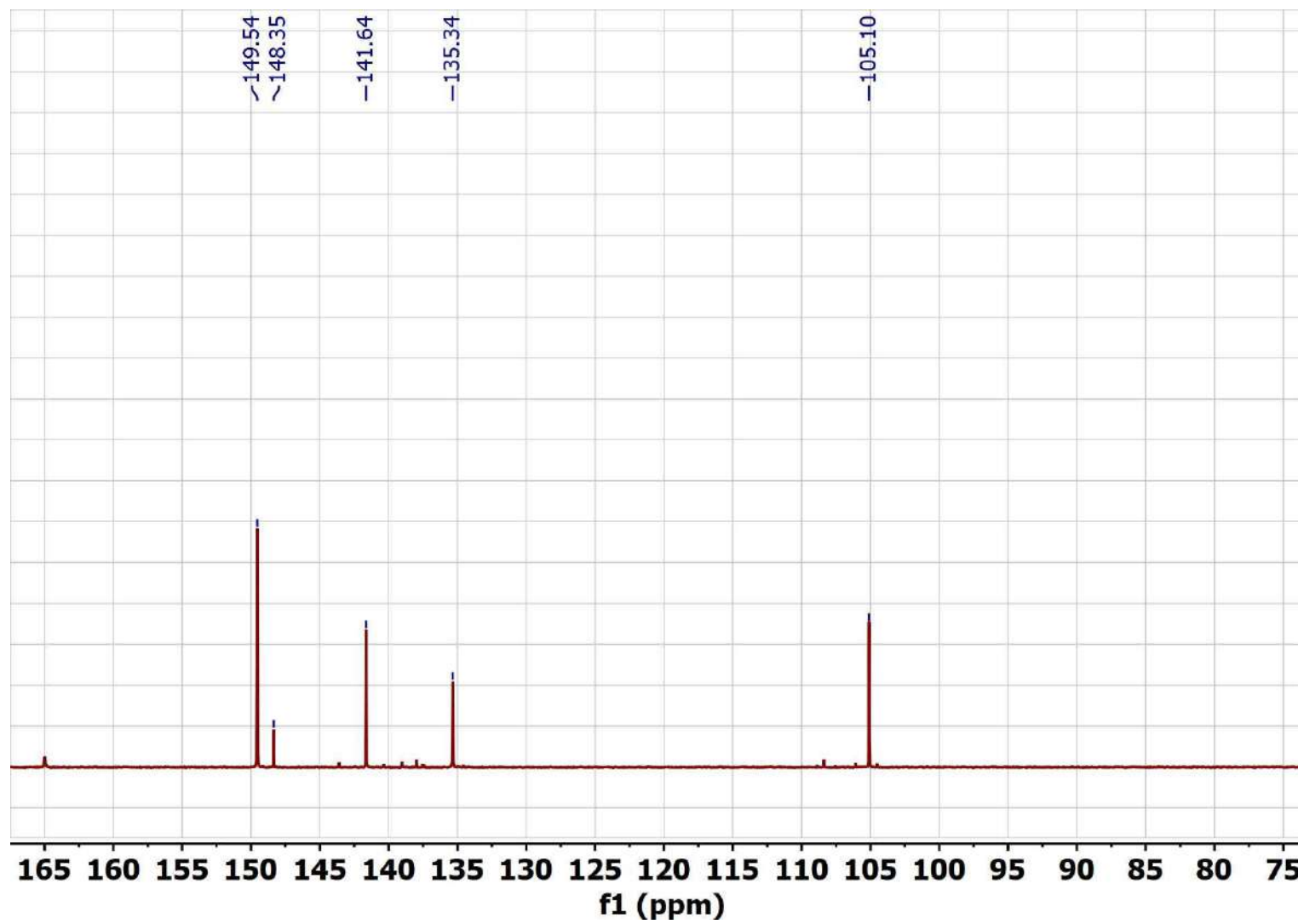
$^{11}\text{B}$  NMR spectrum of  ${}^n\text{Bu}_4\text{NL}^2$  in  $\text{CD}_2\text{Cl}_2$ .



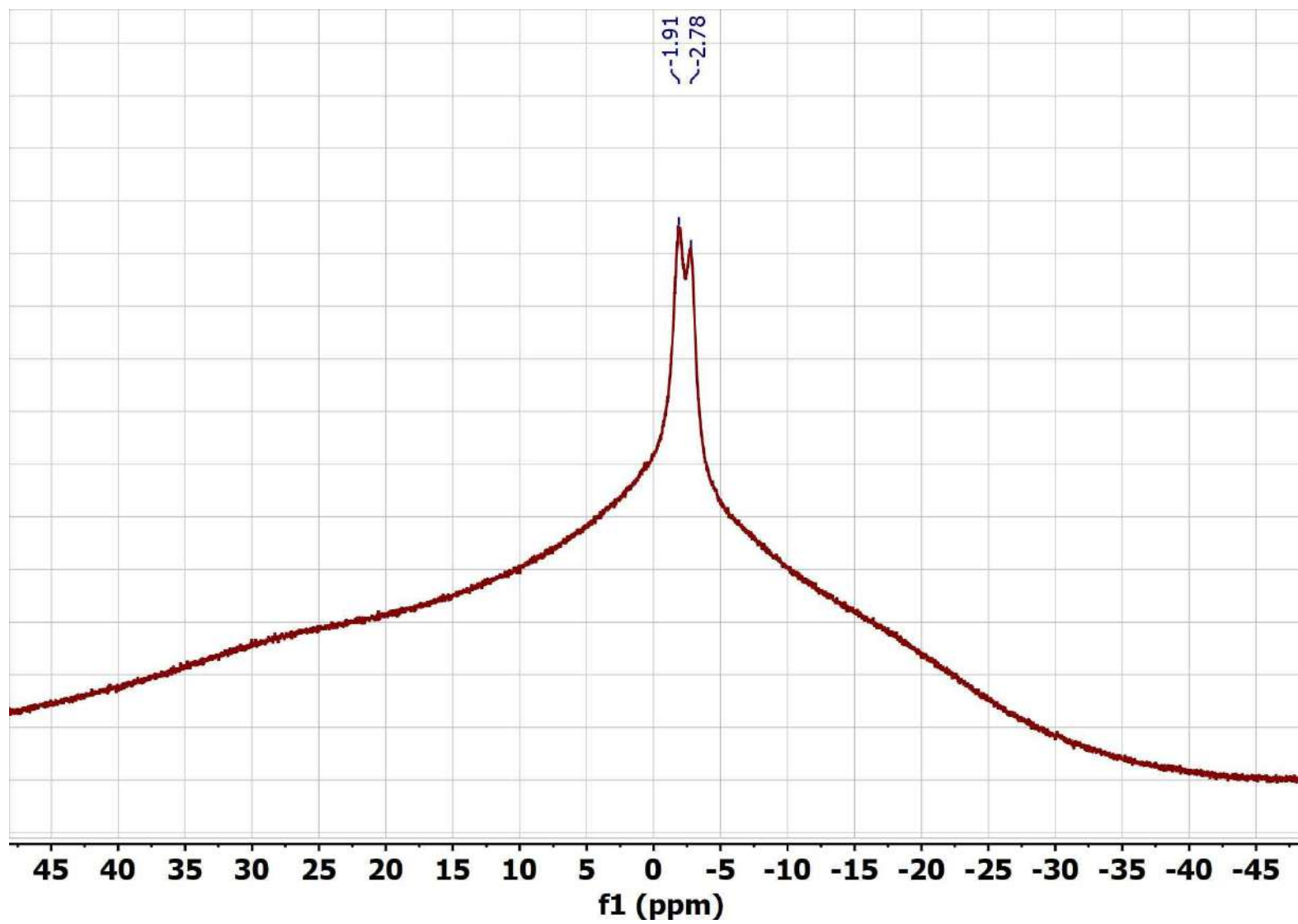
$^1\text{H}$  NMR spectrum (aromatic region) of  ${}^n\text{Bu}_4\text{NL}^3$  in  $\text{CD}_2\text{Cl}_2$ .



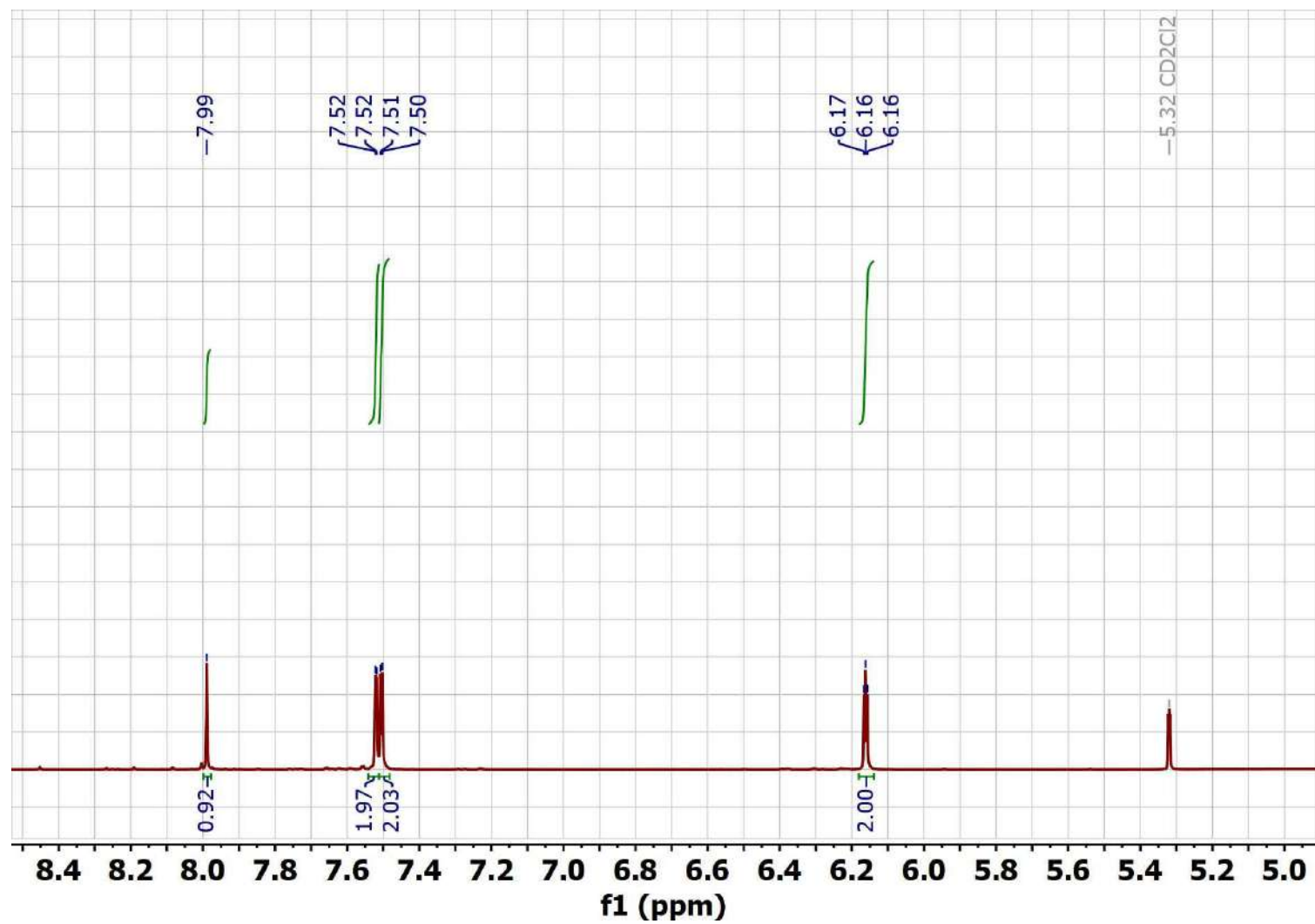
$^{13}\text{C}$  NMR spectrum (aromatic region) of  $n\text{Bu}_4\text{NL}^3$  in  $\text{CD}_2\text{Cl}_2$ .



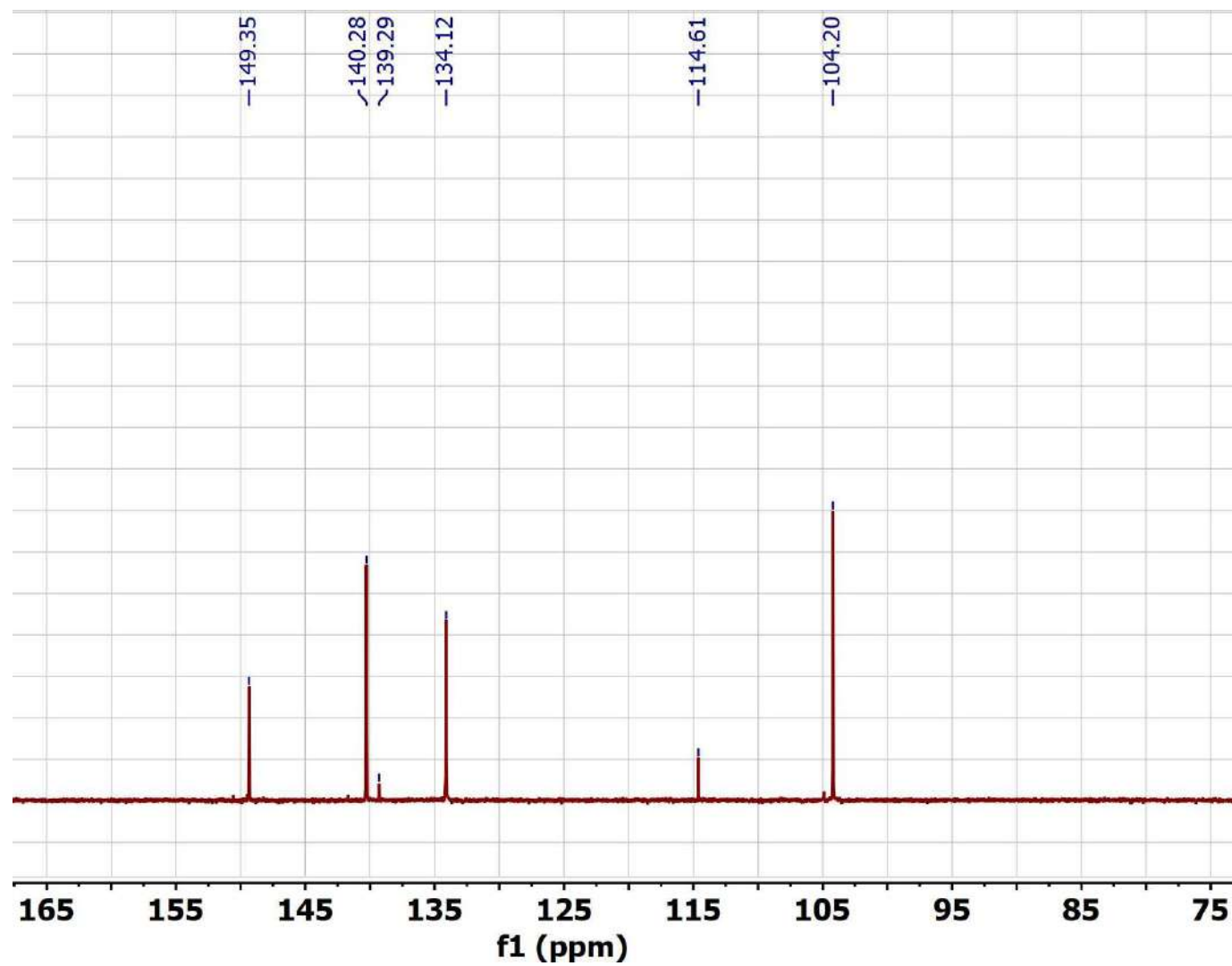
$^{11}\text{B}$  NMR spectrum of  ${}^n\text{Bu}_4\text{NL}^3$  in  $\text{CD}_2\text{Cl}_2$ .



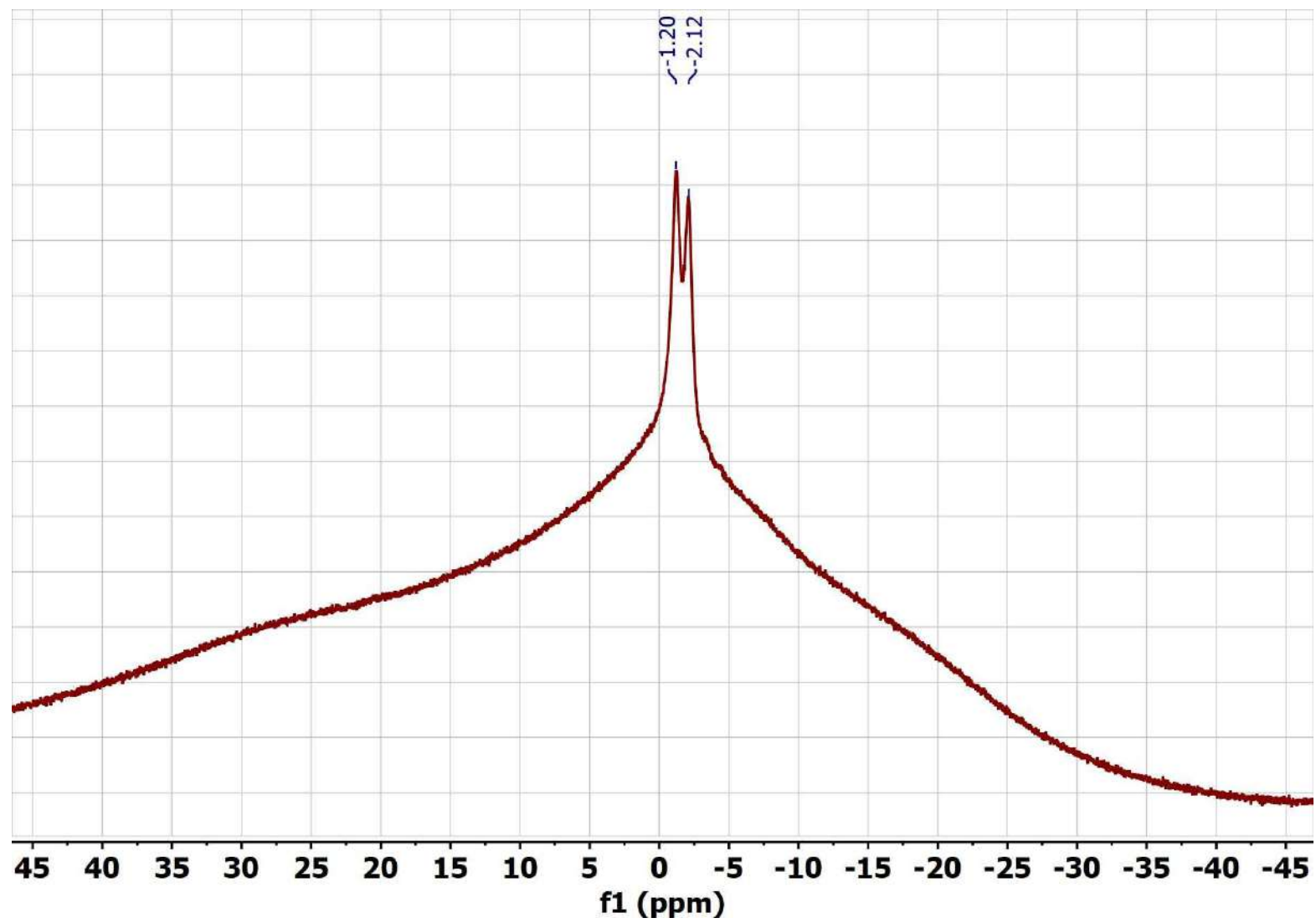
$^1\text{H}$  NMR spectrum (aromatic region) of  ${}^n\text{Bu}_4\text{NL}^4$  in  $\text{CD}_2\text{Cl}_2$ .



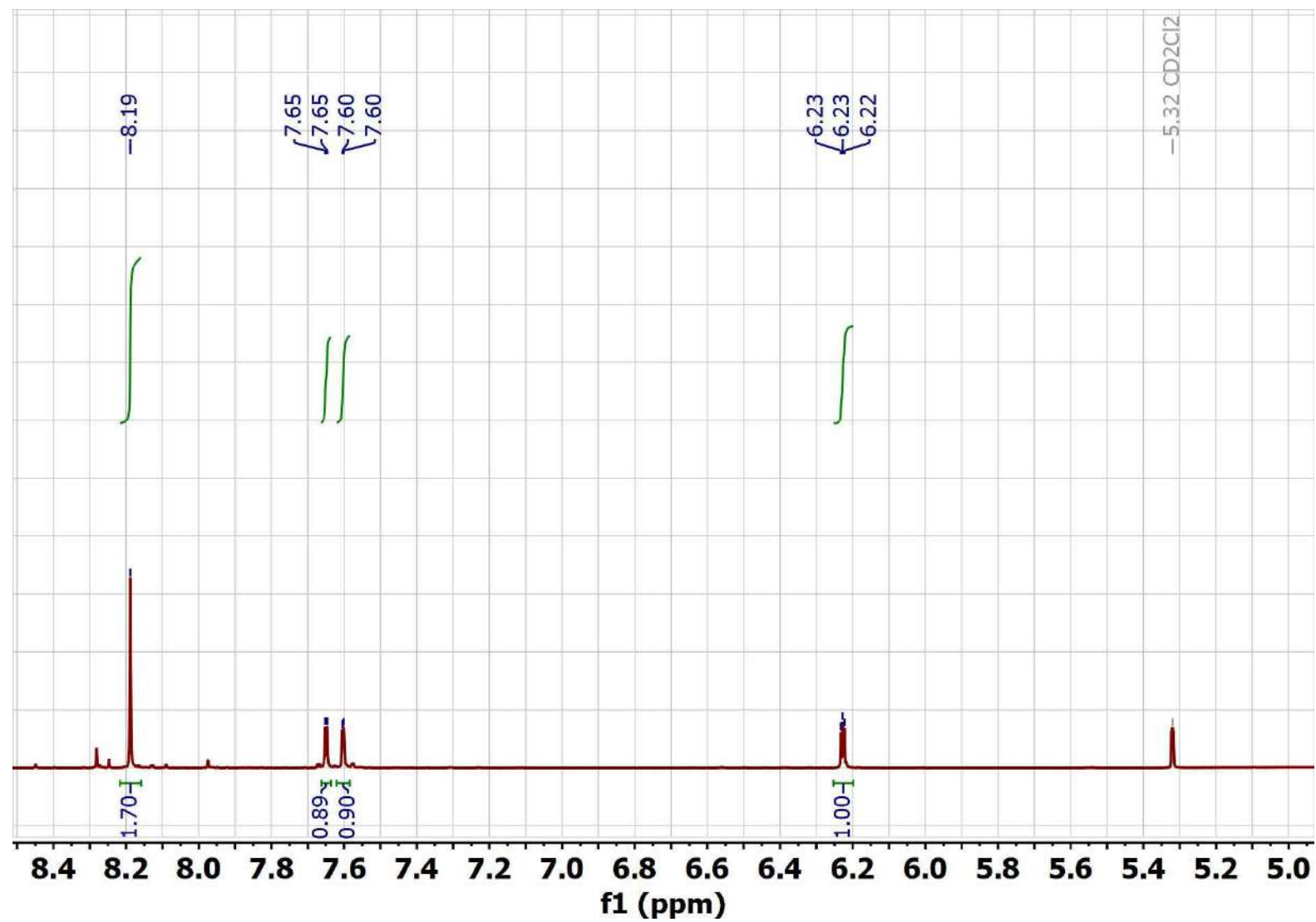
$^{13}\text{C}$  NMR spectrum (aromatic region) of  $n\text{Bu}_4\text{NL}^4$  in  $\text{CD}_2\text{Cl}_2$ .



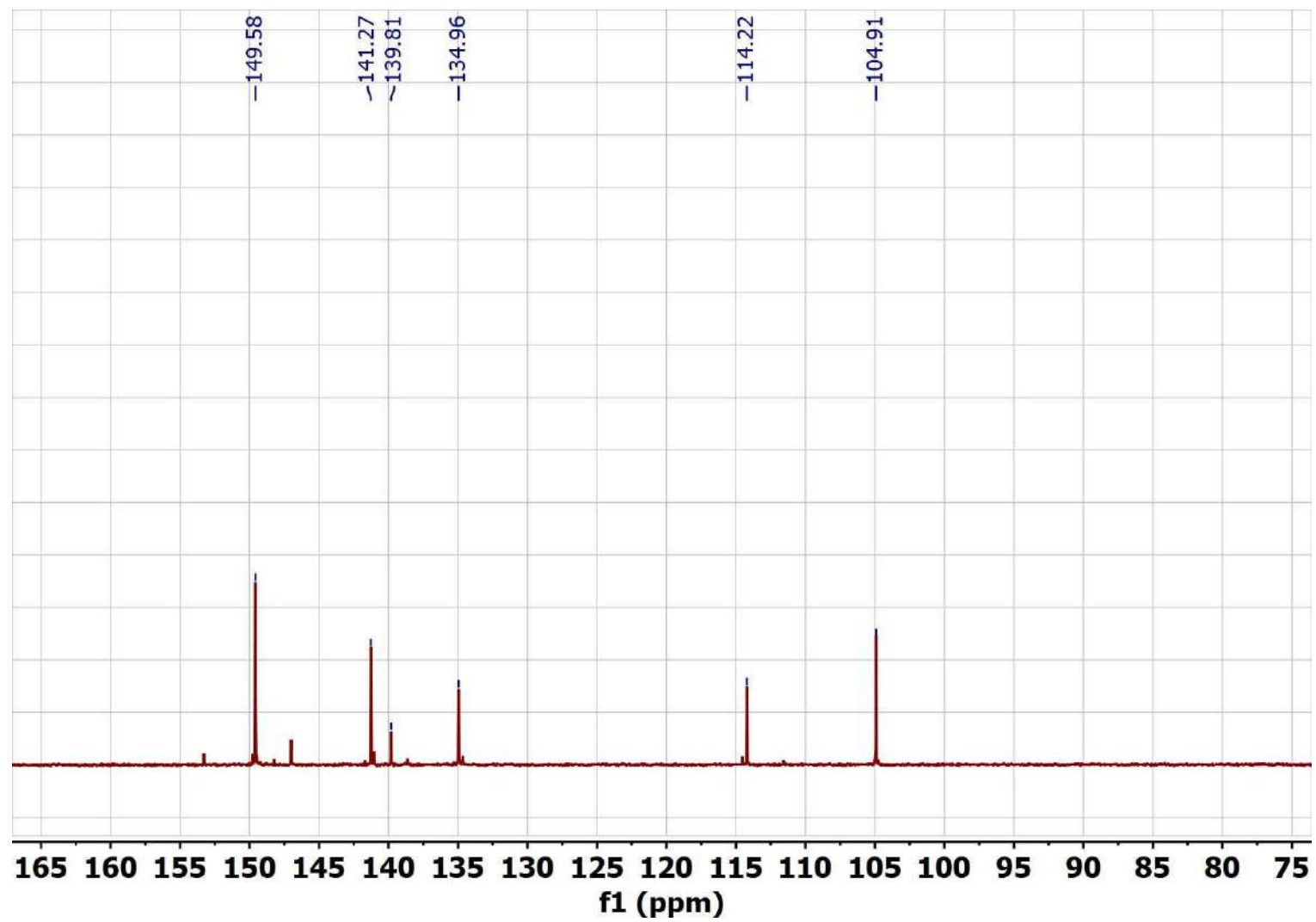
$^{11}\text{B}$  NMR spectrum of  $^n\text{Bu}_4\text{NL}^4$  in  $\text{CD}_2\text{Cl}_2$ .



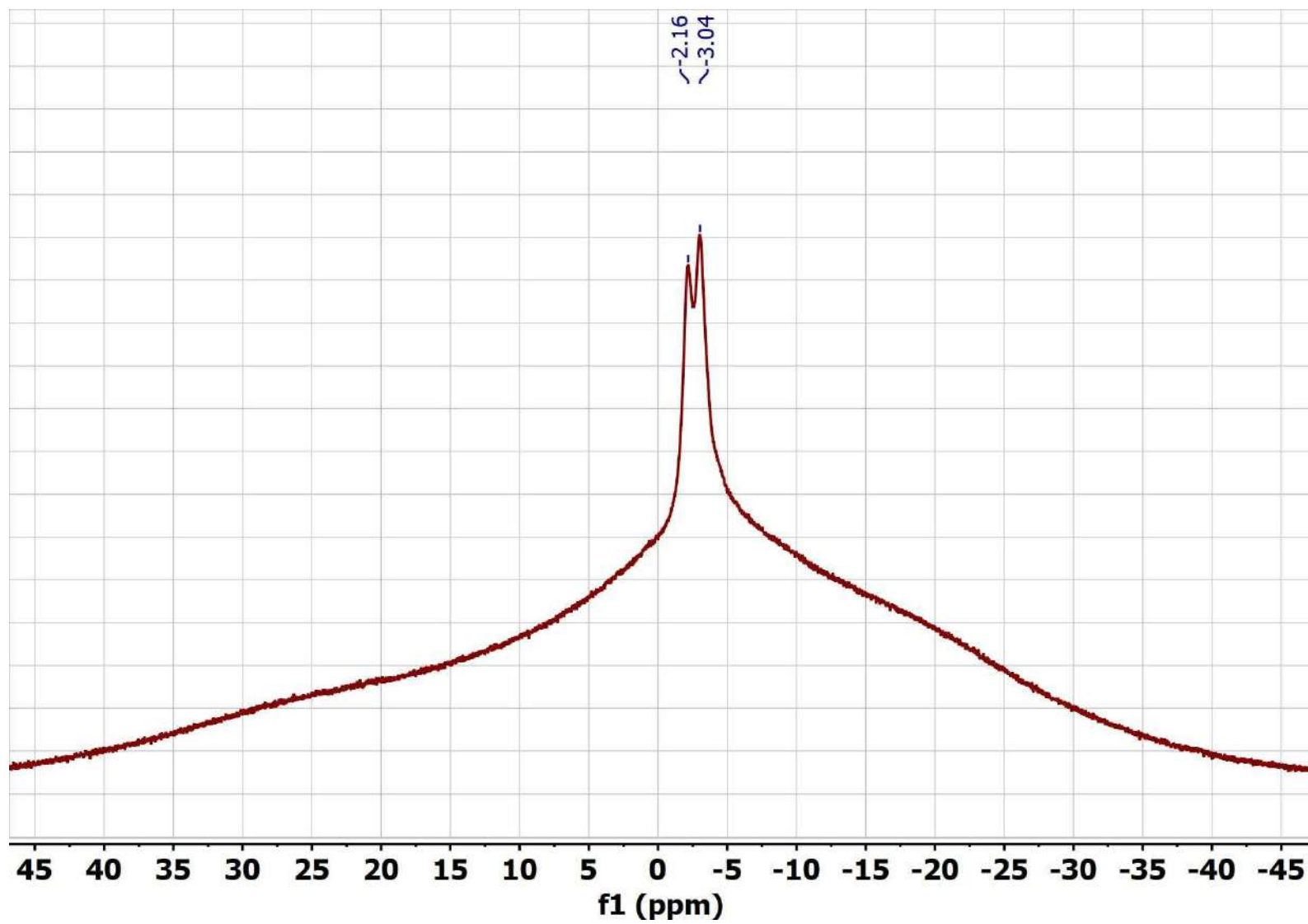
$^1\text{H}$  NMR spectrum (aromatic region) of  ${}^n\text{Bu}_4\text{NL}^5$  in  $\text{CD}_2\text{Cl}_2$ .



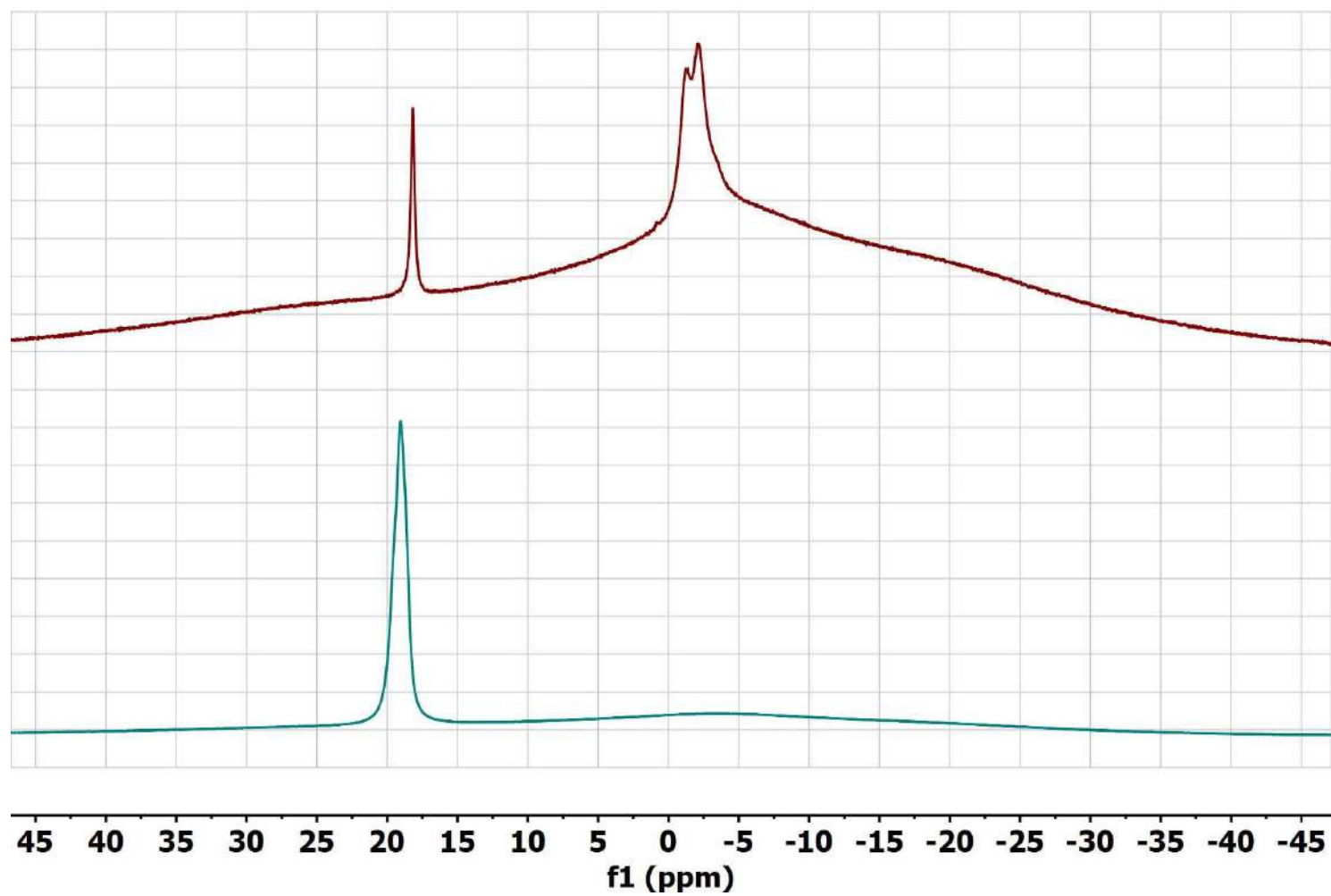
$^{13}\text{C}$  NMR spectrum (aromatic region) of  $n\text{Bu}_4\text{NL}^5$  in  $\text{CD}_2\text{Cl}_2$ .



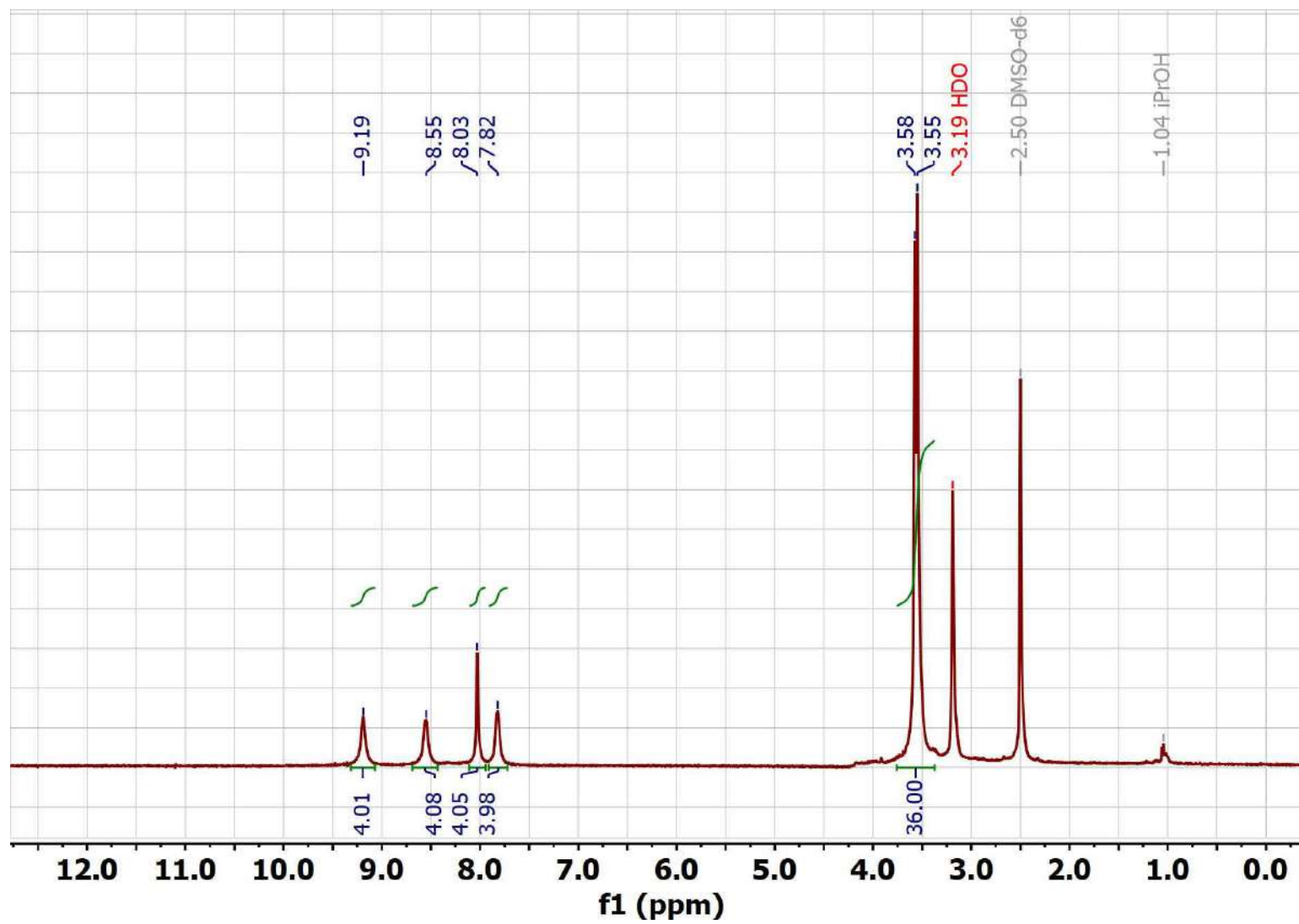
$^{11}\text{B}$  NMR spectrum of  ${}^n\text{Bu}_4\text{NL}^5$  in  $\text{CD}_2\text{Cl}_2$ .



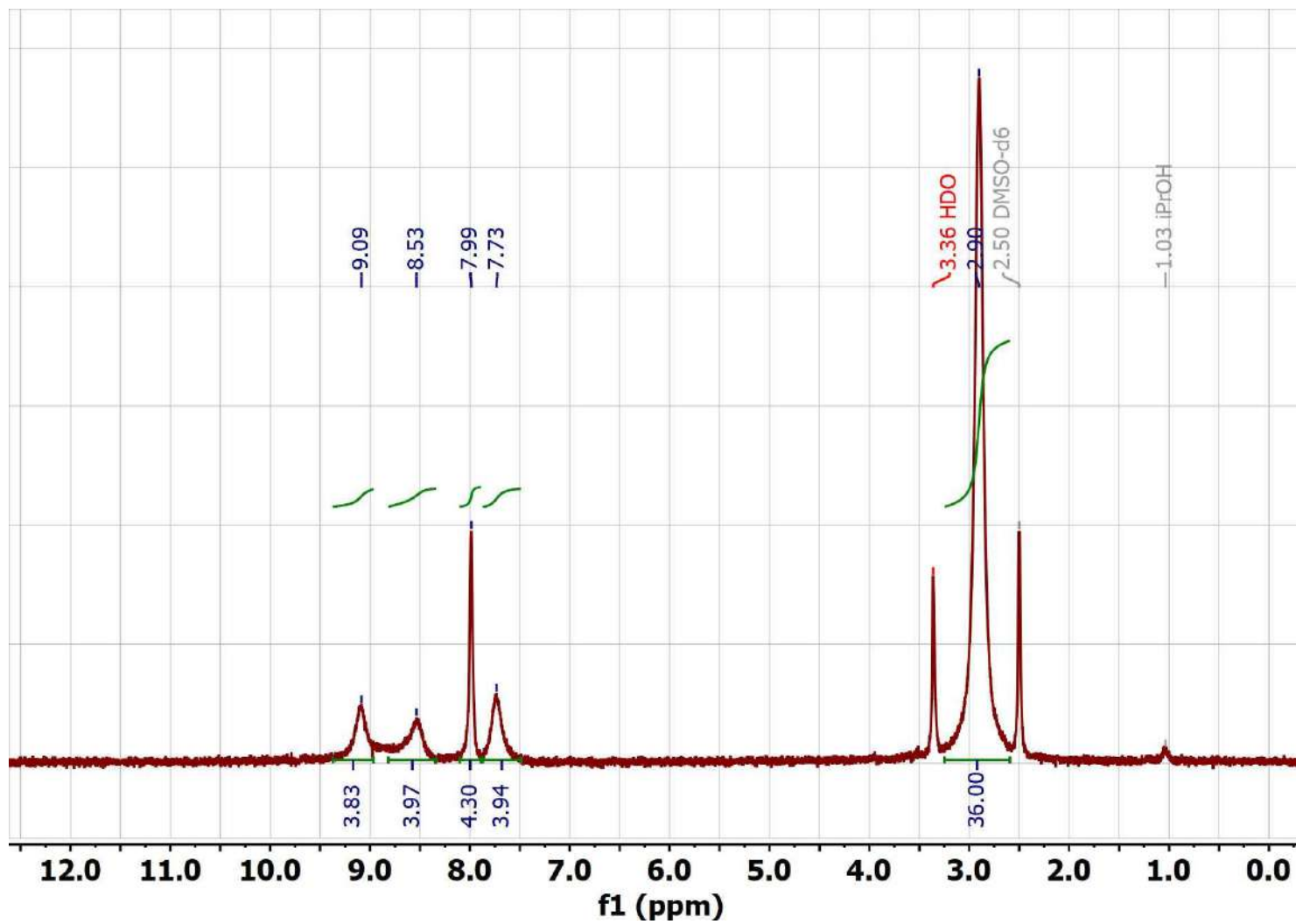
$^{11}\text{B}$  NMR spectra of crude  ${}^n\text{Bu}_4\text{NL}^2$  (maroon line) and  $\text{H}_3\text{BO}_3$  (cyan line) acquired for the solutions in  $\text{CD}_3\text{OD}$ .



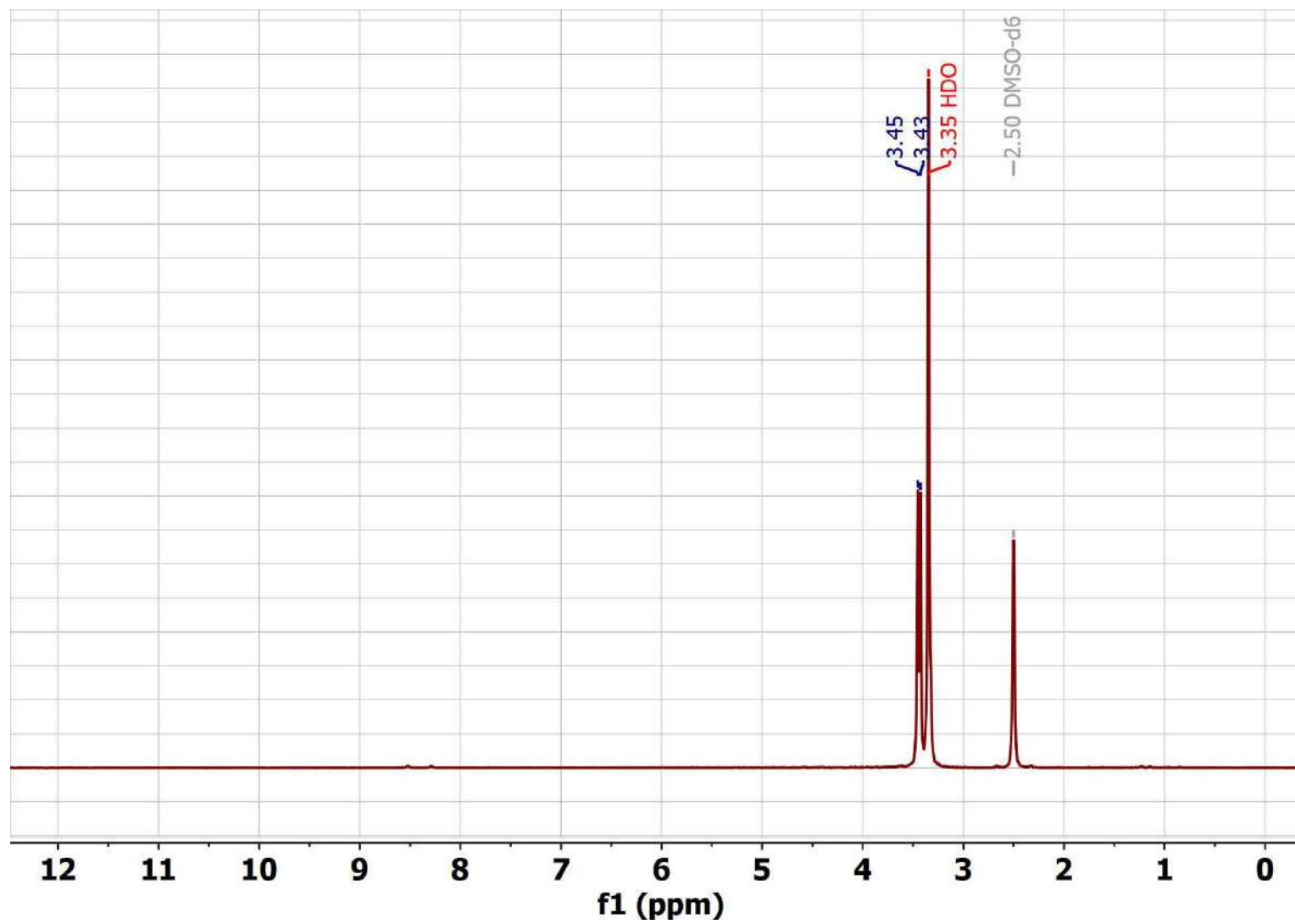
$^1\text{H}$  NMR spectrum of  $[\text{Y}_2(\text{L}^8)_3(\text{phen})_2]$  (**14**) in  $\text{DMSO-}d_6$ .



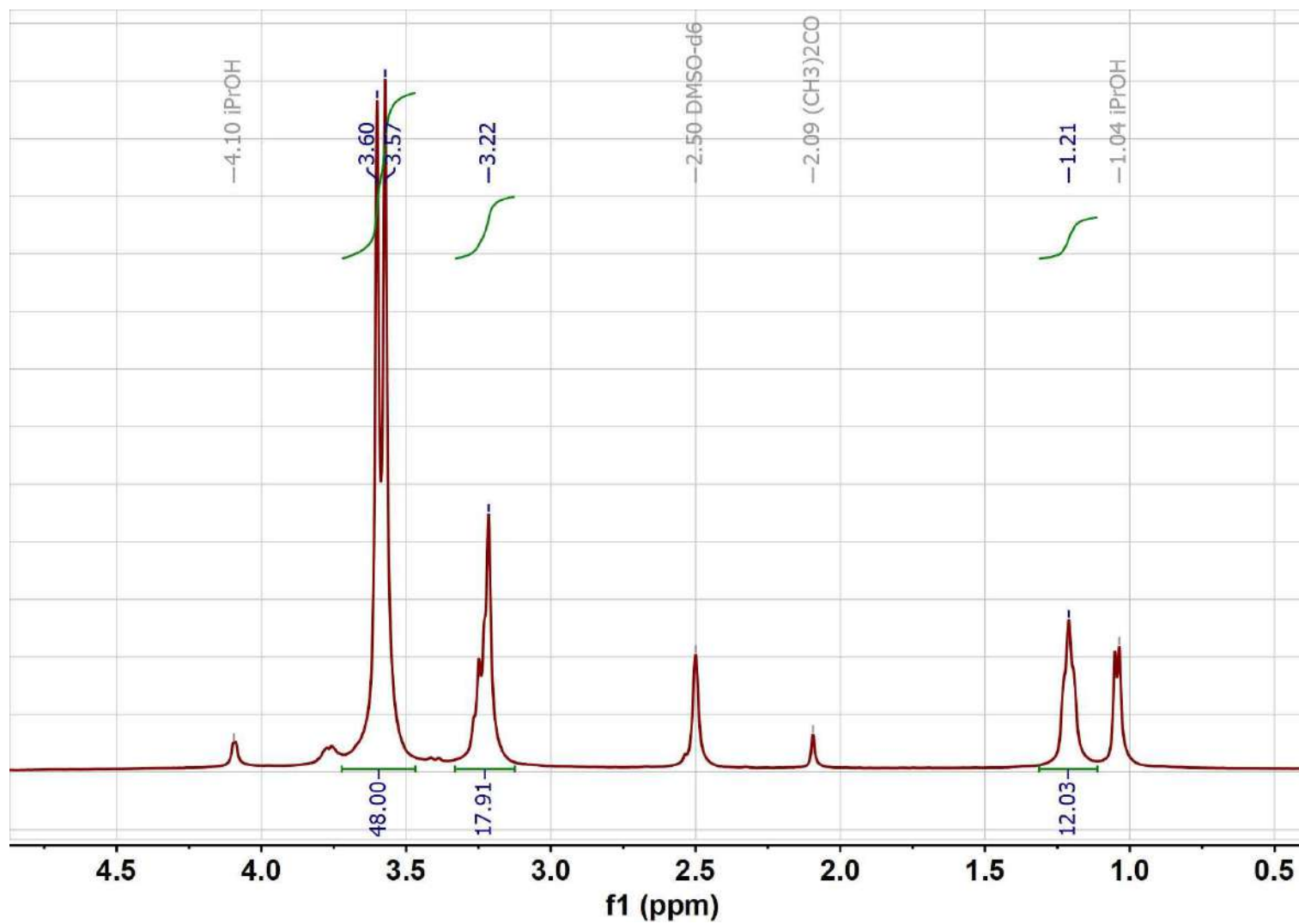
$^1\text{H}$  NMR spectrum of  $[\text{Eu}_2(\text{L}^8)_3(\text{phen})_2]$  (**10**) in  $\text{DMSO-}d_6$ .



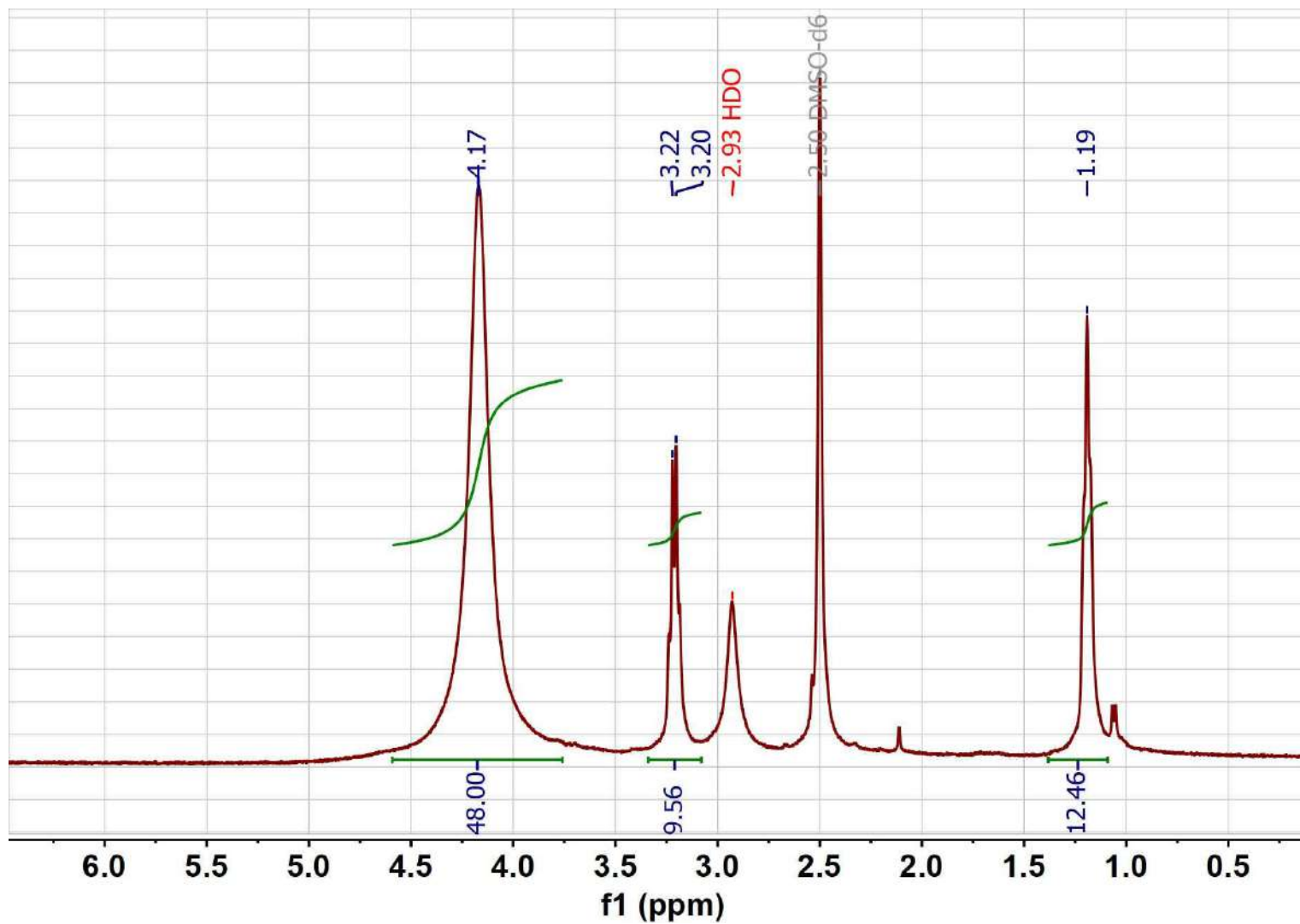
$^1\text{H}$  NMR spectrum of  $\text{Na}_2\text{L}^8$  in  $\text{DMSO-}d_6$ .



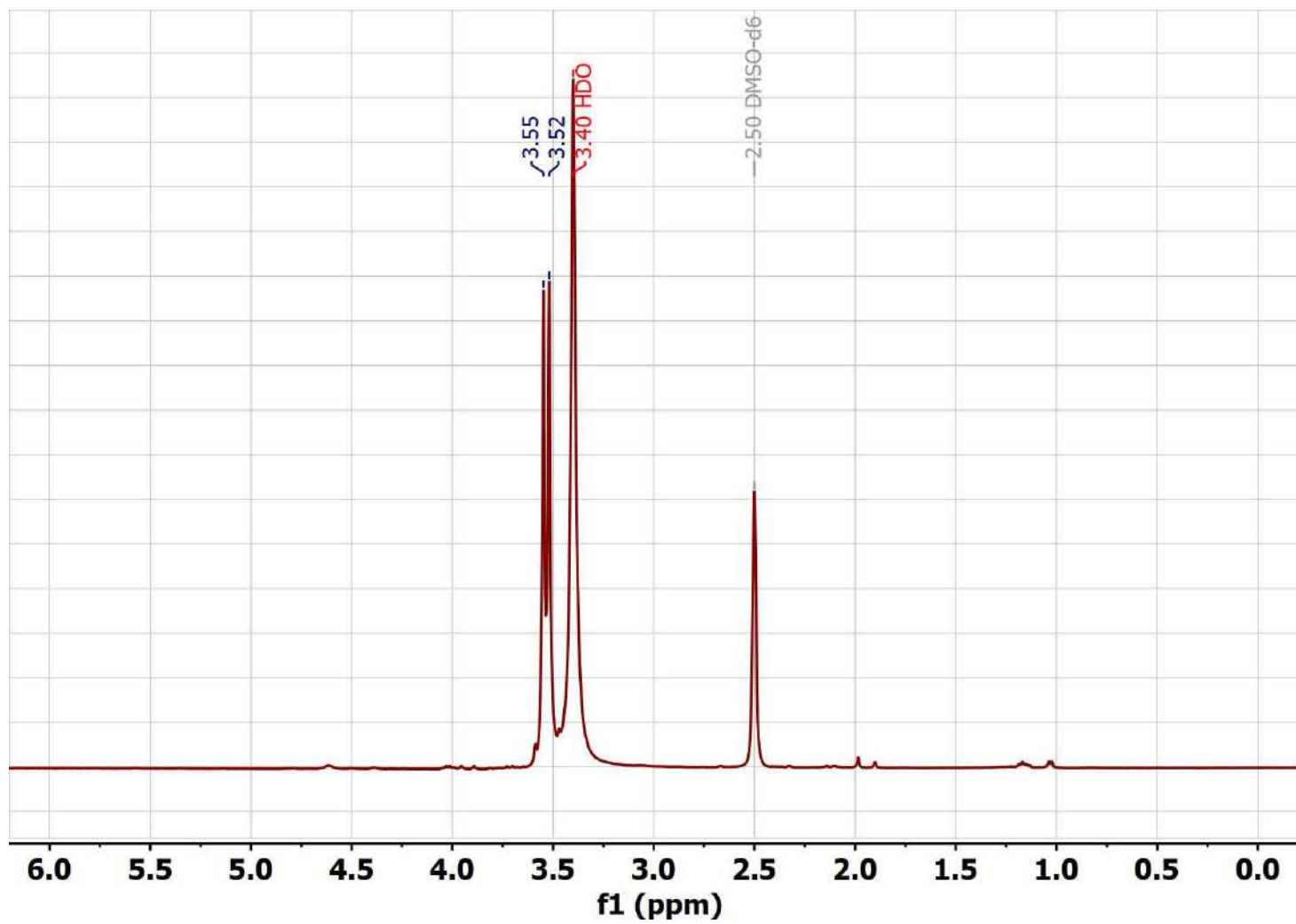
$^1\text{H}$  NMR spectrum of  $\text{NEt}_4[\text{NaLa}_2(\text{L}^8)_4(\text{H}_2\text{O})]$  (**15**) in  $\text{DMSO-}d_6$ .



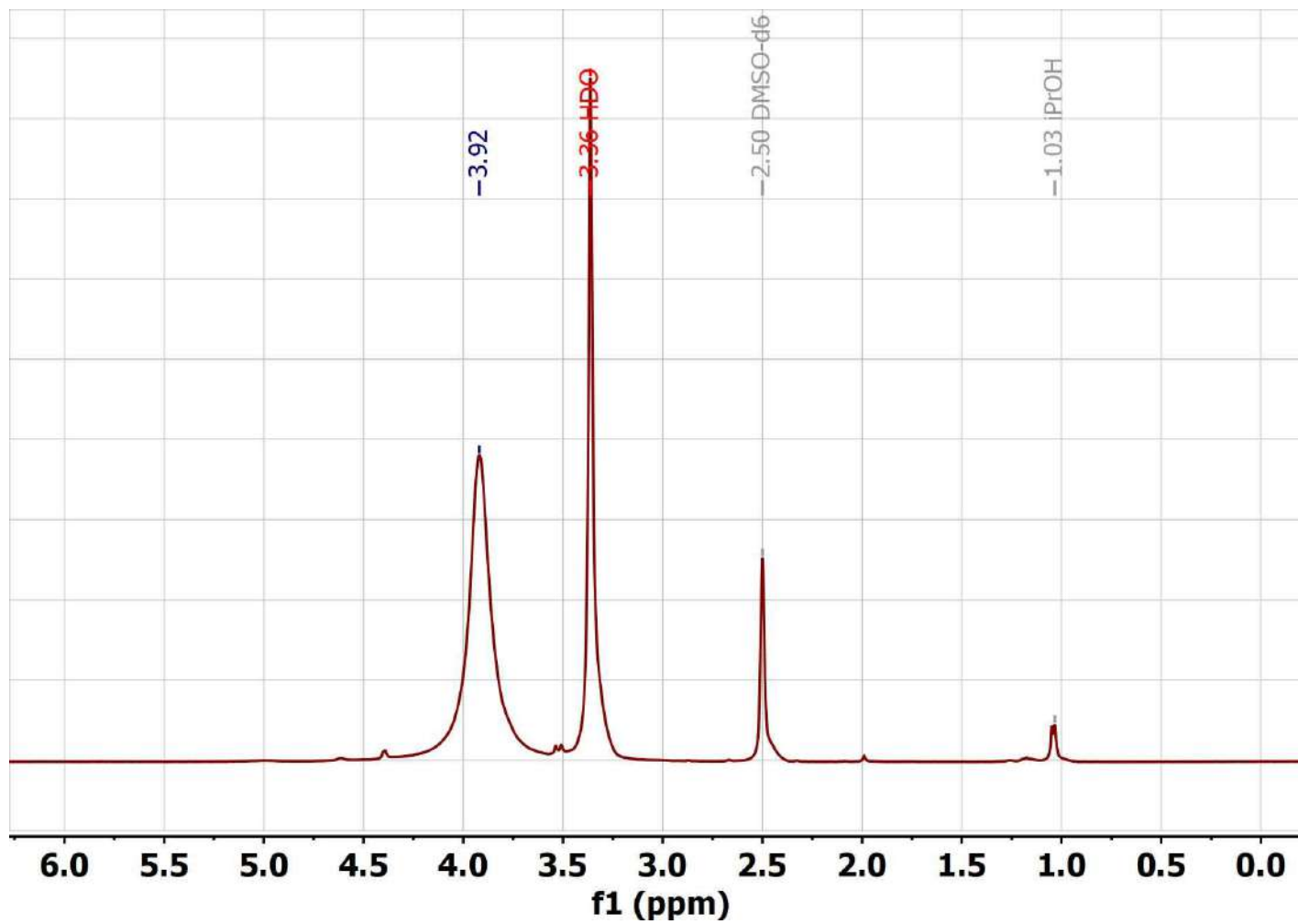
$^1\text{H}$  NMR spectrum of  $\text{NEt}_4[\text{NaNd}_2(\text{L}^8)_4(\text{H}_2\text{O})]$  (**16**) in  $\text{DMSO-}d_6$ .



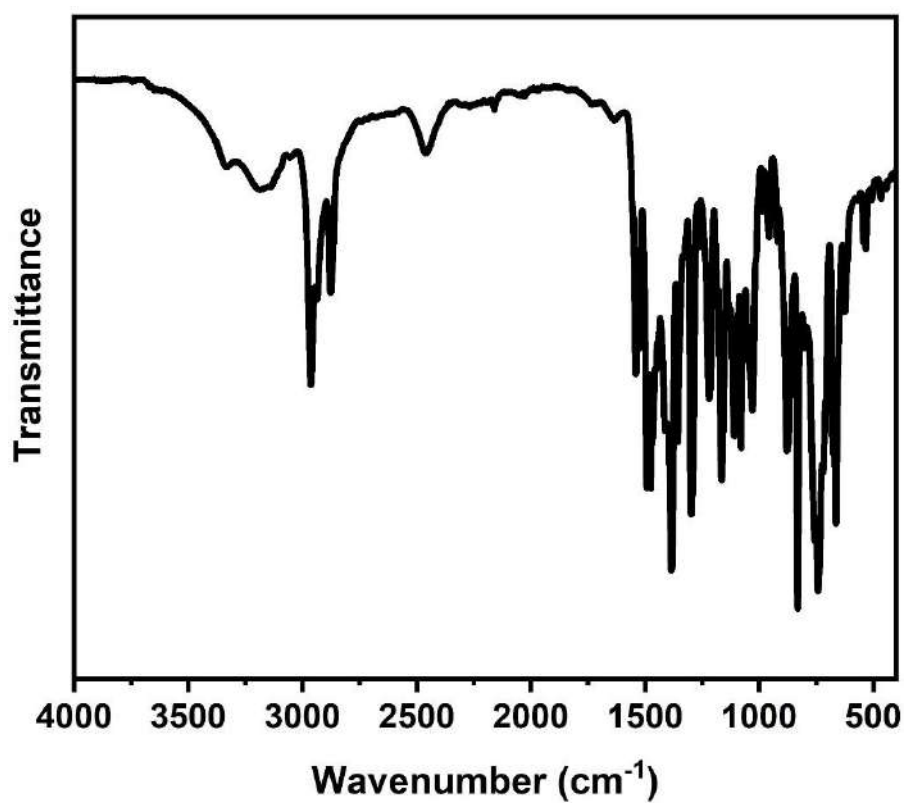
$^1\text{H}$  NMR spectrum of  $\text{Na}[\text{NaLa}_2(\text{L}^8)_4(\text{H}_2\text{O})]\cdot 2\text{H}_2\text{O}$  (**17**) in  $\text{DMSO-}d_6$ .



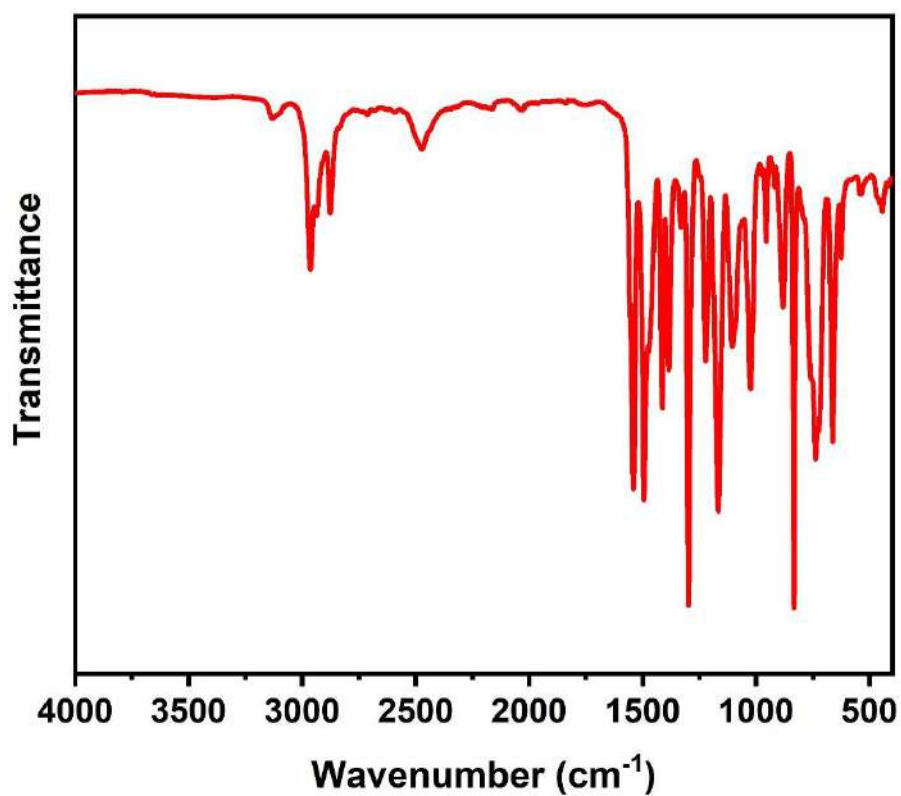
$^1\text{H}$  NMR spectrum of  $\text{Na}[\text{NaNd}_2(\text{L}^8)_4(\text{H}_2\text{O})]\cdot 2\text{H}_2\text{O}$  (**18**) in  $\text{DMSO-}d_6$ .



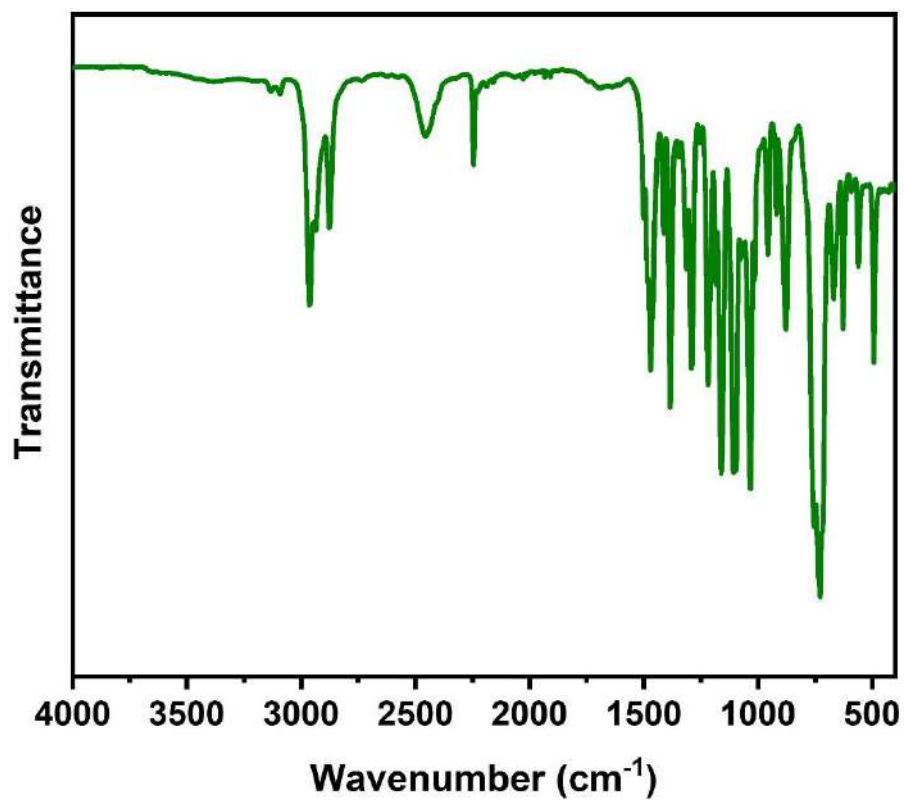
## IR spectra



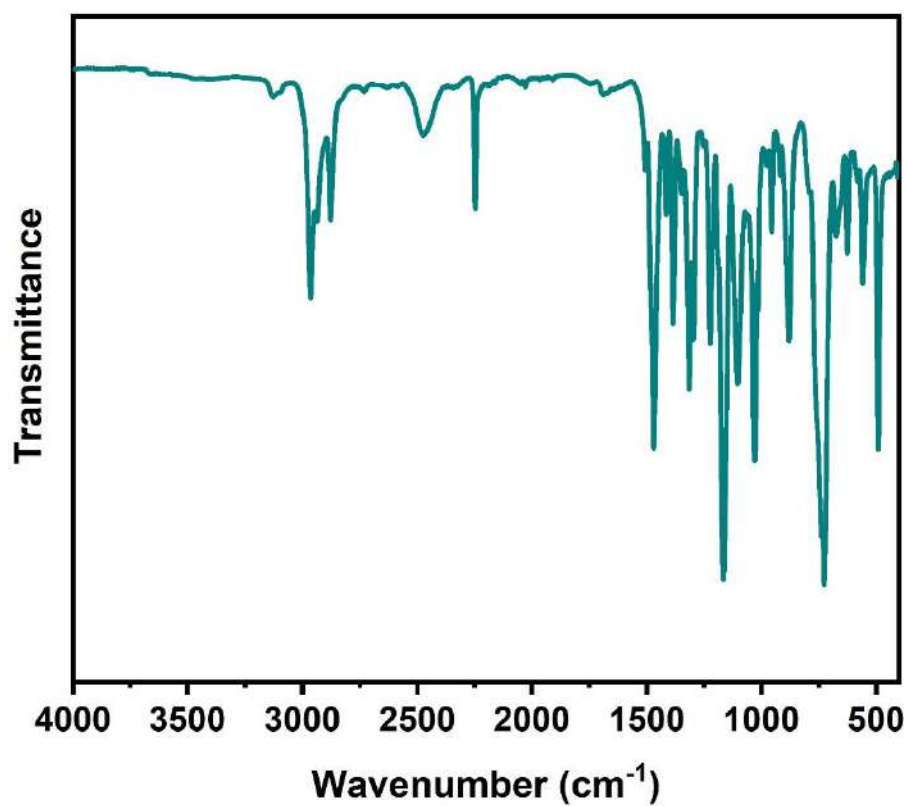
IR spectrum of <sup>n</sup>Bu<sub>4</sub>NL<sup>2</sup>.



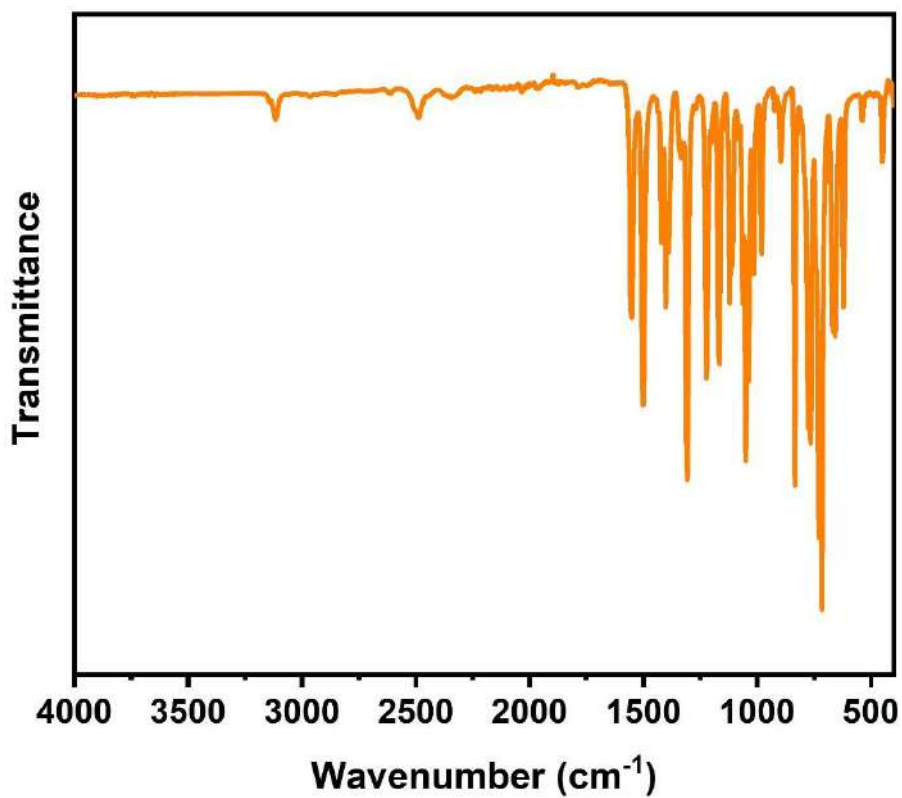
IR spectrum of <sup>n</sup>Bu<sub>4</sub>NL<sup>3</sup>.



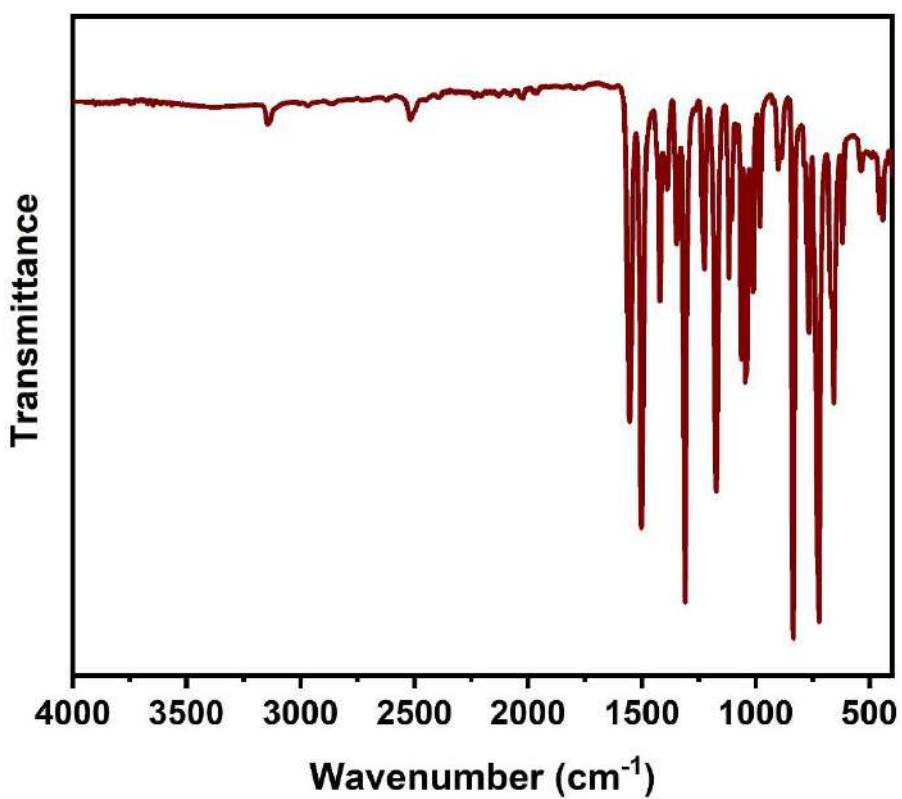
IR spectrum of  ${}^n\text{Bu}_4\text{NL}^4$ .



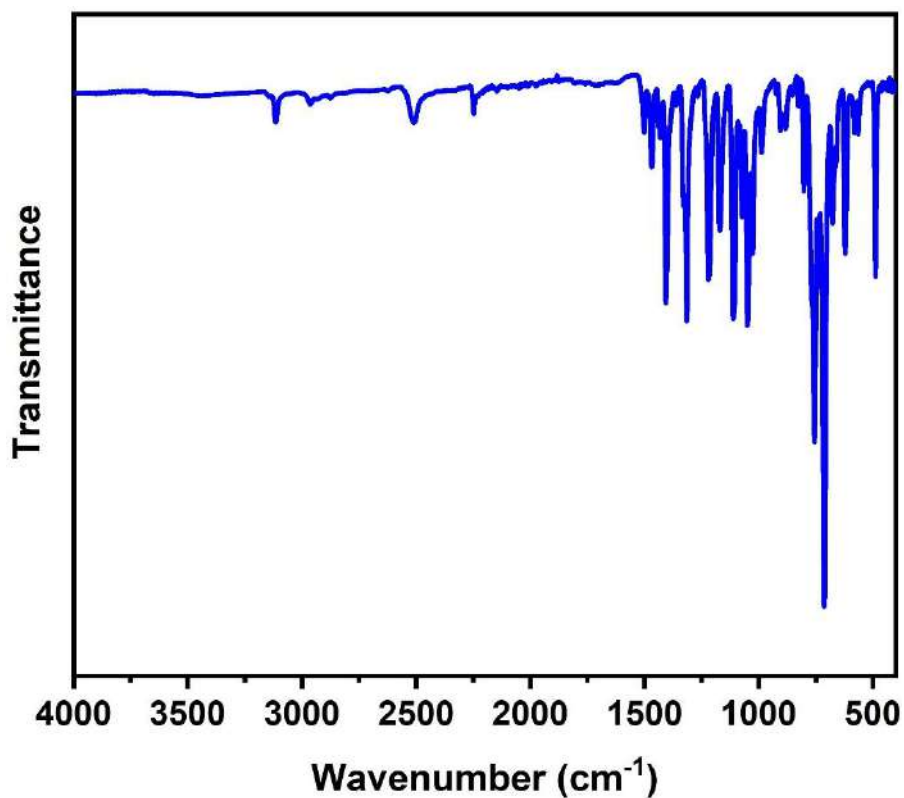
IR spectrum of  ${}^n\text{Bu}_4\text{NL}^5$ .



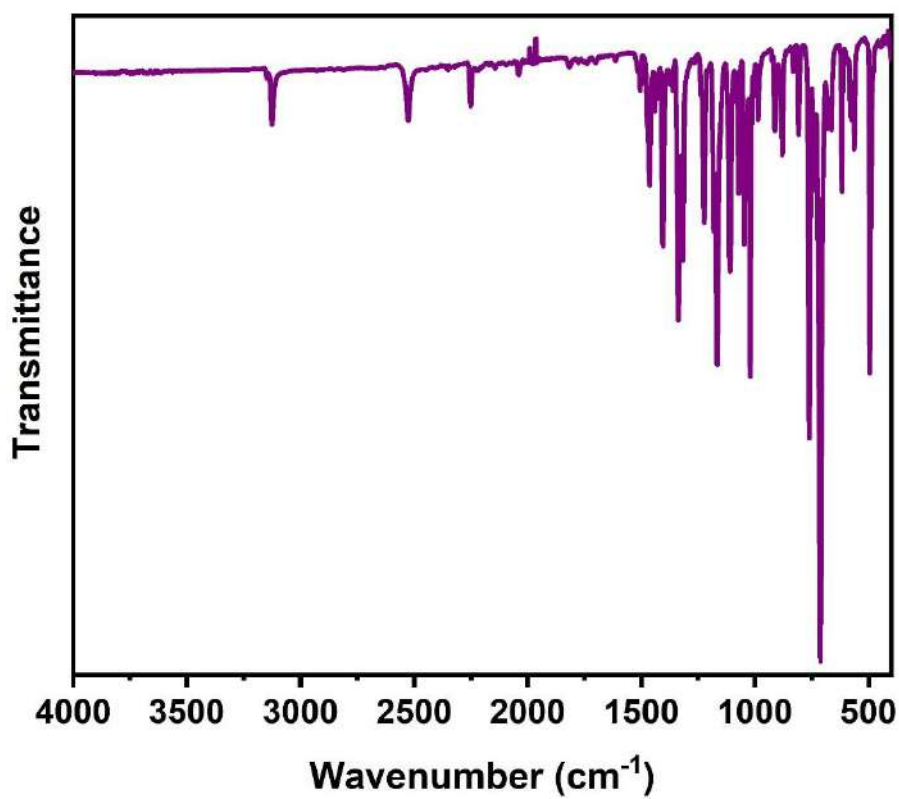
IR spectrum of complex 2.



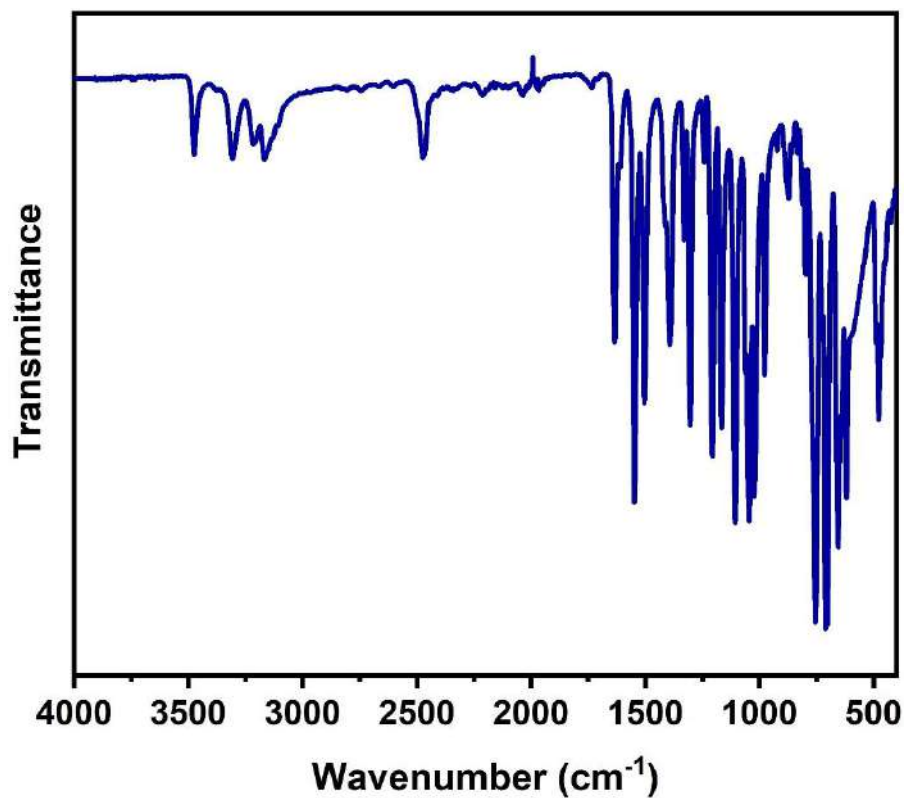
IR spectrum of complex 3.



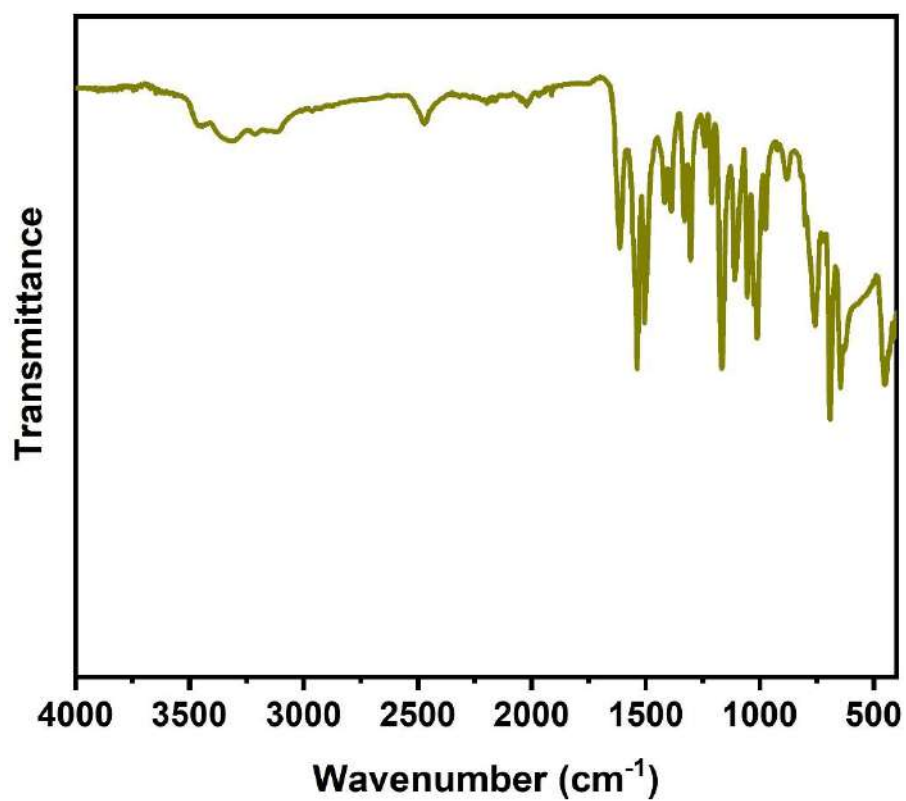
IR spectrum of complex 4.



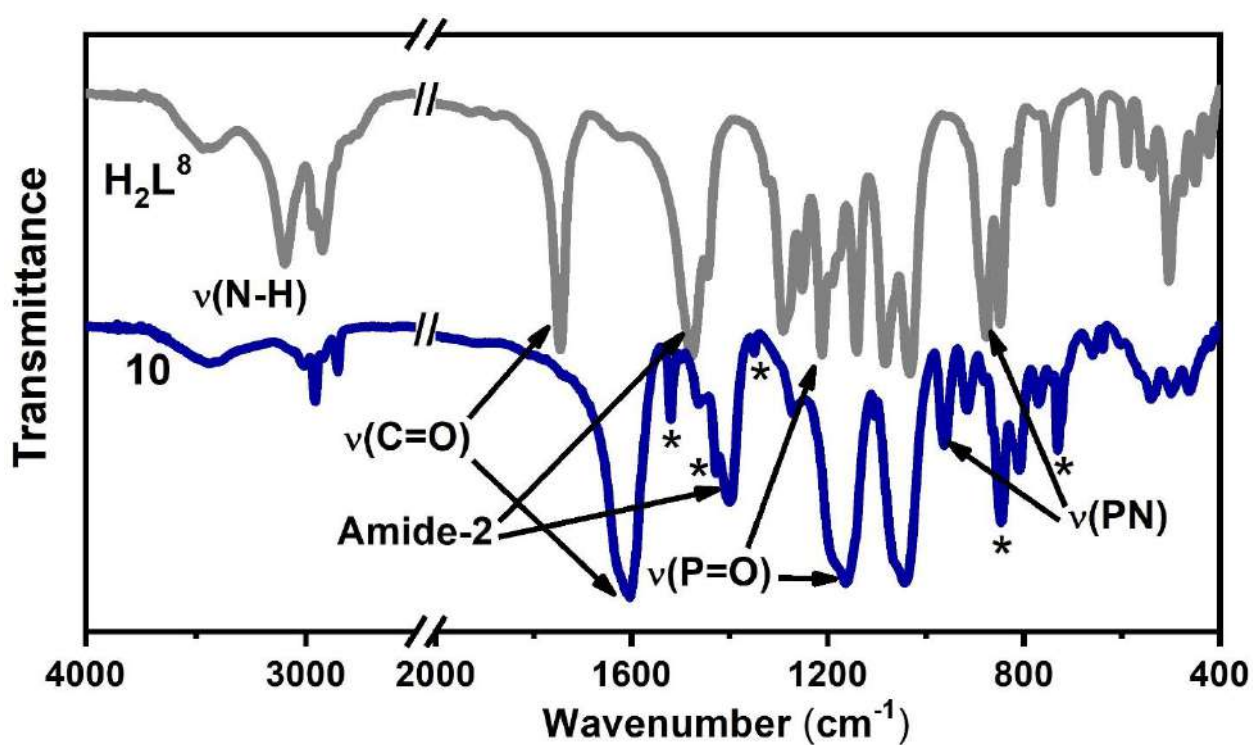
IR spectrum of complex 5.



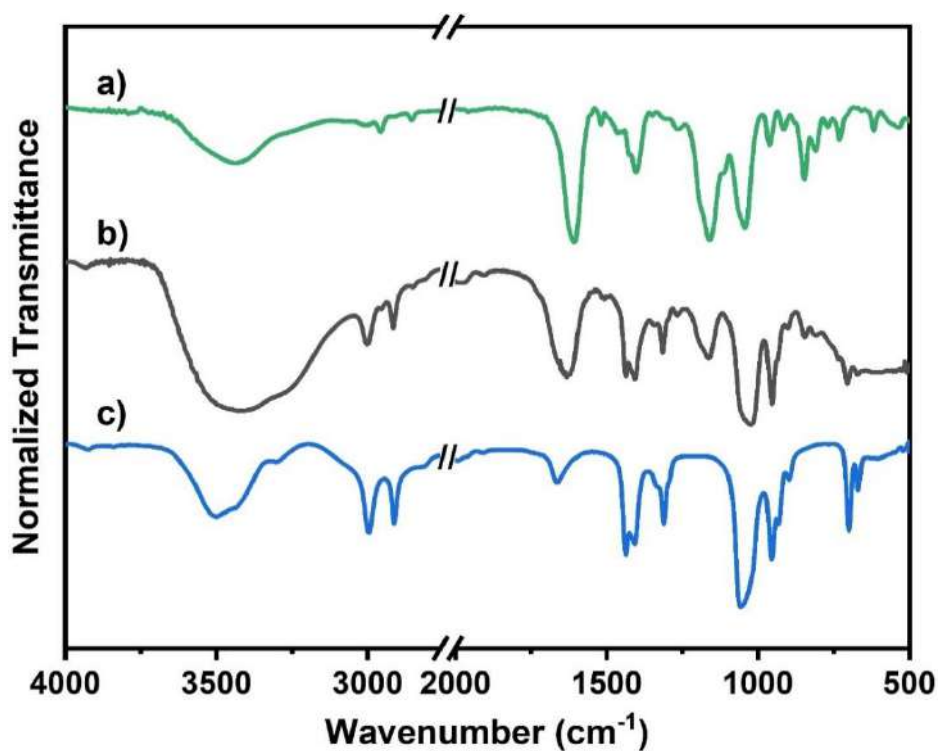
IR spectrum of complex 6.



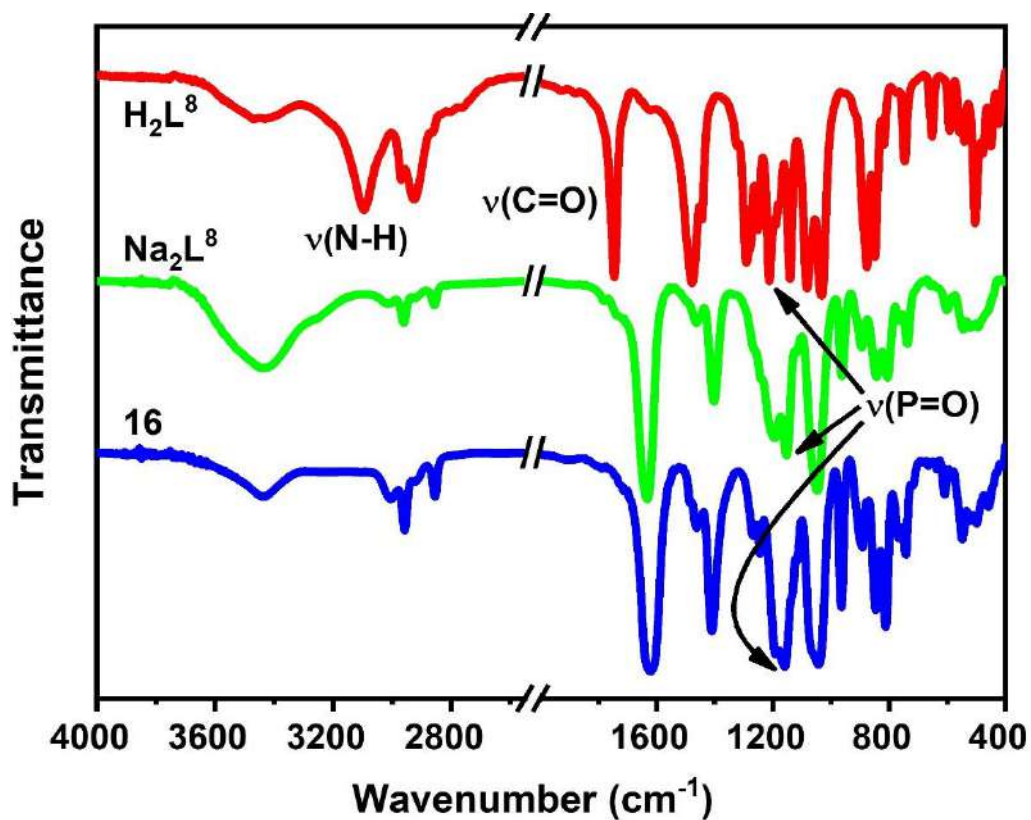
IR spectrum of complex 7.



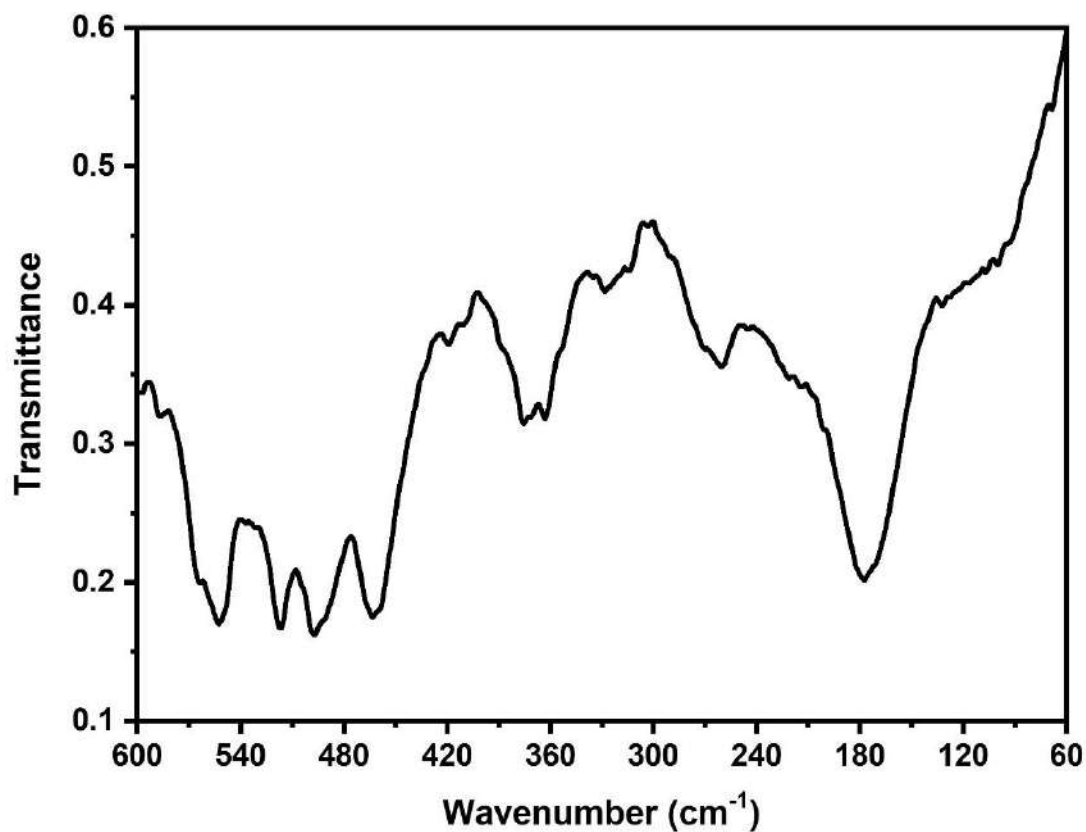
IR spectra of  $\text{H}_2\text{L}^8$  and  $[\text{Eu}_2(\text{L}^8)_3(\text{phen})_2]$  (**10**). 1,10-Phenanthroline absorption bands are marked with asterisk.



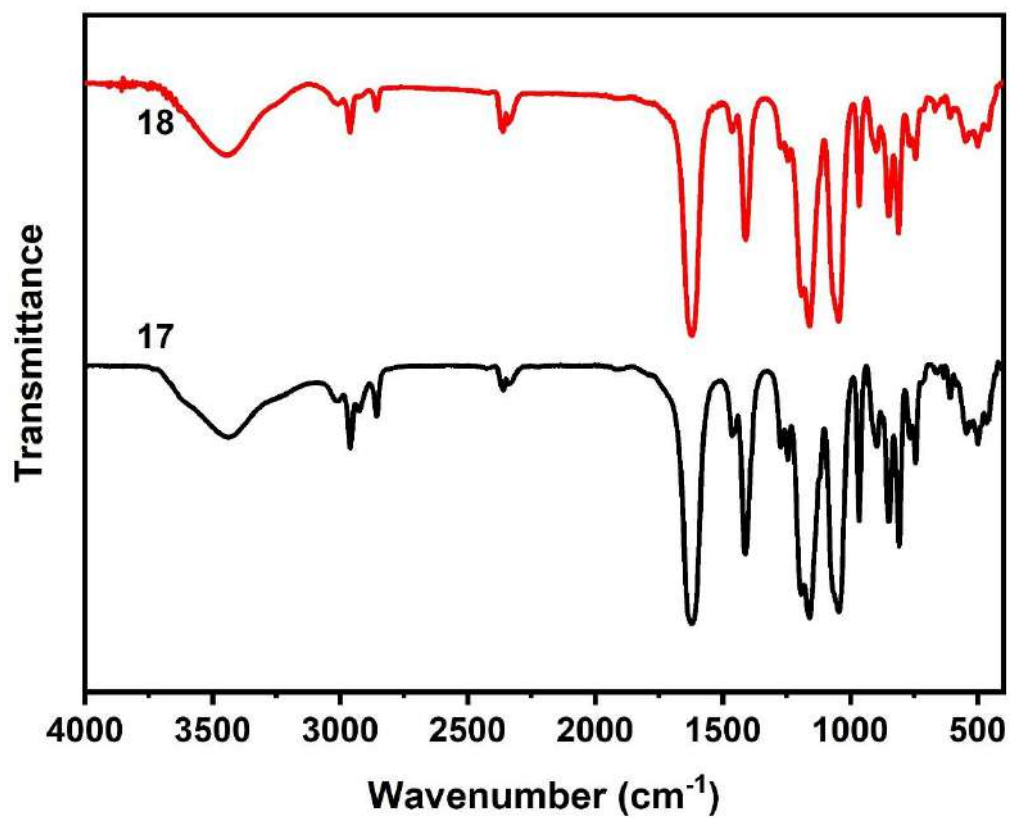
IR spectra of  $[\text{Nd}_2(\text{L}^8)_3(\text{phen})_2]$  in KBr pellet (a), in solution in DMSO (b) and IR spectrum of DMSO (c).



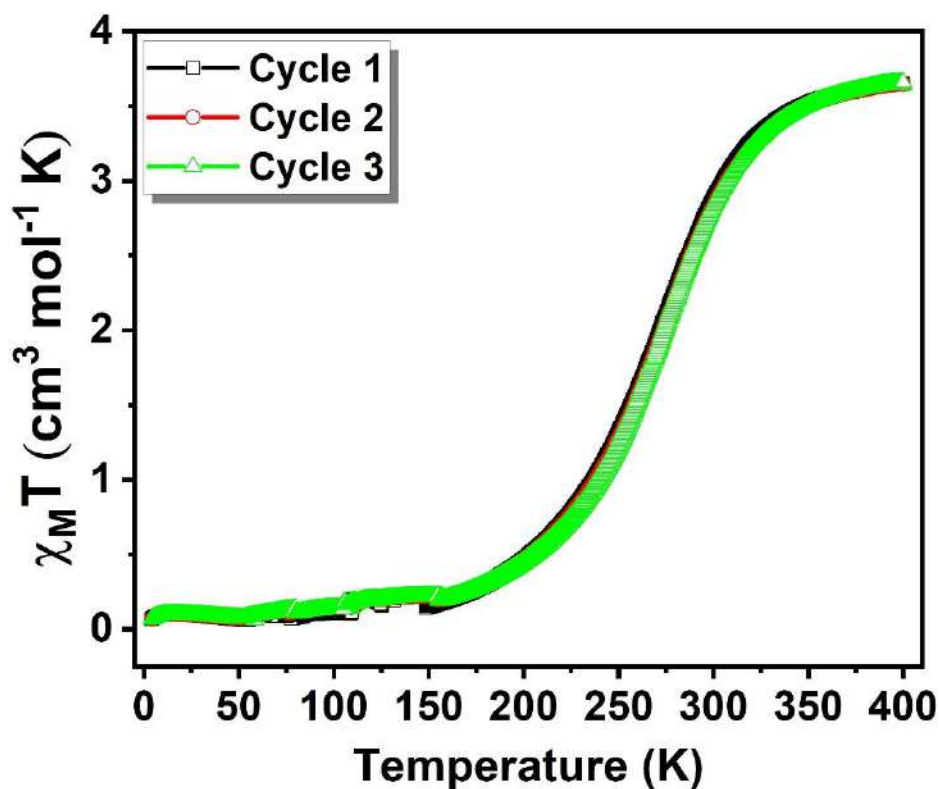
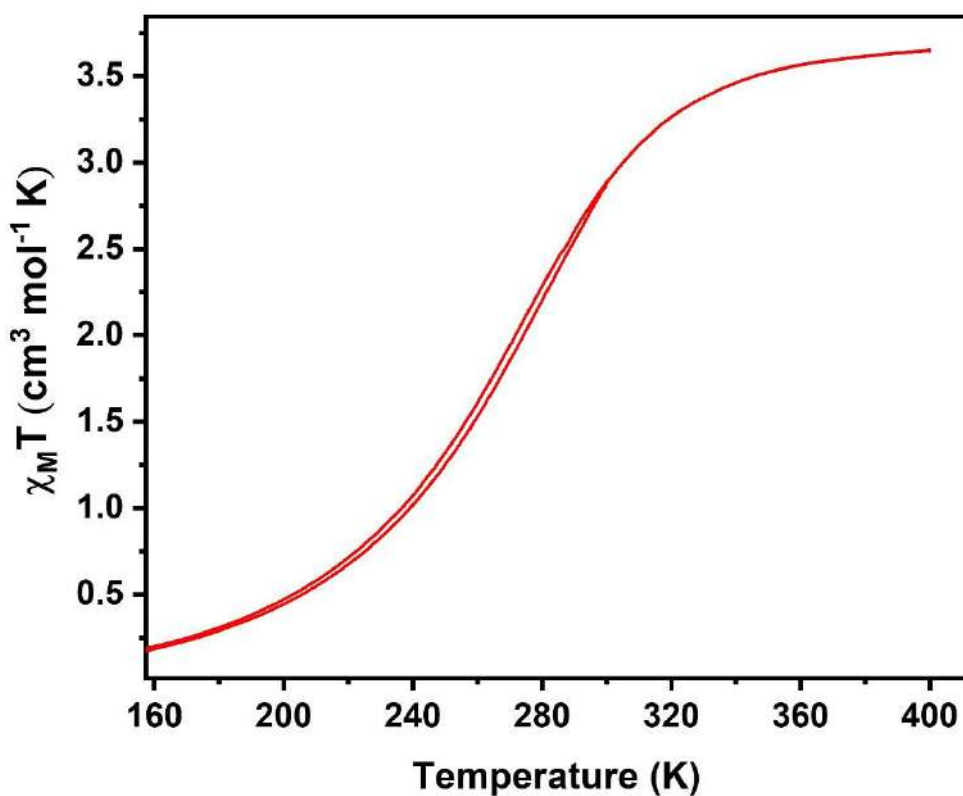
IR spectra of neutral ligand  $H_2L^8$ , its sodium salt  $Na_2L^8$  and complex **16**.



IR spectrum of complex **16** in 60–600  $cm^{-1}$  region.

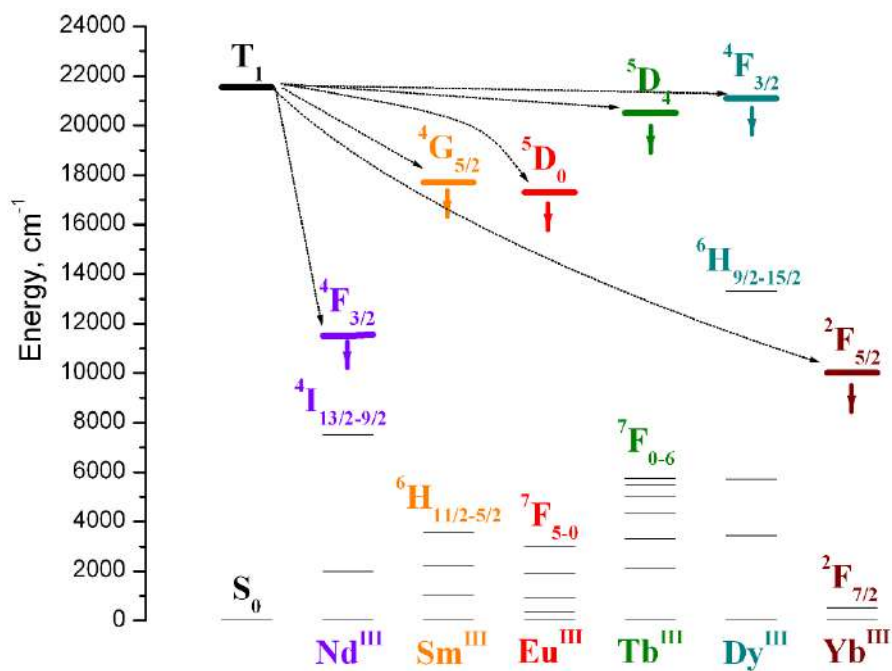


IR spectra of the complexes **17** (black line) and **18** (red line).

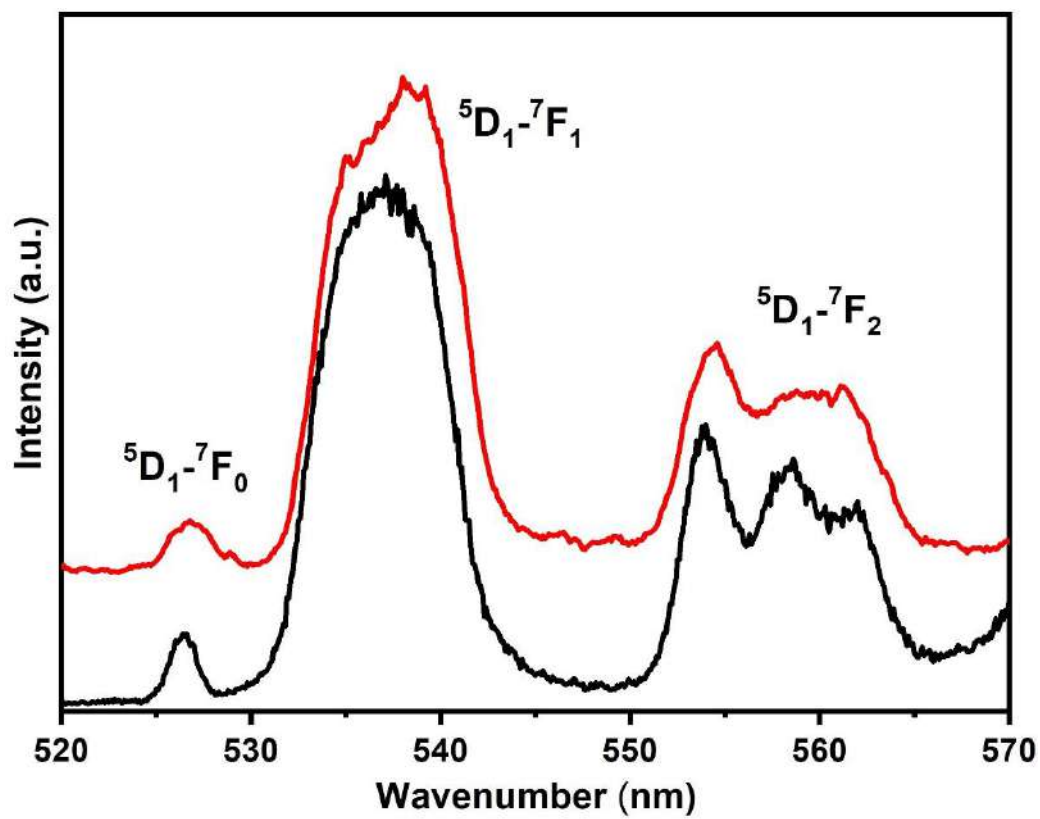
Variable-temperature SQUID magnetometry data for complex **6**Thermal variation of molar magnetic susceptibility of **6** over three consecutive heating/cooling cycles.

Zoomed in region of the SCO demonstrating appearance of a narrow hysteresis loop.

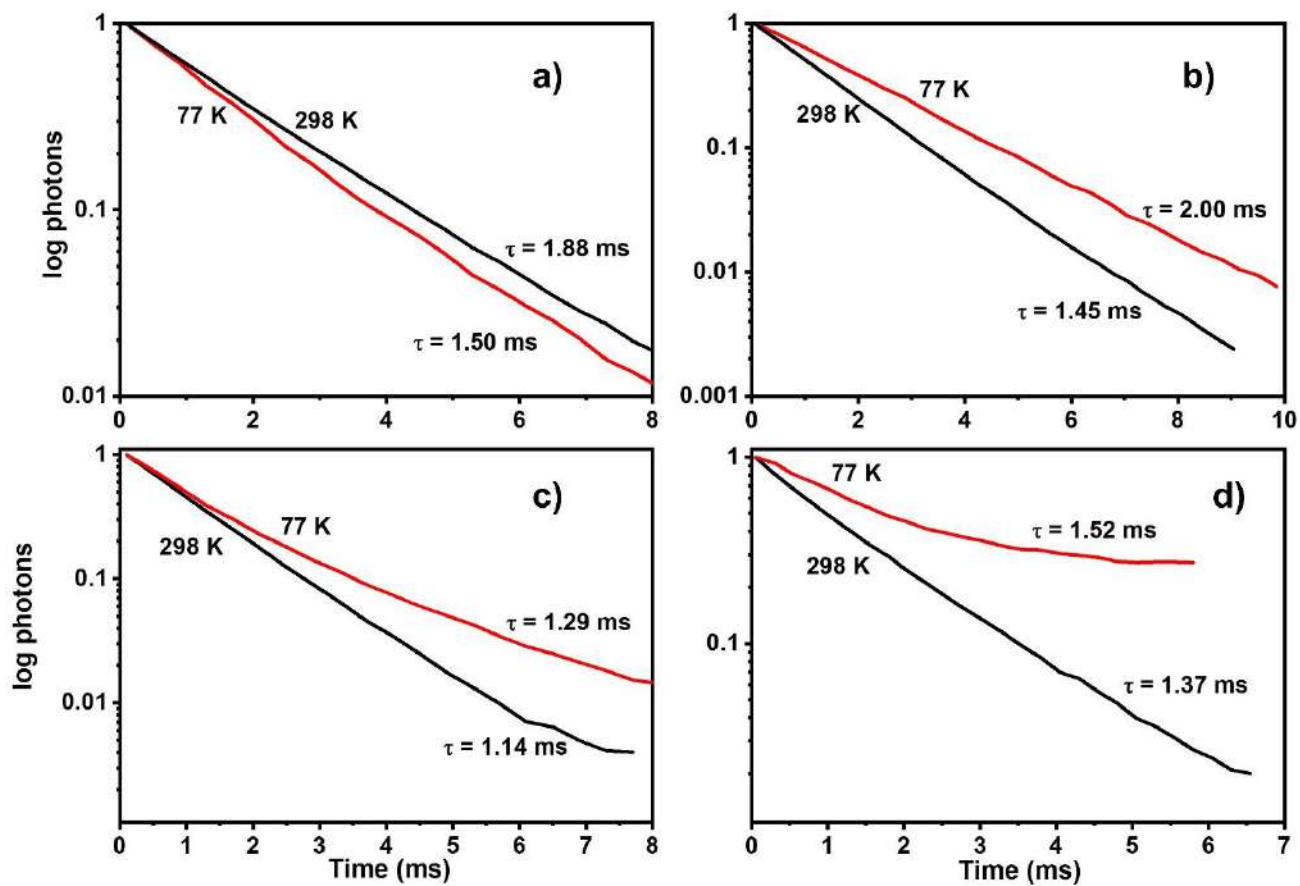
Simplified energy diagram showing the lowest lanthanide excited states and the estimated ligands lowest triplet state in the obtained complexes



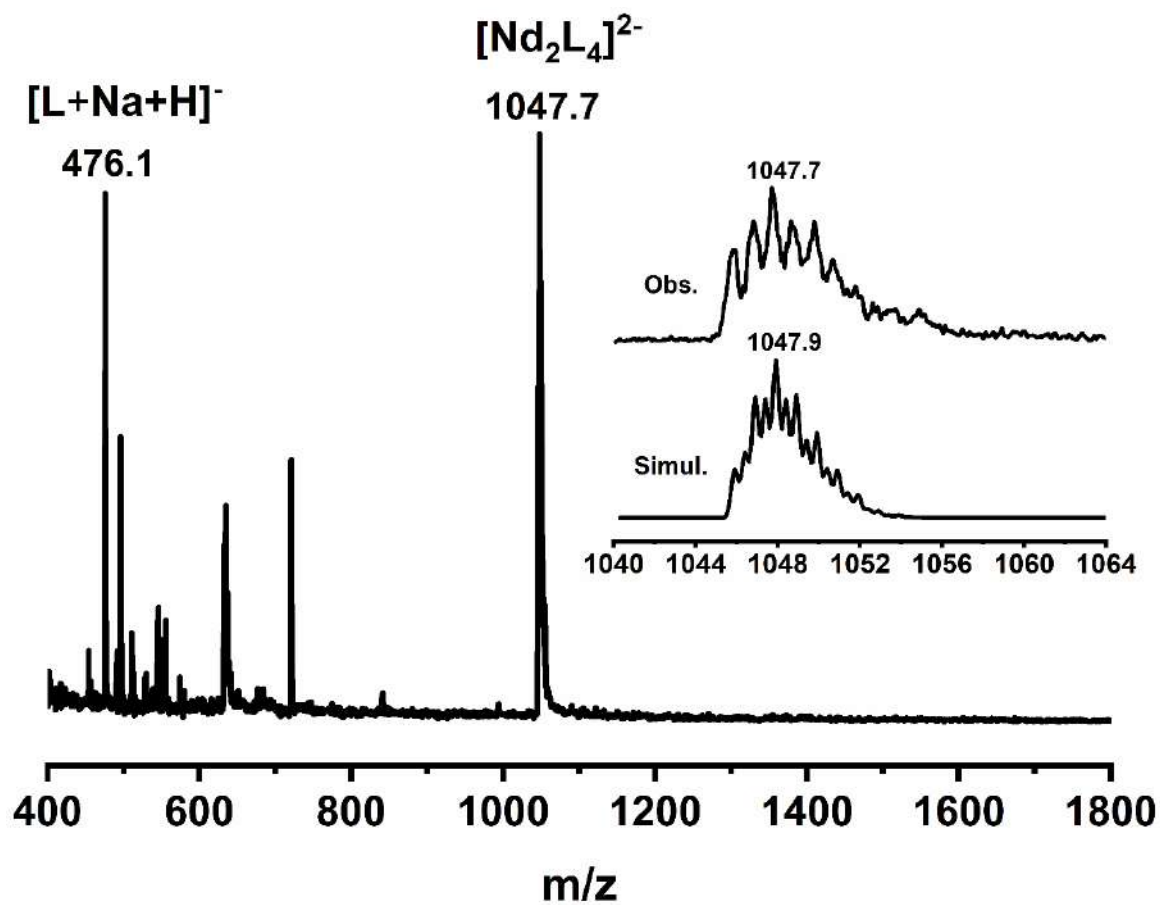
$^5D_0$  luminescence of the solid complex **10** at 298 K (black line) and 77 K (red line)



Decay luminescence curve for solid **10** and **11** (a and b, respectively) and for the complexes in solution in DMSO (c and d, respectively)



LDI mass spectrum of **16** with inset, depicting the simulated (Simul.) and observed (Obs.) isotopic pattern





Cite this: *New J. Chem.*, 2022, 46, 11734

# Solvatomorphism, polymorphism and spin crossover in bis[hydrotris(1,2,3-triazol-1-yl)borate]iron(II)†

Oleksandr Ye. Horniichuk,<sup>ab</sup> Karl Ridier,<sup>ib</sup> Gábor Molnár,<sup>ib</sup> Volodymyr O. Kotsyubynsky,<sup>c</sup> Sergiu Shova,<sup>d</sup> Vladimir M. Amirkhanov,<sup>ib</sup> Il'ya A. Gural'skiy,<sup>\*a</sup> Lionel Salmon<sup>ib</sup>\*<sup>b</sup> and Azzedine Bousseksou<sup>b</sup>

Solvatomorphism and polymorphism play a crucial role in defining the characteristics of spin crossover (SCO) in coordination compounds. In this paper we describe a detailed characterization of the SCO bis[hydrotris(1,2,3-triazol-1-yl)borate]iron(II) complex ([Fe(HB(1,2,3-tz)<sub>3</sub>)<sub>2</sub>]) **1**. Five solvatomorphs of **1**·**2Solv** (where Solv = DMSO, MeOH, and CHCl<sub>3</sub>), **1**·**7DMSO** and **1**·**2DMF**·**H<sub>2</sub>O** were obtained via recrystallization from the respective organic solvents. Solvatomorphs **1**·**2MeOH** and **1**·**2CHCl<sub>3</sub>** undergo single-crystal-to-single-crystal transformations leading to **1** upon heating above 313 K. Single-crystal X-ray diffraction analysis revealed π–π stacking and C–H···N contacts between molecules of the complex both in the solvated and desolvated crystals. The spin crossover and thermal properties of **1** and its solvates were investigated by means of calorimetry, thermogravimetry, Mössbauer spectroscopy, variable temperature magnetic susceptibility, Raman spectroscopy and powder X-ray diffraction measurements. The anhydrous [Fe(HB(1,2,3-tz)<sub>3</sub>)<sub>2</sub>] complex, obtained via dehydration of dodecahydrate, undergoes structural phase transitions upon the first heating in the 303–493 K range followed by reversible, gradual spin crossover upon further thermal cycling, with a transition temperature of  $T_{1/2} = 373$  K.

Received 25th March 2022,  
Accepted 18th May 2022

DOI: 10.1039/d2nj01471h

rsc.li/njc

## Introduction

Switchable molecular materials showing spin crossover (SCO) properties<sup>1</sup> have attracted the attention of many research groups as they can be used for the fabrication of functional devices, finding their application in information storage, molecular electronics, photonics, sensing and construction of mechanical actuators.<sup>2–6</sup> In this context, the ability to fabricate

high quality, pure and homogeneous thin films of SCO materials is crucial. To this aim, vacuum thermal deposition provides a powerful means.<sup>7,8</sup> However, there are only a handful of spin crossover complexes that could be deposited by this technique.<sup>9–23</sup> Among these, only a few sublimable SCO complexes undergo spin transition above room temperature, namely [Fe(pypyr(CF<sub>3</sub>)<sub>2</sub>(phen))] (pypyr = 2-(2'-pyridyl)pyrrolide, phen = 1,10-phenanthroline),<sup>15</sup> [Fe(HB(pz)<sub>3</sub>)<sub>2</sub>] (pz = pyrazolyl-1-yl)<sup>22,23</sup> and [Fe(HB(1,2,4-tz)<sub>3</sub>)<sub>2</sub>] (tz = triazol-1-yl),<sup>21</sup> the two latter belonging to the tris(1-azolyl)borate family of compounds.<sup>24</sup> For Fe-pypyr thin films, the transition temperature  $T_{1/2}$  is reduced from 390 K for the bulk compound to approximately 330 K, whereas the two other complexes display similar SCO properties in bulk and thin film forms ( $T_{1/2} \approx 393$  K and 335 K for the pyrazolyl and triazolyl derivatives, respectively). Notably, the high-quality thin films of [Fe(HB(1,2,4-triazol-1-yl)<sub>3</sub>)<sub>2</sub>] that were vacuum-deposited in the 20–200 nm thickness range showed an abrupt SCO without any fatigue over more than 10 million thermal switching cycles, which could be exploited in photonic, electronic, sensor, actuator and temperature damping devices.<sup>21,25–29</sup> The synthesis of [Fe(HB(1,2,3-triazol-1-yl)<sub>3</sub>)<sub>2</sub>] **1** (Chart 1), a structural isomer of its 1,2,4-triazolyl counterpart, was described by Jenkins *et al.*,<sup>30</sup> but there is no report on the SCO properties of this compound. In order to find out how the change of the exodentate nitrogen atom position from 4 to 3 in the triazolyl

<sup>a</sup> Taras Shevchenko National University of Kyiv, Department of Chemistry, 64 Volodymyrska St., 01601 Kyiv, Ukraine. E-mail: illia.guralskiy@univ.kiev.ua

<sup>b</sup> LCC, CNRS and Université de Toulouse (UPS, INP), 205 route de Narbonne, F-31077 Toulouse, France

<sup>c</sup> Department of Material Science and New Technology, Vasyl Stefanyk Precarpathian National University, Ivano-Frankivsk 76018, Ukraine

<sup>d</sup> “Petru Poni” Institute of Macromolecular Chemistry, 41A Aleea Gr. Ghica Voda, 700487 Iasi, Romania

† Electronic supplementary information (ESI) available: Table S1: crystal structure and refinement data for the solvatomorphs, Fig. S1–S4: crystal structures of some solvatomorphs with intermolecular interactions displayed, Fig. S5: packing diagram of **1**·**7DMSO**, Fig. S6: X-ray diffraction patterns for DMSO solvatomorph, Fig. S7: TGA and DTA curves for **1**·**12H<sub>2</sub>O**, Fig. S8: simulated and experimental PXRD patterns of **1**, Fig. S9: variable temperature Raman spectroscopy data for **1**, Fig. S10: Mössbauer spectra of **1**·**12H<sub>2</sub>O** and polymorphs of **1**. CCDC 2161993–2161998. For ESI and crystallographic data in CIF or other electronic format see DOI: <https://doi.org/10.1039/d2nj01471h>



Chart 1 Molecular structure of  $[\text{Fe}(\text{HB}(1,2,3\text{-triazol-1-yl})_3)_2]$  (**1**).

ring impacts the crystalline structure and SCO properties of the complex, as well as to analyze its solvato/polymorphism, we report herein the single crystal structure of **1** (both in solvated and desolvated forms) as well as its physical properties investigated by Mössbauer spectroscopy and variable-temperature magnetic susceptibility, Raman spectroscopy, powder X-ray diffraction, calorimetry and thermogravimetry. A review of polymorphism in spin crossover complexes has been reported by Tao *et al.*<sup>31</sup> Such polymorphs are generally obtained serendipitously as a mixture of crystals as illustrated by studies of Ruben and collaborators.<sup>32</sup> On the other hand, numerous examples of solvatomorphs in SCO complexes have also been reported mainly in the polymeric Fe(II) Hofmann type and in molecular Fe(II) and Fe(III) compounds.<sup>33–47</sup> These solvatomorphs result from a mixture of crystals obtained serendipitously, by a vapor-induced single-crystal-to-single-crystal transformation or growing crystals by liquid–liquid diffusion methods. In the present case, solvatomorphs were obtained by changing the solvent during the recrystallization procedure.

## Methods

Infrared spectra were recorded on a PerkinElmer 1725 spectrometer. Elemental analysis (for C, H and N) was performed using a PerkinElmer 2400 series II Instrument. Single-crystal X-ray diffraction analysis was performed on an Oxford-Diffraction XCALIBUR E CCD diffractometer with graphite-monochromated Mo-K $\alpha$  radiation. Unit cell determination and data integration were carried out using the CrysAlisPro package from Oxford Diffraction. Multi-scan correction for absorption was applied. All the structures were solved using an intrinsic phasing method using SHELXT and refined by full-matrix least-squares on  $F^2$  with SHELXL<sup>48,49</sup> using the graphic interface of Olex2.<sup>50</sup> Non-hydrogen atoms were refined anisotropically. Aromatic hydrogen atoms were geometrically fixed and refined using a riding model. Variable temperature powder X-ray diffraction patterns were recorded using a Panalytical X'Pert diffractometer equipped with a Cu X-ray tube, a Ge(111) incident beam monochromator ( $\lambda = 1.5406 \text{ \AA}$ ) and an X'Celerator detector. Variable-temperature Raman spectra were acquired by means of an Xplora (Horiba) Raman microspectrometer, using the 532 nm line of a Nd-YAG laser (0.1 mW). The sample temperature was controlled using a Linkam THMS600 liquid

nitrogen cryostat. Differential thermal analysis and thermogravimetric (DTA-TG) data were acquired simultaneously using a PerkinElmer Diamond thermal analyzer under a  $100 \text{ ml min}^{-1}$  nitrogen flow at  $10 \text{ K min}^{-1}$ . DSC analysis was carried out on a Netzsch DSC 3500 Sirius instrument under nitrogen purging gas ( $20 \text{ ml min}^{-1}$ ) at a heating/cooling rate of  $10 \text{ K min}^{-1}$ . Variable-temperature magnetic susceptibility data were obtained at cooling and heating rates of  $2 \text{ K min}^{-1}$  under a field of 1 kOe using a Quantum Design MPMS magnetometer. <sup>57</sup>Fe-Mössbauer spectra were recorded using a constant acceleration Mössbauer spectrometer with a <sup>57</sup>Co source. Fitting of the experimental data was performed using Recoil software.<sup>51</sup>

## Materials and synthesis

Commercial reactants and solvents were used directly without further purification. The tris(1,2,3-triazolyl)borate ligand (NaL) and its neutral  $[\text{Fe}(\text{HB}(1,2,3\text{-tz})_3)_2]$  iron(II) complex (hereafter FeL<sub>2</sub> or **1**) were synthesized according to experimental procedures reported in the literature.<sup>30</sup> The coordination compound isolated from the mother aqueous solution appears as dodecahydrate. The anhydrous powder form can be obtained *via* heating the hydrate above  $90 \text{ }^\circ\text{C}$ .

**FeL<sub>2</sub>·12H<sub>2</sub>O (1·12H<sub>2</sub>O)**.  $\text{C}_{12}\text{H}_{38}\text{B}_2\text{FeN}_{18}\text{O}_{12}$  ( $M = 704.07$ ). Anal. calc.: C, 20.47; H, 5.44; N, 35.81%. Found: C, 20.55; H, 5.42; N, 35.55%.

**FeL<sub>2</sub> (1)**.  $\text{C}_{12}\text{H}_{14}\text{B}_2\text{N}_{18}\text{Fe}$  ( $M = 487.88$ ). Anal. calc.: C, 29.55; H, 2.89; N, 51.68%. Found: C, 29.51; H, 2.86; N, 51.57%.

## Results and discussion

### X-ray crystallography

Complex **1** is soluble in polar solvents, such as water, methanol, dimethylsulfoxide (DMSO), dimethylformamide (DMF) and poorly soluble in the much less polar chloroform. The complex tends to form solvates, which can be easily crystallized from the above-mentioned solvents. The number of solvent molecules per one molecule of the complex depends on the nature of the solvent. For instance, in the case of DMSO, the formation of two solvates **1·2DMSO** and **1·7DMSO** was observed serendipitously from attempts of recrystallization of **1** under the same condition. The methanol- or chloroform-based solvates appear only as **1·2MeOH** and **1·2CHCl<sub>3</sub>**, respectively. The dimethylformamide solvate tends to crystallize with inclusion of one water molecule to form **1·2DMF·H<sub>2</sub>O**. The solvatomorphs **1·2MeOH** and **1·2CHCl<sub>3</sub>** crystallize in monoclinic space groups  $P2_1/n$  and  $P2_1/c$ , respectively. **1·2DMF·H<sub>2</sub>O** crystallizes in the orthorhombic  $Pbcn$  space group. In the case of DMSO-based solvatomorphs, **1·2DMSO** crystallizes in the triclinic  $P\bar{1}$  space group, while **1·7DMSO** adopts a trigonal  $R\bar{3}c$  space group. DMSO molecules in the latter crystals are disordered over six and over two positions, respectively. Upon long-term exposure to ambient air ( $\sim$ hours to days), crystals of solvatomorphs tend to lose their solvents. This process is followed by disintegration of the crystals along with structural changes and can be promoted by heating. Remarkably, crystals of **1·2CHCl<sub>3</sub>** and

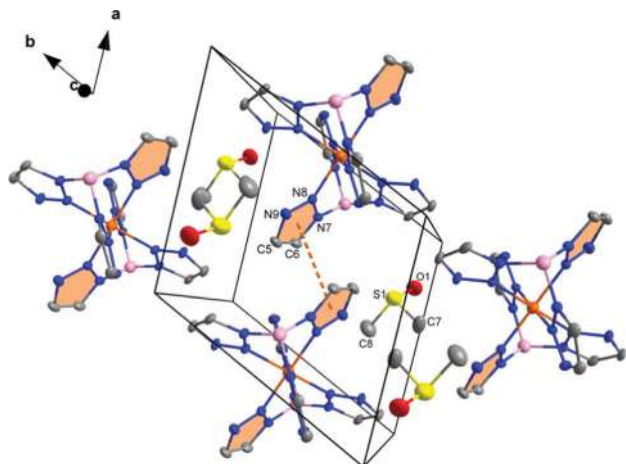


Fig. 1 Crystal structure of **1-2DMSO** showing intermolecular  $\pi$ - $\pi$  stacking interactions developing along the *a* axis. Hydrogen atoms are omitted for clarity. Displacement ellipsoids are drawn at 50% probability level.

**1-2MeOH** undergo single-crystal-to-single-crystal transformations upon heating. When heated at 313 K for one day, solvatomorph **1-2CHCl<sub>3</sub>** completely loses its solvent to form stable crystals of **1**. The same transformation occurs in the case of its methanol counterpart, but the latter requires heating at 323 K for two days. Incomplete solvent loss can be observed in **1-7DMSO**: after two days of evaporation, the single crystal degrades to a powder, the diffraction pattern of which is consistent with the simulated one for **1-2DMSO** (Fig. S7, ESI<sup>†</sup>).

The desolvated compound **1** crystallizes in the monoclinic  $P2_1/c$  space group with 2 molecules of  $\text{FeL}_2$  per unit cell (Fig. 1). It should be noted that the crystals used for refining the structure were obtained *via* a solid-state crystal-to-crystal

transformation. This huge structural rearrangement is related to a chloroform solvent loss, namely *ca.* 25% of the volumic contraction occurs (1412 to 1063 Å<sup>3</sup>) that leads to low quality multi-twin crystals. Three domains were considered upon the refinement. The room temperature (low spin state) unit cell volume per molecule in the crystals of **1** (531.8 Å<sup>3</sup>) is greater when compared to its 1,2,4-triazolyl isomer (516.6 Å<sup>3</sup>).<sup>52</sup> While the structure of  $[\text{Fe}(\text{HB}(1,2,3\text{-tz})_3)_2]$  is less dense, the mean intermolecular  $\text{Fe}\cdots\text{Fe}$  separation (8.49 Å) is slightly shorter in **1** than in the 1,2,4-triazolyl isomer (8.87 Å). The coordination spheres of iron(II) ions in the solvatomorphs (as well as in **1**) have slightly distorted  $[\text{FeN}_6]$  octahedral geometries (see Table S2, ESI<sup>†</sup>). The Fe-N distances lie in the range from 1.952(3) to 1.972(2) Å, while the mean value of coordination octahedra volume ( $V_p$ ) is 10.05 Å<sup>3</sup>, as expected for the low spin iron(II).<sup>53</sup> Considering all the solvatomorphs, the average value of the octahedral distortion parameter  $\sum |90^\circ - \theta_{\text{N-Fe-N}}|$  equals 21.66°. Unfortunately, the high spin structure of **1** could not be assessed because crystals crash at the corresponding high temperatures. Indeed, single crystals of **1**, obtained *via* crystal-to-crystal transformation through thermally induced solvent loss, appear as low quality, highly cracked at room temperature, while further heating is a trigger for crystal degradation.

In the crystals of most of the solvatomorphs, as well as in **1**,  $\pi$ - $\pi$  stacking interactions play a key role in the packing of  $\text{FeL}_2$  molecules. The interactions occur between aromatic 1,2,3-triazolyl rings of adjacent complex molecules (Fig. 1 and Fig. S1-S5, ESI<sup>†</sup>). It is noteworthy that these interactions are spread along one direction in **1-2DMSO**; however they are bidirectional in **1** (Fig. S1, ESI<sup>†</sup>) and in the rest of the solvatomorphs where they are observed. The centroid-centroid distances range from 3.560(3) to 3.6959(17) Å (Table 1). Another type of interaction

Table 1 Intermolecular  $\text{FeL}_2$ - $\text{FeL}_2$  interaction parameters

$\pi$ - $\pi$ stacking interactions			
Compound	$C_{\text{ring}} - C'_{\text{ring}}$ (Å)	$C_{\text{ring}}\text{-plane}'$ (Å)	Dihedral angle (°)
<b>1-2DMSO</b>	3.640(4)	3.298(7)	25.03
<b>1-2MeOH</b>	3.560(3)	3.275(4)	23.08
<b>1-2CHCl<sub>3</sub></b>	3.6959(17)	3.375(3)	24.05
<b>1-2DMF·H<sub>2</sub>O</b>	3.684(3)	3.377(4)	23.56
<b>1</b>	3.594(17)	3.28(3)	24.13
C-H $\cdots$ N interactions			
D-H $\cdots$ A	D $\cdots$ A (Å)	$\angle$ (D-H $\cdots$ A) (°)	
<b>1-2DMSO</b>			
C3-H3 $\cdots$ N3	3.440(7)	150.0(3)	
C6-H6 $\cdots$ N3	3.349(6)	137.6(3)	
<b>1-2MeOH</b>			
C2-H2 $\cdots$ N6	3.279(4)	146.1(2)	
C6-H6 $\cdots$ N3	3.196(4)	133.3(2)	
<b>1-2CHCl<sub>3</sub></b>			
C6-H6 $\cdots$ N3	3.377(3)	153.97(14)	
<b>1-2DMF·H<sub>2</sub>O</b>			
C2-H2 $\cdots$ N6	3.290(4)	135.7(3)	
C4-H4 $\cdots$ N9	3.345(4)	144.0(2)	
<b>1</b>			
C2-H2 $\cdots$ N6	3.14(3)	150.4(17)	
C6-H6 $\cdots$ N3	3.25(3)	134(2)	

that holds molecules of the complex together in the crystal lattices of **1** and **1·Solv** is represented by rather weak C–H···N interactions. The exodentate nitrogen atoms and C–H moieties of 1,2,3-triazolyl rings of neighboring FeL<sub>2</sub> molecules are involved in such intermolecular interactions (Fig. 2 and Fig. S2–S5, ESI†). Similar to  $\pi$ – $\pi$  stacking interactions, C–H···N contacts propagate along *a* and *b* crystallographic directions (Fig. S2, ESI†); however the structure of **1·2CHCl<sub>3</sub>** reveals only a single propagation direction (Fig. S4, ESI†). The parameters of the respective C–H···N contacts are gathered in Table 1. In **1·2DMSO** and **1·2DMF·H<sub>2</sub>O**, the oxygen-containing polar solvents are bound to molecules of **1** via C–H···O contacts (Fig. 2 and Fig. S5a, ESI†). In **1·7DMSO**, the molecules of FeL<sub>2</sub> do not display any direct contacts with each other but interact through solvent molecules by means of C–H···O contacts (Fig. S6, ESI†). In **1·2MeOH**, a hydrogen bonding occurs involving the proton of the OH moiety of the solvent and the exodentate nitrogen atom of the triazolyl ring of the complex ( $d(\text{O} \cdots \text{N}) = 2.867(4)$  Å, Fig. S3a, ESI†). Chloroform molecules in **1·2CHCl<sub>3</sub>** reveal C–H···N and C–H···Cl interactions with FeL<sub>2</sub> molecules (Fig. S4, ESI†).

### Spin crossover properties

A plot of molar magnetic susceptibility as a function of temperature is shown on Fig. 3. Temperature dependent magnetic measurements were conducted by first heating the powder of **1·12H<sub>2</sub>O** from 250 K to 400 K, followed by cycling the as obtained dehydrated sample of **1** in the same temperature range at a rate of 2 K min<sup>−1</sup>.

Compound **1** undergoes a virtually complete, gradual spin crossover between the low spin ( $S = 0$ ) and the high spin ( $S = 2$ ) states, with a transition temperature  $T_{1/2} = 373$  K. We must note that the SCO is not fully completed at 400 K, which is the highest attainable temperature by our magnetometer, but variable-temperature Raman spectroscopic measurements conducted in the 303–433 K range reveal the flattening of the SCO curve slightly above 400 K (see Fig. S9b, ESI†). On the other

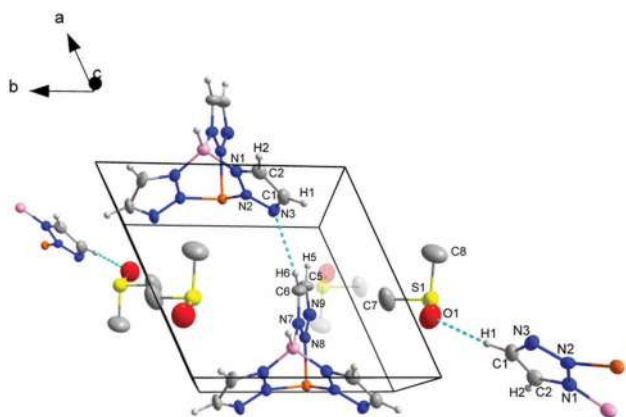


Fig. 2 Crystal structure of **1·2DMSO** showing intermolecular C–H···N and C–H···O contacts. Parts of the complex molecules are omitted for clarity. Displacement ellipsoids are drawn at 50% probability level. Hydrogen atoms in the solvent molecules are omitted for clarity.

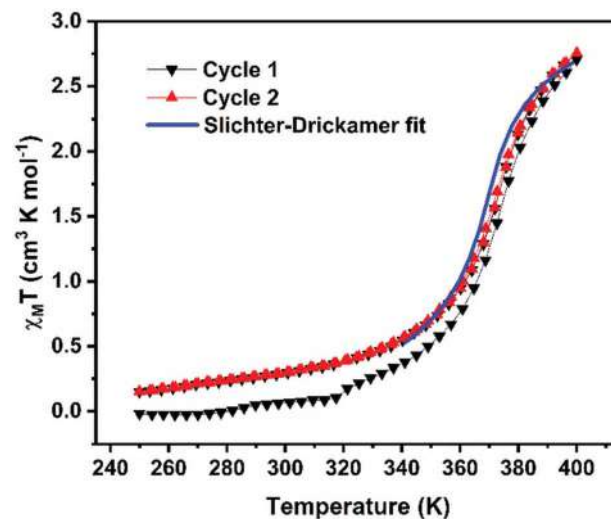


Fig. 3  $\chi_M T$  vs.  $T$  plot, recorded over two thermal cycles starting with the powder sample **1·12H<sub>2</sub>O**. The Slichter–Drickamer fit was performed for the second heating curve.

hand, room temperature Mössbauer spectra recorded both for **1·12H<sub>2</sub>O** and for the anhydrous powder **1** evidence only a low spin ferrous species (see Fig. S10, ESI†). The variable temperature magnetic data could be conveniently fitted by the conventional Slichter–Drickamer (SD) model<sup>37</sup> (see Fig. 3), providing estimation of the enthalpy change ( $\Delta H = 14$  kJ mol<sup>−1</sup>), entropy change ( $\Delta S = 38$  J K<sup>−1</sup> mol<sup>−1</sup>) and cooperativity ( $\Gamma = 5387 \pm 52$  J mol<sup>−1</sup>) associated with the SCO phenomenon. One can remark here the relatively low entropy change and high cooperativity of the spin crossover in **1**, similar to the values reported previously for the 1,2,4-triazolyl isomer ( $\Delta S = 48$  J K<sup>−1</sup> mol<sup>−1</sup>,  $\Gamma = 5700 \pm 50$  J mol<sup>−1</sup>).<sup>54</sup>

At first glance, one may ascribe the different magnetic behavior on the first heating to solvent loss. Indeed, TG-DTA data acquired for compound **1·12H<sub>2</sub>O** reveal dehydration in the temperature range between *ca.* 313 and 363 K (Fig. 4). However, the DSC curve obtained for the hydrated powder displays several intense and broad endothermic peaks during the first heating (Fig. 5), which cannot be solely ascribed to the water loss, but also denote other (overlapped) physical phenomena, including obviously the SCO, but also various structural changes (*vide infra*). Remarkably, the DSC trace on cooling and on successive thermal cycling display a single exothermic (endothermic) peak at 366 K (373 K) on cooling (heating). The peak temperature as well as the associated enthalpy change of *ca.* 14 kJ mol<sup>−1</sup> agrees with the SD fit of the magnetic susceptibility data, allowing us to assign this peak to the sole SCO phenomenon.

In order to further investigate the possible interplay between solvent loss, structural changes and SCO in **1**, powder XRD measurements at variable temperatures were carried out in the 333–493 K temperature range following heating of **1·12H<sub>2</sub>O** at 328 K for 1 h. The powder patterns recorded at 333, 363 and 393 K are substantially different – denoting successive dehydration/structural changes (Fig. 6). Of particular interest is that

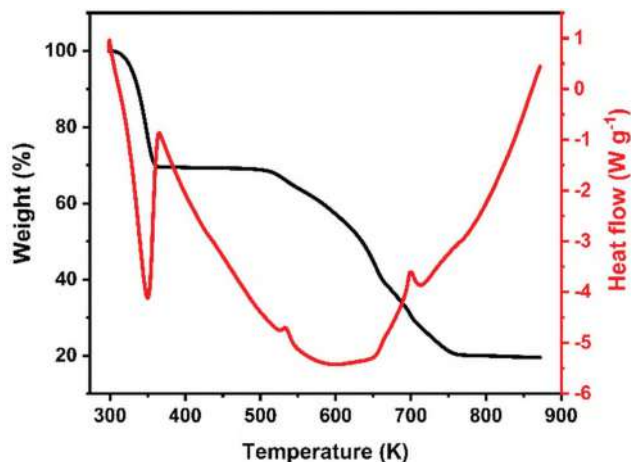


Fig. 4 TGA and DTA curves for  $1 \cdot 12\text{H}_2\text{O}$ .

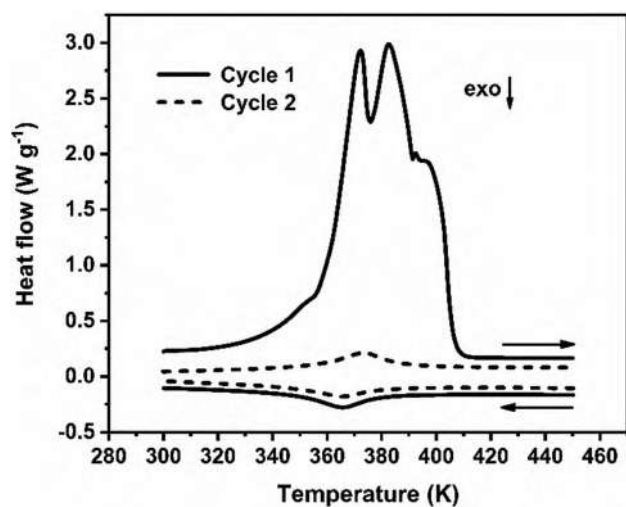


Fig. 5 DSC curves recorded starting with crystalline powder sample of  $1 \cdot 12\text{H}_2\text{O}$  at  $10 \text{ K min}^{-1}$  rate over two successive heating/cooling cycles.

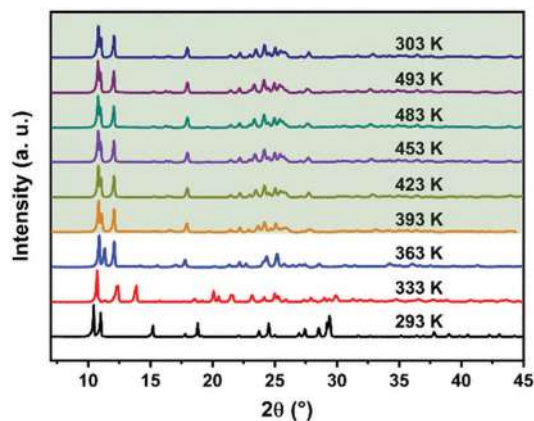


Fig. 6 Powder X-ray diffraction patterns for bulk powders of  $1 \cdot 12\text{H}_2\text{O}$  (293 K) and  $1$  recorded at different temperatures.

the experimental powder pattern recorded at 363 K shows the best match with the diffraction pattern simulated using the single crystal structural data of  $1$  (see Fig. S8, ESI†). Then, further heating up to 493 K and cooling back to 303 K does not reveal any substantial change in the diffractograms (apart from small shifts and broadening of the peak positions – depending on the temperature). This finding is in line with the calorimetric and magnetic measurements, pointing to the occurrence of a very gradual and reversible SCO following a first heating of the sample up to *ca.* 400 K.

## Conclusions

In the present work, we report the crystal structures of solvated and desolvated forms of bis[hydrotris(1,2,3-triazol-1-yl)borate]iron(II) as well as their spin crossover properties. Similar to other unsubstituted tris(1-azoly)borate iron(II) complexes, the complex exhibits reversible spin crossover above room temperature. The SCO in this complex is gradual and is centred at 373 K. Interestingly, the first heating of the hydrated complex is accompanied by a series of structural phase transitions resulting in different polymorphic phases of the compound. Crystal structures of the anhydrous complex and most of the solvatomorphs share the same types of interactions between the molecules of complex, including  $\pi$ - $\pi$  stackings and weak C-H...N hydrogen bond interactions. In the course of this work, we have also evidenced the possibility of sublimating complex  $1$ , which opens attractive perspectives for the deposition of thin films and will be the subject of our further research.

## Conflicts of interest

There are no conflicts to declare.

## Acknowledgements

The authors acknowledge the financial support from the Ministry of Education and Science of Ukraine (grant 22BF037-09) and the courage of the Armed Forces of Ukraine that made the submission of this manuscript possible. We acknowledge Laure Vendier and Jean-Francois Meunier (LCC) for performing variable temperature PXRD and magnetic measurements, respectively. OYH acknowledges the French Embassy in Ukraine and Campus France for a BGF scholarship.

## Notes and references

- 1 P. Gütllich, A. Hauser and H. Spiering, *Angew. Chem., Int. Ed. Engl.*, 1994, 33, 2024–2054.
- 2 in *Spin Crossover in Transition Metal Compounds I*, ed. P. Gütllich and H. A. Goodwin, Springer Berlin Heidelberg, Berlin, Heidelberg, 2004, vol. 233–235.
- 3 in *Spin-Crossover Materials: Properties and Applications*, ed. M. A. Halcrow, John Wiley & Sons Ltd, Oxford, UK, 2013.

- 4 A. Bousseksou, Spin crossover phenomenon, *C. R. Chim.*, 2018, **21**, 12, 1055–1300.
- 5 K. Senthil Kumar and M. Ruben, *Coord. Chem. Rev.*, 2017, **346**, 176–205.
- 6 G. Molnár, S. Rat, L. Salmon, W. Nicolazzi and A. Bousseksou, *Adv. Mater.*, 2018, **30**, 1–23.
- 7 K. S. Kumar and M. Ruben, *Angew. Chem., Int. Ed.*, 2021, **60**, 7502–7521.
- 8 L. Kipgen, M. Bernien, F. Tuzcek and W. Kuch, *Adv. Mater.*, 2021, **33**, 2008141.
- 9 A. Pronschinske, R. C. Bruce, G. Lewis, Y. Chen, A. Calzolari, M. Buongiorno-Nardelli, D. A. Shultz, W. You and D. B. Dougherty, *Chem. Commun.*, 2013, **49**, 10446.
- 10 H. Naggert, J. Rudnik, L. Kipgen, M. Bernien, F. Nickel, L. M. Arruda, W. Kuch, C. Näther and F. Tuzcek, *J. Mater. Chem. C*, 2015, **3**, 7870–7877.
- 11 V. Davesne, M. Gruber, M. Studniarek, W. H. Doh, S. Zafeiratos, L. Joly, F. Sirotti, M. G. Silly, A. B. Gaspar, J. A. Real, G. Schmerber, M. Bowen, W. Weber, S. Boukari, V. Da Costa, J. Arabski, W. Wulfhekel and E. Beurepaire, *J. Chem. Phys.*, 2015, **142**, 194702.
- 12 M. Gruber, T. Miyamachi, V. Davesne, M. Bowen, S. Boukari, W. Wulfhekel, M. Alouani and E. Beurepaire, *J. Chem. Phys.*, 2017, **146**, 092312.
- 13 M. Bernien, D. Wiedemann, C. F. Hermanns, A. Krüger, D. Rolf, W. Kroener, P. Müller, A. Grohmann and W. Kuch, *J. Phys. Chem. Lett.*, 2012, **3**, 3431–3434.
- 14 O. Iasco, M.-L. Boillot, A. Bellec, R. Guillot, E. Rivière, S. Mazerat, S. Nowak, D. Morineau, A. Brosseau, F. Miserque, V. Repain and T. Mallah, *J. Mater. Chem. C*, 2017, **5**, 11067–11075.
- 15 S. Rohlf, M. Gruber, B. M. Flöser, J. Grunwald, S. Jarausch, F. Diekmann, M. Kalläne, T. Jasper-Toennies, A. Buchholz, W. Plass, R. Berndt, F. Tuzcek and K. Rosnagel, *J. Phys. Chem. Lett.*, 2018, **9**, 1491–1496.
- 16 T. Jasper-Tönnies, M. Gruber, S. Karan, H. Jacob, F. Tuzcek and R. Berndt, *J. Phys. Chem. Lett.*, 2017, **8**, 1569–1573.
- 17 M. Atzori, L. Poggini, L. Squillantini, B. Cortigiani, M. Gonidec, P. Bencok, R. Sessoli and M. Mannini, *J. Mater. Chem. C*, 2018, **6**, 8885–8889.
- 18 T. Palamarciuc, J. C. Oberg, F. El Hallak, C. F. Hirjibehedin, M. Serri, S. Heutz, J.-F. Létard and P. Rosa, *J. Mater. Chem.*, 2012, **22**, 9690.
- 19 A. Mosey, A. S. Dale, G. Hao, A. N'Diaye, P. A. Dowben and R. Cheng, *J. Phys. Chem. Lett.*, 2020, **11**, 8231–8237.
- 20 S. Beniwal, S. Sarkar, F. Baier, B. Weber, P. A. Dowben and A. Enders, *J. Phys.: Condens. Matter*, 2020, **32**, 324003.
- 21 V. Shalabaeva, S. Rat, M. D. Manrique-Juarez, A.-C. Bas, L. Vendier, L. Salmon, G. Molnár and A. Bousseksou, *J. Mater. Chem. C*, 2017, **5**, 4419–4425.
- 22 T. Mahfoud, G. Molnár, S. Cobo, L. Salmon, C. Thibault, C. Vieu, P. Demont and A. Bousseksou, *Appl. Phys. Lett.*, 2011, **99**, 9–11.
- 23 L. Salmon, G. Molnár, S. Cobo, P. Oulié, M. Etienne, T. Mahfoud, P. Demont, A. Eguchi, H. Watanabe, K. Tanaka and A. Bousseksou, *New J. Chem.*, 2009, **33**, 1283.
- 24 S. Trofimenko, *Scorpionates: The Coordination Chemistry of Polypyrazolylborate Ligands*, Imperial College Press, 1999.
- 25 M. D. Manrique-Juarez, F. Mathieu, V. Shalabaeva, J. Cacheux, S. Rat, L. Nicu, T. Leïchlé, L. Salmon, G. Molnár and A. Bousseksou, *Angew. Chem., Int. Ed.*, 2017, **56**, 8074–8078.
- 26 V. Shalabaeva, K. Ridier, S. Rat, M. D. Manrique-Juarez, L. Salmon, I. Séguy, A. Rotaru, G. Molnár and A. Bousseksou, *Appl. Phys. Lett.*, 2018, **112**, 013301.
- 27 Y. Zhang, K. Ridier, V. Shalabaeva, I. Séguy, S. Pelloquin, H. Camon, S. Calvez, L. Routaboul, L. Salmon, G. Molnár and A. Bousseksou, *J. Mater. Chem. C*, 2020, **8**, 8007–8011.
- 28 K. Ridier, Y. Zhang, M. Piedrahita-Bello, C. M. Quintero, L. Salmon, G. Molnár, C. Bergaud and A. Bousseksou, *Adv. Mater.*, 2020, **32**, 1–5.
- 29 K. Ridier, A. C. Bas, Y. Zhang, L. Routaboul, L. Salmon, G. Molnár, C. Bergaud and A. Bousseksou, *Nat. Commun.*, 2020, **11**, 1–9.
- 30 B. C. Hughes, Z. Lu and D. M. Jenkins, *Chem. Commun.*, 2014, **50**, 5273–5275.
- 31 J. Tao, R.-J. Wei, R.-B. Huang and L.-S. Zheng, *Chem. Soc. Rev.*, 2012, **41**, 703–737.
- 32 I. Šalitroš, O. Fuhr and M. Ruben, *Materials*, 2016, **9**, 585.
- 33 M. Ohba, K. Yoneda, G. Agustí, M. C. Muñoz, A. B. Gaspar, J. A. Real, M. Yamasaki, H. Ando, Y. Nakao, S. Sakaki and S. Kitagawa, *Angew. Chem.*, 2009, **121**, 4861–4865.
- 34 J. J.-M. Amooore, S. M. Neville, B. Moubaraki, S. S. Iremonger, K. S. Murray, J.-F. Létard and C. J. Kepert, *Chem. – Eur. J.*, 2010, **16**, 1973–1982.
- 35 R.-J. Wei, B. Li, J. Tao, R.-B. Huang, L.-S. Zheng and Z. Zheng, *Inorg. Chem.*, 2011, **50**, 1170–1172.
- 36 C. Bartual-Murgui, A. Akou, H. J. Shepherd, G. Molnár, J. A. Real, L. Salmon and A. Bousseksou, *Chem. – Eur. J.*, 2013, **19**, 15036–15043.
- 37 J. S. Costa, S. Rodríguez-Jiménez, G. A. Craig, B. Barth, C. M. Beavers, S. J. Teat and G. Aromí, *J. Am. Chem. Soc.*, 2014, **136**, 3869–3874.
- 38 R. Kulmaczewski, H. J. Shepherd, O. Cespedes and M. A. Halcrow, *Inorg. Chem.*, 2014, **53**, 9809–9817.
- 39 R. Kulmaczewski, J. Olguín, J. A. Kitchen, H. L.-C. Feltham, G. N.-L. Jameson, J. L. Tallon and S. Brooker, *J. Am. Chem. Soc.*, 2014, **136**, 878–881.
- 40 A. Santoro, L. J. Kershaw Cook, R. Kulmaczewski, S. A. Barrett, O. Cespedes and M. A. Halcrow, *Inorg. Chem.*, 2015, **54**, 682–693.
- 41 M. B. Bushuev, D. P. Pishchur, V. A. Logvinenko, Y. V. Gatilov, I. V. Korolkov, I. K. Shundrina, E. B. Nikolaenkova and V. P. Krivopalov, *Dalton Trans.*, 2016, **45**, 107–120.
- 42 S. Rodríguez-Jiménez, H. L.-C. Feltham and S. Brooker, *Angew. Chem., Int. Ed.*, 2016, **55**, 15067–15071.
- 43 C. Bartual-Murgui, C. Codina, O. Roubeau and G. Aromí, *Chem. – Eur. J.*, 2016, **22**, 12767–12776.
- 44 A. Djemel, O. Stefanczyk, M. Marchivie, E. Trzop, E. Collet, C. Desplanches, R. Delimi and G. Chastanet, *Chem. – Eur. J.*, 2018, **24**, 14760–14767.
- 45 T. Boonprab, P. Harding, K. S. Murray, W. Phonsri, S. G. Telfer, A. Alkaş, R. Ketkaew, Y. Tantirungrotechai, G. N.-L. Jameson and D. J. Harding, *Dalton Trans.*, 2018, **47**, 12449.

- 46 S. Vela and H. Paulsen, *Dalton Trans.*, 2019, **48**, 1237–1245.
- 47 F.-L. Yang, W.-H. Wu, Y.-Q. Wang, X. Chen, B.-B. Liang, H.-L. Mi, G.-L. Zhang, X.-Y. Chen and Y. Shi, *Cryst. Growth Des.*, 2021, **21**, 6671–6683.
- 48 G. M. Sheldrick, *Acta Crystallogr., Sect. C: Struct. Chem.*, 2015, **71**, 3–8.
- 49 G. M. Sheldrick, *Acta Crystallogr., Sect. A: Found. Crystallogr.*, 2008, **64**, 112–122.
- 50 O. V. Dolomanov, L. J. Bourhis, R. J. Gildea, J. A.-K. Howard and H. Puschmann, *J. Appl. Crystallogr.*, 2009, **42**, 339–341.
- 51 K. Lagarec and D. G. Rancourt, *Nucl. Instrum. Methods Phys. Res., Sect. B*, 1997, **129**, 266–280.
- 52 S. Rat, K. Ridier, L. Vendier, G. Molnár, L. Salmon and A. Bousseksou, *CrystEngComm*, 2017, **19**, 3271–3280.
- 53 P. Guionneau, M. Marchivie, G. Bravic, J.-F. Létard and D. Chasseau, in *Spin Crossover in Transition Metal Compounds II*, ed. P. Gütlich and H. A. Goodwin, Springer Berlin Heidelberg, Berlin, Heidelberg, 2004, pp. 97–128.
- 54 C. P. Slichter and H. G. Drickamer, *J. Chem. Phys.*, 1972, **56**, 2142–2160.



# Efficient Sensitized Luminescence of Binuclear Ln(III) Complexes Based on a Chelating Bis-Carbacylamidophosphate

O. Y. Horniichuk<sup>1</sup> · N. S. Kariaka<sup>1</sup> · S. S. Smola<sup>2</sup> · N. V. Rusakova<sup>2</sup> · V. O. Trush<sup>1</sup> · T. Y. Sliva<sup>1</sup> · V. M. Amirkhanov<sup>1</sup>

Received: 14 September 2020 / Accepted: 9 April 2021 / Published online: 26 April 2021

© The Author(s), under exclusive licence to Springer Science+Business Media, LLC, part of Springer Nature 2021

## Abstract

Binuclear rare earth complexes  $\text{Ln}_2\text{L}_3\text{phen}_2$  ( $\text{Ln}^{\text{III}} = \text{Nd}^{\text{III}}, \text{Sm}^{\text{III}}, \text{Eu}^{\text{III}}, \text{Tb}^{\text{III}}, \text{Dy}^{\text{III}}, \text{Yb}^{\text{III}}$  and  $\text{Y}^{\text{III}}$ ) with bis-CAPh type ligand - tetramethyl  $\text{N,N}'$ -(2,2,3,3,4,4-hexafluoro-1,5-dioxopentane-1,5-diyl)bis(phosphoramidate) ( $\text{H}_2\text{L}$ ) and 1,10-phenanthroline (phen) were synthesized and characterized by elemental analysis, IR, NMR, absorption and luminescence spectroscopy. Luminescence measurements were performed for all the complexes in solid state and for the  $\text{Eu}^{\text{III}}$ ,  $\text{Tb}^{\text{III}}$  and  $\text{Y}^{\text{III}}$  complexes - in solution in DMSO as well. The effective energy transfer from organic ligands to  $\text{Ln}^{\text{III}}$  ions strongly sensitizes the  $\text{Ln}^{\text{III}}$  ions emission and under excitation by UV light, the complexes exhibited bright characteristic emission of lanthanide metal centers. It was found that the energy level of the ligands lowest triplet state in the complexes matches better to resonance level of  $\text{Eu}^{\text{III}}$  rather than  $\text{Tb}^{\text{III}}$  ion. Depending on temperature the emission decay times of solid europium and terbium complexes were in the range of 1.5–2.0 ms. In solid state at room temperature the  $\text{Eu}^{\text{III}}$  complex possess intense luminescence with very high intrinsic quantum yield 91% and decay time equal 1.88 ms.

**Keywords** Bis-carbacylamidophosphate · Rare earth elements · Binuclear coordination compounds · Photoluminescence · Sensitization

## Introduction

Over past several decades, there has been much interest in design and synthesis of lanthanide complexes due to their attractive luminescent properties (high color purity of emitted light, relatively long luminescence decay times and large Stokes shifts), which make them promising as luminescent components for optical devices and as labels in fluorescence-based bioassays [1–6]. Despite the extremely interesting features of  $4f$ -luminescence a significant drawback is the inability of  $\text{Ln}^{\text{III}}$  optical centers to absorb light efficiently (extinction coefficient of three-charged lanthanide cations is within  $\epsilon \approx 1$ – $10 \text{ M}^{-1}\cdot\text{cm}^{-1}$  [7]) and easy deactivation of the  $\text{Ln}^{\text{III}}$  excited

states by high-energy vibrations, particularly OH, NH and CH oscillators [8, 9]. To achieve strong  $\text{Ln}^{\text{III}}$  luminescence in coordination compounds the metal coordination sphere should be saturated with bulky organic ligands, providing the “antenna effect”.

Among the most famous groups of lanthanide complexes there are mixed ligand ternary complexes with  $\beta$ -diketones, carbacyl- (CAPh) and sulfonyl-amidophosphates (SAPh), carboxylic acids etc. and ancillary ligand such as 2,2-bipyridine or 1,10-phenanthroline [10–20]. Such complexes are known to be studied as emitting layers in technology of light conversion molecular devices [21–23]. It was observed that incorporation of a neutral ligand (like 2,2'-bipyridine or 1,10-phenanthroline, etc.) in lanthanide complexes, raises their luminescence effectiveness [24, 25]. As excellently luminescent lanthanide coordination compounds also binuclear  $\text{Ln}^{\text{III}}$  complexes based on bis-diketones are worth to be mentioned. Recently some such complexes were reported [26–34] and it was shown that they can exhibit higher luminescence intensity than their mononuclear analogs.

Complexes based on carbacylamidophosphates – P,N substitutes of  $\beta$ -diketones – are in the focus of our scientific interests. Compared to  $\beta$ -diketones the structure of CAPhs

✉ N. S. Kariaka  
natalia\_kariaka@i.ua

<sup>1</sup> Inorganic Chemistry Department, Taras Shevchenko National University of Kyiv, 12, Lva Tolstogo St, Kyiv 01601, Ukraine

<sup>2</sup> Lanthanide chemistry department, A. V. Bogatsky Physicochemical Institute of National Academy of Sciences of Ukraine, 86 Lustdorfska doroga, Odesa 65080, Ukraine

suggests the possibility to decrease the multiphonon quenching of lanthanide emission and to increase the ligand affinity to Ln<sup>III</sup> ion allowing to obtain thermo- and photo-stable Ln<sup>III</sup> coordination compounds with effective luminescence [35]. In our previous work [36] we have approbated for the first time bis-chelating carbacylamidophosphate – N,N'-(2,2,3,3,4,4-hexafluoro-1,5-dioxopentane-1,5-diyl)bis(phosphoramidate) (H<sub>2</sub>L, Fig. 1) as a ligand for obtaining complexes Ln<sub>2</sub>L<sub>3</sub>phen<sub>2</sub> (Ln = Nd<sup>III</sup>, Eu<sup>III</sup> and Y<sup>III</sup>, phen = 1,10-phenanthroline). As a development of this study and in frames of our systematic investigations of CAPH based lanthanide coordination compounds in this work a series of binuclear rare-earth complexes Ln<sub>2</sub>L<sub>3</sub>phen<sub>2</sub> (Ln<sup>III</sup> = Nd<sup>III</sup>, Sm<sup>III</sup>, Eu<sup>III</sup>, Tb<sup>III</sup>, Dy<sup>III</sup>, Yb<sup>III</sup> and Y<sup>III</sup>) was obtained and characterized by elemental analysis, IR, NMR, absorption and luminescent spectroscopy.

## Experimental Section

### Materials and Synthesis

All reagents and solvents were used of commercial grade without further purification.

N,N'-(2,2,3,3,4,4-hexafluoro-1,5-dioxopentane-1,5-diyl)bis(phosphoramidate) (H<sub>2</sub>L) was synthesized by known multistep method starting from dimethyl hexafluoropentanedioate [37].

Coordination compounds Ln<sub>2</sub>L<sub>3</sub>phen<sub>2</sub> were obtained according to Scheme 1:

Ln(NO<sub>3</sub>)<sub>3</sub>·6H<sub>2</sub>O (0.1 mmol) was dissolved in methyl alcohol (2 ml) and HC(OC<sub>2</sub>H<sub>5</sub>)<sub>3</sub> (0.1 ml, 0.6 mmol) as dehydrating agent was added to the solution. Afterwards, the solution was boiled for a minute, cooled down to room temperature and then added to a solution of H<sub>2</sub>L (0.068 g, 0.15 mmol) and of triethylamine (0.041 ml, 0.30 mmol) in methanol. Finally a solution of 1,10-phenanthroline (0.018 g, 0.1 mmol) in methanol was added to the resulting mixture to give an oily precipitation colored as respective metal aqua ion. The obtained mixture was boiled for 5 min. Then the leach was decanted. The precipitation was thoroughly washed with 2-propanol, filtered off and dried on air. Yield was ~75%. The obtained complexes are colored like as respective metal aqua ion, well soluble in dimethyl sulfoxide (DMSO) and *N,N*-dimethylformamide (DMFA).

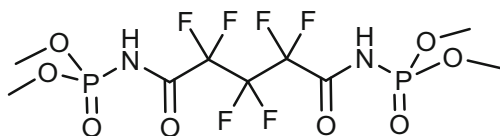


**Fig. 1** Structure of N,N'-(2,2,3,3,4,4-hexafluoro-1,5-dioxopentane-1,5-diyl)bis(phosphoramidate) (H<sub>2</sub>L)

**Nd<sub>2</sub>L<sub>3</sub>phen<sub>2</sub>:** C<sub>51</sub>H<sub>52</sub>N<sub>10</sub>O<sub>24</sub>P<sub>6</sub>F<sub>18</sub>Nd<sub>2</sub> (M = 2005.31). Anal. calc.: Nd, 14.4; C, 30.55; H, 2.61; N, 6.98%. Found: Nd, 14.6; C, 30.57; H, 2.63; N, 6.95%. FT-IR (KBr, cm<sup>-1</sup>): 3008, 2958, 2855 [w, ν(CH)], 1608 [vs, ν(C=O)], 1519 [m, ν(CC), phen], 1424 [m, ν(CC), phen], 1403 [s, ν(Amide 2)], 1350 w, 1160 [vs, ν(P=O)], 1043 [vs, δ(POC)], 962 [m, ν(PN)], 916 w, 847 s, 810 m, 770 w, 731 m, 534 w, 498 w, 463 w. <sup>1</sup>H NMR (DMSO-d<sub>6</sub>), δ =: 9.08 (br, 4H, phen); 8.46 (br, 4H, phen); 7.96 (br, 4H, phen); 7.76 (br, 4H, phen); 4.12 (br, 36H, L<sup>2-</sup>).

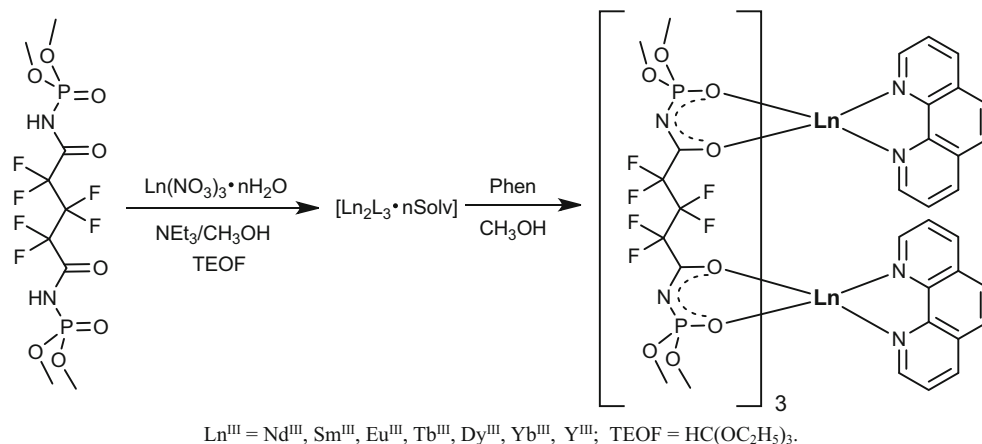
**Sm<sub>2</sub>L<sub>3</sub>phen<sub>2</sub>:** C<sub>51</sub>H<sub>52</sub>N<sub>10</sub>O<sub>24</sub>P<sub>6</sub>F<sub>18</sub>Sm<sub>2</sub> (M = 2017.55). Anal. calc.: Sm, 14.9; C, 30.36; H, 2.60; N, 6.94%. Found: Sm, 15.0; C, 30.38; H, 2.63; N, 6.92%. FT-IR (KBr, cm<sup>-1</sup>): 3002, 2958, 2856 [w, ν(CH)], 1604 [vs, ν(C=O)], 1521 [m, ν(CC), phen], 1427 [m, ν(CC), phen], 1403 [s, ν(Amide 2)], 1350 w, 1162 [vs, ν(P=O)], 1041 [vs, δ(POC)], 963 [m, ν(PN)], 916 w, 809 m, 770 w, 731 m, 540 w, 498 w, 460 w. <sup>1</sup>H NMR (DMSO-d<sub>6</sub>), δ =: 9.48 (br, 4H, phen); 8.96 (br, 4H, phen); 8.43 (br, 4H, phen); 8.22 (br, 4H, phen); 3.99 (br, 36H, L<sup>2-</sup>).

**Eu<sub>2</sub>L<sub>3</sub>phen<sub>2</sub>:** C<sub>51</sub>H<sub>52</sub>N<sub>10</sub>O<sub>24</sub>P<sub>6</sub>F<sub>18</sub>Eu<sub>2</sub> (M = 2020.75). Anal. calc.: Eu, 15.0; C, 30.31; H, 2.59; N, 6.93%. Found: Eu, 15.4; C, 30.33; H, 2.60; N, 6.90%. FT-IR (KBr, cm<sup>-1</sup>): 3008, 2958, 2855 [w, ν(CH)], 1604 [vs, ν(C=O)], 1520 [m, ν(CC), phen], 1428 [m, ν(CC), phen], 1399 [s, ν(Amide 2)], 1350 w, 1163 [vs, ν(P=O)], 1043 [vs, δ(POC)], 962 [m, ν(PN)], 916 w, 846 s, 809 m, 770 w, 731 m, 541 w, 500 w, 462 w. <sup>1</sup>H NMR (DMSO-d<sub>6</sub>), δ =: 9.09 (br, 4H, phen); 8.53 (br, 4H, phen); 7.99 (br, 4H, phen); 7.73 (br, 4H, phen); 2.90 (br, 36H, L<sup>2-</sup>). Thermal gravimetric studies of the europium complex showed its thermal stability to over 200 °C [36].

**Tb<sub>2</sub>L<sub>3</sub>phen<sub>2</sub>:** C<sub>51</sub>H<sub>52</sub>N<sub>10</sub>O<sub>24</sub>P<sub>6</sub>F<sub>18</sub>Tb<sub>2</sub> (M = 2034.68). Anal. calc.: Tb, 15.6; C, 30.11; H, 2.58; N, 6.88%. Found: Tb, 15.9; C, 30.14; H, 2.61; N, 6.86%. FT-IR (KBr, cm<sup>-1</sup>): 3007, 2958, 2854 [w, ν(CH)], 1610 [vs, ν(C=O)], 1522 [m, ν(CC), phen], 1427 [m, ν(CC), phen], 1404 [s, ν(Amide 2)], 1350 w, 1165 [vs, ν(P=O)], 1042 [vs, δ(POC)], 964 [m, ν(PN)], 918 w, 847 s, 811 m, 770 w, 731 m, 536 w, 501 w, 464 w.

**Dy<sub>2</sub>L<sub>3</sub>phen<sub>2</sub>:** C<sub>51</sub>H<sub>52</sub>N<sub>10</sub>O<sub>24</sub>P<sub>6</sub>F<sub>18</sub>Dy<sub>2</sub> (M = 2041.83). Anal. calc.: Dy, 15.9; C, 30.00; H, 2.57; N, 6.86%. Found: Dy, 16.3; C, 30.04; H, 2.59; N, 6.84%. FT-IR (KBr, cm<sup>-1</sup>): 3007, 2959, 2856 [w, ν(CH)], 1607 [vs, ν(C=O)], 1522 [m, ν(CC), phen], 1424 [m, ν(CC), phen], 1405 [s, ν(Amide 2)], 1350 w, 1164 [vs, ν(P=O)], 1043 [vs, δ(POC)], 964 [m, ν(PN)], 918 w, 812 m, 771 w, 730 m, 540 w, 498 w, 462 w.

**Yb<sub>2</sub>L<sub>3</sub>phen<sub>2</sub>:** C<sub>51</sub>H<sub>52</sub>N<sub>10</sub>O<sub>24</sub>P<sub>6</sub>F<sub>18</sub>Yb<sub>2</sub> (M = 2062.93). Anal. calc.: Yb, 16.8; C, 29.69; H, 2.54; N, 6.79%. Found: Yb, 17.1; C, 29.72; H, 2.58; N, 6.76%. FT-IR (KBr, cm<sup>-1</sup>): 3011, 2958, 2856 [w, ν(CH)], 1607 [vs, ν(C=O)], 1522 [m, ν(CC), phen], 1427 [m, ν(CC), phen], 1406 [s, ν(Amide 2)], 1350 w, 1165 [vs, ν(P=O)], 1041 [vs, δ(POC)], 964 [m, ν(PN)], 920 w, 847 s, 813 m, 771 w, 731 m, 540 w, 498 w, 462 w.

**Scheme 1** Synthesis route of  $\text{Ln}_2\text{L}_3\text{phen}_2$  complexes

**$\text{Y}_2\text{L}_3\text{phen}_2$ :**  $\text{C}_{51}\text{H}_{52}\text{N}_{10}\text{O}_{24}\text{P}_6\text{F}_{18}\text{Y}_2$  ( $M = 1894.64$ ). Anal. calc.: Y, 9.4; C, 32.33; H, 2.77; N, 7.39%. Found: Y, 9.7; C, 32.35; H, 2.79; N, 7.35%. FT-IR (KBr,  $\text{cm}^{-1}$ ): 3004, 2958, 2855 [w,  $\nu(\text{CH})$ ], 1613 [vs,  $\nu(\text{C}=\text{O})$ ], 1522 [m,  $\nu(\text{CC})$ , phen], 1428 [m,  $\nu(\text{CC})$ , phen], 1406 [s,  $\nu(\text{Amide } 2)$ ], 1350 w, 1165 [vs,  $\nu(\text{P}=\text{O})$ ], 1043 [vs,  $\delta(\text{POC})$ ], 964 [m,  $\nu(\text{PN})$ ], 919 w, 847 s, 813 m, 771 w, 732 m, 542 w, 495 w, 466 w.  $^1\text{H}$  NMR (DMSO- $d_6$ ),  $\delta$  =: 9.19 (br, 4H, phen); 8.55 (br, 4H, phen); 8.03 (s, 4H, phen); 7.83 (br, 4H, phen); 3.56 (d,  $J = 11.1$  Hz, 36H,  $\text{L}^{2-}$ ).  $^{31}\text{P}$  NMR (DMSO- $d_6$ ),  $\delta = 10.03$ .

## Methods

IR measurements were performed on a Perkin–Elmer Spectrum BX spectrometer on solid state samples in form of KBr pellets and for the neodymium complex solution in DMSO with concentration close to saturated solution, placing a drop of the solution between KBr pellets.

NMR spectra for solutions in DMSO- $d_6$  were obtained on an AVANCE 400 Bruker NMR spectrometer at room temperature. Typical concentrations of the complexes in DMSO solutions in experiments were in range 0.005–0.01  $\text{mol}/\text{dm}^3$ .

Elemental analyses (C, H, and N) were performed on an EL III Universal CHNOS Elemental Analyzer and by using standard titrimetric methods for lanthanide ions.

The absorption spectra for the neodymium complex were recorded on an UV VIS spectrophotometer Specord M 40 Carl Zeiss for solid samples and on KSVU-23 “LOMO” spectrometer using quartz cell of 1 cm path length for the complex 0.008  $\text{mol}/\text{dm}^3$  solution in DMSO.

Photoluminescence excitation and emission spectra of the complexes were measured at 298 and 77 K on a Fluorolog FL 3–22 (Horiba Jobin Yvon) spectrofluorimeter coupled to a R928 Hamamatsu photomultiplier, using the right angle detection mode. The excitation source was a 450 W Xe arc lamp. The emission spectra were corrected for detection and optical spectral response of the spectrofluorimeter and the excitation spectra were corrected for the spectral distribution of the lamp

intensity using a photodiode reference detector. All the spectra were acquired through an UV filter (350 nm cut-off). Solid samples for photoluminescence measurements at room temperature were loaded in a solid sample cuvette supplied with Fluorolog FL 3–22 or in quartz capillaries in case of experiments at 77 K. Concentrations of the complexes solutions in DMSO for photoluminescence measurements were  $(1.0\text{--}5.0) \times 10^{-4}$   $\text{mol}/\text{dm}^3$ . The solution was placed in quartz cuvettes in case of experiment at room temperature or in quartz capillaries in case of experiments at 77 K. The luminescence lifetime measurements were acquired with the same instrument using a pulsed Xe–Hg lamp (6 mcs pulse at half width and 20–30 mcs low-intensity tail). The luminescence lifetime values are averages of at least three independent measurements which were made by monitoring the decay at the maxima of the emission spectra. The decays were analyzed with Origin 9.2.257. The decay time values were estimated with an error of 10%. Phosphorescence spectra were registered for the  $\text{Y}^{\text{III}}$  complex in solid state and for its frozen 0.001  $\text{mol}/\text{dm}^3$  solution in DMSO at 77 K, enforcing a 0.05 ms delay, and repeating measurements at least 3 times.

## Results and Discussion

### NMR Spectra

$^1\text{H}$  NMR spectrum of complex  $\text{Y}_2\text{L}_3\text{phen}_2$  displays a doublet at  $\delta$  3.57 assigned to protons of ester groups of CAPH ligands and a series of peaks in region of  $\delta$  7.8–9.2 assigned to 1,10-phenanthroline ligands (Fig. S1). By integrating of areas of peaks corresponding to the both ligands it was found that their ratio ( $\text{L}^{2-}:\text{phen}$ ) in the complex equals 3:2. No signal of amide protons of CAPH ligand was found in the  $^1\text{H}$  NMR spectrum of the complex  $\text{Y}_2\text{L}_3\text{phen}_2$  which is a consequence of coordination of N,N'-(2,2,3,3,4,4-hexafluoro-1,5-dioxopentane-1,5-diyl)bis(phosphoramidate) to  $\text{Y}^{3+}$  ion in a double deprotonated form. Deprotonation of the CAPH ligand in

**Table 1** Assignments of the main IR absorption bands for the synthesized compounds,  $\text{cm}^{-1}$ 

Compound	Band assignment				
	$\nu(\text{N-H})$	$\nu(\text{C=O})$	$\nu(\text{Amide-II})$	$\nu(\text{P=O})$	$\nu(\text{P-N})$
H <sub>2</sub> L	3095	1746	1478	1212	877
Ln <sub>2</sub> L <sub>3</sub> phen <sub>2</sub>	–	1604–1613	1399–1406	1160–1165	962–964

Y<sub>2</sub>L<sub>3</sub>phen<sub>2</sub> also leads to the shift of the signal of OCH<sub>3</sub>-groups in the complex <sup>1</sup>H NMR spectrum to high field compared to the spectrum of H<sub>2</sub>L [37]. For paramagnetic lanthanides (Nd<sup>III</sup>, Sm<sup>III</sup>, Eu<sup>III</sup>) complexes the signals in their <sup>1</sup>H NMR spectra are broadened and shifted but L<sup>2-</sup>:phen ratio gained through the results of peaks integration remains to be equal 3:2. For the rest of the obtained complexes the <sup>1</sup>H NMR spectra were not informative.

## IR Spectra

The characteristic IR spectra data for H<sub>2</sub>L and the complexes are given in Table 1 and shown in the Fig. S2. The complexes have similar IR spectra with resembling position of characteristic bands, suggesting the similar coordination modes. An absence of  $\nu(\text{N-H})$  absorption band in the region near  $3100\text{ cm}^{-1}$  in the IR spectra of the complexes indicates the coordination of CAPH-ligands to rare earth ions in double deprotonated form which is in good agreement with <sup>1</sup>H NMR data. The low frequency shift of  $\nu(\text{P=O})$  and  $\nu(\text{C=O})$  bands and high frequency shift of  $\nu(\text{P-N})$  bands in the IR spectra of the complexes with respect to H<sub>2</sub>L spectrum point to participation of the both phosphoryl and carbonyl groups in metal binding and existence of  $\pi$ -conjugation in –OCNPO-chelating core. A number of bands with middle and low intensity at  $1520, 1430, 1350, 846$  and  $733\text{ cm}^{-1}$  points to the presence of 1,10-phenanthroline ligands in the complexes (Fig. S2, supplementary materials). The IR spectrum of the neodymium complex concentrated solution in DMSO is shown in Fig. S3. Only the most intense absorption bands of

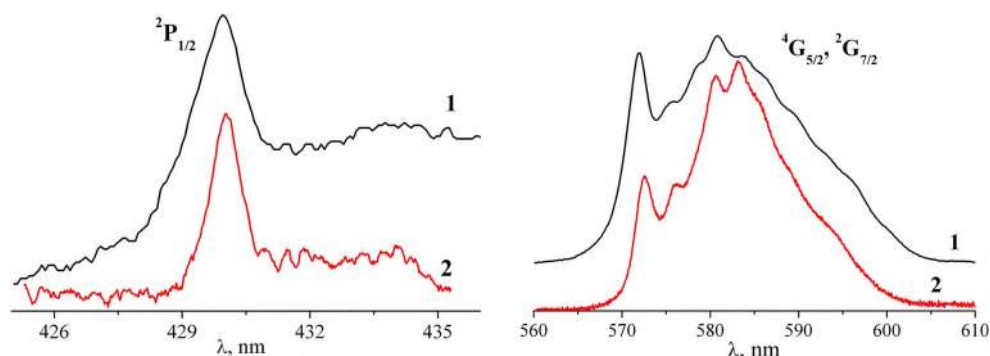
the complex, which do not overlap with the solvent absorption bands, can be observed in the spectrum. The position of  $\nu(\text{P=O})$  absorption band is the same for the complex in KBr pellet and in solution, while  $\nu(\text{C=O})$  and  $\delta(\text{POC})$  absorption bands slightly moved for near  $20\text{ cm}^{-1}$  to higher or lower frequencies respectively. Considering an insignificant difference in positions of characteristic absorption bands in the IR spectra for the solid complex and its solution the retention of CAPH ligand type of coordination in the complex in solution in DMSO can be concluded.

## Absorption Spectra of the Nd<sup>III</sup> Complex

Among the lanthanide (III) ions Nd<sup>III</sup> has been used most frequently as an absorption probe for Ln-ligand interactions. The absorption band associated with  $^4I_{9/2} \rightarrow ^4G_{5/2}$  and  $^2G_{7/2}$  transitions of Nd<sup>III</sup> exhibits strong “hypersensitive” behaviour [38–40]. The intensity of these bands is mostly influenced among all the *f-f* transitions due to the changes in the nearest surrounding of the Nd<sup>III</sup> ion, making it particularly suitable for probing the coordination environment around the ion. View of the spectra in the region of  $^4I_{9/2} \rightarrow ^2P_{1/2}$  transition indicates the splitting of the ground level in the ligand field of the Nd<sup>III</sup> environment [41].

The absorption spectra of the neodymium complex were recorded at 293 K in the ranges of  $^4I_{9/2} \rightarrow ^2P_{1/2}$  and  $^4I_{9/2} \rightarrow ^4G_{5/2}, ^2G_{7/2}$  transitions for solid sample and for the complex 0.008 M solution in DMSO (Fig. 2). A single band with maximum at  $430.0\text{ nm}$  in region of  $^4I_{9/2} \rightarrow ^2P_{1/2}$  transition points on identical or very similar neodymium ions positions in the complex. In the region of  $^4I_{9/2} \rightarrow ^4G_{5/2}, ^2G_{7/2}$  transitions the electronic absorption spectra of the complex Nd<sub>2</sub>L<sub>3</sub>phen<sub>2</sub> show absorption features similar to those reported previously for mononuclear neodymium coordination compounds based on different CAPH and SAPH ligands with a coordination number of the central atom of 8 [16, 42, 43]. From the similar bands positions in the spectra of solid Nd<sub>2</sub>L<sub>3</sub>phen<sub>2</sub> complex and its solution it can be concluded that in solution the central ion of the complex is eight coordinated and the Nd<sup>III</sup>-ligand bond covalence is the same as for the solid sample.

**Fig. 2** Normalized absorption spectra of Nd<sub>2</sub>L<sub>3</sub>phen<sub>2</sub> solid sample (1) and solution in DMSO (2) in the regions of  $^4I_{9/2} \rightarrow ^2P_{1/2}$  (left panel) and  $^4I_{9/2} \rightarrow ^4G_{5/2}, ^2G_{7/2}$  (right panel) transitions



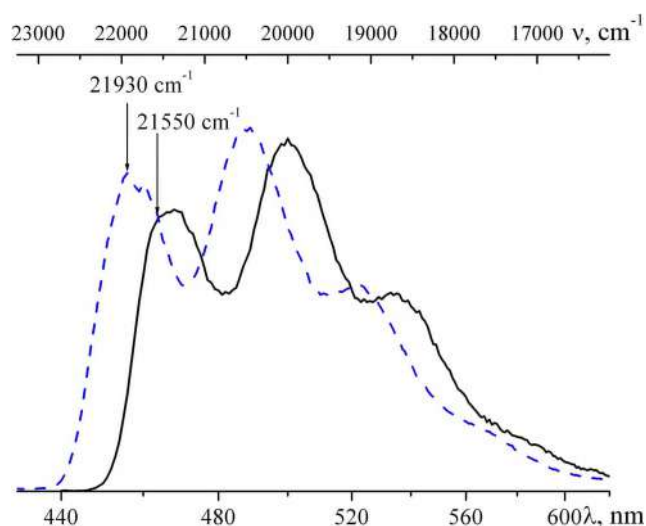


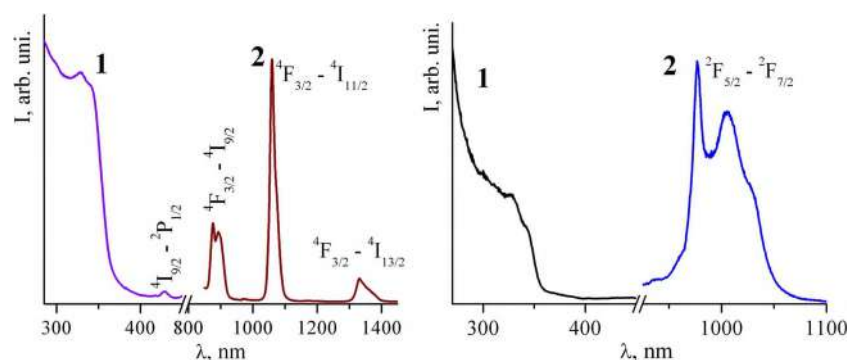
**Fig. 3** The phosphorescence spectra of  $Y_2L_3phen_2$  complex at 77 K ( $\lambda_{exc} = 330$  nm) in solid state (solid line) and for frozen solution in DMSO (dashed line)

### The $Y^{III}$ Complex Phosphorescence Spectra

It is well known that the energy level matching between the lowest ligand triplet state and excited levels of  $Ln^{III}$  ions plays an important role in determining the luminescent properties of complexes. Energy level of the lowest ligands triplet state (LLTS) for the complexes under study ( $21,550\text{ cm}^{-1}$ ) was calculated from the shortest wavelength peak [44] of the phosphorescence spectrum of solid  $Y_2L_3phen_2$  complex (Fig. 3, solid line). LLTS is obviously higher than emissive levels of  $Nd^{III}$ ,  $Sm^{III}$ ,  $Eu^{III}$ ,  $Tb^{III}$ ,  $Dy^{III}$  and  $Yb^{III}$  ions. The energy gaps between the ligands lowest triplet state and emissive levels of the mentioned lanthanides in the complexes under study are  $10,050$ ,  $3850$ ,  $4250$ ,  $1050$ ,  $450$  and  $11,550\text{ cm}^{-1}$  respectively (Fig. S4).

In 0.001 M solution in DMSO the phosphorescence spectrum of the  $Y^{III}$  complex was shifted to higher frequencies for  $380\text{ cm}^{-1}$  (Fig. 3, dashed line) due to the complex interaction with the solvent.

**Fig. 4** Luminescence excitation (1) and luminescence (2) spectra of  $Nd_2L_3phen_2$  (left panel) and  $Yb_2L_3phen_2$  (right panel) solid samples at 293 K



### Luminescence Properties of the $Nd^{III}$ , $Sm^{III}$ , $Eu^{III}$ , $Tb^{III}$ , $Dy^{III}$ and $Yb^{III}$ Complexes

The excitation and emission spectra of the obtained complexes are shown in the Figs. 4–5. The excitation spectra were recorded by monitoring the strongest emission bands of corresponding lanthanide ions. The spectra consist of a broad intense band in the 250–380 nm region, which can be assigned to the  $\pi-\pi^*$  electronic transitions of the ligands, and of less intense and narrow bands of  $f-f$  transitions of the lanthanide ions. Such a ratio of the bands' intensities points on efficient sensitization of lanthanide luminescence by organic ligands. Upon excitation by UV light all the complexes show characteristic  $Ln^{III}$  emission with a series of narrow bands corresponding to the respective lanthanide ion. No ligand fluorescence was observed in the emission spectra of the complexes pointing on efficient energy transfer from ligands to lanthanides.

The spectroscopic properties of  $Nd^{III}$  and  $Yb^{III}$  complexes emitting in the near-infrared (NIR) range have been increasingly studied in recent times [45–49] because of their diagnostic or tagging applications. Considering that in the coordination compounds under study the energy level of lowest ligands triplet state was higher than emissive levels of  $Nd^{III}$  ( ${}^4F_{3/2}$ ,  $\sim 11,500\text{ cm}^{-1}$ ) and  $Yb^{III}$  ( ${}^2F_{5/2}$ ,  $\sim 10,000\text{ cm}^{-1}$ ) ions the luminescence excitation and luminescence spectra for the complexes  $Nd_2L_3phen_2$  and  $Yb_2L_3phen_2$  were recorded (Fig. 4). Upon excitation of the complex  $Nd_2L_3phen_2$  by UV light at 330 nm, characteristic  $Nd^{III}$   $4f$ -luminescence was observed in IR spectral region (Fig. 4, left panel). The observed bands were assigned to the  ${}^4F_{3/2} \rightarrow {}^4I_{9/2}$ ,  ${}^4F_{3/2} \rightarrow {}^4I_{11/2}$  and  ${}^4F_{3/2} \rightarrow {}^4I_{13/2}$  transitions. The bands, observed in the emission spectra of the complex  $Yb_2L_3phen_2$ , were assigned to the  ${}^2F_{5/2} \rightarrow {}^2F_{7/2}$  transition of the  $Yb^{III}$  ion (Fig. 4, right panel). The electronic line corresponding to the  ${}^2F_{5/2}(0) \rightarrow {}^2F_{7/2}(0)$  transition has a maximum at 977.0 nm. The board peaks in region 1000–1050 nm arise from the  $M_J$  splitting of  ${}^2F_{7/2}$  state as the consequence of ligand-field effects.

The luminescence excitation and luminescence spectra of the complexes, emitting in the visible spectral range are shown in Fig. 5.

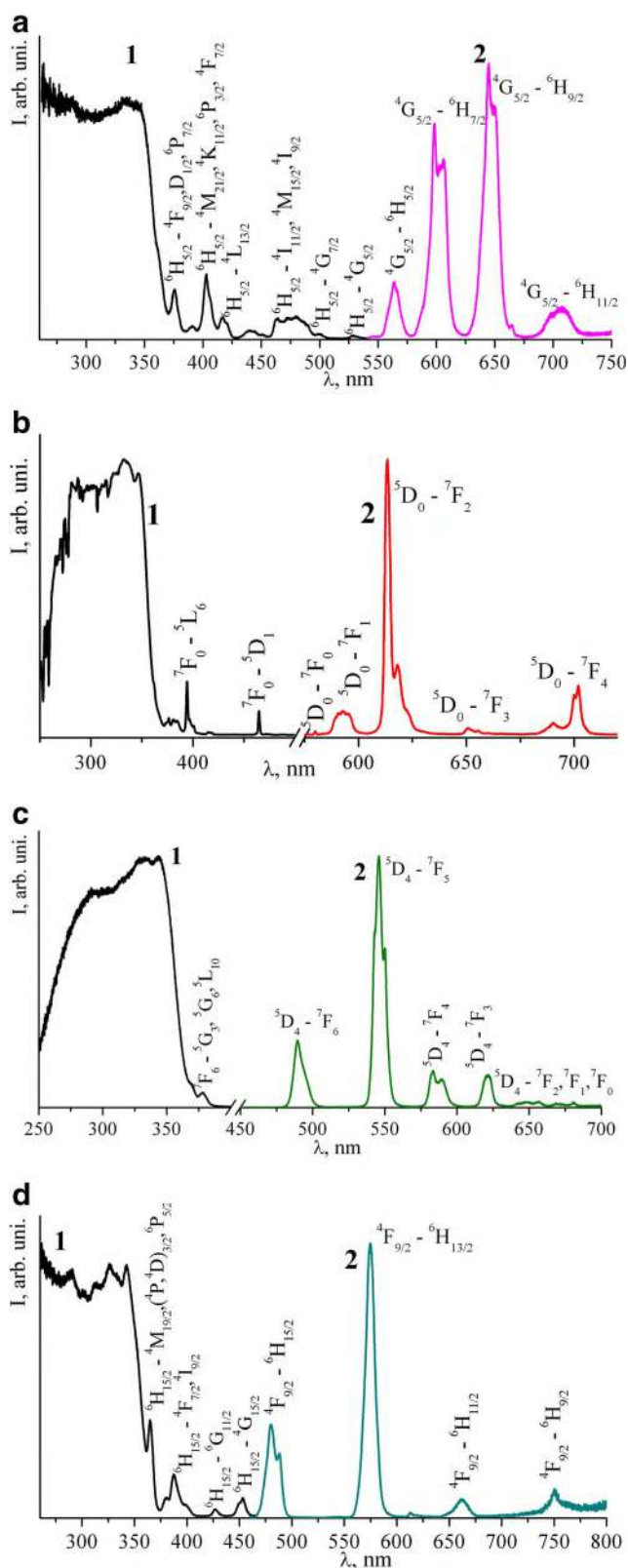


**Fig. 5** Luminescence excitation (1) and luminescence (2) spectra of the complexes  $\text{Sm}_2\text{L}_3\text{phen}_2$  (a),  $\text{Eu}_2\text{L}_3\text{phen}_2$  (b),  $\text{Tb}_2\text{L}_3\text{phen}_2$  (c),  $\text{Dy}_2\text{L}_3\text{phen}_2$  (d) solid samples at 293 K

$\text{Sm}^{\text{III}}$  compounds are the objects of extensive studies because of their application as luminescence orange emitters for laser active materials [50–52].  $\text{Sm}^{\text{III}}$  exhibits an orange emission, which is normally much weaker than  $\text{Eu}^{\text{III}}$  and  $\text{Tb}^{\text{III}}$  emission due to the small energy gap between excited and ground states, that makes multiphonon relaxation much easier. Upon excitation by UV light at 330 nm the complex  $\text{Sm}_2\text{L}_3\text{phen}_2$  shows orange 4f-emission (Fig. 5a). Similar to ternary  $\text{Sm}^{\text{III}}$   $\beta$ -diketone based complexes [53] the band of magnetic dipole forbidden and electronic-dipole allowed hypersensitive transition  $^4\text{G}_{5/2} \rightarrow ^6\text{H}_{9/2}$  ( $\lambda_{\text{max}} = 645$  nm) dominates in the emission spectrum of the complex  $\text{Sm}_2\text{L}_3\text{phen}_2$ . A band of transition  $^4\text{G}_{5/2} \rightarrow ^6\text{H}_{7/2}$  ( $\lambda_{\text{max}} = 598$  nm) is less intense and the bands of  $^4\text{G}_{5/2} \rightarrow ^6\text{H}_{5/2}$  ( $\lambda_{\text{max}} = 564$  nm) and  $^4\text{G}_{5/2} \rightarrow ^6\text{H}_{11/2}$  ( $\lambda_{\text{max}} = 708$  nm) transitions are of the lowest intensity.

Extensive research into  $\text{Eu}^{\text{III}}$  and  $\text{Tb}^{\text{III}}$  complexes possessing long luminescent lifetimes has focused on their use as labels and biological probes [54–60] or as emitting components in electroluminescent devices for light-emitting diodes [21–23]. The luminescence properties of  $\text{Eu}_2\text{L}_3\text{phen}_2$  and  $\text{Tb}_2\text{L}_3\text{phen}_2$  complexes were investigated at room temperature and at 77 K as well as in solution in DMSO (Figs. 5, 6 and 7 and S5). At both temperatures the solid europium complex exhibited  $^5\text{D}_0$  and  $^5\text{D}_1$  emission (Figs. 5b and S5). The  $^5\text{D}_0$  emission spectra of the  $\text{Eu}^{\text{III}}$  complex, solid state and solution, are dominated by the band of the  $^5\text{D}_0 \rightarrow ^7\text{F}_2$  transition (Figs. 5b, 6). High intensity of  $^5\text{D}_0 \rightarrow ^7\text{F}_2$  band compared to the  $^5\text{D}_0 \rightarrow ^7\text{F}_1$  points to low symmetry of the  $\text{Eu}^{\text{III}}$  coordination environment in the complex under study. The intensity ratio of the bands of  $^5\text{D}_0 \rightarrow ^7\text{F}_2$  and  $^5\text{D}_0 \rightarrow ^7\text{F}_1$  transitions (red/orange ratio) was found to be independent on temperature and equal 6.5 for the solid sample and 3.9 for the complex solution, which can be due to increasing of symmetry of  $\text{Eu}^{\text{III}}$

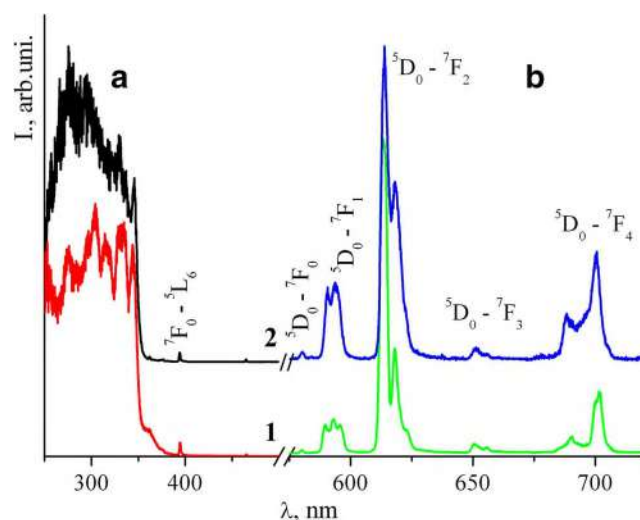


**Fig. 6** Luminescence excitation (a) and  $^5\text{D}_0$  luminescence (b) spectra of the complex  $\text{Eu}_2\text{L}_3\text{phen}_2$  in solid state (1) and for frozen solution in DMSO (2) at 77 K

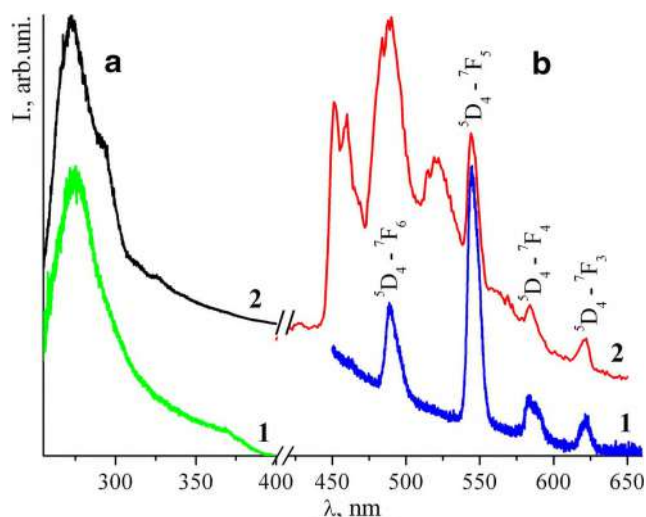


**Fig. 7** Luminescence excitation (a) and luminescence (b) spectra of the complex  $Tb_2L_3phen_2$  in solution in DMSO at 298 K (1) and at 77 K (2)

ion surroundings in the complex solution compared to the solid sample. The obtained red/orange ratio for the solid sample is comparable with that found for mononuclear CAPH based europium complexes with 1,10-phenanthroline [15, 16, 60]. One component band of  $^5D_0 \rightarrow ^7F_0$  transition is observed at 580.1 nm in the both spectra measured for solid sample and solution.

The typical luminescence decay profiles for europium and terbium complexes in a semilog scale are shown in Fig. S5. All decay curves for solid samples are well reproduced by single exponential function, which suggests that only one species exists in the excited states of the complexes. The luminescence decay time of the europium complex did not depend on the excitation wavelength but decreased slightly with the temperature lowering (Table S1). In the solution luminescence decay time for the complex  $Eu_2L_3phen_2$  was found to be equal 1.2 ms that is lower compared to solid sample and can be a result of quenching of  $Eu^{III}$  luminescence by the solvent molecules.

Some luminescence characteristics (radiative ( $A_r$ ) and non-radiative ( $A_{nr}$ ) decay rates, observed ( $\tau_{obs}$ ) and radiative

( $\tau_{RAD}$ ) luminescence lifetime and  $^5D_0$  intrinsic quantum yield ( $Q_{Ln}^{Ln}$ ) for solid state complex  $Eu_2L_3phen_2$  and some selected mixed-ligand europium complexes with  $\beta$ -diketones and CAPHs and 1,10-phenanthroline are given in Table 2. The  $^5D_0$  intrinsic quantum yield ( $Q_{Ln}^{Ln}$ ) for the europium complex was estimated from the emission spectrum and measured  $^5D_0$  luminescence lifetime:

$$Q_{Ln}^{Ln} = \tau_{obs} / \tau_{RAD}$$

whereby  $\tau_{RAD}$  is the radiative lifetime of  $^5D_0$  state estimated from emission data using the following equation:  $1/\tau_{RAD} = A_{MD,0} \cdot n^3 \cdot (I_{tot}/I_{MD})$  [61, 62], with  $A_{MD,0}$  being equal to  $14.65 \text{ s}^{-1}$ ,  $n$  considered to be 1.5 (a value commonly encountered for coordination compounds) and ( $I_{tot}/I_{MD}$ ) is the ratio of the total integrated emission from the  $Eu (^5D_0)$  level to the integrated intensity of MD transition  $^5D_0 \rightarrow ^7F_1$  [63, 64]. It should be noted that a small change in the refractive index leads to significant changes in the  $\tau_{RAD}$  value, therefore, the results of this calculation should be used taking into account the possible deviation from the exact value.

The total decay rates ( $A_r + A_{nr}$ ) for the europium complex under study are dominated by radiative contribution ( $A_r$ ) resulting in very high intrinsic quantum yield equal 91%, which is significantly higher compared to the most of the mentioned in the Table 2 related mixed-ligand europium complexes with 1,10-phenanthroline. The observed ( $\tau_{obs}$ ) and radiative ( $\tau_{RAD}$ ) luminescence lifetimes for the complex  $Eu_2L_3phen_2$  are comparable with those found for CAPH based mixed-ligand europium complexes of general formula  $Eu(CAPH)_3phen$  and higher compared to bis- $\beta$ -diketones based binuclear mixed-ligand europium complexes of general formula  $Eu_2(\text{bis-}\beta\text{-dik})_3phen_2$ .

Unlike the europium complex the luminescence decay time of  $Tb_2L_3phen_2$  increase with the temperature decreasing: at room temperature:  $\tau_{obs}$  for the terbium complex equals 1.45 ms and at 77 K it is 2.00 ms (Fig. S5). Considering rather small energy gap between the ligands lowest triplet state and  $^5D_4$  emissive level of

**Table 2** Selected luminescence characteristics for  $Eu_2L_3phen_2$  and some mixed-ligand europium complexes with bis- $\beta$ -diketones and CAPH type ligands and 1,10-phenanthroline at 298 K

Complex	$\lambda_{exc}$ , nm	$I(^5D_0 \rightarrow ^7F_2) / I(^5D_0 \rightarrow ^7F_1)$	$\tau_{obs}$ , ms (293 K)	$\tau_{RAD}$ , ms	$A_r$ , $s^{-1}$	$A_{nr}$ , $s^{-1}$	$Q_{Ln}^{Ln}$ , %	Ref.
$Eu_2L_3phen_2$	280	6.5	1.88	2.06	485	28	91	this work
$Eu(Pip)_3phen$	337	8.7	1.58	1.78	564	68	89	[15]
$EuL^1_3phen$	254	4.6	1.58	2.85	346	286	55	[16]
$EuL^2_3phen$	254	5.7	1.54	2.03	494	156	76	[60]
$Eu_2(BTP)_3phen_2$	324	7.3	0.91	1.17	857	246	78	[33]
$Eu_2(BTB)_3phen_2$	—	15.6	0.55	1.16	853	973	47	[26]

HPip = 2,2,2-trichloro-N-(dipiperidin-1-ylphosphoryl)acetamide,  $HL^1$  = dimethyl-N-benzoylamidophosphate,  $HL^2$  = N-(diphenylphosphoryl)benzamide, BTP = 1,3-bis(4,4,4-trifluoro-1,3-dioxobutyl)-phenyl, BTB = 3,3'-bis(4,4,4-trifluoro-1,3-dioxobutyl)biphenyl

Tb<sup>III</sup> ion in the complex under study ( $\Delta E = 1050 \text{ cm}^{-1}$ ), an activation of nonradiative processes in Tb<sub>2</sub>L<sub>3</sub>phen<sub>2</sub> upon temperature increasing can be due to energy back transfer from terbium to ligands. It is known that in Tb<sup>III</sup> complexes the ligand to metal energy transfer processes are efficient if the energy gap between the lowest ligand triplet state and <sup>5</sup>D<sub>4</sub> emissive level of Tb<sup>III</sup> ( $\Delta E$ ) exceeds  $1850 \text{ cm}^{-1}$  [65].

The emission spectrum of the terbium complex in solution at 298 K is very similar to that recorded for the solid sample, while at 77 K both Tb<sup>III</sup> centered luminescence and the ligands phosphorescence was observed in the emission spectrum (Fig. 7). According to the phosphorescence spectrum of the Y<sup>III</sup> complex in solution in DMSO (Fig. 3) the energy gaps between the ligands lowest triplet state and emissive levels of Tb<sup>III</sup> ion equals  $1430 \text{ cm}^{-1}$ , that is rather small and makes possible back from terbium to ligands energy transfer and enables rather effective ligand phosphorescence. The luminescence decay time of the terbium complex in solution was dependent on temperature (Fig. S5). At room temperature  $\tau_{\text{obs}} = 1.37 \text{ ms}$  was similar to that found for solid sample. At 77 K the decay curve departs from monoexponentiality probably due to the ligands phosphorescence.

The Dy<sup>III</sup> luminescence mainly takes place from <sup>4</sup>F<sub>9/2</sub> level. The <sup>4</sup>F<sub>9/2</sub> level is separated from the lower lying state <sup>6</sup>F<sub>1/2</sub> by about  $7500 \text{ cm}^{-1}$ , therefore multiphonon relaxation process is of low efficiency. In the visible range, the Dy<sup>III</sup> ion possesses two intense fluorescence bands located at 480 nm (blue region) and 570 nm (yellow region), corresponding to the <sup>4</sup>F<sub>9/2</sub> → <sup>6</sup>H<sub>15/2</sub> and <sup>4</sup>F<sub>9/2</sub> → <sup>6</sup>H<sub>13/2</sub> transitions, respectively. The yellow emission (<sup>4</sup>F<sub>9/2</sub> → <sup>6</sup>H<sub>13/2</sub>) of Dy<sup>III</sup> is called hypersensitive transition and its intensity strongly depends on Dy<sup>III</sup> ion coordination environment. Therefore, the luminescence of Dy<sup>III</sup> ion can be successfully used as structural probe of the chemical environment and recently Dy<sup>III</sup> complexes have been studied as emitting layers in OLEDs for white light generation. For complex Dy<sub>2</sub>L<sub>3</sub>phen<sub>2</sub> the <sup>4</sup>F<sub>9/2</sub> → <sup>6</sup>H<sub>13/2</sub> yellow emission ( $\lambda_{\text{max}} = 575 \text{ nm}$ ) is dominant in its luminescence spectrum, indicating that Dy<sup>III</sup> ion is located in low-symmetry local site environment (Fig. 5d). A band of transition <sup>4</sup>F<sub>9/2</sub> → <sup>6</sup>H<sub>15/2</sub> ( $\lambda_{\text{max}} = 480 \text{ nm}$ ) is of a less intense and the bands of <sup>4</sup>F<sub>9/2</sub> → <sup>6</sup>H<sub>11/2</sub> ( $\lambda_{\text{max}} = 662 \text{ nm}$ ) and <sup>4</sup>F<sub>9/2</sub> → <sup>6</sup>H<sub>9/2</sub> ( $\lambda_{\text{max}} = 750 \text{ nm}$ ) transitions are of the lowest intensity.

## Conclusions

A series of binuclear thermally stable luminescent rare earth complexes Ln<sub>2</sub>L<sub>3</sub>phen<sub>2</sub> (Ln<sup>III</sup> = Nd<sup>III</sup>, Sm<sup>III</sup>, Eu<sup>III</sup>, Tb<sup>III</sup>, Dy<sup>III</sup>, Yb<sup>III</sup> and Y<sup>III</sup>) with chelating bis-CAPh type ligand N,N'-(2,2,3,3,4,4-hexafluoro-1,5-dioxopentane-1,5-diyl)bis(phosphoramidate) and additional ligand 1,10-phenantroline was synthesized and the spectroscopic properties of complexes were studied.

Under excitation by UV light, the complexes exhibited bright characteristic emission of the lanthanide metal centers due to effective energy transfer from organic ligands to Ln<sup>III</sup> ions.

The europium and terbium complexes were found to be luminescent both in solid and solution in DMSO with emission decay time in range of 1.2–2.0 ms depending on temperature.

The energy level of the ligands lowest triplet state in the complexes was found to match better to resonance level of Eu<sup>III</sup> than to Tb<sup>III</sup> ion. In solid state at room temperature the Eu<sup>III</sup> complex possess very high intrinsic quantum yield 91% and decay time equals 1.88 ms.

Based on our results, a series of novel bis--carbacylamidophosphate based lanthanide complexes with optimized luminescence properties for potential applications in photonic devices can be proposed.

**Supplementary Information** The online version contains supplementary material available at <https://doi.org/10.1007/s10895-021-02733-0>.

**Contributions** All the authors (O. Y. Homichuk, N. S. Kariaka, S. S. Smola, N. V. Rusakova, V. O. Trush, T. Y. Sliva, V. M. Amirkhanov) made substantial contribution while preparing the manuscript.

**Funding** This work was supported by the Ministry of Education and Science of Ukraine (Project no. 19BF037–05).

The publication contains the results of studies conducted by President's of Ukraine grant for competitive projects (Project no. 19BF037–06).

**Data Availability** Not applicable.

## Declarations

**Consent to Participate** Not applicable.

**Consent for Publication** Not applicable.

**Conflict of Interest** The authors declare that they have no competing financial interests or personal relationships that could have appeared to influence the work reported in this paper.

## References

- Bunzli J-CG (1989) Luminescent Probes. In: Bunzli J-CG, Choppin GR (eds) Lanthanide probes in life, chemical and earth sciences: theory and practice. Elsevier, Amsterdam, pp 219–293
- Blasse G, Grabmaier BC (1994) Luminescent materials. Springer-Verlag, Berlin
- Glover PB, Ashton PR, Childs LJ, Rodger A, Kercher M, Williams RM, De Cola L, Pikramenou Z (2003) Hairpin-shaped Heterometallic luminescent lanthanide complexes for DNA intercalative recognition. *J Am Chem Soc* 125:9918–9919. <https://doi.org/10.1021/ja029886s>
- Bunzli J-CG, Comby S, Chauvin AS, Vandevyver CDB (2007) New opportunities for lanthanide luminescence. *J Rare Earth* 25: 257–274. [https://doi.org/10.1016/S1002-0721\(07\)60420-7](https://doi.org/10.1016/S1002-0721(07)60420-7)

5. Eliseeva SV, Bunzli J-CG (2010) Lanthanide luminescence for functional materials and bio-sciences. *Chem Soc Rev* 39:189–227. <https://doi.org/10.1039/B905604C>
6. Bunzli J-CG (2016) Lanthanide luminescence: from a mystery to rationalization, understanding, and applications. In: Bunzli J-C, Pecharsky V (eds) *Handbook on the physics and chemistry of rare earths*. Elsevier, Amsterdam, pp 141–177
7. Bunzli J-CG (2015) On the design of highly luminescent lanthanide complexes. *Coord Chem Rev* 293–294:19–47. <https://doi.org/10.1016/j.ccr.2014.10.013>
8. Beeby A, Clarkson IM, Dickins RS, Faulkner S, Parker D, Royle L, de Sousa AS, Gareth Williams JA, Woods M (1999) Non-radiative deactivation of the excited states of europium, terbium and ytterbium complexes by proximate energy-matched OH, NH and CH oscillators: an improved luminescence method for establishing solution hydration states. *J Chem Soc Perkin Trans 2*:493–504. <https://doi.org/10.1039/A808692C>
9. Maas H, Currao A, Calzaferri G (2002) Encapsulated lanthanides as luminescent materials. *Angew Chem Int Ed* 41:2495–2497. [https://doi.org/10.1002/1521-3773\(20020715\)41:14<2495::AID-ANIE2495>3.0.CO;2-G](https://doi.org/10.1002/1521-3773(20020715)41:14<2495::AID-ANIE2495>3.0.CO;2-G)
10. Xiang N-J, Leung LM, So S-K, Gon M-L (2006) Preparation and photoluminescence of a novel  $\beta$ -diketone ligand containing electrotransporting group and its europium(III) ternary complex. *Spectrochim Acta Part A* 65:907–911. <https://doi.org/10.1016/j.saa.2006.01.030>
11. Binnemans K (2005) Rare-earth beta-diketonates. In: Gschneider KA Jr, Bunzli J-C, Pecharsky VK (eds) *Handbook on the physics and chemistry of rare earths*. Elsevier, Amsterdam, pp 107–272
12. Oczko G, Legendziewicz J, Trush V, Amirkhanov V (2003) X-ray analysis and excited state dynamics in a new class of lanthanide mixed chelates of the type  $\text{LnPh}\beta_3\text{-Phen}$  (Ln = Sm, Eu, Gd, Tb). *New J Chem* 27:948–956. <https://doi.org/10.1039/B211044J>
13. Cybińska J, Legendziewicz J, Trush V, Reisfeld R, Saraidarov T (2008) Structural characteristic and luminescence properties of first known example of a pair of europium(III) complexes of phosphoroazo-derivative of  $\beta$ -diketone with inner and both inner and outer sphere 2,2'-bipyridine. *J Alloy Compd* 451:264–269. <https://doi.org/10.1016/j.jallcom.2007.04.183>
14. Gawryszewska P, Moroz OV, Trush VA, Kulesza D, Amirkhanov VM (2011) Structure and sensitized near-infrared luminescence of Yb(III) complexes with sulfonylamidophosphate type ligand. *J Photochem Photobiol A* 217:1–9. <https://doi.org/10.1016/j.jphotochem.2010.06.033>
15. Litsis OO, Ovchinnikov VA, Scherbatskii VP, Nedilko SG, Sliva TY, Dyakononko VV, Shishkin OV, Davydov VI, Gawryszewska P, Amirkhanov VM (2015) Lanthanide mixed-ligand complexes of the  $[\text{Ln}(\text{CAPH})_3(\text{Phen})]$  and  $[\text{La}_x\text{Eu}_{1-x}(\text{CAPH})_3(\text{Phen})]$  (CAPH = carbacylamidophosphate) type. A comparative study of their spectral properties. *Dalton Trans* 44:15508–15522. <https://doi.org/10.1039/c5dt02557e>
16. Kariaka NS, Trush VA, Gawryszewska P, Dyakononko VV, Shishkina SV, Sliva TY, Amirkhanov VM (2016) Spectroscopy and structure of  $[\text{LnL}_3\text{bipy}]$  and  $[\text{LnL}_3\text{phen}]$  complexes with CAPH type ligand dimethylbenzoylamidophosphate. *J Lumin* 178:392–399. <https://doi.org/10.1016/j.jlumin.2016.06.018>
17. Yan B, Zhang HJ, Wang SB, Ni JZ (1998) Photophysical properties of some binary and ternary complexes of rare earth ions with aminobenzoic acids and 1,10 phenanthroline. *Monatsh Chem* 129:151–158. <https://doi.org/10.1007/PL00010151>
18. Yan B, Zhang HJ, Wang SB, Ni JZ (1998) Spectroscopic study of luminescence and energy transfer of binary and ternary complexes of rare earth with aromatic carboxylic acids and 1,10-phenanthroline. *Spectrosc Lett* 31:603–613. <https://doi.org/10.1080/00387019808002753>
19. Zheng J-R, Ren N, Zhang J-J, Zhang D-H, Yan L-Z, Wu K-Z (2012) Synthesis, characterization and thermochemical properties of four new lanthanide complexes with 3,5-diisopropylsalicylic acid and 1,10-phenanthroline. *Thermochim Acta* 547:31–37. <https://doi.org/10.1016/j.tca.2012.08.005>
20. Wankar S, Limaye SN (2015) Luminescence and electronic spectral studies of some synthesized lanthanide complexes using benzoic acid derivative and o-Phenanthroline. *J Fluoresc* 25:787–794. <https://doi.org/10.1007/s10895-015-1573-6>
21. Binnemans K (2009) Lanthanide-based luminescent hybrid materials. *Chem Rev* 109:4283–4374. <https://doi.org/10.1021/cr8003983>
22. Kido J, Okamoto Y (2002) Organo lanthanide metal complexes for electroluminescent materials. *Chem Rev* 102:2357–2368. <https://doi.org/10.1021/cr010448y>
23. Xu H, Sun Q, An Z, Wei Y, Liu X (2015) Electroluminescence from europium(III) complexes. *Coord Chem Rev* 293–294:228–249. <https://doi.org/10.1016/j.ccr.2015.02.018>
24. Yan S, Zhang H-J, Ni J-Z (2008) Synthesis, luminescence properties and energy transfer of binary and ternary rare earth complexes with aromatic acids and 1,10-phenanthroline. *Chin J Chem* 15:242–249. <https://doi.org/10.1002/cjoc.19970150308>
25. Zhang H-J, Yan B, Wang S-B, Ni (1997) The photophysical properties of binary and ternary complexes of rare earths with conjugated carboxylic acids and 1,10-phenanthroline. *J Photochem and Photobiol A* 109:223–228. [https://doi.org/10.1016/S1010-6030\(97\)00144-5](https://doi.org/10.1016/S1010-6030(97)00144-5)
26. Li H-F, Yan P-F, Chen P, Yan W, Xu H, Li G-M (2012) Highly luminescent bis-diketone lanthanide complexes with triple-stranded dinuclear structure. *Dalton Trans* 41:900–907. <https://doi.org/10.1039/C1DT11496D>
27. Bassett AP, Magennis SW, Glover PB, Lewis DJ, Spencer N, Parsons S, Williams RM, De Cola L, Pikramenou Z (2004) Highly luminescent, triple- and quadruple-stranded, dinuclear Eu, Nd, and Sm(III) lanthanide complexes based on bis-diketonate ligands. *J Am Chem Soc* 126:9413–9424. <https://doi.org/10.1021/ja048022z>
28. Li H-F, Li G-M, Chen P, Sun W-B, Yan P-F (2012) Highly luminescent lanthanide complexes with novel bis- $\beta$ -diketone ligand: synthesis, characterization and photoluminescent properties. *Spectrochim Acta Part A: Molecular and Biomolecular Spectroscopy* 97:197–210. <https://doi.org/10.1016/j.saa.2012.05.078>
29. Liu S, He P, Wang H, Shi J, Gong M (2009) A luminescent quadruple stranded dinuclear Eu(III) complex based on 2,8-bis(4',4'-trifluoro-1',3'-dioxobutyl)-dibenzothiophene for light-emitting diodes. *Inorg Chem Commun* 12:506–508. <https://doi.org/10.1016/j.inoche.2009.04.004>
30. Luo Y-M, Chen Z, Tang R-R, Xiao L-X, Peng H-J (2008) Investigations into the synthesis and fluorescence properties of Eu(III), Tb(III), Sm(III) and Gd(III) complexes of a novel bis- $\beta$ -diketone-type ligand. *Spectrochim Acta Part A: Molecular and Biomolecular Spectroscopy* 69:513–516. <https://doi.org/10.1016/j.saa.2007.04.029>
31. Albrecht M, Schmid S, Dehn S, Wickleder C, Zhang S, Bassett AP, Pikramenou Z, Fröhlich R (2007) Diastereoselective formation of luminescent dinuclear lanthanide(III) helicates with enantiomerically pure tartaric acid derived bis( $\beta$ -diketonate) ligands. *New J Chem* 31:1755–1762. <https://doi.org/10.1039/B705090A>
32. He P, Wang HH, Yan HG, Hu W, Shi JX, Gong ML (2010) A strong red-emitting carbazole based europium(III) complex excited by blue light. *Dalton Trans* 39:8919–8924. <https://doi.org/10.1039/c0dt00424c>
33. Gu H, Hou Y, Xu F and Wang S. (2015) Electrospinning preparation, thermal, and luminescence properties of  $\text{Eu}_2(\text{BTP})_3(\text{Phen})_2$

- complex doped in PMMA: colloid Polym Sci 293: 2201–2208. <https://doi.org/10.1007/s00396-015-3614-8>
34. Chu W, Shi X, Gu H, Wang B, Sun Z (2013) Crystal Structure and Highly Luminescent Properties Studies of Bis- $\beta$ -diketonate Lanthanide Complexes. *Inorg Chem* 52:5013–5022. <https://doi.org/10.1021/ic302726z>
  35. Amirkhanov V, Ovchinnikov V, Trush V, Gawryszewska P, Jerzykiewicz LB (2014) Powerful new ligand systems: Carbacylamidophosphates (CAPH) and Sulfonylamidophosphates (SAPh). In: Gawryszewska P, Smolenski P (eds) Ligands synthesis, characterisation and role in biotechnology. Nova Science Publishers, New York, pp 199–248
  36. Homichuk OY, Kariaka NS, Trush VO, Smola SS, Sliva TY, Rusakova NV, Amirkhanov VM (2019) Synthesis and investigation of binuclear rare earth complexes based on bis-chelating carbacylamidophosphate (Ukr.). *Voprosy khimii i khimicheskoi tekhnologii* no. 5: 27–33. <https://doi.org/10.32434/0321-4095-2019-126-5-27-33>
  37. Trush VA, Gubina KE, Gumeniuk YO, Sliva TY and Konovalova IS (2012) Tetramethyl N,N'-(2,2,3,3,4,4-hexafluoro-1,5-dioxopentane-1,5-diy)bis-(phosphoramidate). *Acta Cryst E68*: 1127. <https://doi.org/10.1107/S1600536812011191>, TetramethylN,N'-(2,2,3,3,4,4-hexafluoro-1,5-dioxopentane-1,5-diy)bis(phosphoramidate)
  38. Jergensen CK, Judd BR (1964) Hypersensitive pseudoquadrupole transitions in lanthanides. *Molec Phys* 8:281–290. <https://doi.org/10.1080/00268976400100321>
  39. Choppin GR, Henrie DE, Buijs K (1966) Environmental effects on  $f$ - $f$  transitions. I. Neodymium(III). *Inorg Chem* 5:1743–1748. <https://doi.org/10.1021/ic50044a023>
  40. Henrie DE, Choppin GR (1968) Environmental effects on  $f$ - $f$  transitions. II. “Hypersensitivity” in some complexes of trivalent neodymium. *J Chem Phys* 49:477–481. <https://doi.org/10.1063/1.1670099>
  41. Gawryszewska P, Sokolnicki J, Legendziewicz J (2005) Photophysics and structure of selected lanthanide compounds. *Coord Chem Rev* 249:2489–2509. <https://doi.org/10.1016/j.ccr.2005.06.021>
  42. Kariaka NS, Trush VA, Medvediev VV, Dyakonenko VV, Shishkin OV, Smola SS, Fadeyev EM, Rusakova NV, Amirkhanov VM (2016) Coordination compounds based on CAPH type ligand: synthesis, structural characteristics and luminescence properties of *tetrakis*-complexes CsLnL<sub>4</sub> with dimethylbenzoylamidophosphate. *J Coord Chem* 69:123–134. <https://doi.org/10.1080/00958972.2015.1115024>
  43. Olyshevets IP, Dyakonenko VV, Shyshkina SV, Trush VO, Sliva TY, Amirkhanov VM (2018) Synthesis, structural and spectral studies of anionic tetrakis-complexes of lanthanides CsLnL<sub>4</sub> with SAPh-ligand – dimethyl(phenylsulfonyl)amidophosphate (Ukr.). *Voprosy khimii i khimicheskoi tekhnologii*, no. 6: 56–62. <https://doi.org/10.32434/0321-4095-2018-121-6-56-62>
  44. Gutierrez F, Tedeschi C, Maron L, Daudey J-P, Poteau R, Azema J, Tisnès P, Picard C (2004) Quantum chemistry-based interpretations on the lowest triplet state of luminescent lanthanides complexes. Part 1. Relation between the triplet state energy of hydroxamate complexes and their luminescence properties. *J Chem Soc Dalton Trans* 9:1334–1347. <https://doi.org/10.1039/b316246j>
  45. Shevchuk SV, Rusakova NV, Turianskaya AM, Korovin YV, Nazarenko NA, Gren AI (1998) Infrared luminescence of ytterbium ion in complexes with calix[4]resorcinarenes. *J Fluoresc* 8:225–228. <https://doi.org/10.1023/A:1022505716725>
  46. Quici S, Cavazzini M, Marzanni G, Accorsi G, Armaroli N, Ventura B, Barigelletti F (2005) Visible and near-infrared intense luminescence from water-soluble lanthanide [Tb(III), Eu(III), Sm(III), Dy(III), Pr(III), ho(III), Yb(III), Nd(III), Er(III)] complexes. *Inorg Chem* 44:529–537. <https://doi.org/10.1021/ic0486466>
  47. Zhang J, Petoud S (2008) Ligand for the efficient sensitization of four near-infrared luminescent lanthanide Cations: Nd<sup>3+</sup>, Er<sup>3+</sup>, Tm<sup>3+</sup>, and Yb<sup>3+</sup>. *Chem Eur J* 14:1264–1272. <https://doi.org/10.1002/chem.200701068>
  48. Comby S, Bunzli J-CG (2007) Lanthanide near-infrared luminescence in molecular probes and devices. In: Gscheidner KA Jr, Bunzli J-CG, Pecharsky VK (eds) Handbook on the physics and chemistry of rare earth, vol 37. Elsevier Science, Amsterdam, pp 217–470
  49. Gawryszewska P, Moroz OV, Trush VA, Amirkhanov VM, Lis T, Sobczyk M, Siczek M (2012) Spectroscopy and structure of Ln<sup>III</sup> complexes with Sulfonylamidophosphate-type ligands as sensitizers of visible and near-infrared luminescence. *ChemPlusChem* 77:482–496. <https://doi.org/10.1002/cplu.201200026>
  50. Solarz P, Sobczyk M (2012) Spectroscopic properties of Sm<sup>3+</sup> in KZnLa(PO<sub>4</sub>)<sub>2</sub> in IR–VUV region. *Opt Mater* 34:1826–1832. <https://doi.org/10.1016/j.optmat.2012.05.011>
  51. Sobczyk M, Szymański D (2013) A study of optical properties of Sm<sup>3+</sup> ions in  $\alpha$ -Na<sub>3</sub>Y(VO<sub>4</sub>)<sub>2</sub> single crystals. *J Lumin* 142:96–102. <https://doi.org/10.1016/j.jlumin.2013.03.062>
  52. Sobczyk M, Korzeniowski K, Guzik M, Cybińska J, Gerasymchuk Y, Trush VA, Legendziewicz J (2018) Spectroscopic behaviour of Na[Sm(SP)<sub>4</sub>] (where SP = C<sub>6</sub>H<sub>5</sub>S(O)<sub>2</sub>NP(O)(OCH<sub>3</sub>)<sub>2</sub><sup>-</sup>) and its polymeric material-new orange emitting phosphors. *J Lumin* 193: 90–97. <https://doi.org/10.1016/j.jlumin.2017.08.064>
  53. Brito HF, Malta OL, Felinto MCFC, Teotonio EES, Menezes JFS, Silva CFB, Tomiyama CS, Carvalho CAA (2002) Luminescence investigation of the Sm(III)- $\beta$ -diketonates with sulfoxides, phosphine oxides and amides ligands. *J Alloys and Comps* 344:293–297. [https://doi.org/10.1016/S0925-8388\(02\)00372-9](https://doi.org/10.1016/S0925-8388(02)00372-9)
  54. Mathis G (1993) Rare earth cryptates and homogeneous fluoroimmunoassays with human sera. *Clin Chem* 39:1953–1959
  55. Hemmila I, Mikkala V-M, Takalo H (1997) Development of luminescent lanthanide chelate labels for diagnostic assays. *J Alloys Comps* 249:158–162. [https://doi.org/10.1016/S0925-8388\(96\)02834-4](https://doi.org/10.1016/S0925-8388(96)02834-4)
  56. Bazin H, Trinquet E, Mathis G (2002) Time resolved amplification of cryptate emission: a versatile technology to trace biomolecular interactions. *Rev Mol Biotechnol* 82:233–250. [https://doi.org/10.1016/S1389-0352\(01\)00040-X](https://doi.org/10.1016/S1389-0352(01)00040-X)
  57. Hemmil I, Laitala V (2005) Progress in lanthanides as luminescent probes. *J Fluoresc* 15:529–542. <https://doi.org/10.1007/s10895-005-2826-6>
  58. Ghose S, Trinquet E (2008) Laget, H. Bazin, G. Mathis, rare earth cryptates for the investigation of molecular interactions *in vitro* and in living cells. *J Alloys Comps* 451:35–37. <https://doi.org/10.1016/j.jallcom.2007.04.054>
  59. Montgomery CP, Murray BS, New EJ, Paj R, Parker D (2009) Cell-penetrating metal complex optical probes: targeted and responsive systems based on lanthanide luminescence. *Acc Chem Res* 42:925–937. <https://doi.org/10.1021/ar800174z>
  60. Kariaka NS, Trush VA, Smola SS, Fadeyev EM, Odynets IV, Sliva TY, Amirkhanov VM (2016) *Tris*-(diphenylphosphryl)benzamide lanthanides (III) trinitrates as a basis for creating the luminophore materials. *Dopov Nac Acad Nauk (Ukr)* 5:85–94. <https://doi.org/10.15407/DOPOVIDI2016.05.085>
  61. van der Tol EB, van Ramesdonk HJ, Verhoeven JW, Steemers FJ, Kerver EG, Verboom W, Reinhoudt DN (1998) Tetraazatriphenylenes as extremely efficient antenna Chromophores for luminescent lanthanide ions. *Chem Eur J* 4: 2315–2323. [https://doi.org/10.1002/\(SICI\)1521-3765\(19981102\)4:11<2315::AID-CHEM2315>3.0.CO;2-E](https://doi.org/10.1002/(SICI)1521-3765(19981102)4:11<2315::AID-CHEM2315>3.0.CO;2-E)
  62. Werts MHV, Jukes RTF, Verhoeven JW (2002) The emission spectrum and the radiative lifetime of Eu<sup>3+</sup> in luminescent lanthanide

- complexes. *Phys Chem Chem Phys* 4:1542–1548. <https://doi.org/10.1039/B107770H>
63. Bunzli J-CG, Eliseeva SV (2011) Basics of lanthanide photophysics. In: Hänninen P, Härmä H (eds) *Lanthanide luminescence: Photophysical, Analytical and Biological Aspects*, Springer Series on Fluorescence, pp 1–46
64. de Sa GF, Malta OL, de Mello DC, Simas AM, Longo RL, Santa-Cruz PA, da Silva EF (2000) Spectroscopic properties and design of highly luminescent lanthanide coordination complexes. *Coord Chem Rev* 196:165–195. [https://doi.org/10.1016/S0010-8545\(99\)00054-5](https://doi.org/10.1016/S0010-8545(99)00054-5)
65. Latva M, Takalo H, Mikkala VM, Matachescu C, Rodríguez-Ubis JC, Kankare J (1997) Correlation between the lowest triplet state energy level of the ligand and lanthanide(III) luminescence quantum yield. *J Lumin* 75:149–169. [https://doi.org/10.1016/S0022-2313\(97\)00113-0](https://doi.org/10.1016/S0022-2313(97)00113-0)

**Publisher's Note** Springer Nature remains neutral with regard to jurisdictional claims in published maps and institutional affiliations.



Cite this: *New J. Chem.*, 2021, 45, 22361

## Novel quadruple-stranded heterometallic Ln<sub>2</sub>Na complexes hosting sodium ions inside the cryptand-like cavity†

Oleksandr Ye. Horniichuk,<sup>a</sup> Victor A. Trush,<sup>a</sup> Nataliia S. Kariaka,<sup>a</sup> Svitlana V. Shishkina,<sup>b</sup> Viktoriya V. Dyakonenko,<sup>b</sup> Olga V. Severinovskaya,<sup>c</sup> Paula Gawryszewska,<sup>d</sup> Kostiantyn V. Domasevitch,<sup>a</sup> Adam Watras<sup>e</sup> and Vladimir M. Amirkhanov<sup>a</sup>

Coordination compounds of lanthanides  $\text{NEt}_4[\text{NaLn}_2\text{L}_4(\text{H}_2\text{O})]$ ,  $\text{Na}[\text{NaLn}_2\text{L}_4(\text{H}_2\text{O})]\cdot 2\text{H}_2\text{O}$  ( $\text{Ln} = \text{La}^{3+}$ ,  $\text{Nd}^{3+}$ ) with the bis-chelating carbacylamidophosphate ligand tetramethyl *N,N'*-(2,2,3,3,4,4-hexafluoro-1,5-dioxopentane-1,5-diyl)bis(phosphoramidate) ( $\text{H}_2\text{L}$ ) were obtained for the first time *via* reactions of  $\text{Na}_2\text{L}$  with lanthanide nitrates. The complexes were characterized by IR and NMR spectroscopy and laser desorption/ionization mass spectrometry. From X-ray diffraction analysis, it was established that the complex anions in the obtained compounds have a structure of a quadruple-stranded helicate, which encapsulates a sodium cation and a molecule of water into the negatively charged environment of the ligand fluorine and carbonyl oxygen atoms. Upon excitation by the 266 nm harmonic line of the Nd:YAG pulsed laser, the  $\text{NEt}_4[\text{NaNd}_2\text{L}_4(\text{H}_2\text{O})]$  complex exhibits IR-emission at 300 and 77 K with the  ${}^4\text{F}_{3/2}$  emission lifetime of 2  $\mu\text{s}$ .

Received 10th September 2021,  
Accepted 2nd November 2021

DOI: 10.1039/d1nj04353f

rsc.li/njc

## Introduction

Helicates are polymeric supramolecular assemblies wherein the coordinated polydentate ligands are wrapped about metal ions lying on a helical axis.<sup>1</sup> This family of supramolecular compounds has a range of applications from building blocks for more complex supramolecular architectures and molecular recognition to liquid crystalline materials.<sup>2–10</sup> Lanthanide helicates are interesting objects for luminescence applications<sup>11–13</sup> since

they experience an advantage from the helical architecture, which encapsulates the lanthanide ions, protecting them from external interactions with luminescence quenchers and allowing the combination of two or more emission centers in one molecule.<sup>1</sup> The number of coordinated ligands determines whether double-, triple- or quadruple-stranded helicates are obtained. The aforementioned types of helical edifices have been reported to form with metal ions of p-, d-, and f-block elements.<sup>14–18</sup> Among the types of helicates, quadruple-stranded ones are less prevalent in the literature since they are more challenging to obtain. According to the predictions of Claude Piguet *et al.*,<sup>1</sup> the first quadruple-stranded helicates with a saturated coordination sphere of metal ions were synthesized by combining oligomonodentate ligands and square-planar central ions.<sup>18,19</sup> The other predicted strategy implies the use of oligobidentate ligands with eight-coordinate antiprismatic metal centers and leads to binuclear quadruple-stranded species based on lanthanide ions.<sup>17,20,21</sup> However, the crystallization of such compounds remains a challenge. There are only a few structurally characterized binuclear quadruple-stranded lanthanide helicates.<sup>22–24</sup> Raymond and coworkers described in detail the geometrical features of binuclear quadruple-stranded architectures, using the example of the structure of Th(IV) complexes with bis-acylpyrazolinone ligands that they achieved.<sup>25</sup> In recent works, Yan *et al.* reported a series of homochiral quadruple-stranded Ln(III) assemblies, where their helicity can be preorganized by chiral ligands of a certain absolute con-

<sup>a</sup> Faculty of Chemistry, Taras Shevchenko National University of Kyiv, 12, Lva Tolstogo str., 01033, Kyiv, Ukraine.

E-mail: oleksandr.horniichuk@univ.kiev.ua

<sup>b</sup> STC "Institute for Single Crystals", National Academy of Science of Ukraine, 60, Nauky Ave., 61001, Kharkiv, Ukraine

<sup>c</sup> Chuiko Institute of Surface Chemistry of National Academy of Sciences of Ukraine, 17 General Naumov Str., Kyiv, 03164, Ukraine

<sup>d</sup> Faculty of Chemistry, University of Wrocław, 14, F. Joliot-Curie, 50-383 Wrocław, Poland

<sup>e</sup> INTiBS PAN, Okolna 2, 50-422 Wrocław, Poland

† Electronic supplementary information (ESI) available: Synthetic procedure for  $\text{H}_2\text{L}$ , Fig. S1: fragment of crystal structure of **4**; Fig. S2: IR spectrum of **2** in 60–600  $\text{cm}^{-1}$  range, Fig. S3: IR spectra of **3** and **4**; Fig. S4–S8:  ${}^1\text{H}$  NMR spectra of  $\text{Na}_2\text{L}$ , and the complexes **1–4**; Table S1: structure refinement data for **2–4**; Table S2: Ln<sup>3+</sup> coordination geometry analysis in **2–4** using SHAPE 2.1 software; Table S3: IR data for the free ligand, its sodium salt and the complexes. CCDC 2062595, 2082894 and 2082895. For ESI and crystallographic data in CIF or other electronic format see DOI: 10.1039/d1nj04353f

figuration.<sup>26,27</sup> The team of researchers also succeeded in obtaining a molecular switch as quadruple-stranded Eu(III) helicate with a diarylethene-derived bis-chelating ligand.<sup>24</sup>

Helicates may serve as host molecules since they often contain internal cavities of the metallamacrocyclic fashion, which can adopt small ions or molecules.<sup>28,29</sup> There is a known series of helicates with p- and d-block metal ions which encapsulates alkali metal ions in a cryptate-like manner.<sup>5,14,28,30–33</sup> Triple-helical binuclear lanthanide metallacryptates with potassium or even magnesium cations in the cavity have been reported as well.<sup>34,35</sup> Nevertheless, there is no information on quadruple-helical binuclear lanthanide metallacryptates with s-block metal ion guests.

A promising class of ligands to design binuclear helicates is represented by bis- $\beta$ -diketones:bis-bidentate “brothers” of  $\beta$ -diketones and good candidates for the development of lanthanide-based luminescent materials, since their homobinuclear complexes are much more efficient compared to monometallic  $\beta$ -diketonate analogues.<sup>17,21,36–41</sup> It is noteworthy that in most of the reported helicates based on bis- $\beta$ -diketone ligands, the latter are featured by perfluorinated moieties promoting crystallization of the complex owing to weak C–H...F interactions.<sup>23,36</sup>

Taking into account the structural advantages of bis- $\beta$ -diketones, we developed a new bis-chelating ligand of the bis-carbacylamidophosphate type. Carbacylamidophosphates (CAPH) represent a family of versatile ligands, which are P,N-substituted structural analogues of  $\beta$ -diketones.<sup>42</sup>

Herein, we report the synthesis, structure and properties of lanthanide binuclear quadruple-helical sodium-hosting anionic metallacryptates with the bis-chelating carbacylamidophosphate ligand tetramethyl *N,N'*-(2,2,3,3,4,4-hexafluoro-1,5-dioxopentane-1,5-diyl)bis(phosphoramidate) (Scheme 1).

## Experimental

### Methods

IR spectra were recorded on a PerkinElmer Spectrum BX spectrometer on samples in the form of a KBr pellet. FTIR spectrum of **2** in nujol suspensions was collected using a Bruker IFS66/S FITIR spectrometer in the 60–600  $\text{cm}^{-1}$  region.  $^1\text{H}$  NMR investigations were performed using a WR-400 Bruker NMR spectrometer at room temperature in DMSO- $d_6$ . Emission spectra at 77 and 300 K were recorded using a Hamamatsu PMA-12 photonic multichannel analyzer equipped with BT-CCD line with corrected response in the whole range (350–1100 nm). As an excitation source, the fourth harmonic ( $\lambda_{\text{exc}} = 266 \text{ nm}$ ) of a Nd:YAG laser was used ( $f = 10 \text{ Hz}$ ,  $t_{\text{pulse}} < 20 \text{ ns}$ ,

$E_{\text{pulse}} = 10 \text{ mJ}$ ). For measurement at 77 K a Linkam THMS600 cooling/heating stage was used. Decay curves were recorded using a McPherson spectrometer equipped with Hamamatsu R928 and R5108 photomultiplier tubes and a Tektronix MDO-4052 digital oscilloscope. The excitation source was the same as for emission spectra. MS analysis was performed by the method of laser desorption/ionization on an Autoflex II (Bruker Daltonics, Germany) mass spectrometer with a nitrogen laser ( $\lambda = 337 \text{ nm}$ ). Experiments were carried out in linear mode for negative ions in the mass range 100 to 2000 a.m.u. The resulting mass spectra were obtained by assuming the data of 200 laser shots and processing by the software FlexAnalysis (Bruker Daltonics, Germany). Elemental analyses (C, H, and N) were performed on an EL III Universal CHNOS Elemental Analyzer.

### Materials and synthesis

Lanthanide nitrates  $\text{Ln}(\text{NO}_3)_3 \cdot 6\text{H}_2\text{O}$  (Ln = La, Nd) of commercial grade were used without further purification.

The synthesis and structure of the ligand – tetramethyl *N,N'*-(2,2,3,3,4,4-hexafluoro-1,5-dioxopentane-1,5-diyl)bis(phosphoramidate) were reported by our group earlier.<sup>43</sup> The ligand synthesis in the current work was carried out with a slightly modified procedure (Scheme 1).

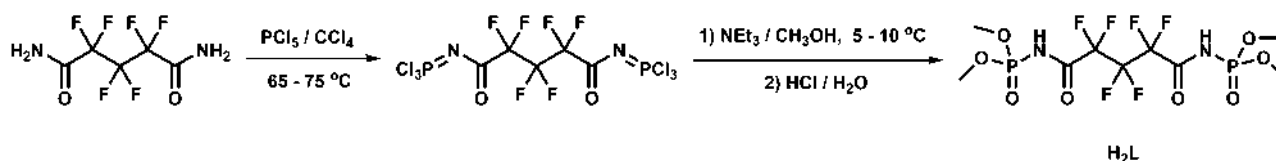
### Synthesis of $\text{Na}_2\text{L}$

In order to obtain the desired complexes, we used the sodium salt of the ligand, which was synthesized according to the previously described methods.<sup>42,44</sup>

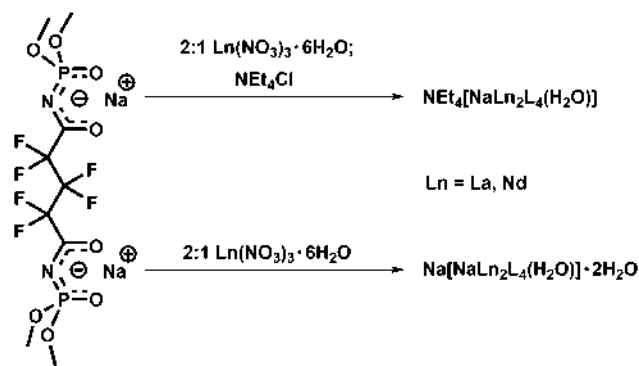
**$\text{Na}_2\text{L}$ .** Yield: 93%; IR (KBr,  $\text{cm}^{-1}$ ): 1630s ( $\nu(\text{C}=\text{O})$ ), 1406m (amide-2), 1202s ( $\nu(\text{P}=\text{O})$ );  $^1\text{H}$  NMR (400 MHz, DMSO- $d_6$ , 25 °C):  $\delta = 3.44 \text{ ppm}$  (d,  $J = 11.0 \text{ Hz}$ , 12H);  $\text{C}_9\text{H}_{12}\text{N}_2\text{O}_8\text{P}_2\text{F}_6\text{Na}_2$  ( $M = 498.12$ ). Anal. calc.: C, 21.70; H, 2.43; N, 5.62%. Found: C, 21.72; H, 2.46; N, 5.58%.

The synthesis of the helicates 1–4 was performed according to Scheme 2.

**Synthesis of  $\text{NET}_4[\text{NaLn}_2\text{L}_4(\text{H}_2\text{O})]$  [Ln = La (**1**), Nd (**2**)].**  $\text{Ln}(\text{NO}_3)_3 \cdot 6\text{H}_2\text{O}$  (0.1 mmol) was dissolved in 2-propanol (2.5 ml), afterwards a dehydrating agent – triethyl orthoformate (0.15 ml, 0.9 mmol) was added to the solution and the latter was heated to boiling for 1 minute. The obtained solution was cooled to room temperature, then mixed with the combined solutions of  $\text{Na}_2\text{L}$  (0.100 g, 0.2 mmol) and  $\text{NET}_4\text{Cl}$  (0.008 g, 0.05 mmol) in acetone (10 ml). The obtained mixture was heated and boiled for a minute, then cooled to room temperature. After the filtration of  $\text{NaNO}_3$  and  $\text{NaCl}$  precipitate, the clear solution was allowed to stand for a few days to yield colorless (**1**) and lilac-colored (**2**) prismatic crystals of the desired products. The complexes are moderately



Scheme 1 Synthesis of tetramethyl *N,N'*-(2,2,3,3,4,4-hexafluoro-1,5-dioxopentane-1,5-diyl)bis(phosphoramidate) ( $\text{H}_2\text{L}$ ).



Scheme 2 Synthesis routes of 1–4.

soluble in polar solvents, mainly in methanol, acetonitrile and acetone.

It is notable that double excess of  $\text{NET}_4\text{Cl}$  does not influence the final composition of the complex.

$\text{NET}_4[\text{NaLa}_2\text{L}_4(\text{H}_2\text{O})]$  (1). Yield: 60%; IR (KBr,  $\text{cm}^{-1}$ ): 1621s ( $\nu(\text{C}=\text{O})$ ), 1411m (amide-2), 1159s ( $\nu(\text{P}=\text{O})$ );  $^1\text{H}$  NMR (400 MHz,  $\text{DMSO-d}_6$ , 25 °C):  $\delta$  = 3.59 ppm (d,  $J$  = 11.2 Hz, 48H,  $\text{L}^{2-}$ ), 3.25 ppm (q,  $J$  = 7.0 Hz, 8H,  $\text{NET}_4^+$ ), 1.21 ppm (t,  $J$  = 7.0 Hz, 12H,  $\text{NET}_4^+$ );  $\text{C}_{44}\text{H}_{70}\text{N}_9\text{O}_{33}\text{P}_8\text{F}_{24}\text{NaLa}_2$  ( $M$  = 2257.63). Anal. calc.: C, 23.41; H, 3.13; N, 5.58%. Found: C, 23.03; H, 3.08; N, 5.59%.

$\text{NET}_4[\text{NaNd}_2\text{L}_4(\text{H}_2\text{O})]$  (2). Yield: 62%; IR (KBr,  $\text{cm}^{-1}$ ): 1623s ( $\nu(\text{C}=\text{O})$ ), 1410m (amide-2), 1160s ( $\nu(\text{P}=\text{O})$ );  $^1\text{H}$  NMR (400 MHz,  $\text{DMSO-d}_6$ , 25 °C):  $\delta$  = 4.17 ppm (br, 48H,  $\text{L}^{2-}$ ), 3.21 ppm (q,  $J$  = 7.1 Hz, 8H,  $\text{NET}_4^+$ ), 1.19 ppm (t,  $J$  = 7.1 Hz, 12H,  $\text{NET}_4^+$ );  $\text{C}_{44}\text{H}_{70}\text{N}_9\text{O}_{33}\text{P}_8\text{F}_{24}\text{NaNd}_2$  ( $M$  = 2268.30). Anal. calc.: C, 23.30; H, 3.11; N, 5.56%. Found: C, 22.55; H, 3.07; N, 5.51%.

**Synthesis of  $\text{Na}[\text{NaLn}_2\text{L}_4(\text{H}_2\text{O})] \cdot 2\text{H}_2\text{O}$  [Ln = La (3), Nd (4)].** The procedure is mainly the same as for  $\text{NET}_4[\text{NaLn}_2\text{L}_4]$ , excluding the use of  $\text{NET}_4\text{Cl}$ . The resulting crystalline products have color and solubility similar to 1 and 2.

$\text{Na}[\text{NaLa}_2\text{L}_4(\text{H}_2\text{O})] \cdot 2\text{H}_2\text{O}$  (3). Yield: 61%; IR (KBr,  $\text{cm}^{-1}$ ): 1622s ( $\nu(\text{C}=\text{O})$ ), 1412m (amide-2), 1160s ( $\nu(\text{P}=\text{O})$ );  $^1\text{H}$  NMR (400 MHz,  $\text{DMSO-d}_6$ , 25 °C):  $\delta$  = 3.53 ppm (d,  $J$  = 11.2 Hz, 48H,  $\text{L}^{2-}$ ).  $\text{C}_{36}\text{H}_{54}\text{N}_8\text{O}_{35}\text{P}_8\text{F}_{24}\text{Na}_2\text{La}_2$  ( $M$  = 2186.43). Anal. calc.: C, 19.78; H, 2.49; N, 5.13%. Found: C, 19.81; H, 2.53; N, 5.09%.

$\text{Na}[\text{NaNd}_2\text{L}_4(\text{H}_2\text{O})] \cdot 2\text{H}_2\text{O}$  (4). Yield: 64%; IR (KBr,  $\text{cm}^{-1}$ ): 1624s ( $\nu(\text{C}=\text{O})$ ), 1411m (amide-2), 1161s ( $\nu(\text{P}=\text{O})$ );  $^1\text{H}$  NMR (400 MHz,  $\text{DMSO-d}_6$ , 25 °C):  $\delta$  = 3.92 ppm (br, 48H,  $\text{L}^{2-}$ );  $\text{C}_{36}\text{H}_{54}\text{N}_8\text{O}_{35}\text{P}_8\text{F}_{24}\text{Na}_2\text{Nd}_2$  ( $M$  = 2197.09). Anal. calc.: C, 19.68; H, 2.48; N, 5.10%. Found: C, 19.73; H, 2.50; N, 5.07%.

### X-Ray crystallography

The X-ray diffraction data on 2 were collected and examined on an Xcalibur 3 diffractometer equipped with CCD sapphire and graphite-monochromated  $\text{MoK}\alpha$  radiation ( $\lambda$  = 0.71073 Å). The diffraction data for 3 were collected at 173 K using a Stoe IPDS-2T diffractometer. For 4, the measurements were performed on a Stoe Stadivari diffractometer with a Dectris Pilatus 300K detector and with an Cu microfocus source ( $\text{Cu-K}\alpha$ ,  $\lambda$  = 1.54186 Å) at 173 K. Face-indexed numerical absorption correction using X-RED and X-SHAPE<sup>45,46</sup> was applied. The structures

were solved by a direct method and refined against  $F^2$  using the full-matrix least-squares method in anisotropic approximation for all atoms except hydrogen using the SHELXTL software package.<sup>47,48</sup> For the structure of 2, H atoms were located from the difference maps of electron density and refined by a “riding” model with  $U_{\text{iso}} = 1.2U_{\text{eq}}$  of the carrier non-hydrogen atom.

In case of the complexes 3 and 4, the refinement met severe problems associated with disorder of the structure components and possible twinning. A significant residual electron density peaks near La (Nd) ions indicated contributions from the second domain. We were not successful to index and integrate the diffraction data as a two-domain system or to derive the appropriate twinning scheme. Therefore, La (Nd) ions were considered as disordered, with partial contribution factors of 0.93, 0.07 (3) and 0.95, 0.05 (4) suggested by the refinement of thermal parameters. Only major components of the disorder were then refined anisotropically. More importantly, the interlay of two chemically identical helicate moieties of opposite chirality resulted in equal disorder of the organic linkage and either encapsulated or outer Na cations. Refinements in acentric space group  $P1$  did not provide an ordered model, while preserving all features of the disorder. This was resolved with partial occupancy factors of 0.5 for all atoms of two unique ligands and two unique Na ions. With the exception of peripheral C-atoms of methoxy groups, it was possible to refine the anisotropic model. A set of restraints was applied to improve the refinement stability. In particular, similarity restraints were used for thermal motion of some closely separated components of the disorder as well as for some chemically identical bonds of P–OCH<sub>3</sub> fragments. Due to the nature of the disorder, the hydrogen atoms were not added.

The crystal data and structure refinement for the complexes 2, 3 and 4 are given in Table S1 (ESI†).

Final atomic coordinates, geometrical parameters and crystallographic data. CCDC 2062595, 2082894 and 2082895.†

## Results and discussion

### Description of the crystal structures

The single crystals of the complexes were obtained from the solution in 2-propanol/acetone mixture.

The crystal structure of compound 2 is shown in Fig. 1. The complex anion  $[\text{NaNd}_2\text{L}_4(\text{H}_2\text{O})]^-$  has a structure of quadruple-stranded helicate, which encapsulates sodium cation and a molecule of water into the negatively charged environment of the ligand fluorine and carbonyl oxygen atoms, which can also be treated as cryptand-like cavity. The water molecule is located between two neodymium ions lying on helical axis, while the sodium ion is situated at the periphery of the cryptand-like cavity, where it is bound to the oxygen atom of the water molecule, carbonyl oxygen and fluorine atoms of the ligand. Four bis-carbamoylphosphate ligands are coordinated to two crystallographically distinct Nd(III) ions in bidentate-chelating manner *via* oxygen atoms of carbonyl and phosphoryl groups. Oxygen atoms of carbonyl groups act as bridges also

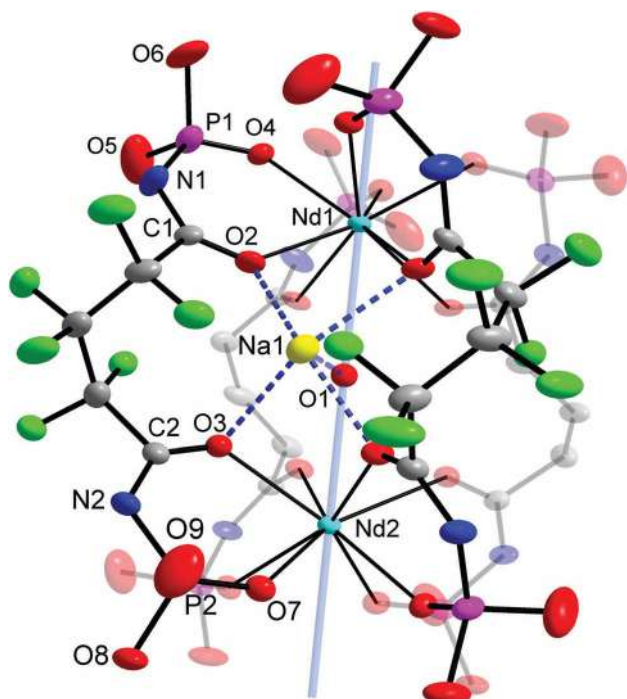


Fig. 1 Structure of the complex anion  $[\text{NaND}_2\text{L}_4(\text{H}_2\text{O})]^-$  in **2**, with the displacement ellipsoids drawn at the 30% probability level (methyl groups are omitted for clarity). The light blue line indicates the axis of the complex, with the O1 atom situated on a center of inversion. The Na1 ion is equally disordered over four inversion-related positions (only one of them is shown here).

binding the sodium ion. Such a structure allows to assume, that the sodium cation may act as a template participating in helicate self-assembly.

The Nd··Nd distance in the complex under study equals 5.703(9) Å that is the shortest reported Ln··Ln distance for quadruple-stranded binuclear lanthanide complexes. The Nd–O(C) bond lengths are of 2.501(7) Å and 2.516(6) Å for Nd1 and Nd2, respectively. The Nd–O(P) bond lengths, respectively, equal 2.429(6) Å and 2.433(6) Å, thus being shorter than those in the case of carbonyl oxygen atoms due to the higher affinity of phosphoryl oxygen to lanthanide ions. The P–O and C–O bond lengths of the ligand in **2** have greater average values compared to such of free ligand ( $d(\text{P–O})_{\text{ligand}} = 1.4598(12)$  Å and  $d(\text{C–O})_{\text{ligand}} = 1.202(2)$  Å<sup>43</sup>) and are equal 1.461(7) Å and 1.22(1) Å, respectively. The average values of P–N and C–N bond lengths of the ligand in the complex are reduced compared to those in the free ligand ( $d(\text{P–N})_{\text{ligand}} = 1.6751(14)$  Å and  $d(\text{C–N})_{\text{ligand}} = 1.361(2)$  Å) (Table 1).

According to the data obtained using the SHAPE 2.1 software,<sup>49</sup> the coordination polyhedra of Nd(III) ions in **2** could be interpreted as a distorted square antiprism (Fig. 2).

There are four  $\text{NET}_4[\text{NaND}_2\text{L}_4(\text{H}_2\text{O})]$  units per unit cell, where both Nd(III) ions are homochiral in each helicate.  $\text{NET}_4^+$  and sodium cations are disordered over four positions.

The average value of OPO angle is 108.98°, consequently the phosphorus atoms surrounding the complex anion have slightly distorted tetrahedral configuration. The values of essential angles and bond distances are given in Table 1.

Table 1 Principal bond lengths and angles in the crystal structures of helicates

Bond length (Å)	Bond length (Å)		
	2	3	4
Ln–O(C)	2.501(7)–2.516(6)	2.557(6)–2.561(12)	2.480(7)–2.487(15)
Ln–O(P)	2.429(6)–2.433(6)	2.435(6)–2.474(5)	2.392(8)–2.440(6)
O–C	1.220(12)–1.222(11)	1.22(2)–1.25(2)	1.28(2)–1.29(3)
P–O	1.444(7)–1.461(7)	1.460(6)–1.481(5)	1.459(10)–1.466(8)
P–N	1.646(10)–1.655(9)	1.613(9)–1.626(9)	1.612(13)–1.623(12)
C–N	1.301(13)–1.303(12)	1.334(19)–1.339(16)	1.28(2)–1.30(3)
Angle (°)			
O–Ln–O	71.3(2)–71.8(2)	70.2(3)–70.66(17)	71.5(4)–72.0(2)
C–O–Ln	136.9(6)–137.0(6)	137.8(11)–140.0(7)	138.4(15)–138.5(9)
P–O–Ln	135.0(4)–135.7(4)	136.6(3)–137.0(4)	135.0(4)–137.0(6)
O–P–O	104.6(5)–113.4(5)	92.4(7)–124.3(6)	99.4(9)–120.6(7)
O–P–N	103.0(5)–119.9(4)	106.2(4)–120.0(4)	104.8(7)–119.3(5)
C–N–P	120.0(7)–122.3(7)	122.6(10)–124.7(10)	124.2(12)–125.0(12)
O–C–N	130.7(9)–132.3(9)	129.1(14)–129.5(15)	127(2)–128.9(15)

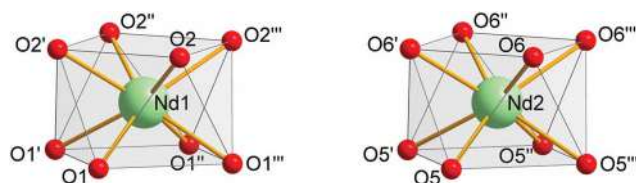


Fig. 2 Polyhedra of Nd1 and Nd2 ions. Twisted square antiprisms (CN = 8).

Unlike the discrete structure of **2**, the crystals of **3** and **4** consist of polymer chains formed by oxygen atoms of  $\text{OCH}_3$  and phosphoryl moieties and outer-sphere sodium cations (Fig. 3 and Fig. S1, ESI<sup>†</sup>). The complexes under consideration are hydrates, since they also contain two molecules of water in their outer-spheres. Considered water molecules tend to bind the outer-sphere sodium. The other significant attribute of helicates **3** and **4** lies in the presence of opposite helicity species in the same unit cell in 1 : 1 ratio, which is not likely to the crystals of **2** with one definite helicity. Both lanthanide ions in the helicate units are crystallographically equivalent.

### Spectroscopic studies

**IR spectroscopy.** The obtained complexes have very similar IR spectra (Fig. S3, ESI<sup>†</sup>). The IR spectra of  $\text{H}_2\text{L}$ ,  $\text{Na}_2\text{L}$  and **2** are shown in Fig. 4. The spectrum of  $\text{H}_2\text{L}$  exhibits N–H stretching vibration band at 3095  $\text{cm}^{-1}$ , while in the spectra of the complexes, as well as  $\text{Na}_2\text{L}$ , this band is absent. This fact indicates the coordination of the ligand to lanthanide ions in the deprotonated form. The other vibration bands sensitive towards deprotonation and coordination are C=O, P=O stretching vibrations and amide II band. Comparing the spectra of the complexes to the spectrum of the neutral ligand, it could be easily noticed that C=O, P=O and amide II bands are bathochromically shifted, compared to such in  $\text{H}_2\text{L}$  by 122–125  $\text{cm}^{-1}$ , 68–72  $\text{cm}^{-1}$  and 51–53  $\text{cm}^{-1}$ , respectively. The shift of these stretching bands is caused by the bond order decreasing as a result of ligand deprotonation and coordination that is in agreement with X-ray data for the complex and neutral ligand.<sup>43</sup>

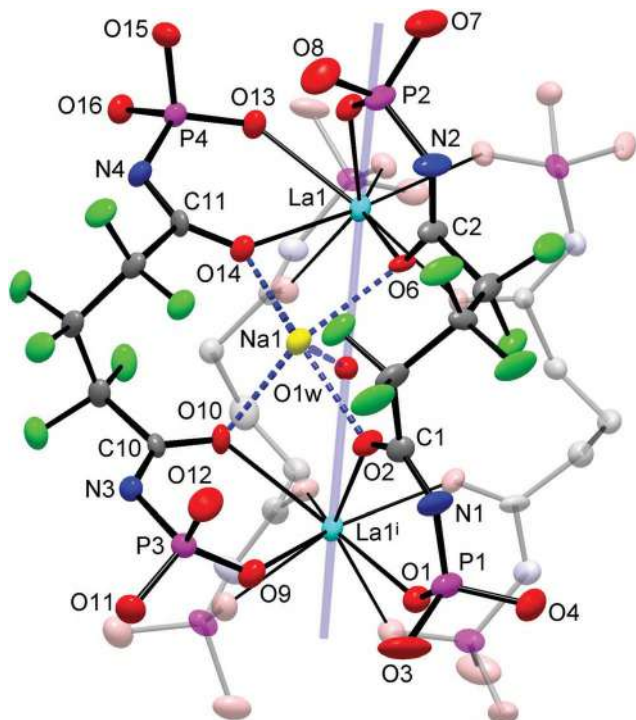


Fig. 3 Structure of the complex anion  $[\text{NaLa}_2\text{L}_4(\text{H}_2\text{O})]^-$  in **3**, with the displacement ellipsoids drawn at the 30% probability level. Only one orientation of the disordered ligands is shown and  $\text{CH}_3$  groups are omitted for clarity. The blue line indicates the axis of the complex, with the O1w atom situated on a center of inversion. The Na1 ion is equally disordered over two inversion-related positions (only one of them is shown here). Symmetry code: (i)  $-x, -y, -z$ .

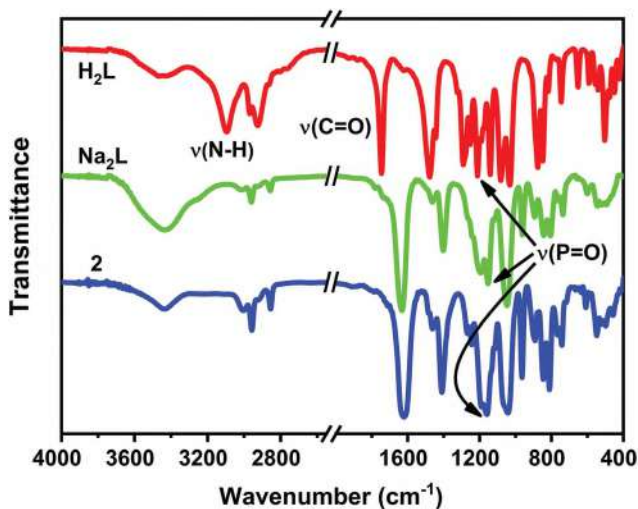


Fig. 4 IR spectra of the neutral ligand ( $\text{H}_2\text{L}$ ), its sodium salt ( $\text{Na}_2\text{L}$ ) and complex **2**.

The IR spectrum of complex **2** in region  $60\text{--}600\text{ cm}^{-1}$  is shown on the Fig. S2 (ESI<sup>†</sup>). The bands of Ln–O stretching modes, OLnO bending modes and chelate ring “breathing” can be observed in this region. The chelate rings are characterized by three types of vibrations: chelate ring breathing, in-plane

bending and out-of-plane bending. These modes are observed in  $625\text{--}840$ ,  $420\text{--}540$  and  $180\text{--}395\text{ cm}^{-1}$  regions.<sup>50,51</sup> Some of these bands are split due to coupling with  $\nu(\text{Ln}\text{--}\text{O})$  and  $\delta(\text{OLnO})$  vibrations. The  $\nu(\text{Ln}\text{--}\text{O})$  stretching vibrations are strongly coupled with the chelate ring deformations.<sup>52</sup> Therefore, the bands sensitive to changes in the metal could be observed, even above  $400\text{ cm}^{-1}$ . Theoretical calculations for mononuclear neodymium CAPH-based complexes showed that the  $\nu(\text{Ln}\text{--}\text{O})$  stretching motions couple with the chelate ring vibrations with their contribution  $10\text{--}30\%$ .<sup>51</sup> These bands are observed in the broad frequency region  $630\text{--}320\text{ cm}^{-1}$ . The bending vibrations OLnO are observed as broad and middle-intensity bands in the IR spectrum in the region  $50\text{--}280\text{ cm}^{-1}$ .

Based on the previously reported data for CAPH-based lanthanide complexes<sup>50,51</sup> the vibrations in the IR spectrum of complex **2** at  $336$ ,  $352$ ,  $375$ ,  $387$ ,  $410$ ,  $463$ ,  $497$  and  $552\text{ cm}^{-1}$  were assigned to Ln–O stretching modes coupled with the chelate ring “breathing”. The bands at  $270$  and  $170\text{ cm}^{-1}$  and their shoulders were assigned to OLnO bending modes coupled with the chelate ring “breathing”.

**<sup>1</sup>H NMR spectroscopy.** When considering the <sup>1</sup>H NMR spectrum of  $\text{H}_2\text{L}$ , there could be found two types of signals: one of them is associated with the protons of four methoxy-groups and appears in the spectrum as a doublet at  $3.74\text{ ppm}$ , the other one is broadened signal at  $11.38\text{ ppm}$ , which corresponds to NH protons. In the spectra of  $\text{Na}_2\text{L}$  and complexes, the signals of amide protons are absent. The signals of the protons in methoxy groups in the spectra of  $\text{Na}_2\text{L}$  and diamagnetic complexes **1** and **3** are shifted to high field compared to those in  $\text{H}_2\text{L}$  and come out as doublets at  $3.44$ ,  $3.59$  and  $3.53\text{ ppm}$ , respectively. The upfield shift is caused by redistribution of electron density in the ligand molecule as a consequence of deprotonation, coordination and  $\pi$ -conjugation in the chelate cycle. In the spectra of **2** and **4**, the signal of protons from methoxy-groups is downfield shifted to  $4.17$  and  $3.92\text{ ppm}$ , respectively, due to the paramagnetic nature of Nd(III). For compounds **1** and **2**, the integral intensity ratio of tetraethylammonium proton signals to ligand proton signals agrees with X-ray data and confirms the established composition of complexes.

**Photoluminescent properties of complex 2.** The  $\text{NET}_4[\text{NaNd}_2\text{L}_4(\text{H}_2\text{O})]$  complex exhibits IR-emissions at  $300$  and  $77\text{ K}$  upon excitation by the  $266\text{ nm}$ -harmonic lines of the Nd:YAG pulsed laser. The emission spectra are shown in Fig. 5. The narrow bands at around  $900$  and  $1060\text{ nm}$  were assigned to  ${}^4\text{F}_{3/2} \rightarrow {}^4\text{I}_{9/2}$  and  ${}^4\text{F}_{3/2} \rightarrow {}^4\text{I}_{11/2}$  transitions of Nd(III) ion. When the temperature decreases from  $300$  to  $77\text{ K}$ , the radiative relaxation channel of the  ${}^4\text{F}_{3/2}$  level changes. This is evidenced from the change in the relative intensities of the transitions, in  $300\text{ K}$   $I({}^4\text{F}_{3/2} \rightarrow {}^4\text{I}_{9/2}) < I({}^4\text{F}_{3/2} \rightarrow {}^4\text{I}_{11/2})$ , and in  $77\text{ K}$   $I({}^4\text{F}_{3/2} \rightarrow {}^4\text{I}_{9/2}) > I({}^4\text{F}_{3/2} \rightarrow {}^4\text{I}_{11/2})$ . The integral intensity ratio of  ${}^4\text{F}_{3/2} \rightarrow {}^4\text{I}_{9/2}/{}^4\text{F}_{3/2} \rightarrow {}^4\text{I}_{11/2}$  equals  $0.97$  at  $300\text{ K}$  and  $1.3$  at  $77\text{ K}$ .

In the case of inorganic Nd compounds, due to the relatively large energy gap between the  ${}^4\text{F}_{3/2}$  and  ${}^4\text{I}_{15/2}$  levels (about  $5500\text{ cm}^{-1}$ ), the participation of multi-phonon relaxation in the depopulation of the  ${}^4\text{F}_{3/2}$  level is relatively small and the

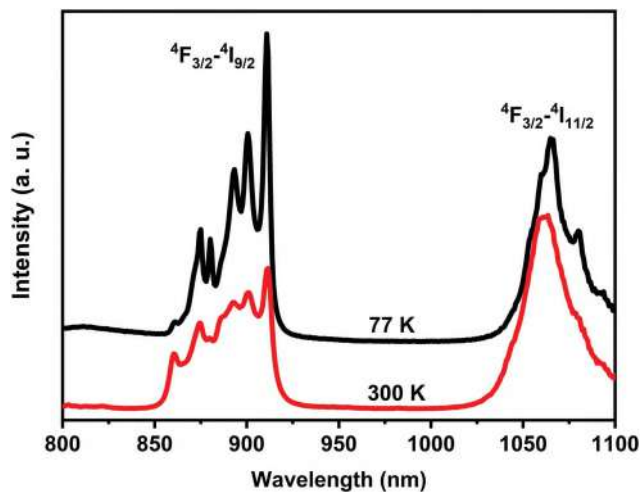


Fig. 5 The emission spectra of the  $\text{NEt}_4[\text{NaNd}_2\text{L}_4(\text{H}_2\text{O})]$  complex at 300 and 77 K,  $\lambda_{\text{exc}} = 266$  nm.

lifetime of the  ${}^4\text{F}_{3/2}$  level can reach about  $150 \mu\text{s}$ .<sup>53</sup> The situation is different regarding the Nd coordination compounds. Organic ligands have high-energy vibrations and are effective in quenching the Nd emission by the so-called multi-phonon quenching process. This is an extremely effective mechanism for the non-radiative conversion of the energy of  $\text{Ln}^{3+}$  electronic states into molecular group resonant vibrational states. The emission is quenched as a result of coupling with, for example, high-energy vibrations of  $\nu(\text{OH})$  of water or  $\nu(\text{CH})$  of aliphatic groups. To reduce this quenching process, the CH groups in our ligand have been partially replaced with CF groups, which are characterized by much lower vibration energy. The lifetime of the  ${}^4\text{F}_{3/2}$  emission level spans from 0.1 to about  $5 \mu\text{s}$  for Nd compounds with organic ligands.<sup>54–56</sup> A slight extension of this value is observed in fluorinated coordination compounds ( $\sim 25 \mu\text{s}$ ).<sup>54</sup> However, in the case of the  $\text{NEt}_4[\text{NaNd}_2\text{L}_4(\text{H}_2\text{O})]$  complex with the fluorinated ligand, the  ${}^4\text{F}_{3/2}$  emission lifetime is very short ( $2 \mu\text{s}$ ) and is non-exponential, as shown in Fig. 6. The

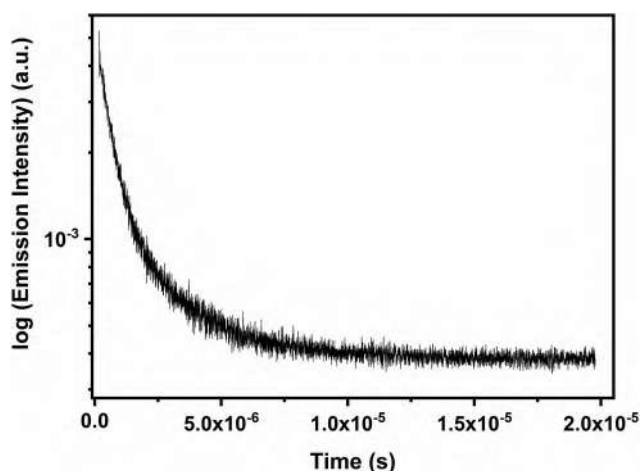


Fig. 6 Decay luminescence curve for  $\text{NEt}_4[\text{NaNd}_2\text{L}_4(\text{H}_2\text{O})]$  at 300 K.

average lifetime was calculated using eqn (1).<sup>57</sup> The non-exponential character of the lifetime is due to the ion–ion energy transfer. As shown in the crystallographic part, the distance  $\text{Nd} \dots \text{Nd}$  equals  $5.703(9) \text{ \AA}$ . At such close distances between Nd ions, the  ${}^4\text{F}_{3/2}$  emission quenching occurs through the cross-relaxation process.<sup>58</sup> The cross-relaxation process is possible if there is a neighboring neodymium ion in the ground state in the vicinity of the excited Nd(III) ion. The excited Nd(III) ion undergoes the  ${}^4\text{F}_{3/2} \rightarrow {}^4\text{I}_{15/2}$  transition and the adjacent ion undergoes the  ${}^4\text{I}_{9/2} \rightarrow {}^4\text{I}_{15/2}$  transition, thus both ions occupy the  ${}^4\text{I}_{15/2}$  levels. Narrow energy gaps between levels below the  ${}^4\text{I}_{15/2}$  state favor multi-phonon relaxation, and the ions revert to the ground state along the non-radiative pathway. The cross-relaxation process is possible due to the coincidence of energy differences between  ${}^4\text{F}_{3/2} - {}^4\text{I}_{15/2}$  and  ${}^4\text{I}_{9/2} - {}^4\text{I}_{15/2}$ .

Due to the above-mentioned emission quenching process, such dimer systems may not be of interest in terms of photo-physical properties. On the other hand, we have shown that the Nd–Nd distance allows the non-radiative interionic energy transfer. Thus, the investigated ligand can be used, *e.g.*, to design heteronuclear complexes for luminescence thermometry, showing interionic temperature-dependent energy transfer.

$$\tau = \frac{\int_0^{\infty} I(t) dt}{\int_0^{\infty} I(t) dt} \quad (1)$$

### Mass spectrometry

The helicate **2** was also characterized by laser desorption/ionization mass spectrometry. The mass spectrum of **2**, recorded in the negative ionization mode, displays a cluster of peaks possessing the correct isotopic distribution, which corresponds to doubly charged anion  $[\text{Nd}_2\text{L}_4]^{2-}$  species (Fig. 7). In contrast to the crystal structure data, the single-charged anion associate  $[\text{Nd}_2\text{L}_4 + \text{Na} + \text{H}_2\text{O}]^-$  is not observed. The mass spectra of the rest of the compounds exhibit similar patterns.

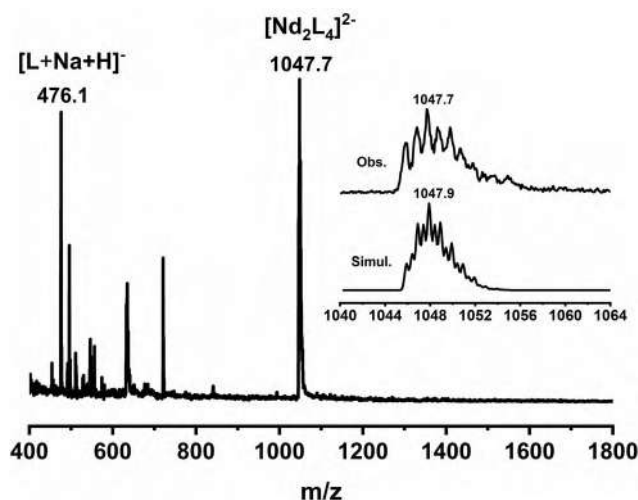


Fig. 7 LDI mass spectrum of **2**, with inset depicting the simulated (Simul.) and observed (Obs.) isotopic pattern.

## Conclusions

The first examples of lanthanide binuclear tetrakis-complexes based on bis-chelating carbacylamidophosphate were synthesized and characterized.

It was found that the complex anions in the obtained compounds have a structure of quadruple-stranded helicate, which encapsulates sodium cation and a molecule of water into a cryptand-like cavity. Following the trend of CAPH-based lanthanide mononuclear tetrakis-complexes, complex 2 has a discrete structure, while crystals of 3 and 4 consist of polymer chains formed by oxygen atoms of OCH<sub>3</sub> and phosphoryl moieties and outer-sphere sodium cations.

The mass spectrum of 2, recorded in the negative ionization mode, showed the prevailing presence of a doubly-charged anion [Nd<sub>2</sub>L<sub>4</sub>]<sup>2-</sup> in the sample, thus pointing to the instability of [Nd<sub>2</sub>L<sub>4</sub> + Na + H<sub>2</sub>O]<sup>-</sup> associate during the experiment.

Complex 2 was found to be luminescent in the IR spectral region with the <sup>4</sup>F<sub>3/2</sub> emission lifetime equal 2 μs. The bis-carbacylamidophosphate ligand belongs to the new family of bis-chelating ligands and can be used to obtain Ln complexes as model systems for the study of interionic energy transfer as well as for the design of heteronuclear luminescent lanthanide materials based on this process.

## Author contributions

Oleksandr Ye. Horniichuk – investigation, visualization, writing – original draft; Victor A. Trush – supervision, writing – review and editing; Nataliia S. Kariaka – investigation, writing – original draft; Svitlana V. Shishkina – formal analysis; Viktoriya V. Dyakonenko – investigation, formal analysis; Olga V. Severinovskaya – investigation; Paula Gawryszewska – investigation, writing – original draft; Kostiantyn V. Domasevitch – investigation, visualization; Adam Watras – investigation; Vladimir M. Amirkhanov – supervision, writing – review and editing.

## Conflicts of interest

There are no conflicts to declare.

## Acknowledgements

This work was supported by the Ministry of Education and Science of Ukraine (Project no. 19BF037-05). The publication contains the results of studies conducted by President's of Ukraine grant for competitive projects (Project no. 19BF037-06).

## Notes and references

- 1 C. Piguet, G. Bernardinelli and G. Hopfgartner, *Chem. Rev.*, 1997, **97**, 2005–2062.
- 2 C. O. Dietrich-Buchecker and J.-P. Sauvage, *Angew. Chem., Int. Ed. Engl.*, 1989, **28**, 189–192.
- 3 C. O. Dietrich-Buchecker, J.-P. Sauvage, A. De Cian and J. Fischer, *J. Chem. Soc., Chem. Commun.*, 1994, 2231–2232.
- 4 C. Dietrich-Buchecker, G. Rapenne and J. P. Sauvage, *Chem. Commun.*, 1997, 2053–2054.
- 5 M. Albrecht and O. Blau, *Chem. Commun.*, 1997, 345–346.
- 6 B. Hasenknopf, J. M. Lehn, B. O. Kneisel, G. Baum and D. Fenske, *Angew. Chem., Int. Ed. Engl.*, 1996, **35**, 1838–1840.
- 7 M. J. Hannon, V. Moreno, M. J. Prieto, E. Moldrheim, E. Sletten, I. Meistermann, C. J. Isaac, K. J. Sanders and A. Rodger, *Angew. Chem., Int. Ed.*, 2001, 879–884.
- 8 I. Meistermann, V. Moreno, M. J. Prieto, E. Moldrheim, E. Sletten, S. Khalid, P. Mark Rodger, J. C. Peberdy, C. J. Isaac, A. Rodger and M. J. Hannon, *Proc. Natl. Acad. Sci. U. S. A.*, 2002, **99**, 5069–5074.
- 9 E. Moldrheim, M. J. Hannon, I. Meistermann, A. Rodger and E. Sletten, *J. Biol. Inorg. Chem.*, 2002, **7**, 770–780.
- 10 A. El-ghayoury, L. Douce, A. Skoulios and R. Ziessel, *Angew. Chem., Int. Ed.*, 1998, **37**, 2205–2208.
- 11 C. Piguet, A. F. Williams, J. C. G. Bünzli, G. Bernardinelli and G. Hopfgartner, *J. Am. Chem. Soc.*, 1993, **115**, 8197–8206.
- 12 A. S. Chauvin, S. Comby, B. Song, C. D. B. Vandevyver, F. Thomas and J. C. G. Bünzli, *Chem. – Eur. J.*, 2007, **13**, 9515–9526.
- 13 E. Deiters, B. Song, A.-S. Chauvin, C. D. B. Vandevyver and J.-C. G. Bünzli, *New J. Chem.*, 2008, **32**, 1140.
- 14 M. Albrecht, S. Schmid, M. deGroot, P. Weis and R. Fröhlich, *Chem. Commun.*, 2003, 2526–2527.
- 15 C. Piguet, G. Bernardinelli and A. F. Williams, *Inorg. Chem.*, 1989, **28**, 2920–2925.
- 16 A. F. Williams, C. Piguet and G. Bernardinelli, *Angew. Chem., Int. Ed. Engl.*, 1991, **30**, 1490–1492.
- 17 A. P. Bassett, S. W. Magennis, P. B. Glover, D. J. Lewis, N. Spencer, S. Parsons, M. Williams, L. De Cola and Z. Pikramenou, *J. Am. Chem. Soc.*, 2004, **126**, 9413–9424.
- 18 D. A. McMorran and P. J. Steel, *Angew. Chem.*, 1998, **110**, 3495–3497.
- 19 T. D. Owens, F. J. Hollander, A. G. Oliver and J. A. Ellman, *J. Am. Chem. Soc.*, 2001, **123**, 1539–1540.
- 20 M. Albrecht, S. Schmidt, S. Dehn, C. Wickleder, S. Zhang, A. P. Bassett and R. Fröhlich, *New J. Chem.*, 2007, **31**, 1755–1762.
- 21 S. Liu, P. He, H. Wang, J. Shi and M. Gong, *Inorg. Chem. Commun.*, 2009, **12**, 506–508.
- 22 J. Yuan, S. Sueda, R. Somazawa, K. Matsumoto and K. Matsumoto, *Chem. Lett.*, 2003, **32**, 492–493.
- 23 P. Chen, H. Li, W. Sun, J. Tang, L. Zhang and P. Yan, *CrystEngComm*, 2015, **17**, 7227–7232.
- 24 Y. Zhang, Y. Zhou, T. Gao, P. Yan and H. Li, *Chem. Commun.*, 2020, **56**, 13213–13216.
- 25 J. Xu and K. N. Raymond, *Angew. Chem.*, 2006, **118**, 6630–6635.
- 26 G. Han, Y. Zhou, Y. Yao, Z. Cheng, T. Gao, H. Li and P. Yan, *Dalton Trans.*, 2020, **49**, 3312–3320.
- 27 Y. Zhou, Y. Yao, Z. Cheng, T. Gao, H. Li and P. Yan, *Inorg. Chem.*, 2020, **59**, 12850–12857.
- 28 M. Albrecht and S. Kotila, *Angew. Chem., Int. Ed. Engl.*, 1996, **35**, 1208–1210.
- 29 A. Bilyk and M. M. Harding, *J. Chem. Soc., Chem. Commun.*, 1995, 1607–1698.

## Paper

- 30 M. Albrecht and S. Kotila, *Angew. Chem., Int. Ed. Engl.*, 1995, **34**, 2134–2137.
- 31 M. Albrecht, H. Röttele and P. Burger, *Chem. – Eur. J.*, 1996, **2**, 1264–1268.
- 32 R. W. Saalfrank, A. Dresel, V. Seitz, S. Trummer, F. Hampel, M. Teichert, D. Stalke, C. Stadler, J. Daub, V. Schünemann and A. X. Trautwein, *Chem. – Eur. J.*, 1997, **3**, 2058–2062.
- 33 M. Albrecht, M. Schneider and H. Röttele, *Angew. Chem., Int. Ed.*, 1999, **38**, 557–559.
- 34 M. Albrecht, O. Osetska, R. Fröhlich, J. C. G. Bünzli, A. Aebischer, F. Gumy and J. Hamacek, *J. Am. Chem. Soc.*, 2007, **129**, 14178–14179.
- 35 X. Zhu, C. He, D. Dong, Y. Liu and C. Duan, *Dalton Trans.*, 2010, **39**, 10051–10055.
- 36 H. Li, P. Yan, P. Chen, Y. Wang, H. Xu and G. Li, *Dalton Trans.*, 2012, **41**, 900–907.
- 37 J. Shi, Y. Hou, W. Chu, X. Shi, H. Gu, B. Wang and Z. Sun, *Inorg. Chem.*, 2013, **52**, 5013–5022.
- 38 Y. Hou, J. Shi, W. Chu and Z. Sun, *Eur. J. Inorg. Chem.*, 2013, 3063–3069.
- 39 J. Leng, H. Li, P. Chen, W. Sun, T. Gao and P. Yan, *Dalton Trans.*, 2014, **43**, 12228–12235.
- 40 B. Li, H. Li, P. Chen, W. Sun, C. Wang, T. Gao and P. Yan, *Phys. Chem. Chem. Phys.*, 2015, **17**, 30510–30517.
- 41 C. Fu, L. Chen, X. Wang and L. Lin, *ACS Omega*, 2019, **4**, 15530–15538.
- 42 V. Amirkhanov, V. Ovchinnikov, V. Trush, P. Gawryszewska and L. B. Jerzykiewicz, in *Powerful new ligand systems: Carbacylamidophosphates (CAPH) and Sulfonylamidophosphates (SAPH) in Ligands: Synthesis, Characterization and Role in Biotechnology*, ed. P. Gawryszewska and P. Smoleński, Nova Science Publishers, New York, 2014, ch. 7, pp. 199–248.
- 43 V. A. Trush, K. E. Gubina, Y. O. Gumeniuk, T. Y. Sliva and I. S. Konovalova, *Acta Crystallogr., Sect. E: Struct. Rep. Online*, 2012, **68**, o1127.
- 44 V. M. Amirkhanov and V. A. Trush, *Z. Obs. Khim.*, 1995, **65**, 1120–1124.
- 45 Stoe and Cie, X-RED, Stoe & Cie GmbH, Darmstadt, Germany, 2001.
- 46 Stoe and Cie, X-SHAPE, Stoe & Cie GmbH, Darmstadt, Germany, 1999.
- 47 G. M. Sheldrick, *Acta Crystallogr., Sect. A: Found. Crystallogr.*, 2008, **64**, 112–122.
- 48 G. M. Sheldrick, *Acta Crystallogr., Sect. C: Struct., Chem.*, 2015, **71**, 3–8.
- 49 M. Lluell, D. Casanova, J. Girera, P. Alemany and S. Alvarez, *SHAPE 2.1*, Universitat de Barcelona, Barcelona, Spain, 2013.
- 50 W. Amirkhanov, C. Jaficzak, L. Macalik, J. Hanuza and J. Legendziewicz, *J. Appl. Spectrosc.*, 1995, **62**, 613–624.
- 51 J. Sokolnicki, J. Legendziewicz, W. Amirkhanov, V. Ovchinnikov, L. Macalik and J. Hanuza, *Spectrochim. Acta, Part A*, 1999, **55**, 349–367.
- 52 J. Fujita, A. E. Martell and K. Nakamoto, *J. Chem. Phys.*, 1962, **36**, 339–345.
- 53 M. Sobczyk, *Opt. Mater.*, 2013, **35**, 852–859.
- 54 S. Comby and J. C. G. Bünzli, Lanthanide Near-Infrared Luminescence in Molecular Probes and Devices, in *Handbook on the Physics and Chemistry of Rare Earth*, 1st edn, ed. K. Gschneidner, J. C. G. Bünzli and V. Pecharsky, Elsevier Science BV, Amsterdam, 2007, ch. 235, pp. 217–470.
- 55 E. Kasprzycka, V. A. Trush, L. Jerzykiewicz, V. M. Amirkhanov, A. Watras, J. Sokolnicki, O. L. Malta and P. Gawryszewska, *Dyes Pigm.*, 2019, **160**, 439–449.
- 56 Y. H. Pham, V. A. Trush, M. Korabik, V. M. Amirkhanov and P. Gawryszewska, *Dyes Pigm.*, 2020, **186**, 108986.
- 57 M. Inokuti and F. Hirayama, *J. Chem. Phys.*, 1965, **43**, 1978–1989.
- 58 G. Blasse and B. C. Grabmaier, *Luminescent Materials*, Springer-Verlag Berlin Heidelberg, 1994.

# High-Sensitivity Microthermometry Method Based on Vacuum-Deposited Thin Films Exhibiting Gradual Spin Crossover above Room Temperature

Oleksandr Ye. Horniichuk, Karl Ridier, Lijun Zhang, Yuteng Zhang, Gábor Molnár, Lionel Salmon,\* and Azzedine Bousseksou\*



Cite This: *ACS Appl. Mater. Interfaces* 2022, 14, 52140–52148



Read Online

ACCESS |

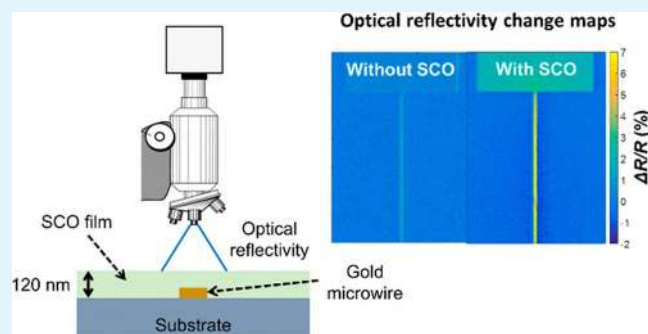
Metrics & More

Article Recommendations

Supporting Information

**ABSTRACT:** We report on the fabrication, characterization, and microthermometry application of high-quality, nanometric thin films, with thicknesses in the range 20–200 nm, of the molecular spin-crossover complex  $[\text{Fe}(\text{HB}(1,2,3\text{-triazol-1-yl})_3)_2]$ . The films were obtained by vacuum thermal evaporation and characterized by X-ray diffraction, UV spectrophotometry, and atomic force microscopy. The as-deposited films are dense and crystalline with a preferred [011] orientation of the monoclinic crystal lattice normal to the substrate surface. The films exhibit a gradual spin conversion centered at ca. 374 K spanning the 273–473 K temperature range, irrespective of their thickness. When deposited on a micro-electronic device, these films can be used to enhance the UV-light thermorefectance coefficient of reflective surfaces by more than an order of magnitude, allowing for high-sensitivity thermorefectance thermal imaging.

**KEYWORDS:** spin crossover, vacuum thermal evaporation, thin films, thermorefectance imaging, microthermometry



than an order of magnitude, allowing for high-sensitivity thermorefectance thermal imaging.

## 1. INTRODUCTION

With the continuous advancement of micro- and nanotechnologies, the development of noninvasive thermometry techniques, capable of measuring and imaging the temperature at the micro- and nanoscale, is of paramount importance for various technological fields, such as photonics, microelectronics, and biomedicine.<sup>1–9</sup> The most common, industry standard, thermal imaging methods rely on optical thermometry techniques, which consist in tracking an optical response (Planck blackbody emission,<sup>10–12</sup> Raman scattering,<sup>4</sup> luminescence,<sup>13</sup> or optical reflectivity<sup>14–17</sup>) of the investigated object's surface to a temperature change.<sup>1</sup> Importantly, an extension to these conventional thermo-optical techniques can be provided by deposition on the investigated surface of temperature-sensitive materials, such as liquid crystals<sup>18</sup> or lumino-phores,<sup>9,13,19–23</sup> to enhance the thermally induced optical contrast of the surface and then the achievable thermal sensitivity and the accuracy of the temperature measurement.

In this context, molecular spin-crossover (SCO) compounds constitute an attractive class of thermoresponsive materials. These transition-metal complexes, which can reversibly switch between their low-spin (LS) and high-spin (HS) electronic configurations, exhibit drastic alterations of their optical properties (absorption coefficient and refractive index) under the effect of a temperature change.<sup>24–26</sup> Depending on the

crystal packing and/or the strength of the intermolecular interactions in the material, a variety of thermal SCO behaviors have been reported, from very gradual conversions over a wide temperature range to abrupt transitions, with or without thermal hysteresis loop (memory effect).<sup>27</sup> Interestingly, these different possible characteristics of the thermal spin transition enable various thermometric and thermal imaging approaches, thus providing an appealing scope for thermometry (see Figure 1).<sup>28</sup> (N.B. It is worth noting that this type of classification of thermometry approaches also applies to other classes of phase-change materials as well, such as liquid crystals.)

As shown in Figure 1a, and as already demonstrated experimentally,<sup>29</sup> a SCO thin film exhibiting a thermal hysteresis loop can be used to detect *ex situ* the overshoot of a certain threshold temperature, thus allowing for thermal memory application. As the thermally induced optical changes can be read out *a posteriori*, the key interest here is that the temperature distribution can be mapped using slow and high-

Received: August 2, 2022

Accepted: October 31, 2022

Published: November 14, 2022



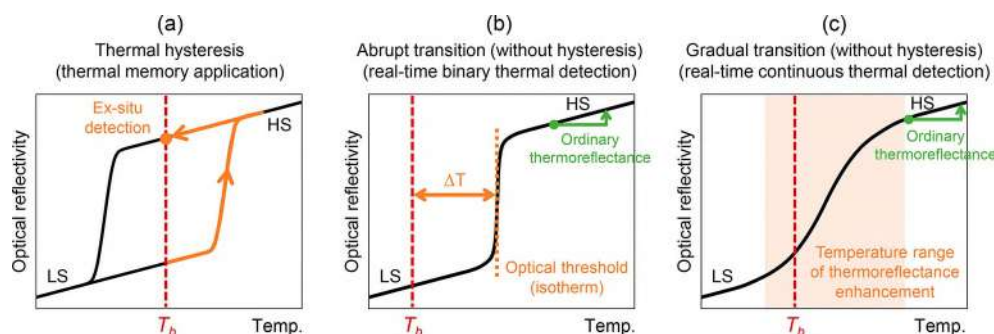


**Figure 1.** Schematic representation of the thermal evolution of the optical reflectivity of a SCO thin film, showing that different possible thermometric applications can be envisioned depending on the characteristics of the thermal spin transition of the film: (a) thermal memory application (transition with thermal hysteresis), (b) real-time binary thermal sensing (abrupt transition without hysteresis), and (c) real-time continuous thermal sensing (gradual transition without hysteresis).  $T_b$  refers to the base (ambient) temperature of the device under study.

resolution imaging methods, such as scanning probe microscopies,<sup>30</sup> to probe fast and spatially localized transient thermal events, which would be hardly detectable using conventional, real-time optical methods.

On the contrary, the absence of the thermal hysteresis loop allows for real-time thermometry. Interestingly, different applications can be envisioned depending on the abruptness of the thermal spin transition. For instance, the use of a SCO film with an abrupt thermal transition ( $\Delta T < 10$  K) allows a binary detection of the surface temperature because a brusque change of the optical reflectivity occurs at the transition temperature, bringing out a well-defined isotherm (Figure 1b). This approach was recently demonstrated using the SCO complex  $[\text{Fe}(\text{HB}(1,2,4\text{-triazol-1-yl})_3)_2]$  which displays an abrupt spin transition centered at 337 K.<sup>31</sup> A great advantage of this approach is that real-time contour maps of the surface temperature distribution can be achieved without any prior thermal calibration of surface properties. Moreover, we have shown that this binary thermal detection method can also afford for high-resolution surface temperature maps, which can be obtained by scanning the base (ambient) temperature  $T_b$  of the device under study (controlled with a heating/cooling stage).<sup>31</sup> However, these surface temperature maps cannot be acquired in real time (since it requires to scan the base temperature of the studied device).

Finally, as shown in Figure 1c, another method would consist in using a thin film with a gradual thermal SCO and to carry out conventional thermorefectance measurements, allowing a continuous and real-time monitoring of the absolute temperature of the surface, provided that a careful thermal calibration of the optical reflectivity is performed beforehand. In this case, the main interest of the SCO film would be to amplify the thermally induced change of the reflectivity of the surface and then to enhance the achievable thermal sensitivity (i.e., the thermorefectance coefficient). To date, however, no thermorefectance-based thermal imaging method utilizing gradual SCO is reported, mainly due to the lack of appropriate samples. Indeed, for this application, the need arises for high-quality, dense, homogeneous SCO thin films displaying a fully reproducible, hysteresis-free, gradual spin conversion above room temperature, capable of withstanding long-term thermal cycling and exhibiting an overall large thermally induced change of optical reflectivity.

In this work, we demonstrate that the molecular SCO complex  $[\text{Fe}(\text{HB}(1,2,3\text{-triazol-1-yl})_3)_2]$ , **1** (see molecular and crystal structures, Figure S1),<sup>32</sup> fulfills the above-mentioned

conditions and can then be used as an accurate, continuous surface temperature sensor, probed by optical reflectivity. Indeed, contrary to its structural isomer  $[\text{Fe}(\text{HB}(1,2,4\text{-triazol-1-yl})_3)_2]$ , which was used in a previous work as a binary temperature sensor,<sup>31</sup> the polycrystalline bulk powder of **1** presents a stable, gradual spin transition centered at around 373 K, spanning over a wide temperature range (ca. 320–430 K).<sup>32</sup> Here, we show that the complex **1** is sublimable and can be deposited in the form of high-quality, homogeneous thin films by vacuum thermal evaporation, in which the SCO properties are retained. The structural, morphological, and electronic properties of the films were investigated using grazing-incidence X-ray diffraction (GIXRD), atomic force microscopy (AFM), and variable-temperature ultraviolet–visible (UV–vis) spectrophotometry. For surface thermal imaging purposes, Joule-heated metallic microwires, fabricated on top of glass and silicon substrates, were coated with nanometric films of **1**, and their response to local temperature changes was probed by optical reflectivity.

## 2. EXPERIMENTAL SECTION

**2.1. Thin Film Fabrication and Characterization.** Thin films of **1** were obtained by means of thermal evaporation in a PREVAC thermal deposition system at a base pressure of ca.  $9 \times 10^{-7}$  mbar. The bulk powder of the complex, synthesized as reported in refs 32 and 33, was heated at 210 °C in a quartz crucible and evaporated at a rate of  $0.04 \text{ \AA s}^{-1}$ . The film thickness and the evaporation rate were followed *in situ* using a quartz crystal microbalance. The thickness of the films was verified *ex situ* by spectral reflectance measurements (F20, Filmetrics) and by AFM (SmartSPM, Horiba). The films were deposited onto crystalline silicon (100 orientation) and amorphous fused silica substrates, which were cleaned beforehand via 5 min sonication in acetone and ethanol.

The GIXRD experiments were performed in ambient conditions by means of a PANalytical X'Pert PRO MPD system using Cu K $\alpha$  radiation (45 kV and 40 mA) and a parallel-beam configuration. The incident beam optics consisted of a mirror with a  $1/32^\circ$  divergence slit. A parallel plate collimator ( $0.18^\circ$ ) and Soller slits ( $0.04^\circ$ ) were mounted on the path of the diffracted beam. An X'Celerator detector in receiving slit mode was used for X-ray collection. AFM surface topography analysis was conducted in amplitude-modulation mode at room temperature using the SmartSPM. The temperature-dependent absorbance spectra of the thin films were collected at wavelengths between 200 and 600 nm using a Cary 50 (Agilent Technologies) spectrophotometer and a Linkam FTIR-600 heating–cooling stage. The sample chamber was purged with dry nitrogen, and spectra were acquired in the 253–453 K range with a  $2 \text{ K min}^{-1}$  rate.

**2.2. Microthermometry Experiments.** Gold microwires (length 1–2 mm, thickness 250 nm, and width 2–16  $\mu\text{m}$ ) were patterned on

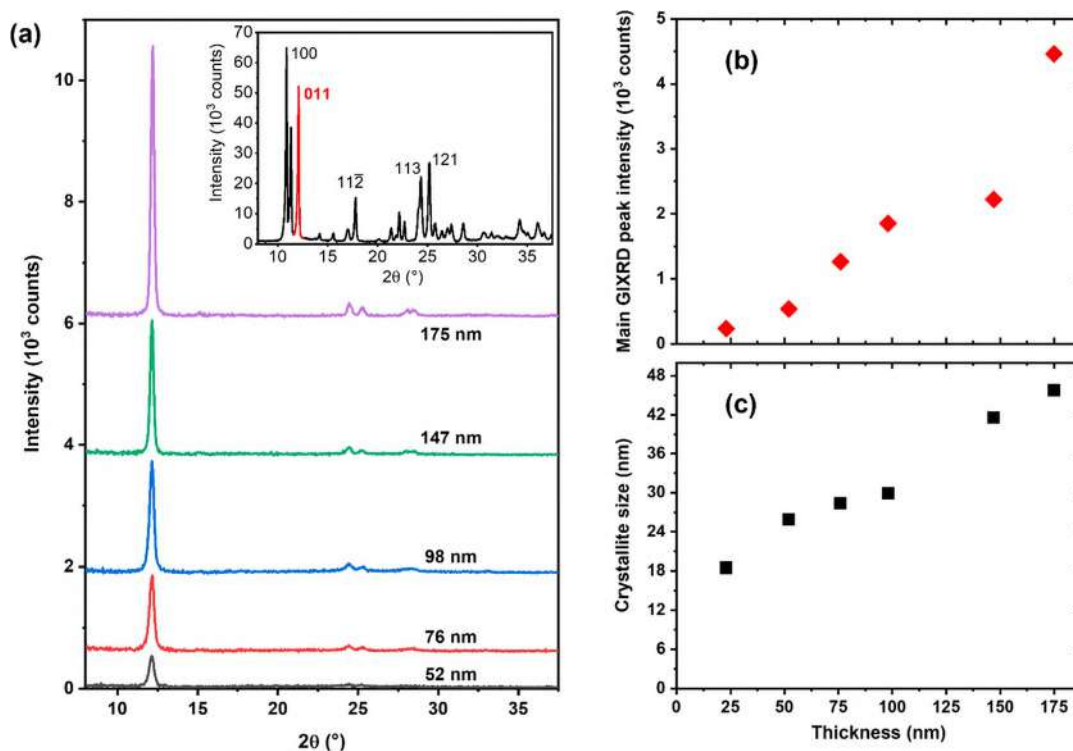


**Figure 2.** Crystallinity of the films. (a) XRD patterns of nanocrystalline thin films of **1** with various thicknesses, deposited on Si substrates. The inset shows the XRD pattern of the microcrystalline powder of **1**. (b) Intensity of the 011 reflection as a function of the film thickness. (c) Average size of the crystalline domains (calculated for the 011 reflection using the Scherrer method) as a function of the film thickness.

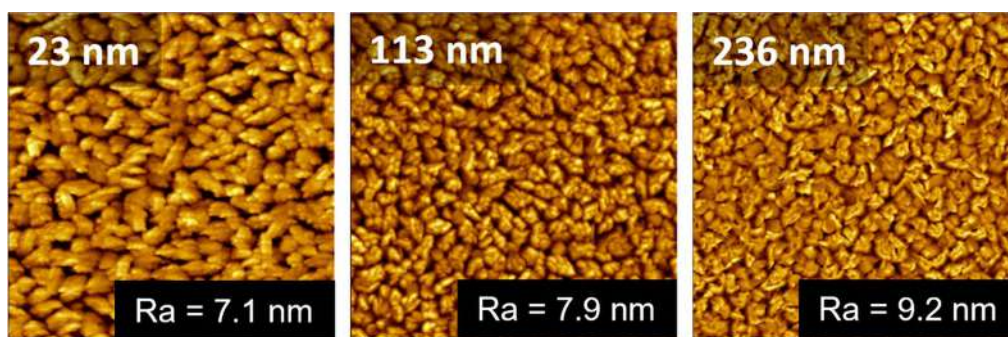


**Figure 3.** Morphology of the films. Representative AFM topography images of films of **1** with different thicknesses (23, 113, and 236 nm) deposited on silicon substrates. The scan size is  $5 \times 5 \mu\text{m}^2$ .

glass and thermally oxidized silicon substrates by a photolithography method, as reported earlier.<sup>29,31,34</sup> The substrates (and the micro-wires) were then coated with a 120 nm thick film of **1** by vacuum thermal evaporation. The SCO-coated chip was connected to a sourcemeter (Keithley 2611A) via an eight-track connector<sup>31</sup> and mounted on a variable-temperature microscope stage (Linkam Scientific Instruments, LTS120) to control the base temperature ( $T_b$ ) of the entire circuit. The microwire electrical characterizations and operation were performed by applying current and not voltage bias to guarantee a reproducible Joule heating. Optical reflectivity images were recorded at  $\lambda = 310$  nm (LED source) and  $\lambda = 452$  nm (halogen lamp with a spectral range reduced by a band-pass filter) using a custom-made optical microscope (compatible with UV light) equipped with a  $\times 5$  magnification objective (numerical aperture, NA = 0.12) and a CCD camera (Andor Technology Clara, 1392  $\times$  1040 pixels of 6.45  $\mu\text{m}$  size).

### 3. RESULTS AND DISCUSSION

**3.1. Fabrication and Characterization of [Fe(HB(1,2,3-Triazol-1-yl)<sub>3</sub>)<sub>2</sub>] Films.** Thin films of **1** were deposited by vacuum thermal evaporation with thicknesses in the 20–200 nm range. The X-ray diffraction patterns of the films reveal an intense peak at  $2\theta = 12.15^\circ$  (Figure 2a) which points to crystallinity and preferential crystallographic orientation of the as-deposited films. Figure 2a also shows the diffraction pattern of the microcrystalline bulk powder, which displays a similar peak at  $2\theta = 12.09^\circ$ . In the simulated PXRD pattern of **1**<sup>32</sup> this peak corresponds to the 011 reflection. We can thus suggest that crystallites in the films grow preferentially with the [011] direction of the monoclinic unit cell normal to the substrate surface. This observation was systematically confirmed, irrespective of the substrate material (silicon or fused silica) and the film thickness. The diffractograms did not undergo significant changes upon long-term storage (months) of the films in ambient conditions. It is interesting to note here that

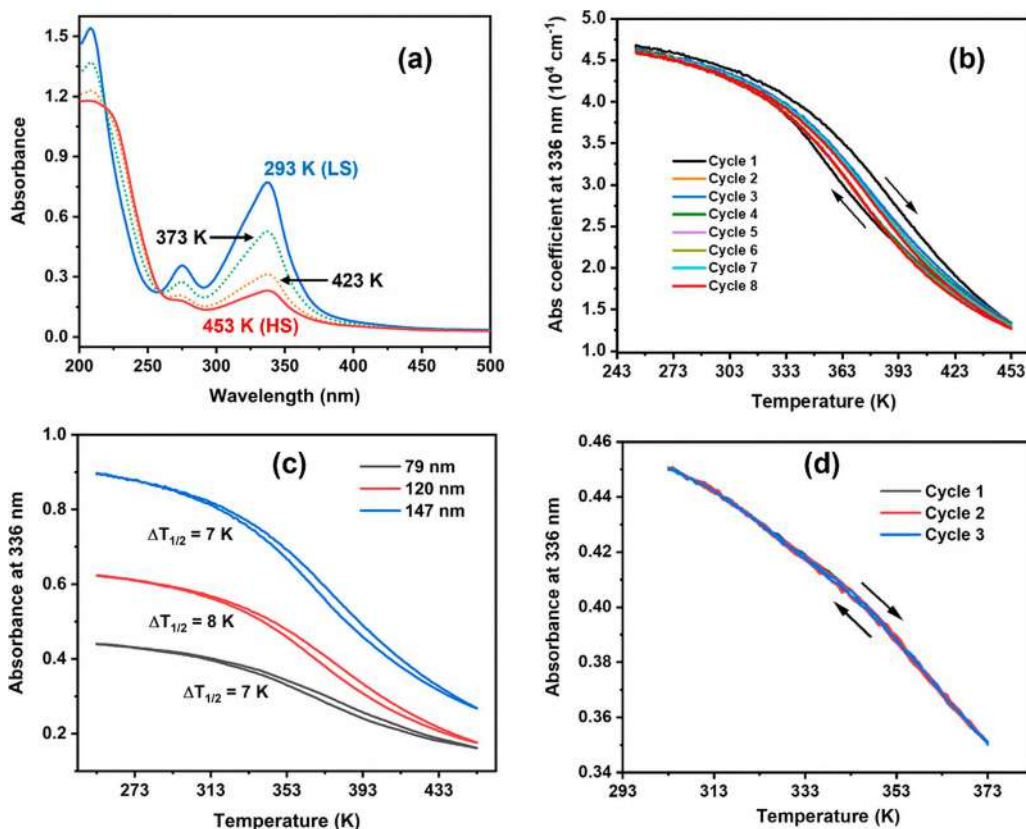


**Figure 4.** SCO properties of the films. (a) Optical absorbance spectra of a 175 nm thick film of **1** on fused silica substrate, acquired at selected temperatures. (b) Temperature dependence of the absorbance at 336 nm of the same 175 nm film upon eight heating–cooling cycles between 253 and 453 K. (c) Thermal variation of the absorbance at 336 nm for a 79, 120, and 147 nm thick film of **1** upon heating–cooling cycles between 253 and 453 K. (d) Thermal variation of the optical absorbance at 336 nm for a 79 nm thick film of **1** upon three heating–cooling cycles from 303 to 373 K.

the complex  $[\text{Fe}(\text{HB}(1,2,4\text{-triazol-1-yl})_3)_2]$ , which is the structural isomer of **1**, forms an amorphous film upon vacuum thermal deposition, and only a subsequent solvent vapor annealing affords for the formation of a textured crystalline film.<sup>35</sup> The 011 diffraction peak intensity of the as-deposited films of **1** correlates with the thickness, indicating a similar degree of crystallinity and texture for each film in the investigated thickness range (Figure 2b). From the width of the 011 diffraction peak, the average size of the coherent crystalline domains can be calculated using the Scherrer equation.<sup>36</sup> As for the absolute values, care must be taken because the peak widths were corrected for instrument broadening but not for other possible effects, such as microstrain. Nevertheless, the tendency shown in Figure 2c clearly evidences that the size of the crystalline domains grows steadily with the film thickness.

Representative AFM surface topography data of films of **1** with different thicknesses, deposited on fused silica substrates, are shown in Figure 3. The nanocrystalline surface morphology of the films is obvious with roughness average (Ra) values typically between 7 and 11 nm. The particle morphology does not substantially depend on the film thickness or the nature of the substrate (see Figure S2), but one can notice a more dense packing in the thicker films.

To investigate the SCO properties in the thin films of **1**, variable-temperature UV–vis spectrophotometry measurements were conducted over three to eight heating–cooling cycles between 253 and 453 at a 2 K min<sup>-1</sup> rate. The

measurements were performed for the films deposited on transparent fused silica substrates. The room-temperature absorbance spectra of the films display three absorption bands with maxima at 208, 275, and 336 nm (Figure 4a). The absorbance level of these bands decreases upon heating, while a fourth band appears at 230 nm and exhibits higher absorbance at high temperatures (Figure 4a). As a result, the variable temperature spectra are characterized by two isosbestic points at ca. 220 and 260 nm. Taking into account the high absorption coefficients associated with these peaks, we can safely assign them to charge transfer (metal-to-ligand and/or ligand-to-metal) transitions.

We use the thermal evolution of the highest intensity absorption band at 336 nm to follow the occurrence of a spin-state change in the films. Typical transition curves, displayed in Figure 4b, reveal a very gradual spin conversion between the LS and HS states, similar to the one observed in the bulk powder.<sup>32</sup> The transition temperature is centered around  $374 \pm 2$  K, independently of the film thickness (Figure 4c). The transition is virtually complete at 273 K (pure LS state), whereas a residual LS fraction of ca. 5–10% is still observed at 453 K. (N.B. Heating above ca. 453 K leads to the degradation of the films.) A notable, unusual characteristic of the SCO in the films of **1** is the occurrence of a thermal hysteresis, which is not expected for such a gradual spin conversion. At the first heating–cooling cycle this thermal hysteresis loop is usually broad reaching up to 35 K in width, while on further cycling it narrows down to ca. 7 K. Importantly, we found, however, that

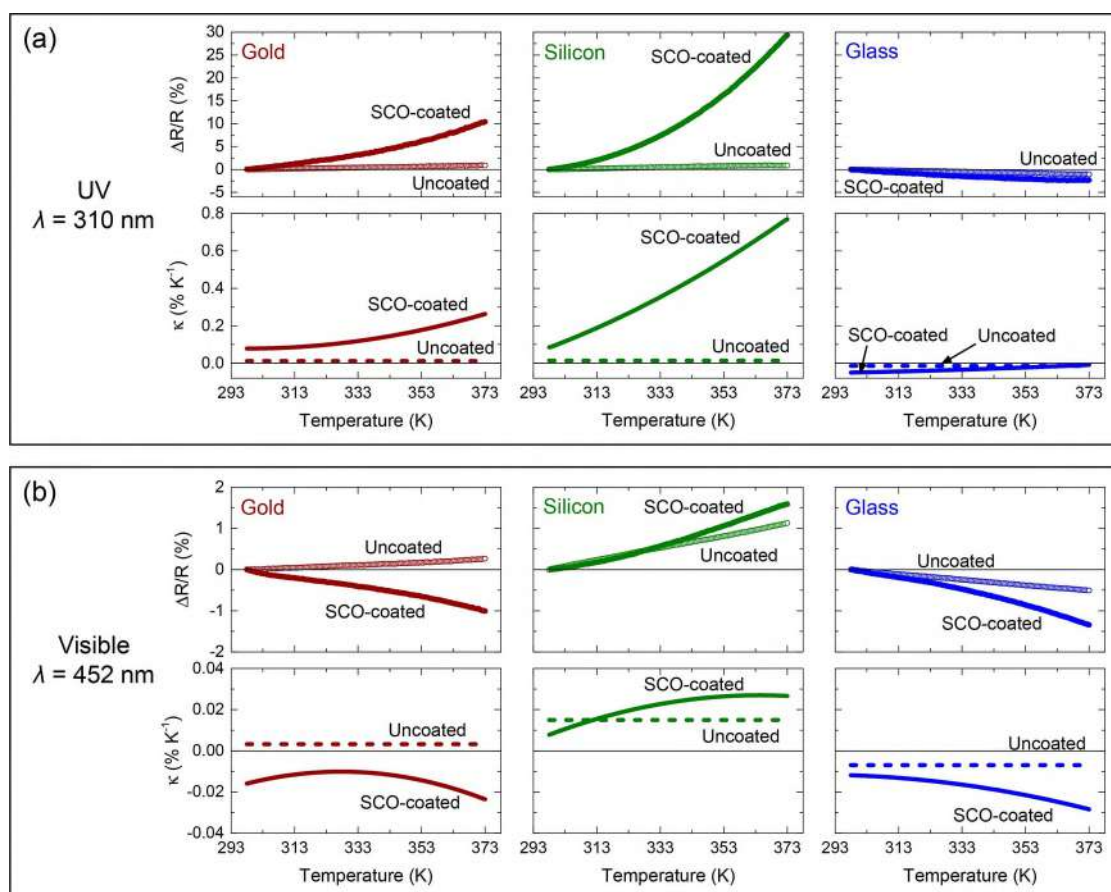


**Figure 5.** Thermal calibrations of the optical reflectivity. (a) Thermal evolution of the relative optical reflectivity change,  $\Delta R/R = (R - R_{298K})/R_{298K}$  (top panel), and of the corresponding thermorefectance coefficient,  $\kappa = d(\Delta R/R)/dT$  (bottom panel), measured at  $\lambda = 310$  nm on SCO-coated and uncoated surfaces of gold, silicon, and glass. (b) Thermal evolution of the relative optical reflectivity change,  $\Delta R/R$  (top panel), and of the corresponding thermorefectance coefficient,  $\kappa$  (bottom panel), measured at  $\lambda = 452$  nm on SCO-coated and uncoated surfaces of gold, silicon, and glass. For each measurement, the surface was heated from 298 to 373 K at a temperature scan rate of 2 K  $\text{min}^{-1}$ .

reducing the thermal cycling span leads to a narrowing of the hysteresis loop. Indeed, reducing the end temperature from 453 to 393 K results in a 4 K wide hysteresis loop, whereas the thermal hysteresis can be completely removed by limiting the heating of the sample to 373 K, leading to perfectly reversible and reproducible spin-transition curves (Figures 4d and S3).

To summarize the somewhat unusual SCO properties of the vacuum-deposited films of **1**, we can say that they display a very gradual spin conversion between ca. 273 and 473 K, similar to that of the bulk powder. Up to ca. 373 K (i.e., the half-transition), the SCO is perfectly reversible, without any thermal hysteresis, thus providing scope for real-time thermometry applications. However, when heating above this temperature, a more and more broad thermal hysteresis loop opens. This hysteresis obviously does not refer to the usually encountered cooperative phenomena in SCO materials. Instead, it is likely an indication of small, irreversible changes in the material when cycling at high temperature. Because of this phenomenon, accurate thermal sensing is not possible in the full 373–453 K range, but still it is possible to acquire thermal images. Finally, above ca. 453 K, the films start to degrade, presumably due to the sublimation of the molecules. At present, we have no unequivocal explanation for the opening of the thermal hysteresis loop above 373 K. Preliminary AFM and GIXRD data acquired on samples cycled at high temperatures reveal the existence of structural

changes in the films as well as a visible modification of their surface morphology (see Figure S4), but further work will be necessary to reach a clear-cut conclusion.

**3.2. Microthermometry Application of [Fe(HB(1,2,3-Triazol-1-yl)<sub>3</sub>)<sub>2</sub>] Films.** Taking advantage of the above-mentioned properties, we have undertaken experiments to explore the use of thin films of **1** as a temperature sensor, probed by optical reflectivity, for mapping and measuring the surface temperature through thermorefectance thermal imaging. Indeed, the role of the SCO film is to enhance the thermorefectance properties of surfaces in a broad temperature range—especially in the UV spectral domain where a drastic change of the optical absorbance occurs when switching between the LS and HS states; the improved thermorefectance involving an increased thermally induced change in optical reflectivity and therefore a greater thermal sensitivity for measuring the surface temperature.

Figure 5a (top panels) shows the thermal evolution of optical reflectivity,  $\Delta R/R = (R - R_{298K})/R_{298K}$ , at  $\lambda = 310$  nm (close to the maximum absorbance wavelength) on SCO-coated (120 nm) and uncoated gold, silicon, and glass surfaces. Remarkably, the presence of the SCO layer significantly enhances the thermorefectance properties of surfaces, providing a relative change of the reflectivity by +29.4%, +10.4%, and -2.4% on silicon, gold, and glass surfaces, respectively, in the temperature range between 298 and 373 K.

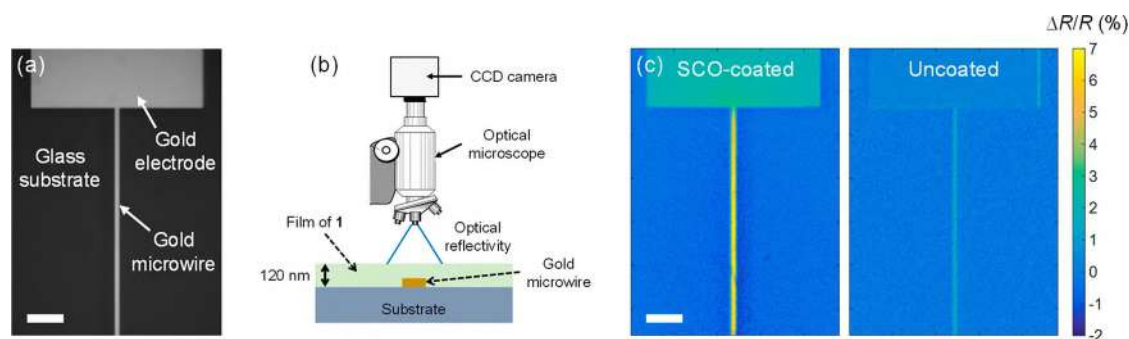


**Figure 6.** Thermal sensitivity improvement. (a) Optical reflectivity  $R$  image of a Joule-heated gold microwire (2 mm long and 16  $\mu\text{m}$  wide) on top of a glass substrate. (b) Scheme of the experimental setup. (c) Relative change of optical reflectivity ( $\lambda = 310$  nm),  $\Delta R/R = (R_{\text{ON}} - R_{\text{OFF}})/R_{\text{OFF}}$ , following the application of an electrical current of 65 mA in the wire, for (left) an SCO-coated surface and (right) an uncoated surface. In both cases, the base temperature  $T_b$  of the chip was maintained at 298 K. The scale bars are 100  $\mu\text{m}$ .

By comparison, on uncoated surfaces, these relative changes (ordinary thermoreflectance) remain moderate: +0.9% on silicon and gold surfaces and  $-1.1\%$  on glass. The observed changes are much greater on silicon (and to a lesser extent on gold), which is a reflective surface in the UV range (compared to glass). On these surfaces, the optical reflectivity is found to increase with temperature ( $\Delta R/R > 0$ ), which is compatible with a progressive reduction of the absorbance of the SCO film at this wavelength upon the spin transition. Figure 5a (bottom panels) depicts the thermal evolution of the corresponding thermoreflectance coefficient ( $\kappa$ ), defined as  $\kappa = d(\Delta R/R)/dT$ , on the various investigated surfaces ( $\lambda = 310$  nm). While  $\kappa$  is virtually constant for uncoated surfaces in the temperature range 298–373 K,  $\kappa = +0.013\% \text{ K}^{-1}$ ,  $+0.012\% \text{ K}^{-1}$ , and  $-0.014\% \text{ K}^{-1}$  for silicon, gold, and glass surfaces, respectively, the thermoreflectance coefficient is not constant on SCO-coated surfaces due to the spin-transition phenomenon. On SCO-coated silicon,  $\kappa$  varies from  $0.085\% \text{ K}^{-1}$  at 298 K to  $0.77\% \text{ K}^{-1}$  at 373 K. In other words, the thermoreflectance coefficient (i.e., the thermal sensitivity) is multiplied by 6.5 at 298 K up to a factor of 59 at 373 K due to the presence of the SCO layer. On gold,  $\kappa$  changes from  $0.078\% \text{ K}^{-1}$  to  $0.26\% \text{ K}^{-1}$  when heating from 298 to 373 K, which corresponds to an increase of the thermoreflectance coefficient by a factor of 6.5 and 22 at 298 and 373 K, respectively, compared to the pristine gold surface. Finally, the effect is less advantageous on transparent glass substrates where  $\kappa$  changes from  $-0.050\% \text{ K}^{-1}$  to  $-0.009\% \text{ K}^{-1}$  when heating from 298 to 373 K, which means that the thermal sensitivity is increased by a factor 3.6 (in absolute value) at 298 K but becomes lower than the ordinary thermoreflectance at high temperature. One should note here that further enhancements of the thermoreflectance coefficient can be anticipated, for instance, by using a light source matching the wavelength of maximum absorbance (336 nm) and/or by increasing the thickness of the SCO film. However, in both cases, the price to pay would be an increasing disturbance of the surface temperature caused by the presence of the SCO film (i.e., increased invasiveness), which is particularly detrimental for fast (<ms) temperature monitoring. As with the optical absorbance measurements, it should be noted that no notable difference is observed in these thermal calibration curves between heating and cooling modes (see Figure S5), which signifies that the performance of the SCO film, in terms of thermal change of the optical reflectivity, is fully reversible in the temperature range 298–373 K.

Interestingly, as shown in Figure 5b, only a slight improvement of the thermoreflectance properties is evidenced on the SCO-coated surfaces in the visible range ( $\lambda = 452$  nm), i.e., in a spectral domain out of the SCO-dependent absorption band of the film. This result indicates that most of the change of the optical reflectivity along the spin transition arises from the variation of the absorption properties of the film rather than a simple change of the refractive index. On the whole, these measurements show that the presence of the SCO thin film entails a substantial increase of the thermoreflectance properties in the UV range by more than 1 order of magnitude compared to the ordinary thermoreflectance, especially on reflective surfaces like gold or silicon, which consequently implies a sizable enhancement of the sensitivity (in terms of optical reflectivity signal) to any change of the surface temperature.

To investigate the potential of this SCO thin film in terms of thermoreflectance thermal imaging, we fabricated a variety of Joule-heated gold microwires (length 1–2 mm, thickness 250 nm) on top of glass and oxidized silicon chips by means of photolithography (see Figure 6a). The surface of the chips was then entirely covered with a 120 nm thick film of **1**. Note that due to its insulating nature, the presence of the molecular films of **1** on the surface is not invasive and does not perturb the electrical performance of the device.

Optical reflectivity images ( $\lambda = 310$  nm) of a SCO-coated microwire (length 2 mm, width 16  $\mu\text{m}$ ) on a glass substrate were acquired by optical microscopy at  $T = 298$  K (see Figure 6b), in both ON ( $I \neq 0$ ) and OFF ( $I = 0$ ) states of the heating device. Figure 6c (left) shows a map of the relative change of optical reflectivity,  $\Delta R/R = (R_{\text{ON}} - R_{\text{OFF}})/R_{\text{OFF}}$ , following the application of an electrical current of 65 mA in the wire. A strong increase of the optical reflectivity is observed on the wire and, to a lesser extent, on the electrode. On the glass substrate, in the immediate vicinity of the wire, a slight decrease of the reflectivity is also observed, which is compatible with an increase of the temperature following the application of the electrical current. (As indicated in Figure 5a, we recall that the optical reflectivity increases/decreases on gold/glass surface following a temperature rise.) For comparison, the same experiment was performed with an identical microwire on an uncoated, pristine chip. As shown in Figure 6c (right), the variation of optical reflectivity associated with the application of the same electrical current (65 mA) is considerably lower than that observed for the SCO-coated surface, which demonstrates the substantial gain provided by

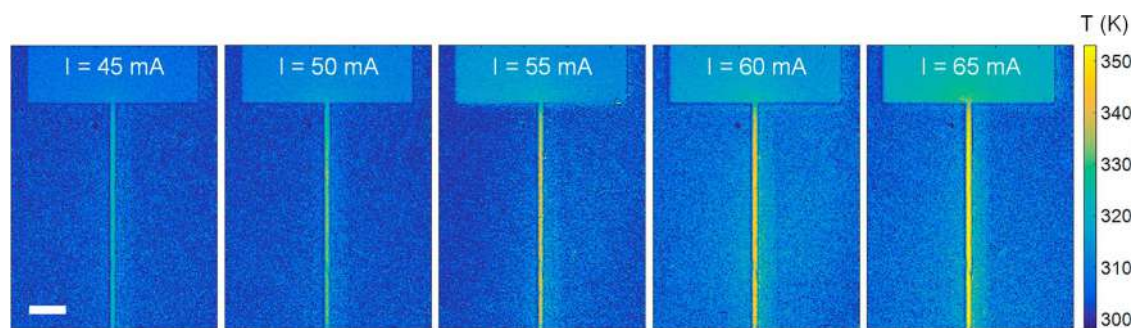


**Figure 7.** Quantitative microthermometry. Temperature maps of a SCO-coated, 16  $\mu\text{m}$  wide gold microwire on top of a glass substrate for various applied electrical currents ranging from 45 to 65 mA ( $T_b = 298$  K). The maps are deduced from the optical reflectivity ( $\lambda = 310$  nm) images,  $\Delta R/R = (R_{\text{ON}} - R_{\text{OFF}})/R_{\text{OFF}}$ , of the SCO-coated surface. The pixel size of the temperature maps is  $2.6 \times 2.6 \mu\text{m}^2$ . The scale bar is 100  $\mu\text{m}$ .

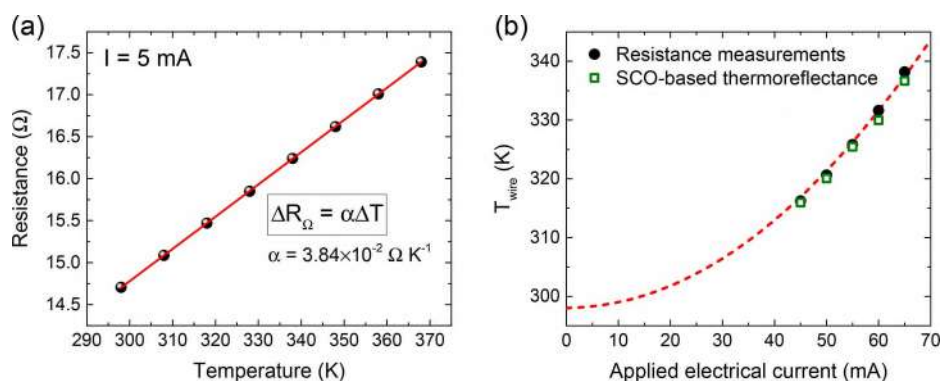


**Figure 8.** Comparison with electrical resistance measurements. (a) Variation of the electrical resistance  $R_\Omega$  of the microwire, measured at low-bias current (5 mA), as a function of the base temperature ( $T_b$ ) of the substrate, controlled with a variable-temperature stage. The linear temperature coefficient of the wire is  $\alpha = 3.84 \times 10^{-2} \Omega \text{K}^{-1}$ . (b) Average temperature of the Joule-heated wire,  $T_{\text{wire}}$ , for various applied electrical currents ranging from 45 to 65 mA ( $T_b = 298$  K), inferred from SCO-based thermoreflectance thermal imaging (open squares) and from electrical resistance measurements (filled circles). The red dotted line indicates the typical quadratic evolution of the resistance (and thus of the wire temperature) with the applied electrical current.

the thermosensitive SCO layer in terms of thermoreflectance properties and, therefore, in terms of thermal sensitivity.

Taking advantage of this enhanced thermal sensitivity, we were able to deduce accurate temperature maps of the Joule-heated microwires. Indeed, on the basis of thermal calibration curves of the optical reflectivity shown in Figure 5a, the reflectivity ( $\Delta R/R$ ) map measured in Figure 6c (left) can be easily transformed into a temperature map, by simply converting the measured value of  $\Delta R/R$ , on each pixel of the image, into a temperature value. As shown in Figure 7, this procedure allowed us to map the temperature field of the surface with a micrometric spatial resolution for different values of the applied electrical current. As expected, these temperature maps show that the heating is mainly localized on the gold microwire, while a progressive diffusion of heat is also observed into the substrate and the metallic electrode when increasing the electrical current, as already reported in our previous study.<sup>31</sup> (N.B. However, it should be noted that the temperature gradients observed on the surrounding glass substrate are less marked than in our previous study<sup>31</sup> mainly because of the use, in the present work, of wider Joule-heating wires (16  $\mu\text{m}$  wide instead of 1  $\mu\text{m}$  wide) which generate less pronounced thermal gradients.) From these temperature maps, we can deduce an average temperature of the Joule-heated microwire  $T_{\text{wire}}$  of 315.9, 320.0, 325.4, 329.9, and 336.6 K for an applied current of 45, 50, 55, 60, and 65 mA, respectively. These values are reported in Figure 8b (open squares).

To validate the results obtained with our SCO-based thermometry technique, we also determined the average temperature of the Joule-heated microwire by measuring its electrical resistance. Indeed, the thermal variation induced by the applied current generates a change of electrical resistance  $\Delta R_\Omega$ , proportional to the mean temperature rise of the wire:  $\Delta R_\Omega = \alpha \Delta T_{\text{wire}}$ . To determine the value of  $\alpha$ , a thermal calibration of the resistance of the microwire was performed by measuring the evolution of  $R_\Omega$  at low-bias current (5 mA) for various base temperatures ( $T_b$ ) of the chip. A linear dependence is observed, giving a value of  $\alpha = 3.84 \times 10^{-2} \Omega \text{K}^{-1}$  (Figure 8a). Therefore, in the course of the thermoreflectance measurements, the resistance was simultaneously measured for each value of the applied electrical current, providing a reliable comparative means to monitor in real time the actual average temperature  $T_{\text{wire}}$  of the Joule-heated wire. Figure 8b summarizes the values of  $T_{\text{wire}}$  obtained from the two methods for the different applied electrical currents bias, the chip being kept at room temperature ( $T_b = 298$  K). As shown in Figure 8b, and as expected, the temperature of the wire increases with the current following a typical quadratic evolution (Joule effect). Importantly, we notice that the temperature values obtained from these two techniques are in very good agreement, the observed relative difference being typically 2–5% and always lower than 2 K.

On the whole, these data demonstrate the possibility of using SCO thin films of 1 for imaging the surface temperature at the micrometric scale with a thermal accuracy of the order of

~1 K (using a simple CCD-based optical detection) by taking advantage of a ca. 1 order of magnitude enhancement of the UV-light thermorefectance coefficient brought into by the presence of the SCO layer. We have not investigated the ultimate spatial and temporal resolution of our SCO-based thermometer, which would require more sophisticated equipment, but the enhanced thermorefectance coefficient is obviously a key asset in this context. Furthermore, the fact that the films operate in the UV spectral range is clearly advantageous for imaging submicrometer features. For example, a powerful NA = 0.9 microscope objective could provide a 0.35  $\mu\text{m}$  spot imaging at a wavelength of 310 nm. As for the temporal resolution, the limiting factor is the heat diffusion rate in the film, the molecular SCO phenomenon being intrinsically faster.<sup>37</sup> Indeed, due to their low thermal diffusivity, the thermalization process of such SCO films is completed in ~1  $\mu\text{s}$ ,<sup>37</sup> which thus defines the accessible temporal resolution of our surface thermometer. Experiments on similar molecular films indicate that a 100 nm thick film of **1** could potentially afford for temperature measurements down to the microseconds time scale.<sup>31</sup>

Overall, the thermometric characteristics demonstrated in the present work are virtually comparable to those obtained with the compound [Fe(HB(1,2,4-triazol-1-yl)<sub>3</sub>)<sub>2</sub>],<sup>31</sup> in terms of accessible thermal, spatial, and temporal resolution. However, it is worth emphasizing that the thermometric approaches used in these two cases are totally different, each having their advantages and disadvantages. The use of [Fe(HB(1,2,4-triazol-1-yl)<sub>3</sub>)<sub>2</sub>] (abrupt spin transition) allowed for a binary detection of the surface temperature, working on any surface without the need of thermal calibration procedure of the optical reflectivity. However, in this case, surface temperature maps could not be acquired in real time. Conversely, in this work, we show that the use of compound **1** allows for real-time thermal imaging, based on a prior thermal calibration of the optical reflectivity. However, as the enhancement of the thermorefectance coefficient induced by the SCO film is surface dependent, this thermometry method is not equally effective on all surfaces.

#### 4. CONCLUSIONS

We have fabricated and characterized the structural, morphological, and spin-transition properties of vacuum-deposited thin films (20–200 nm) of the molecular SCO complex [Fe(HB(1,2,3-triazol-1-yl)<sub>3</sub>)<sub>2</sub>]. These dense, textured, nanocrystalline films are shown to maintain a gradual spin conversion between ca. 273 and 473 K, as observed for the bulk powder of this compound. To our best knowledge, this is only the third SCO film, fabricated by thermal evaporation, which displays above-room-temperature SCO and the first that fulfills requirements for real-time thermal imaging applications on a wide temperature range. We demonstrate that the very gradual spin-state conversion in these films affords for a novel, quantitative, microthermometry approach, wherein the SCO film is used to enhance, in some cases by more than 1 order of magnitude, the UV-light thermorefectance coefficient of the coated surface. We show that the key property for this thermal sensitivity gain is the pronounced change of the UV absorbance of the films upon the spin transition.

This work extends the limited portfolio of SCO compounds for demanding microthermometry applications and highlights once again the technological interest of this family of stimulative responsive molecular materials. Yet, it remains crucial to

develop further high-quality thin films and other micro–nano objects of SCO materials displaying robust, near-room-temperature SCO combined with the desired (optical, electrical, and mechanical) functionalities.<sup>38–41</sup>

#### ■ ASSOCIATED CONTENT

##### Supporting Information

The Supporting Information is available free of charge at <https://pubs.acs.org/doi/10.1021/acsami.2c13834>.

Molecular and crystal structure for [Fe(HB(1,2,3-triazol-1-yl)<sub>3</sub>)<sub>2</sub>], AFM topography images, thermal variation of the optical absorbance and optical reflectivity, grazing incidence X-ray diffraction patterns (PDF)

#### ■ AUTHOR INFORMATION

##### Corresponding Authors

Lionel Salmon – LCC, CNRS and Université de Toulouse (UPS, INP), F-31077 Toulouse, France; [orcid.org/0000-0002-8064-8960](https://orcid.org/0000-0002-8064-8960); Email: [lionel.salmon@lcc-toulouse.fr](mailto:lionel.salmon@lcc-toulouse.fr)

Azzedine Bousseksou – LCC, CNRS and Université de Toulouse (UPS, INP), F-31077 Toulouse, France; Email: [azzedine.bousseksou@lcc-toulouse.fr](mailto:azzedine.bousseksou@lcc-toulouse.fr)

##### Authors

Oleksandr Ye. Horniichuk – LCC, CNRS and Université de Toulouse (UPS, INP), F-31077 Toulouse, France; Faculty of Chemistry, Taras Shevchenko National University of Kyiv, 01033 Kyiv, Ukraine

Karl Ridier – LCC, CNRS and Université de Toulouse (UPS, INP), F-31077 Toulouse, France

Lijun Zhang – LCC, CNRS and Université de Toulouse (UPS, INP), F-31077 Toulouse, France

Yuteng Zhang – LCC, CNRS and Université de Toulouse (UPS, INP), F-31077 Toulouse, France

Gábor Molnár – LCC, CNRS and Université de Toulouse (UPS, INP), F-31077 Toulouse, France

Complete contact information is available at:

<https://pubs.acs.org/doi/10.1021/acsami.2c13834>

##### Notes

The authors declare no competing financial interest.

#### ■ ACKNOWLEDGMENTS

O.Y.H. acknowledges the French Embassy in Ukraine and Campus France for a BGF scholarship.

#### ■ REFERENCES

- (1) Kim, M. M.; Giry, A.; Mastiani, M.; Rodrigues, G. O.; Reis, A.; Mandin, P. Microscale Thermometry: A Review. *Microelectron. Eng.* **2015**, *148*, 129–142.
- (2) Brites, C. D. S.; Lima, P. P.; Silva, N. J. O.; Millán, A.; Amaral, V. S.; Palacio, F.; Carlos, L. D. Thermometry at the Nanoscale. *Nanoscale* **2012**, *4* (16), 4799–4829.
- (3) Mecklenburg, M.; Hubbard, W. A.; White, E. R.; Dhall, R.; Cronin, S. B.; Aloni, S.; Regan, B. C. Nanoscale Temperature Mapping in Operating Microelectronic Devices. *Science* (80-.). **2015**, *347* (6222), 629–632.
- (4) Zani, V.; Pedron, D.; Pilot, R.; Signorini, R. Contactless Temperature Sensing at the Microscale Based on Titanium Dioxide Raman Thermometry. *Biosensors* **2021**, *11* (4), 102.
- (5) Jauffred, L.; Samadi, A.; Klingberg, H.; Bendix, P. M.; Oddershede, L. B. Plasmonic Heating of Nanostructures. *Chem. Rev.* **2019**, *119* (13), 8087–8130.

- (6) Chen, C.; Shen, T.; Du, Z.; Zhang, J.; Wang, J.; Marconnet, A.; Pan, L. Microscale Two-Dimensional (2D) Temperature Mapping by Ratiometric Fluorescence Imaging under Orthogonal Excitations. *Exp. Therm. Fluid Sci.* **2018**, *94*, 168–171.
- (7) Mykhaylyk, V.; Kraus, H.; Zhydachevskyy, Y.; Tsiurma, V.; Luchechko, A.; Wagner, A.; Suchocki, A. Multimodal Non-Contact Luminescence Thermometry with Cr-Doped Oxides. *Sensors* **2020**, *20* (18), 5259.
- (8) Ghifari, N.; Rassouk, S.; Hayat, Z.; Taleb, A.; Chahboun, A.; El Abed, A. I. Dye-Doped ZnO Microcapsules for High Throughput and Sensitive Optofluidic Micro-Thermometry. *Micromachines* **2020**, *11* (1), 100.
- (9) Rocha, J.; Brites, C. D. S.; Carlos, L. D. Lanthanide Organic Framework Luminescent Thermometers. *Chem. - A Eur. J.* **2016**, *22* (42), 14782–14795.
- (10) Teyssie, D.; Thiery, L.; Cretin, B. Near-Infrared Thermography Using a Charge-Coupled Device Camera: Application to Microsystems. *Rev. Sci. Instrum.* **2007**, *78* (3), 034902.
- (11) Fletcher, D. Thermal Microscopy with a Microfabricated Solid Immersion Lens. *Microscale Thermophys. Eng.* **2003**, *7* (4), 267–273.
- (12) Goodson, K. E.; Asheghi, M. Near-Field Optical Thermometry. *Microscale Thermophys. Eng.* **1997**, *1* (3), 225–235.
- (13) Jaque, D.; Vetrone, F. Luminescence Nanothermometry. *Nanoscale* **2012**, *4* (15), 4301–4326.
- (14) Tessier, G.; Bardoux, M.; Boué, C.; Filloy, C.; Fournier, D. Back Side Thermal Imaging of Integrated Circuits at High Spatial Resolution. *Appl. Phys. Lett.* **2007**, *90* (17), 171112.
- (15) Christofferson, J.; Maize, K.; Ezzahri, Y.; Shabani, J.; Wang, X.; Shakouri, A. Microscale and Nanoscale Thermal Characterization Techniques. *J. Electron. Packag.* **2008**, *130* (4), 041101–041106.
- (16) Cahill, D. G.; Ford, W. K.; Goodson, K. E.; Mahan, G. D.; Majumdar, A.; Maris, H. J.; Merlin, R.; Phillpot, S. R. Nanoscale Thermal Transport. *J. Appl. Phys.* **2003**, *93* (2), 793–818.
- (17) Christofferson, J.; Shakouri, A. Thermoreflectance Based Thermal Microscope. *Rev. Sci. Instrum.* **2005**, *76* (2), 024903.
- (18) Csendes, A.; Székely, V.; Rencz, M. Thermal Mapping with Liquid Crystal Method. *Microelectron. Eng.* **1996**, *31* (1–4), 281–290.
- (19) Zhou, J.; del Rosal, B.; Jaque, D.; Uchiyama, S.; Jin, D. Advances and Challenges for Fluorescence Nanothermometry. *Nat. Methods* **2020**, *17* (10), 967–980.
- (20) van Swieten, T. P.; van Omme, T.; van den Heuvel, D. J.; Vonk, S. J. W.; Spruit, R. G.; Meirer, F.; Garza, H. H. P.; Weckhuysen, B. M.; Meijerink, A.; Rabouw, F. T.; Geitenbeek, R. G. Mapping Elevated Temperatures with a Micrometer Resolution Using the Luminescence of Chemically Stable Upconversion Nanoparticles. *ACS Appl. Nano Mater.* **2021**, *4* (4), 4208–4215.
- (21) Lu, Z.; Li, Y.; Qiu, W.; Rogach, A. L.; Nagl, S. Composite Films of CsPbBr<sub>3</sub> Perovskite Nanocrystals in a Hydrophobic Fluoropolymer for Temperature Imaging in Digital Microfluidics. *ACS Appl. Mater. Interfaces* **2020**, *12* (17), 19805–19812.
- (22) Runowski, M.; Woźny, P.; Stopikowska, N.; Martín, I. R.; Lavin, V.; Lis, S. Luminescent Nanothermometer Operating at Very High Temperature—Sensing up to 1000 K with Upconverting Nanoparticles (Yb<sup>3+</sup>/Tm<sup>3+</sup>). *ACS Appl. Mater. Interfaces* **2020**, *12* (39), 43933–43941.
- (23) Chen, Y.; Tran, T. N.; Duong, N. M. H.; Li, C.; Toth, M.; Bradac, C.; Aharonovich, I.; Solntsev, A.; Tran, T. T. Optical Thermometry with Quantum Emitters in Hexagonal Boron Nitride. *ACS Appl. Mater. Interfaces* **2020**, *12* (22), 25464–25470.
- (24) *Spin-Crossover Materials: Properties and Applications*; Halcrow, M. A., Ed.; John Wiley & Sons Ltd.: Oxford, UK, 2013.
- (25) Kumar, K. S.; Ruben, M. Emerging Trends in Spin Crossover (SCO) Based Functional Materials and Devices. *Coord. Chem. Rev.* **2017**, *346*, 176–205.
- (26) Bousseksou, A.; Molnár, G. The Spin-Crossover Phenomenon: Towards Molecular Memories. *Comptes Rendus Chim.* **2003**, *6* (8–10), 1175–1183.
- (27) Gütllich, P.; Goodwin, H. A. *Spin Crossover—An Overall Perspective* **2012**, *1*, 1–47.
- (28) Salmon, L.; Molnár, G.; Zitouni, D.; Quintero, C.; Bergaud, C.; Micheau, J. C.; Bousseksou, A. A Novel Approach for Fluorescent Thermometry and Thermal Imaging Purposes Using Spin Crossover Nanoparticles. *J. Mater. Chem.* **2010**, *20* (26), S499–S503.
- (29) Kraieva, O.; Quintero, C. M.; Suleimanov, I.; Hernandez, E. M.; Lagrange, D.; Salmon, L.; Nicolazzi, W.; Molnár, G.; Bergaud, C.; Bousseksou, A. High Spatial Resolution Imaging of Transient Thermal Events Using Materials with Thermal Memory. *Small* **2016**, *12* (46), 6325–6331.
- (30) Nandi, S. K.; Puyoo, E.; Nath, S. K.; Albertini, D.; Baboux, N.; Das, S. K.; Ratcliff, T.; Elliman, R. G. High Spatial Resolution Thermal Mapping of Volatile Switching in NbO<sub>x</sub>-Based Memristor Using In Situ Scanning Thermal Microscopy. *ACS Appl. Mater. Interfaces* **2022**, *14* (25), 29025–29031.
- (31) Ridier, K.; Bas, A. C.; Zhang, Y.; Routaboul, L.; Salmon, L.; Molnár, G.; Bergaud, C.; Bousseksou, A. Unprecedented Switching Endurance Affords for High-Resolution Surface Temperature Mapping Using a Spin-Crossover Film. *Nat. Commun.* **2020**, *11* (1), 3611.
- (32) Horniichuk, O. Y.; Ridier, K.; Molnár, G.; Kotsyubynsky, V. O.; Shova, S.; Amirkhanov, V. M.; Gural'skiy, I. A.; Salmon, L.; Bousseksou, A. Solvatomorphism, Polymorphism and Spin Crossover in Bis[Hydrotris(1,2,3-Triazol-1-Yl)Borate]Iron(II). *New J. Chem.* **2022**, *46* (24), 11734–11740.
- (33) Hughes, B. C.; Lu, Z.; Jenkins, D. M. The Final Unadorned Tris(Azoly)Borate: Finishing What Trofimenko Started in 1966. *Chem. Commun.* **2014**, *50* (40), S273–S275.
- (34) Quintero, C. M.; Kraieva, O.; Carcenac, F.; Lagrange, D.; Yaremchuk, N. A.; Molnár, G.; Bergaud, C. Joule Heated Metallic Microwire Devices for Sub-Microsecond T-Jump Experiments. *Microelectronics J.* **2015**, *46* (12), 1167–1174.
- (35) Shalabaeva, V.; Rat, S.; Manrique-Juarez, M. D.; Bas, A.-C.; Vendier, L.; Salmon, L.; Molnár, G.; Bousseksou, A. Vacuum Deposition of High-Quality Thin Films Displaying Spin Transition near Room Temperature. *J. Mater. Chem. C* **2017**, *5* (18), 4419–4425.
- (36) Langford, J. I.; Wilson, A. J. C. Scherrer after Sixty Years: A Survey and Some New Results in the Determination of Crystallite Size. *J. Appl. Crystallogr.* **1978**, *11* (2), 102–113.
- (37) Ridier, K.; Bas, A.; Shalabaeva, V.; Nicolazzi, W.; Salmon, L.; Molnár, G.; Bousseksou, A.; Lorenc, M.; Bertoni, R.; Collet, E.; Cailleau, H. Finite Size Effects on the Switching Dynamics of Spin-Crossover Thin Films Photoexcited by a Femtosecond Laser Pulse. *Adv. Mater.* **2019**, *31* (25), 1901361.
- (38) Li, D.; Tong, Y.; Bairagi, K.; Kelai, M.; Dappe, Y. J.; Lagoute, J.; Girard, Y.; Rousset, S.; Repain, V.; Barreteau, C.; Brandbyge, M.; Smogunov, A.; Bellec, A. Negative Differential Resistance in Spin-Crossover Molecular Devices. *J. Phys. Chem. Lett.* **2022**, *13* (32), 7514–7520.
- (39) Gavara-Edo, M.; Córdoba, R.; Valverde-Muñoz, F. J.; Herrero-Martín, J.; Real, J. A.; Coronado, E. Electrical Sensing of the Thermal and Light-Induced Spin Transition in Robust Contactless Spin-Crossover/Graphene Hybrid Devices. *Adv. Mater.* **2022**, *34* (33), 2202551.
- (40) Konstantinov, N.; Tauzin, A.; Noubé, U. N.; Dragoe, D.; Kundys, B.; Majjad, H.; Brosseau, A.; Lenertz, M.; Singh, A.; Berciaud, S.; Boillot, M.-L.; Doudin, B.; Mallah, T.; Dayen, J.-F. Electrical Readout of Light-Induced Spin Transition in Thin Film Spin Crossover/Graphene Heterostructures. *J. Mater. Chem. C* **2021**, *9* (8), 2712–2720.
- (41) Boix-Constant, C.; García-López, V.; Navarro-Moratalla, E.; Clemente-León, M.; Zafra, J. L.; Casado, J.; Guinea, F.; Mañas-Valero, S.; Coronado, E. Strain Switching in van Der Waals Heterostructures Triggered by a Spin-Crossover Metal-Organic Framework. *Adv. Mater.* **2022**, *34* (11), 2110027.